PRAMANA

journal of physics

Vol. 47 No. 1
July 1996

NDIAN ACADEMY OF SCIENCES
ndian National Science Academy
ndian Physics Association

Editor

R Nityananda
Raman Research Institute, Bangalore

Associate Editor

H R Krishnamurthy
Indian Institute of Science, Bangalore

Editorial Board

G S Agarwal, *Physical Research Laboratory, Ahmedabad*
V Balakrishnan, *Indian Institute of Technology, Madras*
J K Bhattacharjee, *Indian Assoc. for the Cultivation of Science, Calcutta*
D N Bose, *Indian Institute of Technology, Kharagpur*
B M Deb, *Panjab University, Chandigarh*
Rohini M Godbole, *Indian Institute of Science, Bangalore*
S Kailas, *Bhabha Atomic Research Centre, Bombay*
R K Kaul, *The Institute of Mathematical Sciences, Madras*
A V Khare, *Institute of Physics, Bhubaneswar*
T Padmanabhan, *Inter-Univ. Centre for Astronomy and Astrophysics, Pune*
R Ramaswamy, *Jawaharlal Nehru University, New Delhi*
A K Raychaudhuri, *Indian Institute of Science, Bangalore*
K C Rustagi, *Centre for Advanced Technology, Indore*
E V Sampathkumaran, *Tata Institute of Fundamental Research, Bombay*
Abhijit Sen, *Institute for Plasma Research, Gandhinagar*
S K Sikka, *Bhabha Atomic Research Centre, Bombay*
Y Singh, *Banaras Hindu University, Varanasi*

Editor of Publications of the Academy

V K Gaur
C-MMACS, NAL, Bangalore

Annual Subscription Rates
(1996)

All countries except India (Price includes AIR MAIL charges)	US$ 200
India	Rs. 200

Annual subscriptions for **individuals** for India and abroad are Rs. 75/- and $50 respectively.

All correspondence regarding subscription should be addressed to the **Circulation Department** of the Academy

---

Editorial Office

Indian Academy of Sciences, C V Raman Avenue,
P.B. No. 8005, Bangalore 560 080, India

Telephone: 334 2546
Telex: 845-2178 ACAD IN
Telefax: 91-80-334 6094

Email: pramana@ias.ernet.in

© 1996 by the Indian Academy of Sciences. All rights reserved.

Pramana – journal of physics

Volume 47
1996

Published by
Indian Academy of Sciences
Bangalore 560 080, India

Editor

R Nityananda
Raman Research Institute, Bangalore

Associate Editor

H R Krishnamurthy
Indian Institute of Science, Bangalore

Editorial Board

G S Agarwal, *Physical Research Laboratory, Ahmedabad*
V Balakrishnan, *Indian Institute of Technology, Madras*
J K Bhattacharjee, *Indian Assoc. for the Cultivation of Science, Calcutta*
D N Bose, *Indian Institute of Technology, Kharagpur*
B M Deb, *Panjab University, Chandigarh*
Rohini M Godbole, *Indian Institute of Science, Bangalore*
S Kailas, *Bhabha Atomic Research Centre, Bombay*
R K Kaul, *The Institute of Mathematical Sciences, Madras*
A V Khare, *Institute of Physics, Bhubaneswar*
T Padmanabhan, *Inter-Univ. Centre for Astronomy and Astrophysics, Pune*
R Ramaswamy, *Jawaharlal Nehru University, New Delhi*
A K Raychaudhuri, *Indian Institute of Science, Bangalore*
K C Rustagi, *Centre for Advanced Technology, Indore*
E V Sampathkumaran, *Tata Institute of Fundamental Research, Bombay*
Abhijit Sen, *Institute for Plasma Research, Gandhinagar*
S K Sikka, *Bhabha Atomic Research Centre, Bombay*
Y Singh, *Banaras Hindu University, Varanasi*

Editor of Publications of the Academy

V K Gaur
C-MMACS, NAL, Bangalore

Annual Subscription Rates
(1996)

All countries except India (Price includes AIR MAIL charges)	US$ 200
India	Rs. 200

Annual subscriptions for **individuals** for India and abroad are Rs. 75/- and $50 respectively.

All correspondence regarding subscription should be addressed to the **Circulation Department** of the Academy

---

Editorial Office

Indian Academy of Sciences, C V Raman Avenue,
P.B. No. 8005, Bangalore 560 080, India

Telephone: 334 2546
Telex: 845-2178 ACAD IN
Telefax: 91-80-334 6094

Email: pramana@ias.ernet.in

© 1996 by the Indian Academy of Sciences. All rights reserved.

Pramana–journal of physics

CONTENTS–VOLUME 47

(July–December 1996)

Number 1

Review

Quantum theory of continuous measurements and its applications in quantum optics.....*M D Srinivas* 1

Research Articles

Magnetized cylindrically symmetric universe in general relativity.....*Raj Bali and Mahbub Ali* 25

Stationary rotating string world models with a magnetic field.....*L K Patel and S D Maharaj* 33

A model of the universe with decaying vacuum energy.....*Abdussattar and R G Vishwakarma* 41

Cross sections and other parameters of e^--H_2O scattering ($E_i \geqslant 50$ eV).....*K N Joshipura and Minaxi Vinodkumar* 57

New method for the evaluation of the RKR potential-integrals for diatomic molecules.....*Suresh Chandra, A K Sharma and Z H Khan* 65

(e, $2e$) triple differential cross section for ionization-excitation of helium.....*Seema Gupta and M K Srivastava* 79

Positron scattering from alkaline-earth elements.....*Ritu Raizada and K L Baluja* 87

Number 2

The origins of phase stability in ordered and disordered Ni–Pt alloys.....*Prabhakar P Singh* 99

Analytic solution of the BCS gap equation in D dimensions ($D = 1, 2, 3$), at finite temperatures.....*Arun Bhardwaj and Satish K Muthu* 109

Internal irradiation effects in ^{239}Pu doped $K_2Ca_2(SO_4)_3$: EPR, TSL and PAS investigations.....*T K Seshagiri, V Natarajan, A R Dhobale and M D Sastry* 125

Raman study of phase transition in ferroelectric $Ba_{0.95}Ca_{0.05}TiO_3$ ..... *Rekha Rao, A P Roy, B A Dasannacharya, S Balakumar, R Ilangovan and P Ramasamy* 145

Pressure-induced structural and electronic transition in $KTb(MoO_4)_2$ through Raman and optical studies ..... *A Jayaraman, S K Sharma, S Y Wang, S R Shieh, L C Ming and S-W Cheong* 151

Measurement of optical constants of thin polymer films using spectrally resolved white light interferometry ..... *V Nirmal Kumar, Y Chandrasekhar and D Narayana Rao* 163

Magnetic studies in mesoscopic length scale using polarized neutron spectrometer at Dhruva reactor, Trombay ..... *Sk Mohammad Yusuf and L Madhav Rao* 171

Number 3

The Painlevé property, integrability and chaotic behaviour of a two-coupled Duffing oscillators ..... *S Rajasekar and S Paul Raj* 183

Stochastic motion of a charged particle in a magnetic field: I Classical treatment ..... *Jagmeet Singh and Sushanta Dattagupta* 199

Stochastic motion of a charged particle in a magnetic field: II Quantum Brownian treatment ..... *Sushanta Dattagupta and Jagmeet Singh* 211

Radiative decays of heavy mesons with heavy quark symmetry ..... *A K Giri, L Maharana and R Mohanta* 225

Electromagnetic form factors nucleons in a relativistic square-root potential model of independent quarks ..... *S N Jena and M R Behera* 233

Weak correlation theory of electron hydrogen atom ionization collisions .... *J N Das and K Chakrabarti* 249

Surface enhanced Raman scattering studies of acetophenone on colloidal silver particles ..... *S Edwin Jayaraj, V Ramakrishnan, S Perumal and M Gurunathan* 255

Errata 261

Number 4

Symmetric scattering in electron and positron impact ionization of metastable 2*s*-state hydrogen atoms ..... *J N Das and S Dhar* 263

Structure of some liquid transition metals using integral equation theory .... *O Akinlade, A M Umar and L A Hussain* 271

Nonlinear travelling waves in ϕ^6 polarizable model ..... *Nabonita D Chowdhury and Sankar P Sanyal* 283

A model of knock-out of oxygen by charged particle irradiation of Bi-2212 .....*S K Bandyopadhyay, Pintu Sen, P Barat, P Mukherjee, S K Das and B Ghosh* 309

Enhanced third harmonic generation in periodic structures..... .....*V Mahalakshmi, Jolly Jose and S Dutta Gupta* 317

Radiation stabilization of U^{5+} in CaO matrix and its thermal stability: Electron paramagnetic resonance and thermally stimulated luminescence studies.....*V Natarajan, T K Seshagiri and M D Sastry* 325

Impurity mediated mechanism of photorefractive effect in $BaTiO_3$: A combination of Sangster and piezoelectric effects..... .....*M D Sastry, M Moghbel and Putcha Venkateswarlu* 331

Number 5

Dynamics of the logistic map under discrete parametric perturbation..... .....*P P Saratchandran, V M Nandakumaran and G Ambika* 339

Relativistic operator description of photon polarization..... .....*Arvind and N Mukunda* 347

Poincaré sphere representation for three state systems.....*Joseph Samuel* 361

Quantum motion over a finite one-dimensional domain: With and without dissipation.....*Ashok Pimpale* 371

Nonadiabatic gravitational collapse in multidimensional spacetime..... .....*B Bhui* 379

A class of stationary rotating string cosmological models..... .....*L K Patel and Naresh Dadhich* 387

Approximate analytical lower bounds on 'double asymptotic scaling' variables and physics at HERA.....*A Saikia* 393

Measurement and analysis of excitation functions for alpha induced reactions on iodine and cesium.....*N P M Sathik M Afzal Ansari, B P Singh and R Prasad* 401

Brief Report

Radiative decays of heavy baryons with heavy quark symmetry..... .....*A K Giri, L Maharana and R Mohanta* 411

Number 6

The partial distribution functions and effective pair potentials of some H-bonded liquids from diffraction data.....*S Sarkar and R N Joarder* 419

Higher order elastic constants generalized Gruneisen parameters of elastic waves and low temperature thermal expansion of gadolinium..... .....*S Sindhu and C S Menon* 435

A stochastic model for solidification I. The basic equations their analysis and solution.....*Shobha Dass, Gautam Johri and Lakshman Pandey* 447

Energy transfer in $CaSiO_3$ phosphors doped with Ce^{3+} and Tb^{3+}..... .....*R V Subrahmanyam, Shishir Jain, Ashish Verma and S Sivaraman* 471

Electron paramagnetic resonance studies in photorefractive crystals I: Hyperfine interaction and photo induced charge transfer in $^{233}U^{5+}$ and $^{238}U^{5+}$ doped. $LiNbO_3$.....*N K Porwal, Mithlesh Kumar and M D Sastry* 481

Determination of thermal effusivity of solids by a photoacoustic scanning technique.....*J Philip and A A Sudhakaran* 493

Subject Index..... 505

Author Index..... 509

Quantum theory of continuous measurements and its applications in quantum optics

M D SRINIVAS
Department of Theoretical Physics, University of Madras, Madras 600 025, India
*Address from September 1996: Centre for Policy Studies, 2 Thyagarajapuram, Mylapore, Madras 600 004, India

MS received 16 February 1996; revised 23 April 1996

Abstract. We present an overview of the quantum theory of continuous measurements and discuss some of its important applications in quantum optics. Quantum theory of continuous measurements is the appropriate generalization of the conventional formulation of quantum theory, which is adequate to deal with counting experiments where a detector monitors a system continuously over an interval of time and records the times of occurrence of a given type of event, such as the emission or arrival of a particle.

We first discuss the classical theory of counting processes and indicate how one arrives at the celebrated photon counting formula of Mandel for classical optical fields. We then discuss the inadequacies of the so called quantum Mandel formula. We explain how the unphysical results that arise from the quantum Mandel formula are due to the fact that the formula is obtained on the basis of an erroneous identification of the coincidence probability densities associated with a continuous measurement situation. We then summarize the basic framework of the quantum theory of continuous measurements as developed by Davies. We explain how a complete characterization of the counting process can be achieved by specifying merely the measurement transformation associated with the change in the state of the system when a single event is observed in an infinitesimal interval of time.

In order to illustrate the applications of the quantum theory of continuous measurements in quantum optics, we first derive the photon counting probabilities of a single-mode free field and also of a single-mode field in interaction with an external source. We then discuss the general quantum counting formula of Chmara for a multi-mode electromagnetic field coupled to an external source. We explain how the Chmara counting formula is indeed the appropriate quantum generalization of the classical Mandel formula. To illustrate the fact that the quantum theory of continuous measurements has other diverse applications in quantum optics, besides the theory of photodetection, we summarize the theory of 'quantum jumps' developed by Zoller, Marte and Walls and Barchielli, where the continuous measurements framework is employed to evaluate the statistics of photon emission events in the resonance fluorescence of an atomic system.

Keywords. Quantum theory of measurements; counting experiments; continuous measurements; photon counting probabilities; quantum jumps.

PACS Nos 03·65; 03·80; 42·50

1. Introduction

The conventional formulations of quantum theory deal only with single instantaneous measurements, or at best with a sequence of instantaneous measurements performed on a system. However there are many physical situations, which are commonly met

with, where an experiment is performed over an extended interval of time to test whether some events occur and if so when. We can cite for instance the measurement of the time of decay of a particle, or of the times of arrival of particles in a detector, etc. In each of these so called counting experiments, there is a continuous interaction of the apparatus with the system and information is acquired continuously as to whether a given type of event has occurred or not.

An appropriate generalization of the conventional formulation of quantum mechanics, a quantum theory of continuous measurements, was first formulated by Davies [1–4], twenty-five years ago. This has proved to be the appropriate framework for discussing counting experiments satisfactorily from a foundational point of view [5]. In fact it was shown quite some time ago [6, 7] that the photon counting experiments in quantum optics are best discussed in this framework of the quantum theory of continuous measurements. In recent years, this framework has found several applications mainly in quantum optics, but also in other contexts. In this paper we shall present an overview of the quantum theory of continuous measurements and discuss some of its important applications in quantum optics.

In § 2, we first introduce some of the basic probability densities, namely the exclusion and coincidence probability densities, associated with a counting process [8]. We explain how, for classical optical fields, one arrives at the celebrated photon counting formula of Mandel [9, 10], which gives the probability that m-photons are detected in an interval of time $[0, t]$. We then discuss the inadequacies of the quantum counting formula obtained by Mandel [11]. While it is often claimed that the quantum Mandel formula has been derived in an important article by Kelley and Kleiner [12], it is indeed the case that there is just no satisfactory derivation of this formula from the fundamental principles of quantum theory [6]. Many of the unphysical features of the quantum Mandel formula have been well-known and were noted long ago by Mollow [13], Scully and Lamb [14] and others. Still there seems to be considerable confusion [15], which shows up sometimes even in current literature [16–18], on the applicability of the quantum Mandel formula, and it may therefore be useful to clarify the issues involved.

In § 3, we summarize the basic framework of the quantum theory of continuous measurements. We explain how, under some simplifying assumptions, a complete characterization of the counting process can be achieved by merely specifying, apart from the Hamiltonian H characterizing the evolution of the system when no measurements are made, the measurement transformation $\rho \to J(\rho)$ which describes the change in the state of the system when a single event is observed in an infinitesimal interval of time. We show how the quantum theory of continuous measurements provides a systematic prescription for calculating all the basic probability densities, the counting formula and, in fact, the entire counting statistics of the process.

In order to illustrate the applications of the general framework of continuous measurements in quantum optics, we first derive the photon counting probabilities for a single-mode free field [6] in § 4. In this particular case, the counting formula derived from the continuous measurement theory turns out to be the same as that obtained by Mollow [13], Scully and Lamb [14] and others, on the basis of a master equation approach. These authors consider the evolution of the composite system, detector + field, over an interval of

with the entire 'history' of outcomes recorded by the detector in the interval $[0, t]$ and provides a general prescription for evaluating the probability densities associated with each counting history. After considering the photon counting statistics of a single-mode free field in some detail, we describe how the framework of continuous measurements can equally be employed to obtain the photon counting statistics of 'open' systems such as a single-mode field in continuous interaction with external sources [19].

In § 5 we discuss the general quantum counting formula derived by Chmara [20], for a multi-mode electromagnetic field coupled to an external source. We explain how the Chmara counting formula is indeed the appropriate quantum generalization of the classical Mandel formula. Chmara's analysis also brings forth very clearly the distinction between the coincidence probability densities of the counting process as calculated from the first principles (the basic principles of the quantum theory of measurement), and the correlation functions which were erroneously identified with the coincidence probability densities in the Kelley and Kleiner approach [12].

In order to illustrate the fact that the quantum theory of continuous measurements has other diverse applications in quantum optics, besides the theory of photodetection, we briefly outline in § 6 the theory of 'quantum jumps' developed by Zoller, Marte and Walls [21] and Barchielli [22]. These authors employ the continuous measurements framework to evaluate the statistics of photon emission events in the resonance fluorescence of an atomic system and account for the interesting phenomenon of the occurrence of dark periods in the fluorescence of a three-level system [23]. In recent years, the quantum theory of continuous measurements and some related approaches have been widely employed in quantum optics as well as in other contexts. We refer the reader to a sample of the growing literature on the subject.

2. The inadequacies of the quantum Mandel formula

We begin with a brief summary of the classical theory of photodetection. The basic random quantity measured by a photodetector is the number of photons detected in any interval $[0, t]$ and hence the object of most of the theories of photodetection is to arrive at a formula for the probability $p(m; [0, t])$ that m-photons are detected in the time interval $[0, t]$. Such a photon counting formula for the case of a fluctuating classical optical field was first derived by Mandel [9, 10] based on the assumption that the counting probabilities in different intervals are statistically independent. Mandel's result has been shown to be applicable to a very general class of situations by means of the methods of classical probability theory, in particular the so called coincidence approach to classical counting processes [8, 24]. In this approach the basic probability densities are the so called exclusion probability density (EPD) $p_{[0,t]}(t_1, t_2, \ldots, t_m)$ and the coincidence probability density (CPD) $h_{[0,t]}(t_1, t_2, \ldots, t_m)$, which are defined as follows:

$p_{[0,t]}(t_1, t_2, \ldots, t_m)\mathrm{d}t_1\,\mathrm{d}t_2 \ldots \mathrm{d}t_m$ is the probability that one count is observed in each of the intervals $[t_i, t_i + \mathrm{d}t_i]$, $i = 1, 2, \ldots, m$, while no counts are observed in the rest of the interval $[0, t]$ in which the counting experiment is performed.

$h_{[0,t]}(t_1, t_2, \ldots, t_m)\mathrm{d}t_1\,\mathrm{d}t_2 \ldots \mathrm{d}t_m$ is the probability that one count is observed in each of the intervals $[t_i, t_i + \mathrm{d}t_i]$, $i = 1, 2, \ldots, m$, with no other restrictions put on the counts registered in the rest of the interval $[0, t]$ in which the counting experiment is performed.

CPD, and we can also derive the EPD from the set of all CPD and vice versa [8]. The counting probability can be expressed in terms of the EPD via the relation

$$p(m;[0,t]) = \int_0^t \mathrm{d}t_m \ldots \int_0^{t_3} \mathrm{d}t_2 \int_0^{t_2} \mathrm{d}t_1 \, p_{[0,t]}(t_1, t_2, \ldots, t_m). \tag{1}$$

For a fluctuating optical field, the basic random quantity is the associated analytic signal [25] $V_\mu(\mathbf{r}, t)$ and the related intensity

$$I(t) = \sum_\mu \int\int_D \int V_\mu^*(\mathbf{r}, t)\, V_\mu(\mathbf{r}, t) \mathrm{d}^3\mathbf{r}, \tag{2}$$

where D is the volume of the detector. The fundamental physical assumption made in the classical theory of photodetection is that the CPD of the counting process is given by [8, 24]

$$h_{[0,t]}(t_1, t_2, \ldots, t_m) = \lambda^m \langle I(t_1) I(t_2) \ldots I(t_m) \rangle, \tag{3}$$

where $\lambda > 0$ is a parameter characterizing the efficiency of the detector. The above assumption (3), for the CPD, can be shown to be equivalent to the following assumption for the EPD of the process

$$p_{[0,t]}(t_1, t_2, \ldots, t_m) = \lambda^m \langle I(t_1) I(t_2) \ldots I(t_m) \mathrm{e}^{-\lambda \int_0^t I(t')\mathrm{d}t'} \rangle. \tag{4}$$

From (1), (4), we obtain the Mandel formula for the classical optical fields

$$p(m;[0,t]) = \left\langle \frac{(\lambda U)^m}{m!} \mathrm{e}^{-\lambda U} \right\rangle, \tag{5}$$

where

$$U = \int_0^t I(t')\mathrm{d}t'. \tag{6}$$

The photon-counting statistics as given by (5), (6) is characteristic of the so called doubly-stochastic Poisson process with the random intensity function $I(t)$.

One of the landmarks in the development of the quantum theory of optical fields in the early sixties was the discovery of the quantum Mandel formula [11] for the photon counting probabilities

$$p(m;[0,t]) = \mathrm{Tr}\left[\rho : \frac{(\lambda U)^m}{m!} \mathrm{e}^{-\lambda U} : \right], \tag{7}$$

where ρ is the density operator characterizing the state of the electromagnetic field at $t = 0$, and the operator U is given by

$$U = \int_0^t I(t')\mathrm{d}t', \tag{8}$$

where the intensity operator $I(t)$ is given by

$$I(t) = \sum_\mu \int\int_D \int A_\mu^-(\mathbf{r}, t) A_\mu^+(\mathbf{r}, t) \mathrm{d}^3\mathbf{r}, \tag{9}$$

where $A_\mu^+(\mathbf{r}, t)$ and $A_\mu^-(\mathbf{r}, t)$ are respectively the positive and negative frequency parts of the vector potential operator characterizing the electromagnetic field. In (7), the symbol :: indicates that the operators enclosed must be placed in the normal order, namely that the creation operators are placed to the left and the annihilation operators to the right. Further, the creation operators are to be placed in the ascending time order from left to right, followed by the annihilation operators placed in the descending time order. Of course, for the case of the free electromagnetic field, the time ordering is no longer necessary [12].

The quantum Mandel formula has been widely applied and has led to important results and insights. However, by the late sixties itself, it became clear [13, 14] that there are several problems with the quantum Mandel formula, if it is taken seriously as the quantum formula for counting probabilities. To get an idea of the unphysical results that arise from the quantum Mandel formula, let us consider the case of a single-mode free field, for which (7)–(9) reduce to

$$p(m; [0, t]) = \mathrm{Tr}\left[\rho : \frac{(a^\dagger a \lambda t)^m}{m!} \mathrm{e}^{-a^\dagger a \lambda t} :\right] \tag{10}$$

which can be expressed as

$$p(m; [0, t]) = \sum_{k=m}^{\infty} \binom{k}{m} (\lambda t)^m (1 - \lambda t)^{k-m} \langle k | \rho | k \rangle. \tag{11}$$

If we now take the initial state of the field to be a number operator eigenstate, $\rho = |n\rangle \langle n|$, then we get

$$p(m; [0, t]) = \binom{n}{m} (\lambda t)^m (1 - \lambda t)^{n-m} \tag{12}$$

for $n > m$. Clearly, the above result (12) can be interpreted as a counting probability only so long as $\lambda t < 1$, for otherwise it will lead to *negative probabilities*. There are of course states for which (10) yields non-negative probabilities for all λt, as for example the coherent state, $\rho = |z\rangle \langle z|$, for which case (10) gives

$$p(m; [0, t]) = \frac{(|z|^2 \lambda t)^m}{m!} \mathrm{e}^{-|z|^2 \lambda t}. \tag{13}$$

Another difficulty with the quantum Mandel formula (10) shows up when we consider the average number of photons detected in the interval $[0, t]$. From (10), we get

$$\sum_{m=0}^{\infty} m\, p(m; [0, t]) = \mathrm{Tr}[\rho a^\dagger a] \lambda t. \tag{14}$$

Thus the mean number of photons detected *exceeds* the mean number of photons initially present in the field, when $\lambda t > 1$, and even *diverges* when $t \to \infty$.

The above difficulties were noted by Mollow [13], who also derived the following formula for the counting probabilities for the single-mode free field, based on a master equation approach

$$p(m; [0, t]) = \sum_{k=m}^{\infty} \binom{k}{m} (1 - \mathrm{e}^{-\lambda t})^m (\mathrm{e}^{-\lambda t})^{k-m} \langle k | \rho | k \rangle. \tag{15}$$

The counting probabilities given by the Mollow formula are always non-negative. Also the mean value of the counts obtained in the interval $[0, t]$, as calculated from (15), is

$$\sum_{m=0}^{\infty} m\, p(m; [0, t]) = \mathrm{Tr}[\rho a^{\dagger} a](1 - e^{-\lambda t}) \tag{16}$$

which is always less than the mean number of photons initially present in the field. Further, in the limit $\lambda t \ll 1$, (15) and (16) go over to the Mandel formula results (11), (14).

It has been argued by Mandel [15] that both the formulae (11) and (15) are valid. He contends that λ in (11) is indeed such that $\lambda t < 1$ always! Mandel also argues that while the Mollow formula (15) applies to the case of a 'closed' system, the Mandel formula (11) applies to the more common situation of an 'open' system where photons are continuously replenished by a source, so that the mean value of the number of photons counted can easily exceed the mean value of the number of photons initially present in the field. We shall return to this question of the photon counting probabilities for an open system, later, in § 4.

The basic problem with the quantum Mandel formula is that there is just *no satisfactory derivation* of the formula from the fundamental principles of quantum theory [6]. The standard derivation of the quantum Mandel formula, due to Kelley and Kleiner [12], involves the following identification of the CPD of the counting process

$$h_{[0,t]}[t_1, t_2, \ldots, t_m) = \mathrm{Tr}[\rho{:}I(t_1)I(t_2)\ldots I(t_m){:}]. \tag{17}$$

From the quantum theory of successive measurements, which we shall discuss in the next section, it can easily be seen that the right-hand-side of (17) is the joint probability density for obtaining one count each during a sequence of 'm' measurements performed during the infinitesimal intervals $[t_i, t_i + \mathrm{d}t_i]$, $i = 1, 2, \ldots, m$, with no measurements being performed in the rest of the interval $[0, t]$. On the other hand, the left-hand-side of (17) is the CPD of a counting process where the detector performs *continuous measurements over the entire interval* $[0, t]$; and the CPD is the joint probability density that one count occurs in each of the intervals $[t_i, t_i + \mathrm{d}t_i]$ in this situation of continuous measurements. The CPD are thus to be obtained by summing over the joint probabilities for all possible counting histories in $[0, t]$ which satisfy the condition that one count is observed in each of the intervals $[t_i, t_i + \mathrm{d}t_i]$. While in classical physics the joint probabilities, in the two different situations mentioned above, turn out to be the same, it is a profound feature of quantum theory that the statistics of the outcomes of experiments performed during the intervals $[t_i, t_i + \mathrm{d}t_i]$, $i = 1, 2, \ldots, m$ *depends* on whether or not measurements were carried out during the rest of the interval $[0, t]$. It is this fundamental feature of quantum theory which makes the Kelley and Kleiner identification (17) for the CPD untenable and renders their derivation of the quantum Mandel formula infructuous. We shall again return to this point in § 5, when we discuss the general quantum counting formula derived by Chmara.

3. Quantum theory of continuous measurements

Before taking up the quantum theory of continuous measurements let us summarize how a sequence of instantaneous measurements are handled in conventional quantum

theory. Let us consider an ensemble of systems characterized by a density operator ρ at time $t = 0$. Let the time evolution of the system in the absence of measurements be given by the unitary transformation

$$\rho \to U(t)\rho U^{-1}(t) = e^{-(i/\hbar)Ht}\rho e^{(i/\hbar)Ht}. \tag{18}$$

Let A be an observable (self-adjoint operator), with a purely discrete spectrum, given by

$$A = \sum_i \alpha_i P^A(\alpha_i), \tag{19}$$

where $\{\alpha_i\}$ are the eigenvalues of A and $P^A(\alpha_i)$ the projection operator onto the subspace spanned by all the eigenvectors of A associated with α_i. Let B be another observable with a purely discrete spectrum such that

$$B = \sum_j \beta_j P^B(\beta_j). \tag{20}$$

We now consider a situation where an ensemble of systems, in state ρ at $t = 0$, is subjected to the sequence of two 'instantaneous' measurements, that of A at time t_1 followed by a measurement of B at time $t_2 > t_1$. Now the joint probability $p(\alpha_i t_1, \beta_j t_2)$ that the outcome α_i is observed in the A-measurement and the outcome β_j is observed in the B-measurement, is given by the well-known Wigner formula [26]

$$\begin{aligned} p(\alpha_i t_1, \beta_j t_2) = \mathrm{Tr}[&P^B(\beta_j)U(t_2 - t_1)P^A(\alpha_i)U(t_1)\rho \\ &\times U^{-1}(t_1)P^A(\alpha_i)U^{-1}(t_2 - t_1)P^B(\beta_j)]. \end{aligned} \tag{21}$$

If we adopt the Heisenberg picture of evolution, the above result (21) can be expressed as

$$p(\alpha_i t_1, \beta_j t_2) = \mathrm{Tr}[P^{B(t_2)}(\beta_j)P^{A(t_1)}(\alpha_i)\rho P^{A(t_1)}(\alpha_i)P^{B(t_2)}(\beta_j)]. \tag{22}$$

In order to derive the joint probabilities (21) or (22) for successive measurements, it is essential to use the so called 'collapse postulate', which is the prescription that the state ρ of a system immediately prior to the $A(t_1)$-measurement, undergoes the change

$$\rho \to \frac{P^{A(t_1)}(\alpha_i)\rho P^{A(t_1)}(\alpha_i)}{\mathrm{Tr}[P^{A(t_1)}(\alpha_i)\rho]} \tag{23}$$

if the outcome α_i is realized in the measurement. The joint probability formula (21) or (22) can be viewed as involving a sequence of two measurement transformations

$$\rho \to P^{A(t_1)}(\alpha_i)\rho P^{A(t_1)}(\alpha_i) \to P^{B(t_2)}(\beta_j)P^{A(t_1)}(\alpha_i)\rho P^{A(t_1)}(\alpha_i)P^{B(t_2)}(\beta_j) \tag{24}$$

each of which is a linear, positive transformation on the class of (non-normalized) density operators, which do not increase the trace. Such transformations are known as 'operations' in the literature on measurement theory [4].

An important feature of the quantum-theoretic joint probabilities (21), which was noted long ago by de Broglie [27, 28] is that in general

$$\sum_{\alpha_i} p(\alpha_i t_1, \beta_j t_2) \neq \mathrm{Tr}[\rho P^{B(t_2)}(\beta_j)] \tag{25}$$

while we always have

$$\sum_{\beta_j} p(\alpha_i t_1, \beta_j t_2) = \mathrm{Tr}[\rho P^{A(t_1)}(\alpha_i)]. \tag{26}$$

The left hand side of the inequality (25) refers to a situation where the ensemble of systems in state ρ at time $t = 0$, is subjected to the sequence of two observations, $A(t_1)$ followed by $B(t_2)$. On the other hand the right hand side of the inequality (25) refers to a situation where the ensemble of systems, in state ρ at time $t = 0$, is subjected only to the measurement of $B(t_2)$. In classical physics the statistics of the outcomes of $B(t_2)$ would be the *same in both the situations.* The crucial feature (25) of the quantum-theoretic probabilities, that the statistics of outcomes of $B(t_2)$ in general depends on whether or not a measurement of $A(t_1)$ was carried out earlier has been termed the 'quantum interference of probabilities' by de Broglie.

We shall now discuss an appropriate generalization of the conventional framework of quantum mechanics which is adequate to describe continuous measurements. The class of continuous measurements we consider are the counting experiments where a detector monitors a system over a continuous interval of time and records all those instants at which a given type of event (absorption or emission of a particle, or decay of a particle, etc.) occurs. We shall only consider time-stationary processes which also satisfy the regularity condition that not more than one event can occur in any infinitesimal interval of time. Under these conditions, a quantum theory of continuous measurements can be developed merely on the basis of two basic measurement transformations $\rho \to J(\rho)$ and $\rho \to S_t(\rho)$ defined as follows [1–6].

If ρ is the state of the system at time t and one event has been observed during the interval $[t, t + \mathrm{d}t]$, then the unnormalized state at time $t + \mathrm{d}t$ is $J(\rho)\mathrm{d}t$ and the probability for this event is

$$p(t)\mathrm{d}t = \mathrm{Tr}[J(\rho)]\mathrm{d}t. \tag{27}$$

Again, if ρ is the state of the system at time t and if no events are observed in the interval $[t, t + \tau]$ then $S_\tau(\rho)$ is the unnormalized state at time $t + \tau$ and the probability of detecting no events in the interval $[t, t + \tau]$ is

$$p[0; [t, t + \tau]) = \mathrm{Tr}[S_\tau(\rho)]. \tag{28}$$

From the above definitions, and in analogy with the Wigner joint probability formula (21), we can easily see that the EPD of our counting process are given by

$$p_{[0,t]}(t_1, t_2, \ldots, t_m) = \mathrm{Tr}[S_{t-t_m} J S_{t_m - t_{m-1}} \ldots J S_{t_1}(\rho)], \tag{29}$$

where ρ is the state of the system at $t = 0$. From (29) we obtain the basic counting probabilities

$$p(m; [0, t]) = \int_0^t \mathrm{d}t_m \int_0^{t_m} \mathrm{d}t_{m-1} \ldots \int_0^{t_2} \mathrm{d}t_1 \times \mathrm{Tr}[S_{t-t_m} J S_{t_m - t_{m-1}} \ldots J S_{t_1}(\rho)]. \tag{30}$$

In order that the EPD (29) and the counting probabilities (30) be non-negative, we need to stipulate that J and S_t are linear positive transformations on the class of

(non-normalized) density operators, which do not increase the trace. The fact that in any counting process

$$p[0, t_1 + t_2] = \text{probability for detecting no events in } [0, t_1 + t_2]$$
$$= \text{joint probability for detecting no events in } [0, t_1] \text{ and none in } [t_1, t_1 + t_2] \tag{31}$$

leads to the condition

$$S_{t_1} S_{t_2} = S_{t_1 + t_2} \tag{32}$$

for all t_1, t_2, which means that $t \to S_t$ is a semigroup. Finally, the total probability requirement

$$\sum_{m=0}^{\infty} p(m; [0, t]) = 1 \tag{33}$$

may be shown to be equivalent to the condition

$$\frac{\mathrm{d}}{\mathrm{d}t} \mathrm{Tr}[S_t(\rho)]\Big|_{t=0} = -\mathrm{Tr}[J(\rho)] \tag{34}$$

for all ρ. An important result of the general theory of quantum counting processes, developed by Davies [1–4], is that the above conditions imposed on the measurement transformations J, S_t, essentially suffice to characterize the counting process completely.

The state of the entire ensemble at any time t, obtained by pooling together all the systems irrespective of their counting history, is given by another measurement transformation $\rho \to T_t(\rho)$, which can be expressed in terms of J and S_t as follows:

$$T_t(\rho) = S_t(\rho) + \sum_{m=1}^{\infty} \int_0^t \mathrm{d}t_m \int_0^{t_m} \cdots \int_0^{t_2} \mathrm{d}t_1$$
$$\times S_{t - t_m} J S_{t_m - t_{m-1}} \cdots J S_{t_1}(\rho). \tag{35}$$

It can be shown that

$$\mathrm{Tr}[T_t(\rho)] = \mathrm{Tr}[\rho] \tag{36}$$

for all ρ, which is just the preservation of the normalization of the density operator of the entire ensemble, and is equivalent to the total probability requirement (33). Also

$$T_{t_1} T_{t_2} = T_{t_1 + t_2} \tag{37}$$

for all t_1, t_2, which shows that $t \to T_t$ is also a semigroup. Finally, T_t also satisfies the integral equation

$$T_t = S_t + \int_0^t T_{t - t'} J S_{t'} \mathrm{d}t'. \tag{38}$$

The measurement transformations $\rho \to T_t(\rho)$, which give the state of the entire ensemble – irrespective of the counting history – at any time in the counting experiment, are indeed very important, as the CPD of the counting process can be straightaway

expressed in terms of them as follows:

$$h_{[0,t]}(t_1, t_2, \ldots, t_m) = \mathrm{Tr}[T_{t-t_m} J T_{t_m - t_{m-1}} \ldots J T_{t_1}(\rho)], \tag{39}$$

where of course the last T_{t-t_m} can be dropped because of (36). The measurement transformations J, S_t and T_t suffice to express in a succinct and transparent manner all the probabilities associated with a counting process [6].

Thus, a general quantum counting process is completely characterized by the measurement transformations J, S_t which satisfy the various requirements mentioned above. In general, J and S_t can be chosen more or less independently, except for the condition (34) which imposes a certain relation between them. However, it so happens that all the important physical applications of the quantum theory of continuous measurements, including the ones that we shall discuss later, seem to be based on a certain *canonical prescription* for obtaining S_t in terms of the measurement transformation J (associated with the detection of an event in an infinitesimal interval of time) and the Hamiltonian H characterizing the evolution of the system in the absence of the detector. To describe this canonical prescription for obtaining S_t given J and H, we first define the positive operator R on the Hilbert space by

$$\mathrm{Tr}[J(\rho)] = \mathrm{Tr}[\rho R] \tag{40}$$

for all ρ. For instance if

$$J(\rho) = \sum_i V_i \rho V_i^\dagger, \tag{41}$$

where V_i are some operators on the Hilbert space, then

$$R = \sum_i V_i^\dagger V_i. \tag{42}$$

Now if H is the Hamiltonian of the system in the absence of the detector, then the 'no-count' transformation $\rho \to S_t(\rho)$ can be taken to be

$$S_t(\rho) = \mathrm{e}^{-(i/\hbar)\tilde{H}t} \rho \mathrm{e}^{(i/\hbar)\tilde{H}^\dagger t}, \tag{43}$$

where

$$\tilde{H} = H - \frac{i\hbar}{2} R. \tag{44}$$

The above prescription for S_t clearly satisfies the condition (34) and has the special feature that it transforms pure states into pure states. Given this canonical choice (43), (44) for S_t, we see that all the counting probabilities are completely determined once we specify J, the measurement transformation associated with the detection of an event in an infinitesimal interval of time, and the Hamiltonian H of the system in the absence of the detector. Finally we may note that for a such a canonical counting process, the density operator

$$\rho(t) = T_t(\rho) \tag{45}$$

characterizing the entire ensemble of systems, irrespective for their counting history,

$$\frac{\mathrm{d}}{\mathrm{d}t}\rho(t) = \frac{-i}{\hbar}[H, \rho(t)] + J(\rho(t)) - \tfrac{1}{2}(R\rho(t) + \rho(t)R)$$

$$= \frac{-i}{\hbar}(\tilde{H}\rho(t) - \rho(t)\tilde{H}^{\dagger}) + J(\rho(t)). \tag{46}$$

4. Photon counting probabilities for a single-mode field

In order to illustrate the general theory of continuous measurements outlined above, we first consider the photon counting statistics of a single-mode free field [6]. The Hamiltonian of the system in the absence of the detector is

$$H = \hbar\omega a^{\dagger}a \tag{47}$$

and the measurement transformation specifying the change in the state of the field when the detector detects one photon, is assumed to be

$$J(\rho) = \lambda a\rho a^{\dagger}. \tag{48}$$

Here we consider a detector which, typically like the photoelectric detector, detects a photon by absorption and converts an n-photon state into an $(n-1)$-photon state. Measurement transformations such as (48) are clearly different from the projection-operator based transformations (24) employed in conventional quantum theory.

From (40) and (48), we get

$$R = \lambda a^{\dagger}a \tag{49}$$

and making the canonical choice (44) we obtain

$$\tilde{H} = \left(\hbar\omega - \frac{i\hbar\lambda}{2}\right)a^{\dagger}a \tag{50}$$

and

$$S_t(\rho) = \mathrm{e}^{-(i\omega + \lambda/2)a^{\dagger}at}\rho\mathrm{e}^{(i\omega - \lambda/2)a^{\dagger}at}. \tag{51}$$

From (29), we obtain the EPD

$$p_{[0,t]}(t_1, t_2, \ldots, t_m) = \sum_{k=m}^{\infty} \lambda^m m! \binom{k}{m} \langle k|\rho|k\rangle$$

$$\times \exp\{-\lambda(t_1 + t_2 + \cdots + t_m) - \lambda(k-m)t\}. \tag{52}$$

An interesting feature of the above EPD is that it depends only on the sum $(t_1 + t_2 + \ldots + t_m)$. From (30), (52), we obtain the counting probability

$$p(m; [0,t]) = \sum_{k=m}^{\infty} \binom{k}{m} (1 - \mathrm{e}^{-\lambda t})^m (\mathrm{e}^{-\lambda t})^{k-m} \langle k|\rho|k\rangle \tag{53}$$

which is indeed identical with the counting formula (15) obtained by Mollow [13]. Mollow [13], Scully and Lamb [14] and others [29] have obtained the counting

formula (53) for the single-mode free field by first considering the evolution of the composite system, detector + field, over the interval $[0, t]$ and then evaluating the probability that m-photons have been absorbed by the detector. On the other hand, the quantum theory of continuous measurements is a general framework which deals with the actual 'history' of the outcomes recorded by the detector and gives the basic ansatz (29) for calculating the EPD, from which the entire counting statistics can be derived.

We now consider the measurement transformation $\rho \to T_t(\rho)$ which gives the change in the state of the entire ensemble at any stage in the continuous measurement. From (46), (48) and (49), we obtain for $\rho(t) = T_t(\rho)$ the equation

$$\frac{\mathrm{d}\rho(t)}{\mathrm{d}t} = \frac{-i}{\hbar}[\hbar\omega a^\dagger a, \rho(t)] + \frac{\lambda}{2}(2a\rho a^\dagger - a^\dagger a\rho - \rho a^\dagger a), \tag{54}$$

which turns out to be the well-known master equation for a damped harmonic oscillator [30]. The solution of (54) can be written explicitly [31]

$$T_t(\rho) = \sum_{k=0}^{\infty} \frac{(1-\mathrm{e}^{-\lambda t})^k}{k!} \mathrm{e}^{-(i\omega+\lambda/2)a^\dagger a t} a^k \rho a^{\dagger k} \mathrm{e}^{(i\omega-\lambda/2)a^\dagger a t}. \tag{55}$$

In particular, we may note [6] that

$$T_t(|z\rangle\langle z|) = |z(t)\rangle\langle z(t)|, \tag{56}$$

where

$$z(t) = z\mathrm{e}^{-(i\omega+\lambda/2)t}. \tag{57}$$

This fact, that a coherent state transforms into a coherent state under the action of T_t, leads to the factorization property for the CPD when the field is in a coherent state to start with. From (56), (57) we obtain

$$\begin{aligned} h_{[0,t]}(t_1, t_2, \ldots, t_m) &= \mathrm{Tr}[T_{t-t_m} J T_{t_m - t_{m-1}} \cdots J T_{t_1}(|z\rangle\langle z|)] \\ &= \prod_{i=1}^{m} (\lambda|z|^2 \mathrm{e}^{-\lambda t_i}) \\ &= \prod_{i=1}^{m} h_{[0,t]}(t_i). \end{aligned} \tag{58}$$

In fact, it can also be shown [6] that the coherent states have an important physical property that the counting probabilities in any two disjoint intervals are statistically independent.

We refer the reader to the literature [6, 32–34] for further discussion regarding the CPD and other counting probabilities for various particular states of the electromagnetic field. Here, we note only one other result that the counting probabilities (53) can be expressed in a form analogous to the Mandel formula

$$p(m; [0, t]) = \mathrm{Tr}\left[\rho : \frac{\Omega^m}{m} \mathrm{e}^{-\Omega} :\right], \tag{59}$$

where

$$\Omega = a^\dagger a(1 - \mathrm{e}^{-\lambda t}) \tag{60}$$

which can also be written as

$$\Omega = \lambda \int_0^t a^\dagger e^{(i\omega - \lambda/2)t'} a e^{-(i\omega + \lambda/2)t'} dt'. \tag{61}$$

As mentioned earlier in § 2, Mandel [15] has argued that the counting probabilities (53), derived from the theory of continuous measurements, are applicable only to a closed system "in which field and detector are both contained in some cavity, and any photons not absorbed by the detector at one time are available for detection at later times"; these probabilities are not applicable to a situation "in which light falls on the photodetector and any unabsorbed photons propagate away". Further, Mandel has also argued that the counting formula (53) is not applicable to the usual experimental conditions, "because the laser is not really a closed system. Some photons are emitted or absorbed by the detector, but they are continuously replenished by the source...". Mandel's above comments perhaps implies the doubt that these are not merely the limitations of the counting formula (53), but also of the general quantum theory of continuous measurements, for Mandel concludes his critique with the remark that "sound mathematical argument and sound physics are not always the same thing" [15].

Since the counting probabilities (53) are for a single-mode field, it is true that the photons that are not absorbed are present everywhere as it were, and hence are always available for detection. In other words the spatial location and size of the detector are not relevant in this case. Hence Mandel's first observation above is indeed valid, but that will be so for any calculation involving a single-mode field. The volume and location of a detector will play a crucial role when we consider the photodetection of a multi-mode electromagnetic field, and that can be very well carried out in the general framework of the continuous measurement theory, as we shall show in the next section.

The other observation of Mandel is that the counting probabilities (53) do not pertain to a situation where the field is being replenished by a source of photons; this is also a valid point. However this is just a characteristic of the system for which we have calculated the photon counting probabilities, and is not in any way a limitation of the quantum theory of continuous measurements. The counting probabilities (53) have been derived specifically for the case of a single-mode free field, where the Hamiltonian of the system, while not interacting with the detector, is given by (47). However, it is quite straight forward to apply the general formalism of continuous measurements for the photodetection of a single-mode field which is not undergoing free evolution, but is coupled to an external source, as we shall explain below [19].

For the photodetection of the single-mode field coupled to an external source, we can continue with the same measurement transformation

$$J(\rho) = \lambda a \rho a^\dagger \tag{62}$$

as before, but change the Hamiltonian of the system from (47) to the following:

$$H = \hbar\omega a^\dagger a + (f^* a + f a^\dagger), \tag{63}$$

where f is an arbitrary complex number. Then we get

$$\tilde{H} = \hbar\omega a^\dagger a + (f^* a + f a^\dagger) - \frac{i\hbar}{2}\lambda a^\dagger a. \tag{64}$$

Now, following the same sequence of steps that we took in the case of the single-mode free field, we arrive at the following counting formula for a single-mode field coupled to an external source

$$p(m;[0,t]) = \mathrm{Tr}\left[\rho : \frac{\Omega^m}{m!} e^{-\Omega} :\right], \tag{65}$$

where

$$\Omega = \lambda \int_0^t \tilde{a}^\dagger(t')\tilde{a}(t')\,dt' \tag{66}$$

where

$$\tilde{a}(t) = z_0 I + (a - z_0 I)e^{-(i\omega + \lambda/2)t}, \tag{67}$$

where I is the identity operator and

$$z_0 = \frac{-if}{i\omega + (\lambda/2)}. \tag{68}$$

It can be shown that the mean number of photons detected in the interval $[0,t]$ essentially behaves as $|z_0|^2 \lambda t$ for the large times t.

Thus the general formalism of the quantum theory of continuous measurements is not in any sense restricted to a consideration of only closed systems. In fact it is also possible to further generalize the theory outlined in § 3 to situations where the evolution of the system in the absence of the detector is not governed by a Hamiltonian, but is of a more general type described by some master equation. This only involves making appropriate modifications in the prescription (43), (44) for the "no count" measurement transformation S_t, which we will not consider here.

5. Quantum counting formula of Chmara

We now briefly outline the general quantum counting formula derived by Chmara [20] for photocount measurements performed on a multi-mode electromagnetic field coupled to an external source. As we shall explain below, the Chmara counting formula is indeed the appropriate quantum generalization of classical Mandel formula (5), (6) for the photon counting probabilities.

For the change in the state of the electromagnetic field $\rho \to J(\rho)$ when one photon has been detected in an infinitesimal interval of time, Chmara adopts the same measurement transformation which was implicit in the work of Kelley and Kleiner [12]

$$J(\rho) = \sum_{\mu,\mu'} \int d^3\mathbf{r} \int d^3\mathbf{r}'\, C_{\mu\mu'}(\mathbf{r},\mathbf{r}') A_\mu^+(\mathbf{r}) \rho A_{\mu'}^-(\mathbf{r}') \tag{69}$$

where $C_{\mu\mu'}(\mathbf{r},\mathbf{r}')$ is a function which characterizes the location and senstivity of the detector, and should satisfy

$$C_{\mu\mu'}(\mathbf{r},\mathbf{r}')^* = C_{\mu'\mu}(\mathbf{r}',\mathbf{r}). \tag{70}$$

For many purposes, we could simplify (69) into the following form

$$J(\rho) = \lambda \sum_\mu \int_D d^3\mathbf{r} A_\mu^+(\mathbf{r}) \rho A_\mu^-(\mathbf{r}), \tag{71}$$

where λ is a parameter, dependent on the sensitivity of the detector, and the integration is over the volume of the detector. In (69) or (71), $A_\mu^-(\mathbf{r})$ and $A_\mu^+(\mathbf{r})$ are respectively the negative and positive frequency parts of the vector potential at the initial time. $A_\mu^-(\mathbf{r})$ has the usual mode expansion

$$A_\mu^-(\mathbf{r}) = \sum_{\lambda=1,2} \int \mathrm{d}^3\mathbf{k} \left(\frac{\hbar}{2\omega(2\pi)^3}\right)^{1/2} \mathrm{e}_\mu^{*\lambda}(\mathbf{k}) \mathrm{e}^{-\mathrm{i}\mathbf{k}\cdot\mathbf{r}} a_\lambda^\dagger(\mathbf{k}). \tag{72}$$

From (40) it follows that

$$R = \sum_{\mu,\mu'} \int \mathrm{d}^3\mathbf{r} \int \mathrm{d}^3\mathbf{r}' C_{\mu\mu'}(\mathbf{r},\mathbf{r}') A_{\mu'}^-(\mathbf{r}') A_\mu^+(\mathbf{r}) \tag{73}$$

which reduces to the form

$$R = \lambda \sum_\mu \int_D \mathrm{d}^3\mathbf{r} A_\mu^-(\mathbf{r}) A_\mu^+(\mathbf{r}). \tag{74}$$

For the evolution of the system in the absence of detector, Chmara employs the Hamiltonian

$$H = \sum_{\lambda=1,2} \int \mathrm{d}^3\mathbf{k} \left\{\hbar\omega a_\lambda^\dagger(\mathbf{k}) a_\lambda(\mathbf{k}) - \left(\frac{\hbar}{2\omega}\right)^{1/2} (j_\lambda^*(\mathbf{k}) a_\lambda(\mathbf{k}) + j_\lambda(\mathbf{k}) a_\lambda^\dagger(\mathbf{k})\right\}, \tag{75}$$

where $j_\lambda(\mathbf{k})$ are c-numbers which are the Fourier transforms of the transverse part of the external sources. (75) is the usual Hamiltonian of an electromagnetic field coupled to external sources. If no measurements are made, the time evolution of the field operators are given by the standard Heisenberg picture equations

$$\frac{\mathrm{d}}{\mathrm{d}t} A_\mu^\pm(\mathbf{r},t) = \frac{i}{\hbar}[H, A_\mu^\pm(\mathbf{r},t)]. \tag{76}$$

Now, employing the canonical prescription for the no-count measurement transformation, given by (43), (44), Chmara derives the following expression for the EPD

$$\begin{aligned} p_{[0,t]}(t_1, t_2, \ldots, t_m) &= \mathrm{Tr}[S_{t-t_m} J S_{t_m - t_{m-1}} \ldots J S_{t_1}(\rho)] \\ &= \mathrm{Tr}[\rho : \tilde{I}(t_1)\tilde{I}(t_2)\ldots\tilde{I}(t_m)\mathrm{e}^{-\int_0^t \tilde{I}(t')\mathrm{d}t'} :], \end{aligned} \tag{77}$$

where

$$\tilde{I}(t) = \sum_{\mu,\mu'} \int \mathrm{d}^3\mathbf{r} \int \mathrm{d}^3\mathbf{r}' C_{\mu\mu'}(\mathbf{r},\mathbf{r}') \tilde{A}_\mu^-(\mathbf{r}',t) \tilde{A}_\mu^+(\mathbf{r},t), \tag{78}$$

where $\tilde{A}_\mu^\pm(\mathbf{r},t)$ are determined by the non-Hamiltonian evolution equation

$$\begin{aligned} \frac{\mathrm{d}}{\mathrm{d}t} \tilde{A}_\mu^\pm(\mathbf{r},t) &= \frac{i}{\hbar}[H, \tilde{A}_\mu^\pm(\mathbf{r},t)] \\ &\quad + \sum_{\nu',\nu''} \int \mathrm{d}^3\mathbf{r}' \int \mathrm{d}^3\mathbf{r}'' C_{\nu'\nu''}(\mathbf{r}',\mathbf{r}'') A_{\nu''}^-(\mathbf{r}'') \tilde{A}_\mu^\pm(\mathbf{r},t) A_{\nu'}^+(\mathbf{r}') \end{aligned}$$

From the EPD (77), we immediately obtain the Chmara formula

$$p(m;[0,t]) = \mathrm{Tr}\left[\rho{:}\frac{\Omega^m}{m!}\mathrm{e}^{-\Omega}{:}\right], \tag{80}$$

where

$$\Omega = \int_0^t \tilde{I}(t')\mathrm{d}t'. \tag{81}$$

Clearly the Chmara counting formula is very similar to the quantum Mandel formula (7), (8) in appearance, except that the time-dependent 'intensities' $\tilde{I}(t)$, whose time-integrals are involved, do not satisfy the usual Heisenberg picture equation (76) involving only the Hamiltonian of the system in the absence of the detector, but evolve according to the non-Hamiltonian evolution equation (79).

There is a transparent way of understanding the evolution equation (79). Associated with the measurement transformations $\rho \to J(\rho)$ and $\rho \to T_t(\rho)$ are the so called "dual" transformations $A \to J^*(A)$, $A \to T_t^*(A)$, defined for each operator A on the Hilbert space, via the equations

$$\mathrm{Tr}[J(\rho)A] = \mathrm{Tr}[\rho J^*(A)] \tag{82}$$

$$\mathrm{Tr}[T_t(\rho)A] = \mathrm{Tr}[\rho T_t^*(A)] \tag{83}$$

for all ρ and A. Then the evolution equation (79) can be easily seen to be

$$\frac{\mathrm{d}}{\mathrm{d}t}\tilde{A}_\mu^\pm(\mathbf{r},t) = \frac{i}{\hbar}[H,\tilde{A}_\mu^\pm(\mathbf{r},t)] + J^*(\tilde{A}_\mu^\pm(\mathbf{r},t)) - \tfrac{1}{2}(R\tilde{A}_\mu^\pm(\mathbf{r},t) + \tilde{A}_\mu^\pm(\mathbf{r},t)R). \tag{84}$$

Equation (84) can be seen to be the 'dual' of eq. (46) satisfied by $T_t(\rho)$. Hence, we can write the solution of (79) as

$$\tilde{A}_\mu^\pm(\mathbf{r},t) = T_t^*(A_\mu^\pm(\mathbf{r})). \tag{85}$$

Further from the special form of J, H as given by (69) and (75), it can be shown that

$$\tilde{I}(t) = T_t^*(R), \tag{86}$$

where $A_\mu^\pm(\mathbf{r})$ and R are as given by (72) and (73).

The crucial step in the derivation of the counting formula (80) by Chmara is that, given the measurement transformation J as in (69) and the Hamiltonian of the system in the absence of the detector as in (75), the evolution of the total ensemble of systems in the counting experiment, namely $\rho \to T_t(\rho)$, is such that coherent states of the electromagnetic field are transformed into coherent states. This once again leads to the important property of the coherent states that the associated counting probabilities for disjoint intervals of time are statistically independent, even in the general case of the photodetection of a multi-mode electromagnetic field coupled to an external source. Chmara [20] has further demonstrated that such statistical independence holds also in the case of several photodetectors.

The photon counting formulae, (59)–(61) and (65)–(68), obtained in § 4 for a single-mode field, can be easily seen to be particular cases of the Chmara counting formula

(80), (81). In fact our discussion above clearly shows that the Chmara counting formula is the appropriate quantum generalization of the classical Mandel formula (5), (6).

Finally a remark about the CPD of the counting process. From the EPD (77) it can be shown that the CPD of our counting process are given by

$$h_{[0,t]}(t_1, t_2, \ldots, t_m) = \mathrm{Tr}[\rho{:}\tilde{I}(t_1)\tilde{I}(t_2)\ldots\tilde{I}(t_m){:}]. \tag{87}$$

The above relation can also be obtained by employing the usual definition of CPD

$$h_{[0,t]}(t_1, t_2, \ldots, t_m) = \mathrm{Tr}[T_{t-t_m} J T_{t_m - t_{m-1}} \ldots J T_{t_1}(\rho)] \tag{88}$$

and making use of the property that under the transformation $\rho \to T_t(\rho)$ the coherent states evolve into coherent states, in a manner analogous to Chmara's derivation [20] of the EPD (77).

The CPD (87) are correlation functions of the "intensities" $\tilde{I}(t)$ whose time evolution is given by the non-Hamiltonian evolution equation (79). Clearly the CPD (84) are significantly different from the correlation functions which occur on the right hand side of eq. (17) and which were assumed to be the CPD of the counting process by Kelley and Kleiner [12]. If we introduce the unitary transformation $\rho \to \mathscr{U}_t(\rho)$ which gives the evolution of the system in the absence of the detector, namely

$$\mathscr{U}_t(\rho) = \mathrm{e}^{-(i/\hbar)Ht} \rho \mathrm{e}^{(i/\hbar)Ht} \tag{89}$$

then the correlation functions (17) considered by Kelley and Kleiner can be actually expressed as

$$\mathrm{Tr}[\mathscr{U}_{t-t_m} J \mathscr{U}_{t_m - t_{m-1}} \ldots J \mathscr{U}_{t_1}(\rho)] = \mathrm{Tr}[\rho{:}I(t_1)I(t_2)\ldots I(t_m){:}]. \tag{90}$$

Thus the correlation functions considered by Kelley and Kleiner are clearly the joint probability densities that one count is observed in each of the infinitesimal intervals $[t_i, t_i + \mathrm{d}t_i]$ when *no* measurements are performed during the rest of the interval $[0, t]$. Hence these correlation functions have nothing to do with CPD which are joint probability densities when a continuous measurement is performed over the entire interval $[0, t]$ and which have to be evaluated as per (88). From Chmara's analysis we are thus able to clearly understand where Kelley and Kleiner went wrong, and how the CPD of the counting process have to be correctly identified on the basis of the quantum theory of continuous measurements.

6. The photon emission process – quantum jumps

The final example we shall consider is one where the quantum theory of continuous measurements is employed to discuss the statistics of photon emission events in the resonance fluorescence of an atom in interaction with radiation. The developments in laser spectroscopy which have made it possible to observe the fluorescence light emitted by a single atom or ion, have revived the good old issue of 'quantum jumps' occurring in atomic systems. What we shall outline is the calculation of the photon emission statistics in the resonance fluorescence of a three-level atom which shows periods of darkness when two transitions, one weak and one strong, are simultaneously driven. By applying the quantum theory of continuous measurements, Zoller, Marte and Walls [21] and Barchielli [22] obtained the complete photon emission statistics.

It can be shown [22] that the definition and properties of the so called 'delay function', introduced by Cohen-Tannoudji and Dalibard [23] in their explanation of the dark periods in the fluorescence, follow naturally from this theory.

We consider a three-level atom in the so called V-configuration. The Hamiltonian of the system, in the absence of any detector, is

$$H = \sum_{j=1}^{2} \left\{ \frac{1}{2}\Omega_j(|0\rangle\langle j| + |j\rangle\langle 0|) - \Delta_j |j\rangle\langle j| \right\}, \tag{91}$$

where $|0\rangle$ is the ground state and $|1\rangle, |2\rangle$ are the excited states of the atom. Ω_1, Ω_2 are the Rabi frequencies and Δ_1, Δ_2 the detuning parameters of the $1 \leftrightarrow 0$ and $2 \leftrightarrow 0$ transitions respectively. Associated with $1 \to 0$ and $2 \to 0$ emission events in any infinitesimal interval of time, are the measurement transformations $\rho \to J_j(\rho), j = 1, 2$, given by

$$J_j(\rho) = \Gamma_j |0\rangle\langle j| \rho |j\rangle\langle 0|, \tag{92}$$

$j = 1, 2$ where Γ_1, Γ_2 are the natural transition rates. Note that each of these transitions can take place from a superposed state, but would always leave the system in the ground state. It is also important to note that we are here concerned only with the consequent changes in the state of the atomic system, whenever the detector registers a photon emission event.

Since there are now two types of basic events characterized by the measurement transformations $J_j, j = 1, 2$, the canonical prescription for obtaining the 'no count' measurement transformation S_t would involve the associated operators R_j defined as in (40) by

$$\mathrm{Tr}[J_j(\rho)] = \mathrm{Tr}[\rho R_j], \tag{93}$$

$j = 1, 2$, for all ρ. From (92), we obtain

$$R_j = \Gamma_j |j\rangle\langle j|, \tag{94}$$

$j = 1, 2$. Now the appropriate generalization of (43), (44) can be easily seen to be

$$S_t(\rho) = \mathrm{e}^{-(i/\hbar)\tilde{H}t} \rho \mathrm{e}^{(i/\hbar)\tilde{H}^\dagger t}, \tag{95}$$

where

$$\tilde{H} = H - \frac{i\hbar}{2} R_1 - \frac{i\hbar}{2} R_2. \tag{96}$$

From (91), (94), we obtain

$$\tilde{H} = \sum_{j=1}^{2} \left\{ \frac{\Omega_j}{2}(|0\rangle\langle j| + |j\rangle\langle 0|) - \left(\Delta_j + \frac{i\hbar\Gamma_j}{2} \right) |j\rangle\langle j| \right\}. \tag{97}$$

The EPD of the process are of the form $p_{[0,t]}(\nu_1 t_1, \nu_2 t_2, \ldots, \nu_m t_m)$ which is the joint probability density that the emission event associated with $\nu_j \to 0$ transition ($\nu_j = 1, 2$) is observed around the time t_j, $j = 1, 2, \ldots, m$, with no other emission being observed in the interval $[0, t]$. From the basic principles of the continuous measurement theory, these EPD are given by a prescription analogous to (29), as below:

$$p_{[0,t]}(\nu_1 t_1, \nu_2 t_2, \ldots, \nu_m t_m) = \mathrm{Tr}(S_{t-t_m} J_{\nu_m} \ldots J_{\nu_1} S_{t_1}(\rho)] \tag{98}$$

for all $\nu_j = 1, 2$, $j = 1, 2, \ldots, m$. If we now employ (92), which expresses the fact that each emission event leaves the system in the ground state, it follows that the EPD (98) factorize in the following manner:

$$p_{[0,t]}(\nu_1 t_1, \nu_2 t_2, \ldots, \nu_m t_m)$$
$$= \Gamma_{\nu_1} \langle \nu_1 | S_{t_1}(\rho) | \nu_1 \rangle \prod_{j=2}^{m} W_{\nu_j}(t_j - t_{j-1})$$
$$\times \operatorname{Tr}[S_{t-t_m}(|0\rangle\langle 0|)] \tag{99}$$

for all $\nu_j = 1, 2$, $j = 1, 2, \ldots, m$, where ρ is the state of the atom at $t = 0$, and

$$W_j(\tau) = \Gamma_j \langle j | S_\tau(|0\rangle\langle 0|) | j \rangle$$
$$= \Gamma_j |\langle j | e^{-(i/\hbar)\tilde{H}\tau} | 0 \rangle|^2 \tag{100}$$

for $j = 1, 2$, is the probability density that if an emission has occurred at some time, the next emission event is of type $j \to 0$ ($j = 1, 2$), and occurs at time τ later.

Equations (99), (100) which give the EPD, completely characterize the statistics of the photon emission events. For instance the 'delay function' introduced by Cohen-Tannoudji and Dalibard [23] can be expressed as

$$W(\tau) = \sum_{j=1}^{2} W_j(\tau) = \sum_{j=1}^{2} \Gamma_j |\langle j | e^{-(i/\hbar)\tilde{H}\tau} | 0 \rangle|^2. \tag{101}$$

$W(\tau)$ clearly has the interpretation of being the probability density that if an emission event occurred at some time, the next emission event occurs at time τ later. Barchielli [22] has shown that the delay function (101) satisfies.

$$\int_0^\infty W(\tau) d\tau = 1 \tag{102}$$

and that if we set

$$e^{-(i/\hbar)\tilde{H}t} | 0 \rangle = \sum_{k=0}^{2} a_k(t) | k \rangle \tag{103}$$

then $a_k(t)$ satisfy the equations derived the Cohen-Tannoudji and Dalibard [23] using the master equation approach involving the so called 'dressed atoms'.

It may be of interest to note that the master equation obeyed by the density operator, $\rho(t) = T_t(\rho)$, characterizing the entire ensemble of systems with their diverse emission histories, will have the following form, instead of (46):

$$\frac{d}{dt}\rho(t) = -\frac{i}{\hbar}[H, \rho(t)] + \sum_{j=1}^{2} J_j(\rho(t)) - \sum_{j=1}^{2} (R_j \rho(t) + \rho(t) R_j)$$
$$= -\frac{i}{\hbar}(\tilde{H}\rho(t) - \rho(t)\tilde{H}^\dagger) + \sum_{j=1}^{2} J_j(\rho(t)). \tag{104}$$

If we use the particular form of J_j and $\tilde{H}$ as given by (92) and (97), then equation (104) will reduce to the well-known optical Bloch equation for an atomic system [35].

Finally we may note that the above analysis of resonance fluorescence in a three-level atom can be easily extended to the case of 'quantum jumps' in a general n-level system driven by external fields.

7. Discussion

In this article we have presented an overview of the quantum theory of continuous measurements as the appropriate generalization of conventional quantum mechanics for discussing physical situations where there is a continuous interaction of the apparatus with the system and information is acquired continuously as to whether a given type of event has occured or not. We have also outlined some of the important applications of this formalism in quantum optics. The two important classes of applications that we have discussed in some detail are the following: 1) Analysis of the photon counting statistics of an electromagnetic field which may be interacting with an external source. 2) Analysis of the statistics of photon emission events in the resonance fluorescence of an atomic system.

The quantum theory of continuous measurements as discussed in this paper has been extensively applied in quantum optics as well as in other contexts, especially in the last few years. We shall presently refer the reader to a sample of the growing literature on this subject. At the outset we should mention that an important problem which has not received any serious attention is the study of the physical consequences of the general quantum counting formula of Chmara, which as explained in § 5 is the appropriate quantum generalization of the classical Mandel formula.

Some of the mathematical aspects of the quantum theory of continuous measurements and possible generalizations of this framework to include more general stochastic processes have been studied by Barchielli and co-workers [36, 37]. Barchielli, Belavkin and co-workers have also studied the relation of this formalism to the so called quantum stochastic calculus and have utilized this relation for applications in quantum optics and also to develop a theory of gravity-wave detectors [38–43].

A large class of applications of the quantum theory of measurements in quantum optics, with particular emphasis on photon counting experiments, have been studied by Milburn, Walls, Gardiner and co-workers [44–51]. In recent years Milburn and co-workers have also developed a theory of continuous measurements of an electromagnetic field in a cavity with feedback [52–55]. The general theory of measurements in cavity electrodynamics has been reviewed by Meystre [56, 57]. There have also been interesting investigations on the influence of pump statistics on the output of a laser or micro-maser by Marte, Herzog, Ritsch and co-workers [58–61].

The photon counting statistics of a single-mode field has been extensively studied by Ueda and co-workers [31–33, 62, 63] who have evaluated the counting probabilities for a large class of physically interesting states of the field. We may also note the work of Marian, Ban and co-workers [64, 65, 34] in this context. Ueda and co-workers have also studied the case of photon counting experiments performed on two correlated modes [66].

Ueda and co-workers [67, 68] and Ban [69] have investigated in detail the nature of measurement performed by a photo-detector. Different models of photodetection are envisaged in the work of Lee [70–73]. Ban [74, 75] has developed a theory of electron

systems and the phenomena of quantum jumps have been further investigated by Grochmalicki, Hegerfeldt, Milburn and co-workers [77–81]. An alternative formalism based on the Monte-Carlo simulation of the atomic master equation in terms of stochastic evolution of atomic wave functions has been developed by Zoller, Dalibard and co-workers [82–85]. Carmichael [16, 86] has discussed another formalism referred to as the 'trajectories approach' which is based on the quantum theory of open systems. Both these formalisms start from different foundational points of view, but for all physically meaningful quantities such as the EPD, CPD and the counting statistics of the process, they lead to the same result as the quantum theory of continuous measurements.

Recently Agarwal, Perinova and co-workers [87–89] have discussed the interesting possibility of preparing particular quantum states by means of continuous measurements. Continuous measurements have also been proposed as a possible way of preventing decoherence in the entangled states of an n-atom system in recent investigations on the models of quantum computers based on cavity quantum electrodynamics [90].

In conclusion we may state that the quantum theory of continuous measurements is indeed an essential and significant generalization of the conventional formulation of quantum mechanics. It has proved to be a coherant and satisfactory framework for discussing counting experiments and all situations of continual observations which cannot be handled within the conventional formulation of quantum mechanics. There are likely to be many more applications of this theory in quantum optics as well as in other fields.

References

[1] E B Davies, *Commun. Math. Phys.* **15**, 277 (1969)
[2] E B Davies, *Commun. Math. Phys.* **19**, 83 (1970)
[3] E B Davies, *Commun. Math. Phys.* **22**, 5 (1971)
[4] E B Davies, *Quantum theory of open systems* (Academic Press, New York, 1976)
[5] M D Srinivas, *J. Math. Phys.* **18**, 2138 (1977)
[6] M D Srinivas and E B Davies, *Opt. Acta* **28**, 981 (1981)
[7] A S Holevo, *Sov. Math.* **26**, 1 (1982); *Izv. Vuz. Mat.* **26**, 3 (1982)
[8] O Macchi, *Adv. Appl. Probab.* **7**, 83 (1975)
[9] L Mandel, *Proc. Phys. Soc.* **72**, 1037 (1958)
[10] L Mandel, *Proc. Phys. Soc.* **74**, 233 (1959)
[11] L Mandel, in *Progress in optics* edited by E Wolf (North Holland, Amsterdam, 1963) vol. 2, p. 183
[12] P L Kelley and W H Kleiner, *Phys. Rev.* **A136**, 316 (1964)
[13] B R Mollow, *Phys. Rev.* **168**, 1896 (1968)
[14] M O Scully and W E Lamb Jr., *Phys. Rev.* **179**, 368 (1969)
[15] L Mandel, *Opt. Acta* **28**, 1447 (1981)
[16] H J Carmichael, *An open systems approach to quantum optics* (Springer Verlag, New York, 1993)
[17] D F Walls and G J Milburn, *Quantum optics* (Springer Verlag, New York, 1994)
[18] L Mandel and E Wolf, *Optical Coherence and Quantum Optics* (Cambridge, 1995)

[19] M D Srinivas and E B Davies, *Opt. Acta* **29**, 235 (1982)
[20] W Chmara, *J. Mod. Opt.* **34**, 455 (1987)
[21] P Zoller, M Marte and D F Walls, *Phys. Rev.* **A35**, 198 (1987)
[22] A Barchielli, *J. Phys.* **A20**, 6341 (1987)
[23] C Cohen-Tannoudji and J. Dalibard, *Europhys. Lett.* **1**, 441 (1986)
[24] M D Srinivas, *Pramana – J. Phys.* **17**, 203 (1981)
[25] M Born and E Wolf, *Principles of optics* (Pergamon, New York, 1980)
[26] E P Wigner, in *Foundations of quantum mechanics* edited by B d'Espagnat (Academic Press, New York, 1971) p. 1
[27] L de Broglie, *La Rev. Sci.* **87**, 259 (1947)
[28] L de Broglie, *Physics and microphysics* (Hutchinson, New York, 1955)
[29] A Selloni,P Schwendimann, A Quattropani and H P Balthes, *J. Phys.* **A11**, 1427 (1978)
[30] G S Agarwal, in *Progress in optics* edited by E Wolf (North Holland, Amsterdam, 1973) vol. 11, p. 1
[31] M Ueda, *Quantum Opt.* **1**, 131 (1989)
[32] M Ueda, N Imoto and T Ogawa, *Phys. Rev.* **A41**, 3891 (1990)
[33] T Ogawa, M Ueda and N Imoto, *Phys. Rev. Lett.* **66**, 1046 (1991)
[34] M Ban, *Phys. Rev.* **A51**, 1604 (1995)
[35] G S Agarwal, *Quantum statistical theories of Spontaneous emission and their relation to other problems* (Springer Verlag, New York, 1974)
[36] A Barchielli, L Lanz and G M Prosperi, *Nuovo Cimento* **B72**, 79 (1982)
[37] A Barchielli, L Lanz and G M Prosperi, *Found. Phys.* **13**, 779 (1983)
[38] A Barchielli and G Lupieri, *J. Math. Phys.* **26**, 2222 (1985)
[39] A Barchielli, *Phys. Rev.* **D32**, 347 (1985)
[40] A Barchielli, *Phys. Rev.* **D34**, 1642 (1986)
[41] A Barchielli, *Quantum Opt.* **2**, 423 (1990)
[42] V P Belavkin and P Staszewski, *Rep. Math. Phys.* **29**, 213 (1991)
[43] A Barchielli and V P Belavkin, *J. Phys.* **A24**, 1495 (1991)
[44] G J Milburn and D F Walls, *Phys. Rev.* **A30**, 56 (1984)
[45] D F Walls, M J Collet and G J Milburn, *Phys. Rev.* **D32**, 3208 (1985)
[46] G J Milburn, *Phys. Rev.* **A36**, 744 (1987)
[47] G J Milburn, in *Quantum optics V* edited by J D Harvey and D F Walls (Springer Verlag, New York, 1989) p. 90
[48] C W Gardiner, in *Quantum optics V* edited by J D Harvey and D F Walls (Springer Verlag, New York, 1989) p. 98
[49] C A Holmes, G J Milburn and D F Walls, *Phys. Rev.* **A39**, 2493 (1989)
[50] C W Gardiner, *Quantum noise* (Springer Verlag, New York, 1991)
[51] G J Milburn, in *Atomic and molecular physics and quantum optics* edited by H A Bachor *et al* (World Scientific, Singapore, 1992) p. 435
[52] H M Wiseman and G J Milburn, *Phys. Rev.* **A46**, 2853 (1992)
[53] A Liebman and G J Milburn, *Phys. Rev.* **A47**, 634 (1993)
[54] H M Wiseman and G J Milburn, *Phys. Rev.* **A47**, 642 (1993)
[55] A Liebman and G J Milburn, *Phys. Rev.* **A51**, 736 (1995)
[56] P Meystre, in *Progress in optics* edited by E Wolf (North Holland, Amsterdam, 1992) vol. 30, p. 263
[57] P Meystre, *Phys. Rep.* **219**, 243 (1992)
[58] M A M Marte and P Zoller, *Phys. Rev.* **A40**, 5774 (1989)
[59] M A M Marte and P Zoller, *Quantum Opt.* **2**, 229 (1990)
[60] U Herzog, *Phys.Rev.* **A50**, 783 (1994)
[61] K Ellinger and H Ritsch, *J. Mod. Opt.* **42**, 2127 (1995)
[62] M Ueda, *Phys. Rev.* **A41**, 3875 (1990)
[63] M Ueda, N Imoto, H Nagaoka and T Ogawa, *Phys. Rev.* **A46**, 2859 (1992)
[64] P Marian and T A Marian, *Phys. Rev.* **A47**, 4487 (1993)
[65] P Marian and T A Marian, *Phys. Lett.* **A198**, 163 (1995)
[66] M Ueda, N Imoto and T Ogawa, *Phys. Rev.* **A41**, 6331 (1990)

[67] N Imoto, M Ueda and T Ogawa, *Phys. Rev.* **A41**, 4127 (1990)
[68] M Ueda and M Kitagawa, *Phys. Rev. Lett.* **68**, 3424 (1992)
[69] M Ban, *Phys. Rev.* **A49**, 5078 (1994)
[70] C T Lee, *Phys. Rev.* **A48**, 2285 (1993)
[71] C T Lee, *Phys. Rev.* **A49**, R633 (1994)
[72] C T Lee, *Phys. Rev.* **A49**, 4888 (1994)
[73] C T Lee, *Phys. Rev.* **A51**, 3386 (1995)
[74] M Ban, *Phys. Lett.* **A172**, 337 (1993)
[75] M Ban, *Phys. Rev.* **A49**, 4142 (1994)
[76] M D Srinivas, *Pramana – J. Phys.* **17**, 217 (1981)
[77] J Grochmalicki and M Lewenstein, *Phys. Rev.* **A40**, 2517 (1989)
[78] G C Hegerfeldt and T S Wilser, in *Classical and quantum systems – Foundations and symmetries* edited by W Scherer *et al* (World Scientific, Singapore, 1992) p. 104
[79] G C Hegerfeldt, *Phys. Rev.* **A47**, 449 (1993)
[80] M J Gagen and G J Milburn, *Phys. Rev.* **A47**, 1467 (1993)
[81] H M Wiseman and G J Milburn, *Phys. Rev.* **A47**, 1652 (1993)
[82] R Dum, P Zoller and H Ritsch, *Phys. Rev.* **A45**, 4879 (1992)
[83] C W Gardiner, A S Parkins and P Zoller, *Phys. Rev.* **A46**, 4363 (1992)
[84] R Dum, A S Parkins, P Zoller and C W Gardiner, *Phys. Rev.* **A46**, 4382 (1992)
[85] K Molmer, Y Castin and J Dalibard, *J. Opt. Soc. Am.* **B10**, 524 (1993)
[86] H J Carmichael, S Singh, R Vyas and P R Rice, *Phys. Rev.* **A39**, 1200 (1989)
[87] G S Agarwal, M O Scully and H Walther, *Phys. Scr.* **T48**, 128 (1993)
[88] G S Agarwal, M Graf, M Orszag, M O Scully and H Walther, *Phys. Rev.* **A49**, 4077 (1994)
[89] V Perinova, A Luks and J Krepelka, *Phys. Rev.* **A53**, 525 (1996)
[90] T Pellizzari, S A Gardiner, J I Cirac and P Zoller, *Phys. Rev. Lett.* **75**, 3788 (1995)

Magnetized cylindrically symmetric universe in general relativity

RAJ BALI and MAHBUB ALI
Department of Mathematics, University of Rajasthan, Jaipur 302 004, India

MS received 30 December 1993; revised 2 December 1995

Abstract. A magnetized cylindrically symmetric universe with two degrees of freedom in which the free gravitational field is Petrov type I degenerate, is obtained. The magnetic field is due to an electric current produced along the x-axis. The distribution consists of an electrically neutral perfect fluid with an infinite electrical conductivity. The behaviour of the model when magnetic field tends to zero and other physical aspects of the model are also discussed.

Keyword. General relativity.

PACS No. 4·20

1. Introduction

Stewart [1] investigated the models as more stable if the matter is supposed to be anisotropic. Ellis and MacCallum [2] obtained a class of homogeneous models for perfect fluid distribution. The anisotropic magnetic fluid models have significant contribution in the evolution of galaxies and stellar bodies. Primordial magnetic fields of cosmological origin have been speculated by Asseo and Sol [3]. FRW models are approximately valid as present day magnetic field strength is very small. In early universe the strength must have been appreciable. The breakdown of isotropy is due to magnetic field. Thorne [4] investigated an LRS Bianchi type I cosmological models containing a magnetic field. Jacobs [5, 6] investigated Bianchi type I cosmological models with magnetic field satisfying barotropic equation of state. Collins [7] gave a qualitative analysis of Bianchi type I models with magnetic field. Roy *et al* [8] obtained Bianchi type I cosmological model with perfect fluid and magnetic field introducing space-like unit vector field orthogonal to the coordinate time. Recently, Bali [9] investigated a magnetized cosmological model in which expansion θ in the model is proportional to σ_1^1, the eigenvalue of shear tensor σ_i^j for perfect fluid distribution. Bali and Tyagi [10] investigated stiff magnetofluid cosmological model for perfect fluid distributions. Bali and Ali [11], to appear in IJTP obtained magnetized cosmological model with two degrees of freedom for perfect fluid distribution in general relativity. Roy and Prakash [12] obtained a plane symmetric cosmological model with an incident magnetic field for perfect fluid distribution in which the gravitational field is of Petrov type I degenerate. Roy *et al* [13] investigated a cylindrically symmetric universe with two degrees of freedom in general relativity in which free gravitational field is Petrov type I degenerate.

In this paper we have obtained a magnetized cylindrically symmetric universe with two degrees of freedom in general relativity in which free gravitational field is of Petrov type I degenerate. The magnetic field is due to an electric current along x-axis. The distribution consists of an electrically neutral perfect fluid with an infinite electrical conductivity.

Let us consider an anisotropic homogeneous universe with two degrees of freedom in the form

$$dS^2 = A^2(dx^2 - dt^2) + C^2dz^2 + (B^2 + D^2)dy^2 + 2CDdydz, \tag{1.1}$$

where the metric potentials A, B, C, D are function of time alone. The energy momentum tensor is got in the form

$$T_i^j = (\varepsilon + p)v_iv^j + pg_i^j + E_i^j, \tag{1.2}$$

where E_i^j is the electromagnetic field given by Lichnerowicz (1967) as

$$E_i^j = \bar{\mu}[|h|^2(v_iv^j + \tfrac{1}{2}g_i^j - h_ih^j)], \tag{1.3}$$

where ε is the density, p the pressure and v^i the flow vector satisfying

$$g_{ij}v^iv^j = -1. \tag{1.4}$$

$\bar{\mu}$ is the magnetic permeability and h_i the magnetic flux vector defined by

$$h_i = \frac{\sqrt{-g}}{2\bar{\mu}}\varepsilon_{ijkl}F^{kl}v^j, \tag{1.5}$$

where F_{kl} is the electromagnetic field tensor and ε_{ijkl} the Levi-Civita tensor density. A semi colon stands for covariant differentiation. We assume that the coordinates are comoving so that $v^1 = 0 = v^2 = v^3$ and $v^4 = 1/A$. We take the incident magnetic field to be in the direction of x-axis, so that $h_1 \neq 0$, $h_2 = 0 = h_3 = h_4$. This leads to $F_{12} = F_{13} = 0$, by virtue of (1.5). We also find that $F_{14} = F_{24} = F_{34} = 0$ due to the assumption of the inifinite conductivity of the fluid. Thus, the only non-vanishing component of F_{ij} is F_{23}. The first set of Maxwell's equations

$$F_{ij;k} + F_{jk;i} + F_{ki;j} = 0$$

leads to $F_{23} = \text{constant} = H$(say).

Hence

$$h_1 = \frac{AH}{\bar{\mu}BC} \tag{1.6}$$

The Einstein's field equations

$$R_{ij} - \tfrac{1}{2}Rg_{ij} + \Lambda g_i^j = -8\pi T_i^j$$

for the line element (1.1) are

$$\frac{1}{A^2}\left\{\frac{A_4B_4}{AB} + \frac{A_4C_4}{AC} - \frac{B_4C_4}{BC} - \frac{B_{44}}{B} - \frac{C_{44}}{C}\right\} - \frac{1}{4}\left[\frac{CD_4 - DC_4}{ABC}\right]^2 - \Lambda$$
$$= 8\pi\left(p - \frac{H^2}{2\bar{\mu}B^2C^2}\right), \tag{1.7}$$

$$-\frac{1}{A^2}\left\{\frac{A_{44}}{A}+\frac{B_{44}}{B}-\frac{A_4^2}{A^2}\right\}-\frac{1}{2}\frac{DC}{A^2B^2}\left(\frac{D}{C}\right)_{44}+\frac{1}{2}\frac{DC}{A^2B^2}\left(\frac{D}{C}\right)_4\left(\frac{B_4}{B}-\frac{3C_4}{C}\right)$$
$$-\frac{3}{4}\left[\frac{CD_4-DC_4}{ABC}\right]^2-\Lambda=8\pi\left(p+\frac{H^2}{2\bar{\mu}B^2C^2}\right), \tag{1.8}$$

$$-\frac{1}{A^2}\left\{\frac{A_{44}}{A}+\frac{C_{44}}{C}-\frac{A_4^2}{A^2}\right\}+\frac{1}{2}\frac{DC}{A^2B^2}\left(\frac{D}{C}\right)_{44}-\frac{1}{2}\frac{DC}{A^2B^2}\left(\frac{D}{C}\right)_4\left(\frac{B_4}{B}-\frac{3C_4}{C}\right)$$
$$+\frac{1}{4}\left[\frac{CD_4-DC_4}{ABC}\right]^2-\Lambda=8\pi\left(p+\frac{H^2}{2\bar{\mu}B^2C^2}\right), \tag{1.9}$$

$$\frac{1}{A^2}\left\{\frac{A_4B_4}{AB}+\frac{A_4C_4}{AC}+\frac{B_4C_4}{BC}\right\}-\frac{1}{4}\left[\frac{CD_4-DC_4}{ABC}\right]^2+\Lambda=8\pi\left(\varepsilon+\frac{H^2}{2\bar{\mu}B^2C^2}\right) \tag{1.10}$$

and

$$\left(\frac{D}{C}\right)_{44}-\left(\frac{D}{C}\right)_4\left(\frac{B_4}{B}-\frac{3C_4}{C}\right)=0. \tag{1.11}$$

2. Solution of the field equations

Equations (1.7)–(1.11) are five equations in six unknowns A, B, C, D, ε and p. For complete determination of this set, we need an extra condition. We assume that the free gravitational field is Petrov type I degenerate which leads to

$$C_{12}^{12}=C_{13}^{13}.$$

This implies that

$$\frac{C_{44}}{C}-\frac{B_{44}}{B}+\frac{2A_4}{A}\left(\frac{B_4}{B}-\frac{C_4}{C}\right)=\left[\frac{CD_4-DC_4}{BC}\right]^2. \tag{2.1}$$

Equation (1.11) leads to

$$\frac{CD_4-DC_4}{BC}=\frac{K}{C^2}, \tag{2.2}$$

where K is a constant of integration. From eqs (1.7), (1.8), (1.9) and (1.11), we have

$$\frac{A_4B_4}{AB}+\frac{A_4C_4}{AC}-\frac{B_4C_4}{BC}-\frac{C_{44}}{C}+\left(\frac{A_4}{A}\right)_4=-\frac{1}{2}\left[\frac{CD_4-DC_4}{BC}\right]^2-\frac{8\pi H^2A^2}{\bar{\mu}B^2C^2}, \tag{2.3}$$

$$\frac{C_{44}}{C}-\frac{B_{44}}{B}=\left[\frac{CD_4-DC_4}{BC}\right]^2. \tag{2.4}$$

From eqs (2.1), (2.2) and (2.4), we have

$$\frac{C_{44}}{C}-\frac{B_{44}}{B}=\frac{K^2}{C^4} \tag{2.5}$$

and

$$\frac{A_4}{A}\left(\frac{B_4}{B}-\frac{C_4}{C}\right)=0. \tag{2.6}$$

Since $B \neq C$, (2.6) on integration leads to

$$A = \text{constant} = \alpha(\text{say}). \tag{2.7}$$

From (2.3), (2.4) and (2.7), we have

$$\frac{B_{44}}{B}+\frac{C_{44}}{C}+\frac{2B_4C_4}{BC}=\frac{L}{B^2C^2}, \tag{2.8}$$

where $L=\alpha^2 b$ and $b=16\pi H^2/\bar{\mu}$.

Putting $B=e^{u+v/2}$ and $C=e^{u-v/2}$ in (2.5) and (2.8), we have

$$e^u v_4=\sqrt{M-K^2e^{2v}} \tag{2.9}$$

and

$$\mu f f'=L, \tag{2.10}$$

where M is a constant of integration. Equation (2.10) leads to

$$f^2=\log(N\mu)^{2L}, \tag{2.11}$$

where

$$(BC)=\mu \text{ and } \mu_4=f(\mu). \tag{2.12}$$

Also equation (2.9) leads to

$$e^{-v}=\frac{K}{\sqrt{M}}\cosh\phi, \tag{2.13}$$

where $\phi=P-\sqrt{2M}/L\{\log(N\mu)^L\}^{1/2}$.

From (2.2), (2.12) and (2.13), we have

$$\frac{D}{C}=R-\frac{\sqrt{M}}{K}\tanh\phi, \tag{2.14}$$

where P and R are constants of integration.

From (2.12), (2.13) and (2.14), we have

$$B^2=\frac{\sqrt{M}}{K}\mu\,\text{sech}\,\phi, \tag{2.15}$$

$$C^2=\frac{K}{\sqrt{M}}\mu\cosh\phi, \tag{2.16}$$

$$D^2=\frac{K\mu}{\sqrt{M}}\left(R-\frac{\sqrt{M}}{K}\tanh\phi\right)^2\cosh\phi \tag{2.17}$$

and

$$CD=\frac{K}{\sqrt{M}}\mu\left(R-\frac{\sqrt{M}}{K}\tanh\phi\right)\cosh\phi. \tag{2.18}$$

Hence, the metric (1.1) reduces to the form

$$dS^2 = \alpha^2(dx^2 - dt^2) + \frac{\mu}{\sqrt{M}} K \cosh\phi\, dz^2 + K\left\{\left(\frac{\mu R^2}{\sqrt{M}} + \frac{\mu\sqrt{M}}{K^2}\right)\cosh\phi - \frac{2\mu R}{K}\sinh\phi\right\} dy^2 + \frac{2\mu}{\sqrt{M}} K\left(R\cosh\phi - \frac{\sqrt{M}}{K}\sinh\phi\right) dy\, dz. \quad (2.19)$$

After suitable transformations, the metric reduces to the form

$$dS^2 = \alpha^2\left(dX^2 - \frac{dT^2}{\log T}\right) + 2T\cosh\phi\, dZ^2 + \left\{\left(2TR^2 + \frac{T}{2}\right)\cosh\phi - 2TR\sinh\phi\right\} dY^2 + 4T\left(R\cosh\phi - \frac{1}{2}\sinh\phi\right) dY\, dZ. \quad (2.20a)$$

In the absence of magnetic field, the metric (2.20a) reduces to the form

$$dS^2 = \alpha^2\left(dX^2 - \frac{dT^2}{\log T}\right) + 2T\cosh\phi\, dZ^2 + \left[\left(2TR^2 + \frac{T}{2}\right)\cosh\phi - 2TR\sinh\phi\right] dY^2 + 4T\left(R\cosh\phi - \frac{1}{2}\sinh\phi\right) dY\, dZ, \quad (2.20b)$$

where $\phi = P - (\log T)^{1/2}$.

3. Some physical and geometrical features

The pressure and density for the model (2.20a) are given by

$$8\pi p = \frac{1}{\alpha^2 T^2}\left(\frac{1}{4}\log T - \frac{9}{16} + \frac{\alpha}{8}\right) - \Lambda, \quad (3.1)$$

$$8\pi\varepsilon = \frac{1}{\alpha^2 T^2}\left(\frac{1}{4}\log T - \frac{1}{16} - \frac{\alpha}{8}\right) + \Lambda. \quad (3.2)$$

The model has to satisfy the reality condition (Ellis (1971)) (i) $\varepsilon + p > 0$ and (ii) $\varepsilon + 3p > 0$.

The condition (i) leads to

$$T^{1/2} > \exp\left(\frac{5}{8}\right). \quad (3.3)$$

The condition (ii) leads to

$$T > \exp\left(\frac{7}{4} - \frac{\alpha}{4} + 16\pi\Lambda\alpha^2 T^2\right) \quad (3.4)$$

which gives condition on Λ. From (3.3) and (3.4), we find that reality conditions are satisfied.

The scalar of expansion θ calculated for the flow vector v^i is given by

$$\theta = \frac{1}{\sqrt{T}}(\log T)^{1/2}. \quad (3.5)$$

The rotation ω is identically zero and the components of shear tensor is given by

$$\sigma_1^1 = -\frac{1}{3\alpha T}(\log T)^{1/2}, \tag{3.6}$$

$$\sigma_2^2 = \frac{1}{\alpha T}\left[\frac{1}{6}(\log T)^{1/2} - LR\right], \tag{3.7}$$

$$\sigma_3^3 = \frac{1}{\alpha T}\left[\frac{1}{6}(\log T)^{1/2} + LR\right], \tag{3.8}$$

$$\sigma_3^2 = \frac{1}{2\alpha T}. \tag{3.9}$$

The non-vanishing components of the conformal curvature tensor are

$$C_{12}^{12} = C_{13}^{13} = -\tfrac{1}{2}C_{23}^{23} = \frac{1}{6\alpha^2 T^2}\left(\frac{1}{2}\log T - \frac{3}{8}\right). \tag{3.10}$$

The model (2.20a) does not exist between $T = 0$ and $T = 1$. At $T = 1$, $\theta = 0$. Hence it starts from rest and goes on expanding till $T = \infty$ when θ is zero again. The model in general represents expanding, shearing and non-rotating universe since $\lim_{T\to\infty}$, $\sigma/\theta \neq 0$. Hence, the model does not approach isotropy for large values of T. The ratio of magnetic energy to material energy is given by

$$\frac{E_4^4}{\varepsilon} = \frac{\sqrt{2}L^{3/2}\alpha T}{4\left[\frac{1}{2}\log T - \frac{L}{8} - \frac{L\alpha}{4} + 8\pi\Lambda a^2 T^2\right]}. \tag{3.11}$$

Since $\lim_{T\to 0} E_4^4/\varepsilon \to 0$, the material energy is more dominant than magnetic energy.

In the absence of magnetic field, the pressure and density for the model (2.20b) are given by

$$8\pi p = \frac{1}{\alpha^2 T^2}\left(\frac{1}{4}\log T + \frac{\alpha}{8} - \frac{9}{16}\right) - \Lambda, \tag{3.12}$$

$$8\pi\varepsilon = \frac{1}{\alpha^2 T^2}\left(\frac{1}{4}\log T - \frac{\alpha}{8} - \frac{1}{16}\right) + \Lambda. \tag{3.13}$$

The expansion θ, the components of shear tensor and non-vanishing components of conformal curvature tensor in the absence of magnetic field are given by

$$\theta = \frac{1}{\alpha T}(\log T)^{1/2}, \tag{3.14}$$

$$\sigma_1^1 = -\frac{1}{3\alpha T}(\log T)^{1/2}, \tag{3.15}$$

$$\sigma_2^2 = \frac{1}{6\alpha T}(\log T)^{1/2}, \tag{3.16}$$

$$\sigma_3^3 = \frac{1}{6\alpha T}(\log T)^{1/2}, \tag{3.17}$$

$$\sigma_3^2 = \frac{1}{2\alpha T} \tag{3.18}$$

and

$$C_{12}^{12} = C_{13}^{13} = -\frac{1}{2}C_{23}^{23}$$

$$= \frac{1}{6\alpha^2 T^2}\left(\frac{1}{2}\log T - \frac{3}{8}\right). \tag{3.19}$$

The reality condition $(\varepsilon + p) > 0$ leads to

$$T^{1/2} > \exp\left(\frac{5}{8}\right).$$

The condition $(\varepsilon + 3p) > 0$ leads to

$$T > \exp\left(\frac{7}{4} - \frac{\alpha}{4} + 16\pi\Lambda\alpha^2 T^2\right)$$

which gives condition on Λ. Thus reality conditions are satisfied for T. The model in the absence of magnetic field starts expanding with a big bang at $T = 0$ and it stops at $T = 1$. In the absence of magnetic field, the model in general represents expanding, shearing, non-rotating and Petrov type I degenerate universe in general. Since $\lim_{T\to\infty} \sigma/\theta$ does not tend to zero, the model does not approach isotropy for large values of T.

Acknowledgements

The authors are thankful to the referee for his valuable comments for the improvement of the paper.

References

[1] B W Stewart, *J. Phys.* **A15**, 2419 (1982)
[2] G F R Ellis and M A H MacCallum, *Commun. Math. Phys.* **12**, 108 (1969)
[3] E Asseo and H Sol, *Phys. Rep.* **6**, 148 (1987)
[4] K S Thorne, *Astrophys. J.* **148**, 51 (1967)
[5] K C Jacobs, *Astrophys. J.* **153**, 661 (1968)
[6] K C Jacobs, *Astrophys. J.* **155**, 379 (1969)
[7] C B Collins, *Commun. Math. Phys.* **27**, 37 (1972)
[8] S R Roy, S Narain and J P Singh, *Aust. J. Phys.* **2**, 239 (1985)
[9] R Bali, *Int, J. Theor. Phys.* **25**, 7 (1986)
[10] R Bali and A Tyagi, *Int. J. Theor. Phys.* **27**, 5 (1988)
[11] R Bali and M Ali, *Int. J. Theor. Phys.* (1996) to appear
[12] S R Roy and S Prakash, *Indian J. Phys.* **B52**, 47 (1978)
[13] S R Roy, R Bali and S Prakash, *Proc. Indian Acad. Sci.* **A87**, 181 (1978)

— journal of
physics

July 1996
pp. 33–39

Stationary rotating string world models with a magnetic field

L K PATEL[1,2] and S D MAHARAJ[1]
[1]Department of Mathematics and Applied Mathematics, University of Natal, Private Bag X10, Dalbridge 4014, South Africa
[2]Permanent address: Department of Mathematics, Gujarat University, Ahmedabad 380009, India

MS received 18 December 1995; revised 26 April 1996

Abstract. Following the techniques used by Letelier and Stachel some new physically relevant stationary solutions of string cosmology with magnetic field are presented. In these solutions, the flow vector of matter has non-zero rotation and the cosmological constant is taken to be non-zero. Previously known solutions are derived as particular cases from our class of solutions. Some string models with vanishing cosmological constant are also discussed.

Keywords. Cosmology; strings; magnetic fields.

PACS Nos 04·20; 98·90

1. Introduction

In recent times, the study of cosmic strings has received the attention of many investigators. The present day observations of the universe do not rule out the possibility of the existence of large scale networks of strings in the early universe [1]. It is believed that cosmic strings give rise to density perturbations which lead to galaxy formations [2]. The cosmic strings possess stress energy and are coupled to the gravitational field. Detailed accounts of various features of cosmic strings are given by Vilenkin [3], Gott [4] and Garfinkle [5].

Cosmic strings in the framework of general relativity have been discussed by Letelier [6] and Stachel [7]. They have given the energy momentum tensor for string distribution in the form

$$M_{ik} = \rho v_i v_k - \lambda w_i w_k, \tag{1}$$

where

$$v^i v_i = -w^i w_i = 1, \quad v^i w_i = 0. \tag{2}$$

Here ρ denotes the energy density of a cloud of strings with particles attached to them and λ is the string tension density. The unit time-like vector v^i is the flow vector and the unit space-like vector w^i specifies the direction of the strings. The particle density associated with the configuration is given by

$$\rho_p = \rho - \lambda. \tag{3}$$

The energy conditions imply $\rho \geqslant 0, \rho_p \geqslant 0$, leaving the sign of string tension density λ unrestricted.

The energy momentum tensor E_{ik} for source-free electromagnetic fields is given by

$$E_{ik} = -g^{lm}F_{il}F_{km} + \tfrac{1}{4}g_{ik}F_{im}F^{lm}, \tag{4}$$

where

$$F_{ik} = A_{i;k} - A_{k;i} \tag{5}$$

and

$$F^{ik}_{;k} = 0. \tag{6}$$

Here F_{ik} is the electromagnetic field tensor and A_i is the electromagnetic 4-potential and a semi-colon indicates covariant differentiation. In the present paper we shall use Einstein field equations in the form

$$R_{ik} - \tfrac{1}{2}Rg_{ik} = -8\pi[M_{ik} + E_{ik}] - \Lambda g_{ik}, \tag{7}$$

where Λ is the cosmological constant.

The string cosmological models with a magnetic field are discussed by Banerjee *et al* [8], Chakraborty [9] and Tikekar and Patel [10, 11]. All these models are non-static and the flow vector v^i is irrotational. Patel and Dadhich [12] have constructed some stationary rotating string models with non-zero cosmological constant. The main purpose of the present article is to introduce an axial magnetic field in the string world models discussed earlier by Patel and Dadhich [12].

Note that rotation plays an important role in the structure and equilibrium configurations of elementary particles, and also in astrophysical bodies. For example the nature of pulsars, which are widely accepted as rotating neutron stars, can only be properly described by including the effects of rotation. During the last three decades many researchers have introduced rotation in the general theory of relativity in discussions of rotating cosmological models. Rotation is likely to significantly affect the behaviour of the gravitational field in the early universe. As we are attempting to model the early universe in terms of networks of strings, rotation should be included in our analysis to determine its effect on the field.

The occurrence of magnetic fields on galactic scales is a well-established fact today, and their importance for a variety of astrophysical phenomena is generally acknowledged as pointed out by Zeldovich *et al* [13]. Also Harrison [14] has suggested that magnetic fields could have a cosmological origin. As a natural consequence we should include magnetic fields in the energy-momentum tensor of the early universe. Therefore rotating string models with magnetic fields may have physical significance for early universe cosmology.

2. The metric and the field equations

We consider a Gödel-type stationary line element in the form

$$ds^2 = (dt + H\,dy)^2 - \alpha^2\,dy^2 - dz^2 - dx^2, \tag{8}$$

where H and α are functions of x only.

$$\theta^1 = \mathrm{d}x, \quad \theta^2 = \alpha \mathrm{d}y, \quad \theta^3 = \mathrm{d}z, \quad \theta^4 = \mathrm{d}t + H\,\mathrm{d}y \tag{9}$$

to write the metric in the form

$$\mathrm{d}s^2 = (\theta^4)^2 - (\theta^1)^2 - (\theta^2)^2 - (\theta^3)^2 = g_{(ab)}\theta^a\theta^b. \tag{10}$$

Here and in what follows the bracketed indices indicate tetrad components. Thus $g_{(ab)} = \mathrm{diag}\{-1, -1, -1, 1\}$ are tetrad components of the metric tensor g_{ik}. Using Cartan's equations of structure one can easily obtain the tetrad components $R_{(ab)}$ of the Ricci tensor for the metric (8). The nonzero $R_{(ab)}$ are given by

$$R_{(11)} = R_{(22)} = \frac{\alpha''}{\alpha} - \frac{H'^2}{2\alpha^2}, \quad R_{(44)} = -\frac{H'^2}{2\alpha^2},$$

$$R_{(24)} = -\frac{1}{2\alpha}\left(H'' - \frac{H'\alpha'}{\alpha}\right). \tag{11}$$

Here and in what follows a prime indicates differentiation with respect to x.

It is easy to see that the field equation (7) can be expressed in the tetrad form as

$$R_{(ab)} = -8\pi[\rho v_{(a)}v_{(b)} - \lambda w_{(a)}w_{(b)}] + 4\pi(p+\lambda)g_{(ab)} - 8\pi E_{(ab)} + \wedge g_{(ab)}. \tag{12}$$

We use comoving coordinates and take the string direction as z-direction. Therefore we have

$$v_{(a)} = (0,0,0,1) \quad w_{(a)} = (0.0,1,0). \tag{13}$$

It is an easy task to check that v_i and w_i given by (13) satisfy the condition (2).

We wish to consider an axial magnetic field along z-axis. Therefore the electromagnetic 4-potential A_i can be taken as

$$A_i = (0, \psi, 0, 0), \tag{14}$$

where ψ is a function of x only and the coordinates are named as $x^1 = x$, $x^2 = y$, $x^3 = z$, $x^4 = t$. Therefore the only non-vanishing component F_{12} of the electromagnetic field tensor is given by $F_{12} = -\psi'$. The Maxwell equation (6) lead to

$$\psi' = K\alpha, \tag{15}$$

where K is a constant of integration. The surviving E_{ik} are found to have the expressions

$$E_{11} = E_{44} = -E_{33} = E_{24}/H = E_{22}|_{(H^2+\alpha^2)} = \tfrac{1}{2}K^2. \tag{16}$$

The tetrad components $E_{(ab)}$ of E_{ik} can be obtained from

$$E_{(ab)} = \mathrm{e}^i_{(a)}\mathrm{e}^k_{(b)}E_{ik}, \quad \mathrm{e}^i_{(a)}\theta^a = \mathrm{d}x^i.$$

The surviving $E_{(ab)}$ are given by

$$E_{(11)} = E_{(22)} = -E_{(33)} = E_{(44)} = \tfrac{1}{2}K^2. \tag{17}$$

In view of (10), (13) and (17), the field equation (12) give the following non-trivial relations:

$$R_{(24)} = 0, \tag{18}$$

$$R_{(11)} = -4\pi(\rho + \lambda) - 8\pi E_{(11)} - \Lambda, \tag{19}$$

$$\Lambda = 4\pi(\lambda - \rho) - 8\pi E_{(33)}, \tag{20}$$

$$R_{(44)} = -8\pi E_{(44)} + 4\pi(\lambda - \rho) + \Lambda, \tag{21}$$

where $R_{(ab)}$ are given by (11).

Equation (18) is easily integrable. The solution of this equation is

$$\frac{H'}{\alpha} = \text{constant} = m, \quad \text{say.} \tag{22}$$

From (20), (21) and (22) we obtain

$$\Lambda = -\tfrac{1}{4}m^2 + 4\pi K^2. \tag{23}$$

It is interesting to note that the cosmological constant Λ depends upon the magnetic field also. From (19) and (20) we get

$$8\pi\lambda = \frac{m^2}{2} - 8\pi K^2 - \frac{\alpha''}{\alpha}, \tag{24}$$

$$8\pi\rho = m^2 - 8\pi K^2 - \frac{\alpha''}{\alpha}. \tag{25}$$

Obviously the strings satisfy the equation of state $\rho = \lambda + (m^2/16\pi)$.

From the results (24) and (25) we have

$$8\pi\rho_p = \frac{m^2}{2}. \tag{26}$$

Note that ρ_p is independent of magnetic field and is always positive.

We have checked that the velocity field v_i given by (13) has vanishing expansion, shear and acceleration. But the rotation Ω of the velocity field v_i is non-zero and it is given by

$$\Omega = \sqrt{2}m. \tag{27}$$

As the metric potential α remains undetermined, we can have many rotating string models with a magnetic field. In the next section we shall give some physically relevant explicit solutions of the equations (22)–(25).

From the results (26) and (27) it is clear that the rotation Ω and the particle density ρ_p are intimately linked. The rotating character of the string is determined by the component Ω. The vanishing of Ω implies the vanishing of ρ_p. Thus in the absence of rotation, we have $\rho = \lambda$ and consequently we regain string-dust cosmological models.

3. Explicit solutions

Case (i): $\Lambda = 0$.

If the cosmological constant Λ is zero, we have $m^2 = 16\pi K^2$. In this case we obtain

$$8\pi\lambda = -\frac{\alpha''}{\alpha}, \quad 8\pi\rho = 8\pi K^2 - \frac{\alpha''}{\alpha}, \quad \Omega = 4\sqrt{2\pi}K. \tag{28}$$

Here two particular cases are noteworthy.

Case (ia): $\alpha'' = 0$ (i.e. $\alpha = x$).

In this case string tension density λ vanishes. The line element in this case becomes

$$ds^2 = (dt + 4K\sqrt{\pi}x dy)^2 - x^2 dy^2 - dx^2 - dz^2. \tag{29}$$

This metric represents a dust-filled stationary rotating universe with magnetic field whose density is given by $\rho = K^2$. Thus the rotation and the density entirely depend upon the magnetic field. When the magnetic field is switched off, the metric (29) reduces to

$$ds^2 = dt^2 - x^2 dy^2 - dx^2 - dz^2. \tag{30}$$

The metric (30) is a flat metric. The required simple transformation is $X = x\cos y$, $Y = x \sin y$. Thus the matter-free limit of this rotating dust model is a flat metric.

Case (ib): $\alpha''/\alpha = -n^2$.

In this case we have

$$8\pi\lambda = n^2, \quad 8\pi\rho = 8\pi K^2 + n^2, \quad \Omega = 4\sqrt{2\pi}K. \tag{31}$$

When the magnetic field is removed, we get a static string-dust solution obtained earlier by Patel and Dadhich [12]. The geometry of this solution is described by the metric

$$ds^2 = \left(dt + \frac{4K\sqrt{\pi}}{n}\sin nx\, dy\right)^2 - \cos^2 nx\, dy^2 - dx^2 - dz^2. \tag{32}$$

Case (ii): $\lambda = 0$.

In this case we have

$$8\pi\rho = 8\pi\rho_p = \frac{m^2}{2}, \quad \Omega = \sqrt{2}m, \quad \frac{\alpha''}{\alpha} = \frac{m^2}{2} - 8\pi K^2. \tag{33}$$

The subcase $\alpha'' = 0$ has been considered in case (i). Here there are two subcases to be considered.

Case (iia): $m^2 > 16\pi K^2$.

Let us put $m^2 - 16\pi K^2 = 2a^2$. We have in this case

$$\Lambda = -\frac{a^2}{2}, \quad \alpha = e^{ax}, \; H = \frac{m}{a}e^{ax}, \quad 8\pi\rho = a^2 + 8\pi K^2. \tag{34}$$

The line element of this case is

$$ds^2 = \left(dt + \frac{m}{a}e^{ax}dy\right)^2 - e^{2ax}dy^2 - dx^2 - dz^2. \tag{35}$$

The metric (35) represents the Gödel [15] universe with a magnetic field.

Case (iib): $m^2 < 16\pi K^2$.

Let us put $m^2 - 16\pi K^2 = -2b^2$, i.e. $m^2 = 16\pi K^2 - 2b^2$. Note that here we cannot remove the magnetic field. In this case we have

$$\Lambda = \frac{b^2}{2}, \quad 8\pi\rho = 8\pi K^2 - b^2, \quad \alpha = \cos bx,$$

$$H = \frac{m}{b}\sin bx, \quad \Omega = \sqrt{2}m. \tag{36}$$

The final form of the metric of this subcase is

$$ds^2 = \left(dt + \frac{m}{b}\sin bx\, dy\right)^2 - \cos^2 bx\, dy^2 - dx^2 - dz^2. \tag{37}$$

When $\rho = 0$, i.e. $b^2 = 8\pi K^2$, the rotation vanishes and the metric (37) reduces to the metric of a simple magnetic universe discussed by Patel and Vaidya [16]. Thus the metric (37) represents a dust-filled generalization of the simple magnetic universe discussed by Patel and Vaidya [16].

Case (iii): Takabayashi strings.

Let us assume that the string distribution has the equation of state

$$\rho = (1 + W)\lambda, \tag{38}$$

where W is a positive constant. Such strings are known as Takabayashi strings.

The substitution of ρ and λ from (25) and (24) in the result (38) yields the differential equation

$$\frac{\alpha''}{\alpha} = \frac{m^2(W-1) - 16\pi W K^2}{2W}. \tag{39}$$

The solution of (39) depends upon the values of the constants m, W and K. In this case we have

$$8\pi\rho = \frac{m^2(1+W)}{2W}, \quad 8\pi\lambda = \frac{m^2}{2W}, \quad \Lambda = -\tfrac{1}{4}m^2 + 4\pi K^2. \tag{40}$$

As $W > 0$, the energy conditions are satisfied. Let us put

$$m^2(W-1) - 16WK^2 = 2W\varepsilon a^2. \tag{41}$$

Then

$$\alpha = \begin{cases} x \\ e^{ax} \\ \cos ax \end{cases} \quad \text{when} \quad \varepsilon = \begin{cases} 0 \\ 1 \\ -1 \end{cases}. \tag{42}$$

In each case we can write the explicit forms of the line elements. For the sake of brevity we shall not give these details here. When the magnetic field is switched off (i.e. $K = 0$), we get the solution for Takabayashi strings discussed by Patel and Dadhich [12].

4. Discussion

Note that the solutions presented in this paper are all homogeneous. This essentially follows because of our particular choice for the function α; other choices of α are certainly possible. Clearly there exists forms for α which would lead to inhomogeneous solutions. We provide a simple example of a solution which is inhomogeneous in nature. Let us assume that $m^2 - 8\pi K^2 = 4a^2$, i.e. $m^2 - 8\pi K^2$ is positive. Also take $\alpha = \cosh^2 ax$. Then we have

$$8\pi\rho = 2a^2 \operatorname{sech}^2 ax, \quad 8\pi\lambda = 8\pi\rho - \tfrac{1}{2}m^2,$$

$$H = \frac{m}{2}\left[x + \frac{1}{2a}\sinh 2ax\right].$$

The geometry of this inhomogeneous rotating string model is described by the line element

$$ds^2 = \left[dt + \frac{m}{2}\left(x + \frac{1}{2a}\sinh 2ax\right)dy\right]^2 - dx^2 - dz^2 - \cosh^4 ax\, dy^2,$$

where a is determined by the above relationship.

There are few exact solutions to the Einstein equations for cosmic strings available in the literature. We have made an attempt to obtain more exact solutions so that our understanding of cosmic strings may be improved. It would be interesting to find non-static generalizations of the solutions discussed above.

Acknowledgements

L K Patel wishes to thank the University of Natal for hospitality and Gujarat University for leave of absence. The authors thank Prof. A K Raychaudhuri for useful comments.

References

[1] T W S Kible, *J. Phys.* **A9**, 1357 (1976)
[2] Ya B Zeldovich, *Mon. Not. R. Astron. Soc.* **192**, 663 (1980)
[3] A Vilenkin, *Phys. Rev.* **D24**, 2082 (1981)
[4] J R Gott, *Astrophys. J.* **288**, 422 (1985)
[5] D Garfinkle, *Phys. Rev.* **D32**, 1323 (1985)
[6] P S Letelier, *Phys. Rev.* **D20**, 1294 (1979)
[7] J Stachel, *Phys. Rev.* **D21**, 2171 (1980)
[8] A Banerjee, A K Sanyal and S Chakraborty, *Pramana – J. Phys.* **34**, 1 (1990)
[9] S Chakraborty, *Indian J. Pure Appl. Phys.* **29**, 31 (1991)
[10] R Tikekar and L K Patel, *Gen. Relativ. Gravit.* **24**, 31 (1992)
[11] R Tikekar and L K Patel, *Pramana – J. Phys.* **42**, 483 (1994)
[12] L K Patel and N Dadhich, to be published (1996)
[13] Ya B Zeldovich, A A Ruzmainkin and D D Sokoloff, *Magnetic fields in Astrophysics* (New York, Gordon and Breach, 1993)
[14] E R Harrison, *Phys. Rev. Lett.* **30**, 188 (1973)
[15] K Gödel, *Rev. Mod. Phys.* **21**, 447 (1949)
[16] L K Patel and P C Vaidya, *Curr. Sci.* **40**, 278 (1971)

A model of the universe with decaying vacuum energy

ABDUSSATTAR and R G VISHWAKARMA
Department of Mathematics, Banaras Hindu University, Varanasi 221 005, India

MS received 8 February 1996; revised 13 May 1996

Abstract. The consequences of taking the total active gravitational mass of the universe phasewise constant together with a decaying vacuum energy in the background of Robertson–Walker space-time are investigated. The model so determined admits a contracted Ricci-collineation along the fluid flow vector v^i. It is geometrically closed but ever-expanding and does not possess the initial singularity, horizon, entropy, monopole or cosmological constant problems of the standard big bang cosmology. Estimates of the present matter, radiation and vacuum energy densities, the age of the universe and the present values of the deceleration parameter and the scale factor are also obtained.

Keywords. RW space-time; cosmological constant-time variation; vacuum energy; active gravitational mass.

PACS No. 98·80

1. Introduction

In recent times the cosmological constant Λ has interested theoreticians and observers for various reasons [1]. The non-trivial role of the vacuum in the early universe generates a Λ-term in the Einstein field equations that leads to the inflationary phase [2]. The inflationary cosmology postulates that during an early exponential phase, the vacuum energy was a large cosmological constant. Therefore, in view of the smallness of the cosmological constant observed at present, it is natural to assume that the cosmological constant Λ, representing the energy density of vacuum, is a variable dynamic degree of freedom which being initially very large relaxes to its small present value in an expanding universe. The idea of a dynamically decaying cosmological constant with cosmic expansion has been considered by several authors in the past few years [3–8]. Linde [9] has proposed that Λ is a function of temperature and is related to the process of broken symmetries. Gasperini [6] in this regard, argues that the cosmological constant Λ can also be interpreted as a measure of the temperature of cosmic vacuum which should decrease, like the radiation temperature, with cosmic expansion.

In the present paper, a time-varying cosmological constant representing the energy density of vacuum is considered within the framework of general relativity. Motivation is given for taking the total active gravitational mass of an isotropic and homogeneous universe phasewise constant and a model of the universe is investigated. It is found that the vacuum decays differently in the different phases of evolution depending upon the equation of state of the matter content. The resulting model is geometrically closed but

2. The field equations

The universe is assumed to be filled with distribution of matter represented by the energy-momentum tensor of a perfect fluid

$$T_{ij} = (\rho + p)v_i v_j + p g_{ij}, \quad \text{(in the units with } c = 1\text{)}, \tag{2.1}$$

where ρ is the energy density of the cosmic matter and p is its pressure. The geometry of an isotropic and homogeneous universe is described by the Robertson–Walker metric

$$ds^2 = -dt^2 + R^2(t)\left\{\frac{dr^2}{(1-kr^2)} + r^2(d\theta^2 + \sin^2\theta\, d\phi^2)\right\} \tag{2.2}$$

characterized by its scale factor $R(t)$ and the curvature parameter $k(= \pm 1, 0)$. The gravitational effects of matter and vacuum in the universe together control the nature of expansion and provide a tool to determine $R(t)$ and k through the Einstein field equations

$$R_{ij} - \tfrac{1}{2}R^h_h g_{ij} = -8\pi G\left(T_{ij} - \frac{\Lambda(t)}{8\pi G}g_{ij}\right). \tag{2.3}$$

In view of the vanishing divergence of the Einstein tensor, Λ would become constant in the absence of matter (i.e. for $T_{ij} = 0$) implying that the presence of matter is essential for a time-varying Λ. Thus the incorporation of a time-dependent cosmological constant $\Lambda(t)$ in the Einstein field equations amounts to assuming that in the presence of the usual energy momentum tensor of the matter content T_{ij} of the universe, there is an additional piece $-(\Lambda/8\pi G)g_{ij}$ which may be regarded as the energy momentum tensor of vacuum

$$T^{(\text{vac})}_{ij} = -\frac{\Lambda}{8\pi G}g_{ij}, \tag{2.4}$$

representing a perfect fluid with its energy density ρ_v and homogeneous, isotropic pressure p_v satisfying the equation of state

$$p_v = -\rho_v = -\frac{\Lambda}{8\pi G}. \tag{2.5}$$

Thus the total energy momentum tensor of the universe due to the matter and the vacuum can be written as

$$T^{(\text{tot})}_{ij} \equiv T_{ij} + T^{(\text{vac})}_{ij} = (\rho_t + p_t)v_i v_j + p_t g_{ij}, \tag{2.6}$$

where $\rho_t = \rho + \rho_v$ and $p_t = p + p_v$. Obviously it is the total energy momentum tensor, due to the matter and the vacuum, which is conserved and not the two separately. However, the representation of Λ term by (2.4) and (2.5) is only a gross way of describing the vacuum. One would really like to replace Λ by a term that gives a proper description of the physics of the vacuum as T_{ij} does for the matter. But the main thing which is

lacking for a unified theory of gravitation and particle physics is a proper energy momentum tensor for the vacuum [10]. In the context of (2.1), (2.2) and (2.5), the field equation (2.3) yields

$$-\frac{\ddot{R}}{R}=\frac{4\pi G}{3}(\rho+3p-2\rho_v)\equiv\frac{4\pi G}{3}(\rho_t+3p_t) \tag{2.7}$$

and

$$\frac{\dot{R}^2}{R^2}+\frac{k}{R^2}=\frac{8\pi G}{3}(\rho+\rho_v)\equiv\frac{8\pi G}{3}\rho_t. \tag{2.8}$$

Equation (2.7) may be deemed as an analogue of the Newtonian force law and suggests that the force per unit mass at each space-time point is determined by the active gravitational mass density $(\rho+3p)$ causing an attractive force together with the vacuum energy acting as a repulsive force. It is this repulsive force which drives expansion, with the classical de-Sitter inflation, in the early vacuum dominated universe. Here we note that the gravitational pull is exerted not only by ρ, as in the Newtonian theory, but rather by $(\rho+3p)$ which exhibits a relativistic effect. It is this additional pressure and internal energy contribution to the gravitational force which is the major cause of the problem of gravitational collapse in general relativity.

In the standard model (with $\rho_v=0$), (2.7) and (2.8) obtain $\rho R^3=$ constant in the present pressureless phase of evolution which can be interpreted as the conservation of the active gravitational mass of the comoving sphere of radius R. As there is no justification of conferring a special status upon the present epoch, we speculate that this constancy feature of the active gravitational mass is met not only in the present phase of evolution but in the early phases too. We thus assume that in the presence of pressure, the active gravitational mass is constant, i.e.

$$(\rho+3p)R^3=\text{constant}. \tag{2.9}$$

It may be noted that $\rho R^3=$ constant is a consequence of the field equations in the absence of pressure, whereas $(\rho+3p)R^3=$ constant is the result of the restriction that we have imposed on the model.

Equation (2.9), taken together with the energy-momentum conservation equation

$$\dot{\rho}+3(\rho+p)\frac{\dot{R}}{R}=0, \tag{2.10}$$

leads to

$$p^3=K(\rho+3p)^2,\quad K=\text{constant}\geqslant 0, \tag{2.11}$$

which is the equation of state for the perfect fluid constituting the matter content of the universe. It is a physically reasonable equation of state since

$$\frac{dp}{d\rho}=\frac{2}{3}\cdot\frac{p}{(\rho+p)}, \tag{2.12}$$

indicating that $dp/d\rho<1/3$ for $\rho>p$. The equation of state (2.11) taken together with the field equations leads to big bang models which we have already discussed [11].

In the presence of ρ_v, where the active gravitational mass density is modified as $(\rho_t + 3p_t)$ or equivalently as $(\rho + 3p - 2\rho_v)$, (2.9) representing the conservation of the active gravitational mass is then modified as

$$(\rho_t + 3p_t)R^3 \equiv (\rho + 3p - 2\rho_v)R^3 = \text{constant} = A(\text{say}), \tag{2.13}$$

and the energy-momentum conservation equation (2.10) is replaced by

$$\dot{\rho}_t + 3(\rho_t + p_t)\frac{\dot{R}}{R} = 0. \tag{2.14}$$

It may be noted that the constant A appearing in (2.13) may assume different values (even zero and negative ones) in the different phases of evolution specially for a decaying vacuum energy which may generate relativistic or non-relativistic particles. This is because the total active gravitational mass A is the resultant of two components; (i) a gravitational attraction caused by the material part $(\rho + 3p)$ and (ii) a repulsion produced by the vacuum. The value of A at any epoch therefore depends upon the relative contribution of these two components and hence on the relative dominance of matter and vacuum at that epoch. In the early vacuum dominated phase, $A < 0$ as (2.13) indicates. As soon as the vacuum balances its material counterpart, A becomes zero. When the vacuum further reduces and gets dominated by matter, A becomes positive. Thus the total active gravitational mass is conserved phasewise only and not throughout the evolution. The non-conservation of the active mass across phases may be a result of two phase transitions occurring in the early universe which lead to the restoration of the originally broken symmetry between weak, strong and electromagnetic interactions and thus results in a number of striking and unusual effects which take place during the phase transitions. Almost all elementary particles become massless, weak and strong interactions become long-range like electromagnetic interactions and large inhomogeneities in the energy density is created forming black holes which, after the phase transition, are soon evaporated due to the Hawking effect [12]. These phase transitions also account for the changes in $\ddot{R}$ via the discontinuities in A as is clear from

$$\ddot{R} = -\frac{4\pi GA}{3R^2}, \tag{2.15}$$

which may be obtained from (2.7) and (2.13).

As the conservation laws are closely related with the symmetry properties of the physical systems, it is natural to look for the symmetry of the space-time linked with the conservation law (2.13). In this connection, we note that a space-time is said to admit Ricci-collineation along a field vector η^i [13] if $\mathcal{L}_\eta R_{ij} = 0$, where $\mathcal{L}_\eta$ denotes the Lie-derivative along η^i. If the Ricci tensor is Lie-transported along η^i, then there exists a conservation law generator of the form $[R^j_m \eta^m]_{;j} = 0$ [14] and if Einstein's field equation (2.3) is satisfied, this can be written as $[T^j_m \eta^m + (\rho_v - \frac{1}{2}T)\eta^j]_{;j} = 0$ which provides the symmetries of the stress energy tensor depending upon the specific character of the symmetry vector η^i. Also a space-time is said to admit a family of contracted Ricci-collineation if $g^{ij}\mathcal{L}_\eta R_{ij} = 0$ which leads to a conservation law generator of the form $[\sqrt{-g}\{T^j_m \eta^m + (\rho_v - \frac{1}{2}T)\eta^j\}]_{;j} = 0$ [15]. Now we recall the symmetries of the

Robertson–Walker metric belonging to the family of contracted Ricci-collineation discussed by Green *et al* [16] for the symmetry vector proportional to the fluid flow vector v^i. Out of the three possible choice for $\mathcal{L}R_{ij}$ studied by them, the one having $\mathcal{L}R_{ij} = \lambda(R_{ij} - \frac{1}{4}R^h_h g_{ij})$ leads to a symmetry vector $\eta^i = \psi v^i$ given by $\psi = \text{constant}/\dot{R}R^2$. Thus, in view of (2.15) which is a consequence of the conservation law (2.13), it follows that the space time admits a contracted Ricci-collineation along the fluid flow vector v^i. The conservation law (2.13) also follows directly from the conservation law generator $[\sqrt{-g}\{T^j_m\eta^m + (\rho_v - \frac{1}{2}T)\eta^j\}]_{;j} = 0$ for the symmetry vector $\eta^i = \text{constant} \times v^i$ and T_{ij} given by (2.1).

It may also be noted that the left hand side of (2.7) is the Gaussian curvature of the two dimensional surface specified by varying r and t, keeping θ and ϕ constant in (2.2) and may be considered as the curvature of the isotropic, homogeneous space-time (2.2). Thus (2.7) indicates that the curvature of the space-time is governed by the total active gravitational mass density of the universe which continuously rolls down in an expanding universe, as (2.13) indicates. This consequently transforms the space-time from a state of large curvature to a state of flatness as $t \to \infty$.

The integration of (2.15) gives

$$\dot{R}^2 = \frac{8\pi GA}{3R} + B, \tag{2.16}$$

where B is a constant of integration. It is important to note that (2.16), whose integral supplies the time-variation of the scale factor $R(t)$, is independent of k – at least in the absence of any further constraint imposed on the model. It may be noted that in the standard model, three competing terms drive the universal expansion: a matter term, a cosmological constant term and a curvature term, via (2.8), for an universe which is respectively open, flat and closed as $k = -1, 0$ and $+1$. In the present case, the curvature index $k = \pm 1, 0$ plays its role via the equation of state and the initial conditions.

Equations (2.8), (2.13) and (2.16) may be used to obtain

$$\rho_t \equiv \rho + \rho_v = \frac{A}{R^3} + \frac{3(B+k)}{8\pi GR^2} \tag{2.17}$$

and

$$p_t \equiv p - \rho_v = -\frac{(B+k)}{8\pi GR^2}. \tag{2.18}$$

One can observe that the different suitable choices of B and k in (2.18) may obtain the variations of ρ_v, in the present pressureless phase of evolution, as obtained by various authors in their models [3,4]. If one chooses B and k in such a way that $B + k = \delta$, where δ is a positive constant of order 1, one would get $\rho_v = \delta/8\pi GR^2$ as obtained by Chen and Wu [3] from a dimensional analysis made in the spirit of quantum cosmology. For $B = 2$ with $k = 1$, (2.18) gives $\rho_v = 3/8\pi GR^2$ and (2.16)–(2.18) give $\rho = \rho_c (\equiv 3H^2/8\pi G)$ as obtained by Ozer and Taha [4].

As we have only two independent equations (2.17) and (2.18) in three unknowns ρ, p and ρ_v, we need an extra equation to solve the system uniquely. This is supplied by the equation of state of the matter content. We assume that the energy density of the

Thus the assumption (2.13), taken together with Einstein's field equations, determines the time variation of the scale factor $R(t)$ and leaves the vacuum energy density ρ_v to be treated on the same footing as the material energy densities ρ_m and ρ_r so that like ρ_m and ρ_r, ρ_v too varies differently in the different phases of evolution.

Equations (2.17) and (2.18), together with (2.16) imply that

$$\rho + p = \rho_c, \quad \text{provided we take } B = 2k. \tag{2.20}$$

However, $k = -1$ demands $\rho_v < 0$ for $p = 0$. Equation (2.20), taken together with (2.19), suggests that

$$\frac{\rho}{\rho_c} \simeq \begin{cases} \frac{3}{4}, & \text{when } \rho \simeq \rho_r \gg \rho_m \text{ (in the early radiation dominated universe),} \\ 1, & \text{when } \rho \simeq \rho_m \gg \rho_r \text{ (in the present matter dominated universe).} \end{cases} \tag{2.21}$$

This favours the presence of some sort of dark matter which has not been detected so far.

The total-energy conservation equation (2.14), which may alternatively be written as

$$\frac{\mathrm{d}}{\mathrm{d}t}(\rho R^3) + p\frac{\mathrm{d}R^3}{\mathrm{d}t} + R^3\frac{\mathrm{d}\rho_v}{\mathrm{d}t} = 0, \tag{2.22}$$

suggests that the change in the entropy of matter content of the universe, given by

$$T\mathrm{d}S \equiv \mathrm{d}(\rho R^3) + p\mathrm{d}R^3 = -R^3\mathrm{d}\rho_v, \tag{2.23}$$

is always increasing for a decaying vacuum energy though the total entropy, of matter and vacuum taken together, remains conserved as is clear from (2.14). Thus there is a spontaneous creation of matter in the form of radiation out of the vacuum energy provided $\dot{\rho}_v < 0$, which is the case in our model as we shall see later on. This can also be seen by integrating (2.22) which, in the early pure radiation era ($\rho_m = 0$) with the equation of state given by (2.19), gives

$$\rho_r = \rho_{r0}\left(\frac{R_0}{R}\right)^4 - \frac{1}{R^4}\int_{R_0}^{R} R'^4\frac{\mathrm{d}\rho_v}{\mathrm{d}R'}\mathrm{d}R', \tag{2.24}$$

where $\rho_r = \rho_{r0}$ at $R = R_0$. The subscript zero stands for the value of the quantity at $t = 0$. When matter and radiation are both present ($\rho = \rho_m + \rho_r$), equation (2.22) reads

$$\frac{\mathrm{d}}{\mathrm{d}t}(\rho_m R^3) + \frac{\mathrm{d}}{\mathrm{d}t}(\rho_r R^3) + p\frac{\mathrm{d}R^3}{\mathrm{d}t} + R^3\frac{\mathrm{d}\rho_v}{\mathrm{d}t} = 0. \tag{2.25}$$

Vacuum coupling primarily to matter would imply the continuous creation of baryon-antibaryon pairs. Naively, one would expect this effect to be greatly suppressed relative to radiation production. Moreover, observations so restrict the size of such a matter creation term that one would get [5]

$$\frac{\mathrm{d}}{\mathrm{d}t}(\rho_m R^3) \simeq 0, \tag{2.26}$$

so that (2.24) may be considered approximately valid for the radiation component in both—the radiation dominated as well as matter dominated eras, which shows that for $\dot{\rho}_v < 0$ with $\dot{R} > 0$, the vacuum generates a positive contribution to ρ_r. Even when $\rho_{r0} = 0$, (2.24) is valid and the vacuum energy then represents the curvature of the empty space-time which soon makes the universe non-empty by generating radiation. Thus the radiation will be created from a decaying vacuum energy all the time transforming the space-time from a state of large curvature to a state of flatness as $t \to \infty$.

We thus see that the energy momentum tensor of vacuum represented by (2.4), which is a negative field, acts just like a creation field proposed by Hoyle and Narlikar [17] operating through the interaction of a zero rest mass scalar filed C of negative energy, with matter. Because of its negative energy, the C-field has a repulsive effect tending to expand the space-time as does the positive cosmological constant Λ. In fact continuous creation can be accounted for with the equations of conventional general relativity plus an equation of state that includes negative pressure and a positive matter density [18].

The model is now completely specified in dynamical structure. The provisions for an initial condition and an equation of state, which is supplied by (2.19), determine its physical content. In the following sections, we investigate its cosmological consequences, starting with the initial phase of pure radiation.

3. The very early universe

We choose the initial time $t = 0$, when $\rho_{r0} = \dot{R} = 0$ and hence the whole vacuum energy is then locked up in potential form in the curvature of empty space-time. With this, (2.16), (2.17) and (2.18) suggest that $A = -3kR_0/4\pi G$, $B = 2k$ and $\rho_{v0} = 3k/8\pi G R_0^2$. As ρ_v is always positive in this model, we have $k > 0$ so that

$$k = 1, \quad A = -\frac{3R_0}{4\pi G} \text{ and } B = 2. \tag{3.1}$$

It is noteworthy that the initial conditions necessarily require the curvature index k to be positive. Further, the curvature can be looked upon as being generated by the Λ term which, as evolution proceeds, itself generates the radiation as evidenced by (2.24).

By the use of (3.1), (2.15) reduces to

$$\ddot{R} = \frac{R_0}{R^2}, \tag{3.2}$$

which indicates that $\ddot{R} > 0$ implying that the expansion is being driven by some general (non-exponential) type of inflation throughout the era. With (3.1), the solution of (2.16) obtains

$$R = R_0 \operatorname{cosec}^2 \psi, \quad t = \frac{R_0}{\sqrt{2}}\left(\ln \cot \frac{\psi}{2} + \operatorname{cosec} \psi \cot \psi\right). \tag{3.3}$$

The parameter ψ appearing in (3.3) can be eliminated, giving

$$t = \frac{R_0}{\sqrt{2}} \ln\left(\frac{\sqrt{R} + \sqrt{R - R_0}}{\sqrt{R_0}}\right) + \sqrt{\frac{R(R - R_0)}{2}}. \tag{3.4}$$

With (3.1), equations (2.17) and (2.18) obtain

$$\rho_r = \frac{\alpha}{R^2}\left[1 - \frac{R_0}{R}\right], \tag{3.5}$$

$$\rho_v = \frac{\alpha}{R^2}\left[1 - \frac{R_0}{3R}\right], \tag{3.6}$$

where $\alpha = 9/16\pi G$. The differentiation of (3.5) and (3.6) with respect to the cosmic time t yields

$$\dot{\rho}_r = -\frac{2\alpha\dot{R}}{R^4}\left[R - \frac{3}{2}R_0\right], \tag{3.7}$$

$$\dot{\rho}_v = -\frac{2\alpha\dot{R}}{R^4}[R - \tfrac{1}{2}R_0], \tag{3.8}$$

which indicate that for $\dot{R} \gtrless 0$, $\dot{\rho}_r \lessgtr 0$ according as $R \gtrless 1{\cdot}5R_0$ while $\dot{\rho}_v \leqslant 0$ throughout the era implying that the vacuum is continuously decaying in this era and transforming into radiation whose energy density ρ_r, which is zero initially, reaches its maximum at $R = 1{\cdot}5R_0$ or equivalently at $t = 1{\cdot}24R_0$. Thereafter, it begins to decrease which may be a result of fast expansion of the universe. As soon as the created radiation reaches thermal equilibrium, it may be characterized by its temperature T given by

$$\rho_r = \frac{\pi^2}{30}N(T)\,T^4, \tag{3.9}$$

in suitable units. Here the effective number of spin degrees of freedom $N(T)$ at temperature T is given by

$$N(T) = N_b(T) + \tfrac{7}{8}N_f(T), \tag{3.10}$$

where $N_b(T)$ and $N_f(T)$ correspond to bosons and fermions respectively. We assume $N(T)$ to be constant throughout the pure radiation era. From (3.5) and (3.9), we have

$$T = \left[\frac{30\alpha}{\pi^2 N}\right]^{1/4}\left[\frac{1}{R^2}\left(1 - \frac{R_0}{R}\right)\right]^{1/4}. \tag{3.11}$$

Thus the temperature T is zero initially. It remains finite for all finite values of t and reaches a maximum at $t = 1{\cdot}24R_0$, given by

$$T_{max} = \left[\frac{40\alpha}{9\pi^2 N R_0^2}\right]^{1/4}. \tag{3.12}$$

The model although starts from a cold state but need not, however, be much different from a hot initiation, for a small R_0, since the temperature increases very rapidly within a time scale of order R_0.

In order to have an estimate of R_0, we relate it with the Planck mass M_{pl}, by assuming that

$$T_{max} = M_{pl} = G^{-1/2}. \tag{3.13}$$

This amounts to

$$R_0 \simeq 0{\cdot}28 M_{\rm pl}^{-1} N^{-1/2} \simeq 2{\cdot}3 \times N^{-1/2} \times 10^{-20} (\text{GeV})^{-1}. \tag{3.14}$$

Thus the maximum temperature, at $R = 1{\cdot}5R_0$, is achieved at a very early time, at $t \simeq 10^{-44}$ sec.

For $R \gg 1{\cdot}5R_0$, (3.4) obtains

$$R \simeq \sqrt{(2)}t. \tag{3.15a}$$

Hence for $R \gg 1{\cdot}5R_0$, (3.5), (3.6) and (3.11) reduce to

$$\rho_{\rm r} \simeq \rho_{\rm v} \simeq \frac{\alpha}{(\sqrt{2}t)^2}, \tag{3.15b}$$

and

$$T \simeq \left[\frac{30\alpha}{\pi^2 N}\right]^{1/4} \frac{1}{(\sqrt{2}t)^{1/2}}. \tag{3.15c}$$

The corresponding expressions for these variables in the standard model are given by

$$R_{\rm SM} \sim t^{1/2}, \tag{3.16a}$$

$$\rho_{\rm rSM} = \frac{\alpha}{(\sqrt{6}t)^2} \tag{3.16b}$$

and

$$T_{\rm SM} = \left[\frac{30\alpha}{\pi^2 N}\right]^{1/4} \frac{1}{(\sqrt{6}t)^{1/2}}. \tag{3.16c}$$

Thus for $R \gg 1{\cdot}5R_0$, the values of the radiation energy density and temperature attained at time t in the standard model are attained at time $\sqrt{3}t$ in the present model. We thus see that although the present model is clearly different from the standard model in several respects such as cold initiation, non-adiabaticity and regularity at $t = 0$, it possesses for $T \geqslant T_{\rm max}$ almost the same thermal history as the standard model. However, the time dependence of R in the present model is altogether different from that of the standard model which may be effective in solving the horizon problem. As the universe is geometrically closed ($k = 1$) in the present model, it is possible to determine the time $t = t_{\rm cau}$ when the whole universe becomes causally connected. This is given by [4, 19]

$$\int_0^{t_{\rm cau}} \frac{{\rm d}t}{R(t)} = \int_0^1 \frac{{\rm d}r}{\sqrt{(1-r^2)}} = \frac{\pi}{2} \tag{3.17}$$

which, by the use of (3.3), obtains

$$t_{\rm cau} \simeq 2{\cdot}4R_0 \simeq 0{\cdot}68 M_{\rm pl}^{-1} N^{-1/2} \tag{3.18}$$

indicating that the global causal connection in the present model has been established at a very early time – of the order of Planck time. Thus the present model does not have a horizon problem. When the global causality is established, the maximum temperature is surpassed and the whole universe attains the temperature $T_{\rm cau}$, given by

$$T_{\rm cau} = 0{\cdot}859 T_{\rm max}, \tag{3.19}$$

which indicates that the whole universe becomes causally connected soon after attaining the Planck temperature.

4. Period of rest mass generation

Equations (3.5) and (3.6) indicate that as R becomes larger than R_0, ρ_v gradually tends to ρ_r. When $\rho_v = \rho_r$ at $R = R_1$ (say), which may be taken as the first phase transition in the model, $A = \ddot{R} = 0$, as (2.13) and (2.15) indicate, and the universe starts to expand linearly. In this phase, the radiation energy is converted into rest mass by some mechanism until the rest mass density ρ_m attains a maximum, say at $R = R_2$ which may be taken as the second phase transition leading to $\ddot{R} < 0$. Assuming that the early part of the evolution is very small compared to the matter dominated universe, one observes that R_2 may not be much larger than R_{eq} (where $\rho_m = \rho_r$) and hence one may take $R_2 \simeq R_{eq}$ with no consequence. The possibility of two phase transitions occurring in the present model is consistent with unified gauge field theories.

As $A = 0$ in this period, (2.13) suggests that

$$\rho + 3p - 2\rho_v = 0. \tag{4.1}$$

Now we consider the viscous effects of radiation in this phase, where the motion is one of pure expansion, by replacing the hydrostatic pressure p by p' given by

$$p' = p - \xi\theta, \tag{4.2}$$

where ξ is the coefficient of bulk viscosity and $\theta = 3\dot{R}/R$ is the volume expansion rate. The customary expression for ξ for a radiative fluid is given by [20]

$$\xi = \beta\rho_r, \tag{4.3}$$

where β is a constant of order unity. For $R \gg R_0$, (3.5) and (3.6) suggest that $\rho_v \simeq \rho_r \simeq \alpha/R^2$. Though this holds in the pure radiation era for $R \leqslant R_1$, it may be taken approximately valid in the rest mass generation period too as the latter period may not be very large. Thus (4.1), together with (2.19), (4.2) and (4.3), obtains

$$\rho_m R^3 \simeq 9\alpha\beta\dot{R}. \tag{4.4}$$

Thus $\rho_m R^3 \simeq$ constant, as $\ddot{R} = 0$ in this period. This indicates that the universe might have turned matter dominated by some dissipative mechanism in the rest mass generation period itself.

5. The matter and radiation era

In this period of evolution $R \geqslant R_2$ and (2.26) holds which implies that the total rest mass energy $E_m = \rho_m R^3$, remains approximately constant:

$$\rho_m R^3 = E_m^p, \tag{5.1}$$

where 'p' stands for the present value of the quantity.

Observations [8, 21] indicate that the present cosmic energy density ρ is very close to its corresponding critical value ρ_c. In our model, (2.21) indicates that $\rho \simeq \rho_c$ for $B = 2$ with $k = 1$ in the present matter dominated phase. We therefore, maintain $B = 2$ in this phase too in order to be in agreement with observations.

density ρ_r^p and at most it is of the order of ρ_r^p [5]. Also from (2.18) together with $B=2$ and $k=1$, we conclude that $\rho_v^p > \frac{1}{3}\rho_r^p$. These constraints form limits for the present value of ρ_v as $\frac{1}{3}\rho_r^p < \rho_v^p \lesssim \rho_r^p$ implying

$$\rho_v^p = \left(1 - \frac{w}{2}\right)\rho_r^p, \quad 0 \lesssim w < 4/3, \tag{5.3}$$

w being a dimensionless pure number. With (5.3), (5.2) gives the value of A in this era as

$$A = E_m^p + wE_r^p. \tag{5.4}$$

Equations (2.17) and (2.18), in this phase, thus yield

$$\rho_r = \frac{\alpha}{R^2}\left[1 + \gamma\frac{R_p}{R}\right] \tag{5.5}$$

and

$$\rho_v = \frac{\alpha}{R^2}\left[1 + \frac{\gamma}{3}\frac{R_p}{R}\right], \tag{5.6}$$

where $\gamma = (4\pi wG/3)\rho_r^p R_p^2$ is a positive dimensionless number. Equation (5.5) indicates that the total radiation content of the universe E_r, which is given by

$$E_r \equiv \rho_r R^3 = \alpha\gamma R_p + \alpha R, \tag{5.7}$$

is a function of R and increases as R increases. This is altogether different from the case in Ozer-Taha model [4] which has a decreasing E_r in a certain interval of time, in spite of radiation always being created.

Equations (5.1) and (5.5) imply that

$$\rho_m \gtrless \rho_r \quad \text{according as} \quad R \lessgtr \frac{1}{\alpha}\left(E_m^p - \frac{3w}{4}E_r^p\right). \tag{5.8}$$

Thus $\rho_m = \rho_r$ is obtained at (i) $R = R_{eq} (\simeq R_2)$ and (ii) $R = 1/\alpha(E_m^p - (3w/4)E_r^p) = R_{eq}^{II}$ (say).

Thus a second era of radiation dominance starts at R_{eq}^{II} which, for the estimates of R_p, ρ_r^p and ρ_m^p as obtained later on, is found to be $R_{eq}^{II} \simeq 9{\cdot}6 \times 10^{47}(\text{GeV})^{-1}$.

The time-dependence of the scale factor $R(t)$ in this era may be obtained from (2.16) as

$$R = \frac{3A}{8\alpha}(\cosh 2\psi - 1), \quad t = \frac{3A}{8\sqrt{2\alpha}}(\sinh 2\psi - 2\psi) + C, \tag{5.9a}$$

where A is given by (5.4) and C, the constant of integration, is some function of R_2. Equation (5.9a) indicates that $R \to \infty$ and $t \to \infty$ although $k = 1$.

Equation (5.9a) may alternatively be written as

$$t = [8^{-1}R(4R + 3\alpha^{-1}A)]^{1/2} + 16^{-1}A\,3\sqrt{2}\alpha^{-1} \times \ln\left[\frac{\sqrt{4R + 3\alpha^{-1}A} - 2\sqrt{R}}{\sqrt{4R + 3\alpha^{-1}A} + 2\sqrt{R}}\right] + C. \tag{5.9b}$$

The radiation energy density ρ_r, at present, is given by

$$\rho_r^p = \frac{\pi^2 N(T_p) T_p^4}{30}. \tag{5.10}$$

For the variation of ρ_r given by (5.5), one can observe, along the lines of Ozer–Taha [4], that $N(T_p) = 43/11$ in the present model. Hence (5.10), with the experimental value of $T_p = 2{\cdot}7°K$, yields

$$\rho_r^p \simeq 3{\cdot}8 \times 10^{-51}(\text{GeV})^4. \tag{5.11}$$

Equation (2.20) may now be used to obtain the present total (non-vacuum) energy density $\rho_p (= \rho_m^p + \rho_r^p)$ as

$$\rho_p = \frac{2\alpha}{3} H_p^2 - \tfrac{1}{3}\rho_r^p. \tag{5.12}$$

Taking $H_p = 75\,\text{km s}^{-1}\text{Mpc}^{-1}$ as favoured by the recent observations, (hence $\rho_c^p = 4{\cdot}4 \times 10^{-47}(\text{GeV})^4$), we get

$$\rho_p \simeq 4{\cdot}4 \times 10^{-47}(\text{GeV})^4. \tag{5.13}$$

Thus the present universe is matter dominated with $\rho_p \simeq \rho_c^p \simeq \rho_m^p$.

In order to obtain an estimate of the present values of the observables R_p and ρ_v^p, one may use (5.11) in (5.5) and (5.3) giving

$$R_p = \left[\frac{\alpha}{(1-\frac{3}{4}w)\rho_r^p}\right]^{1/2} = (1-\tfrac{3}{4}w)^{-1/2} \times 8{\cdot}4 \times 10^{43}(\text{GeV})^{-1}, \tag{5.14}$$

$$\rho_v^p = \left(1 - \frac{w}{2}\right) \times 3{\cdot}8 \times 10^{-51}(\text{GeV})^4. \tag{5.15}$$

Another important quantity is the deceleration parameter q defined by $q = -R\ddot{R}/\dot{R}^2$ which, from (2.15) and (2.16) obtains

$$q = \left[2 + \frac{8\alpha R}{3A}\right]^{-1}, \tag{5.16}$$

so that the present value of q is given by

$$q_p \simeq \tfrac{1}{2}\left[1 - 0{\cdot}00012\left(1 - w\frac{\rho_r^p}{\rho_m^p}\right)\right] \simeq \tfrac{1}{2}, \tag{5.17}$$

independently of w. Although w, which is not exactly known, occurs in the expressions for R_p and ρ_v^p, it is possible to find the estimates of these quantities as the maximum uncertainty in the value of w is $\frac{4}{3}$ which does not much effect the values of these observables given by (5.14) and (5.15).

We thus have

$$R_p \gtrsim 8{\cdot}4 \times 10^{43}(\text{GeV})^{-1}, \quad \rho_v^p \lesssim 3{\cdot}8 \times 10^{-51}(\text{GeV})^4. \tag{5.18}$$

The present value of the cosmological constant is then obtained as

$$\Lambda_p \lesssim 6{\cdot}4 \times 10^{-88}(\text{GeV})^2, \tag{5.19}$$

which is well within the upper limit of the observed value of Λ_p found as $10^{-82}(\text{GeV})^2$ [22].

Assuming that the early evolution (pure radiation era followed by the rest mass generation regime) lasts for a very small time and the maximum part of the evolution is matter dominated, we can drop the constant of integration C in (5.9) giving the approximate age of the universe as

$$t_p \simeq \tfrac{2}{3} \cdot H_p^{-1} \simeq 8{\cdot}9 \times 10^9 \text{ years}, \tag{5.20}$$

which is approximately the same as in the standard model. Thus the model has the same age problem as does the standard model. That is, the age of the universe is smaller than $12\text{–}18 \times 10^9$ yrs, the age of the globular clusters. However, the comparison of the age of the universe from observations with that from models is some what inconclusive [23]. Moreover, there is still an uncertainty in the value of H_p which varies by a factor of $2{:}50 \leqslant H_p \leqslant 100\,\text{kms}^{-1}\,\text{Mpc}^{-1}$ rendering the age of the universe in our model as $6{\cdot}7\text{–}13{\cdot}3 \times 10^9$ yrs.

Finally we consider the monopole problem of the standard cosmology. Although our discussion so far has not been field theoretic as the present model is presented in purely classical terms, the model does solve the monopole problem associated with grand unified theories. The present monopole number density is found to be given by [24]

$$n_M(t_p) \simeq d_H^{-3}(t_c)\left[\frac{R(t_c)}{R_p}\right]^3, \tag{5.21}$$

where t_c is the time of monopole production corresponding to the grand unifications – phase transition-temperature $T_c \simeq 10^{15}$ GeV and $d_H(t_c)$ is the horizon distance at time $t = t_c$ defined by [19]

$$d_H(t_c) = R(t_c)\int_0^{r_H(t_c)} \frac{dr}{\sqrt{1-kr^2}} = R(t_c)\int_0^{t_c} \frac{dt'}{R(t')}, \tag{5.22}$$

which with (3.3), obtains

$$d_H(t_c) = \sqrt{2}\,R(t_c)\ln\left[\frac{\sqrt{R(t_c)} + \sqrt{R(t_c) - R_0}}{\sqrt{R_0}}\right]. \tag{5.23}$$

Noting that $R(t_c) \gg R_0$, we have

$$d_H(t_c) \simeq \sqrt{2}\,R(t_c)\ln\left[2\sqrt{\frac{R(t_c)}{R_0}}\right], \tag{5.24}$$

which, by the use of (3.11) and (3.12), obtains

$$d_H(t_c) \simeq \sqrt{2}\,R(t_c)\ln\left[108^{1/4}\left(\frac{T_{max}}{T_c}\right)\right], \tag{5.25}$$

where we have taken $N(T_c) = N(T_{max})$. Now (5.21) yields

$$n_M(t_p) \simeq \left[\sqrt{2}\,R_p \ln\left\{108^{1/4}\left(\frac{T_{max}}{T_c}\right)\right\}\right]^{-3}. \tag{5.26}$$

For R_p given by (5.18) and $T_{max} = M_{pl} = 1{\cdot}22 \times 10^{19}$ GeV, (5.26) gives $n_M(t_p) \lesssim 5 \times 10^{-136}(\text{GeV})^3$. Thus for monopoles of mass 10^{16} GeV, the present monopole energy density $\lesssim 5 \times 10^{-120}(\text{GeV})^4$ indicating that the present cosmic energy density is clearly far from being dominated by monopoles.

6. Conclusions

Assuming the total active gravitational mass of the universe phasewise constant, we have investigated a cosmological model admitting a contracted Ricci-collineation along the fluid flow vector. The resulting model is geometrically closed ($k = 1$) but ever expanding and is free from the main problems of big bang cosmology, viz. the initial singularity, horizon, entropy, monopole and cosmological constant problems. The physical picture of the model is described in three phases:

Phase 1: The universe evolves from rest with $S = T = \rho = 0$ and $R = R_0$. Radiation is created by the unfolding of space time curvature, as is clear from (2.24), heating up the universe to a maximum temperature $T_{max} = M_{pl}$ at $t = 1{\cdot}24R_0$ with $\rho_r = \rho_{r\,max}$ too. Shortly after attaining T_{max}, the universe is globally casually connected at $t = 2{\cdot}4R_0$ with $T_{cau} \simeq 0{\cdot}86T_{max}$. For $t \gg R_0$, $T(t) \sim t^{-1/2}$ and $\rho_r \sim t^{-2}$ as in the standard model while $R(t) \sim t$ which is different from $R(t) \sim t^{1/2}$ of the standard model. This phase is vacuum dominated, however, for $R \gg R_0$, $\rho_v \to \rho_r$.

Phase 2: As soon as ρ_v equals to ρ_r at $R = R_1$, $\ddot{R} = 0$ and the universe starts to expand linearly. This is interpreted as the first phase transition in the model. Rest mass emerges from the created radiation and reaches a maximum at $R = R_2 \simeq R_{eq}$, which has been taken as the second phase transition in the model resulting in the reversal of sign of $\ddot{R}$. Though the mechanism of generation of rest mass is not known, it is possible to infer from the dissipative effects of radiation that the whole rest mass content of the universe would have been generated in this period itself and the universe turned matter dominated.

Phase 3: This is the present phase of matter dominance with $\ddot{R} < 0$. For the present radiation temperature $T_p = 2{\cdot}7°\text{K}$ and the present value of the Hubble parameter $H_p = 75\,\text{kms}^{-1}\,\text{Mpc}^{-1}$, the predicted values of some observables are found. These include $\rho_r^p = 3{\cdot}8 \times 10^{-51}(\text{GeV})^4$, $\rho_m^p \simeq 4{\cdot}4 \times 10^{-47}(\text{GeV})^4$, $R_p \gtrsim 8{\cdot}4 \times 10^{43}(\text{GeV})^{-1}$, $q_p \simeq \frac{1}{2}$, the age of the universe $t_p \simeq 8{\cdot}9 \times 10^9$ years, $\Lambda_p \lesssim 6{\cdot}4 \times 10^{-88}(\text{GeV})^2$ and the present monopole energy density $\lesssim 5 \times 10^{-120}(\text{GeV})^4$. The value of Λ_p is well within the experimental limit which is remarkable since the initial value of Λ is very large.

Acknowledgement

We would like to thank Prof. S R Roy for discussing some points related to this work.

References

[2] Ya B Zeldovich, *Sov. Phys. JETP* **14**, 1143 (1968); Usp **11**, 384 (1968)
A D Sakharov, *Sov. Phys. Dokl.* **12**, 1040 (1968)
L H Ford, *Phys. Rev.* **D11**, 3370 (1975)
E Steeruwitz, *Phys. Rev.* **D11**, 3378 (1975)
P J E Peebles and B Ratra, *Astrophys. J.* **325**, L17 (1988)
[3] W Chen and Y S Wu, *Phys. Rev.* **D41**, 695 (1990)
[4] M Ozer and M O Taha, *Phys. Lett.* **B171**, 363 (1986); *Nucl. Phys.* **B287**, 776 (1987)
[5] K Freese, F C Adams, J A Frieman and E Mottola, *Nucl. Phys.* **B287**, 797 (1987)
[6] M Gasperini, *Phys. Lett.* **B194**, 347 (1987); *Class. Quant. Gravit.* **5**, 521 (1988)
[7] J C Carvalho, J A S Lima and I Waga, *Phys. Rev.* **D46**, 2404 (1992)
M S Berman, *Phys. Rev.* **D43**, 1075 (1991); *Gen. Relativ. Gravit.* **23**, 465 (1991)
D Kalligas, P Wesson and C W F Everitt, *Gen. Relativ. Gravit.* **24**, 351 (1992)
A-M M Abdel-Rehman, *Gen. Relativ. Gravit.* **22**, 655 (1990)
A Beesham, *Int. J. Theor. Phys.* **25**, 1295 (1986)
[8] E W Kolb and M S Turner, *The early universe* (Addition-Wesley, New York, 1990)
[9] A D Line, *JETP Lett.* **19**, 183 (1974)
[10] P S Wesson, *Gravity, particles and astrophysics* (Reidel, Dordrecht, 1980) p. 36
[11] Abdussattar and R G Vishwakarma, *Curr. Sci.* **69**, 924 (1995)
[12] A D Linde, *Rep. Prog. Phys.* **42**, 389 (1979)
[13] G H Katzin, J Levine and W R Davis, *J. Math. Phys.* **10**, 617 (1969)
[14] C D Collinson, *Gen. Relativ. Gravit.* **1**, 137 (1970)
[15] W R Davis, L H Green and L K Norris, *Nuovo Cimento* **B34**, 256 (1976)
[16] L H Green, L K Norris, D R Jr Oliver and W R Davis, *Gen. Relativ. Gravit.* **8**, 731 (1977)
[17] F Hoyle and J V Narlikar, *Proc. R. Soc. London* **A273**, 1 (1963)
[18] W H McCrea, *Proc. R. Soc. London* **A206**, 562 (1951)
J Pachner, *Mon. Not. R. Astron. Soc.* **131**, 173 (1965)
N Rosen, *Int. J. Theor. Phys.* **2**, 189 (1969)
[19] S Weinberg, *Gravitation and cosmology* (Wiley, New York, 1972)
[20] M O Calvao, H P de Oliveira, D Pavon and J M Salim, *Phys. Rev.* **D45**, 3869 (1992); and the references therein
[21] K A Olive, *Phys. Rep.* **190**, 307 (1990)
[22] S W Hawking, *Phys. Lett.* **B134**, 403 (1984)
[23] A Sandage, B Katem and M Sandage, *Ap. J. Suppl.* **46**, 41 (1981)
A Sandage, *Ap. J.* **252**, 553 (1982)
J N Islam, An introduction to mathematical cosmology (Cambridge Univ. Press, 1992)
[24] R H Brandenberger, *Rev. Mod. Phys.* **57**, 1 (1985); and the references therein

Cross sections and other parameters of $e^- - H_2O$ scattering ($E_i \geqslant 50$ eV)

K N JOSHIPURA and MINAXI VINODKUMAR*
Department of Physics, Sardar Patel University, Vallabh Vidyanagar, Gujarat 388 120, India
*V. P. & R. P. T. P. Science College, Vallabh Vidyanagar, Gujarat 388 120, India

MS received 11 April 1996; revised 27 June 1996

Abstract. Our previous theoretical work on $e^- - H_2O$ scattering has been modified and extended to intermediate and high energies E_i. Using the Bethe plot, we compare the present inelastic cross-sections with the experimental ionization cross sections. Total cross-sections are analytically represented as $Q_{TOT}(cm^2) = a.(E_i\,eV)^{-b}$ and the parameters 'a' and 'b' are discussed for molecules H_2O, NH_3 and CH_4 in the range $E_i = 100$–1000 eV.

Keywords. Electron-molecule scattering; total cross-sections; Bethe plot.

PACS No. 34·80

1. Introduction

Collisions of electrons with water molecules have been the target of theoretical and experimental investigation since long. Our recent paper [1], hereafter referred to as paper I, dealt with calculations on vibrationally elastic $e^- - H_2O$ scattering at intermediate energies $E_i = 10$–300 eV. We treated the $e^- - H_2O$ interaction potentials in spherical models and the nonspherical interaction, mainly the molecular dipole potential was treated separately. The overall effect of electronic excitation and ionization was included through the imaginary part [2] of the complex spherical optical potential. All the terms of this complex potential were constructed by starting with an accurate spherically averaged charge density of the target molecule. A number of experimental results are also available for various cross-sections of the $e^- - H_2O$ system [3, 4]. Our total cross-sections given in paper I are in agreement with the experimental results of Sueoka *et al* [3] which in turn, are on the lower side of a number of other measurements e.g., those of Zecca *et al* [4]. Further, paper I demonstrated that it is more appropriate to consider the target charge density to be distorted dynamically by the polarization effect of the projectile.

In the present paper, two corrections have been introduced over the previous work. The absorption potential of Staszewska *et al* [2] V_{abs} vanishes at or below the threshold of electronic excitation Δ_{gap}. Paper I employed $\Delta_{gap} = I$, the ionization energy of H_2O which is 12·6 eV. More appropriately Δ_{gap} should correspond to the actual energy of excitation to the (first or low-lying) electronic energy level of the target. Presently, we have considered $\Delta_{gap} = 10{\cdot}2$ eV which is the excitation energy for the important transition $X^1A_1 \rightarrow {}^3A_1$ in H_2O (see ref. [5]). Further the Bethe plot of our total

inelastic cross-sections Q_{inel} is also given here. This now compares meaningfully well with the experimental ionization cross-sections $Q(H_2O^+)$.

Secondly the vibrational excitation cross-sections calculated recently by Nishimura and Itikawa [6] though important at low and intermediate energies only, may be added incoherently to define the grand total cross-sections. Thus the present work incorporates these two changes and reports grand total cross-sections Q_{TOT} at intermediate and high energies $E_i = 50$–2000 eV. We have also discussed here the scaling laws, or the fitting formulas to investigate the functional dependence of cross-sections on incident energy, especially, above 100 eV. A comparison in this regard has also been made with other 10-electron systems viz., CH_4 and NH_3. A consistent picture of E_i-dependence of Q_{TOT} emerges for all the three 10-electron systems. Theoretical expressions in this paper are given in a.u., unless specified otherwise.

2. Theoretical aspects

Potentials and scattering calculations

Katase *et al* [7] have given a simple but accurate spherical single-centre charge-density of H_2O in the form

$$\rho_0(r) = \frac{1}{4\pi}\left[a_1 \exp\left(\frac{-r}{b_1}\right) + a_2 r \exp\left(\frac{-r}{b_2}\right)\right], \tag{1}$$

where $a_1 = 4478$, $a_2 = 125$, $b_1 = 0{\cdot}0602$ and $b_2 = 0{\cdot}322$.

Ab initio accurate charge-density of molecules can be calculated using quantum chemistry techniques. This allows for a proper treatment of correlation and exchange potentials of the electron-molecule system [8, 9]. However, in the present case the model charge-density of (1) accurately reproduces the charge distribution in H_2O, given in refs [10–12]. It has a convenient form for carrying out the electron scattering calculations [1].

Considering $\rho_0(r)$ as the static or unperturbed charge-density of the target, we construct the dynamically distorted charge-density, as in [1]

$$\rho'(r, E_i) = \rho_0(r) + \rho_{pol}(r, E_i), \tag{2}$$

where ρ_{pol}, the polarized part of the charge-density based on the dynamic polarization potential is given by (5) and (7) of paper I. At high enough electron-energies ($\geqslant 500$ eV), as the polarization effect dwindles, $\rho'(r, E_i)$ merges with $\rho_0(r)$, as expected. Now, the complex spherical optical potential of $e^- - H_2O$ system consists of static, exchange, polarization and absorption terms. Starting with (1) and (2) given here, we construct all the terms of the optical potential as in [1]. In particular the parameter Δ_{gap} in the V_{abs} of ref. [2] is now chosen to have a more realistic value 10·2 eV, as explained in § 1. This improvement is significant at intermediate energies (say $\leqslant 300$ eV) only. Details of the scattering calculations are given in paper I and are not repeated here. We have calculated the total cross-sections for (elastic + inelastic) scattering viz.,

$$Q_T^S(E_i) = Q_{el}(E_i) + Q_{inel}(E_i), \tag{3}$$

where Q_{el} is the total elastic cross section within the complex potential. The superscript S in Q_T^S refers to the spherical interactions. The total inelastic cross section Q_{inel} shows the cumulative effect of all electronic excitations and the direct ionization, so that $Q_{inel} > Q(H_2O^+)$ at a particular E_i. Our model does not include dissociative ionization processes and vibrational and rotational excitations. The non-spherical dipole potential dominant at low to intermediate energies, was considered incoherently in [1]. Following this approach for the present energy range, we define the grand total cross-sections of $e^- - H_2O$ scattering, i.e.,

$$Q_{TOT}(E_i) = Q_T^S(E_i) + Q_{01}(D, E_i) + Q_{vib}(E_i). \tag{4}$$

We have followed paper I to obtain the dipole rotational excitation cross section $Q_{01}(D, E_i)$. These are the total cross-sections for the electron impact $0 \rightarrow 1$ rotational excitation, calculated in the Born approximation for the molecular dipole of strength D. The vibrationally inelastic integral cross-sections $Q_{vib}(E_i)$ determined by Nishimura and Itikawa [6] and included here are quite small for $E_i \geqslant 30$ eV.

The Bethe plot and the fitting formulas

It is well-known that at high energies the total inelastic cross-sections obey the Bethe asymptotic formula, as given by Inokuti [13]. This is

$$\frac{Q_{inel}}{4\pi a_0^2}\frac{E_i}{R} = (-M_{tot}^2)\ln\left(\frac{E_i}{R}\right) + M_{tot}^2 \ln[4C_{tot}] + O\left(\frac{R}{E_i}\right), \tag{5}$$

where a_0 is the Bohr-radius and R is the Rydberg unit of energy. The parameter M_{tot}^2 measuring the slope of the Bethe plot, is the square of the total dipole-matrix element. This formula is presently applied to our Q_{inel} results as well as to the total (direct) ionization cross-sections $Q(H_2O^+)$ recently measured by Srivastava [14].

We next consider the E_i-dependence of the total electron scattering cross-sections Q_{TOT} of H_2O vis-a-vis the other two well-known 10-electron molecules CH_4 and NH_3. Nishimura and Tawara [15] have given the following fitting formulas for CH_4 and other hydrocarbons, applicable to intermediate energies.

$$Q_{TOT} = \frac{a}{\sqrt{E_i}}. \tag{6a}$$

$$= b\sqrt{\frac{\alpha_0}{E_i}}. \tag{6b}$$

These two expressions, with 'a' and 'b' as typical molecular parameters and α_0 as the target polarizability, emphasize $E_i^{-1/2}$ dependence of the cross-sections in the range 50–500 eV.

Zecca *et al* [16] found that their measured values for NH_3, SiH_4 and H_2S targets are in accordance with the following formula, based on the Yukawa potential with the Born approximation, at $E_i > 200$ eV.

$$Q_{TOT}(E_i) = \frac{\sigma_0 B}{B + \sigma_0 E_i}. \tag{7}$$

The present theoretical results on H_2O are based on the partial wave analysis of the complex optical potential. This consists of short-range (static + exchange) potentials, intermediate range absorption potential and the long range polarization potential. Hence we have represented the grand-total cross-sections Q_{TOT}(in cm^2) in a general form, as a function of energy (eV), viz.,

$$Q_{TOT}(E_i) = a(E_i)^{-b}, \tag{8}$$

where 'a' and 'b' are our target-dependent parameters. This formula is found to be suitable for the present results in the range 100–1000 eV. Now, in order to apply (8) to the other 10-electron systems CH_4 and NH_3, we calculated their cross-sections through our modified additivity rule for e^--molecule scattering at high energies as given in [17]. Here the cross-sections of short-range atomic potentials in the molecule, i.e. $Q_{SR}(i)$ are added together and the long range (polarization) contribution $Q_{pol}(M)$ is considered at the direct molecular level. Thus, with 'n' atoms in a molecule

$$Q_{TOT}(E_i) = \sum_{i=1}^{n} Q_{SR}(i) + Q_{pol}(M). \tag{9}$$

This formulation goes over to the simple 'additivity rule' [18, 19] at high energies. The cross-sections of H_2O, CH_4 and NH_3 are found to have an identical E_i dependence, as discussed in the next section.

3. Results, discussion and conclusion

In a spherical model for H_2O, the total elastic cross-sections Q_{el} and the total inelastic cross-sections Q_{inel} are calculated to obtain $Q_T^S(E_i)$, vide eq. (3). The present values of Q_{inel} are somewhat higher (up to about 300 eV) than the previous values [1], in view of our choice of Δ_{gap}. The present values lie above the total (direct) ionization cross-sections $Q(H_2O^+)$ of Srivastava [14], as it should be. The grand-total cross-sections Q_{TOT} are obtained incoherently through (4).

We now discuss the results of the present calculations in terms of the analytical fits given in (5) and (8). Consider figure 1 which shows the graphical representation of the fitting formula of (5) for $e^- - H_2O$ scattering. Both the present Q_{inel} as well as the experimental $Q(H_2O^+)$ plotted here, are found to obey this relation at high energies (above 100 eV) and yield straight lines with an identical slope $M_{tot}^2 = 4{\cdot}28$. This quantity is related to the optical oscillator strength of the molecule. The present value of M_{tot}^2 differs from that in an earlier calculation [20] wherein the ionization energy is taken in place of Δ_{gap}.

Let us next consider our results on the grand total cross-sections Q_{TOT} calculated for the energy range $E_i = 50$–2000 eV. In figure 2, these cross-sections are plotted as functions of energy, and compared with some of the experimental data. For H_2O, our theoretical results are now in a very good agreement with the measurements of Zecca *et al* [4] throughout the present energy range. The experimental data of Sueoka *et al* [3] available up to 300 eV are on the lower side. Thus the present results are in a good general accord with the relevant experiments, and the modifications done here over paper I are meaningful.

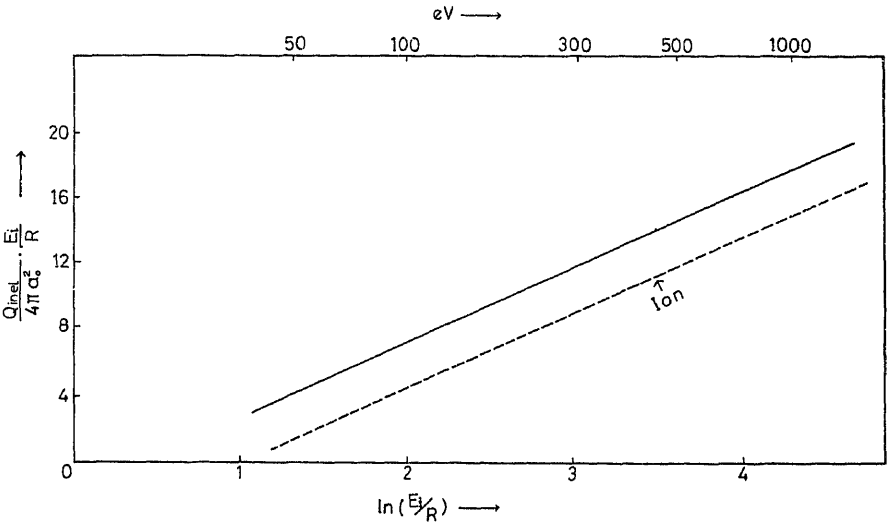

Figure 1. Bethe plots for H_2O. ——— present Q_{inel}; --- experimental $Q(H_2O^+)$, vide ref. [14].

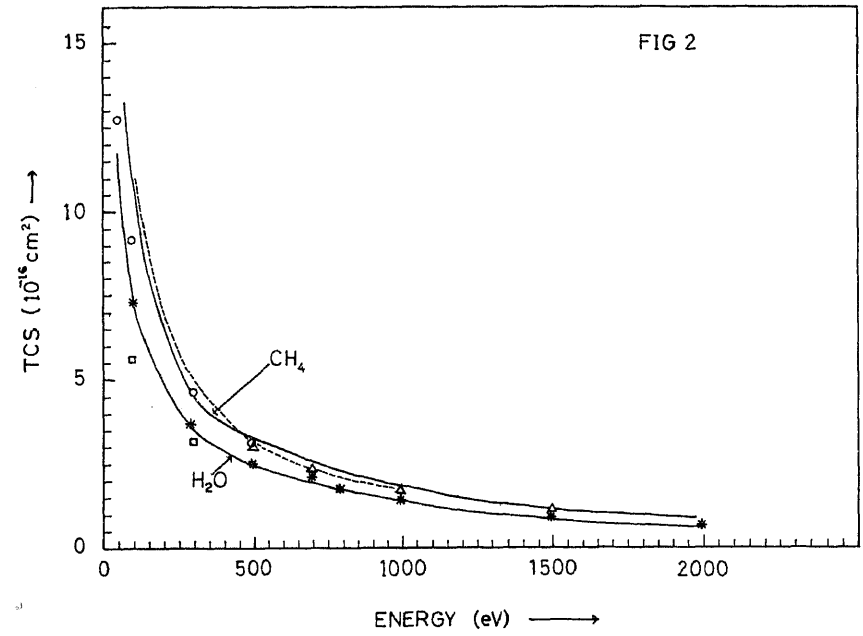

Figure 2. Total (elastic + inelastic) cross-sections at various energies. Lower curve——— present H_2O results. (□ Sueoka *et al* [3], ∗ Zecca *et al* [4]). Upper curve——— represents our results for CH_4 (eq. 9), --- Jiang *et al* [19]. Experimental data for CH_4: ○ Dababneh *et al* [21], Δ Zecca *et al* [16].

Table 1. The fitting parameters of eq. (8).

System	a	b	Polarizability Å^3
H_2O	239·94	0·742	1·45
NH_3	307·25	0·753	2·26
CH_4	352·24	0·757	2·59

We next examine the energy dependence of the total cross-sections of iso-electronic systems H_2O, NH_3 and CH_4, in the energy range 100–1000 eV. For this purpose we calculated the Q_{TOT} for NH_3 and CH_4 by employing (9). In figure 2 the cross-sections of only H_2O and CH_4 are shown, for simplicity. For CH_4 our results compare favourably with other theoretical [19] as well as experimental [16, 21] results. Now the present results are fitted to the analytical formula of (8). The constants 'a' and 'b' for the present targets are given in table 1. Here Q_{TOT} is in 10^{-16} cm^2 and E_i is in eV.

We observe from table 1 that all the three 10-electron systems exhibit a similar dependence of Q_{TOT} viz., $(E_i)^{-0.75}$, since 'b' is practically the same for all of them. The other parameter, 'a' is different for each of these molecules and appears to depend on their polarizability α_0. This is clear from the polarizabilities given in table 1. With the parameters given here, eq. (8) very accurately reproduces our theoretical results for all the three molecules in the energy range 100–1000 eV. A similar analysis should be extended to HF molecule, which also has 10 electrons.

Thus in this paper we have considered some more aspects of total electron scattering cross-sections of H_2O at intermediate and high impact energies. Our previous results are now improved and extended to facilitate further studies. Our total inelastic cross-sections are consistent with the measured ionization cross-sections, barring dissociative ionization. Our Q_{inel} values obey the well-known Bethe formula, (5). As regards the total cross-sections Q_{TOT}, systematic relations are confirmed here for the target sequence H_2O–NH_3–CH_4. At a fixed E_i the cross-sections increase along this sequence, but tend to merge at high enough energies. The present results follow the energy dependence given through (8) and table 1.

It would be desirable to consider accurate *ab initio* charge-densities and corresponding static-exchange potentials in e-molecule scattering.

Acknowledgement

One of the authors (KNJ) is thankful to the University Grants Commission, New Delhi, for a major research project.

References

[1] K N Joshipura, Minaxi Vinodkumar and P M Patel, *Pramana – J. Phys.* **43**, 495 (1994)
[2] G Staszewska, D Schwenke, D Thirumalai and D G Truhlar, *Phys. Rev.* **A28**, 2740 (1983)
[3] O Sueoka, S Mori and Y Katayama, *J. Phys.* **B19**, L373 (1986); *J. Phys.* **B20**, 3237 (1987)

5] M T Lee, S E Michelin, T Kroin, L E Machado and L M Brescansin, *J. Phys.* **B28**, 1859 (1995)
6] T Nishimura and Y Itikawa, *J. Phys.* **B28**, 1995 (1995)
7] A Katase, K Ishibashi, Y Matsuomoto, T Sakae, S Maezono, E Murakami, K Watanabe and H Maki, *J. Phys.* **B19**, 2715 (1986)
8] K B Ghose and S Pal, *J. Chem. Phys.* **99**, 945 (1993)
9] S Pal, K B Ghose and H Meyer, *Int. J. Quant. Chem.* **55**, 291 (1995)
0] K E Banyard and N H March, *J. Chem. Phys.* **26**, 1416 (1957)
1] D G Thompson and F A Gianturco, *Chem. Phys. Lett.* **14**, 110 (1976)
2] Arvind Jain, A N Tripathi and Ashok Jain, *Phys. Rev.* **A37**, 2893 (1988)
3] M Inokuti, *Rev. Mod. Phys.* **43**, 297 (1971)
4] S K Srivastava, private communication (1995)
5] H Nishimura and H Tawara, *J. Phys.* **B24**, L363 (1991)
6] A Zecca, G P Karwasz and R S Brusa, *Phys. Rev.* **A45**, 2777 (1992)
7] Minaxi Vinodkumar, P M Patel and K N Joshipura, *Prajna – J. Sardar Patel University*, **5**, 79 (1995)
8] K N Joshipura and P M Patel, *Z. Phys.* **D29**, 269 (1994)
9] Y Jiang, J Sun and L Wan, *Phys. Rev.* **A52**, 398 (1995)
0] A Jain and K L Baluja, *Phys. Rev.* **A45**, 202 (1992)
1] M S Dababneh, Y F Hsieh, W E Kauppila, C K Kwan, S J Smith, T S Stein and M N Uddin, *Phys. Rev.* **A38**, 1207 (1988)

New method for the evaluation of the RKR potential-integrals for diatomic molecules

SURESH CHANDRA[1,2], A K SHARMA[3] and Z H KHAN[3]
[1]School of Sciences, Indira Gandhi National Open University, New Delhi 110068, India
[2]Inter-University Centre for Astronomy and Astrophysics, Post Bag 4, Ganeshkhind, Pune 411 007, India
[3]Department of Physics, Jamia Millia Islamia, New Delhi 110025, India

MS received 26 October 1995; revised 27 May 1996

Abstract. We present a new method for the evaluation of the RKR potential-integrals for diatomic molecules. This method is straightforward and fast, and the calculations can be performed to an accuracy better than any other method.

Keywords. Diatomic molecules; potential energy curve.

PACS Nos 30; 31·15

1. Introduction

The classical left- and right-hand turning points, $r_{\min}$ and $r_{\max}$, of the RKR potential-energy curve, for a diatomic molecule, are given by [1, 2]

$$r_{\min} = (f/g + f^2)^{1/2} - f, \quad r_{\max} = r_{\min} + 2f,$$

where the Klein f and g integrals are defined as

$$f(\text{cm}) = \left(\frac{h}{8\pi^2 \mu c}\right)^{1/2} \int_{-\Delta}^{t} [U - E(v, J)]^{-1/2} \, \mathrm{d}s \tag{1}$$

and

$$g(\text{cm}^{-1}) = \left(\frac{8\pi^2 \mu c}{h}\right)^{1/2} \int_{-\Delta}^{t} \frac{\partial E}{\partial [J(J+1)]} [U - E(v, J)]^{-1/2} \, \mathrm{d}s, \tag{2}$$

where

$$s = v + \tfrac{1}{2}, \quad t = v' + \tfrac{1}{2}.$$

v is the vibrational quantum number, and v' is the vibrational quantum number of the vibrational level (with $J = 0$) for which the turning points are to be calculated. The energy of the level is given by

$$U = \sum_{i=0} Y_{i,0} t^i \tag{3}$$

and the energy of the vib-rotational levels, in a diatomic molecule, can be expressed as

$$E(v, J) = \sum_{i,j} Y_{i,j} \left(v + \frac{1}{2}\right)^i [J(J+1)]^j. \tag{4}$$

Equations (11) and (12) are obviously free from the problem of the singularity, as the integrands of the integrals approach to zero at the upper limit of the integrals, but the final expressions are too complicated, as there are nested summations and the calculation would take a long time. Due to the same reason, the accuracy of the calculations may also be affected. Fleming and Rao [12] tested the accuracy of their method by comparing their results with those of Mantz *et al* [10]. The difference between the two sets of the values was less than 0·0000005 Å for r_{min} and less than 0·0000010 Å for r_{max}.

Before Fleming and Rao [12], Zeleznik [8] and Mantz *et al* [10] also, independently, could succeed to remove the singularity of the integrals. But since the evaluation of these methods [8, 10] was more difficult [12] than that of Fleming and Rao [12], the latter [12] was adopted for the evaluation of the RKR potential-energy curves.

2.3 *Kirschner and Watson* [14]

The method of Kirschner and Watson [14] is as follows. Equations (6) and (7) can be written as

$$f(\mathrm{cm}) = \left(\frac{h}{8\pi^2\mu c}\right)^{1/2} \int_0^{E_{v'}} \frac{1}{\omega_v [E_{v'} - E_v]^{1/2}} \mathrm{d}E_v \tag{13}$$

and

$$g(\mathrm{cm}^{-1}) = \left(\frac{8\pi^2\mu c}{h}\right)^{1/2} \int_0^{E_{v'}} \frac{B_v}{\omega_v [E_{v'} - E_v]^{1/2}} \mathrm{d}E_v, \tag{14}$$

where

$$E_v = \sum_{i=0}^{n} Y_{i0} s^i \quad E_{v'} = \sum_{i=0}^{n} Y_{i0} t^i \quad \omega_v = \sum_{i=1}^{n} Y_{i0} i s^{i-1} \quad B_v = \sum_{i=0}^{n} Y_{i1} i s^i.$$

They calculated $E_{v'}$, $1/\omega_{v'}$ and $B_{v'}/\omega_{v'}$ for each value of v', and then fitted to the expressions

$$\frac{1}{\omega_{v'}} = \sum_{i=1}^{\infty} \alpha_n E_{v'}^n, \tag{15}$$

$$\frac{B_{v'}}{\omega_{v'}} = \sum_{i=1}^{\infty} \beta_n E_{v'}^n \tag{16}$$

to evaluate α_n and β_n by a least squares fit to polynomials of any degree. The degree of the polynomial was increased until the fit was satisfactory. The coefficients α_n and β_n were then inserted in the equations

$$f(\mathrm{cm}) = \left(\frac{h}{8\pi^2\mu c}\right)^{1/2} \sum_{n=0}^{\infty} \frac{n!}{(n+\frac{1}{2})(n-\frac{1}{2})\ldots\frac{1}{2}} \alpha_n E_{v'}^{n+1/2} \tag{17}$$

and

$$g(\mathrm{cm}^{-1}) = \left(\frac{8\pi^2\mu c}{h}\right)^{1/2} \sum_{n=0}^{\infty} \frac{n!}{(n+\frac{1}{2})(n-\frac{1}{2})\ldots\frac{1}{2}} \beta_n E_{v'}^{n+1/2}. \tag{18}$$

Obviously, in this procedure, it is a very difficult task to evaluate α_n and β_n for every v' from (15) and (16), respectively.

The procedure of Telle and Telle [15] can be understood in the following manner. The expressions (6) and (7) can be rearranged as

$$f(\mathrm{cm}) = \left(\frac{h}{8\pi^2\mu c}\right)^{1/2} \int_{-\Delta}^{t} (t-s)^{-1/2} \left[\sum_{k=1}^{n} t^{k-1} \left(\sum_{i=k}^{n} Y_{i,0} s^{i-k}\right)\right]^{-1/2} \mathrm{d}s \quad (19)$$

and

$$g(\mathrm{cm}^{-1}) = \left(\frac{8\pi^2\mu c}{h}\right)^{1/2} \int_{-\Delta}^{t} (t-s)^{-1/2} \left[\sum_{i=0}^{n} Y_{i,1} s^{i}\right] \left[\sum_{k=1}^{n} t^{k-1} \left(\sum_{i=k}^{n} Y_{i,0} s^{i-k}\right)\right]^{-1/2} \mathrm{d}s. \quad (20)$$

The substitution $t - s = \tau^2$, in the expressions (19) and (20), gives

$$f(\mathrm{cm}) = 2\left(\frac{h}{8\pi^2\mu c}\right)^{1/2} \int_{0}^{\sqrt{t+\Delta}} \left[\sum_{k=1}^{n} t^{k-1} \left(\sum_{i=k}^{n} Y_{i,0} (t-\tau^2)^{i-k}\right)\right]^{-1/2} \mathrm{d}\tau \quad (21)$$

and

$$g(\mathrm{cm}^{-1}) = 2\left(\frac{8\pi^2\mu c}{h}\right)^{1/2} \int_{0}^{\sqrt{t+\Delta}} \left[\sum_{i=0}^{n} Y_{i,1} (t-\tau^2)^{i}\right] \left[\sum_{k=1}^{n} t^{k-1} \left(\sum_{i=k}^{n} Y_{i,0} (t-\tau^2)^{i-k}\right)\right]^{-1/2} \mathrm{d}\tau. \quad (22)$$

These expressions are also free from the problem of singularity. However, due to the existence of nested summations, the calculations would be slow. Furthermore, since we have to evaluate τ^2, and not the linear expression, the accuracy of these results would be affected. Nevertheless, Telle and Telle [15] claimed that the turning point of their calculations agreed to better than 1×10^{-7} Å with those of Dickinson [11], Fleming and Rao [12], and Kirschner and Watson [14].

2.5 *Remark*

One point to be noted here is that all these authors discussed about the accuracy of their results by comparing them with the existing values of other methods. But all of them are doing the calculations by numerical integration and the integrands in their final integrals are *quite complicated.* Therefore, the accuracy of their results may not be as good as mentioned by them. However, the accuracy of all the methods have to be almost the same. The accuracy of the quadrature method cannot be very high as the number of points cannot be taken to be very large. After comparing the results of the quadrature method with those obtained from the other methods, the accuracy has been claimed to be up to seven-figures. Unfortunately, no experimental results are available so that one could have a better estimation about the accuracy. But, fortunately, for a limited number of the Dunham coefficients, there are analytical expressions, which can play an important role for deciding about the accuracy of the results. When we compared the results of the quadrature method with those obtained from the analytical expressions (see §4), we found that the quadrature method could reproduce the

analytical results up to five-figures or sometime up to six-figures. It shows that the accuracy of all these methods may not be as good as reported by the authors, as they have compared the results of one with that of the other.

3. Present approach

Recent calculations [17] show that the Einstein A-coefficients for some vib-rotational transitions, depending on the potential-energy curve, particularly for large rotational quantum numbers J and/or large vibrational quantum numbers v, are very sensitive to the potential-energy curve. Therefore, in order to get reliable results, one should try to get the potential-energy curve as accurate as possible. In the following text, we discuss about our method for the evaluation of the RKR potential-integrals. The accuracy of this method is better than that of the other methods.

In order to have a feeling about the nature of the singularity, we considered the Dunham coefficients for $^{12}C^{16}O$ given by Farrenq *et al* [18], and plotted the arguments given by

$$f' = \left[\sum_{i=1}^{n} Y_{i,0}(t^i - s^i)\right]^{-1/2} \tag{23}$$

and

$$g' = \left[\sum_{i=0}^{n} Y_{i,1} s^i\right]\left[\sum_{i=1}^{n} Y_{i,0}(t^i - s^i)\right]^{-1/2} \tag{24}$$

of the integrals (6) and (7), for $v' = 2$, in figure 1. In the figure, the upper curve is for g', whereas the lower one is for f'. Further, we calculated the values of the integrands, and their gradients, $\partial f'/\partial s$ and $\partial g'/\partial s$, and we report here, in table 1, some values of $f', g', \partial f'/\partial s$ and $\partial g'/\partial s$, in the region near the singularity. The values in table 1, for $s = 2{\cdot}5$, are calculated very close to the singularity. The figure along with table 1 shows that there is the region from $(t-\varepsilon)$ to t, where $\varepsilon \approx 10^{-2}$, in which the integrands f' and g' have enormously large gradient. The rest of the integrals, from $-\Delta$ to $(t-\varepsilon)$, can be evaluated with the help of the well-known and very accurate methods for numerical integration, e.g., Simpson method. Therefore, in the present approach, each of the Klein f and g integrals has been divided into two parts: (i) from $-\Delta$ to $(t-\varepsilon)$ and (ii) from $(t-\varepsilon)$ to t:

$$f(\mathrm{cm}) = \left(\frac{h}{8\pi^2 \mu c}\right)^{1/2}\left[\int_{-\Delta}^{t-\varepsilon}\left[\sum_i Y_{i,0}(t^i - s^i)\right]^{-1/2} \mathrm{d}s + F\right] \tag{25}$$

and

$$g(\mathrm{cm}^{-1}) = \left(\frac{8\pi^2 \mu c}{h}\right)^{1/2}\left[\int_{-\Delta}^{t-\varepsilon}\left[\sum_i Y_{i,1} s^i\right]\left[\sum_i Y_{i,0}(t^i - s^i)\right]^{-1/2} \mathrm{d}s + G\right]. \tag{26}$$

The second parts are denoted by F and G, respectively. The first part is evaluated by the Simpson method for numerical integration. The second parts are evaluated analytically in the following manner:

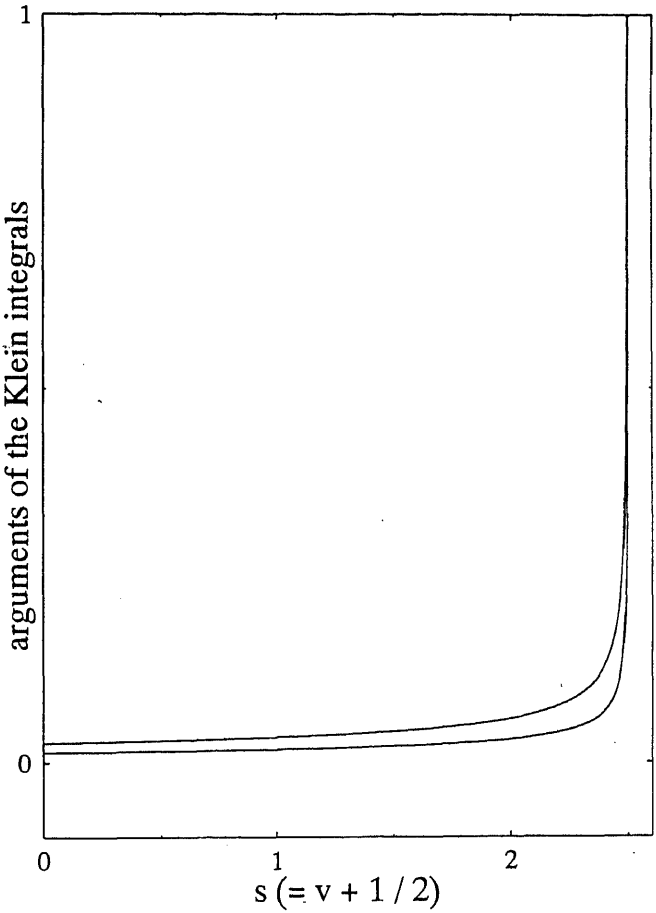

Figure 1. Variation of the arguments f' and g' (eqs (23) and (24)) for $v' = 2$, for $^{12}C^{16}O$, using the Dunham coefficients of Farrenq *et al* [18]. The upper curve is for g', whereas the lower one is for f'.

Table 1. Integrands and their gradients.

s	f'	g'	$\partial f'/\partial s$	$\partial g'/\partial s$
2·450	9·7492E − 02	0·1841	0·9752	1·840
2·455	0·1028	0·1941	1·142	2·155
2·460	0·1090	0·2058	1·363	2·572
2·465	0·1165	0·2200	1·665	3·142
2·470	0·1259	0·2376	2·098	3·959
2·475	0·1379	0·2603	2·758	5·205
2·480	0·1542	0·2910	3·855	7·274
2·485	0·1780	0·3361	5·934	11·20
2·490	0·2180	0·4116	10·90	20·58
2·495	0·3083	0·5820	30·83	58·20
2·500	1·2366E + 05	2·3342E + 05	1·9890E + 18	3·7543E + 18

Using $r = t - s$, (27) can be rearranged as

$$F = \int_0^{\varepsilon} r^{-1/2}[A - rB + r^2 C - r^3 D + r^4 E]^{-1/2} \mathrm{d}r, \tag{28}$$

where

$$A = Y_{10} + 2tY_{20} + 3t^2 Y_{30} + 4t^3 Y_{40} + 5t^4 Y_{50} + 6t^5 Y_{60} + 7t^6 Y_{70} + 8t^7 Y_{80} + 9t^8 Y_{90} + \ldots$$

$$B = Y_{20} + 3tY_{30} + 6t^2 Y_{40} + 10t^3 Y_{50} + 15t^4 Y_{60} + 21t^5 Y_{70} + 28t^6 Y_{80} + 36t^7 Y_{90} + \ldots$$

$$C = Y_{30} + 4tY_{40} + 10t^2 Y_{50} + 20t^3 Y_{60} + 35t^4 Y_{70} + 56t^5 Y_{80} + 84t^6 Y_{90} + \ldots$$

$$D = Y_{40} + 5tY_{50} + 15t^2 Y_{60} + 35t^3 Y_{70} + 70t^4 Y_{80} + 126t^5 Y_{90} + \ldots$$

$$E = Y_{50} + 6tY_{60} + 21t^2 Y_{70} + 56t^3 Y_{80} + 126t^4 Y_{90} + \ldots$$

Here, we have taken the terms up to r^4 and it can be easily extended to higher powers of r, depending upon the requirement of the accuracy of the results. Equation (28) can be written as

$$F = \int_0^{\varepsilon} r^{-1/2} A^{-1/2} \left[1 - \frac{rB - r^2 C + r^3 D - r^4 E}{A}\right]^{-1/2} \mathrm{d}r. \tag{29}$$

Using the relation

$$(1-x)^{-1/2} = 1 + \frac{1}{2}x + \frac{3}{8}x^2 + \frac{5}{16}x^3 + \frac{35}{128}x^4 + \ldots$$

in (29) and retaining the terms up to r^4 only, on integration we get

$$F = \frac{\varepsilon^{1/2}}{A^{1/2}}\left[2 + \varepsilon\left[\frac{B}{3A}\right] + \frac{2}{5}\varepsilon^2\left[\frac{3B^2}{8A^2} - \frac{C}{2A}\right] + \frac{2}{7}\varepsilon^3\left[\frac{5}{16}\frac{B^3}{A^3} - \frac{3}{4}\frac{BC}{A^2} + \frac{D}{2A}\right] + \frac{2}{9}\varepsilon^4\left[\frac{35}{128}\frac{B^4}{A^4} - \frac{15}{16}\frac{B^2 C}{A^3} + \frac{3}{4}\frac{BD}{A^2} + \frac{3}{8}\frac{C^2}{A^2} - \frac{E}{2A}\right]\right]. \tag{30}$$

Now,

$$G = \int_{t-\varepsilon}^{t}\left[\sum_i Y_{i,1} s^i\right]\left[\sum_i Y_{i,0}(t^i - s^i)\right]^{-1/2} \mathrm{d}s. \tag{31}$$

Using $r = t - s$, (31) can be rearranged as

$$G = \int_0^{\varepsilon} r^{-1/2}[a - rb + r^2 c - r^3 d + r^4 e][A - rB + r^2 C - r^3 D + r^4 E]^{-1/2} \mathrm{d}r, \tag{32}$$

where

$$a = Y_{01} + tY_{11} + t^2 Y_{21} + t^3 Y_{31} + t^4 Y_{41} + t^5 Y_{51} + t^6 Y_{61} + t^7 Y_{71} + t^8 Y_{81} + t^9 Y_{91} + \ldots$$

$$b = Y_{11} + 2tY_{21} + 3t^2 Y_{31} + 4t^3 Y_{41} + 5t^4 Y_{51} + 6t^5 Y_{61} + 7t^6 Y_{71} + 8t^7 Y_{81} + 9t^8 Y_{91} + \ldots$$

$$c = Y_{21} + 3tY_{31} + 6t^2 Y_{41} + 10t^3 Y_{51} + 15t^4 Y_{61} + 21t^5 Y_{71} + 28t^6 Y_{81} + 36t^7 Y_{91} + \ldots$$

$$d = Y_{31} + 4tY_{41} + 10t^2 Y_{51} + 20t^3 Y_{61} + 35t^4 Y_{71} + 56t^5 Y_{81} + 84t^6 Y_{91} + \ldots$$

$$e = Y_{41} + 5tY_{51} + 15t^2 Y_{61} + 35t^3 Y_{71} + 70t^4 Y_{81} + 126t^5 Y_{91} + \ldots$$

Here also, we have taken the terms up to r^4. One can consider more terms, depending on the requirement of the accuracy of the results. Following the above mentioned procedure, the final expression for G can be obtained as

$$G = \frac{\varepsilon^{1/2}}{A^{1/2}}\left[2a + \frac{2}{3}\varepsilon\left[\frac{Ba}{2A} - b\right] + \frac{2}{5}\varepsilon^2\left[\frac{3B^2a}{8A^2} - \frac{Ca}{2A} - \frac{Bb}{2A} + c\right] + \frac{2}{7}\varepsilon^3\left[\frac{5}{16}\frac{B^3a}{A^3} - \frac{3}{4}\frac{BCa}{A^2} + \frac{Da}{2A} - \frac{3B^2b}{8A^2} + \frac{Cb}{2A} + \frac{Bc}{2A} - d\right] + \frac{2}{9}\varepsilon^4\left[\frac{35}{128}\frac{B^4a}{A^4} - \frac{15}{16}\frac{B^2Ca}{A^3} + \frac{3}{4}\frac{BDa}{A^2} + \frac{3}{8}\frac{C^2a}{A^2} - \frac{Ea}{2A} - \frac{5}{16}\frac{B^3b}{A^3} + \frac{3}{4}\frac{BCb}{A^2} - \frac{Db}{2A} + \frac{3}{8}\frac{B^2c}{A^2} - \frac{Cc}{2A} - \frac{Bd}{2A} + e\right]\right]. \tag{33}$$

These expressions for F and G look a bit bulky, but they are very simple from the computation point of view. The expressions for F and G, for the given value of v', have to be evaluated one time only, and not on several points taken in the numerical integration. The integrands of the integrals in (25) and (26) are very simple in comparison to the integrands of the methods discussed in the previous section. Thus, the present method is very fast in comparison to the other methods.

The accuracy of the first part of the integrals, here, can be enhanced to any required value by reducing the step-size in the numerical integration. Obviously, the present approach would face less problem of computation time, by reducing the step-size, than the others, as the integrands in the present approach are the simplest ones. The accuracy of the second part of the integrals can be increased by including higher powers of r in (28) and (32). Since the expressions for F and G, for the given value of v', have to be evaluated one time only, the inclusion of the higher powers of r, would not affect the speed of the method.

4. Test for the accuracy

For the limited number of Dunham coefficients, $Y_{0,0}$, $Y_{1,0}$, $Y_{2,0}$, $Y_{0,1}$, and $Y_{1,1}$, Klein f and g integrals can be solved analytically. The analytical expressions are

$$f(\mathrm{cm}) = \left(\frac{h}{8\pi^2\mu c(-Y_{2,0})}\right)^{1/2} \ln\left[\frac{\sqrt{l^2-m}}{\sqrt{l^2+k}-\sqrt{m+k}}\right] \tag{34}$$

and

$$g(\mathrm{cm}^{-1}) = \left(\frac{8\pi^2\mu c}{h(-Y_{2,0})}\right)^{1/2}(-Y_{1,1}) \left(\sqrt{m+k} - (l-n)\ln\left[\frac{\sqrt{l^2-m}}{\sqrt{l^2+k}-\sqrt{m+k}}\right]\right), \tag{35}$$

where

$$k = \frac{Y_{0,0}}{(-Y_{2,0})}, \quad l = \frac{Y_{1,0}}{2(-Y_{2,0})}, \quad m = \frac{U - Y_{0,0}}{(-Y_{2,0})} \quad \text{and} \quad n = \frac{Y_{0,1}}{(-Y_{1,1})}.$$

For the case, $Y_{0,0} = 0$, these expressions are the same as derived by Rees [2], which have been used as the basis for rather extensive calculations by a number of research-groups and can play an important role for checking the accuracy of the present approach. Fortunately, the programme of Le Roy [16] is available to us. We calculated the classical turning points for the Dunham coefficients, $Y_{1,0}$, $Y_{2,0}$, $Y_{0,1}$, and $Y_{1,1}$ for $^{12}C^{16}O$, given by Farrenq *et al* [18], by using (i) the programme for the quadrature method [16], (ii) the analytical expressions (34) and (35) and (iii) the present method (eqs (25) and (26)). (The Dunham coefficient $Y_{0,0}$ for $^{12}C^{16}O$ is zero.) The values of the turning points are given in table 2.

Table 2 shows that the present method reproduces the analytical results atleast up to seven-figures. For some values of v', it reproduces up to eight-figures. The accuracy of the present method, obviously, can be enhanced by including higher powers of r in (28) and (32), and by reducing the step-size in the numerical integration. Nevertheless, in the present form, the accuracy of the present method is better than that of the other methods. Moreover, here we are deciding about the accuracy by comparing our results with those obtained from the analytical expressions.

Table 2. Turning points for the Dunham coefficients $Y_{1,0}$, $Y_{2,0}$, $Y_{0,1}$ and $Y_{1,1}$.

	Quadrature technique		Analytical		Present	
v'	r_{min}	r_{max}	r_{min}	r_{max}	r_{min}	r_{max}
0	1·08330749	1·17877144	1·08331168	1·17876726	1·08331165	1·17876723
2	1·03421758	1·24989222	1·03421947	1·24989035	1·03421944	1·24989032
4	1·00710030	1·29954077	1·00710172	1·29953937	1·00710169	1·29953933
6	0·98719792	1·34249955	0·98719910	1·34249839	0·98719907	1·34249834
8	0·97123407	1·38207159	0·97123511	1·38207057	0·97123508	1·38207053
10	0·95782732	1·41966713	0·95782827	1·41966621	0·95782824	1·41966616
12	0·94624181	1·45605321	0·94624268	1·45605236	0·94624266	1·45605232
14	0·93603079	1·49171041	0·93603160	1·49170962	0·93603157	1·49170957
16	0·92689885	1·52697092	0·92689963	1·52697018	0·92689960	1·52697013
18	0·91863839	1·56208251	0·91863913	1·56208181	0·91863910	1·56208176
20	0·91109649	1·59724198	0·91109719	1·59724131	0·91109717	1·59724126
22	0·90415626	1·63261440	0·90415693	1·63261376	0·90415691	1·63261371
24	0·89772546	1·66834501	0·89772611	1·66834439	0·89772608	1·66834434
26	0·89172928	1·70456716	0·89172991	1·70456656	0·89172989	1·70456651
28	0·88610551	1·74140798	0·88610613	1·74140740	0·88610610	1·74140735
30	0·88080115	1·77899270	0·88080175	1·77899214	0·88080172	1·77899209
32	0·87576998	1·81744825	0·87577056	1·81744771	0·87577053	1·81744765
34	0·87097076	1·85690652	0·87097133	1·85690599	0·87097131	1·85690593
36	0·86636581	1·89750747	0·86636637	1·89750695	0·86636634	1·89750689
38	0·86191980	1·93940243	0·86192035	1·93940192	0·86192033	1·93940186
40	0·85759884	1·98275772	0·85759938	1·98275722	0·85759936	1·98275716

5. Computer programme

The computer programme developed for the present method is available on request from the first author. In the programme one has to put (1) the data for the atomic masses (in atomic units), AMASS(1) and AMASS(2), of the atoms of the diatomic molecule; (2) the Dunham coefficients $Y_{i,0}$ and $Y_{i,1}$ (in cm^{-1}). The indices of the Dunham coefficients is increased by 1, for example, $Y(3,2)$ is used for $Y_{2,1}$.

In the programme, we have used the Dunham coefficients for the CO molecule, given by Farrenq *et al* [18]. The output of the programme is given in Appendix 1, where the Klein integrals F (in cm) and G (in cm^{-1}), the turning points RMIN and RMAX (in Å), and the potential energy (POTENE) (in cm^{-1}) are given for the vibrational quantum number V up to 40.

6. Conclusions

On the basis of the facts mentioned in the previous sections, we can conclude that the present method for the evaluation of the RKR potential-integrals for diatomic molecules is straightforward and fast, and the calculations can be performed to a better accuracy than that of the other methods. In the approach, the accuracy can be enhanced (i) by considering the higher powers of r in (28) and (32) and (ii) by reducing the step-size in the numerical integration of the first part. However, the achievement of the accuracy is limited by the accuracy of the computer used.

Appendix 1

ATOMIC MASSES ARE: 12·00000 15·99491

VIBRATIONAL DUNHAM COEFFICIENTS ARE:

2169·812670	− 13·28787634	1·0411066470E − 02
6·9366407560E − 05	1·6793523060E − 07	2·0592515760E − 09
− 8·4881457070E − 10	1·2397720130E − 11	− 8·2337372780E − 14

ROTATIONAL DUNHAM COEFFICIENTS ARE:

1·931280985	− 1·7504392290E − 02	7·1739170070E − 07
− 2·1463545860E − 08	4·4354039090E − 09	− 1·3610694500E − 10
1·2457857150E − 12	− 2·1251234150E − 14	

V	F	G	RMIN	RMAX	POTENE
0	4·77277D − 10	3·73757D + 06	1·083312	1·178767	1081·5857
1	8·30935D − 10	6·46760D + 06	1·053423	1·219610	3224·8568
2	1·07832D − 09	8·34185D + 06	1·034222	1·249886	5341·6478
3	1·28258D − 09	9·86103D + 06	1·019395	1·275911	7432·0247
4	1·46202D − 09	1·11710D + 07	1·007114	1·299518	9496·0550
5	1·62496D − 09	1·23386D + 07	0·996547	1·321539	11533·8078

V	F	G	RMIN	RMAX	POTENE
6	1·77605D − 09	1·34011D + 07	0·987231	1·342441	13545·3543
7	1·91816D − 09	1·43819D + 07	0·978880	1·362513	15530·7670
8	2·05325D − 09	1·52966D + 07	0·971300	1·381951	17490·1202
9	2·18270D − 09	1·61567D + 07	0·964355	1·400896	19423·4901
10	2·30754D − 09	1·69703D + 07	0·957942	1·419451	21330·9539
11	2·42855D − 09	1·77439D + 07	0·951986	1·437696	23212·5907
12	2·54636D − 09	1·84826D + 07	0·946424	1·455697	25068·4807
13	2·66147D − 09	1·91904D + 07	0·941210	1·473505	26898·7056
14	2·77430D − 09	1·98706D + 07	0·936302	1·491162	28703·3478
15	2·88517D − 09	2·05261D + 07	0·931670	1·508704	30482·4908
16	2·99440D − 09	2·11590D + 07	0·927285	1·526164	32236·2189
17	3·10222D − 09	2·17714D + 07	0·923124	1·543568	33964·6167
18	3·20887D − 09	2·23651D + 07	0·919168	1·560941	35667·7691
19	3·31452D − 09	2·29414D + 07	0·915398	1·578303	37345·7608
20	3·41936D − 09	2·35018D + 07	0·911802	1·595674	38998·6766
21	3·52354D − 09	2·40472D + 07	0·908364	1·613072	40626·6001
22	3·62719D − 09	2·45789D + 07	0·905074	1·630513	42229·6144
23	3·73045D − 09	2·50976D + 07	0·901923	1·648013	43807·8009
24	3·83344D − 09	2·56041D + 07	0·898899	1·665587	45361·2396
25	3·93626D − 09	2·60993D + 07	0·895996	1·683249	46890·0081
26	4·03903D − 09	2·65838D + 07	0·893207	1·701012	48394·1814
27	4·14183D − 09	2·70582D + 07	0·890524	1·718890	49873·8318
28	4·24478D − 09	2·75231D + 07	0·887941	1·736896	51329·0276
29	4·34795D − 09	2·79789D + 07	0·885454	1·755044	52759·8334
30	4·45144D − 09	2·84262D + 07	0·883057	1·773345	54166·3090
31	4·55534D − 09	2·88654D + 07	0·880745	1·791814	55548·5091
32	4·65974D − 09	2·92970D + 07	0·878515	1·810464	56906·4825
33	4·76473D − 09	2·97212D + 07	0·876363	1·829310	58240·2716
34	4·87040D − 09	3·01386D + 07	0·874286	1·848365	59549·9117
35	4·97683D − 09	3·05494D + 07	0·872279	1·867645	60835·4299
36	5·08413D − 09	3·09540D + 07	0·870341	1·887167	62096·8449
37	5·19239D − 09	3·13527D + 07	0·868468	1·906946	63334·1657
38	5·30171D − 09	3·17458D + 07	0·866659	1·927001	64547·3909
39	5·41220D − 09	3·21336D + 07	0·864909	1·947350	65736·5076
40	5·52398D − 09	3·25164D + 07	0·863219	1·968015	66901·4905

Acknowledgements

One of the authors (SC) is grateful to Prof. Dr W H Kegel for fruitful discussions during his visit to Germany under the Scientific Exchange Programme between the I.N.S.A., New Delhi and the D.F.G., Bonn. He is thankful to Dr Bruno Deiss for helpful discussions. We are also grateful to Prof. J V Narlikar for his encouragements. Facilities used at the IUCAA, Pune are thankfully acknowledged.

References

[1] O Klein, *Z. Phys.* **76**, 226 (1932)
[2] A L G Rees, *Proc. Phys. Soc. (London)* **A59**, 998 (1947)
[3] E W Kaiser, *J. Chem. Phys.* **53**, 1686 (1970)
[4] S Weissman, J T Vanderslice and R Battino, *J. Chem. Phys.* **39**, 2226 (1963)
[5] W G Richards and R F Barrow, *Proc. Phys. Soc. (London)* **83**, 1045 (1964)
[6] R N Zare, *J. Chem. Phys.* **40**, 1934 (1964)
[7] F R Gilmore, *J. Quant. Spectrosc. Radiat. Transfer* **5**, 369 (1965)
[8] F J Zeleznik, *J. Chem. Phys.* **42**, 2836 (1965)
[9] W R Jarmain, *J. Quant. Spectrosc. Radiat. Transfer* **11**, 421 (1971)
[10] A W Mantz, J K G Watson, K Narahari Rao, D L Albritton, A L Schmeltekopf and R N Zare, *J. Mol. Spectrosc.* **39**, 180 (1971)
[11] A S Dickinson, *J. Mol. Spectrosc.* **44**, 183 (1972)
[12] H E Fleming and K Narahari Rao, *J. Mol. Spectrosc.* **44**, 189 (1972)
[13] J Tellinghuisen, *J. Mol. Spectrosc.* **44**, 194 (1972); *Comput. Phys. Commun.* **6**, 221 (1974)
[14] S M Kirschner and J K G Watson, *J. Mol. Spectrosc.* **47**, 234 (1973)
[15] H Telle and U Telle, *J. Mol. Spectrosc.* **85**, 248 (1981)
[16] R J Le Roy, Univ. of Waterloo, Chemical Physics Research Report CP-425 (1992)
[17] S Chandra, W H Kegel, R J Le Roy and T Hertenstein, *Astron. Astrophys. Suppl.* **114**, 175 (1995)
[18] R Farrenq, G Guelachvili, A J Sauval, N Grevesse and C B Farmer, *J. Mol. Spectrosc.* **149**, 375 (1991)

$(e, 2e)$ triple differential cross section for ionization-excitation of helium

SEEMA GUPTA and M K SRIVASTAVA
Department of Physics, University of Roorkee, Roorkee 247 667, India

MS received 29 January 1996; revised 27 May 1996

Abstract. Simultaneous ionization and excitation of helium by electron impact is considered in an improved second Born approximation. The wave function of the low energy ejected electron is obtained in the field of residual He^+ ion in 2s-state. The calculation has been done for the process $e^- + He \rightarrow e^- + He^+(2s) + e^-$ in the coplanar asymmetric geometry with Hartree-Fock wave function of Byron and Joachain for the helium ground state and the results are compared with the absolute experimental data of Dupre *et al* [*J. Phys.* **B25**, 259 (1992)] at $\sim 5{\cdot}5$ keV incident energy. Our results are found to increase the ratio of the recoil peak to binary peak intensity by about 30% over the first Born results and thus to bring it closer to the experimental data.

Keywords. Excitation alongwith ionization; two active atomic electrons; second Born approximation.

PACS No. 34·80

1. Introduction

Most of the $(e - 2e)$ studies have been confined to the ionizing processes which leave the residual positive ion in the ground state. However, the related process of simultaneous ionization and excitation of the target by the incoming electron has been studied very little. In this process, one electron is ejected and a second one is transferred to some available excited state of the residual ion. This process therefore provides an interesting link between the widely investigated single ionization $(e - 2e)$ area and the recently emerged double ionization $(e - 3e)$ area. It can proceed via two mechanisms:

(i) The shake-off (SO) mechanism which corresponds to single ionization followed by final state rearrangement.
(ii) The two-step (TS) mechanism in which the projectile interacts with both the atomic electrons.

Several studies have been carried out to probe the sensitivity of triple differential cross section (TDCS) to the initial and final state correlations. The process $e^- + He \rightarrow e^- + He^+(2s, 2p) + e^-$ has been investigated by Cook *et al* [1], Smith *et al* [2], Stefani *et al* [3], Avaldi *et al* [4] and Dupre *et al* [5] in high incident energy experiments. Calculations have been done in the framework of the first Born approximation with various prescriptions for obtaining ejected electron wave function [6–10]. The plane and distorted wave impulse approximations have also been used [2, 11, 12].

Recently a first order calculation with correlated Coulomb wave function of Brauner *et al* [13] has also been tried [14]. It is found that, in the asymmetric kinematics where the dynamics is more important, no single model is able to reproduce angular variation of TDCS at incident energies 645·4 eV, 1585·4 eV and ~5·5 keV where experimental data are available. However these calculations have indicated that the TDCS are not very sensitive to the $e-e$ correlations in the initial state, though they are important to allow collective ionization-excitation of the two target electrons in a first order model. On the other hand a proper description of the ejected electron which takes into account its interaction with the residual excited ion in $n=2$ state of larger spatial extent is crucial and is largely responsible for a larger recoil intensity and for an angular distribution whose shape is no longer made of the usual binary and recoil lobes. These features tend to vanish as the ejected electron energy increases.

In the present paper we investigate the role of (i) dynamic correlations in the continuum final state and (ii) two-step (TS) processes. The second order terms in the scattering amplitude are expected to be quite important up to certain high incident energies. The calculation has been done in the second Born approximation for asymmetric kinematics. A similar calculation was done by Saxena *et al* [15] at an incident energy of 600 eV and the results were compared with those for ionization without excitation. The present calculation differs from this attempt in the sense that the low energy ejected electron wave function is calculated in the static field of the residual ion. Earlier calculations have already underlined the importance of this feature. We have, for this study, considered the simple process $e^- + \mathrm{He} \rightarrow e^- + \mathrm{He}^+(2s) + e^-$ in the asymmetric kinematics at an incident energy of ~5·5 keV with the Hartree-Fock wave function of Byron and Joachain [16] for the helium ground state.

2. Calculation

The triple differential cross section (TDCS) for the ionization of helium may be expressed as

$$\frac{\mathrm{d}^3\sigma}{\mathrm{d}\Omega_a \mathrm{d}\Omega_b \mathrm{d}E_b} = \frac{k_a k_b}{k_0}|F|^2, \tag{1}$$

where F is the direct scattering amplitude and $\mathbf{k}_0$, $\mathbf{k}_a$ and $\mathbf{k}_b$ are the momenta of the incident, scattered and ejected electrons respectively. In the present improved second Born approximation the direct scattering amplitude may be expressed as

$$F_{CB2} = f_{CB1} + f_{CB2}, \tag{2}$$

where f_{CB1} and f_{CB2} are respectively the first and second order Born amplitudes. The amplitude f_{CB1} is given by

$$f_{CB1} = -\frac{1}{2\pi}\left\langle \mathrm{e}^{\mathrm{i}\mathbf{k}_a\cdot\mathbf{r}_0}\Phi_f(\mathbf{r}_1,\mathbf{r}_2)\left|\frac{1}{r_{01}}+\frac{1}{r_{02}}\right|\mathrm{e}^{\mathrm{i}\mathbf{k}_0\cdot\mathbf{r}_0}\Phi_0(\mathbf{r}_1,\mathbf{r}_2)\right\rangle. \tag{3}$$

Here $\mathbf{r}_0$, $\mathbf{r}_1$ and $\mathbf{r}_2$ are the position vectors of the incident and the two target electrons respectively, Φ_0 is the ground state wave function of helium atom which is taken to be

$$\Phi_0(\mathbf{r}_1, \mathbf{r}_2) = u(\mathbf{r}_1)u(\mathbf{r}_2), \tag{4}$$

$$u(\mathbf{r}) = \sum_{i=1}^{2} \gamma_i e^{-\alpha_i r},$$

with

$$\alpha_1 = 1{\cdot}41, \quad \alpha_2 = 2{\cdot}61,$$

$$\gamma_1 = 0{\cdot}73485 \text{ and } \gamma_2 = 0{\cdot}58715.$$

The final state wave function Φ_f is taken to be the symmetrized product of the He^+ excited state (2s) wave function $v(\mathbf{r})$ for the bound electron with the continuum wave function $\psi_{\mathbf{k}_b}^{(-)}$ (orthogonalized to the ground state orbital $u(\mathbf{r})$) for the ejected electron:

$$\Phi_f(\mathbf{r}_1, \mathbf{r}_2) = \frac{1}{\sqrt{2}}[\psi_{\mathbf{k}_b}^{(-)}(\mathbf{r}_1)\, v(\mathbf{r}_2) + \psi_{\mathbf{k}_b}^{(-)}(\mathbf{r}_2)\, v(\mathbf{r}_1)], \tag{5}$$

$$v(\mathbf{r}) = \frac{1}{\sqrt{\pi}}(1 - r)e^{-r}, \tag{6}$$

$$\psi_{\mathbf{k}_b}^{(-)}(\mathbf{r}) = \phi_{\mathbf{k}_b}^{(-)}(\mathbf{r}) - \langle u(\mathbf{r})|\phi_{\mathbf{k}_b}^{(-)}(\mathbf{r})\rangle u(\mathbf{r}). \tag{7}$$

Using (4)–(7) in (3) and integrating with respect to $\mathbf{r}_0$, we get

$$f_{CB1} = -\frac{2^{3/2}}{K^2}\langle v|u\rangle[\langle\phi_{\mathbf{k}_b}^{(-)}(\mathbf{r})|e^{i\mathbf{K}.\mathbf{r}}|u(\mathbf{r})\rangle - \langle u(\mathbf{r})|e^{i\mathbf{K}.\mathbf{r}}|u(\mathbf{r})\rangle$$

$$\langle\phi_{\mathbf{k}_b}^{(-)}(\mathbf{r})|u(\mathbf{r})\rangle], \tag{8}$$

where $\mathbf{K} = \mathbf{k}_0 - \mathbf{k}_a$. The wave function $\phi_{\mathbf{k}_b}^{(-)}(\mathbf{r})$ is written as

$$\phi_{\mathbf{k}_b}^{(-)}(\mathbf{r}) = \phi_{C,\mathbf{k}_b}^{(-)}(\mathbf{r}) + (\phi_{\mathbf{k}_b}^{(-)}(\mathbf{r}) - \phi_{C,\mathbf{k}_b}^{(-)}(\mathbf{r}))$$

$$= \phi_{C,\mathbf{k}_b}^{(-)}(\mathbf{r}) + \chi_{\mathbf{k}_b}^{(-)}(\mathbf{r}), \tag{9}$$

where $\phi_{C,\mathbf{k}_b}^{(-)}$ is the Coulomb wave function (corresponding to $Z = 1$) with appropriate boundary conditions

$$\phi_{C,\mathbf{k}_b}^{(-)} = e^{-\pi\eta/2}\Gamma(1 - i\eta)e^{i\mathbf{k}_b.\mathbf{r}}\,{}_1F_1(i\eta; 1, -ik_b r - i\mathbf{k}_b.\mathbf{r}), \tag{10}$$

$$\eta = -1/k_b.$$

The correction $\chi_{\mathbf{k}_b}^{(-)}(\mathbf{r}) \equiv (\phi_{\mathbf{k}_b}^{(-)}(\mathbf{r}) - \phi_{C,\mathbf{k}_b}^{(-)}(\mathbf{r}))$ is expressed in the partial wave form

$$\chi_{\mathbf{k}_b}^{(-)}(\mathbf{r}) = \sum_{\ell} i^{\ell}(2\ell + 1)(e^{-i\delta_\ell}R_\ell(r) - e^{-i\delta_\ell^C}R_\ell^C(r))P_\ell(\hat{k}_b.\hat{r}). \tag{11}$$

Here, $R_\ell^C(r)$ is the ℓth Coulomb partial wave and δ_ℓ^C is the corresponding phase shift. The radial solution $R_\ell(r)$ and the phase shift δ_ℓ are obtained by solving the radial Schrödinger equation in the static field V_0 of He^+ ion:

$$V_0(r) = \int |v(\mathbf{r}')|^2 \left(\frac{2}{r} - \frac{1}{|\mathbf{r}' - \mathbf{r}|}\right) d\mathbf{r}'. \tag{12}$$

Using (9) and (11) in (8), one finally obtains

$$f_{CB1} = f_{B1} - \frac{2^{7/2}}{K^2}\pi C_1(0)\left[\sum_\ell (2\ell+1)P_\ell(\hat{K}.\hat{k}_b)D_\ell(K) - C_2(K)D_0(0)\right], \quad (13)$$

where

$$C_1(K) = \int v(\mathbf{r})u(\mathbf{r})e^{i\mathbf{k}.\mathbf{r}}d\mathbf{r}, \quad (14)$$

$$C_2(K) = \int u^2(\mathbf{r})e^{i\mathbf{K}.\mathbf{r}}d\mathbf{r} \quad (15)$$

and

$$D_\ell(K) = \int u(r)j_\ell(Kr)[e^{i\delta_\ell}R_\ell(r) - e^{i\delta_\ell^C}R_\ell^C(r)]r^2 dr. \quad (16)$$

The amplitude f_{B1}, is the usual first Born amplitude which is evaluated in the standard way [17, 16]. The second term in (13) represents the correction due to the improved choice, (9), in place of $\phi^{(-)}_{C,\mathbf{k}_b}(\mathbf{r})$ for the ejected electron wave function. The radial integral in (16) is evaluated numerically.

The second Born term f_{CB2} may be written as

$$f_{CB2} = \frac{1}{8\pi^4}\int d\mathbf{q}\frac{1}{q^2 - p^2 - i\varepsilon}M, \quad (17)$$

where

$$M = \frac{16\pi^2}{K_i^2 K_f^2}\langle\Phi_f(\mathbf{r}_1,\mathbf{r}_2)|(e^{-i\mathbf{K}_f.\mathbf{r}_1} + e^{-i\mathbf{K}_f.\mathbf{r}_2} - 2)$$
$$\times (e^{i\mathbf{K}_i.\mathbf{r}_1} + e^{i\mathbf{K}_i.\mathbf{r}_2} - 2)|\Phi_i(\mathbf{r}_1,\mathbf{r}_2)\rangle, \quad (18)$$
$$p^2 = k_0^2 - 2\bar{\omega}, \mathbf{K}_i = \mathbf{k}_0 - \mathbf{q} \text{ and } \mathbf{K}_f = \mathbf{k}_a - \mathbf{q}.$$

The excitation energies of the intermediate states have been approximated by an average excitation energy $\bar{\omega}$ and the sum over them carried out by using the closure property. We have taken $\bar{\omega}$ equal to the ionization energy plus the $n=1$ to $n=2$ excitation energy, $0{\cdot}9 + 1{\cdot}5 = 2{\cdot}4$ a.u. It is essentially a parameter. The results are, however, found to be not very sensitive to this choice. Using (4), (5), (14)–(16) in eq. (18), one obtains

$$M = \frac{16\sqrt{2}\pi^2}{K_i^2 K_f^2}[C_1(K_f)\langle\psi^{(-)}_{\mathbf{k}_b}(\mathbf{r}_1)|e^{i\mathbf{K}_i.\mathbf{r}_1}|u(\mathbf{r}_1)\rangle$$
$$+ C_1(K_i)\langle\psi^{(-)}_{\mathbf{k}_b}(\mathbf{r}_2)|e^{-i\mathbf{K}_f.\mathbf{r}_2}|u(\mathbf{r}_2)\rangle$$
$$+ C_1(0)\langle\psi^{(-)}_{\mathbf{k}_b}(\mathbf{r}_1)|e^{i\mathbf{K}.\mathbf{r}_1} - 2e^{i\mathbf{K}_i.\mathbf{r}_1} - 2e^{i\mathbf{K}_f.\mathbf{r}_1}|u(\mathbf{r}_1)\rangle], \quad (19)$$

which by using (7), (9) and (10) and the partial wave decomposition leads to

$$M = M_C + \frac{16\sqrt{2}\pi^2}{K_i^2 K_f^2}\Bigg[4\pi\sum_\ell (2\ell+1)\{C_1(0)D_\ell(K)P_\ell(\hat{K}.\hat{k}_b) + (C_1(K_f)$$
$$- 2C_1(0)D_\ell(K_i)P_\ell(\hat{K}_i.\hat{k}_b)) + (C_1(K_i) - 2C_1(0))$$
$$\times D_\ell(K_f)P_\ell(\hat{K}_f.\hat{k}_b)\} - 4\pi\{C_2(q) - 2(C_2(K_i) + C_2(K_f))$$
$$+ C_1(K_f)C_2(K_i) + C_1(K_i)C_2(K_f)\}D_0(0)\Bigg], \quad (20)$$

where M_C corresponds to the contribution in the usual second Born amplitude f_{B2} which is evaluated by following the method of Ehrhardt *et al* [17] and Baliyan and Srivastava [18]. The second part in (20) represents the correction due to the choice $\phi^{(-)}_{\mathbf{k}_b}(\mathbf{r})$ rather than the standard Coulomb wave $\phi^{(-)}_{C,\mathbf{k}_b}(\mathbf{r})$ for the ejected electron. The maximum value of ℓ in the summations over ℓ in (13) and (20) has been obtained by comparing the results with $\ell_{max} = 0$, 1 and 2. It is found that taking $\ell_{max} = 1$ is good enough for ejected electron energies E_b up to 10 eV. For larger E_b, a higher ℓ_{max} is perhaps needed. We have, however, taken $\ell_{max} = 2$ in all the cases considered here. The integration over $\mathbf{q}$ in (17) is performed numerically following Srivastava and Sharma [19].

3. Results

Figures 1–3 show our results in the coplanar geometry plotted against the ejected electron angle θ_b for (i) $\theta_a = 0{\cdot}35°$, $E_b = 5$ eV, (ii) $\theta_a = 0{\cdot}32°$, $E_b = 10$ eV and (iii) $\theta_a = 1°$, $E_b = 75$ eV respectively in the first Born approximation B1 (× × ×), second Born approximation B2 (○ ○ ○), improved first Born approximation CB1 (– – –) and improved second Born approximation CB2 (———). The scattered electron energy E_a in every case is 5·5 keV. The theoretical results have been normalized to the absolute experimental data of Dupre *et al* [11] for excitation to $n = 2$(s, p) by multiplying them by the factors shown in the figures. The recoil peak intensity naturally decreases in all cases as E_b increases. The second Born approximation leads to a decrease (increase) in

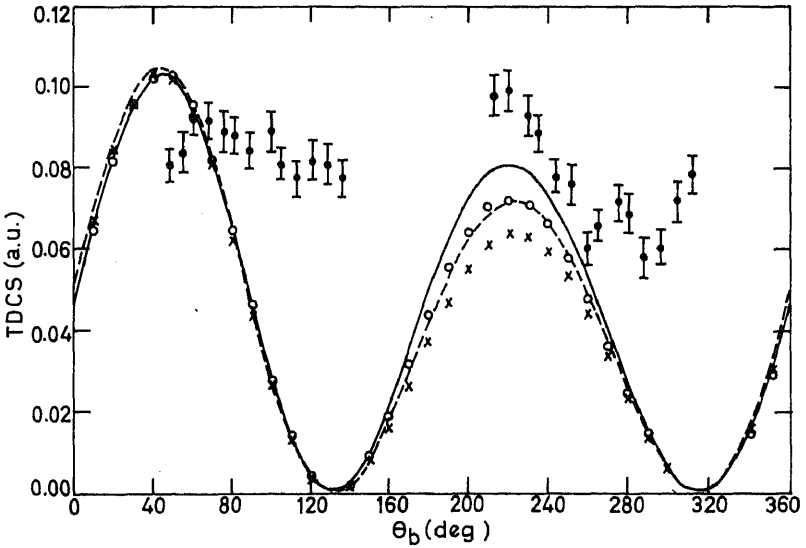

Figure 1. Triple differential cross sections (in a.u.) for the simultaneous ionization and excitation of helium by electron impact at $E_0 = 5570{\cdot}4$ eV, $E_b = 5$ eV and $\theta_a = 0{\cdot}35°$ plotted as a function of ejection angle θ_b. Theoretical results: × × × ×: (B1 × 0·182); – – – –: (CB1 × 0·238); ○ ○ ○ ○: (B2 × 0·190) and ———: (CB2 × 0·25). Experimental data are the absolute measurements of Dupre *et al* [11] for excitation to He^+ (2s, 2p).

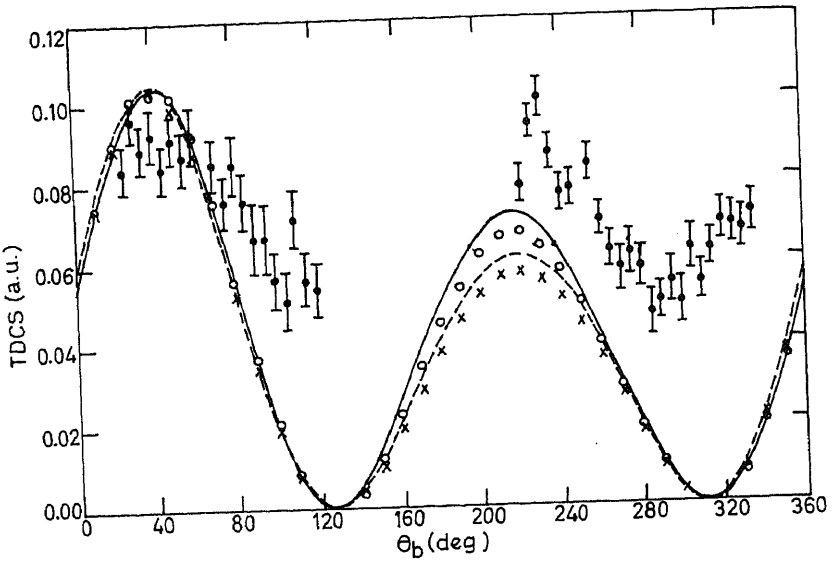

Figure 2. Same as figure 1 but for $E_0 = 5575{\cdot}4$ eV, $E_b = 10$ eV and $\theta_a = 0{\cdot}32°$. Theoretical results: ××××: (B1 × 0·263); ----: (CB1 × 0·370); ○○○○: (B2 × 0·278) and ———: (CB2 × 0·40).

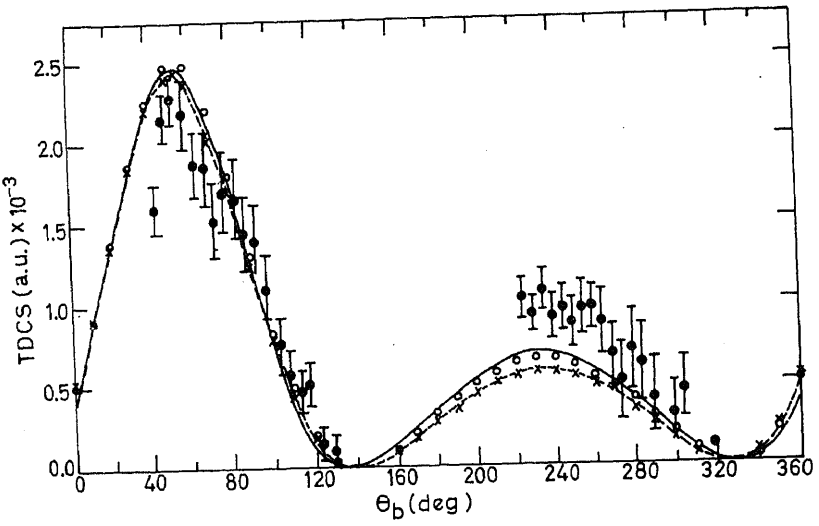

Figure 3. Same as figure 1 but for $E_0 = 5640{\cdot}4$ eV, $E_b = 75$ eV and $\theta_a = 1°$. Theoretical results: ××××: (B1 × 0·65); ----: (CB1 × 1·1); ○○○○: (B2 × 0·7) and ———: (CB2 × 1·2).

the binary (recoil) peak height. This feature is similar to what is found in the case of ionization without excitation. The ratio of the recoil peak to binary peak intensity increases by about 15% in B2 results over B1 at $E_b = 5$ eV (figure 1). This improvement

is little less at $E_b = 10$ eV and $E_b = 75$ eV. The model CB2 leads to an improvement of about 30% in this ratio over the B1 results at $E_b = 5$ and 10 eV. At $E_b = 75$ eV (figure 3), the increase is less, about 12%. The experiments indicate a still larger recoil peak intensity. A possible reason for this inadequacy of the present model could be the use of average excitation energy $\bar{\omega}$ and closure used in the evaluation of the second Born term. A variation of $\bar{\omega}$ within the present model does not lead to much change in the results.

4. Conclusions

The 'improved' second Born approximation is found to increase the ratio of recoil peak to binary peak intensity quite a bit over the value obtained by using the first Born approximation. However this enhancement is not large enough to reproduce the experimental value. The present model also fails to reproduce shallow maxima and minima observed in the angular distribution of TDCS for small ejected electron energies. The second order term is thus important but not enough to reproduce the observed angular distribution of the cross section.

Acknowledgement

One of the authors (SG) would like to thank the University Grants Commission, Government of India for a research fellowship.

References

[1] J P D Cook, I E McCarthy, A T Stelbovics and E Weigold, *J. Phys.* **B17**, 2339 (1984)
[2] A D Smith, M A Coplan, D J Chornay, J H Moore, J A Tossell, J Mrozek, V H Smith Jr and N S Chant, *J. Phys.* **B19**, 969 (1986)
[3] G Stefani, L Avaldi and R Camilloni, *J. Phys.* **B23**, L227 (1990)
[4] L Avaldi, R Camilloni, S Cvejanovics, R A Multari and G Stefani, *Proc. 17th Int. Conf. Phys. Elect. and Atomic Collisions*, Brisbane (1991) p. 175
[5] C Dupre, A Duguet and A Lahmam-Bennani, *Proc. Workshop (e, 2e) Collisions and Related Problem, Rome* edited by G Stefani (1990) p. 9
[6] F Mota-Furtado and P F O'Mahony, *Proc. Workshop (e, 2e) Collisions and Related Problems, Kaiserslautern* edited by H Ehrahardt (1990) p. 7
[7] P F O'Mahony and F Mota-Furtado, *Proc. Workshop (e, 2e) Collisions and Related Problems, Rome* edited by G Stefani (1990) p. 1
[8] O Robaux, R J Tweed and J Langlois, *J. Phys.* **B24**, 457 (1991)
[9] C Dupre, A Lahmam-Bennani, A Duguet, F Mota-Furtado, P F O'Mahony and C Dal Cappello, *J. Phys.* **B25**, 259 (1992)
[10] A Lahmam-Bennani, A Duguet, C Dupre and C Dal Cappello, *J. Electron. Spectrosc. Related Phenomena* **58**, 17 (1992)
[11] F P Larkins, *J. Phys.* **B14**, 1477 (1981)
[12] F P Larkins and J A Richards, *Chem. Phys.* **81**, 329 (1983)
[13] M Brauner, J S Briggs and H Klar, *J. Phys.* **B22**, 2265 (1989)
[14] A Franz and P L Altick, *J. Phys.* **B25**, L257 (1992)
[15] Sushma Saxena, K S Baliyan and M K Srivastava, *J. Phys.* **B20**, L611 (1987)
[16] F W Byron Jr and C J Joachain, *Phys. Rev.* **146**, 1 (1966)
[17] H Ehrhardt, M Fischer, K Jung, F W Byron Jr, C J Joachain and B Piraux, *Phys. Rev. Lett.* **48**, 1807 (1982)
[18] K S Baliyan and M K Srivastava, *J. Phys.* **B19**, 3603 (1986)
[19] M K Srivastava and Sadhana Sharma, *Phys. Rev.* **A37**, 628 (1988)

Positron scattering from alkaline-earth elements

RITU RAIZADA and K L BALUJA
Department of Physics and Astrophysics, University of Delhi, Delhi 110007, India

MS received 28 February 1996; revised 8 May 1996

Abstract. The total (elastic + inelastic) cross sections for e^+ impact on alkaline-earth elements from Be to Ra are calculated by employing a complex spherical optical potential. This potential has static, polarization and absorption components. The positron energy range is from a few eV to several thousand eV. We have compared our elastic cross sections for Mg and Ca with the other available results and the agreement is good for energies above 100 eV. We have also compared our absorption cross sections with e^- ionization cross sections at high energies where our absorption cross sections are in good accord. We have made Bethe plots for e^+ scattering on these elements.

Keywords. Positron; alkaline-earth elements; static potential; optical potential; polarization potential; absorption potential; inelastic and total cross sections; Bethe plot.

PACS Nos 34·80; 34·90

1. Introduction

Since the advent of positron beams of well defined energies, the study of positron scattering from atoms and molecules has become an important branch of research in atomic physics. One of the principal objectives for obtaining cross section data for the scattering of positrons from atoms has been to compare this data with that of electrons. There are interesting differences in the cross sections for the two cases. The Coulomb static field for the electron case is attractive in contrast to the repulsive field experienced by the positrons. The dipole polarization term which arises from the second order perturbation theory is attractive in both cases. Because of the cancellation effects in static and polarization components of the interaction of positron with atoms, the elastic cross sections for positrons are smaller than the corresponding e^- case for energies up to 100 eV. Since the total cross sections for both the cases merge with each other at high energies, the inelastic cross sections for positrons would be higher than the corresponding electron case. At low energies the virtual positronium formation term must be taken into account whereas for electrons it is the exchange effect which is important. There are several interesting articles on positron impact on various targets [1–9].

Most of the experimental and theoretical work has been concentrated on positron impact on H, noble gases, alkali atoms and some diatomic and polyatomic molecules [10–21]. However, there are some calculations of elastic scattering of e^+ by Mg [22] and Ca [23] using a real optical potential. In the present work, we have calculated elastic, inelastic and total cross sections for e^+ impact on alkaline-earth atoms Be, Mg,

Ca, Ba, Sr and Ra. These atoms are characterized by two *s* electrons in their outermost shell. We have employed an optical potential approach in which the positron-atom interaction term is replaced by a complex potential. The real part of this complex potential consists of static and polarization terms and imaginary part accounts for the absorption of flux from the incident positrons. We report elastic, absorption and total cross sections for e^+ impact on all alkaline earth elements from Be to Ra in the energy range 10 eV to few thousand eV.

2. Theory

The basic idea of the optical model potential approach is to reduce many body problems to an equivalent one body problem. Above the first ionization threshold, the interaction between the e^+ and target is represented by a complex optical potential $V_{\text{opt}}(\mathbf{r})$. The scattering function $F(\mathbf{r})$ of the positron satisfies the differential equation

$$(\nabla^2 + k^2 - V_{\text{opt}}(\mathbf{r}))F(\mathbf{r}) = 0, \tag{1}$$

where k^2 is the energy of the incident positron. The optical potential is a complex, non local, non spherically symmetric and energy dependent potential whose evaluation is a formidable task. In the present work we have replaced $V_{\text{opt}}(\mathbf{r})$ by spherically symmetric potential $V_{\text{opt}}(r)$. We represent $V_{\text{opt}}(r)$ by various local potentials of the form [14]

$$V_{\text{opt}}(r) = V_{\text{st}}(r) + V_{\text{pol}}(r) + iV_{\text{abs}}(r). \tag{2}$$

The static potential $V_{\text{st}}(r)$ is calculated from the unperturbed target wavefunctions at the Dirac–Hartree–Fock level [24]. This relativistic potential has been parametrized as a sum of three Yukawa potentials. Its form is

$$V_{\text{st}}(r) = \frac{Z}{r}\sum_{i=1}^{3} A_i e^{-\alpha_i r}, \tag{3}$$

where A_i and α_i are parameters. In principle, these parameters can be determined so that one-electron binding energies agree with Dirac–Hartree–Fock–Slater energy eigenvalues by employing a conventional least-square fitting procedure. However, such a procedure makes the values of A_i and α_i sensitive to the initial estimate. An alternative procedure is to reproduce the expectation values of $\langle r^n \rangle$ where $n = -1, 0, 1, 2, 3$ and 4. The atomic density takes the analytic form

$$\rho(r) = \frac{Z}{r}\sum_i A_i \alpha_i^2 \exp(-\alpha_i r). \tag{4}$$

The form $V_{\text{st}}(r)$ of (3) is not a unique one. Other forms like a sum of exponential terms or a sum of exponential and Yukawa terms can be employed.

$V_{\text{pol}}(r)$ represents the polarization potential which arises due to the distortion of the electronic charge cloud by the incident positron. The effect of polarization is very important for alkaline-earth elements because of the large value of dipole polarizabilities of these atoms. The long range part of the polarization assumes its asymptotic form

$$V_{\text{pol}}(r) = \frac{-\alpha_d}{2r^4}, \quad r > r_c. \tag{5}$$

In the short range part $r < r_c$, the polarization potential is evaluated by calculating the correlation energy $\varepsilon_{corr}(r_s)$ of a single e^+ in a homogeneous electron gas [25]. The correlation energy is calculated from the ground state expectation value of the Hamiltonian which describes the fixed positron interacting with the target electrons. This polarization is different from that of the corresponding short range part of the e^- case [26] because the e^+ distorts the electronic charge cloud differently than the corresponding e^- case. The polarization potential $V_{corr}(r)$ is related to $\varepsilon_{corr}(r_s)$ by

$$V_{corr}(r) = \left[1 - \frac{1}{3} r_s \frac{d}{dr_s}\right] \varepsilon_{corr}(r_s). \tag{6}$$

Its explicit form is given as [14]

(i) for $r_s < 0{\cdot}302$,

$$2V_{corr}(r) = -\frac{1{\cdot}82}{(r_s)^{1/2}} + [0{\cdot}051 \ln(r_s) - 0{\cdot}115]\ln(r_s) + 1{\cdot}167, \tag{7a}$$

(ii) for $0{\cdot}302 \leqslant r_s \leqslant 0{\cdot}56$,

$$2V_{corr}(r) = -0{\cdot}92305 - \frac{0{\cdot}09098}{(r_s)^2} \tag{7b}$$

and

(iii) for $0{\cdot}56 \leqslant r_s \leqslant 8{\cdot}0$,

$$2V_{corr}(r) = -\frac{8{\cdot}764 r_s}{(r_s + 2{\cdot}5)^3} + \frac{0{\cdot}9552 r_s - 13{\cdot}151}{(r_s + 2{\cdot}5)^2} + \frac{2{\cdot}8655}{(r_s + 2{\cdot}5)} - 0{\cdot}6298. \tag{7c}$$

r_c in (5) is the first crossing point of the short and long range parts and r_s is defined by

$$(4/3)\Pi r_s^3 \rho(r) = 1. \tag{8}$$

It may be pointed out that in the limit $r_s \to 0$, $V_{corr}(r)$ diverges. This is due to the strong short-range correlation between the positron and the homogeneous electron gas. When $r_s \to \infty$ (or $\rho(r) \to 0$), $V_{corr}(r)$ is designed such that it approximately reproduces the binding energy of the positronium. Since we know that asymptotically, the polarization potential behaves like $-\alpha/2r^4$, we assume this form beyond the radius r_c. The formulas 7(a–c) have been derived so that the correlation-energy functionals and its derivatives are continuous over the entire range of r_s values. In other words, $V_{corr}(r)$ is a continuous function of r.

Semi-empirical models have been developed to determine the imaginary part $V_{abs}(r)$ of the optical potential for the case of e^- scattering. The imaginary part $V_{abs}(r)$ represents the total loss of flux into all accessible channels. We, in the present work, have employed the semi-empirical form [27–30] $V^-_{abs}(r)$ of e^- case modified as $V^+_{abs}(r)$ for e^+ case as prescribed earlier [14]. These are related as

$$V^+_{abs}(r) = f(k, r)\, V^-_{abs}(r). \tag{9}$$

It is a formidable task to determine the form of $f(k, r)$ from an *ab-initio* point of view. This relation is further dictated by certain conditions which hold in the electron as well

as in the positron case. The imposed conditions for the electron case are that (1) the initially unbound electron is not allowed to fall into the occupied Fermi sea, and (2) the lowest-energy state available to the initially bound electron exceeds the Fermi level by the energy gap (Δ). These conditions are also valid when the incident projectile is a positron. It has been shown [14] that by choosing $f(k,r) = 2/(kr)^{1/2}$, there is a good agreement between calculated total cross sections and the experimental results for Ar, Kr, Xe and Rn. The factor 2 accounts for the fact that exchange is absent in positron scattering. It may be pointed out that a factor of 1/2 approximately accounts for exchange effects in the evaluation of $V^{-}_{abs}(r)$. So to remove this factor, a factor of 2 appears in $V^{+}_{abs}(r)$. The factor $1/(kr)^{1/2}$ approximately accounts for Ps formation at lower energies. It is well known that the positron-atom total cross sections exhibit a sharp rise near the Ps threshold and there is a bell-shaped structure around 20–80 eV depending upon the chosen target. We have introduced the empirical factor $1/(kr)^{1/2}$ to account for this behaviour. The factor $(kr)^{1/2}$ is dimensionless since $f(k,r)$ is dimensionless. The square root factor is only an empirical one. In the present work, we have kept Δ equal to the first ionization potential of the atom.

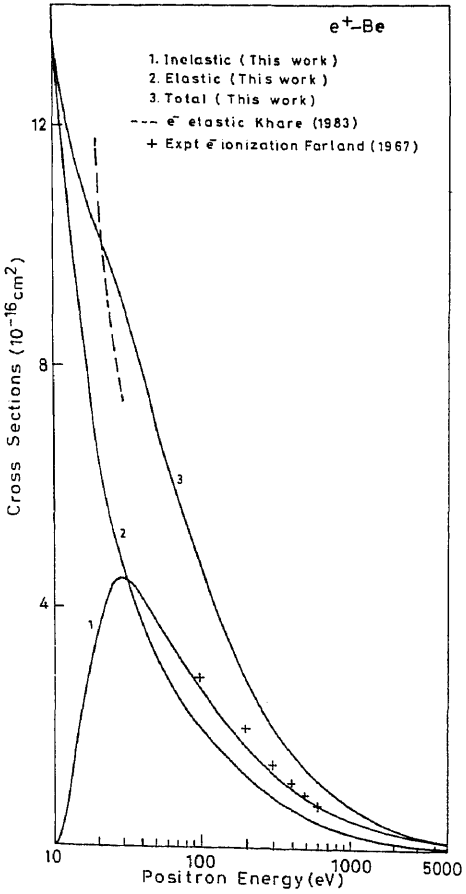

Figure 1. Cross sections for positron impact on Be.

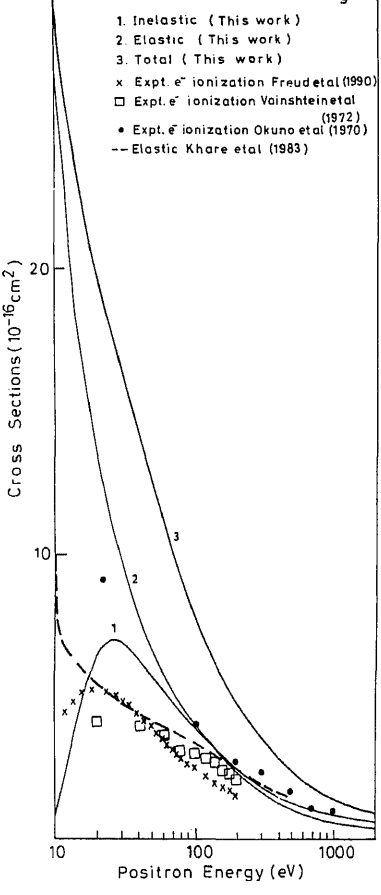

Figure 2. Cross sections for positron impact on Mg.

Since our optical potential is spherically symmetric, we now make a partial wave analysis and get the real and complex phase shifts by using a variable phase approach [14]. The S-matrix and the various cross sections are calculated. We also calculate the polarized Born phase shifts and checked their values against the numerical phase shifts. When the agreement was better than 0·1% at a particular value of the partial wave l_{max}, we switched over entirely to the polarized Born phase shifts for partial waves having value of $l > l_{max}$. Enough partial waves are included to obtain converged results.

3. Results and discussion

In figure 1 we have displayed the elastic, absorption and the total cross sections for e^+-Be scattering systems using our complex optical model potential. We notice a maximum in the absorption cross section around 30 eV. There are no other results available for comparison. However, we show elastic scattering result of e^--Be

as in the positron case. The imposed conditions for the electron case are that (1) the initially unbound electron is not allowed to fall into the occupied Fermi sea, and (2) the lowest-energy state available to the initially bound electron exceeds the Fermi level by the energy gap (Δ). These conditions are also valid when the incident projectile is a positron. It has been shown [14] that by choosing $f(k,r) = 2/(kr)^{1/2}$, there is a good agreement between calculated total cross sections and the experimental results for Ar, Kr, Xe and Rn. The factor 2 accounts for the fact that exchange is absent in positron scattering. It may be pointed out that a factor of 1/2 approximately accounts for exchange effects in the evaluation of $V^{-}_{abs}(r)$. So to remove this factor, a factor of 2 appears in $V^{+}_{abs}(r)$. The factor $1/(kr)^{1/2}$ approximately accounts for Ps formation at lower energies. It is well known that the positron-atom total cross sections exhibit a sharp rise near the Ps threshold and there is a bell-shaped structure around 20–80 eV depending upon the chosen target. We have introduced the empirical factor $1/(kr)^{1/2}$ to account for this behaviour. The factor $(kr)^{1/2}$ is dimensionless since $f(k,r)$ is dimensionless. The square root factor is only an empirical one. In the present work, we have kept Δ equal to the first ionization potential of the atom.

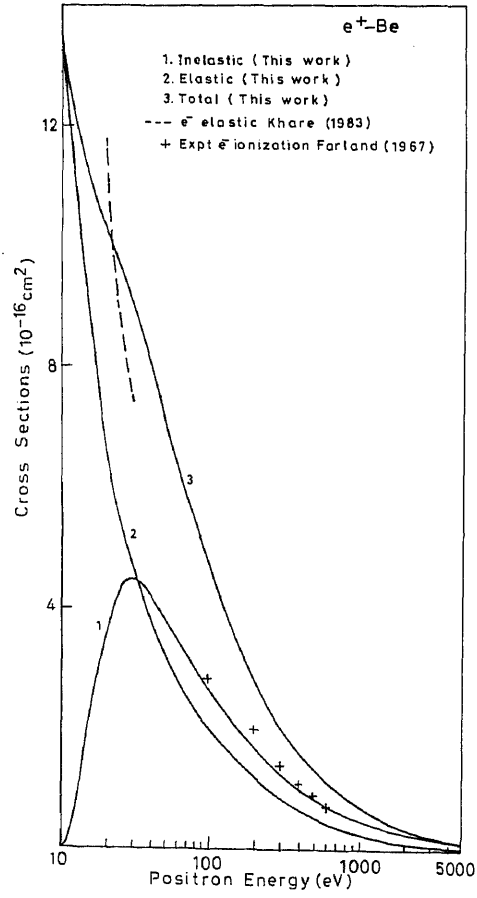

Figure 1. Cross sections for positron impact on Be.

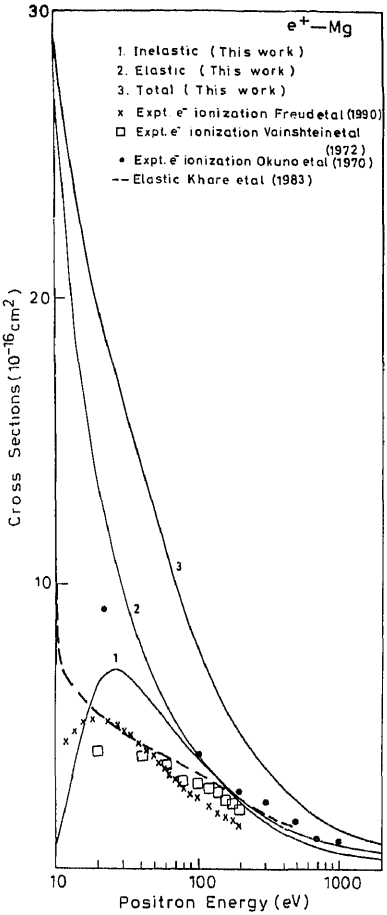

Figure 2. Cross sections for positron impact on Mg.

Since our optical potential is spherically symmetric, we now make a partial wave analysis and get the real and complex phase shifts by using a variable phase approach [14]. The S-matrix and the various cross sections are calculated. We also calculate the polarized Born phase shifts and checked their values against the numerical phase shifts. When the agreement was better than 0·1% at a particular value of the partial wave l_{max}, we switched over entirely to the polarized Born phase shifts for partial waves having value of $l > l_{max}$. Enough partial waves are included to obtain converged results.

3. Results and discussion

In figure 1 we have displayed the elastic, absorption and the total cross sections for e^+-Be scattering systems using our complex optical model potential. We notice a maximum in the absorption cross section around 30 eV. There are no other results available for comparison. However, we show elastic scattering result of e^--Be

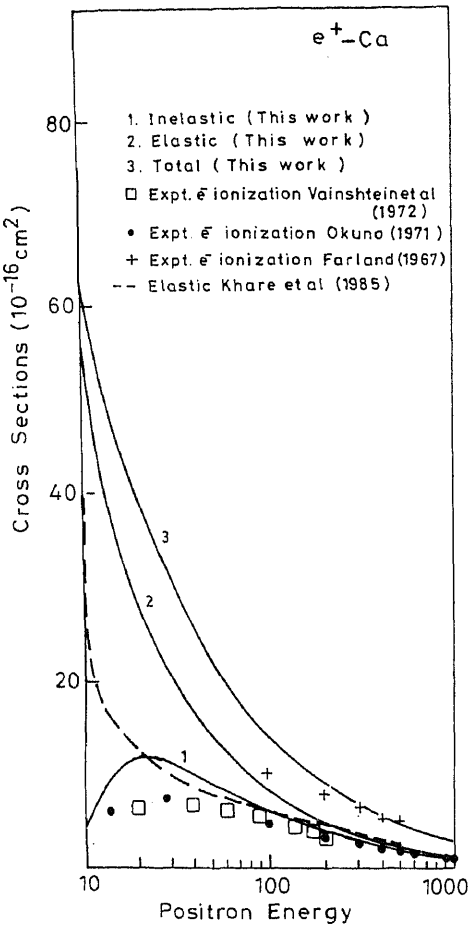

Figure 3. Cross sections for positron impact on Ca.

scattering system which also employed an optical model potential [31]. This calculation was done in the static field approximation (SF), static field polarization approximation (SFP) and static field polarization exchange approximation (SFPE). For polarization potential this calculation employed an empirical energy dependent and spherically symmetric potential [32]. These results were calculated up to 30 eV. We have shown SFP results only in figure 1 because there is no exchange in the positron case. The elastic scattering cross sections for e^- case are higher than the corresponding elastic e^+ cross sections by almost 50% up to 30 eV. The lower cross sections for e^+ case are due to the cancellation effect of repulsive static field and attractive polarization field. The absorption cross section represents the loss of incident e^+-flux into ionization channel and all other accessible excitation channels. Therefore the absorption cross section represents an upper bound to the ionization cross section. There are no results available for e^+ impact ionization of Be. However, it is well-known that at energies

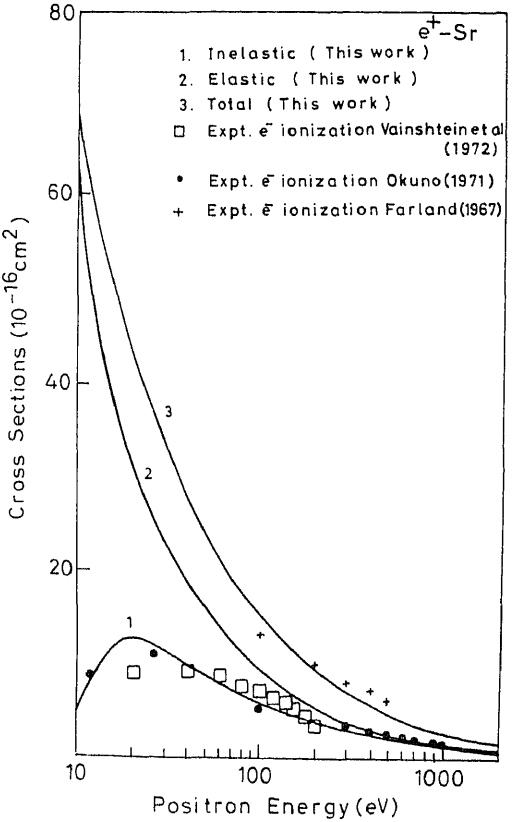

Figure 4. Cross sections for positron impact on Sr.

greater than a few hundred eV, the ionization cross section for e^- and e^+ case merg with each other. Also at such high energies the ionization cross section is the mo important channel in the absorption cross section. The ionization cross section mak the bulk contribution to the absorption cross section. In figure 1 we have displayed th ionization cross section from 100–600 eV for e^- impact on Be using Gryzinski equatio [33]. It is indeed satisfactory to note a good agreement between our absorption cro sections and the experimental e^- ionization cross sections [33].

Figure 2 shows various cross sections for positron-Mg scattering system. We ha also shown the elastic scattering cross sections obtained via a real optical mod potential [22]. This calculation employed Buckingham type polarization potenti The difference in the elastic cross section computed in our model and that of real optic model potential is due to the different polarization potentials used. However abo 100 eV the two calculations agree with each other. We have no knowledge of vario components of absorption cross sections for e^+-Mg scattering. However at hig energies (greater than 400 eV), the ionization channel is the dominant channel amo all the inelastic processes, and therefore we expect our absorption curve to approa from above the ionization curve for e^- or e^+. According to Born approximation e

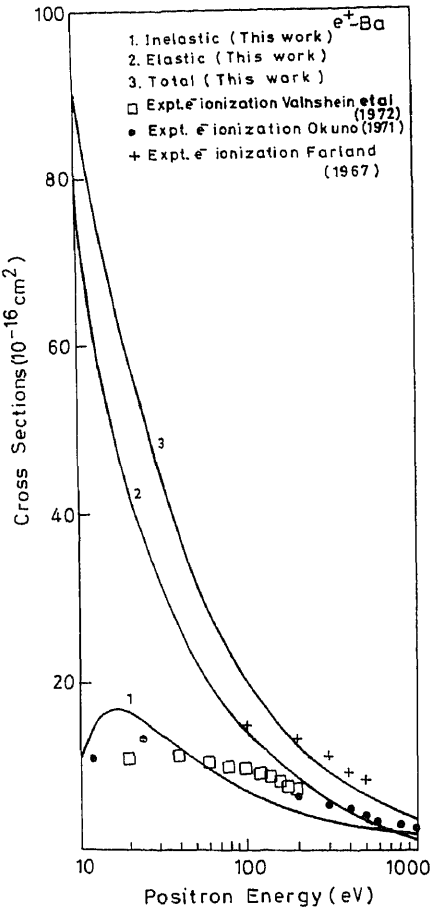

Figure 5. Cross sections for positron impact on Ba.

ionization curve coincide with e^+ ionization curve at high energies. To bring this qualitative features into focus we have shown various ionization cross sections for e^- impact on Mg [34–36]. It is interesting to note that our absorption curve peaks at 26 eV whereas the ionization curve of Freund *et al* peaks at 20 eV. The ionization cross sections of Vainshtein *et al* indicate maximum around 26 eV. It is also interesting to note that our absorption cross section lie above all the ionization cross sections shown. At energies above 200 eV our absorption curve seems to be merging with the ionization curve of Vainshtein *et al*. It is indeed satisfying to note that our simple model is capable of yielding elastic and inelastic cross sections which reveal expected qualitative features. More light on their quantitative aspects can be shed only by doing more calculations by other theoretical means and performing experiments using the positron beam. The measurements of Okudaira *et al* [37] almost agree with Okuno *et al* [36], hence are not shown in the figure.

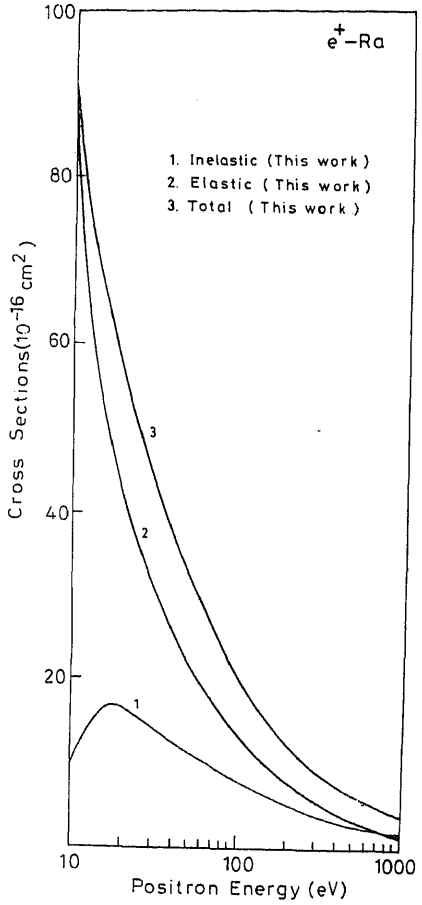

Figure 6. Cross sections for positron impact on Ra.

Our results for e^+ scattering on Ca are displayed in figure 3. Just as in Mg, our elastic cross sections agree with the real optical model potential [23] above 100 eV. Once again our absorption cross sections are close to the e^- ionization cross sections [35, 38] above 100 eV. We have also shown the experimental result of McFarland [33] which lie above our absorption curve. These higher cross sections are probably due to normalization procedure used. This experiment used Gryznski equations for normalization which may not be appropriate.

The cross sections for e^+ scattering on Sr and Ba are depicted in figures 4 and 5 respectively where the elastic, absorption and total cross sections are shown. The absorption cross sections are compared with the ionization cross sections for e^- case. Our absorption cross sections are in good accord with the e^- ionization cross sections [35,38] above 100 eV for Sr. Once again the cross sections measured in chopped crossed beam experiment [33] are above our absorption cross section curve due to normalization process. For Ba, our absorption cross section lie slightly lower than the

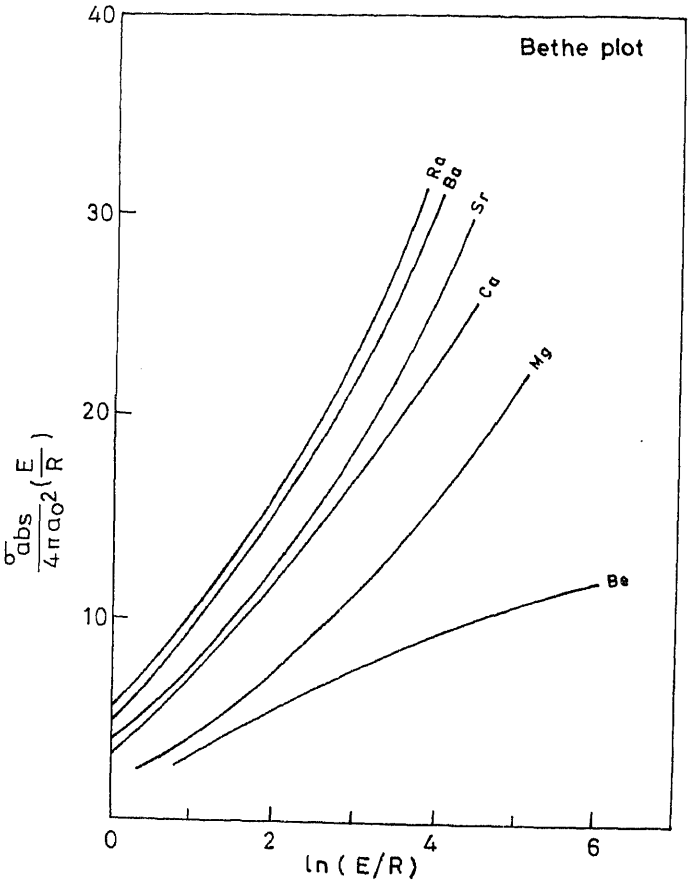

Figure 7. Bethe plot for positron impact on alkaline-earth elements.

ionization cross sections [35, 38] which indicates that the absorption potential may not be accurate for such heavier systems.

Lastly our results for e^+ scattering on Ra are given in figure 6. However there are no other results available for comparison. An interesting aspect of the ionization curve for these alkaline-earth elements reveal a maximum around 30 eV.

To probe further into the study of absorption cross section we have made Bethe plots [39] for e^+ scattering on alkaline earth elements in figure 7. The inelastic cross sections can be conveniently parametrized by Bethe asymptotic formula [39]

$$\frac{\sigma_{\text{abs}}E}{4\pi a_0^2 R} = M_{\text{tot}}^2 \ln(4C_{\text{tot}}E/R), \tag{10}$$

where M_{tot}^2 is the total dipole matrix element [39]. R is the Rydberg energy. We notice that for all the elements, there is a region of linearity at energies above 300 eV. The slope of these curves directly yields the value of M_{tot}^2. The values extracted are $M_{\text{tot}}^2 = 1{\cdot}86$,

17, 6·08, 7·8 and 8·6 for Be, Mg, Ca, Sr, Ba and Ra respectively. We note that the values f M^2_{tot} increases from Be to Ra. This implies that the effect of absorption increases from e to Ra. For energies above 1 keV, we expect our cross sections to merge with the orresponding electron case.

In conclusion, we have shown that a complex spherical model optical potential is apable of producing elastic, absorption and total cross sections for rare earth elements nowing their expected qualitative features. There is internal consistency in our alculations which is embedded in Bethe plots.

eferences

[1] B H Bransden, *Case studies in atomic collision physics* (American, Elsevier, New York, 1969) p. 171
[2] J Wm McGowan, 7th ICPEAC (North Holland, Amsterdam, 1971) p. 295
[3] H S W Massey, *Fundamental interactions in physics* (Plenum Press, New York, 1973) p. 189
[4] P G Coleman, T C Griffith, G R Heyland and T R Killeen, *Atomic Physics* (Plenum Press, New York, 1975) **4**, 355
[5] H S W Massey, *Physics Today* **29**, 42 (1976)
[6] P A Frasner, *Advances in atomic and molecular physics* (Academic Press, New York, 1968) **4**, 63
[7] H S W Massey, E H S Burhop and H B Gilbody, *Electronic and ionic impact phenomena* (University Press, Oxford, 1974) vol. 5, p. 3123 and 3683
[8] *Proceedings of the Positron Workshop*, Macquarie University, Sydney, July 1991 editor: L Parcell Macquair University, Sydney, Australia vol. 173, nos 1–2 (1992)
[9] *Workshop proceedings*, Bielefeld, Germany, 1993 edited by R P McEachran (York University, Ontario, Canada), W. Raith (Universitat Bielefeld, Germany) vol. 89 (1994)
[10] S Zhou, W E Kauppila, C K Kwan and T S Stein, *Phys. Rev. Lett.* **72**, 1443 (1994)
[11] N K Sarkar and A S Ghosh, *J. Phys.* **B27**, 759 (1994)
[12] Igor Bray, *Phys. Rev.* **A49**, R2224 (1994)
[13] J Mitroy, *Aust. J. Phys.* **48**, 645 (1995)
[14] K L Baluja and A Jain, *Phys. Rev.* **A46**, 1279 (1992)
[15] C K Kwan, W E Kauppila, R A Lukaszew, S P Parikh, T S Stein, Y J Wan and M S Dababneh, *Phys, Rev.* **A44**, 1620 (1991)
[16] S P Parikh, W E Kauppila, C K Kwan, R A Lukaszew, D Przybyla, T S Stein and S Zhou, *Phys. Rev.* **A47**, 1535 (1993)
[17] I E Mc Carthy, K Ratnavelu and S Zhou, *J. Phys.* **B26**, 2733 (1993)
[18] K P Sarkar, M Basu and A S Ghosh, *J. Phys.* **B21**, 1649 (1988)
[19] K L Baluja and Ashok Jain, *Phys. Rev.* **A45**, 7838 (1992)
[20] M Charlton, T C Griffith, G R Heyland and G L Wright, *J. Phys.* **B13**, L353 (1980)
[21] K Floeder, D Fromme, W Raith and G Sinapius, *J. Phys.* **B18**, 3347 (1985)
[22] S P Khare, A Kumar and K Lata, *J. Phys.* **B16**, 4419 (1983)
[23] S P Khare, A Kumar and Vijayshri, *J. Phys.* **B18**, 1827 (1985)
[24] F Salvat, J D Martinez, R Mayol and J Parellada, *Phys. Rev.* **A36**, 467 (1987)
[25] A Jain, *Phys. Rev.* **A41**, 2437 (1990)
[26] J K O'Connell and N F Lane, *Phys. Rev.* **A27**, 1893 (1983)
[27] G Statszewska, D W Schwenke, D Thirumalai and D G Truhlar, *J. Phys.* **B16**, L281 (1983)
[28] G Statszewska, D W Schwenke, D Thirumalai and D G Truhlar, *Phys. Rev.* **A28**, 2740 (1983)
[29] G Statszewska, D W Schwenke and D G Truhlar, *J. Chem. Phys.* **81**, 335 (1984)
[30] G Statszewska, D W Schwenke and D G Truhlar, *Phys. Rev.* **A29**, 3078 (1984)
[31] Y D Kaushik, S P Khare and A Kumar, *J. Phys.* **B16**, 3609 (1983)
[32] B L Jhanwar and S P Khare, *J. Phys.* **B9**, L527 (1976)
[33] R H McFarland, *Phys. Rev.* **159**, 20 (1967)
[34] R S Freund, R C Wetzel, R J Shul and T R Hayes, *Phys. Rev.* **A41**, 3575 (1990)

L A Vainshtein, V I Ochkur, V I Rakhovskii and A M Stepanov, *Sov. Phys. – JETP* **34**, 271 (1972)
Y Okuno, K Okuno, Y Kaneko, *J. Phys. Soc. Jpn.* **29**, 164 (1970)
S Okudaira, Y Kaneko and I Kanomata, *J. Phys. Soc. Jpn.* **28**, 1536 (1970)
Y Okuno, *J. Phys. Soc. Jpn.* **31**, 1189 (1971)
M Inokuti, *Reviews of modern physics* **43**, 297 (1971)

PRAMANA
— journal of
physics

© Printed in India

Vol. 47, No. 2,
August 1996
pp. 99–108

The origins of phase stability in ordered and disordered Ni–Pt alloys

PRABHAKAR P SINGH
Department of Physics, Indian Institute of Technology, Bombay 400076, India

MS received 30 April 1996

Abstract. Using the atomic-sphere approximation formulation of the Korringa–Kohn–Rostoker coherent potential approximation (KKR CPA) method, we have studied the effects of relativity on the electronic structure of ordered and substitutionally disordered Ni–Pt alloys. The inclusion of mass-velocity and Darwin terms are found to be essential for describing the experimentally observed ground-state properties. For the stability of disordered Ni–Pt alloys we find that, in addition to relativity, the minimization of charge-transfer effects are important. We also find that the treatment of ordering tendencies based on the band energy term alone is not sufficiently accurate for alloys with charge-transfer effects. Further analysis, in terms of basis functions, densities of states and non-spherically averaged charge densities, indicate the importance of *s*- and *d*-electrons of Pt for the stability of both ordered and disordered Ni–Pt alloys.

Keywords. Phase stability; ordered alloys; disordered alloys.

PACS Nos 71·10, 71·20, 72·15, 71·55

1. Introduction

Recent studies [1–4] of ordered NiPt and AuNi, and substitutionally disordered $Ni_{0.5}Pt_{0.5}$ have clearly shown the importance of including the relativistic terms, the so-called mass-velocity and Darwin terms, in the Hamiltonian for describing accurately their phase stability properties. For those alloy-systems where phase stability is relativity-induced, studies based on inclusion or non-inclusion of relativistic terms provide an opportunity to pinpoint unambiguously the electronic mechanism responsible for their phase stability. In the process one also gains a better understanding of the electronic properties of these alloys.

In this paper we examine the effects of the mass-velocity and Darwin terms, referred to as *R*-terms in the following, on the electronic structure of ordered Ni_3Pt in $L1_2$, NiPt in $L1_0$, and $NiPt_3$ in $L1_2$ phases, and substitutionally disordered $Ni_{0.75}Pt_{0.25}$, $Ni_{0.5}Pt_{0.5}$ and $Ni_{0.25}Pt_{0.75}$ on fcc lattices using our formulation [5] of Korringa–Kohn–Rostoker coherent potential approximation (KKR CPA) method [6, 7] in the atomic-sphere approximation [8]. We have chosen the Ni–Pt system primarily because it demonstrates the improvements, outlined below, of our approach over previous methods, and answers some of the questions raised by recent works on the Ni–Pt system [2–4].

bitals (LMTO) developed by Andersen *et al* [9, 10] and the KKR CPA approach as scribed in [6]. The advantages of our formulation include (a) an efficient calculation electronic structure of ordered and disordered alloys with the same set of approxi-tions for the Hamiltonians in each case, (b) minimization of charge-transfer effects employing charge-neutral spheres [11], (c) a probable improvement over the MT mulation for those alloys where the potential in the interstitial region is not constant, d (d) the calculation of non-spherically averaged charge density [12]. Of course, ASA leads to overlapping atomic spheres, but the error introduced due to such erlaps in the ordered alloys can be minimized with the use of combined correction C) terms [8]. A similar formalism that corrects for the overlap in the disordered oys has also been developed and we are in the process of implementing it in our culations.

Experimentally, at temperatures above 950 K, the Ni–Pt system is found to be stable the form of face-centered-cubic (fcc) solid solution over the whole concentration ge. At lower temperatures the fcc solid solution, depending on concentration, nsforms into ordered Ni_3Pt ($L1_2$), NiPt ($L1_0$) and $NiPt_3$ ($L1_2$), respectively.

Based on our calculations described below, we believe that relativistic effects are ical for the stability of ordered as well as disordered Ni–Pt alloys. The changes uced by relativity mainly affect the *s*- and *d*- (especially t_{2g}) electrons of Pt. Our ults for ordered Ni–Pt alloys are in qualitative agreement with that given in [2, 13]. r disordered Ni–Pt alloys we find that an accurate electronic structure description hin the single-site approach requires not only the inclusion of relativistic terms, in agreement with [3], but also the minimization of charge-transfer effects.

Computational details

e self-consistent electronic structure of ordered phases, Ni, Pt, and Ni_3Pt, NiPt and Pt_3 is calculated with the LMTO–ASA method [8, 9]. To find the best possible nbination of various approximations that are usually made in the ASA, we have ried out an extensive set of calculations involving (i) equal atomic spheres, (ii) rge-neutral atomic spheres, (iii) combined corrections (CC) with (i), and (iv) CC with The calculations (i)–(iv) are performed using the non-relativistic (NR) Schrödinger ation as well as the scalar-relativistic (SR) Dirac equation as a function of volume. e **k**-space integration is carried out using more than 200 **k**-points in the irreducible lges of the Brillouin zones (IBZ).

The KKR–ASA CPA method [5] is used for calculating the self-consistent electronic cture of substitutionally disordered $Ni_{0.75}Pt_{0.25}$, $Ni_{0.5}Pt_{0.5}$ and $Ni_{0.25}Pt_{0.75}$ on attices. The SR and NR calculations in this case are carried out for (v) equal atomic eres and (vi) charge-neutral atomic spheres. During the CPA self-consistency cycle, **k**-points are used in the IBZ. For both ordered and disordered calculations the nange-correlation potential was parametrized as suggested by von Barth and Hedin]. The effective pair interactions (EPI) are calculated using generalized perturbation hod (GPM) in ASA [15].

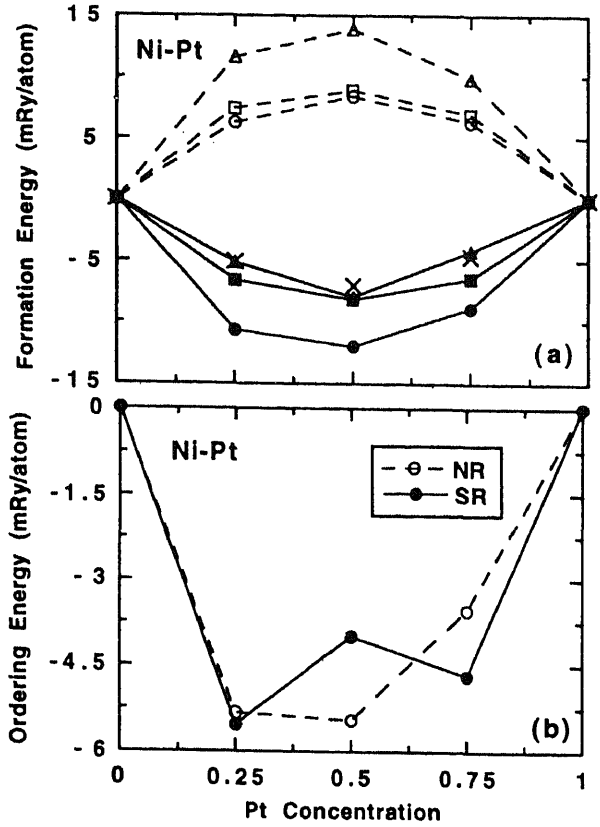

Figure 1. (a) The scalar-relativistic (filled symbols) and the non-relativistic (open symbols) formation energies of Ni–Pt alloys obtained with charge-neutral calculations as described in the text. The circles, the squares and the triangles represent the results of ordered, ordered with combined correction and the disordered calculations, respectively. The experimental heats of formation [16] are shown by crosses. (b) The scalar-relativistic (filled circles) and the non-relativistic (open circles) ordering energies of Ni–Pt alloys obtained with charge-neutral calculations for both ordered and disordered alloys.

3. Results and discussion

The most important results of our calculations are shown in figure 1, where we plot the formation energies of ordered and disordered Ni–Pt alloys given by

$$E^{\text{form}}_{\text{ord(dis)}} = E^{\text{total}}_{\text{ord(dis)}} - E_{\langle\rangle}, \tag{1}$$

where $E^{\text{total}}_{\text{ord(dis)}}$ is the total energy of the ordered (disordered) Ni–Pt alloy calculated with the LMTO–ASA (KKR–ASA CPA) method, and the quantity $E_{\langle\rangle} = cE_{\text{Ni}} + (1-c)E_{\text{Pt}}$ with c being the concentration of Ni, is the average energy of the two pure elemental solids, Ni and Pt. A negative (positive) formation energy indicates that the compound is stable (unstable) with respect to phase separation. In our calculations we find that the

formation energies for ordered Ni–Pt alloys are positive for all sets of NR calculations, indicating phase separation. The results for NR charge-neutral calculations for ordered Ni–Pt alloys are shown in figure 1. The SR calculations predict Ni–Pt alloys to be stable, in agreement with experiment [16]. As for the ordered structures, the calculations carried out in (iv) are expected to be the most accurate, and it is not surprising that the corresponding formation energies are closest to the experimental values as well as to the full-potential calculations of [2].

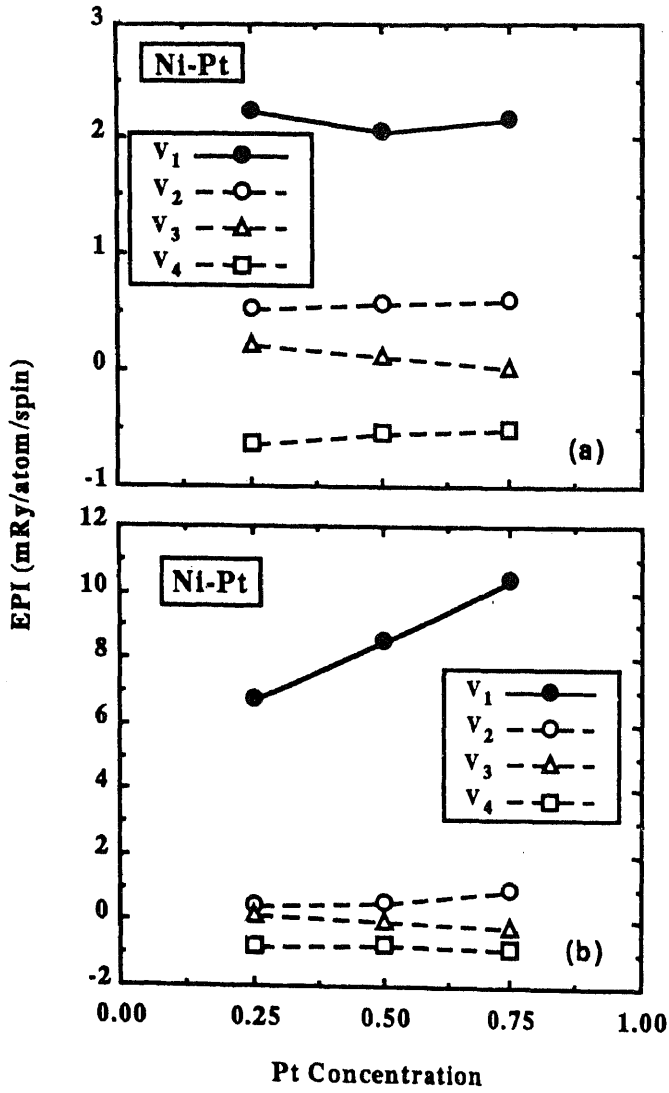

Figure 2. The scalar-relativistic effective pair interactions up to the fourth nearest neighbour obtained with (**a**) equal atomic spheres and (**b**) charge-neutral atomic spheres.

An interesting picture emerges if we consider the disordered-alloy formation energies also shown in figure 1. Within the usual applications of KKR–ASA CPA, where we use equal atomic spheres, the substitutionally disordered alloy is unstable even in the SR case. One of the reasons that make disordered Ni–Pt alloys unstable is the neglect of Madelung-type contribution to the total energy in the single-site CPA. The choice of charge-neutral spheres renders the Madelung-type contribution negligible as well as improves the ASA description of the charge density as in the ordered case. This improvement is reflected by the fact that the SR calculations done with (vi) indicate disordered Ni–Pt alloys to be stable, as can be seen from figure 1. Thus in our opinion, for metallic alloys with essentially no charge-transfer the choice of charge-neutral spheres improves the accuracy over the conventional choice of equal spheres by minimizing the error due to the neglect of Madelung-type contribution within the single-site CPA. This has been examined in some detail in [11]. The other approaches for including the Madelung-type contribution are described in [17, 18].

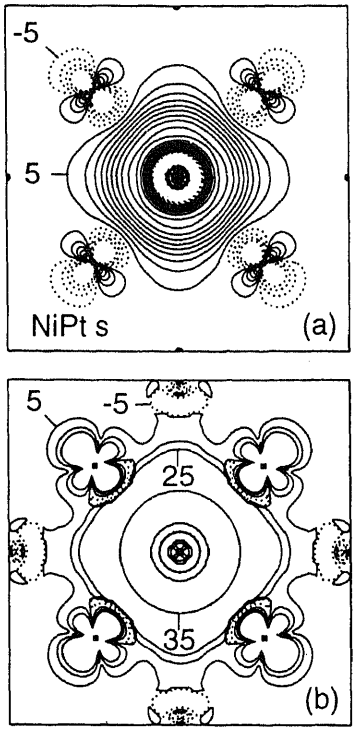

Figure 3. (**a**) The *s*-TB LMTO of $L1_0$ NiPt in (100) plane calculated scalar-relativistically at $a = 7{\cdot}1$ a.u. with charge-neutral spheres. The contours are plotted at intervals of 10, and the values have been multiplied by 10^3. The filled (open) circles indicate the positions of Pt(Ni) atoms. (**b**) The difference in magnitude of scalar-relativistic and non-relativistic *s*-TB LMTOs calculated as in (a). The full (dashed) lines denote increase in SR (NR) values. The contours are plotted at an interval of 10, and the values have been multiplied by 10^4.

Surprisingly, we find that the ordering energy ΔE given by

$$\Delta E = E_{\text{ord}}^{\text{form}} - E_{\text{dis}}^{\text{form}}, \tag{2}$$

and shown in figure 1(b), is negative in all cases which implies that ordering is favoured over disordering. The point to note is that a negative ordering energy does not guarantee a stable ordered state, as can be clearly seen from figures 1(a) and (b). Hence, reliable predictions about the ordering tendencies based on methods that probe only ΔE, such as $S^2(\mathbf{k})$ [3] and generalized perturbation methods [19], can only be made in conjunction with the disordered-alloy formation energy $E_{\text{dis}}^{\text{form}}$.

The effective pair interactions up to the fourth nearest neighbour for both equal atomic spheres and charge-neutral atomic spheres are shown in figure 2. The calculated EPIs predict the stable structure in agreement with the experiments but the ordering energies as well as the ordering temperatures are much higher than that observed experimentally. These results clearly demonstrate the inadequacy of perturbative expansions such as GPM, which are based on band energy term only, for alloys with charge-transfer effects. We also like to note that the overlap effects of ASA may have undesirable effects on GPM which includes only the band energy.

Further insight into the effects of relativity on Ni–Pt system can be obtained by examining the changes in the individual terms that make up the electronic charge density, $\rho(\mathbf{r})$, namely the basis functions and the various elements of the density matrix. As shown in [10, 12] we can calculate the non-spherically averaged charge density $\rho(\mathbf{r})$ for ordered as well as disordered alloys from

$$\rho(\mathbf{r}) = \sum_{RL,R'L'} \chi_{RL}^{\beta}(\mathbf{r}_R) n_{RL,R'L'}^{\beta}(E) \chi_{R'L'}^{\beta,*}(\mathbf{r}_R), \tag{3}$$

where $\chi_{RL}^{\beta}(\mathbf{r}_R)$, $n_{RL,R'L'}^{\beta}(E)$, R and L are the LMTOs, the density matrix, site and angular momentum indices, respectively. The superscript β denotes the most-localized tight-binding (TB) representation of [10]. In the case of disordered alloys the density matrix is given by the imaginary part of the ensemble-averaged Green functions [12].

Table 1. The SR and NR lattice constants a for Ni–Pt system obtained with charge-neutral calculations. The numbers in the brackets correspond to calculations that included combined correction terms. The experimental lattice constants are also given.

	NR	SR	Expt·
Ni	6·625 (6·576)	6·585 (6·536)	6·66
Ni_3Pt	7·001 (6·949)	6·849 (6·809)	
$Ni_{0.75}Pt_{0.25}$	7·010	6·856	
NiPt	7·392 (7·277)	7·117 (7·062)	
$Ni_{0.5}Pt_{0.5}$	7·366	7·122	
$NiPt_3$	7·653 (7·568)	7·364 (7·287)	
$Ni_{0.25}Pt_{0.75}$	7·655	7·374	
Pt	7·925 (7·816)	7·605 (7·501)	7·41

The origins of phase stability

In figure 3(a) we show the s-TB LMTO in the (100) plane of $L1_0$ NiPt calculated with charge-neutral atomic spheres. Because of the contributions coming from the neighbouring sites, the orbital is spherical only close to its own site. To illustrate the effects of relativity on s-TB orbital, we have plotted in figure 3(b) the difference in magnitude of SR and NR $\chi_s^{\beta,\mathrm{NiPt}}$. The decrease in magnitude of $\chi_s^{\beta,\mathrm{NiPt}}$ due to relativistic effects around the nearest-neighbour (nn) Ni atoms and the second nn Pt atoms is obvious. The inclusion of relativity decreases the lattice constants of both ordered and

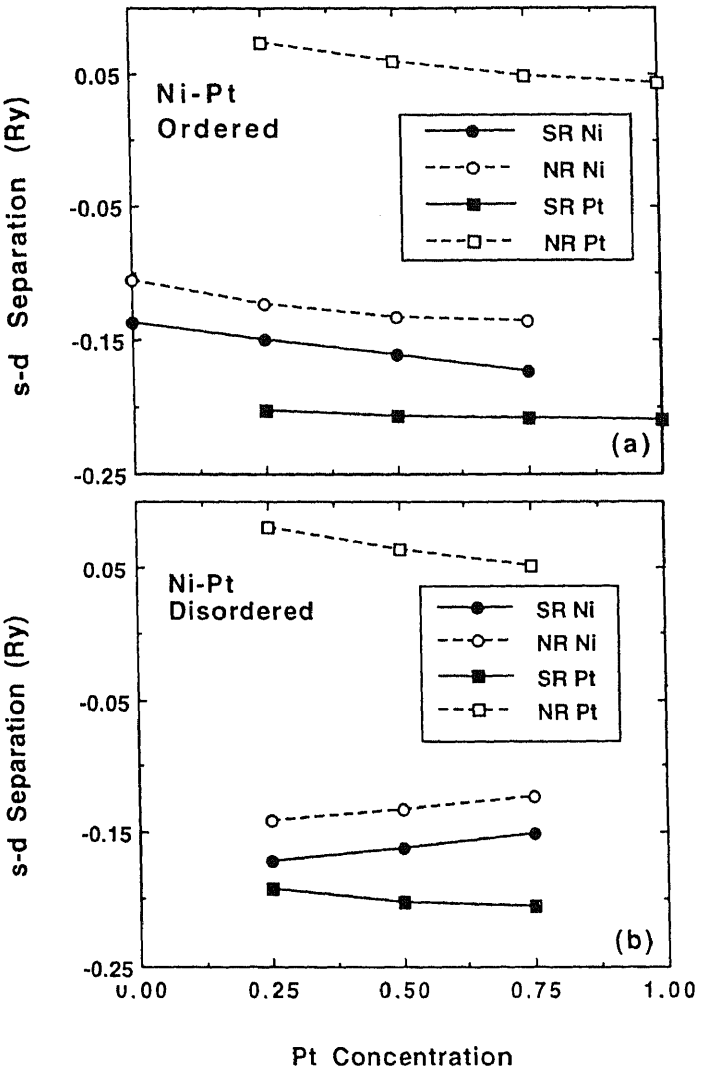

contracts by about 4% due to relativity. Similar contractions take place for ordered and disordered Ni–Pt alloys. The contractions in the lattice constants are due to the fact that the R-terms make the potentials more attractive which pull the wave function inside, thereby reducing the overlap. The deepening of potentials is reflected in the downward movement of the centres of l-bands.

To show the effect that relativity has on the centres of l-bands, we show in figures 4(a) and (b) the separation between the centres of s and d levels of Ni and Pt atoms in the ordered and the disordered alloys, respectively. The change due to relativity in the s–d separation in the Pt sphere over the whole concentration range is $\approx 0{\cdot}25$ Ry, compared to $\approx 0{\cdot}04$ Ry in the Ni sphere. The lowering of the Pt s-band leads to increased s–d hybridization which contributes to the stability of Ni–Pt alloys.

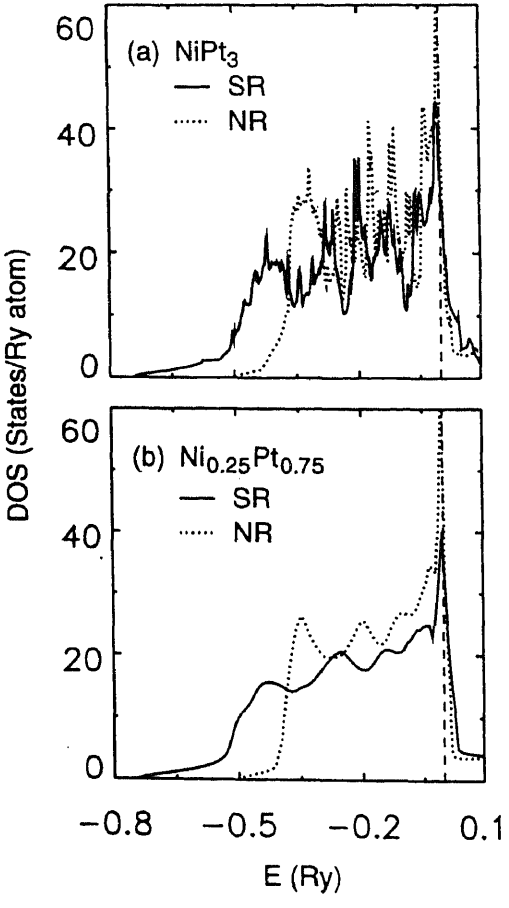

Figure 5. The scalar-relativistic (solid line) and the non-relativistic (dashed lines) total densities of states for (**a**) $L1_2$ $NiPt_3$ and (**b**) substitutionally disordered $Ni_{0{\cdot}25}Pt_{0{\cdot}75}$ calculated at their equilibrium lattice constants.

The changes in the densities of states (DOS) of ordered $NiPt_3$ and disordered $Ni_{0.25}Pt_{0.75}$ alloys due to relativity are shown in figure 5. Most of these differences arise due to the movement of the centres of l-bands due to relativistic effects and subsequent hybridizations. Not surprisingly, these effects get larger as the concentration of Pt is increased. The corresponding results for NiPt are given in [1]. Figure 5 demonstrates the importance of relativity for describing correctly the electronic structures of ordered as well as disordered Ni–Pt alloys.

We have discussed the effects of relativity on the basis functions and the densities of states of Ni–Pt alloys. The changes in the nonspherical charge density due to relativity incorporates changes in the basis functions and the densities of states as well as the changes in the off-diagonal matrix elements of the density matrix, thereby characterizing completely the effects of relativity on the system.

4. Conclusions

Based on our recently formulated approach that provides a consistent and unified framework for studying the electronic structure of ordered as well as disordered alloys, we have examined the effects of mass-velocity and Darwin terms on ordered Ni_3Pt, NiPt and $NiPt_3$ and substitutionally disordered $Ni_{0.75}Pt_{0.25}$, $Ni_{0.5}Pt_{0.5}$ and $Ni_{0.25}Pt_{0.75}$. For both ordered and disordered Ni–Pt alloys we find that (i) the inclusion of mass-velocity and Darwin terms is essential and (ii) the changes induced by these terms mainly affect the s- and d-electrons of Pt.

Acknowledgements

The author would like to thank A Gonis for many helpful discussions. Part of the work was carried out at Lawrence Livermore National Laboratory, USA.

References

[1] Prabhakar P Singh, A Gonis and P E A Turchi, *Phys. Rev. Lett.* **71**, 1605 (1993)
[2] Z W Lu, S-H Wei and A Zunger, *Phys. Rev. Lett.* **66**, 1753 (1991)
Z W Lu, S-H Wei and A Zunger, *Phys. Rev. Lett.* **68**, 1961 (1992)
Z W Lu, S-H Wei and A Zunger, *Europhys. Lett.* **21**, 221 (1993)
[3] F J Pinski, B Ginatempo, D D Johnson, J B Staunton, G M Stocks and B L Gyorffy, *Phys. Rev. Lett.* **66**, 776 (1991)
F J Pinski, B Ginatempo, D D Johnson, J B Staunton, G M Stocks and B L Gyorffy, *Phys. Rev. Lett.* **68**, 1962 (1992)
[4] G Treglia and F Ducastelle, *J. Phys.* **F17**, 1935 (1987)
[5] Prabhakar P Singh, *Solid State Commun.* **76**, 1223 (1990)
Prabhakar P Singh, D de Fontaine and A Gonis, *Phys. Rev.* **B44**, 8578 (1991)
[6] J S Faulkner and G M Stocks, *Phys. Rev.* **B21**, 3222 (1980)
[7] J S Faulkner, *Prog. Mater. Sci.* **27**, 1 (1982)
[8] O K Andersen, *Phys. Rev.* **B12**, 3060 (1975)
[9] O K Andersen and O Jepsen, *Phys. Rev. Lett.* **53**, 2571 (1984)
[10] O K Andersen, Z Pawlowska and O Jepsen, *Phys. Rev.* **B34**, 5253 (1986)
[11] Prabhakar P Singh and A Gonis, *Phys. Rev.* **B49**, 1642 (1994)
[12] Prabhakar P Singh and A Gonis, *Phys. Rev.* **B48**, 2139 (1993)

3] C Amador, W R L Lambrecht and B Segall, *Mater. Res. Soc. Symp. Proc.* **253**, 297 (1992)
4] U von Barth and L Hedin, *J. Phys.* **C5**, 1629 (1972)
5] Prabhakar P Singh and A Gonis, *Phys. Rev.* **B47**, 6744 (1993)
6] R A Walker and J B Darby, *Acta Metall.* **18**, 1761 (1970)
7] D D Johnson and F J Pinski, *Phys. Rev.* **B48**, 11553 (1993)
8] I A Abrikosov, Yu H Vekilov, A V Ruban and D Ya Katz, *Solid State Commun.* **80**, 177 (1991)
9] P E A Turchi, G M Stocks, W H Butler, D M Nicholson and A Gonis, *Phys. Rev.* **B37**, 5982 (1988)

Analytic solution of the BCS gap equation in D dimensions ($D = 1, 2, 3$), at finite temperatures

ARUN BHARDWAJ and SATISH K MUTHU
Department of Physics and Astrophysics, University of Delhi, Delhi 110 007, India

MS received 29 March 1996; revised 11 June 1996

Abstract. The Bardeen–Cooper–Schrieffer (BCS) gap equation is solved analytically in one, two and three dimensions, for temperatures close to zero and T_c. We work in the weak coupling limit, but allow the interaction width $\nu \equiv \hbar\omega_m/E_F$ to lie in the interval $(0, \infty)$ Here, $\hbar\omega_m$ is the maximum energy of a force-mediating boson, and E_F denotes the Fermi energy. We obtain expressions for T_c and ΔC, the jump in the electronic specific heat across $T = T_c$, in the limits $\nu \ll 1$ (the usual phonon pairing) and $\nu > 1$ (non-phononic pairing). This enables us to see how T_c scales with the mediating boson cut off. Our results predict a larger jump in the specific heat for the case $\nu > 1$, compared to $\nu \ll 1$. We also briefly touch upon the role of a van Hove singularity in the density of states.

Keywords. BCS gap equation; phononic and non-phononic pairing; critical temperature; jump in specific heat; van Hove singularity.

PACS No. 74·20

1. Introduction

The epochal discovery of high-temperature superconductivity by Bednorz and Müller [1], has unleashed an unprecedented level of activity. During the last eight years, an enormous amount of data has been collected [2,3]. A correct theoretical explanation is still being sought. Among the myriad proposals dotting the theoretical landscape, the simplest seems to be to retain the usual BCS framework in which electrons form bound pairs, the so-called Cooper pairs. However, the electron-phonon interaction is replaced by other mechanisms like excitons, magnons, etc. Thus, in particular, the Debye cut-off energy $\hbar\omega_D$ is replaced by $\hbar\omega_m$, where $\hbar\omega_m$ can be greater than E_F. It is of considerable interest to study the usual BCS model in this limit.

The motivation for the present work stems from a paper by Walt, Quick and Llano [4], on the analytic solutions of the BCS gap equation in one, two and three dimensions, for arbitrary interaction width $\nu(\nu = \hbar\omega_m/E_F, 0 < \nu < \infty)$ at zero temperature. We extend these results to finite temperatures.

The article is organized as follows: In § 2, we cast the BCS gap equation at $T = 0$ in the notation of Walt, Quick and Llano. Section 3 is devoted to a solution of this equation in D dimensions for $\nu \ll 1$. Section 4 contains solutions for the case $\nu > 1$. This enables us to see how T_c scales with ν. In § 5 we compare the cases $\nu \ll 1$ and $\nu > 1$ and

make a rough numerical estimate of the enhancement of T_c. In § 6 we discuss briefly the role of the presence of a van Hove singularity in the density of states. We conclude by making some general comments on our results.

2. BCS theory at finite temperature

At finite temperature, the BCS gap equation in D dimensions can be written as [5]

$$\Delta_{\mathbf{k}} = \frac{1}{2}\sum_{\mathbf{k}'} V_{kk'} \tanh\left(\frac{(\Delta_{k'}^2 + \xi_{k'}^2)^{1/2}}{2kT}\right) \times \left(\frac{\Delta_{k'}}{(\Delta_{k'}^2 + \xi_{k'}^2)^{1/2}}\right). \tag{1}$$

Here ξ_k represent the single-particle energies measured with respect to the chemical potential μ, i.e.

$$\xi_k = \frac{\hbar^2 k^2}{2m} - \mu. \tag{2a}$$

The interelectronic interaction is assumed to be of the form

$$V_{kk'} = \frac{v_0}{L^D}, \max(0, E_F - \hbar\omega_m) < \varepsilon_{k'}, \varepsilon_{k'} < E_F + \hbar\omega_m$$

$$= 0, \text{ otherwise.} \tag{2b}$$

Here, L is a measure of the size of the system and the coupling strength v_0 is taken to be positive, signifying a net attraction between the electrons; $\varepsilon_k = \hbar^2 k^2/2m$ is the single-particle kinetic energy, E_F is the Fermi energy and $\hbar\omega_m$ is the maximum energy of the force-mediating boson.

In view of the model interaction given by (2b) it follows that

$$\Delta_{\mathbf{k}} = \Delta\theta(\hbar\omega_m - |\xi_k|), \tag{2c}$$

where $\theta(x)$ is the Heaviside step function and the gap parameter Δ is assumed to be isotropic (independent of $\mathbf{k}$). Hence, (1) becomes

$$1 = \frac{v_0}{2L^D}\sum_{\mathbf{k}} \frac{\theta(\hbar\omega_m - |\xi_k|)}{(\Delta^2 + \xi_k^2)^{1/2}} \tanh\left(\frac{(\Delta^2 + \xi_k^2)^{1/2}}{2kT}\right). \tag{3}$$

Changing the summation over $\mathbf{k}$ into integration, one obtains after some algebra,

$$\frac{2}{\lambda} = \int_{E_F - \hbar\omega_m, 0}^{E_F + \hbar\omega_m} d\varepsilon \frac{(\varepsilon/E_F)^{(D-2)/2}}{(\Delta^2 + (\varepsilon - E_F)^2)^{1/2}} \tanh\left(\frac{(\Delta^2 + (\varepsilon - E_F)^2)^{1/2}}{2kT}\right). \tag{4}$$

Here, $\lambda = N(0)v_0$, $N(0)$ being density of states per spin state at the Fermi level. The lower limit of integration is $E_F - \hbar\omega_m$ for the case $E_F > \hbar\omega_m$ and zero for $E_F < \hbar\omega_m$.

Introducing the dimensionless variables ε', ν and δ, defined by

$$\varepsilon' = \frac{\varepsilon}{E_F}, \tag{5a}$$

and

$$\delta = \frac{\Delta}{E_F}, \tag{5c}$$

equation (4) becomes

$$\frac{2}{\lambda} = \int_{1-\nu,0}^{1+\nu} d\varepsilon' \frac{\varepsilon'^{(D-2)/2}}{(\delta^2 + (\varepsilon' - 1)^2)^{1/2}} \tanh\left(\frac{(\delta^2 + (\varepsilon' - 1)^2)^{1/2}}{2kT/E_F}\right). \tag{6a}$$

Using the relation $\tanh x = 1 - \frac{2}{e^{2x}+1}$, (6a) can be rewritten as

$$\frac{2}{\lambda} = \int_{1-\nu,0}^{1+\nu} \frac{\varepsilon'^{(D-2)/2}}{(\delta^2 + (\varepsilon' - 1)^2)^{1/2}} d\varepsilon' - 2 \int_{1-\nu,0}^{1+\nu} \frac{\varepsilon'^{(D-2)/2}}{(\delta^2 + (\varepsilon' - 1)^2)^{1/2}} \times \frac{d\varepsilon'}{[e^{(\delta^2 + (\varepsilon' - 1)^2)^{1/2} E_F/kT} + 1]}. \tag{6b}$$

At $T = 0$, the second term in (6b) gives zero and so it reduces to

$$\frac{2}{\lambda} = \int_{1-\nu,0}^{1+\nu} \frac{\varepsilon'^{(D-2)/2}}{(\delta_0^2 + (\varepsilon' - 1)^2)^{1/2}} d\varepsilon', \text{ with } \delta_0 = \delta(T = 0). \tag{7}$$

The integral on the right can be easily evaluated; we have [4] for $D = 1$, 2 and 3

$$\int_{1-\nu,0}^{1+\nu} \frac{\varepsilon'^{-1/2} d\varepsilon'}{(\delta_0^2 + (\varepsilon' - 1)^2)^{1/2}} = 2\ln\left[\frac{8\nu}{\delta_0(1 + (1-\nu)^{1/2})(1 + (1+\nu)^{1/2})}\right], \quad \nu < 1$$

$$= 2\ln\left[\frac{8\nu^{1/2}}{\delta_0(1 + (1+\nu)^{1/2})}\right], \quad \nu > 1$$

$$\int_{1-\nu,0}^{1+\nu} \frac{d\varepsilon'}{(\delta_0^2 + (\varepsilon' - 1)^2)^{1/2}} = 2\ln\left[\frac{2\nu}{\delta_0}\right], \quad \nu < 1$$

$$= 2\ln\left[\frac{2\nu^{1/2}}{\delta_0}\right], \quad \nu > 1$$

$$\int_{1-\nu,0}^{1+\nu} \frac{\varepsilon'^{1/2} d\varepsilon'}{(\delta_0^2 + (\varepsilon' - 1)^2)^{1/2}} = 2\ln\left[\frac{8\nu}{\delta_0(1 + (1-\nu)^{1/2})(1 + (1+\nu)^{1/2})}\right] + 2(1-\nu)^{1/2} + 2(1+\nu)^{1/2} - 4 \quad \nu < 1$$

$$= 2\ln\left[\frac{8\nu^{1/2}}{\delta_0(1 + (1+\nu)^{1/2})}\right] + 2(1+\nu)^{1/2} - 4, \quad \nu > 1,$$

respectively.

3.1 *Expression for δ near $T=0$*

We start with eq. (6b). Since we are working near $T=0$, the first term can be replaced using (7). This leads to

$$2\ln\left[\frac{\delta}{\delta_0}\right] = -2\int_{1-\nu}^{1+\nu} \frac{\varepsilon'^{(D-2)/2}\mathrm{d}\varepsilon'}{(\delta^2+(\varepsilon'-1)^2)^{1/2}[\mathrm{e}^{(\delta^2+(\varepsilon'-1)^2)^{1/2}E_F/kT}+1]}. \tag{8a}$$

Introducing

$$x=(\varepsilon'-1)\frac{E_F}{kT} \tag{9a}$$

and

$$\delta' = \left(\frac{E_F}{kT}\right)\delta, \tag{9b}$$

in (8a), we have

$$\ln\left[\frac{\delta_0}{\delta}\right] = \int_{-E_F\nu/kT}^{E_F\nu/kT} \frac{(1+kTx/E_F)^{(D-2)/2}\mathrm{d}x}{(\delta'^2+x^2)^{1/2}(\mathrm{e}^{(\delta'^2+x^2)^{1/2}}+1)}.$$

Since close to $T=0$, $E_F\nu/kT$ becomes very large, we can take the upper and lower limits as ∞, $-\infty$, respectively. Hence,

$$\begin{aligned}\ln\left[\frac{\delta_0}{\delta}\right] &= \int_{-\infty}^{\infty} \frac{(1+kTx/E_F)^{(D-2)/2}\mathrm{d}x}{(\delta'^2+x^2)^{1/2}(\mathrm{e}^{(\delta'^2+x^2)^{1/2}}+1)} \\ &= \int_0^{\infty} \frac{\mathrm{d}x}{(\delta'^2+x^2)^{1/2}(\mathrm{e}^{(\delta'^2+x^2)^{1/2}}+1)}[(1+kTx/E_F)^{(D-2)/2} \\ &\quad +(1-kTx/E_F)^{(D-2)/2}]. \end{aligned} \tag{8b}$$

The numerator of the integrand is now expanded binomially to obtain

$$\begin{aligned}\ln\left[\frac{\delta_0}{\delta}\right] &= \int_0^{\infty} \frac{\mathrm{d}x}{(\delta'^2+x^2)^{1/2}(\mathrm{e}^{(\delta'^2+x^2)^{1/2}}+1)} \\ &\quad \times [2+\tfrac{1}{4}(D-2)(D-4)(kTx/E_F)^2+\ldots]. \end{aligned} \tag{10}$$

Also

$$\frac{1}{\mathrm{e}^{(\delta'^2+x^2)^{1/2}}+1} = \mathrm{e}^{-(\delta'^2+x^2)^{1/2}} - \mathrm{e}^{-2(\delta'^2+x^2)^{1/2}} + \mathrm{e}^{-3(\delta'^2+x^2)^{1/2}} - \ldots$$

Equation (10) can now be written in the form

$$\begin{aligned}\ln\left[\frac{\delta_0}{\delta}\right] &= 2\int_0^{\infty} \frac{\mathrm{d}x}{(\delta'^2+x^2)^{1/2}}[\mathrm{e}^{-(\delta'^2+x^2)^{1/2}} - \mathrm{e}^{-2(\delta'^2+x^2)^{1/2}} + \mathrm{e}^{-3(\delta'^2+x^2)^{1/2}} - \ldots] \\ &\quad +\tfrac{1}{4}(D-2)(D-4)(kT/E_F)^2 \int_0^{\infty} \frac{\mathrm{d}x x^2}{(\delta'^2+x^2)^{1/2}}[\mathrm{e}^{-(\delta'^2+x^2)^{1/2}} \\ &\quad -\mathrm{e}^{-2(\delta'^2+x^2)^{1/2}} + \mathrm{e}^{-3(\delta'^2+x^2)^{1/2}} - \ldots]. \end{aligned} \tag{11}$$

Using [6]

$$K_\nu(xz) = \frac{(\pi)^{1/2}}{\Gamma(\nu+\frac{1}{2})}(x/2z)^\nu \int_0^\infty \frac{e^{-x(t^2+z^2)^{1/2}}}{(t^2+z^2)^{1/2}} t^{2\nu}\,dt,$$

equation (11) takes the form

$$\ln\left[\frac{\delta_0}{\delta}\right] = 2[K_0(\delta') - K_0(2\delta') + K_0(3\delta') - \ldots] + \tfrac{1}{4}(D-2)(D-4)$$
$$\times (kT/E_F)^2 \left[\delta' K_1(\delta') - \frac{\delta'}{2}K_1(2\delta') + \frac{\delta'}{3}K_1(3\delta') - \ldots\right]$$
$$= 2\sum_{n=1}^{\infty}(-1)^{n+1}K_0\left(\frac{nE_F\delta}{kT}\right) + \tfrac{1}{4}(D-2)(D-4)\left(\frac{kT}{E_F}\right)^2\left(\frac{E_F\delta}{kT}\right)$$
$$\times \sum_{n=1}^{\infty}\frac{(-1)^{n+1}}{n}K_1\left(\frac{nE_F\delta}{kT}\right).$$

Thus finally

$$\ln\left[\frac{\delta_0}{\delta}\right] = 2\sum_{n=1}^{\infty}(-1)^{n+1}K_0\left(\frac{nE_F\delta}{kT}\right) + \tfrac{1}{4}(D-2)(D-4)\left(\frac{\delta kT}{E_F}\right)$$
$$\times \sum_{n=1}^{\infty}\frac{(-1)^{n+1}}{n}K_1\left(\frac{nE_F\delta}{kT}\right). \tag{12}$$

To obtain the BCS result, we take $n=1$ and retain only the first term. This gives

$$\ln\left[\frac{\delta_0}{\delta}\right] = 2K_0\left(\frac{E_F\delta}{kT}\right). \tag{13}$$

For large values of the argument z, we have [7]

$$K_0(z) = \left(\frac{\pi}{2z}\right)^{1/2} e^{-z}\left(1 - \frac{1}{8z}\right).$$

Equation (13) becomes

$$\ln\left[\frac{\delta_0}{\delta}\right] = 2\left(\frac{\pi kT}{2E_F\delta}\right)^{1/2} e^{-E_F\delta/kT}\left(1 - \frac{kT}{8E_F\delta}\right)$$

or,

$$\delta = \delta_0 - \left(\frac{2\pi\delta_0 kT}{E_F}\right)^{1/2} e^{-E_F\delta/kT}\left(1 - \frac{kT}{8\delta_0 E_F}\right). \tag{14a}$$

In more familiar notation,

$$\Delta = \Delta_0 - (2\pi\Delta_0 kT)^{1/2} e^{-\Delta_0/kT}\left(1 - \frac{kT}{8\Delta_0}\right), \tag{14b}$$

which is the usual BCS result [8].

3.2 *Determination of the T_c equation for general D*

We start with (6a). Since at $T = T_c$, $\delta = 0$, (6a) becomes

$$\frac{2}{\lambda} = \int_{1-\nu}^{1+\nu} \frac{\varepsilon'^{(D-2)/2}}{|\varepsilon' - 1|} \tanh\left(|\varepsilon' - 1| \frac{E_F}{2kT_c}\right) d\varepsilon'$$

$$= \int_{1-\nu}^{1+\nu} \frac{\varepsilon'^{(D-2)/2}}{\varepsilon' - 1} \tanh\left((\varepsilon' - 1) \frac{E_F}{2kT_c}\right) d\varepsilon'. \tag{15a}$$

Introducing the variable y defined by

$$y = (\varepsilon' - 1) \frac{E_F}{2kT_c}, \tag{16}$$

into (15a) yields

$$\frac{2}{\lambda} = \int_{-E_F\nu/2kT_c}^{E_F\nu/2kT_c} \left(1 + \frac{2kT_c y}{E_F}\right)^{(D-2)/2} \frac{\tanh y}{y} dy, \tag{15b}$$

or

$$\frac{2}{\lambda} = \int_0^{E_F\nu/2kT_c} \frac{\tanh y}{y} \left[\left(1 + \frac{2kT_c y}{E_F}\right)^{(D-2)/2} + \left(1 - \frac{2kT_c y}{E_F}\right)^{(D-2)/2}\right] dy. \tag{15c}$$

Integrating by parts and replacing $\tanh(E_F\nu/2kT_c)$ by unity, since $E_F\nu/2kT_c$ is large, we obtain

$$\frac{2}{\lambda} = [(1+\nu)^{(D-2)/2} + (1-\nu)^{(D-2)/2}] \ln\left(\frac{E_F \nu}{2kT_c}\right) - [I_+(T_c) + I_-(T_c)], \tag{17}$$

with

$$I_+(T_c) = \int_0^{E_F\nu/2kT_c} dy \ln y \left[\left(1 + \frac{2kT_c y}{E_F}\right)^{(D-2)/2} \operatorname{sech}^2 y + \frac{kT_c}{E_F}(D-2)\left(1 + \frac{2kT_c y}{E_F}\right)^{(D-4)/2} \tanh y\right], \tag{18a}$$

and

$$I_-(T_c) = \int_0^{E_F\nu/2kT_c} dy \ln y \left[\left(1 - \frac{2kT_c y}{E_F}\right)^{(D-2)/2} \operatorname{sech}^2 y - \frac{kT_c}{E_F}(D-2)\left(1 - \frac{2kT_c y}{E_F}\right)^{(D-4)/2} \tanh y\right], \tag{18b}$$

since $\nu \ll 1$,

$$I_+(T_c) + I_-(T_c) \simeq 2 \int_0^{E_F\nu/2kT_c} \ln y \operatorname{sech}^2 y \, dy \simeq 2 \int_0^{\infty} \ln y \operatorname{sech}^2 y \, dy$$

γ being the Euler–Mascheroni constant.

Hence, (17) yields

$$\frac{2}{\lambda} = [(1+v)^{(D-2)/2} + (1-v)^{(D-2)/2}] \ln\left(\frac{E_F v}{2kT_c}\right) + 2\ln\left(\frac{4e^{\gamma}}{\pi}\right),$$

or

$$kT_c = \frac{E_F v}{2}\left(\frac{4e^{\gamma} e^{-1/\lambda}}{\pi}\right)^{2/[(1+v)^{(D-2)/2} + (1-v)^{(D-2)/2}]} \tag{19}$$

This is the desired expression for T_c.

3.3 *Expression for δ near $T = T_c$*

We start from eq. (6a). Introducing x and δ', as defined by eqs (9a) and (9b), we have

$$\frac{2}{\lambda} = \int_{-E_F v/kT}^{E_F v/kT} \frac{(1+kTx/E_F)^{(D-2)/2}}{(\delta'^2 + x^2)^{1/2}} \tanh\left(\frac{(\delta'^2 + x^2)^{1/2}}{2}\right) dx.$$

Using the well-known expansion [9]

$$\tanh\frac{x}{2} = 4x \sum_{n=0}^{\infty} \frac{1}{\pi^2(2n+1)^2 + x^2},$$

we obtain

$$\frac{2}{\lambda} = 4 \sum_{n=0}^{\infty} \int_{-E_F v/kT}^{E_F v/kT} \frac{(1+kTx/E_F)^{(D-2)/2}}{\pi^2(2n+1)^2 + \delta'^2 + x^2} dx. \tag{20a}$$

Since, near T_c, the size of the gap is very small, we can carry out an expansion in powers of δ'. This leads us to the equation

$$\begin{aligned}\frac{2}{\lambda} &= 4 \sum_{n=0}^{\infty} \int_{-E_F v/kT}^{E_F v/kT} \left(1 + \frac{kTx}{E_F}\right)^{(D-2)/2} \frac{dx}{[\pi^2(2n+1)^2 + x^2]} \\ &\quad - 4\delta'^2 \sum_{n=0}^{\infty} \int_{-E_F v/kT}^{E_F v/kT} \frac{(1+kTx/E_F)^{(D-2)/2}}{[\pi^2(2n+1)^2 + x^2]^2} dx + \ldots \\ &= \int_{-E_F v/kT}^{E_F v/kT} \left(1 + \frac{kTx}{E_F}\right)^{(D-2)/2} \left(\frac{\tanh(x/2)}{x}\right) dx \\ &\quad - 4\delta'^2 \sum_{n=0}^{\infty} \int_{-E_F v/kT}^{E_F v/kT} \frac{(1+kTx/E_F)^{(D-2)/2}}{[\pi^2(2n+1)^2 + x^2]^2} dx. \end{aligned} \tag{20b}$$

At $T = T_c$, we have from (15b), on putting $y = x/2$,

$$\begin{aligned}\frac{2}{\lambda} &= \int_{-E_F v/kT_c}^{E_F v/kT_c} \left(1 + \frac{kT_c x}{E_F}\right)^{(D-2)/2} \left(\frac{\tanh(x/2)}{x}\right) dx \\ &= [(1+v)^{(D-2)/2} + (1-v)^{(D-2)/2}] \ln\left(\frac{E_F v}{2kT_c}\right) + 2\ln\left(\frac{4e^{\gamma}}{\pi}\right).\end{aligned}$$

Thus (20b) becomes

$$[(1+\nu)^{(D-2)/2}+(1-\nu)^{(D-2)/2}]\ln\left(\frac{T}{T_c}\right)$$
$$=-4\delta'^2\sum_{n=0}^{\infty}\int_0^{E_F\nu/kT}\frac{dx}{[\pi^2(2n+1)^2+x^2]^2}\cdot$$
$$\times\left[\left(1+\frac{kTx}{E_F}\right)^{(D-2)/2}+\left(1-\frac{kTx}{E_F}\right)^{(D-2)/2}\right].$$

Simplifying the numerator, using binomial expansions, we obtain

$$[(1+\nu)^{(D-2)/2}+(1-\nu)^{(D-2)/2}]\ln\left(\frac{T}{T_c}\right)$$
$$=-8\delta'^2\left[\sum_{n=0}^{\infty}\int_0^{E_F\nu/kT}\frac{dx}{[\pi^2(2n+1)^2+x^2]^2}\right.$$
$$\left.+\tfrac{1}{8}(D-2)(D-4)(kT/E_F)^2\int_0^{E_F\nu/kT}x^2\,dx\sum_{n=0}^{\infty}\frac{1}{[\pi^2(2n+1)^2+x^2]^2}\right]. \tag{21}$$

The first integral on the R.H.S. can be easily evaluated.

Assuming the upper limit to be ∞, we have

$$\int_0^{\infty}\frac{dx}{[\pi^2(2n+1)^2+x^2]^2}=\frac{1}{4\pi^2(2n+1)^3}. \tag{22a}$$

Using

$$\sum_{n=0}^{\infty}\frac{1}{[\pi^2(2n+1)^2+x^2]^2}=\frac{1}{8x^3}\tanh\frac{x}{2}-\frac{1}{16x^2}\operatorname{sech}^2\frac{x}{2}, \tag{22b}$$

the R.H.S. of (21) becomes

$$-8\delta'^2\left[\sum_{n=0}^{\infty}\frac{1}{4\pi^2(2n+1)^3}+\tfrac{1}{8}(D-2)(D-4)(kT/E_F)^2\right.$$
$$\left.\times\int_0^{E_F\nu/kT}\left(\frac{1}{8x}\tanh\frac{x}{2}-\frac{1}{16}\operatorname{sech}^2\frac{x}{2}\right)dx\right].$$

For evaluating the integral, we substitute $x/2=y$. This gives

$$I=\int_0^{E_F\nu/kT}\left(\frac{1}{8x}\tanh\frac{x}{2}-\frac{1}{16}\operatorname{sech}^2\frac{x}{2}\right)dx$$
$$=\frac{1}{8}\int_0^{E_F\nu/2kT}\frac{\tanh y}{y}\,dy-\frac{1}{8}\int_0^{E_F\nu/2kT}\tanh y\,dy=\frac{1}{8}\left[\ln\left(\frac{2e^{\gamma}E_F\nu}{\pi kT}\right)\right.$$

$$\tfrac{1}{2}[(1+\nu)^{(D-2)/2}+(1-\nu)^{(D-2)/2}]\ln\left(\frac{T}{T_c}\right)=-4\delta'^2\times\frac{1}{4\pi^2}\frac{7}{8}\zeta(3)$$

$$\times\left[1+\frac{\pi^2}{14\zeta(3)}(D-2)(D-4)(kT/E_F)^2\left[\ln\left(\frac{2e^\gamma E_F\nu}{\pi kT}\right)-1\right]\right]. \tag{23}$$

Hence,

$$\Delta^2=\pi^2k^2T_c^2\frac{8}{7\zeta(3)}\left[\frac{(1+\nu)^{(D-2)/2}+(1-\nu)^{(D-2)/2}}{2}\right]\left(1-\frac{T}{T_c}\right)$$

$$\times\left[1-\frac{\pi^2}{14\zeta(3)}(D-2)(D-4)(kT_c/E_F)^2\left[\ln\left(\frac{2e^\gamma E_F\nu}{\pi kT}\right)-1\right]\right]. \tag{24}$$

Neglecting the second term, which is very small compared to the first term and using $\zeta(3)=1.202$, we obtain

$$\Delta=3{\cdot}06kT_c\left[\frac{(1+\nu)^{(D-2)/2}+(1-\nu)^{(D-2)/2}}{2}\right]^{1/2}\left(1-\frac{T}{T_c}\right)^{1/2}. \tag{25}$$

3.4 *Jump in the electronic specific heat at $T=T_c$*

The jump in the specific heat at $T=T_c$ is given by

$$(C_s-C_n)_{T=T_c}=\Delta C=-N(0)\left.\frac{d\Delta^2}{dT}\right|_{T=T_c}, \tag{26a}$$

where the normal specific heat is given by

$$C_n=\frac{2}{3}N(0)k^2\pi^2T. \tag{26b}$$

Using (24) (neglecting the term containing $(kT_c/E_F)^2$), we obtain

$$\frac{d\Delta^2}{dT}=\pi^2k^2T_c^2\frac{8}{7\zeta(3)}\left[\frac{(1+\nu)^{(D-2)/2}+(1-\nu)^{(D-2)/2}}{2}\right]\left(\frac{1}{T_c}\right).$$

Substituting this expression into (26a), we obtain

$$(C_s-C_n)_{T=T_c}=N(0)\pi^2k^2T_c\frac{8}{7\zeta(3)}\left[\frac{(1+\nu)^{(D-2)/2}+(1-\nu)^{(D-2)/2}}{2}\right],$$

or

$$\left.\frac{C_s-C_n}{C_n}\right|_{T=T_c}=1{\cdot}43\left[\frac{(1+\nu)^{(D-2)/2}+(1-\nu)^{(D-2)/2}}{2}\right]. \tag{27}$$

4. Solution of the BCS gap equation in D dimensions for $\nu>1$

4.1 *Expression for δ near $T=0$*

We again start with eq. (6b). Using (7), we have

$$2\ln\left[\frac{\delta}{\delta_0}\right]=-2\int_0^{1+\nu}\frac{\varepsilon'^{(D-2)/2}d\varepsilon'}{(\delta^2+(\varepsilon'-1)^2)^{1/2}[e^{(\delta^2+(\varepsilon'-1)^2)^{1/2}E_F/kT}+1]}. \tag{28a}$$

Introducing x and δ', defined by eqs (9a) and (9b), we obtain

$$\ln\left[\frac{\delta_0}{\delta}\right]=\int_{-E_F/kT}^{E_F\nu/kT}\frac{(1+kTx/E_F)^{(D-2)/2}\,dx}{(\delta'^2+x^2)^{1/2}(e^{(\delta'^2+x^2)^{1/2}}+1)}. \tag{28b}$$

For temperatures close to $T=0$, the limits can be taken as $-\infty$ and $+\infty$, and thus we have the same result as obtained for the case $\nu \ll 1$, viz. that given by eq. (12).

4.2 *Determination of the T_c equation for general D*

Starting from (6a) with $\delta=0$, we have

$$\frac{2}{\lambda}=\int_0^{1+\nu}\frac{\varepsilon'^{(D-2)/2}}{\varepsilon'-1}\tanh\left((\varepsilon'-1)\frac{E_F}{2kT_c}\right)d\varepsilon',$$

or

$$\frac{2}{\lambda}=\int_{-E_F/2kT_c}^{E_F\nu/2kT_c}\left(1+\frac{2kT_cy}{E_F}\right)^{(D-2)/2}\frac{\tanh y}{y}\,dy, \tag{29}$$

with y defined by (16).

Following a procedure similar to the one used in obtaining (17) from (15b), we have

$$\frac{2}{\lambda}=(1+\nu)^{(D-2)/2}\ln\left(\frac{E_F\nu}{2kT_c}\right)-[I_+(T_c)+I_-(T_c)], \tag{30}$$

with

$$I_+(T_c)=\int_0^{E_F\nu/2kT_c}dy\ln y\left[\left(1+\frac{2kT_cy}{E_F}\right)^{(D-2)/2}\operatorname{sech}^2y+\frac{kT_c}{E_F}(D-2)\left(1+\frac{2kT_cy}{E_F}\right)^{(D-4)/2}\tanh y\right], \tag{31a}$$

and

$$I_-(T_c)=\int_0^{E_F/2kT_c}dy\ln y\left[\left(1-\frac{2kT_cy}{E_F}\right)^{(D-2)/2}\operatorname{sech}^2y-\frac{kT_c}{E_F}(D-2)\left(1-\frac{2kT_cy}{E_F}\right)^{(D-4)/2}\tanh y\right]. \tag{31b}$$

Using binomial expansions to approximate the integrands in eqs (31a) and (31b), we have

$$I_+(T_c)+I_-(T_c)=\int_0^{E_F\nu/2kT_c}dy\ln y\times\left[\left(1+(D-2)\frac{kT_cy}{E_F}\right)\operatorname{sech}^2y+(D-2)\frac{kT_c}{E_F}\tanh y\right]+\int_0^{E_F\nu/2kT_c}dy\ln y\left[\left(1-(D-2)\frac{kT_cy}{E_F}\right)\operatorname{sech}^2y-(D-2)\frac{kT_c}{E_F}\tanh y\right].$$

Taking the upper limits in both the integrals to be ∞, we obtain

$$I_+(T_c)+I_-(T_c)=2\int_0^{\infty}\ln y\operatorname{sech}^2y\,dy=-2\ln\left(\frac{4e^{\gamma}}{\pi}\right).$$

Therefore, (30) takes the form

$$\frac{2}{\lambda} = (1+\nu)^{(D-2)/2} \ln\left(\frac{E_F \nu}{2kT_c}\right) + 2\ln\left(\frac{4e^{\gamma}}{\pi}\right), \tag{32}$$

or

$$kT_c = \frac{E_F \nu}{2}\left(\frac{4e^{\gamma} e^{-1/\lambda}}{\pi}\right)^{2(1+\nu)/(1+\nu)^{D/2}} \tag{33}$$

4.3 *Expression for δ near $T = T_c$*

The counterparts of eqs (20a) and (20b) in this case are

$$\frac{2}{\lambda} = 4\sum_{n=0}^{\infty} \int_{-E_F\nu/kT}^{E_F\nu/kT} \frac{(1+kTx/E_F)^{(D-2)/2}}{\pi^2(2n+1)^2 + \delta'^2 + x^2}\,dx, \tag{34a}$$

and

$$\frac{2}{\lambda} = 4\sum_{n=0}^{\infty} \int_{-E_F\nu/kT}^{E_F\nu/kT} \frac{(1+kTx/E_F)^{(D-2)}}{[\pi^2(2n+1)^2 + x^2]}\,dx - 4\delta'^2 \times \sum_{n=0}^{\infty} \int_{-E_F\nu/kT}^{E_F\nu/kT} \frac{(1+kTx/E_F)^{(D-2)/2}}{[\pi^2(2n+1)^2 + x^2]^2}\,dx, \tag{34b}$$

respectively.

The first term in (34b) gives the contribution

$$(1+\nu)^{(D-2)/2} \ln\left(\frac{E_F \nu}{2kT}\right) + 2\ln\left(\frac{4e^{\gamma}}{\pi}\right), \tag{35}$$

in consonance with (32) in which $T = T_c$.

Using (34b) and (35) in conjunction with (32), we obtain

$$(1+\nu)^{(D-2)/2} \ln\left(\frac{T}{T_c}\right) = -4\delta'^2 \sum_{n=0}^{\infty} \int_{-E_F\nu/kT}^{E_F\nu/kT} \frac{(1+kTx/E_F)^{(D-2)/2}}{[\pi^2(2n+1)^2 + x^2]^2}\,dx,$$

$$= -4\delta'^2 \left[2\sum_{n=0}^{\infty} \int_0^{\infty} \frac{dx}{[\pi^2(2n+1)^2 + x^2]^2} + \frac{(D-2)}{2}\frac{kT}{E_F} \times \sum_{n=0}^{\infty}\left(\int_0^{E_F\nu/kT} \frac{x\,dx}{[\pi^2(2n+1)^2 + x^2]^2} - \int_0^{E_F/kT} \frac{x\,dx}{[\pi^2(2n+1)^2 + x^2]^2}\right)\right]. \tag{36}$$

The first integral on the right is given by (22a). Using (22b), we have

$$\int_0^{E_F\nu/kT} x\,dx \sum_{n=0}^{\infty} \frac{1}{[\pi^2(2n+1)^2 + x^2]^2} = \int_0^{E_F\nu/kT} \left(\frac{1}{8x^2}\tanh\frac{x}{2} - \frac{1}{16x}\operatorname{sech}^2\frac{x}{2}\right) dx \simeq \frac{1}{16}\left[1 - \frac{2kT}{E_F\nu}\right]. \tag{37a}$$

Similarly

$$\int_0^{E_F/kT} x\,dx \sum_{n=0}^{\infty} \frac{1}{[\pi^2(2n+1)^2 + x^2]^2} \simeq \frac{1}{16}\left[1 - \frac{2kT}{E_F}\right]. \tag{37b}$$

Using (22a), (37a) and (37b), eq. (36) becomes

$$(1+v)^{(D-2)/2}\ln\left(\frac{T}{T_c}\right) = -4\delta'^2\left[\frac{1}{2\pi^2}\frac{7}{8}\zeta(3)+\frac{(D-2)}{2}(kT/E_F)^2\frac{(v-1)}{8v}\right],$$

or

$$\delta'^2 = \frac{4\pi^2}{7\zeta(3)}(1+v)^{(D-2)/2}\left(1-\frac{T}{T_c}\right)\left[1-\frac{\pi^2}{7\zeta(3)}(D-2)(kT_c/E_F)^2\frac{(v-1)}{v}\right].$$

Since $\delta' = (E_F/kT)\,\delta = \Delta/kT$ (see eqs (9a), (9b) and (5a), (5b), (5c)), we have finally,

$$\Delta^2 = \frac{4\pi^2}{7\zeta(3)}k^2T_c^2(1+v)^{(D-2)/2}\left(1-\frac{T}{T_c}\right) \times\left[1-\frac{\pi^2}{7\zeta(3)}(D-2)(kT_c/E_F)^2\frac{(v-1)}{v}\right]. \tag{38}$$

4.4 *Jump in the specific heat*

Using (26a) and (26b), we obtain

$$\Delta C = N(0)\frac{4\pi^2}{7\zeta(3)}k^2\,T_c(1+v)^{(D-2)/2}\left[1-\frac{\pi^2}{7\zeta(3)}(D-2)(kT_c/E_F)^2\frac{(v-1)}{v}\right].$$

Neglecting the second term in the parentheses, compared to unity, we have

$$\left.\frac{C_s-C_n}{C_n}\right|_{T=T_c} = \frac{6}{7\zeta(3)}(1+v)^{(D-2)/2} = (1{\cdot}43)\frac{(1+v)^{(D-2)/2}}{2}. \tag{39}$$

For $v>3$ and $D=3$, this is greater than 1·43, the usual BCS value. The specific heat measurements in high T_c materials are beset with many difficulties. The lattice contribution to the specific heat dominates the electronic contribution. Moreover, it is difficult to obtain reliable values of the Sommerfeld constant, γ. Nonetheless, in some experiments on Y123 powders one gets a jump in the specific heat, which is twice the BCS prediction [10].

5. Comparison of T_c equations for $v \ll 1$ and $v > 1$ for $D = 3$

It is instructive to compare the T_c equations for the cases $v \ll 1$ and $v > 1$. For the case of $v \ll 1$, $D = 3$, we have from (19)

$$(kT_c)_{BCS} = \frac{E_F v}{2}\left(\frac{4e^{\gamma}e^{-1/\lambda}}{\pi}\right)^{2/((1+v)^{1/2}+(1-v)^{1/2})}, \tag{19a}$$

and for the case of $v > 1$, $D = 3$, (33) gives

$$(kT_c) = \frac{E_F v'}{2}\left(\frac{4e^{\gamma}e^{-1/\lambda}}{\pi}\right)^{2/(1+v')^{1/2}}, \tag{33a}$$

where v' is used for v to distinguish it from the case $v \ll 1$. Dividing (33a) by (19a), we obtain

$$\frac{T_c}{(T_c)_{BCS}} = \frac{v'}{v}\left(\frac{4e^{\gamma}e^{-1/\lambda}}{\pi}\right)^{2[(1/(1+v')^{1/2})-(1/(1+v)^{1/2}+(1-v)^{1/2})]} \tag{40a}$$

Since $v \ll 1$, (40a) can be simplified to give

$$\frac{T_c}{(T_c)_{BCS}} = \frac{\nu'}{\nu}(2{\cdot}27e^{-1/\lambda})^{2(1/(1+\nu')^{1/2}-1/2)}. \tag{40b}$$

Equation (40b) tells us how T_c scales with the parameter ν', characterizing the mediating boson energy cutoff. Clearly there is an enhancement in the value of T_c compared to the BCS value. For example for $\nu' = 3$ we have

$$\frac{T_c}{(T_c)_{BCS}} = \frac{3}{\nu}. \tag{41a}$$

Since $\nu \ll 1$, it follows that

$$\frac{T_c}{(T_c)_{BCS}} \gg 1. \tag{41b}$$

6. Calculation of T_c from the BCS gap equation with a van Hove singularity in the density of states

As remarked earlier, non-phononic mechanisms have been proposed to explain the high transition temperatures exhibited by the new superconducting copper oxides. Apart from this a van Hove singularity in the density of states has been proposed as a T_c enhancement mechanism and as a means to explain the anomalous isotope effect in these materials [10–14].

Let us assume a logarithmic density of states

$$N(\varepsilon) = N(0)\ln\left|\frac{E_F}{\varepsilon - E_F}\right|,$$

$$N(\varepsilon) = N(0)\ln\left|\frac{1}{\varepsilon' - 1}\right|, \qquad (\varepsilon' = \varepsilon/E_F). \tag{42}$$

The equation corresponding to (6a) becomes

$$\frac{2}{\lambda} = \int_{1-\nu,0}^{1+\nu} d\varepsilon' \frac{\varepsilon'^{(D-2)/2}}{(\delta^2 + (\varepsilon'-1)^2)^{1/2}} \tanh\left(\frac{(\delta^2 + (\varepsilon'-1)^2)^{1/2}}{2kT/E_F}\right) \ln\left|\frac{1}{\varepsilon'-1}\right|. \tag{43}$$

At $T = T_c$, $\delta = \Delta/E_F = 0$. Putting $1 - \varepsilon' = x(\varepsilon' < 1)$, $\varepsilon' - 1 = x(\varepsilon' > 1)$ and $xE_F/2kT_c = y$, we get the equation

$$\frac{2}{\lambda} = \int_{E_F\nu/2kT_c, E_F/2kT_c}^{0} \frac{\tanh y}{y}\left(1 - \frac{2kT_c y}{E_F}\right)^{(D-2)/2} \ln\left(\frac{2kT_c y}{E_F}\right) dy$$

$$- \int_0^{E_F\nu/2kT_c} \frac{\tanh y}{y}\left(1 + \frac{2kT_c y}{E_F}\right)^{(D-2)/2} \ln\left(\frac{2kT_c y}{E_F}\right) dy. \tag{44}$$

As long as $\nu \ll 1$, the usual BCS result follows if we take $D = 2$, since the small width of the interaction makes the problem essentially two-dimensional. In this case (44) gives

$$\frac{2}{\lambda} = -2\ln\left(\frac{2kT_c}{E_F}\right)\int_0^{E_F\nu/2kT_c} \frac{\tanh y}{y} dy - 2\int_0^{E_F\nu/2kT_c} \frac{\tanh y}{y} \ln y\, dy. \tag{45}$$

Assuming $\tanh y \simeq y$ for $y \leqslant 1$ and $\tanh y \simeq 1$ for $y > 1$, one obtains

$$kT_c = \frac{eE_F}{2} \exp\left[-\left(\frac{2}{\lambda} - 1 + (\ln v)^2 \right)^{1/2} \right]. \tag{46}$$

This, of course, agrees with (3) obtained by Tsuei *et al* [11]. These authors have shown that for $\lambda = 0{\cdot}12$, $T_F = 5800$ K and $v = 0{\cdot}12$, T_c enhancement is obtained with $T_c = 92$ K. If we use the T_c equation for $D = 3$, $v > 1$ [eq. (33a)], we get the same T_c enhancement with $v = 6{\cdot}83$. Thus it seems that non-phononic mechanisms can lead to high values of T_c without invoking van Hove singularity.

Using (46), Tsuei *et al* [11] have been able to explain the anomalous isotope effect in the superconducting Cu oxides.

7. Conclusions

We have obtained analytic solutions of the BCS gap equation in one, two and three dimensions, for temperatures close to zero and T_c. Our calculations have been carried out in the weak coupling limit ($\lambda = N(0)v_0 \ll 1$). Expressions have been obtained for T_c and ΔC for the cases $v \ll 1$ and $v > 1$, respectively, where v is a measure of the interaction width.

The scaling of T_c with v, for the regime $v > 1$, is given by (33). Equation (41b) shows that there is an enhancement in the value of T_c in this limit. However, precise numerical estimates cannot be made within the framework of the present model. We may also mention that the appearance of non-zero T_c values, in dimensions lower than three, is a consequence of the mean field approximation, on which the usual BCS framework rests. In fact the non local interaction of the BCS reduced Hamiltonian violates the f sum rule [15].

We also find that ΔC, the jump in the electronic specific heat, across T_c, has a larger value than the usual BCS value. Certain experiments have revealed a similar feature in some high T_c materials.

The role of van Hove singularity seems to be crucial in understanding the anomalous isotope effect in new superconducting Cu oxides. A more detailed investigation is needed to make meaningful comments on this. It involves an analysis of (44) for the case $D = 3$, $v > 1$.

Acknowledgements

One of the authors (Arun Bhardwaj) is grateful to the University Grants Commission (UGC) for the financial assistance provided for carrying out this project. The authors are thankful to the Head of the Department of Physics and Astrophysics, University of Delhi, for providing the necessary facilities to carry out this work. They also wish to thank Prof. K K Singh for useful discussions.

References

[1] J G Bednorz and K A Müller, *Z. Phys.* **B64**, 189 (1986)
[2] For a recent comprehensive review see, *Proceedings of the International Conference on Materials and Mechanisms of Superconductivity, Physica* **C235–240** (1994)

[3] R. Batlogg, *Phys. Today*, **44**, 44 (1991)
[4] D M van der Walt, R M Quick, and M de Llano, *J. Math. Phys.* **34**, 3980 (1993)
[5] J R Schrieffer, *Theory of superconductivity* (W A Benjamin, New York, 1964) p. 54
[6] I S Gradshteyn and I M Ryzhik, *Tables of integrals, series and products* (Academic Press, New York, 1994) p. 969
[7] M Abramowitz and I A Stegun (Eds), *Handbook of mathematical functions* (Dover, New York, 1965) p. 378
[8] A L Fetter and J D Walecka, *Quantum theory of many-particle systems* (McGraw-Hill, New York, 1971) p. 449
[9] H Feshbach and P M Morse, *Methods of theoretical physics* (McGraw-Hill, New York, 1953) p. 385
[10] G Burns, *High temperature superconductivity* (Academic Press, New York, 1992) Ch. 5
[11] C C Tsuei, D M Newns, C C Chi and P C Pattnaik, *Phys. Rev. Lett.* **65**, 2724 (1990)
[12] Sujit Sarkar and A N Das, *Phys. Rev.* **B49**, 13070 (1994)
[13] Sujit Sarkar, S Basu and A N Das, *Phys. Rev.* **B51**, 12854 (1995)
[14] R Kishore, *Physica* **C253**, 367 (1995)
[15] P W Anderson, *Phys. Rev.* **110**, 827 (1958)

PRAMANA
— journal of
physics

© Printed in India

Vol. 47, No. 2,
August 1996
pp. 125–132

Internal irradiation effects in ^{239}Pu doped $K_2Ca_2(SO_4)_3$: EPR, TSL and PAS investigations

T K SESHAGIRI, V NATARAJAN, A R DHOBALE and M D SASTRY
Radiochemistry Division, Bhabha Atomic Research Centre, Bombay 400 085, India

MS received 7 October 1995; revised 12 April 1996

Abstract. The electron/hole trapped centres created during internal irradiation in ^{239}Pu doped $K_2Ca_2(SO_4)_3$ were investigated using electron paramagnetic resonance (EPR), thermally stimulated luminescence (TSL) and photoacoustic spectroscopic studies (PAS). These techniques were used to identify the defects and characterize the thermally induced relaxation processes. TSL studies of self (α)/γ-irradiated ^{239}Pu doped $K_2Ca_2(SO_4)_3$ revealed two glow peaks around 400 and 433 K. Plutonium introduced as Pu^{4+} was partly reduced to Pu^{3+} due to self irradiation. This was ascertained from PAS studies. EPR studies carried out on these samples showed the formation of radical ions SO_4^-, SO_3^-, O_3^-, etc. The thermal destruction of SO_4^- ion was found to be associated with the prominent glow peak around 433 K. Pu^{3+} was found to act as luminescent centre for the observed TSL glow. The trap depth for the glow peak at 433 K has been determined from TSL and EPR data.

Keywords. Thermally stimulated luminescence; electron paramagnetic resonance; photo acoustic spectroscopy.

PACS Nos 61·8; 78·6; 76·30

1. Introduction

Rare earth doped mixed sulphate compounds such as $K_2Ca_2(SO_4)_3$, $K_3Na(SO_4)_2$, $K_2Mg_2(SO_4)_3$, etc. are of intense current interest due to their possible role as excellent dosimetric materials and also for their optical properties [1, 2]. In this connection actinide dopants incorporated in mixed sulphate lattices, have unique role due to their α-activity causing auto radiolytic effects thereby facilitating TSL. This role of actinides is besides the more common function as fluroscent activator. Furthermore the existence of actinide ions in multiple valence states facilitates the formation of point defects favourable for enhancing luminescence. The self irradiation effects in actinide doped solids can result in the formation of numerous types of colour centres/radical ions as well as stabilization of actinide ions in unusual valence states of actinide ions [3, 4]. EPR and TSL are two techniques that can be effectively used in tandem to get an insight to the radiation damage centres produced due to internal (α) irradiation. ^{238}U (specific activity 0·74 dpm/μg) exists in oxidation states + 4, + 6 and + 3. The most common among these is UO_2^{2+}, which is known to be strongly fluorescing and is a good activator for intense TSL [5]. Plutonium on the other hand, is not known to give significant fluorescence in the visible region. It is well known that plutonium exists in oxidation states of + 4 and + 3 specially in solids. This is relevant in the formation of

local defect sites in the lattice. Conventionally optical absorption studies are normally used in similar investigations for identifying the metal ion impurities and/or colour centres. For powder samples PAS studies are better suited for the purpose. PAS is a versatile technique that can be used to probe the non-radiative relaxation processes even in weakly fluorescing samples. Thus in the present work on ^{239}Pu doped $K_2Ca_2(SO_4)_3$ we have combined EPR, TSL and PAS techniques to get an insight about the radiation damage centres produced due to internal (self-α) irradiation.

2. Experimental

Samples of Pu (0·5% by weight) doped $K_2Ca_2(SO_4)_3$ were prepared by the method similar to that reported earlier [5]. The incorporation of Pu in the sample has been ascertained by radiometric methods. TSL and PAS studies were carried out on home-built unit [6, 7]. EPR spectra were recorded on a Bruker ESP-300 Spectrometer at X-band frequency. A variable temperature accessory (V-4502) was used for EPR temperature variation experiments. A ^{60}Co gamma source with a dose rate of 2 kGy/h was used for gamma irradiation.

3. Results and discussion

In freshly prepared samples of $K_2Ca_2(SO_4)_3$, no TSL could be observed. However, on samples stored for about 2 weeks (α-dose rate = 10 kGy/hr.), a weak TSL peak around 433 K was observed (heating rate = 150 K/min.). On gamma irradiation of freshly quenched samples, an intense peak around 433 K was observed with a shoulder around 400 K (figure 1). Systematic gamma dose dependence studies have shown the TSL peak at 433 K to saturate after a gamma dose of about 6 kGy. The spectral studies of the TSL glow carried out using narrow band interference filters revealed emission groups around 580 and 485 nm characteristic of Pu^{3+} ion [8, 9]. The intrinsic luminescence of SO_4^{2-} was reported to be around 360 nm in alkaline earth sulphate lattices [10]. Substantial reduction in the intensity of TSL glows were observed when filters transmitting below 380 nm were used. This suggest that SO_4^{2-} does not act as luminescent centre in the mixed sulphate lattices. The trap depth energy values for the

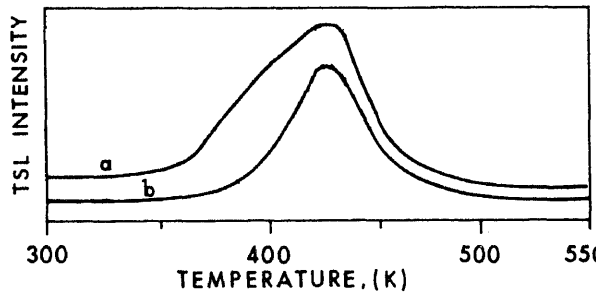

Figure 1. (a) TSL glow curve of γ-irradiated Pu doped $K_2Ca_2(SO_4)_3$ in the 300–550 K temperature range (γ-dose = 3/kGy). (b) TSL glow curve of the γ-irradiated sample recorded after annealing at 400 K for 1 min. (The TSL glow curve

peak at 433 K as determined from different heating rates method and initial rise method are given in table 1.

3.1 *Photo acoustic spectroscopic studies*

No absorption peaks were observed in unirradiated/gamma irradiated samples of undoped $K_2Ca_2(SO_4)_3$. However, on purely self (α) irradiated samples stored for about 24 h absorption bands around 445, 460, 560, 600, 680, 740, 780 and 820 nm are observed. The PAS of Pu doped sample was obtained after subtraction (in digital form) of the blank [undoped $K_2Ca_2(SO_4)_3$] spectrum. Both the sample and blank spectra were corrected for the source intensity variation and were stored in the computer. The difference spectra is shown in figure 2. The absorption peaks around 445, 460, 680, 740 and 820 nm are assigned to Pu^{4+} and those at 560, 600, 780 and 820 nm are assigned to Pu^{3+} on the basis of the absorption spectra reported for Pu ions in solutions in

Table 1. Trap parameters

TSL peak temp.* (K)	Trap depth (eV)			Frequency factor (sec^{-1})
	DHR	IR	EPR	
433	0·87	0·83	0·88	$2·2 \times 10^9$

DHR = Different heating rates method; IR = Initial rise method; * – heating rate = 150 K/min.

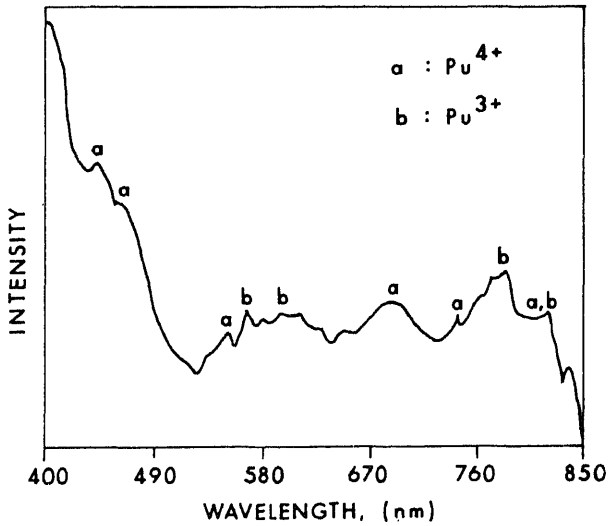

Figure 2. The photoacoustic absorption spectra (corrected for source intensity profile using a black body absorber) of Pu doped $K_2Ca_2(SO_4)_3$ after γ-irradiation (γ-dose = 3 kGy). The spectrum was obtained after subtraction (in digital form) of

literature [11]. Pu^{4+} complexes are also reported to have absorption below 440 nm ($5f^n \rightarrow 5f^{n-1}6d$). The high relative intensity in PAS spectrum below 440 nm can probably be due to predominant non-radiative relaxation. (The PAS intensities and absorption intensities can differ depending on the relative probability of radiative and non-radiative relaxation.) On gamma irradiation no change in the absorption maxima was observed.

3.2 *EPR studies*

The EPR spectrum of ^{239}Pu doped $K_2Ca_2(SO_4)_3$ recorded at room temperature three days after preparation is shown in figure 3. The spectrum contained signals due to SO_3^- ($g = 2{\cdot}0030$), SO_4^- ($g_\perp = 2{\cdot}0116$, $g_\parallel = 2{\cdot}0160$) and O_3^- ($g = 2{\cdot}0130$). These radical ions were found to build up in a period of 15 days and leveled off in intensity afterwards. The build up of the radical ions viz. SO_4^- and SO_3^- as a function of time of self-irradiation is shown in figure 4. In freshly quenched samples subjected to γ-irradiation from ^{60}Co source (dose = 2 kGy), the same radical ions were found to be present. No additional signal could be seen up to a γ-dose of 40 kGy. In uranium doped $K_2Ca_2(SO_4)_3$ reported earlier [5], EPR signals due to SO_2^- were found to overlap with that of SO_3^- line and SO_2^- disappeared around 400 K. In view of the intense SO_3^- signal observed in Pu doped sample, the presence of SO_2^- ion ($g_\perp \simeq 2{\cdot}004$) in smaller amounts could not be ruled out. No EPR signals due to Pu^{3+} could be obtained either at 77 K or at room temperature up to a magnetic field of 12·0 KG, the highest that can be achieved with our magnet. The EPR spectra of gamma irradiated samples recorded at different temperatures are given in figure 5. From the temperature dependence studies of the EPR spectra of irradiated samples carried out in the 300–600 K range, it was found that SO_4^- gets destroyed in the temperaure range 410–420 K suggesting its role in the glow peak observed around 433 K. The radical ion O_3^- showed a reduction in intensity in the

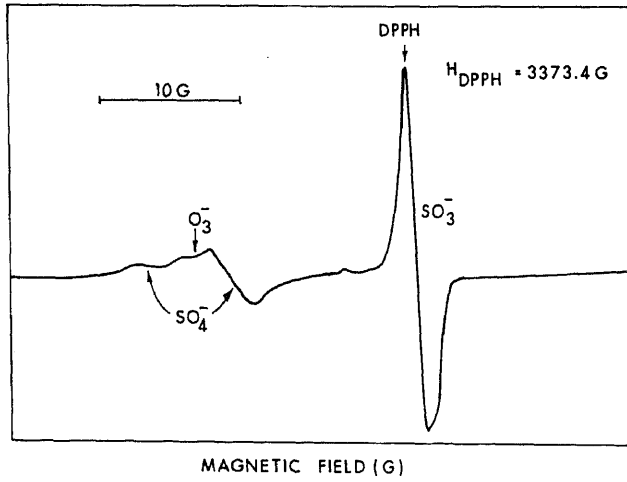

Figure 3. EPR spectrum of self (α)-irradiated Pu doped $K_2Ca_2(SO_4)_3$ (recorded 24 h after preparation of sample) at 300 K (α-dose rate = 3·6 kGy/h).

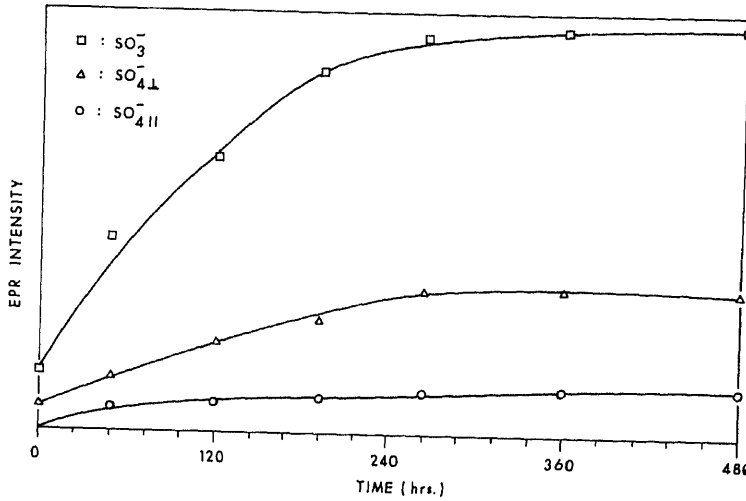

Figure 4. Build up of the radical ions SO_3^- and SO_4^- (as observed by EPR) as a function of period of self (α)-irradiation in ^{239}Pu doped $K_2Ca_2(SO_4)_3$.

380–450 K temperature range while the SO_2^- radical was found to disappear around 400 K. This could probably account for the increase in SO_3^- intensity beyond 400 K.

$$SO_2^- + O_3^- \rightarrow SO_4^{2-} + O;$$

$$SO_2^- + O \rightarrow SO_3^-$$

Essentially SO_3^- is generated out of SO_2^- and O_3^- in a two step process. An increase in SO_3^- signal intensity beyond 380 K was also observed in our studies on Am/Eu doped $SrSO_4$ [12]. The thermal stability plots for the radical ions are given in figure 6. The trap depth value was also determined from the temperature dependence of the EPR signal of the SO_4^- ion for the peak at 433 K by plotting $\ln[-\ln(1-\Delta I/I)]$ vs. $1/T$, where I is the intensity of the EPR signal and ΔI is the amount of decrease of signal at each temperature [13]. The trap depth value, thus determined is included in Table 1.

3.3 *Mechanism for the TSL glows*

(i) *Peak at* 400 K: This peak could not be studied in detail due to its low intensity. It could probably be associated with the thermal destruction of SO_2^- as reported in uranium doped $K_2Ca_2(SO_4)_3$.

(ii) *Peak at* 433 K: Plutonium was doped as Pu^{4+}. It is most likely that Pu^{4+} would go to Ca^{2+} site rather than K^+ site. A tetravalent ion at a divalent site would be a good electron trap. The detection of Pu^{3+} along with Pu^{4+} in PAS studies clearly shows that Pu^{4+} traps an electron purely by internal α/γ irradiation. This is essentially a radiation induced partial reduction of Pu^{4+}. EPR studies have shown the concomitant formation of SO_4^- indicating that electron is released from SO_4^{2-}.

$$SO_4^{2-} \xrightarrow{\alpha/\gamma} SO_4^- + e^-; \quad Pu^{4+} + e^- \rightarrow Pu^{3+}.$$

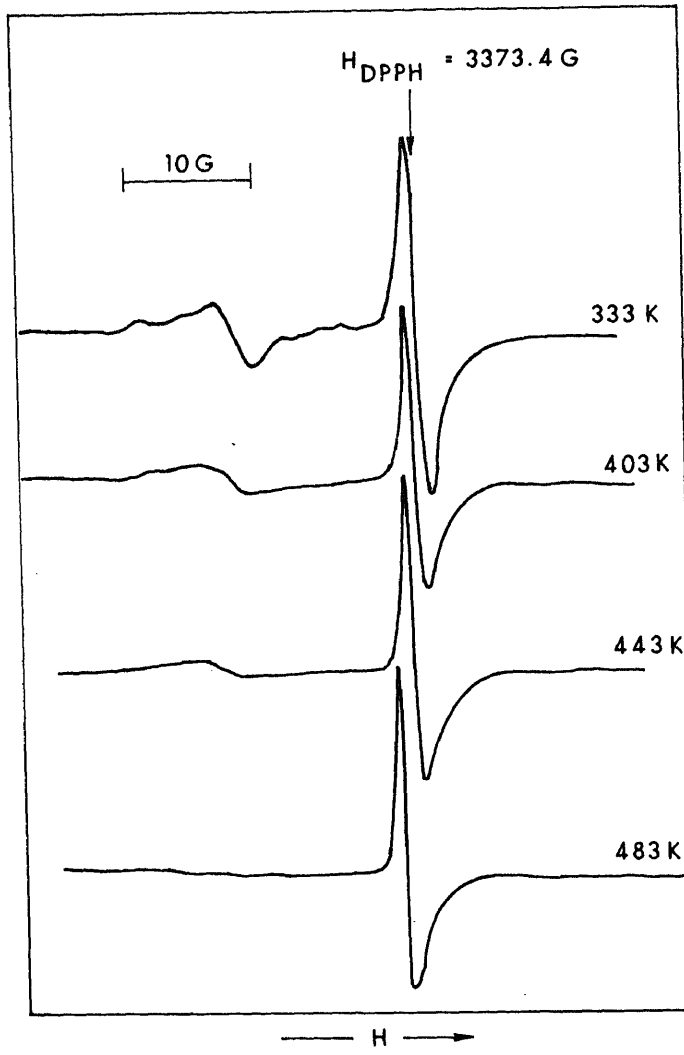

Figure 5. The EPR spectra of γ-irradiated ^{239}Pu doped $K_2Ca_2(SO_4)_3$ recorded at different temperatures (γ-dose = 3 kGy).

On heating to 433 K, the hole on SO_4^- becomes mobile i.e. SO_4^- takes an electron from adjacent SO_4^{2-} so that effectively SO_4^- appears to be mobile. When such an SO_4^- comes closer to Pu^{3+} then the electron transfer from Pu^{3+} to SO_4^- takes place and the reaction products would be SO_4^{2-} and Pu^{4+} with associated liberation of energy.

$$SO_4^- + Pu^{3+} \rightarrow SO_4^{2-} + Pu^{4+} + \text{energy}.$$

The liberated energy can go in to excitation of Pu^{3+}/SO_4^{2-} or both. Pu^{4+} is reported to give fluorescence in the infrared region [8]. Therefore direct excitation of Pu^{4+}

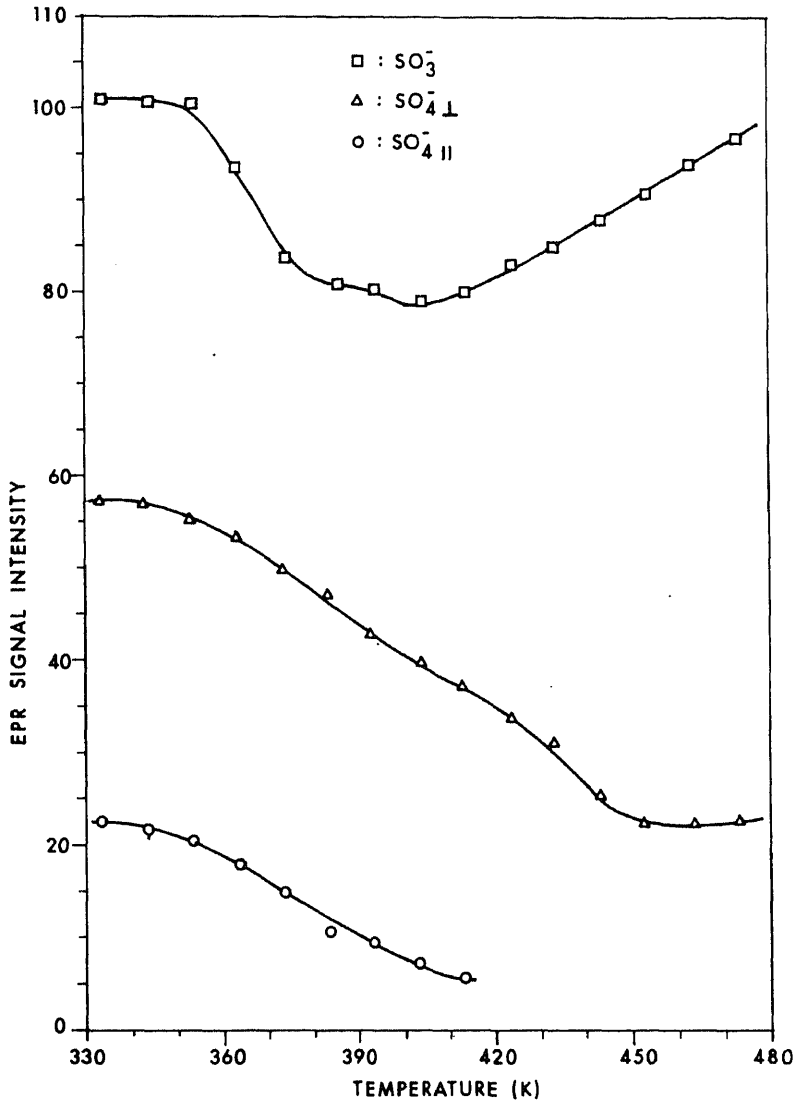

Figure 6. Temperature dependence of intensities of the radical ions SO_4^- and SO_3^- observed in ^{239}Pu doped $K_2Ca_2(SO_4)_3$.

essentially relaxes through non-radiative mechanism. This would not show in TSL. The SO_4^{2-} ion is known to give emission around 360 nm [10]. This energy can be transferred to Pu^{3+} as it has a broad absorption band in that region, resulting in the formation of excited Pu^{3+} which on de-excitation gives Pu^{3+} emission around 485 and 580 nm as seen from TSL spectral studies.

$$Pu^{3+} + SO_4^{2-*} \rightarrow Pu^{3+*} + SO_4^{2-} \rightarrow Pu^{3+} + SO_4^{2-} + h\nu\,(485, 580\,\text{nm}).$$

4. Conclusion

The TSL glow peak at 433 K is associated with the thermal destruction of SO_4^- ion as observed from EPR. The presence of Pu^{4+}/Pu^{3+} in the samples has been confirmed from PAS studies.

Acknowledgement

The authors are thankful to Dr R H Iyer, for his keen interest and encouragement.

References

[1] P D Sahare, S V Moharil and B D Bhasin, *J. Phys.: Appl. Phys.* **D22**, 971 (1989)
[2] M Ohta, M Sakaguchi and M Sato, *Denki Kagaku* **60**, 881 (1993)
[3] T K Seshagiri, A G I Dalvi and M D Sastry, *J. Phys.* **C21**, 5891 (1988)
[4] M D Sastry and A G I Dalvi, in *Handbook on Physics and Chemistry of the actinides* edited by A J Freeman and C Keller (Elsevier Science Publishers, Amsterdam, 1991) ch. 8, p. 411
[5] T K Seshagiri, V Natarajan and M D Sastry, *Pramana – J. Phys.* **44**, 211 (1995)
[6] A G I Dalvi, M D Sastry and B D Joshi, *J. Phys. E Sci. Inst.* **13**, 1106 (1980)
[7] A R Dhobale, Mithlesh Kumar, A G Page and M D Sastry, BARC Report. BARC/1993/E/020
[8] R D McLaughlin, R White, N Edelstein and J G Conway, *J. Chem. Phys.* **48**, 967 (1968)
[9] J J Stacy, N Edelstein and R D McLaughlin, *J. Chem, Phys.* **57**, 4980 (1972)
[10] M L Gaft, L V Bershov, A R Krasnaya and V Ya Yaskolko, *Phys. Chem. Minerals* **11**, 255 (1985)
[11] J M Cleveland, *Chemistry of Plutonium* (Gordon and Breach Science Publishers, New York, 1970) pp. 14–17 and p. 115
[12] A G I Dalvi, M D Sastry, T K Seshagiri and B D Joshi, *J. Phys.* **C17**, 5864 (1984)
[13] R Huzimara, K Asahi and M Takanega, *Nucl. Instrum. Methods* **175**, 8 (1980)

Temperature dependent photoluminescence studies of ZnSe:I single crystals grown by chemical vapor transport

SURUCHI ANAND, PRABHAT VERMA, S C ABBI, K P JAIN, M J TAFRESHI*, K BALAKRISHNAN* and R DHANSEKARAN*
Department of Physics, Indian Institute of Technology, New Delhi 110016, India
*Crystal Growth Centre, Anna University, Madras 600025, India

MS received 23 June 1995; revised 28 June 1996

Abstract. The single crystal ZnSe:I sample was grown by the chemical vapor transport (CVT) method using iodine as the transporting agent. The iodine incorporates itself effectively as a donor in the lattice. The sample shows a ⟨111⟩ optical quality surface and has an absorption edge at 2·55 eV due to a deep impurity band nearly 0·15 eV below the conduction band. The photoluminescence emission spectra of this crystal have been measured for its temperature dependence as well as for excitation energy dependence. The photoluminescence is in accordance with a donor-acceptor complex formation involving iodine activated donors and self-activated acceptors. The configuration coordinate model has been used to explain the temperature dependent changes in the peak position and the bandwidth of the emission band. The decrease in luminescence efficiency with increasing temperature is explained by using a simple model for thermal quenching. The activation energy at low temperature range ($T < 200$ K) is different from that at high temperature range (200 K $< T <$ 300 K).

Keywords. ZnSe; chemical vapor transport; photoluminescence.

PACS Nos 61·50; 78·60

1. Introduction

ZnSe has received great attention [1–4] recently due to its potential and technological importance, as it has a wide band gap of 2·7 eV at room temperature. It shows great promises for the fabrication of blue semiconductors lasers, high efficiency electroluminescent blue/green light emitting diodes (LEDs) and windows for high power lasers. ZnSe is also widely used in the fabrication of modulated heterostructures and optical waveguides both in its binary and alloy forms. ZnSe needs incorporation of *n*- and *p*-type dopants for its use as electroluminescent devices and LEDs. Although *n*-type doping is easily achieved in ZnSe, successful *p*-type doping have been achieved [2, 3] only recently in materials prepared by molecular beam epitaxy (MBE) process. Since MBE is an expensive method, other growth and doping methods should be explored, and the present work reports studies on the ZnSe:I samples grown by the chemical vapor transport (CVT) method using iodine as a transporting agent. These samples are characteri zed by optical transmission, X-ray diffraction and Raman spectroscopy. The photoluminescence for the well characterized crystal is studied in detail.

In the present study, ZnSe:I single crystals have been grown by the CVT technique, which permits growing the sample at lower temperatures than those in other methods (e.g. melt and sublimation methods) using iodine as the transporting agent. The iodine, which incorporates effectively as a dopant in the lattice, produces donor-activated centers and changes the optical properties of the sample. Raman scattering and optical transmission studies have been carried out to characterize the optical properties. The optical phonon positions and widths in the Raman spectra are used to ascertain the crystallinity of the material. The optical transmission spectrum indicates the onset of absorption at 2·55 eV due to iodine impurity, which is 0·15 eV below the band gap of pure ZnSe crystal. This agrees with the previous observation of Lebaccabue *et al* [5] in 1993.

The CVT grown samples exhibited strong photoluminescence band in the red region, centered around 2·015 eV at room temperature. This photoluminescence is ascribed to the donor-acceptor complex formation involving iodine activated donors and self-activated (SA) acceptors. This complex is formed during the photoexcitation and is short-lived ($\approx 10^{-16}$ s). The room temperature photoluminescence studies at various excitation energies show a maximum photoluminescence efficiency for the excitation energy close to 2·5 eV with a peak at 2·015 eV, which is in good agreement with the band gap of 2·55 eV observed in the optical transmission studies. The temperature dependent photoluminescence studies for a fixed excitation laser energy (2·4 eV) show changes in the peak position, bandwidth and intensity of the emission band. As the temperature is changed from 10 to 300 K, the peak position shifts from 2·005 to 2·015 eV, the bandwidth increases from 190 to 280 meV and the intensity decreases by more than an order of magnitude. The temperature variation in the peak position and bandwidth are explained using the configuration coordinate (CC) model [6–8] whereas the temperature variation in the intensity is explained by a simple model for thermal quenching [6, 9]. The activation energies are found to be 11 meV at temperatures below 200 K and 107 meV at higher temperatures.

2. Growth procedure

The process of CVT with iodine as the transporting agent has been widely applied [10–13] to the growth of ZnSe single crystals because of the advantages of its greatly reduced growth temperatures compared to the melt and sublimation methods. In addition to the need of expensive and complex furnaces for the crystal growth by melt and sublimation methods, there are many disadvantages of these methods, like defects produced by thermal strains including dislocations, fracture or twins and uncontrolled impurities incorporation from the crucible. The CVT on the other hand is a simple process with lower growth temperature. For the CVT growth process, the source in the powder form is kept at one end of a quartz ampoule of inner diameter 10 mm and length 250 mm and the crystal is obtained at the other end, when the two ends are maintained at two different temperatures with the source at higher temperature. Figure 1 shows the geometry and the temperature variation in the ampoule during the growth process. Before starting the growth process, the ampoule was subjected to reverse temperature gradient (i.e. the sample end at a higher temperature compared to the source end) for 24 h to remove sticking powders from deposition zone and diminish the active sites.

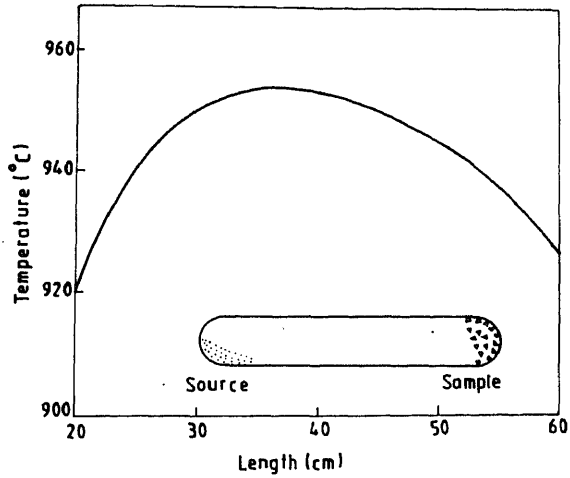

Figure 1. The sketch and the temperature variation in the ampoule for the CVT process.

The source temperature (T_s) and deposition temperature (T_d) values have been optimized for an iodine concentration in order to obtain good quality crystals. The best sample was grown for $T_s = 953°C$, $T_d = 940°C$. The ampoule was loaded with 3g of presynthesized source powder along with iodine at a concentration of $2\,mg/cm^3$ of the empty volume. The ampoule was placed stationarily in a horizontal double zone furnace controlled by Eurotherm controllers with the accuracy of $\pm$ 0·1°C. The source and deposition temperatures were kept at 953 and 940°C respectively. The process was carried out for about 100 h. At the end of the growth process, the furnace was slowly cooled to room temperature at a cooling rate of 50°C/hr to prevent thermal strains. After cooling, the sample chunk was taken out by breaking the tube. The sample chunk was further broken and a crystallite with well-developed smooth shiny surface was chosen. This surface was identified as the $\langle 111 \rangle$ surface by Raman spectroscopy as well as by X-ray Laue diffraction studies.

3. Characterization

The ZnSe:I sample grown by the CVT method was characterized by the optical transmission measurements, X-ray diffraction and Raman scattering studies. The optical transmission measurements were performed by employing the Hitachi-U4300 spectrophotometer in visible-UV ranges. The optical transmission spectra for this sample is shown in figure 2. This figure shows an absorption edge at 489·7 nm (2·55 eV) which is about 0·15 eV below the conduction band. The complex shape of the absorption band also indicates existence of levels deeper into the band gap. The CVT grown sample was also studied by obtaining the X-ray Laue pattern. This study indicates that the sample surface is oriented perpendicular to the $\langle 111 \rangle$ direction.

The quality of the crystal grown by the CVT technique was examined by employing laser Raman spectroscopy. The Raman spectroscopy experiments were performed in

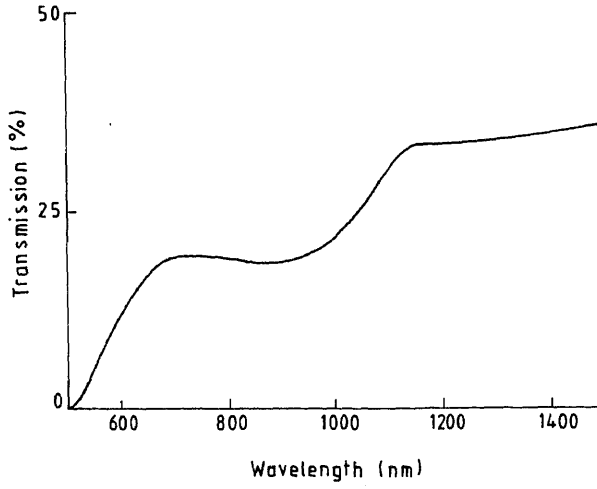

Figure 2. Optical transmission spectrum of CVT grown ZnSe:I.

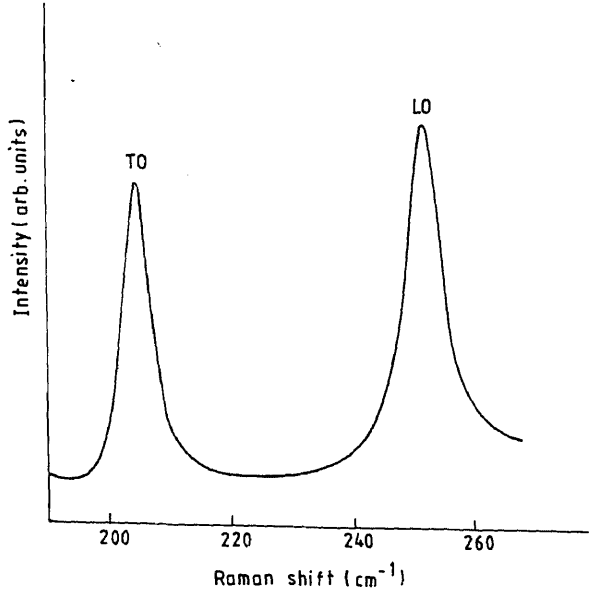

Figure 3. Raman spectrum of CVT grown ZnSe:I showing the TO and LO phonons.

the backscattering geometry with $Z(XX + XY)\bar{Z}$ polarization at room temperature by employing the 514·5 nm line of an argon-ion laser, Ramanor double monochromator and the usual photon counting electronics. The monochromator was calibrated using strong plasma lines of the argon-ion laser and for better accuracy the slit-

References	TO phonon position (cm^{-1})	LO phonon position (cm^{-1})
Mel'nik *et al*	205	252
Islam *et al*	204	251
Anand *et al*	205	251·5
Present work	204	251·5

width of the monochromator was reduced to 100 μm. Figure 3 shows a room temperature Raman spectrum of the sample between 200 and 300 cm^{-1}. The spectrum shows two prominent phonon modes at 251·5 and 204 cm^{-1}, which are identified as the longitudinal optic (LO) and transverse optic (TO) phonons respectively at the center of the Brillouin zone. The LO and TO phonons are observed with comparable intensity in figure 3. According to the momentum selection rules, this is allowed only for the $\langle 111 \rangle$ face in a back scattering geometry Raman spectrum [14]. Thus we conclude that the sample is oriented in the $\langle 111 \rangle$ direction. The peak positions and the symmetry of the Raman lines for the CVT grown ZnSe crystal are in agreement with those obtained for ZnSe single crystals [15–17]. Table 1 gives a comparison between earlier results and our observations. This indicates that the CVT process yields good quality single crystals of ZnSe.

4. Experimental results and discussion

The photoluminescence was excited in the CVT grown ZnSe:I sample using the argon-ion laser, and was dispersed using a double monochromator. The sample was fixed on the cold finger of a cryostat using silver paste and the temperature was regulated down to 10 K from the room temperature using a Helitron closed cycle liquid He cryostat. The temperature of the sample was measured accurately by mounting a Au-Cr thermocouple on the cold finger. The accuracy in the temperature measurement was $\pm 0{\cdot}2$ K. The cryostat was evacuated to 1×10^{-6} torr to avoid condensation of moisture on the sample at low temperatures. The monochromator was calibrated using the strong plasma-lines of the argon-ion laser.

It is generally found that small amounts of copper incorporated intentionally or as an impurity [9], gives an emission band from the grown ZnSe:I crystals. The self-activated emission associated with iodine and the low energy copper emission overlap in the red region of the spectrum at room temperature. As the temperature is decreased the self activated band shifts towards the higher wavelength side whereas the copper emission band shifts towards the lower wavelength side. Therefore the two bands are separated at low temperatures. The copper band is reasonably strong even if the copper concentration is a few part per million. Since copper band is not seen even at low temperatures, we conclude that the CVT grown ZnSe:I sample does not contain any trace of copper.

The photoluminescence was excited in the crystal using various lines of argon-ion laser in the range 2·4 to 2·7 eV with the incident power adjusted to 10 mW for each

line at room temperature. The photoluminescence spectra were obtained in the range 1·750 to 2·250 eV, which show a broad band with the maximum at about 2·015 eV. It is seen that the intensity of the luminescence band first increases and then decreases when the laser energy is varied from 2·4 to 2·7 eV with a maximum at about 2·5 eV. Figure 4 shows the plot of band intensity versus incident energy at room temperature.

The temperature dependent photoluminescence studies were performed for various temperatures between 10 and 300 K using the 2·4 eV laser line. Figure 5 shows the photoluminescence spectra at various temperatures. The spectrum at room temperature shows a broad band with a maximum at about 2·015 eV and the bandwidth is about 280 meV. It can be seen in figure 5 that the peak position shifts towards higher energy side and the bandwidth increases as the temperature is increased from 10 to 300 K. Apart from the changes in the peak position and the bandwidth, the band intensity is also found to decrease with increase in temperature.

The broad peak observed at 2·015 eV which is ascribed to the self activated (SA) luminescence band [5, 11, 13], is typical of the ZnSe:I single crystals. This peak is mainly due to the incorporation of iodine [18] which leads to well-known self-compensation of the iodine-related donors by the SA acceptor, which is a ($V_{Zn}I_{Se}$) complex with Zn vacancy V_{Zn} and iodine on the nearest-neighbor Se site I_{Se}. The complex is formed during the photoexcitation and its decay gives rise to the SA luminescence. The SA luminescence band could be fitted to a Lorenztian line shape confirming the model for photoluminescence involving the formation of a short-lived complex. From the width of the Lorentzian band, the life-time of the complex is estimated as $\approx 10^{-16}$ s.

4.1 *Thermal broadening and shift*

The bandwidth and the peak position for the SA band shows a temperature dependent behavior. It is found that the SA band in the luminescence spectra of the CVT grown

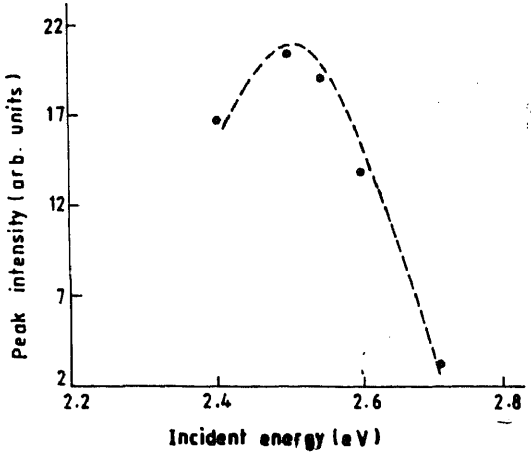

Figure 4. The peak intensity of photoluminescence band at various incident laser energies for the CVT grown ZnSe:I.

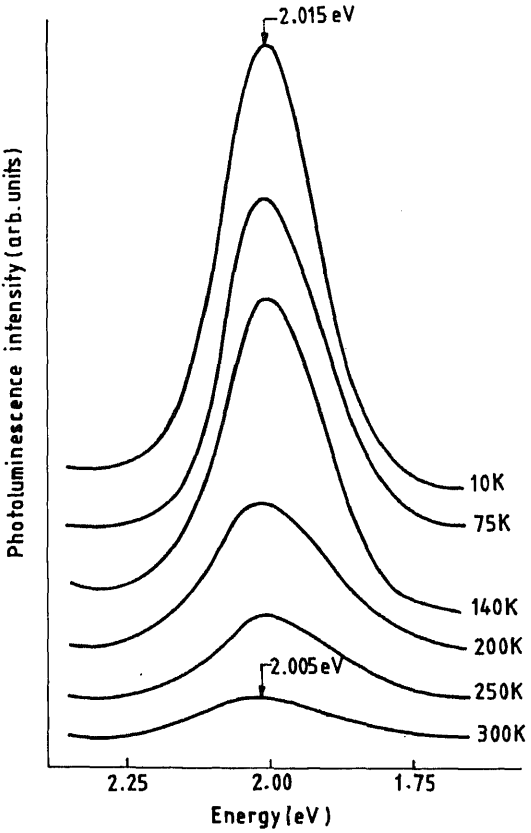

Figure 5. Self-activated photoluminescence spectra for the CVT grown ZnSe:I sample at various temperatures.

sample shifts towards higher energy and its bandwidth increases as the temperature is raised from 10 to 300 K. The temperature dependence of the bandwidth of the SA band can be explained in terms of a simplified form of the configuration coordinate model used for localized centers. According to this model, the temperature dependence of the halfwidth of the emission spectrum is given [6–8] by

$$\Gamma(T) = \Gamma_0 \{\coth(\hbar\omega_e/2k_B T)\}^{1/2}, \tag{1}$$

where ω_e is the frequency of the local vibrational mode associated with excited state of the luminescent centre for the emission process and Γ_0 is a temperature independent term and gives the bandwidth at low temperatures.

Equation (1) has been used to obtain the values of Γ_0 and ω_e for the best fit to the experimental data. The values of Γ_0 and ω_e are estimated to be 190 meV (1520 cm^{-1}) and 26 meV (208·3 cm^{-1}) respectively. The resultant curve is shown in figure 6. The experimental data points fall on this curve reasonably closely. The value of ω_e is close to the TO phonon frequency, which indicates that the TO phonon interacts strongly with the excited state of the luminescent center.

The occupation number in the vibrational level can be assumed to follow the Boltzmann distribution. This introduces a Gaussian factor in the shape function of the emission spectrum, assuming that the displacement between the minima in the coordinate of the excited and ground states is sufficiently large. In the process of emission, the Einstein coefficient for spontaneous emission, which is proportional to the third power of photon energy, has to be taken into consideration. Thus if the emission spectrum is divided by the third power of the photon energy, it should yield a Gaussian curve. This fact was confirmed [19] long time back. Making simple assumptions that the shapes of the CC curve do not change with temperature and the temperature shift in the SA band peak position (E_e) is predominantly due to the temperature change of the occupation number in vibrational levels, Shionoya *et al* [20] derived the expression for the temperature dependent shift of the peak of the emission band using the configuration coordinate model on the basis of the above discussion. This temperature dependence is given by

$$E_e(T) = Ak_BT, \tag{2}$$

where A is a temperature independent coefficient, which includes the frequencies of the local vibrational modes associated with the excited and ground states, and the emission and absorption peak energies at zero temperature. Equation (2) gives a linear temperature dependence of the emission band peak position. Figure 7 shows the best linear fit to our experimental values. The constant A is estimated to be 0·41 from the linear portion of the plot.

4.2 *Thermal quenching*

It is well-known [9] that the photoluminescence from many materials quenches with an increase in temperature. We have also observed a rapid thermal quenching of the SA emission band as the temperature was raised from 10 to 300 K. The curve in figure 8 shows how the intensity (peak height) of self-activated band decreases with increase in

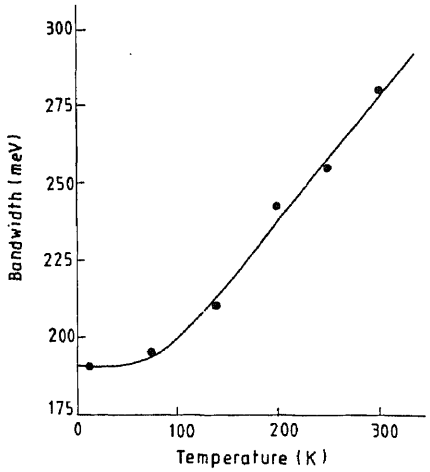

Figure 6. The temperature dependence of photoluminescence bandwidth. The figure shows experimental data points as well as the theoretical curve using eq. (1).

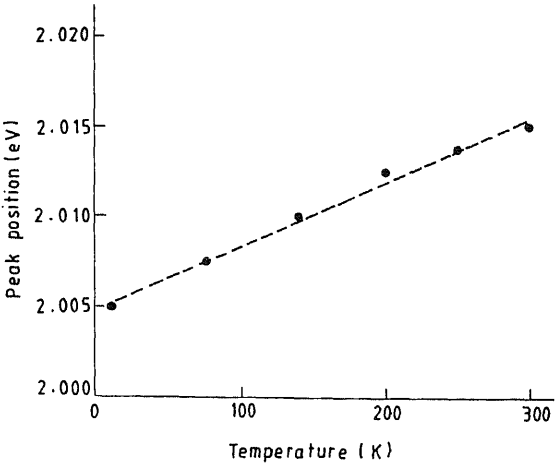

Figure 7. Temperature dependence of the luminescence band peak position showing a linear behavior.

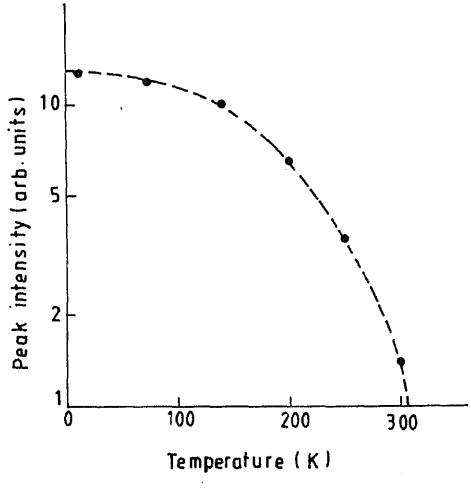

Figure 8. The peak intensity of the photoluminescence band at various temperatures for the CVT grown ZnSe:I sample.

temperature. The intensity of this band decreases slowly in the low temperature range ($T < 200$ K) and falls rapidly at the higher temperatures.

The luminescence efficiency [9, 20], η, which is the normalized value of luminescence intensity, can be described by a simple equation

$$\eta = \{1 + C\exp(-W/k_B T)\}^{-1}, \tag{3}$$

where C is a constant and W is the activation energy for quenching.

Equation (3) was used to fit the experimentally observed values of the luminescence intensity to calculate the best estimations of the constants involved. This equation can

be rewritten as

$$\ln(1/\eta - 1) = -W/k_B T + C', \tag{4}$$

where C' is another constant. According to (4), ln $(1/\eta - 1)$ is linearly dependent on $1/k_B T$. However, the experimental results do not show this linear behavior for the temperature range between 10 and 300 K. A similiar result was observed earlier by Jones *et al* [9]. The plot of the experimental values of $\ln(1/\eta - 1)$ versus $1/k_B T$ is shown in figure 9. Figure 9 shows an average linear dependence at low temperatures ($T < 200$ K) with a slope of 11 meV and an average linear dependence at high temperatures ($T > 200$ K) with a slope of 107 meV. These values of the slopes gives the activation energies in the two temperature ranges. We ascribe the energy of 11 meV and 107 meV to the activation energies for the loss of donor and acceptor concentrations of the conduction and valence bands respectively.

5. Conclusions

ZnSe:I single crystal was grown by the chemical vapor transport (CVT) method using iodine as the transporting agent. The characterization processes such as optical transmission measurements, X-ray diffraction and Raman scattering studies indicate that it is a well-grown single crystal with a good quality optically plane $\langle 111 \rangle$ surface. The sample has an absorption edge at 2·55 eV, which is about 0·15 eV below the bandgap energy. This indicates the presence of a deep impurity band nearly 0·15 eV below the conduction band.

The CVT grown sample was studied for the photoluminescence using various excitation energies between 2·4 and 2·7 eV at room temperature and also for various temperatures between 10 and 300 K when the excitation energy was fixed at 2·4 eV. The room temperature spectra shows a maximum luminescence emission for incident laser energy of about 2·5 eV, with peak position at 2·015 eV. The temperature dependent photoluminescence spectra show that the peak position shifts towards higher side, the bandwidth increases and the intensity decreases as the temperature is increased from 10

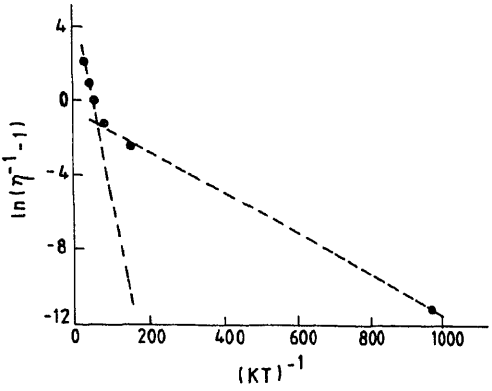

Figure 9. Plot of $\ln(1/\eta - 1)$ versus $1/k_B T$ showing two different slopes at low and at high temperatures.

to 300 K. The shift in the peak position and the bandwidth are explained on the basis of the CC model. It is found that the TO phonon mode interacts strongly with the excited state of the luminescence center. The intensity change is explained by employing a simple model for the thermal quenching of the luminescence band. The activation energies calculated from the thermal quenching process are 11 meV at low temperatures and 107 meV at elevated temperatures.

Acknowledgements

The authors are thankful to Dr R Jayavel and Mr S Balakumar of Crystal Growth Centre, Anna University, for their help in X-ray analysis. One of the authors, KB, is grateful to CSIR, India for the award of Research Associateship. The authors, PV, SCA and KPJ are thankful to the Department of Science and Technology, Govt. of India, for sponsoring the research project.

References

[1] J Kuhl, B K Rhee and W E Born, in *Photon scattering in condensed matter. Proc. IVth Int. Conf.* (Stuttgart, Germany, 1983) pp. 106–108
[2] H Mitsuhashi, A Yahata, T Umoto, A Kamata, M Okajima, K Hirahara and T Bippu, *J. Cryst. Growth* **101**, 818 (1990)
[3] M A Haasa, J Qiu, J M De Puydt and H Cheng, *Appl. Phys. Lett.* **59**, 1272 (1991)
[4] L Ward, in *Handbook of optical constants II* edited by E Palik (Academic, New York, 1991) pp. 737–758
[5] F Leccabue, O demalo Pereira and T H Calderon, *Proc. Int. Workshop* (La Hubana, Cuba, 1993) p. 241
[6] S Shionoya, in *Luminescence of inorganic solids* edited by P Goldberg (Academic, New York, 1966) pp. 206–277
[7] D Curie and J S Prener, in *Physics and chemistry of II–VI compounds* edited by M Aven and J S Prener (Amsterdam, North Holland Publishing Company, 1967) pp. 434–482
[8] G Jones and J Woods, *J. Phys.* **D6**, 1640 (1973)
[9] G Jones and J Woods, *J. Lumin.* **9**, 389 (1974)
[10] E Kaldis, *J. Phys. Chem. Solids* **26**, 1701 (1965)
[11] S G Parker, *J. Cryst. Growth* **9**, 177 (1971)
[12] H Hartmann, *J. Cryst. Growth* **42**, 144 (1977)
[13] S Fujita, H Mimoto, H Takebe and T Noguchi, *J. Cryst. Growth* **47**, 326 (1979)
S Fujita, H Mimoto and T Noguchi, *J. Appl. Phys.* **50**, 1079 (1979)
[14] M Cardona, in *Light scattering in solids* edited by M Cardona and Guntherodt (Springer-Verlag, Berlin Heidelberg, New York, 1982) vol. II, pp. 96–97
[15] N N Mel'nik and E A Vinogradov, *Sov. Phys. Solid State* **18**, 1900 (1976)
[16] S S Islam and K P Jain, *XIIIth Int. Conf. on Raman Spectroscopy*, Germany (1993)
[17] S Anand, Prabhat Verma, K P Jain and S C Abbi, to be published (1996)
[18] J O Fornell and H G Grimmeiss, *J. Appl. Phys.* **64**, 6322 (1988)
[19] H Treptow, *Czech. J. Phys.* **B13**, 115 (1963)
[20] S Shionoya, T Koda, K Era and H Fujiwara, *J. Phys. Soc. Jpn.* **19**, 1157 (1964)

Raman study of phase transition in ferroelectric $Ba_{0.95}Ca_{0.05}TiO_3$

REKHA RAO[1], A P ROY[2], B A DASANNACHARYA[3], S BALAKUMAR[4], R ILANGOVAN[4] and P RAMASAMY[4]
[1]Solid State Physics Division, Bhabha Atomic Research Centre, Mumbai 400 085, India
[2]Spectroscopy Division, Bhabha Atomic Research Centre, Mumbai 400 085, India
[3]Inter-University Consortium for DAE Facilities, University Campus, Khandwa Road, Indore 452 001, India
[4]Crystal Growth Centre, Anna University, Madras 600 025, India

MS received 10 June 1996

Abstract. Raman scattering investigation of phase transition in the ferroelectric $Ba_{0.95}Ca_{0.05}TiO_3$ is reported. The results suggest onset of significant dynamic disorder at 105°C. This corroborates findings of recent structural study regarding large positional disorder associated with Ti and O1 atoms well below the tetragonal to cubic transition temperature (~ 150°C).

Keywords. Raman scattering; phase transition; ferroelectric.

PACS Nos 78·30; 64·60; 77·80

1. Introduction

The tetragonal (ferroelectric) to cubic (paraelectric) phase transition in $BaTiO_3$ (BT) is characterized by a sharp peak in dielectric permittivity around 130°C. Solid solutions like $Ba_{1-x}Sr_xTiO_3$ ($x < 0{\cdot}4$) on the other hand exhibit broadened transitions termed as diffuse phase transitions (DPT). DPT is not necessarily related to crystalline inhomogeneity but it is intrinsic in nature [1]. It is believed that phase changes are influenced by large polarization fluctuations in these systems [2]. It has been shown recently [3] that partial substitution of Ba by Ca results in broadening of the dielectric peak as well as shifting of the peak position to higher temperatures (~ 150°C). In this paper we report detailed Raman scattering investigations in $Ba_{1-x}Ca_xTiO_3$ single crystal having a nominal value of $x = 0{\cdot}05$. Interestingly, the intensities of E and A_1 modes which are Raman active in the tetragonal phase, disappear around 105°C, well before the temperature at which the dielectric function peaks, namely 150°C. We discuss the implication of these observations in conjunction with the results reported using neutron scattering and electron paramagnetic resonance studies.

2. Experimental details

$Ba_{1-x}Ca_xTiO_3$ (BCT) crystals were grown at Crystal Growth Centre, Anna University by Remeika technique using KF as flux. A mixture containing 30% ($BaCO_3 + CaCO_3 + TiO_2$) and 70% KF was taken in Pt crucible and heated to 1200°C. After a certain

soaking time temperature was lowered to 850°C. At this temperature, the flux was decanted and the crystals were cooled to room temperature. The grown crystals were recovered using hot-distilled water. By performing the growth run with a slow cooling rate of 3°C/h, and a soaking period of 15 h, high quality crystals with enhanced size were obtained [4].

The BCT sample used in our experiment was a parallelopiped of $2 \times 5 \times 5\,mm^3$ with the smallest side parallel to c-axis. Neutron diffraction measurements indicate that Ca^{2+} occupies Ba^{2+} site [5, 6]. The crystal space group is P4 mm and room temperature lattice constants are $a = b = 3{\cdot}982$ Å, $c = 4{\cdot}025$ Å [6]. For determining the concentration of Ca, a small crystallite belonging to this lot was subjected to composition analysis using optical emission spectroscopic technique [7] which yielded a value of $x \approx 0{\cdot}05$. Raman spectra were excited using the 5145 Å line of Ar^+ laser in backscattering geometry. The scattered light was analyzed with a home-made double monochromator and detected using a cooled photomultiplier in the photon counting mode [8]. In the tetragonal ferroelectric phase, $A_1(TO)$ and $E(LO, TO)$ polar modes were picked up from the bc face by employing $a(cc)a$ and $a(cb)a$ scattering geometry respectively. The $A_1(LO)$ mode was recorded from the ab face in the $c(aa)c$ scattering geometry. The soft mode in the tetragonal phase has $E(TO)$ symmetry. For the sake of comparison limited measurements were also carried out on a $BaTiO_3$ (BT) crystal.

3. Result and analysis

Existence of an overdamped soft mode in $BaTiO_3$ is well documented in literature [9, 10]. The frequency and damping of the mode are obtained by fitting the Stokes side of Raman spectra to $I(\omega)\alpha(n(\omega)+1)\mathrm{Im}\,G(\omega)$. where $G(\omega) = [\omega_0^2 - \omega^2 + i\Gamma\omega]^{-1}$ is the

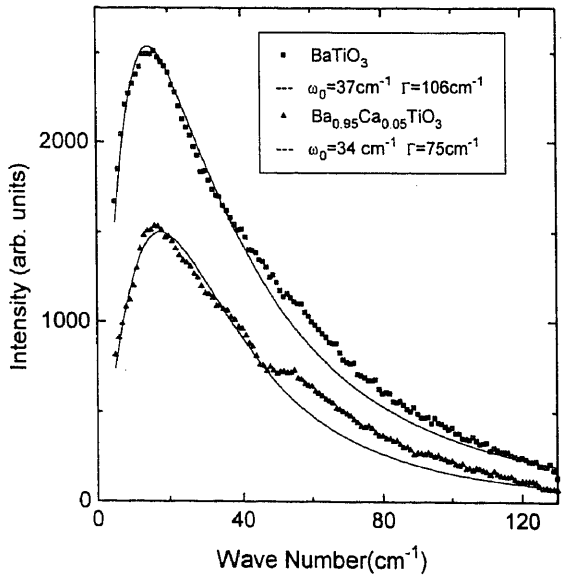

Figure 1. Raman line shapes of the $E(TO)$ mode reduced by Bose population

response of a damped harmonic oscillator with frequency ω_0 and damping parameter Γ. Figure 1 shows the measured Raman line shapes of the soft mode, reduced by the Bose population factor for BT and BCT in the tetragonal (22°C) phase. The continuous line is a fit to the data. For BCT, the analysis yields $\omega_0 = 34\,cm^{-1}$ and $\Gamma = 75\,cm^{-1}$ at 22°C in the tetragonal phase. This may be compared with the corresponding values for BT; $\omega_0 = 37\,cm^{-1}$, $\Gamma = 106\,cm^{-1}$. In BCT we find additional intensity around $65\,cm^{-1}$, the origin of which is not clear.

To monitor the tetragonal (ferroelectric) to cubic (paraelectric) transition in BCT, intensity variation with temperature for the following modes was studied: (i) overdamped E(TO) mode, (ii) A_1(LO) mode at $720\,cm^{-1}$, and (iii) A_1(TO) mode which manifests as a dip at $180\,cm^{-1}$.

The results are presented in figures 2 and 3. It is seen that Raman intensity disappears between 100°C–105°C. Recent neutron diffraction study of structural phase transition in BCT [6] indicates presence of significant Ti disorder at 120°C. On the basis of structural data refinement, a displacement of 0·2 Å is assigned to the Ti ion along the c-axis on either side of its mean position. Since $(c - a)$ which can be taken as a measure of the tetragonality of the unit cell is quite small ($= 0{\cdot}025$ Å) in comparison, the local site symmetry of the TiO_6 octahedron can be regarded as pseudo-cubic. From symmetry arguments it then follows that the modes involving Ti and O atoms will be Raman inactive. It is interesting to note however that even though Raman scattered intensity from the normal modes disappear around 105°C, polarized quasi-elastic light scattering intensity is present in BCT above this temperature. The intensity profile $I_{II}(\omega)$ has been measured from $5\,cm^{-1}$ to $100\,cm^{-1}$ where it merges with the background level. The profile could be fitted to a function of the form $1/(1 + \omega^2\tau^2)$. τ can be regarded as a characteristic time scale for fluctuations in the system. τ varies from 10^{-12} s in the

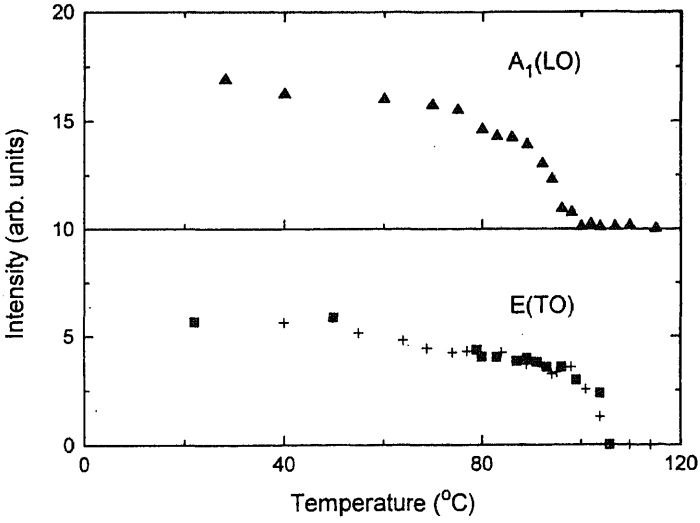

Figure 2. Integrated Raman intensity of A_1(LO) and E(TO) mode in the tetragonal phase of $Ba_{0.95}Ca_{0.05}TiO_3$. Crosses (+) and squares (■) belong to two different runs normalized at room temperature.

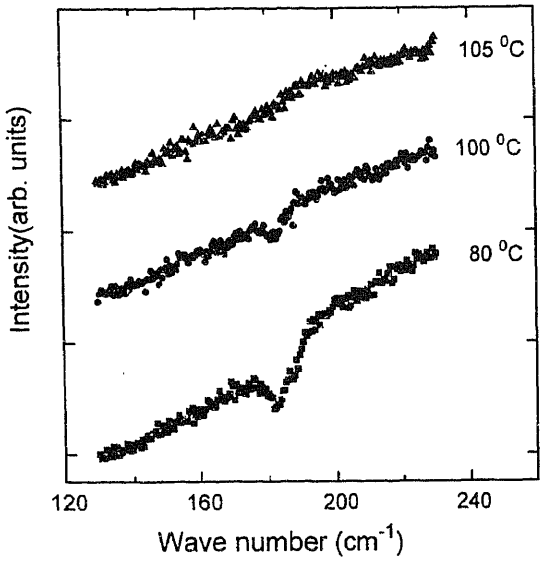

Figure 3. Raman line shape of the A_1(TO) mode at 180 cm^{-1} in $Ba_{0.95}Ca_{0.05}TiO_3$ at three different temperatures.

pre-transition regime to 10^{-11} s in the post-transition regime (transition temperature $\sim 150°C$). The integrated quasi-elastic intensity is plotted as a function of temperature in figure 4. This intensity which we attribute to disorder induced scattering is picked up *only* in the polarized scattering configuration. The above observation is consistent with a picture where dynamical disorder of Ti and O1 atoms is confined primarily along *c*-axis. Further, intensity drops considerably around 150°C. Structural investigations [6] also confirm that positional disorder of Ti and O1 atoms is very much reduced at this temperature as the crystal transforms from tetragonal to cubic phase.

It is of interest to make a comparison with $BaTiO_3$. Raman measurements similar to BCT were carried out. There is evidence for onset of dynamical disorder as the transition temperature ($T_c \sim 130°C$) is approached but *unlike* in BCT, fluctuations in $BaTiO_3$ do not lead to vanishing of Raman intensity below T_c.

The dielectric response (ε') of BCT can be understood on the basis of the results reported here. We note that the rising trend in ε'[3] commences at 100°C where dynamic disorder associated with Ti and O1 atoms also manifest in Raman spectra and ε' peaks around 150°C as the crystal transforms into the paraelectric phase.

The tetragonal → cubic transition in BCT has also been investigated using EPR technique [11]. The EPR signal originates from Fe^{3+} ions residing at Ti sites. The authors find that the signal corresponding to the tetragonal phase disappears at 110°C but the cubic spectrum appears only above 160°C The absence of any signal in the temperature range 110°C–160°C is attributed to dynamic fluctuations in the system with a characteristic time scale of 6×10^{-11} sec. It is interesting to note that the temperature at which the EPR signal for the tetragonal phase disappears is not very different from the temperature at which Raman intensity also vanishes. This is not

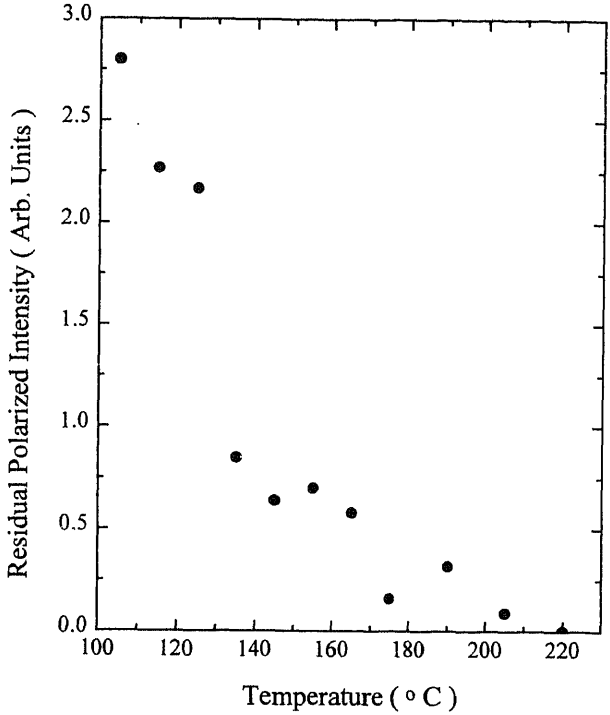

Figure 4. The integrated quasielastic polarized (I_{II}) intensity in the pre- and post-transition regimes for $Ba_{0.95}Ca_{0.05}TiO_3$ ($T_c \sim 150°C$). Since I_{II} is practically temperature independent above 220°C, it has been subtracted out to obtain the contribution arising from dynamic disorder associated with phase change.

surprising since in both EPR and Raman scattering one is essentially probing local symmetry of the TiO_6 octahedron.

Acknowledgement

The authors wish to thank Dr. Dhananjai Pandey, Dr A Sequeira and Dr M D Sastry for many illuminating discussions.

References

[1] L Benguigui and K Bethe, *J. Appl. Phys.* **47**, 2787 (1976)
[2] C N W Darlington and R J Cernik, *J. Phys. Condens. Matter* **4**, 4387 (1992)
[3] V S Tiwari, D Pandey and P Groves, *J. Phys.* **D22**, 837 (1989)
[4] S Balakumar, R Illangovan, C Subramanian and P Ramasamy, *J. Math. Sci. Lett.* **12**, 20 (1993)
[5] V S Tiwari, C Pandey, P S R Krishna, R Chakravarthy and B A Dasannacharya, *Physica* **B174**, 112 (1991)
[6] P U M Sastry, A Sequeira, H Rajagopal, B A Dasannacharya, S Balakumar, R Illangovan and P Ramasamy, *J. Phys. Condens. Matter* **8**, 2905 (1996)

[7] S V N Bhaskara Rao and P S Murty, Private communication (1995)
[8] A P Roy and M L Bansal, *Indian J. Pure Appl. Phys.* **26**, 218 (1988)
[9] G Burns and B A Scott, *Phys. Rev.* **B7**, 3088 (1973)
[10] A Scalabrin, A S Chaves, D S Shim and S P S Porto, *Phys. Status Solidi.* **B79**, 731 (1977)
[11] Y Babu, M D Sastry, B A Dasannacharya, S Balakumar, R Illangovan, P Ramasamy and M D Agarwal, to be published

Pressure-induced structural and electronic transition in $KTb(MoO_4)_2$ through Raman and optical studies

A JAYARAMAN, S K SHARMA, S Y WANG, S R SHIEH, L C MING and S-W CHEONG*
University of Hawaii at Manoa, Hawaii Institute of Geophysics and Planetology, Honolulu, HI 96822, USA
*Lucent Technology, Murray Hill, NJ 07974, USA

MS received 22 March 1996

Abstract. Raman and optical absorption studies under pressure have been conducted on $KTb(MoO_4)_2$ up to 35·5 GPa. A phase transformation occurs at 2·7 GPa when the crystal is pressurized at ambient temperature in a hydrostatic pressure medium. The sample changes to a deep yellow color at the transition and visibly contracts in the *a*-axis direction. The color shifts to red on further pressure increase. The Raman spectral features and the X-ray powder pattern change abruptly at the transition indicating a structural change. The pressure-induced transition appears to be a property of the layer-type alkali rare earth dimolybdates. However, the color change at the transition in $KTb(MoO_4)_2$ is rather unusual and is attributed to a valence change in Tb initiated by the structural transition and consequent intervalence charge transfer between Tb and Mo. *In situ* high pressure X-ray diffraction data suggest that phase II could be orthorhombic with a unit cell having 3 to 4% smaller volume than that of phase I.

Keywords. High pressure Raman spectroscopy; optical spectroscopy; potassium terbium molybdate; electronic transition; phase transition.

PACS Nos 62·50; 64·70; 70·30; 78·20

1. Introduction

The alkali-rare earth double molybdates $M^{1+}Ln^{3+}(MoO_4)_2^{4-}$ have been of considerable interest from a crystal chemistry point of view, and their structural properties have been extensively investigated, in particular by the Russian group [1–4]. The compounds crystallize either in the scheelite or in the distorted scheelite structures having orthorhombic, monoclinic, or triclinic symmetry. The tetrahedral coordination of Mo with respect to the oxygens (MoO_4) [4] is preserved, however. It has been found that the members of the heavier alkali metal and rare earths are stable in a layer-type orthorhombic structure in which the rare earth and (MoO_4) group are in the layer, with the alkali metal ion sandwiched between the layers [4] (see figure 1).

The vibrational properties of the orthorhombic layer-type $KLn(MoO_4)_2$, Ln = Y, Dy to Lu [5, 6], as well as some Cs [7, 8] and Rb [9] members have been reported in the literature. Further, some high pressure-high temperature quenching experiments [10] have reported the occurrence of new pressure-induced denser phases in many $MLn(MoO_4)_2$ systems, as revealed by X-ray powder diffraction studies on quenched products.

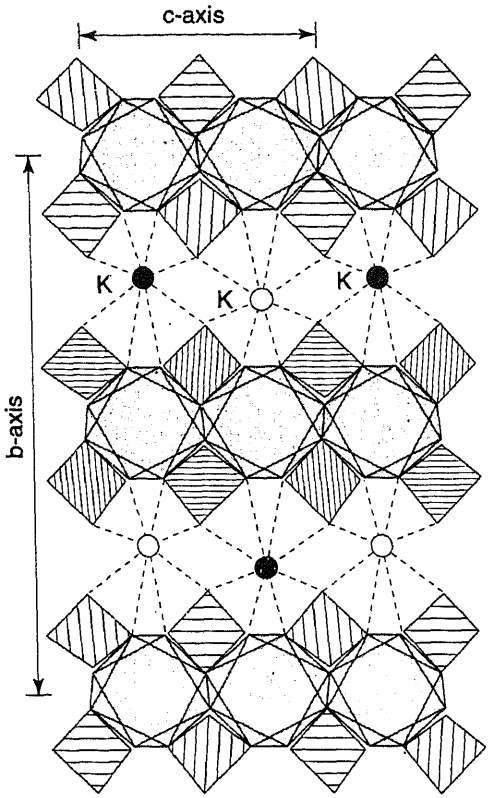

Figure 1. The layer structure of $KLn(MoO_4)_2$ following ref. [4]. The $LnMo_2O_8$ constitute the layers parallel to the *a-c* plane. The LnO_8 polyhedra are linked and form a chain. The K^+ ions act as links between the layers.

We have a continuing interest in the high pressure behaviour of molybdate systems of different complexity and have reported pressure-induced phase transformations including amorphization in $Tb_2(MoO_4)_3$ [11], $Gd_2(MoO_4)_3$ [12] and more recently in $NaLa(MoO_4)_2$ [13] using high pressure Raman, IR and X-ray diffraction studies. We were motivated to study the layer-type double molybdates, exemplified in the potassium based heavy Ln double molybdate $KTb(MoO_4)_2$ (KTMO), for possible pressure-induced phase transitions and their effect on the physical properties. Our choice of $KTb(MoO_4)_2$ was because of its ready availability. Further, the vibrational properties of the isostructural $KY(MoO_4)_2$ [14] and $KDy(MoO_4)_2$ [15] at ambient pressure have been thoroughly investigated by polarized Raman scattering and IR absorption measurements, thus providing a standard for comparison.

We have conducted high pressure Raman scattering measurements up to 35 GPa on KTMO in the diamond cell. Optical microscopic observations as well as some qualitative optical absorption studies were made under high pressure. Some preliminary high pressure X-ray diffraction studies in the diamond cell were also conducted. We have found a rather spectacular pressure-induced phase transition near 2·7 GPa at

ambient temperature, in which the crystal sample abruptly turns deep yellow in color, with a totally different Raman spectrum from that of the starting orthorhombic phase (Pbcn, D_{2h}^{14}). The X-ray diffraction pattern also changes at this pressure. At higher pressures the sample color turns progressively toward orange, then red and finally black near 35 GPa. The sudden change to yellow color at the transition near 2·7 GPa must be the result of an electronic structure change, possibly a change in the valence state of Tb^{3+} to the Tb^{4+} state, and consequent charge transfer between the Tb and Mo metal *d*-orbitals. The crystal structure change is apparent in the Raman spectrum, as well as in X-ray diffraction. These results will be presented and discussed in this paper.

2. Experiments and results

High-pressure Raman scattering measurements were performed using a gasketed Mao–Bell-type diamond anvil cell. For the pressure medium, either the standard 4:1 methanol-ethanol mixture or argon was used. Argon filling into the diamond cell was accomplished in a specially fabricated 2-kilobar high-pressure gas system. In some experiments the sample powder was packed into the hole drilled in the gasket and ressurized directly without any medium. The pressure was calibrated using the well-known ruby fluorescence technique [16] in all cases. The gaskets were from hardened 301 stainless steel, and typically the hole was 200 μm wide and 70–100 μm thick.

Raman measurements were carried out using a Spex Triple spectrometer equipped with a liquid N_2 cooled CCD detector. Spectra were excited using mainly the 514·5 nm line of the argon laser. The power levels were generally in the range of 30–60 mW.

Large flaky crystals of KTMO grown in AT&T Bell laboratories many years ago for possible application as laser hosts were available to us. The crystals were colorless and transparent and could be cleaved very easily in the layer plane (*a*-*c* plane). The lattice parameters were checked by X-ray powder diffraction and were found to be consistent with the published data [10] ($a = 5{\cdot}098 \pm 0{\cdot}004$ Å, $b = 18{\cdot}17 \pm 0{\cdot}03$ Å, $c = 8{\cdot}027 \pm 0{\cdot}003$ Å). The crystals were Eu doped with half atomic per cent Eu substituting for Tb, and the sample was highly fluorescent in the yellow green and red region. However, there was no interference from fluorescence with the Raman spectrum when the 514·5 nm line of the argon laser was used for Raman excitation. In figure 2, the Raman spectrum of a crystal plate of KTMO recorded with the 514·5 nm line is shown. The peaks appearing above 1000 cm^{-1} are the fluorescence peaks from Tb. The Raman spectra recorded at 1 and 3·2 GPa with the sample in the diamond cell are shown in figure 3. The spectrum of the sample abruptly changes near 2·7 GPa and is completely different from that at lower pressures (as shown in figure 3), signifying a pressure-induced phase change. Another interesting fact is that the fluorescence peaks vanish in the high-pressure phase. Upon further increase in pressure the Raman peaks shift to higher wavenumbers but the spectral features do not change up to 22 GPa, the highest pressure reached in the experiment with methanol/ethanol as a pressure medium. On pressure release the high pressure phase was stable down to 0·3–0·2 GPa, as judged by the Raman spectrum, and reverted completely on the release of the pressure to the ambient. When argon was used as the pressure-medium very similar behaviour of the sample was observed.

Optical observation of the sample under a microscope revealed that at the 2·7 GPa phase transition the color of the sample abruptly turns yellow in transmitted light. Also,

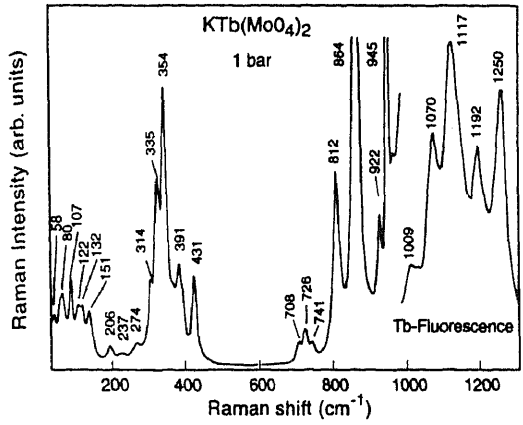

Figure 2. The Raman spectrum of $KTb(MoO_4)_2$ recorded at ambient pressure with 514·5 nm line of the argon laser. The Tb-fluorescence peaks are at the extreme right and they are very strong. Hence they are scaled down by a factor of two compared to the Raman peaks. The latter are listed in table 1.

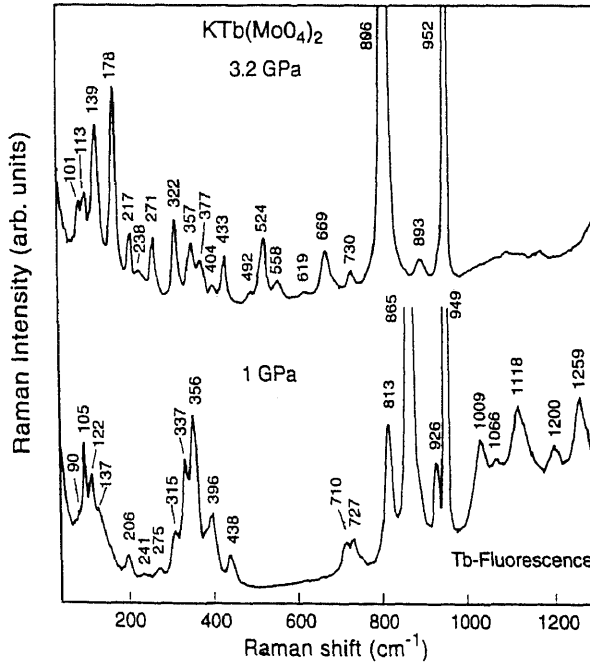

Figure 3. The Raman spectra of $KTb(MoO_4)_2$ single crystal samples recorded at 1 and 3·2 GPa. The lower spectrum is that of the normal orthorhombic Pbcn phase. The upper spectrum is quite different, due to a pressure-induced phase transition. The Tb fluorescence peaks are almost gone in the new phase.

the sample visibly shrinks along the a-axis of the orthorhomic crystal, and the single crystal nature is preserved. On pressure release the sample color continues to be yellow down to 0·3 GPa and then develops striation due to retransformation.

In a different experiment, the powdered sample (synthesized from high purity K_2MoO_4 and $Tb_2(MoO_4)_3$ by heating to 950°C) was presssurized directly without any pressure medium. The Raman spectrum of the powder was identical to that of the crystal. The spectral features changed near 3 GPa; the spectra recorded between 3 and 6 GPa showed Raman peaks of the low pressure as well as the high pressure phases. From the behavior of the stronger high frequency peaks it was clear that the high-pressure phase was growing at the expense of the low-pressure phase in the 3–6 GPa range. Above 6 GPa and up to 30 GPa the Raman spectral features remained more or less the same. The highest pressure reached in the powder run was 35·5 GPa, and only two high-frequency, broad Raman peaks could be seen. There was also a broad background. When pressure was released down to ambient pressure, the sample completely reverted to the original starting phase.

Optical observations on the powder sample revealed a color change near 3 GPa; the powder distinctly turned yellow. The color deepened with pressure, progressively turning orange, red and black. In a microphotograph taken at 35·5 GPa the sample appeared yellow on the outer edge, then orange, red and black in moving toward the center; apparently the result of a large pressure gradient over the sample area. The deepening of the yellow color after the transition and shift toward orange was very clear in single crystal sample runs with methanol/ethanol or argon as the pressure medium in which the maximum pressures reached were lower.

The pressure dependence of the observed Raman peaks is presented in figure 4. The dotted vertical line marks the phase transition pressure. The Raman data for the starting orthorhombic phase are given in table 1 with the assignments from ref. [14]. The Raman peaks observed in the high-pressure phase (phase II) are also listed both near the transition pressure as well as at ambient pressure, the latter obtained from pressure release data and extrapolation.

3. Discussion

The orthorhombic KTMO belongs to the space group D_{2h}^{14-} Pbcn with $Z = 4$ and is isostructural with $KY(MoO_4)_2$(KYMO) [4] and $KDy(MoO_4)_2$(KDMO) [15].Polarized Raman and IR absorption measurements on single crystals of the latter two compounds have been reported by Hanuza and Labuda [14]. They assigned the observed infrared and Raman peaks to vibrational modes obtained from a group theoretical analysis for the space group and polarization studies. Following their work [14] we have labeled the Raman peaks of the orthorhombic KTMO in table 1.

Based on the structural features and the number of bands observed in the IR and Raman spectra of KYMO and KDMO, Hanuza and Labuda [14] have proposed a dimer formation (Mo_2O_8) in the compounds, with two oxygens bridging adjacent MoO_4 tetrahedra. The large spread in the internal stretching mode frequencies of 280 cm^{-1} (from 950 cm^{-1} to 670 cm^{-1}) is unusual for the isolated MoO_4 group and is believed to be the result of additional interaction between the molybdate ions in the unit cell. However, the dimer formation has been questioned by Fomichev and

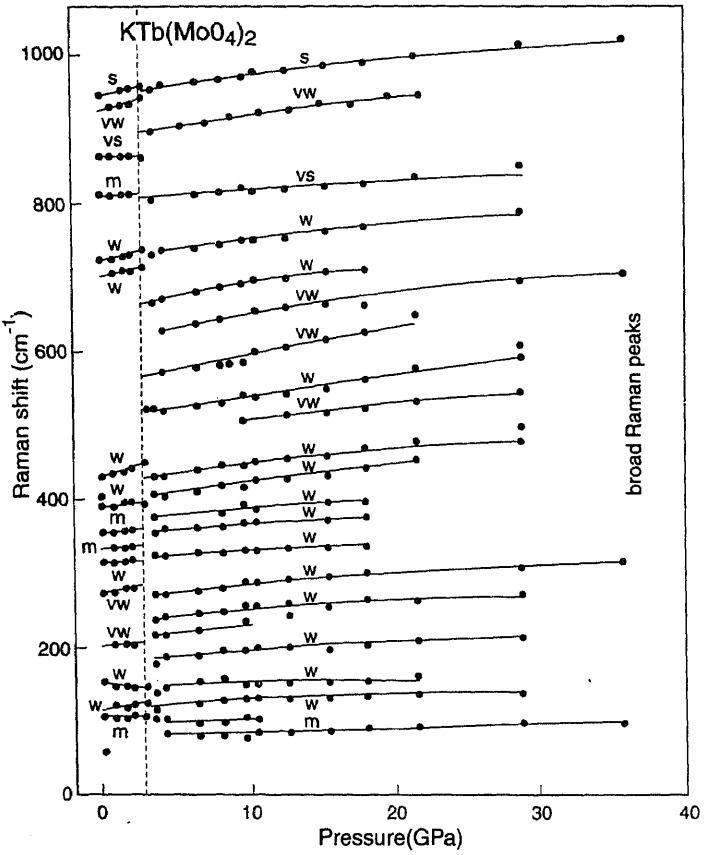

Figure 4. The pressure dependence of the observed Raman peaks in $KTb(MoO_4)_2$ up to 35 GPa. The phase transition at 2·7 GPa is marked by the dashed vertical line. The intensities of the peaks are indicated. At the highest pressure the observed Raman features are broad.

Kondratov [7] who investigated $CsPr(MoO_4)_2$ and compared it with $KDy(MoO_4)_2$. They have calculated the force constants for a number of alkali double molybdates and, in particular, the latter two and arrive at the following conclusions: (1) the interaction between MoO_4 species through "long" bonds affects the nature of the spectra, and (2) the Mo atoms are not purely in tetrahedral coordination with O, and remote O atoms interact to form complicated systems that are intermediate between a structure with discrete tetrahedral anions and condensed systems of complex oxide-polyhedra.

The 2·7 GPa phase transition

Our main objective is to discuss the high-pressure behaviour and, in particular, the pressure-induced phase transitions. The Raman data and optical observations unam-

Table 1. Observed Raman peaks in $KTb(MoO_4)_2$ of phase I and high pressur phase II and their pressure dependence

Mode	Phase I (cm^{-1})	$d\omega/dP$(cm^{-1} GPa) (PI)[a]	(PII)[b]	PhaseII (3·2 GPa)	PII(amb.) (cm^{-1})
ν_1	A_g 945 s[†]	2·5	3	952 s	942
	B_g 922 vw	4	5	893 vw	878
ν_3	A_g 864 vs	0	2	806 vs	799
ν_{br}	A_g 812 m	0	5	730 vw	715
	B_g 741 vw	2·5	5	669 w	652
	B_g 726 vw	1·2	n.d.[c]	619 vw	
	B_g 708 vw	n.d.	5	558 vw	544
$\nu_2 - \nu_4$	A_g 431 w	6·5	5	524 w	508
	A_g 404 vw	0	6	492 vw	474
	A_g 391 w	3·3	3	433 w	420
	A_g 354 m	2·5	3	404 vw	392
	A_g 335 w	1	3	377 w	367
	A_g 314 vw	1	5	357 w	340
	A_g 274 vw	4·5	3	322 w	312
T and R		2·5	3	271 w	260
K-K-T mode	A_g 206 vw	−1	5	238 vvw	223
Y-T mode	A_g 151 w	−2·5	5	217 w	202
	B_g 132 w	n.d.		n.d.	n.d.
	122 w	n.d.		n.d.	n.d.
MoO_4, T-mode	A_g 107 w	−1·3	2·5	178 m	170
R-mode	80	n.d.	3	139 m	132
	58 w	n.d.	2	113, 101 w	104, 96

[a]PI, Phase I; [b]PII, Phase II; [c]n.d., not determined.
[†]s, strong; m, medium; w, weak; vw very weak; vvw, very very weak.

of MoO_4 (ν_1) is only slightly affected (shifts downward by a few cm^{-1}), whereas th antisymmetric stretching mode (ν_3) decreases in frequency by about 60 cm^{-1} in th high pressure phase. Also, the number of modes in the bending region (ν_2 and ν_4) fill the entire range from 700 cm^{-1} to 270 cm^{-1}. Further, there are more Raman peaks i the translational and rotational region, suggestive of a transition to a lower symmetr phase. The small shift of (ν_1) frequency is an indication that the tetrahedral coordina tion for Mo is essentially preserved in the high-pressure phase. The 60 cm^{-1} downwar shift of the (ν_3) may be attributed to the small adjustments of the Mo–O bond lengths i the layer, in response to the observed abrupt shrinkage of the structure parallel to th *a*-axis.

In the layer-type materials, maximum compression will take place along a directio perpendicular to the layer, which in the present case is the *b*-axis of the orthorhombi D_{2h}^{14} phase (see figure 1). At some critical interlayer distance the MoO_4 tetrahedr apparently readjust within the layer to overcome the increase in the electrostati repulsion energy between the oxygens of adjacent layers. We find from pressure Rama studies on isostructural KYMO and KDMO that an analogous pressure-induce

phase transition occurs in the vicinity of 2–3 GPa [17]. Their lattice parameters are very nearly the same as that of KTMO. This similarity indicates that the structural instability is a common behavior for the layer-type alkali rare earth molybdates, and the instability is mainly determined by the interlayer distance and (MoO_4) interactions. For a more detailed understanding, the exact nature of the structural rearrangement in the high-pressure phase would have to be determined.

4. X-ray diffraction results

An earlier study has indicated that potassium RE double molybdates as well as several other alkali RE double molybdates transform under high-pressure and high-temperature treatment (in the range of 2·5–8 GPa and 700–1000°C) to denser phases. In these studies the product quenched to ambient conditions [10] was examined by high pressure X-ray diffraction and was reported to have the β-$KY(WO_4)_2$ structure (C2/*c*) with a volume 13% smaller for the formula unit compared with the original phase in a dozen compounds including KTMO, KYMO and KDMO. The high-pressure phase that we have found in room-temperature compression experiments is not quenchable, and our *in situ* X-ray diffraction data cannot be indexed on the basis of the lattice parameters reported for the quenched phase [10]. Further, the Mo-O coordination is given as 6 for the quenched phase, but there is no Raman evidence [18] for such a coordination increase in our high pressure phase. These considerations lead us to believe that our high pressure phase is different from the above mentioned quenched materials.

Our *in situ* high-pressure X-ray diffraction data on the high-pressure phase (phase II) can be indexed on the basis of an orthorhombic cell. At 2 GPa we find that the new orthorhombic cell has $a = 9{\cdot}58$ Å, $b = 8{\cdot}90$ Å and $c = 8{\cdot}03$ Å, with 4 formula units; the corresponding volume (v) per formula unit calculates to 103·2 cm^3/mol, compared with the 107·5 cm^3/mol at 2 GPa for the orthorhombic cell of phase I. Because the compressibilities of phase I and II are very different, the Δv evaluation would depend on the pressure. At the transition pressure of 2·7 GPa, the Δv would be about $\sim 3\%$, whereas it would be about 7% when evaluated at ambient pressure. This difference in Δv explains our optical observations on the sample during pressurization and pressure release. When the transition (phase I to II) occurs near 2·7 GPa on the increasing pressure cycle, the crystal visibly contracts in the *a*-direction but remains as a single crystal. On the other hand, the reverse transition which occurs almost near the ambient pressure on pressure release breaks up the crystal, because of the large expansion ($\sim 7\%$) associated with the II to I transition. First, parallel lines coincident with the *c*-axis appear in the sample as pressure decreases to 0·2 GPa, followed by breaking up of the crystal when the pressure is completely off.

A complete structure analysis of phase II based on single crystal diffraction data is needed to determine the exact nature of the atomic arrangement and what exactly happens to the MoO_4 and the cationic polyhedra.

The color of the high-pressure phase and its origin

The most spectacular aspect of the 2·7 GPa transition in KTMO is the abrupt change in the color of the sample to a deep yellow color in transmitted light [19]. This strongly

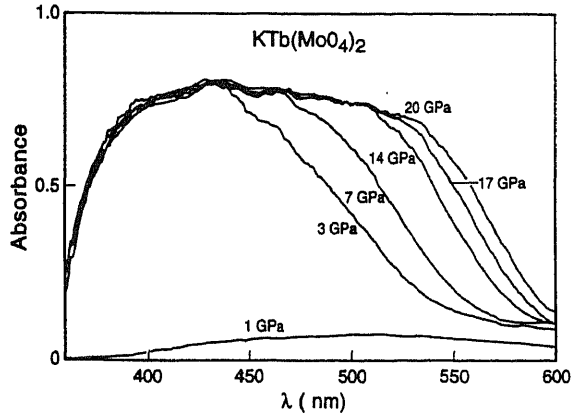

Figure 5. Shows optical absorption by the sample (single crystal) at different pressures. At the 2·7 GPa transition the sample abruptly turns yellow in color, as reflected in the curve for 3 GPa. At higher pressures the absorption shifts toward red (see text for explanation).

suggests a change in the electronic structure in the high-pressure phase. The color deepens and shifts to longer wavelengths with increasing pressure (see figure 5). It is of interest to note that no such color change is seen in the case of KYMO and KDMO, although the same structural phase transition occurs [17] (as deduced from the Raman and X-ray powder diffraction data). Therefore, we believe that the color change is something special to KTMO and attribute this to a charge transfer absorption ($4f-5d$) originating from a change in the valence state of Tb from 3^+ to the 4^+ state. That Tb can exist in these two valence states is well-known. As the material is still an insulator in the high pressure phase, a valence change in Tb must be compensated by a change in the valence state of Mo to the 5^+ state to preserve charge neutrality. This would, then, be a case of intervalence charge transfer between Tb and Mo from Tb^{3+}–$Mo^{6+} \rightarrow Tb^{4+}$–$Mo^{5+}$. An analogous charge transfer mechanism between TI and Re has been proposed for the 10 GPa phase transition observed in $TIReO_4$ [20], in which the colorless sample turned to a dark red color in the high-pressure phase. Our scenario for KTMO is that at the structural transition near 2·7 GPa the oxygens surrounding the Tb ion move closer to the terbium, causing an abrupt increase in the crystal field splitting of the $5d$ state of Tb. This increased splitting brings down the $5d$ energy and facilitates electron transfer from $4f$ into the $5d$. To preserve charge neutrality the promoted electron transfers into the Mo-$4d$ band through the ligand. In the case of Y and Dy compounds the question of valence change does not arise and hence no color change is expected in them, as is actually the case. It must be noted that the phase transition in KTMO is not driven by the electronic instability in Tb but rather the structure change is the one that causes the electronic change. Our experiments on KYMO and KDyMO are proof of this contention.

The Tb fluorescence peaks are almost gone when the 2·7 GPa phase transition takes place (see figure 2). This we believe is another significant evidence that the electronic structure of terbium has changed at the phase transition. An interesting question that

comes up here is, whether the valence state of Tb can be described in terms of an interconfiguration fluctuation leading to a mixed valence state. It is possible that magnetic susceptibility measurements on the high pressure phase could throw some light on the question.

5. Summary and conclusions

The alkali rare earth dimolybdate $KTb(MoO_4)_2$ undergoes a pressure-induced phase transition near 2·7 GPa when pressurized at room temperature in a hydrostatic pressure medium. The phase transition involves a structural rearrangement which is abrupt. The crystal sample contracts visibly in the *a*-axis direction and simultaneously acquires a strong yellow color. The color deepens with further increase in pressure and shifts toward red. The reverse transition occurs at pressures near 0·3 GPa on pressure release, thus exhibiting a large hysteresis. The structural transition is the property of layered alkali-rare earth dimolybdates, but we believe the color change in KTMO is caused by a change in the valence state of Tb from Tb^{3+} to Tb^{4+} and consequent charge transfer to the Mo–*d* state (Tb^{3+}–$Mo^{6+} \rightarrow Tb^{4+}$–$Mo^{5+}$). The electronic transition is triggered by the lowered *d*-state of terbium caused by an abrupt increase of the crystal field (ligand field) splitting because of a shorter Tb–O distance in the high-pressure phase.

Acknowledgement

This work was supported by a grant from the National Science Foundation, Division of Materials Research. This is a contribution from SOEST (No. 4107) and HIGP (No. 898).

References

[1] V K Trunov, V A Fremov and Yu A Velikodnyi, *The crysal chemistry and properties of double molybdates and tungstates*, in Russian (Nauka, Leningrad, 1986) pp. 137
[2] B M Sokolovski, A A Jevdokimov and V K Turnov, *Zh. Neorg. Khim.* **22**, 1499 (1977)
A Vielidodny and V K Turnov, *Zh. Neorg. Khim.* **22**, 1496 (1976)
N N Bushuyev and V K Turnov, *Kristallografiya* **21**, 69 (1976)
[3] R F Klevtzova, L P Kozyeva and P V Klevtzova, *Kristallografiya* **19**, 89 (1974)
R F Klevtzova, *Kristallografiya* **20**, 746 (1975)
P V Klevtzov, W A Winokurov and R F Klevtzova, *Kristallografiya* **18**, 1192 (1973)
P V Klevtzov and L P Kozyeva, *Kristallografiya* **21**, 316 (1976)
P V Klevtzov, L P Kozyeva and A A Pavluk, *Kristallografiya* **20**, 1216 (1975)
[4] R F Klevtzova and S V Borisov, *Dokl. Akad. Nauk. SSSR* **177**, 1334 (1967)
[5] J Hanuza and L Macalik, *Spectrochim. Acta*, **A38**, 61 (1982)
[6] J Hanuza and M Maczka, *Vibrational Spectrosc.* **1**, 85–96 (1994)
[7] V V Fomichev and O I Kondratov, *Russ. J. Inorg. Chem.* **37**, 587 (1992)
[8] V P Gnezdilov, V V Eremenko, N M Neoterenko and V I Fomin, *Optical Spectrosc.* (USSR) **68**, 324 (1990)

[11] A Jayaraman, S K Sharma, Z Wang, S Y Wang, L C Ming and M Manghnani, *J. Phys. Chem. Solids* **54**, 827 (1993)
[12] A Jayaraman, S K Sharma and S Y Wang, *Pramana – J. Phys.* **40**, 357 (1993)
[13] A Jayaraman, S Y Wang and S K Sharma, *Solid State Commun.* **93**, 885 (1995)
S R Shieh, L C Ming and A Jayaraman, *J. Phys. Chem. Solids* **57**, 247 (1996)
[14] J Hanuza and L Labuda, *J. Raman Spectrosc.* **11**, 231 (1981)
[15] J Hanuza and V V Fomitzev, *J. Mol. Struc.* **66**, 1 (1980)
[16] J D Barnett, S Block and G J Piermarini, *Rev. Sci. Instrum.* **44**, 1 (1973)
[17] A Jayaraman, S K Sharma, S Y Wang, S R Shieh, L C Ming and S-W Cheong, *J. Raman Spectrosc.* (in press)
[18] A Jayaraman, S Y Wang and S K Sharma, *Curr. Sci.* **69**, 44 (1995)
[19] A Jayaraman, S Y Wang, S K Sharma, and S-W Cheong, *Curr. Sci.* **70**, 232 (1996)
[20] A Jayaraman, G A Kourouklis and L G Van Uitert, *Phys. Rev.* **B36**, 8547 (1987)

Measurement of optical constants of thin polymer films using spectrally resolved white light interferometry

V NIRMAL KUMAR, Y CHANDRASEKHAR and D NARAYANA RAO
School of Physics, University of Hyderabad, Hyderabad 500046, India

MS received 22 April 1996; revised 15 July 1996

Abstract. Using the spectrally resolved white light interferometry we present our experimental results on the measurement of the optical constants of thin polymer films coated on a transparent substrate. As an extension to our previous work (*J. Opt. Soc. Am.* **B12**, 1559 (1995)) on thick glass plates, we have shown here that this technique can be effectively applied to very thin polymer films also. We have improved the accuracy of our results by using the Sellmeier dispersion formula for fitting the data. From the width and position of the zero-order fringe and the frequency of modulations in the white light spectrum, the refractive index $n(\lambda)$ and thickness t of the thin polymer films are calculated. To study the accuracies involved in the technique, PVA, PMMA and PS films of varied thicknesses are coated on glass plates and the measured values are compared with ellipsometer studies.

Keywords. Optical constants; polymer films; white light interferometry.

PACS Nos 07·60; 78·65

1. Introduction

Thin films are used as planar waveguides for processing optical signals by modulation, switching, frequency conversion, etc. To make the best use of these thin films for devices, it is essential to measure their refractive indices as a function of wavelength $n(\lambda)$ and their geometric thickness t. Depending on the coating mechanism, the thickness of the film could vary from place to place. Hence it becomes important to measure the refractive index and the thickness quite accurately and non-destructively at any specific location of the sample. A variety of techniques is available for their measurement. Most important among them are prism coupling [1], m-line method [2], integrated optical technique [3], ellipsometry [4] and interferometric techniques [5].

In the prism coupling and m-line techniques, (a) the film must be thick enough to support at least two modes to propagate film for determining n and t simultaneously, (b) it is not contact less and is suited for hard films, (c) laser lines over the whole visible range are not easily available. Ellipsometer studies are best suited for very thin films as the reflection coefficients are periodic for phase change larger than 2π. As a result, to determine the accurate values of the thickness, one would require the approximate values of the thickness for thicker films before making the ellipsometric measurements.

Among the optical measuring techniques, interferometry is highly accurate and simple in operation. The technique of spectral analysis of the interferogram is used in

the measurement of differential refractive index of liquid solution [5], construction of a thickness gauge system [6], real time measurement of material dispersion of optical glass [7], and in the measurement of polarization mode dispersion in a single mode optical fiber [8].

When the optical path difference between the two interfering beams $c\tau$ is more than the coherence length $c\tau_c$ of the light beam used, one does not see interference in the spatial domain. However, if the spectrum of the interfering beams is monitored, one observes an interference pattern in the spectral domain, the periodicity of the fringes characteristic of the delay between the two beams. By properly adjusting the path difference between the two arms of the Michelson interferometer, after the introduction of the dispersive material, the zero-order fringe can be made to appear within the region of observation. Using the fringe width and its frequency in the spectral domain, the measurement of refractive index and thickness of thick glass plates has been proposed by us recently [9]. In this communication we extend our investigations to the measurement of optical constants ($n(\lambda)$ and t) of thin polymer films coated on a thick

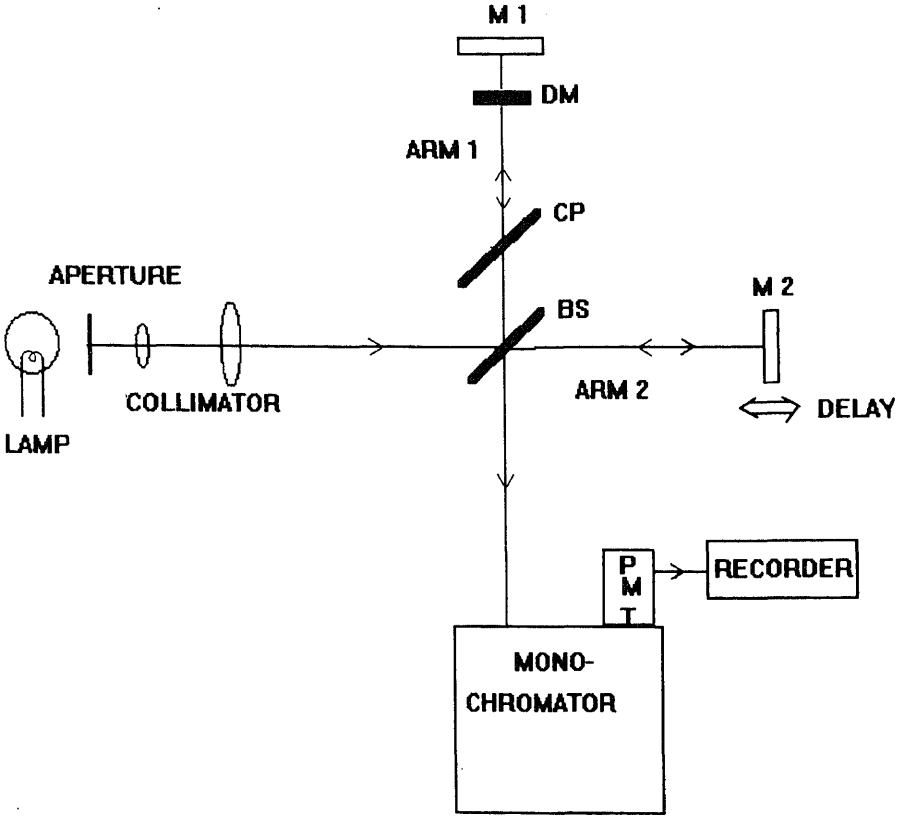

Figure 1. Schematic representation of the experimental set up: Michelson interferometer with the time delay between the interfering beams $\tau > \tau_c$ (τ_c is the correlation time of the source). BS, 50/50 beam splitter; CP, compensating plate; M1, M2, mirrors; DM, dispersive medium.

glass substrate using either spin coating technique or doctor-blade technique and show that this technique would be an alternative for the more expensive ellipsometer.

2. Experimental details

The experimental set up used for the measurements, shown in figure 1, consists of a Michelson interferometer (MI) configuration with a light source of 1 mm aperture illuminated by a 25 W tungsten filament lamp (white light source). The light beam is collimated using proper lens combination and is sent into the two arms of the MI by a 50–50 beam splitter (BS). The dispersion effects of the dielectric film coated beam splitter (with AR coating on the second surface) is compensated by introducing another one of the same material (CP) in the second arm. One mirror M_1 is fixed and another one M_2 is mounted on a translational stage with a movement accuracy of $\pm 5\,\mu$m. Light emerging from the interferometer is imaged onto the slit of a 50 cm grating spectrometer (Jobin-Yvon, HRS-2). The output from the spectrometer, collected with a PMT, is given to a strip-chart recorder (Packard-611). The recorded spectra are later digitized for analysis with a computer.

The glass plates, on which the polymer films are to be coated, are thoroughly cleaned with solvents and then dried with dry nitrogen. Care has been taken to prepare the polymer solution by filtering it. Commercially available polyvinyl alcohol (PVA) (0·3 gm) is dissolved in 10 ml of distilled water. The solution is warmed to make a clear homogeneous solution before filtering. The polymer solution is then coated on the glass substrate using the spin coating technique or doctor blade technique. The coated glass plates are kept in an oven at 40°C for 2 h to make sure that the solvents are completely removed. Similar procedure is followed to prepare the films of polystyrene (PS) dissolved in xylene and polymethyl meta acrylate (PMMA) dissolved in toluene.

3. Theory

Consider interference of two light beams described by the frequency dependent complex field amplitudes $\varepsilon_1(\omega)$ and $\varepsilon_2(\omega)$,

$$\varepsilon(\omega) = a(\omega)\varepsilon_1(\omega) + b(\omega)\varepsilon_2(\omega)\exp(-i\omega\Delta/c), \tag{1}$$

where Δ is the total path delay between the two interfering beams, $a(\omega)$ and $b(\omega)$ are the frequency dependent coefficients which depend on the properties of the beamsplitter.

In the case when both light beams $\varepsilon_1(\omega)$ and $\varepsilon_2(\omega)$ are derived from the same source, the observed spectrum at the output is given by the expression

$$S(\omega) = \tfrac{1}{2}S_0(\omega)[1 + \mathrm{Re}\{\mu_{12}(\omega)\}\cos(\omega\Delta/c + \theta)], \tag{2}$$

where $\mu_{12}(\omega)$ is the complex degree of spectral coherence of the two beams and θ is the constant phase factor. A detailed discussion of the theory has been given in our earlier communications [9, 10].

In terms of wavelength λ, the above expression can be written as

$$S(\lambda) = \frac{1}{2}S_0(\lambda)\left[1 + \mathrm{Re}\{\mu_{12}(\lambda)\}\cos\left(\frac{2\pi\Delta}{\lambda} + \theta\right)\right]. \tag{3}$$

When a glass substrate of refractive index $n(\lambda)$ and thickness t is introduced into one of the beams (say arm 1), the path difference becomes

$$\Delta = n(\lambda)2t - L_0, \tag{4}$$

where $n(\lambda)$ is the refractive index of the material over the entire visible region, given by the modified 5 constant Sellmeier dispersion relation

$$n(\lambda) = A\lambda^4 + B\lambda^2 + C + D/\lambda^2 + E/\lambda^4, \tag{5}$$

with A, B, C, D and E the dispersion constants of the glass substrate. As the refractive index is a function of λ, one can see from (3), a variation in the periodicity of the fringes with λ. The constant L_0 can be chosen such that the total phase difference becomes zero at some wavelength near the centre of the spectrum, where one sees a broad fringe with the periodicity of the fringes changing on either side. Experimentally this is achieved by translating the mirror in arm 2 and visually observing the fringes with a grating.

Equation (3) is modified as

$$S(\lambda) = \frac{1}{2}S_0(\lambda)\left[1 + \mathrm{Re}\{\mu_{12}(\lambda)\}\cos\left(\frac{2\pi(\Delta + \Delta')}{\lambda} + \theta\right)\right] \tag{6}$$

with, $\Delta' = n'(\lambda)2t'$ for the glass plate coated with a polymer film of refractive index n' and thickness t'.

4. Results and discussion

Figures 2(a) and 2(c) show the spectral interference fringes recorded with the transparent glass substrate alone, introduced into one of the arms. The intensity of the interference pattern represents the cosine of the phase at each wavelength of the radiation. After the introduction of the glass plate in arm 1, the broad fringe is brought to the centre of the spectrum by translating the mirror M_2. We refer to this broad fringe as zero-order fringe, which appears for $L_0 = n(\lambda_{st})2t + \theta\lambda_{st}/2\pi$, where λ_{st} is the stationary phase point and corresponds to the wavelength at the centre of the zero-order fringe. Since the variations of the phase i.e., $\mathrm{d}\phi/\mathrm{d}\lambda$ around this point is very slow, this zero-order fringe can be seen to be broad compared to other fringes. The stationary phase point can be located at any point in the spectrum by changing the path difference between the two arms using micrometer. From (3) and (4), one can see that the width of the fringes depends on the refractive index and thickness of the material. The modulated spectrum is fitted using (3) to get the refractive index $n(\lambda)$ and thickness t of the glass plate.

Without disturbing the inteferometer, the coated glass plate is reintroduced in the same arm. A special mount with an aperture is made for this purpose so that the same area of the glass plate is introduced into the interferometer. The spectrum recorded now (figures 2(b) and 2(d)), clearly shows the following interesting features: (1) the stationary phase point is red shifted, and (2) there are more number of fringes in the region of observation, as a result of the excess path seen in this arm. The modulated spectrum obtained with the polymer film coating is fitted with (5). The $n(\lambda)$ and t of the substrate are substituted from the previously calculated values. The values obtained for glass

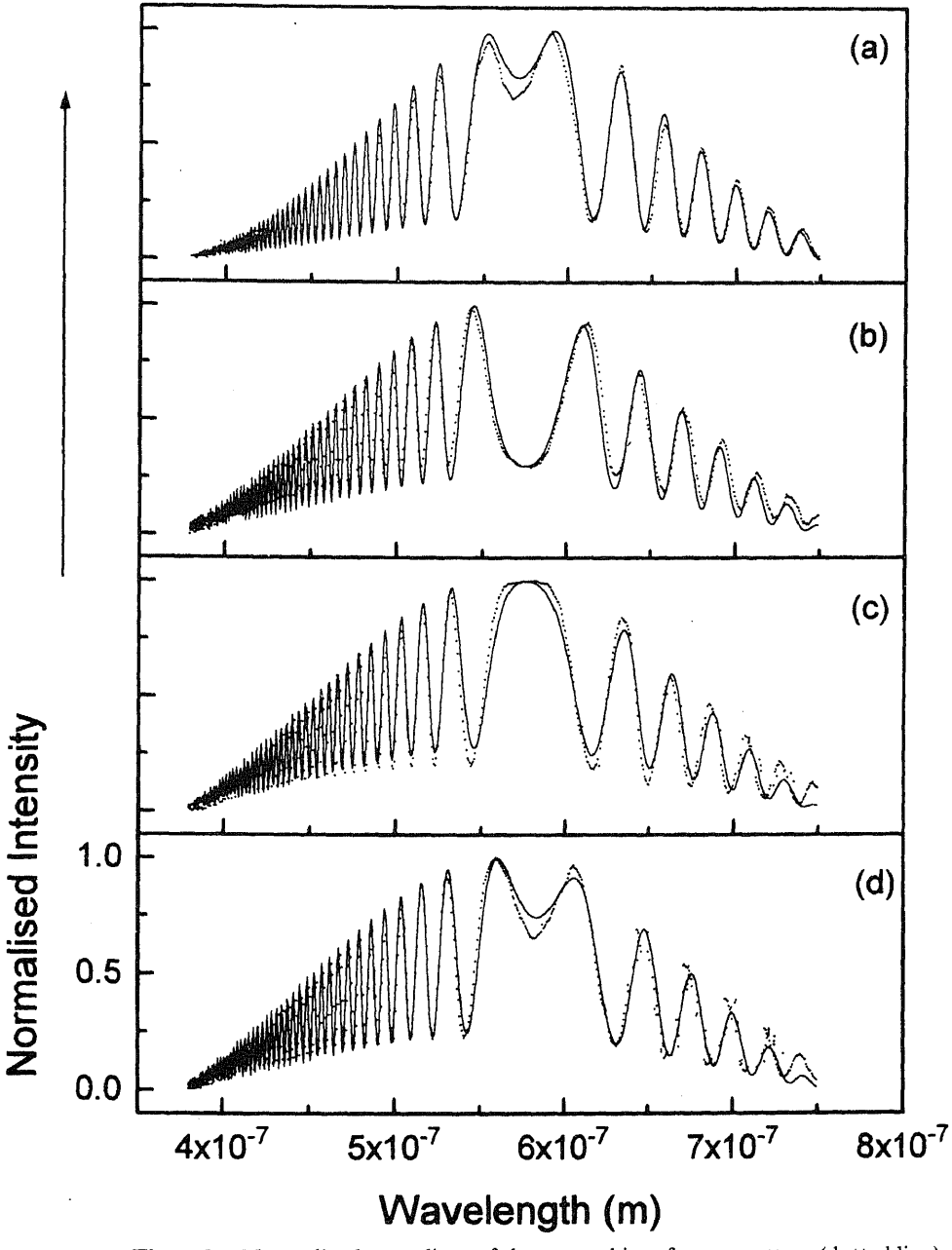

Figure 2. Normalized recordings of the spectral interference pattern (dotted line) and the theoretical fittings (continuous line) for (a) glass plate, (b) glass plate + PVA, (c) glass plate, (d) glass plate + PS.

plates and the polymer films are summarized in table 1. We estimate that the accuracies of the values so derived are in the range of 10^{-5}, that is ± 1 nm for t and $\pm 0{\cdot}00001$ for n. These accuracies are estimated through our theoretical fittings of the experimental data. A change in the fifth decimal place of either $n(\lambda)$ or t (in μm) is found to affect the fitting curves.

Table 1 also gives the values of λ_{st} for the glass substrates and the polymer films. Substituting the fitted values of the dispersion constants A, B, C, D and E of the glass plates and the corresponding constants of the polymer films in (5), the variation in the refractive index of these materials over the entire visible region is calculated and shown in figure 3.

In order to compare the accuracies of the results, we have measured n and t values with an ellipsometer. The back surface of the glass plate was properly grounded to eliminate the reflections from the second surface of the glass plate. The measured values are also given (*) in table 1. Transmission measurements are taken on a spectrometer prior to the ellipsometer studies to get the approximate thickness of the polymer films. Ellipsometer studies could not give any values for the PVA and PMMA films as their refractive indices are either very close to or lower than the glass substrate. This clearly demonstrates the usefulness of the spectral modulations technique for characterizing the thin film refractive indices and thickness over the other techniques. We have also measured the thickness and refractive indices of free standing films of PS of the order of 10–40 μm thickness. Except for the visibility (which was lower for free standing films, as they were not perfectly transparent) of the fringes, we obtained similar results. However, as there is no 1 mm glass plate, the measurement accuracies are expected to be much higher for free standing films.

5. Conclusions

We have developed a simple and relatively inexpensive method that uses a white light source, Michelson interferometer, and a spectrometer to measure simultaneously the thickness t and the refractive index $n(\lambda)$ of thin, transparent films over the entire visible region to an accuracy of about 10^{-5}. The results are compared with ellipsometer measurements and we have demonstrated that the spectral modulation technique gives more accurate values for n and t compared to the other techniques.

Table 1. Measured n and t values of the glass substrate and the polymer films.

Material	n (at 633 nm)	t ($\times 10^{-4}$ m)	λ_{st}($\times 10^{-7}$ m) GP	λ_{st}($\times 10^{-7}$ m) GP + PF
Glass plate	1·52075	9·99981		
PVA	1·50747	0·00333	5·67624	5·75079
PS	1·58294 (1·587)*	0·00323 (0·003237)*	5·78424	5·81699
PMMA	1·48889	0·01544	5·51117	5·72425

*Ellipsometer studies; GP: Glass plate; PF: Polymer film.

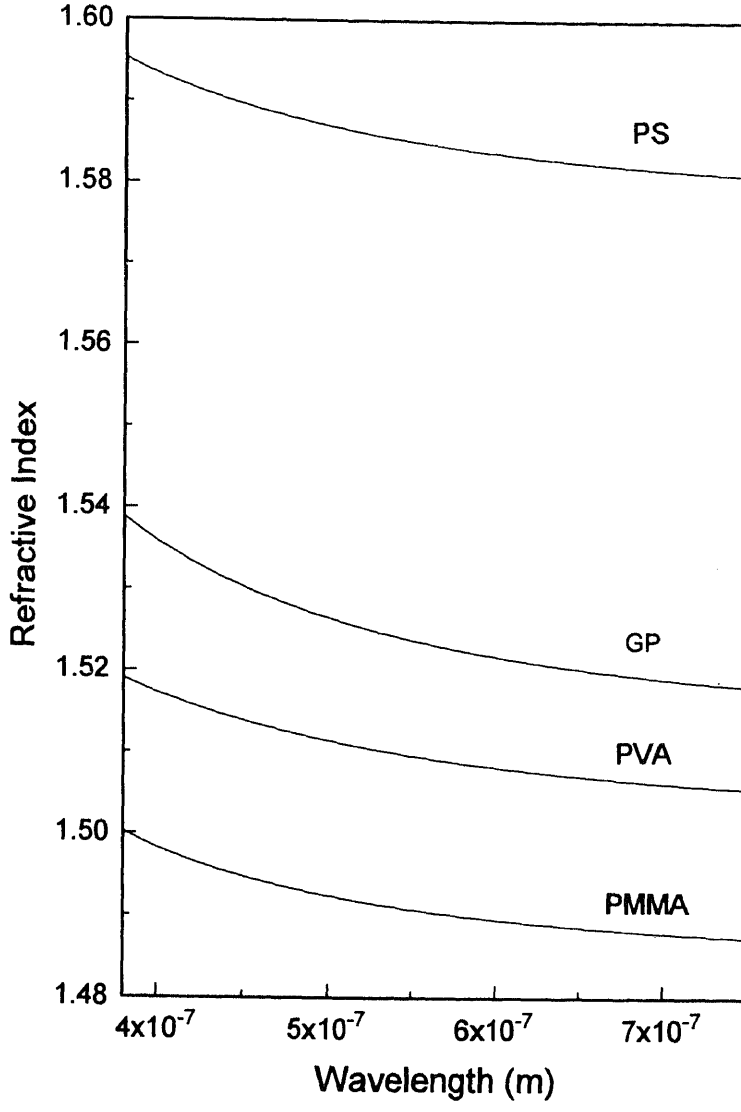

Figure 3. Plot of the refractive index variation with wavelength for the glass plate (GP) (average for all the plates) and the polymers PVA, PS and PMMA over the entire visible region.

Acknowledgements

One of the authors (VNK) acknowledges the financial support from UGC, India. The authors acknowledge the help of Prof. J Kumar, Department of Physics, Lowell University, USA for the ellipsometric studies. This work has been supported by the National Laser Programme, India.

References

[1] R Ulrich and R Torge, *Appl. Opt.* **12**, 2901 (1973)
A C Adams, D P Schinke and C D Capio, *J. Electrochem. Soc.* **126**, 1539 (1979)
[2] Tie-Nan Ding and Elsa Garmire, *Appl. Opt.* **22**, 3177 (1983)
[3] J D Swalen, M Tacke, R Santo and J Fischer, *Opt. Commun.* **18**, 387 (1976)
[4] R M A Azzam and N M Bashara, *Ellipsometry and polarized light* (North-Holland, Amsterdam, 1989)
[5] C Sainz, J E Calatroni and G Tribillon, *Measurements in Science and Technology* **1**, 356 (1990)
[6] J P Goedgebuer, A Lacourt and M Guignard, *Optics and laser technology* **10**, 193 (1978)
[7] C Sainz, P Jourdain, R Escalona and J Calatroni, *Opt. Commun.* **110**, 381 (1994)
[8] X D Cao and D D Meyerhofer, *Opt. Lett.* **19**, 1837 (1994)
[9] V Nirmal Kumar and D Narayana Rao, *J. Opt. Soc. Am.* **B12**, 1559 (1995)
[10] D Narayana Rao and V Nirmal Kumar, *J. Mod. Opt.* **41**, 1757 (1994)

physics pp. 171–182

Magnetic studies in mesoscopic length scale using polarized neutron spectrometer at Dhruva reactor, Trombay

Sk MOHAMMAD YUSUF and L MADHAV RAO*
Solid State Physics Division, *Inter University Consortium for DAE Facilities, Bhabha Atomic Research Centre, Trombay, Mumbai 400 085, India

MS received 4 May 1996

Abstract. The details of construction and principle of polarized neutron spectrometer at Dhruva reactor, Trombay, for neutron depolarization studies have been described. The feasibility in carrying out neutron depolarization studies in order to know the nature of magnetic ordering in various types of magnetic systems on mesoscopic length scale has been shown.

Keywords. Polarized neutron; neutron depolarization study; mesoscopic probe; domain effect; spin glass-like ordering.

PACS Nos 61·12; 75·60; 75·50

1. Introduction

When a polarized neutron beam traverses through an unsaturated ferro/ferrimagnetic material, a change in the state of polarization P arises from the Larmor precession of P around the local magnetic induction B of magnetic domains. This change of polarization of a polarized neutron beam after transmission through a magnetic material is known as neutron depolarization. The classical approach of depolarization was first initiated theoretically in 1941 by Halpern and Holstein [1], later extended by Rekveldt [2,3] and the Leningrad group [4]. The quantum mechanical approach [5] is based on small angle neutron scattering (within the analyzer aperture) by magnetic inhomogeneities. However, both approaches are generally equivalent [6]. The first neutron depolarization (one-dimensional) experiment was performed by Burgy *et al* in 1950 [7] in order to determine the mean domain size in iron. Recently, we have set up a neutron polarization analysis spectrometer (PAS) at Dhruva reactor, Trombay for magnetic scattering studies [8]. In our earlier report [8] the description of the spectrometer and its possible application in polarization analysis mode (in scattering geometry) have been discussed. In principle, this type of polarized neutron spectrometer can be used in different modes, such as, diffraction mode (2-axis configuration), polarization analysis mode (3-axis configuration in scattering geometry) and depolarization mode (3-axis configuration in transmission geometry). Here we report the principle of neutron depolarization, the recent upgradation of PAS suitable for neutron depolarization studies, and possible applications of such studies.

The neutron is an elementary particle with spin quantum number $s = 1/2$ and only one component along an arbitrary axis can be measured. When the average of the spin component of neutrons from a neutron beam is not equal to zero the neutron beam is said to be polarized. The polarization direction is defined as that direction in which the average spin component measured has an extreme. The polarization vector $\mathbf{P}$ of a neutron beam is the expectation value of $\hat{\sigma}$, the Pauli spin operator and can be written as

$$\mathbf{P} = \frac{I_+ - I_-}{I_+ + I_-}\mathbf{P}_0, \tag{1}$$

where $\mathbf{P}_0$ is a unit vector in the direction of the polarization and I_+ and I_- are the neutron beam intensities with + (parallel) and − (antiparallel) spin components along the direction $\mathbf{P}_0$, respectively. In an unsaturated ferromagnet or ferrimagnet, the magnetic domains exert a dipolar field on the neutron polarization and depolarize the neutrons owing to the Larmor precession of the neutron spins in the magnetic field of domains. The time dependence of $\mathbf{P}$ obeys the classical equation of motion and can be given as

$$\frac{d\mathbf{P}}{dt} = \gamma(\mathbf{P} \times \mathbf{B}), \tag{2}$$

where $\gamma = 2\mu_n/\hbar = 1{\cdot}83 \times 10^8$ radians $\sec^{-1}\mathrm{T}^{-1}$. This means that the polarization vector $\mathbf{P}$ precesses around the field direction with frequency $\omega_L = \gamma|\mathbf{B}|$, known as the Larmor precession frequency.

Mitsuda and Endoh derived the wavelength dependent transmitted polarization $P(\lambda)$ [9] in a one-dimensional case which can be written in the most general form as

$$\mathrm{P}(\lambda) = \left[\left\langle \frac{B_\parallel^2}{B^2} \right\rangle_B + \left\langle \frac{B_\perp^2}{B^2} \right\rangle_B \langle \cos(cB\delta\lambda) \rangle_\delta\right]^N, \tag{3}$$

where $B_\parallel$ and $B_\perp$ are the components of the local magnetic induction B parallel and perpendicular to the direction of incident neutron polarization $(-z)$, δ is the mean domain size and λ the neutron wavelength. The constant c is related to the neutron gyromagnetic ratio $g[c = gm/2\pi\hbar = 4{\cdot}63 \times 10^{-10}\,\mathrm{Oe}^{-1}\,\text{Å}^{-2}]$ and N is the average number of the domains along the path of neutrons ($N = d/\delta$, d is the sample thickness). The angular brackets $\langle\rangle_B$ and $\langle\rangle_\delta$ represent the ensemble average over the local induction B in each domain and over the domain size, respectively. In each ferromagnetic domain, the spin component parallel to the induction B does not precess whereas the component perpendicular to B does. The precession angle for a neutron of wavelength λ, travelling a distance δ in a field B is $\phi_\delta = (4{\cdot}63 \times 10^{-10}\,\mathrm{Oe}^{-1}\,\text{Å}^{-2})B\delta\lambda$. In antiferromagnets there is no net magnetization and hence no depolarization is expected in antiferromagnets. (In some special situations depolarization may occur in antiferromagnets due to (a) Bragg scattering within the analyzer aperture and (b) uncompensated ferromagnetic planes at the surface of the sample particle [10].) As the neutron depolarization technique probes the magnetic inhomogeneity on a mesoscopic length scale say, from 100 Å to a few thousand ångströms, magnetic inhomogeneity on

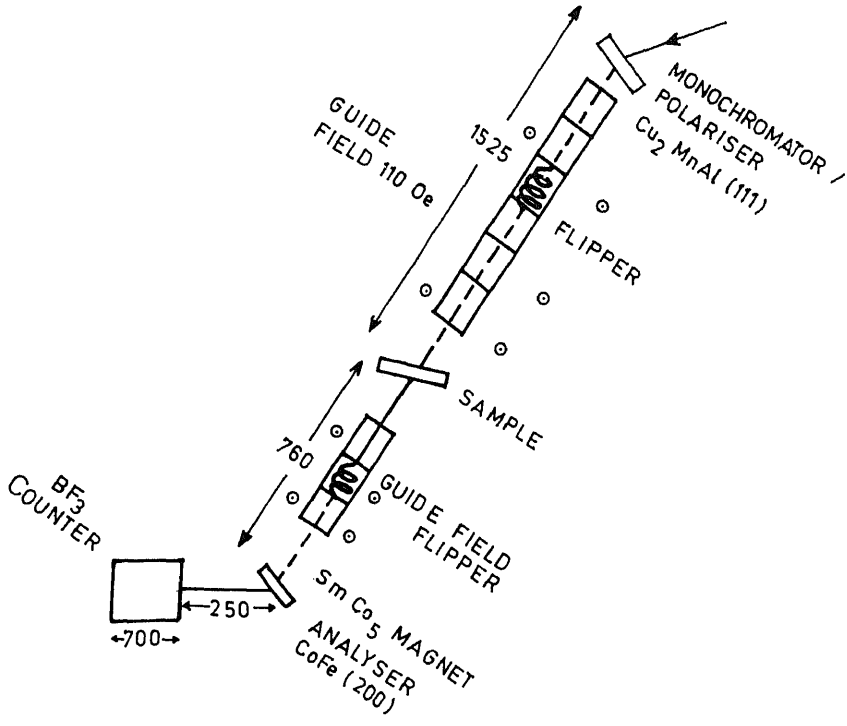

Figure 1. Schematic diagram of the polarized neutron spectrometer for neutron depolarization studies at the Dhruva reactor.

an atomic scale, as in paramagnetic state, has no effect on the neutron polarization, because the temporal spin fluctuation is too fast (10^{-12} s or faster) for the neutron polarization to follow the variation of the magnetic field B acting on the moving thermal neutron. Similarly no depolarization is expected in a true (canonical) spin glass state. In a true spin glass phase the spins are randomly frozen in space on a microscopic length scale and, as a result, the magnetic induction averages out to zero on a mesoscopic length scale. Hence no depolarization is found in true spin-glass systems.

In three-dimensional depolarization study [11, 12] one measures all the nine components of the depolarization matrix: With incident neutron polarization in the direction x, y or z, after transmission, the polarization is measured in all the three directions, namely, x, y and z directions. However, in one-dimensional depolarization study [9, 13] one measures only one component (say z–z component) of the depolarization matrix.

3. Experimental details

The polarized neutron spectrometer is like any unpolarized neutron spectrometer with additional devices such as a polarizing magnet on the 1st axis, an analyzing magnet on the 3rd axis, a magnet at the sample position (2nd axis), magnetic guide modules along the neutron path and two rf flippers. A schematic diagram of neutron polarization

analysis spectrometer (PAS) is shown in figure 1. For details, refer to our earlier report (ref. [8]).

In order to improve the incident neutron flux we have taken the following steps. (a) The $Co_{0.92}Fe_{0.08}(200)$ polarizer-cum-monochromator crystal has been replaced by $Cu_2MnAl(111)$ as the latter has about 3 times higher reflectivity than the former. (b) The incident neutron wavelength is changed from 0·999 Å to 1·201 Å as the peak of the Maxwellian profile of the neutron flux coming out of Dhruva reactor falls around 1·20 Å.

The monochromator-cum-polarizer Cu_2MnAl Heusler alloy is in a single crystal form, rectangular shaped, 50 × 50 × 4 mm (thick) in size. The polarizing plane is the (111) plane in transmission geometry. This crystal is mounted between the pole pieces of a $SmCo_5$ permanent magnet assembly, which provides a vertical uniform field of 2·8 kOe. This assembly is housed on the first axis inside a massive sector-type monochromator drum, 2 m in diameter [14]. The polarization efficiency of the monochromatic ($\lambda = 1{\cdot}201$ Å) neutron beam obtained from this Cu_2MnAl polarizer is $98{\cdot}83 \pm 0{\cdot}01\%$. A similar polarization sensitive analyzer single crystal: either $Cu_2MnAl(111)$ identical to the monochromator/polarizer or $Co_{0.92}Fe_{0.08}(200)$ crystal disc-shaped, 50 mm in diameter and 1·5 mm thick in transmission geometry can be inserted in the pole gap of a $SmCo_5$ magnet assembly mounted on the third axis. The $Co_{0.92}Fe_{0.08}(200)$ and $Cu_2MnAl(111)$ polarizing/analyzing crystals may be considered as devices which have almost 100% reflectivity for up $(+z)$ and down $(-z)$ spin neutrons respectively and almost zero reflectivity for down $(-z)$ and up $(+z)$ spin neutrons, respectively. The purpose of the analyzer crystal is to analyze the spin state of neutrons scattered or transmitted from the sample.

The (222) reflection of Cu_2MnAl has a higher nuclear structure factor than its (111) reflection. As a result, the second order wavelength contamination can, in principle, be problematic. For second order wavelength ($\lambda/2$) contamination measurement, the spectrometer was set at $2\theta_s = 0°$ and a $Cu_2MnAl(111)$ single crystal identical to the polarizer was mounted on the third axis of the spectrometer. After setting the detector at $2\theta_A = 20{\cdot}35°$, corresponding to first order reflection of $\lambda = 1{\cdot}201$ Å and second order reflection of $\lambda/2$, the rocking curve of $Cu_2MnAl(111)$ analyzer crystal was taken. The background corrected integrated intensity obtained from this measurement has contributions both from λ and $\lambda/2$. Then, the detector was set at $2\theta_A = 10{\cdot}18°$ and rocking curve of the analyzer was taken. In this case ($2\theta_A = 10{\cdot}18$) only $\lambda/2$ scattering occurs. From these two independent measurements the $\lambda/2$ contamination was obtained and found to be of the order of 1%, which can be neglected in the data analysis for all practical purposes.

In order to carry out low field neutron depolarization measurements an H-type electromagnet was designed, fabricated and installed at the sample position on the second axis. The schematic diagram of the H-type electromagnet is shown in figure 2. This H-type electromagnet is designed to provide either a horizontal or vertical field. This can carry an APD make closed cycle helium refrigerator for the low temperature measurements in the presence of a magnetic field. The yoke, pole piece and current coil configuration were optimized using a computer program. The magnet consists of four current carrying coils. Each of the two large and two small coils have 1746 and 390

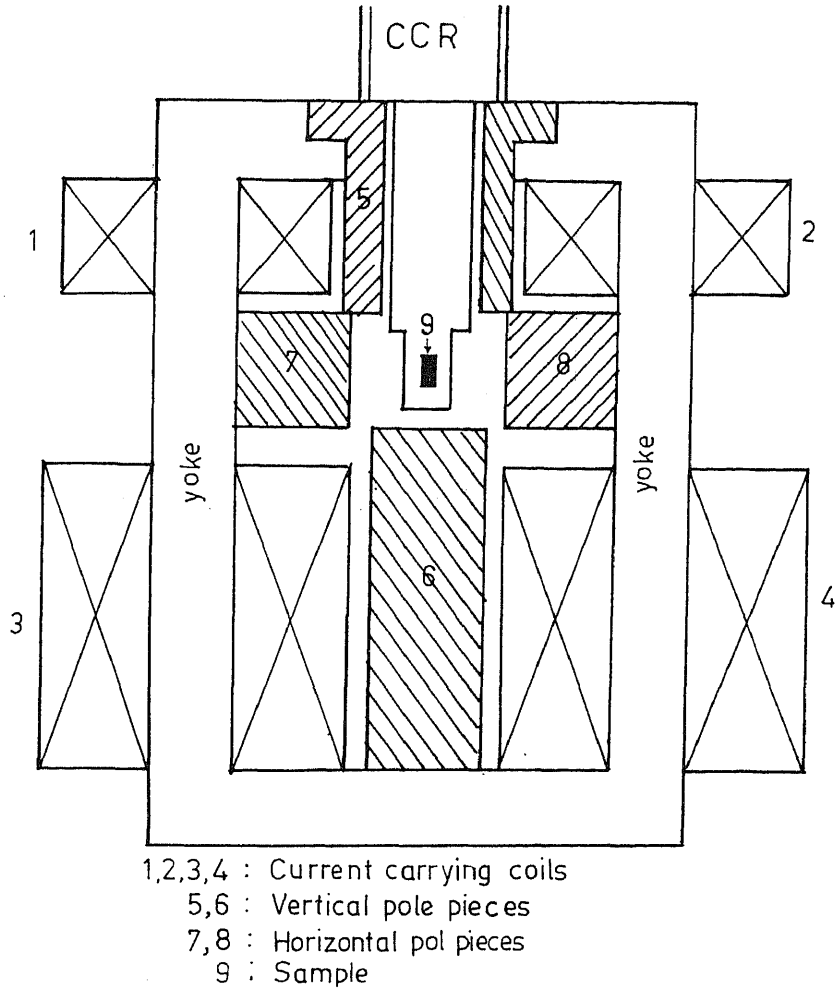

Figure 2. Schematic diagram of the H-type electromagnet along with the closed cycle helium refrigerator used for polarized neutron study. The shaded portions indicate the pole pieces.

respectively. The bobbins are made out of Al with a central gap of 41 × 41 square mm along the axis of the solenoid. The dimensions of the large coils are as follows: internal dimension = 43 × 43 mm, outer dimension = 170 mm diameter and height = 170 mm. The small coils have the following dimensions: internal dimension = 43 × 43 mm, outer dimension = 140 mm diameter and height = 60 mm. The magnet yoke, pole pieces and pole shoes were fabricated out of Tata grade mild steel. The demountable pole shoes are tapered for the purpose of concentrating the magnetic flux. The magnet is air cooled and is operated from electronically controlled constant current DC power supply. The working range of this power supply is 0–100 V DC and 0–10 A current. Several pairs of pole pieces with various pole shoes have been made to have different

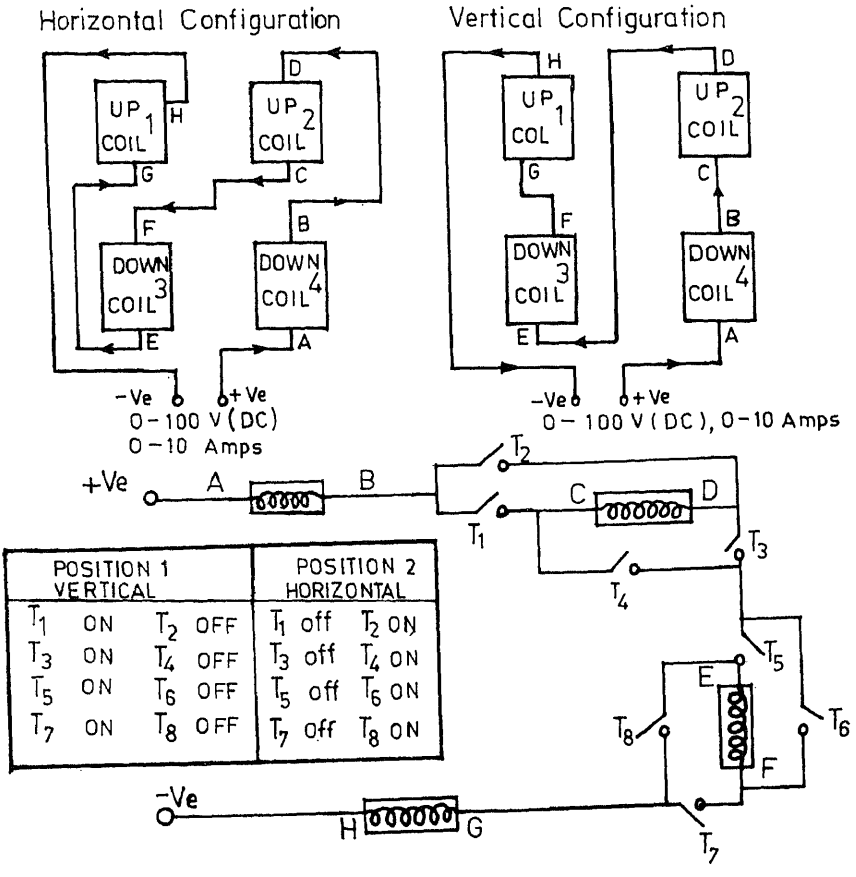

Figure 3. Block diagram of the electrical connections to the current carrying coils for both vertical and horizontal field configurations of the H-type electromagnet.

pole gaps of ~20–60 mm at the sample position with a field homogeneity of about 97·8% in both vertical and horizontal variable field configurations. One such pair is mounted at a time. A proper electrical connection (shown in figure 3) to all four current carrying coils for both vertical and horizontal field configurations have been provided through a rotary switch having 4 poles with 2 way configuration. The value of the measured field with a hollow vertical upper pole piece which can carry a closed cycle refrigerator was found to be 2·2 kOe with a 26 mm pole gap and 5 A current. The measured field values with solid pole pieces of 20 mm pole gap and 5 A current are 3·1 and 2·9 kOe in the vertical and horizontal field configurations, respectively.

In order to carry out low temperature measurements (10–300 K) an APD closed cycle helium refrigerator (CCR) can be easily mounted (using a brass stand) on the H-type electromagnet located on PAS. Figure 4 shows the H-type electromagnet with the CCR mounted on the 2nd axis of the spectrometer. This CCR is a two stage, water-cooled rotary compressor type helium gas cryogenic refrigerator. The sample is

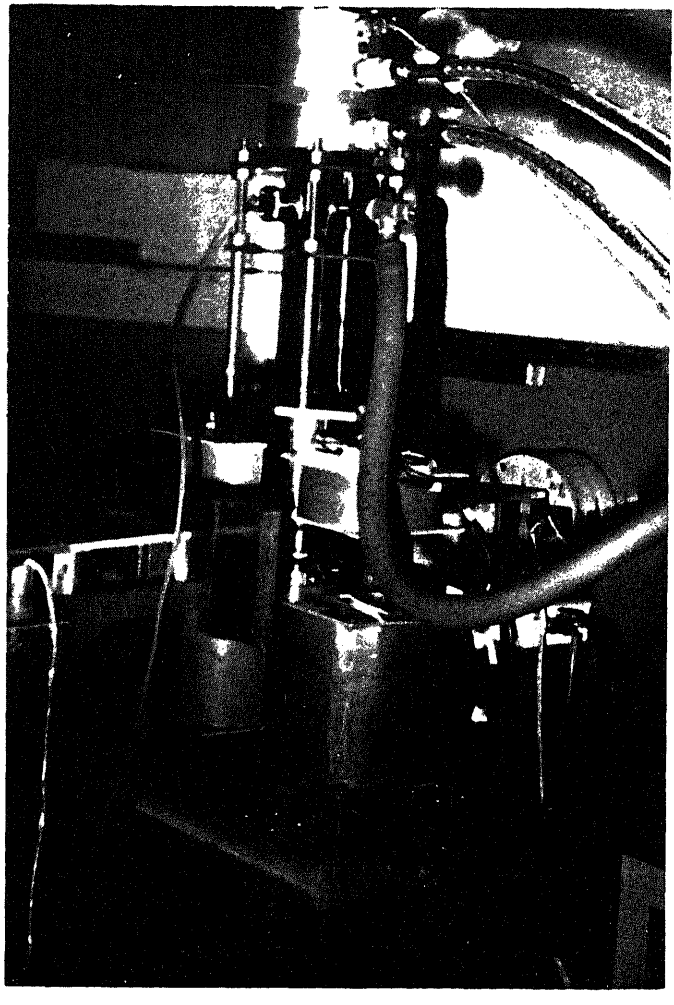

Figure 4. Photograph of the H-type electromagnet with the closed cycle helium refrigerator mounted on the 2nd axis of the polarized neutron spectrometer at the Dhruva reactor.

mounted from the bottom of the cold head. A Scientific Instruments Inc. make of 9650 microprocessor-based digital temperature controller is used for controlling sample temperature with an accuracy better than 0·1 K.

For depolarization measurements it is necessary to reverse the direction of polarization before or after transmission. The principle of resonance inversion is used (as described in ref. [8]) to achieve neutron spin reversal or flipping.

The one-dimensional depolarization measurements are performed with Cu_2MnAl (111) as polarizer and $Co_{0\cdot92}Fe_{0\cdot08}$(200) as analyzer i.e. with the incident neutron beam polarized along the $-z$ direction (vertically down) with a beam polarization of 98·83 $\pm$ 0·01% and the transmitted neutron beam (transmitted through the sample) polarization

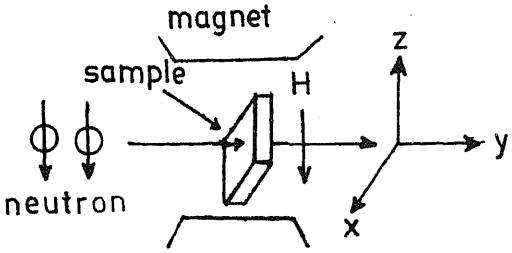

Figure 5. Schematic representation of a neutron depolarization measurem

is measured along the $+z$ direction [15]. The first rf flipper is used before the samp flipping the incident neutron spin.

In neutron depolarization study one measures the polarization ratio (R) [16] of transmitted intensities for $+z$ to that of $-z$ states of incident neutron spin) wh a measure of z–z transmitted polarization. The expression for polarization ratio (R be given in the following form

$$R = \frac{1 - P_i D P_A}{1 + (2f - 1) P_i D P_A},$$

where P_i is the incident beam polarization, P_A is the efficiency of the analyzer cr f is the efficiency of the rf flipper and D is the depolarization coefficient (due t sample under investigation). $P_i D (\equiv P)$ therefore corresponds to the transmitted polarization. In the absence of any depolarization in the sample the depolariz coefficient $D = 1$. When there is total depolarization $D = 0$ (which correspon $R = 1$). Hence the transmitted neutron polarization $P_i D$ decreases as depolariz increases. The measurements of the instrumental parameters P_i, P_A and f are disc in ref. [8].

Flat rectangular aluminium sample holders with different effective thicknesses c 10 mm are used for depolarization studies of powder samples as a function of sa thickness. The powder samples are used in the form of compressed pellets. If the sa is in thin plate form (as in the case of amorphous metallic ribbons), the sample is between two thin aluminium plates. The sample is placed in the neutron beam in a way that its plane surface (xz) remains perpendicular to the propagation dire (y) of the polarized neutron beam (see figure 5). The beam size is restricted a cadmium slit which is within the size of the sample. An external magnetic field c applied on the sample along the $-z$ or x direction using the electromagnet mount the spectrometer. The temperature of the sample can be varied from 300 to 12 K the closed-cycle helium refrigerator with a temperature accuracy of better than

Data acquisition programs for recording data in depolarization mode of oper have been written in Fortran and are stored and accessed by the control system

4. Experimental results

intermetallic compound [17], superparamagnetic Ce_2Fe_{17} alloy [18], disordered ferrites $Zn_{0.5}Co_{0.5}Fe_{2-x}Cr_xO_4$ ($x \sim 0.9$, 1.0) [15] and frustrated $KMnFeF_6$ system [19] in order to understand the magnetic nature of these systems in mesoscopic length scales and hence to resolve the discrepancies between the commonly available results on macroscopic and microscopic length scales. We have also carried out similar studies on $Co_{1.4-x}Zn_xGe_{0.4}Fe_{1.2}O_4$ disordered ferrites [20] and $Fe_{90-x}Ru_xZr_{10}$ amorphous system [21]. In this paper we present illustrative examples of just one composition from each of these two systems.

(a) *$Fe_{90-x}Ru_xZr_{10}$ amorphous system*

A number of amorphous and crystalline materials show sequential paramagnetic–ferromagnetic-spin glass like transition i.e. so called reentrant spin glass transition (RSG), as the sample temperature is lowered. The RSG systems have drawn considerable attention as these investigations have raised a lot of controversy about their exact nature of ordering. For example, recent low field ac susceptibility, dc magnetization (in both low and high field region) and Mössbauer studies of $Fe_{90-x}Ru_xZr_{10}$ amorphous alloys [22, 23] show that Ru substitution destroys ferromagnetism very rapidly and the system goes directly from para to a spin glass-like state for more than 3 at. % of Ru. In order to study the nature of magnetic ordering in the spin glass like phase in $Fe_{85}Ru_5Zr_{10}$ we have carried out zero-field cooled (ZFC) and field-cooled (FC) neutron depolarization studies as a function of temperature and magnetic field.

The sample does not show any depolarization over the entire temperature range either in ZFC or in the FC case, when a field of 7 Oe is applied on the sample. But the same sample when cooled in 1200 Oe, shows field induced time dependent depolarization which led us to do a relaxation study. The relaxation measurement were carried out in the heating cycle (in field cooled case) with a cooling field of 1200 Oe and a measuring field of 7 Oe at 12 K and 80 K by looking at the depolarization caused by the sample. In these measurements, the transmitted neutron counts were measured in crossed polarizer-analyzer mode (i.e. Cu_2MnAl (111) as polarizer and $Co_{0.92}Fe_{0.08}$ (200) as analyzer and with rf flipper off) as a function of time. In this configuration, a higher count rate corresponds to higher depolarization and lower count rate corresponds to lower depolarization. The counting was started after reducing the field value from 1200 Oe to 7 Oe. At each time step the data were collected for about 5 min (normalized to a fixed monitor count).

At 12 K a strong depolarization was observed, which decreases as a function of time (figure 6). The observed decay of depolarization was found to be reasonably well described by a stretched exponential function of the form $N(t) = N_0 \exp[-(t/\tau)^{1-n}]$ with $\tau = 18.4$ h and $n = 0.88$. Present study confirms that at higher Ru concentration, ($x \sim 5$) the ferromagnetic correlation totally disintegrates. At this higher Ru concentration the system shows a true spin glass behaviour when the external field applied on the sample is low, but at relatively higher cooling field the formation of field induced spin-glass cluster is observed. From this field induced observed depolarization, it is apparent that the cluster growth mechanism is involved at a higher cooling field. When the sample ($x = 5$) is cooled in the presence of a higher external field it helps the clusters to grow in the framework of a cluster spin glass phase and cause depolarization. After removal of the field from 1200 Oe to 7 Oe, the clusters start decaying with time, causing

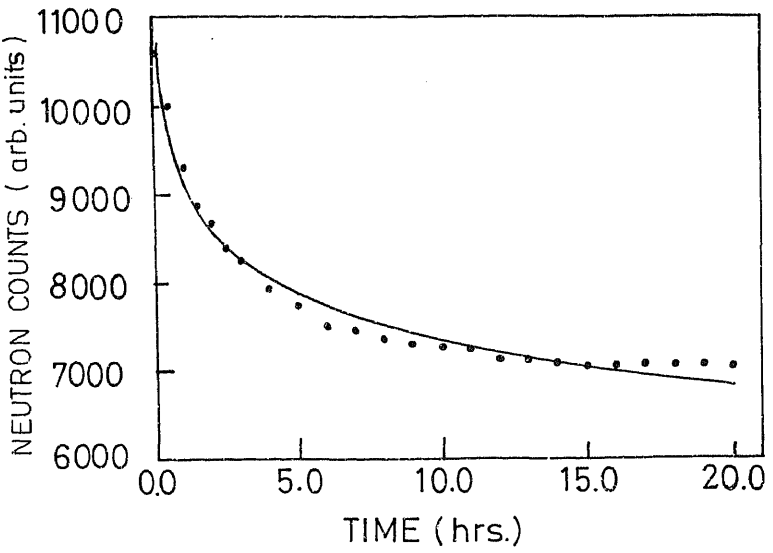

Figure 6. Time variation of depolarization for the amorphous $Fe_{85}Ru_5Zr_{10}$ sample at 12 K, solid line: stretched exponential fitted curve (see text).

the relaxation behaviour as shown in figure 6. The depolarization relaxation essentially scales to the relaxation of magnetization. Hence, figure 6 corresponds to the relaxation of magnetization of field induced spin glass clusters. This kind of slow, stretched exponential relaxation of magnetization are known to be exhibited by spin glass systems [24]. We would like to remark here, that as far as we know, the study of magnetization relaxation through neutron depolarization measurements has not been reported so far in literature.

(b) *Disordered ferrites*

In disordered spinel ferrites very often [25–27] one finds a broad hump in the ac susceptibility curve and a deviation between zero field cooled (ZFC) and field cooled (FC) magnetization (in low field values) around the same temperature where a broad peak occurs in the ac susceptibility curve. These features are normally interpreted as signatures of a spin glass like freezing. Our recent neutron depolarization study on $Zn_{0.5}Co_{0.5}Fe_{2-x}Cr_xO_4$ (with $x = 0.9$ and 1.0) clearly indicated that these macroscopic features (in low field ac susceptibility and magnetization measurements) which mimic a spin glass are not due to any spin glass like freezing but, a signature of kinetic freezing of magnetic domains. Here we will discuss similar results obtained on another disordered ferrite $Co_{1.4-x}Zn_xGe_{0.4}Fe_{1.2}O_4$ with $x = 0.6$. The real part of ac susceptibility curves of $x = 0.4$, 0.5 and 0.6 samples of this series shows a broad maximum around 260, 200 and 120 K, respectively [28]. The low field ZFC and FC data show deviation around the same temperature. These features (for $x = 0.6$) were taken as

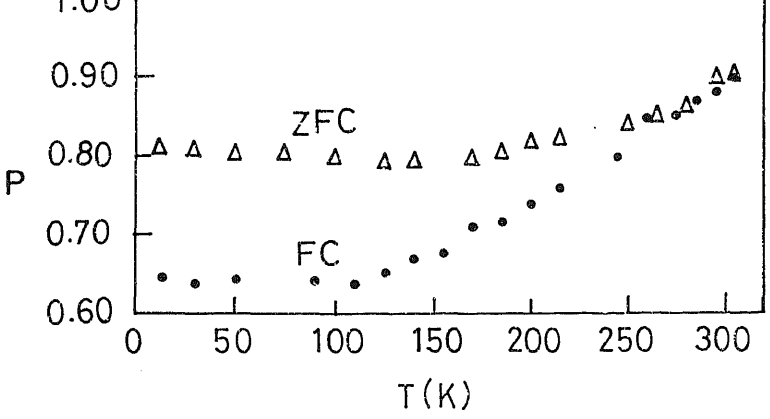

Figure 7. ZFC and FC polarization P versus temperature in a 30 Oe field fo $Co_{0.8}Zn_{0.6}Ge_{0.4}Fe_{1.2}O_4$ ferrite.

structure is confirmed by the presence of significant depolarization up to 12 K, the lowes measured temperature. A continuous drop in both the ZFC and FC transmitted polariza tion right from room temperature (the highest measured temperature) up to about 160 K and 110 K for ZFC and FC cases, respectively, clearly indicates that the ferrimagnetic orde parameter increases with decrease in temperature. The difference between the ZFC and th FC depolarization increases with decrease in temperature until about 110 K and it remain constant below 110 K. There is no indication of breakdown of ferrimagnetic domai structure at any temperature. The observed branching between ZFC and FC depolariza tion clearly tells us that the domain mobility strongly depends upon the cooling process o the sample. The observed higher depolarization in the FC case than in the ZFC cas indicates that, when the sample is cooled in the presence of an external field, it helps th domains to grow. At this low field (the measured field value is 30 Oe) favourably oriente domains grow in size [29]. So a higher depolarization is expected from larger domains. I should be pointed out that our sample contains Co^{2+} ions, and this introduces uniaxia random anisotropy [30]. In the presence of such anisotropy field, the cooling in fiel cooled condition can induce a large unidirectional anisotropy so that very larg domains can be maintained. From the above discussion, it can be inferred that th features in susceptibility and low-field magnetization (which mimic a spin glass lik freezing) do not result from transition to any spin glass-like phase or a breakdown o ferrimagnetic correlation, but can be related to magnetic domain effects.

5. Conclusion

In order to know the nature of magnetic ordering on a mesoscopic length scale 1-dimensional neutron depolarization study can be carried out using polarized neutron spectrometer at Dhruva reactor, Trombay. Using this spectrometer, zero-field cooled depolarization, field cooled depolarization and relaxation study through neutron depolar ization can be carried out over a temperature range of 12 to 300 K and field range of abou

$-3{\cdot}0$ to $+3{\cdot}0$ kOe. From our studies it is evident that interpretation of macroscopic observations alone can be quite misleading. Macroscopic properties of many systems, especially, in systems where frustrations are present, might have some common features but the mesoscopic nature of the system and the underlying physics can be quite different.

Acknowledgements

It is a pleasure to thank Dr K R Rao for his encouragement and support in these studies. Authors also thank Mr R S Kothare for his valuable technical help, Dr P L Paulouse for the $Fe_{90-x}Ru_xZr_{10}$ samples and Prof. R G Kulkarni for the $Co_{1\cdot4-x}Zn_xGe_{0\cdot4}Fe_{1\cdot2}O_4$ samples.

References

[1] O Halpern and T Holstein, *Phys. Rev.* **59**, 960 (1941)
[2] M Th Rekveldt, *J. Phys. (Paris)* **32**, C1–C579 (1971)
[3] M Th Rekveldt, *J. Magn. & Magn. Mater.* **1**, 342 (1976)
[4] A I Okorokov, V V Runov, V I Volkov and A G Gukasov, *Sov. Phys. JETP* **42**, 300 (1976)
[5] B P Toperverg and J Weniger, *Z. Phys.* **B74**, 105 (1989)
[6] R Rosman and M Th Rekveldt, *Z. Phys.* **B79**, 61 (1990)
[7] M Burgy, D J Hughes, J R Wallace, R B Heller and W E Woolf, *Phys. Rev.* **80**, 953 (1950)
[8] L Madhav Rao, Sk M Yusuf and R S Kothare, *Indian J. Pure Appl. Phys.* **30**, 276 (1992)
[9] S Mitsuda and Y Endoh, *J. Phys. Soc. Jpn.* **54**, 1570 (1985)
[10] R Rosman, Magnetic particles studied with neutron depolarization and small-angle neutron scattering, Ph.D. Thesis, Delft University of Technology, 1991
[11] M Th Rekveldt, *Z. Phys.* **259**, 391 (1973)
[12] M Th Rekveldt, *Z. Phys.* **259**, 391 (1973); *J. Magn. & Magn. Mater.* **1**, 342 (1976)
[13] I Mirebeau, S Itoh, S Mitsuda, T Watanabe, Y Endoh, M Hennion and P Calmetters, *Phys. Rev.* **B44**, 5120 (1991) and references therein
[14] P R Vijayaraghavan, *Indian J. Pure Appl. Phys.* **27**, 554 (1989)
[15] Sk M Yusuf and L Madhav Rao, *J. Phys. Condens. Matter* **7**, 5891 (1995)
[16] I Mirebeau, S Itoh, S Mitsuda, T Watanabe, Y Endoh, M Hennion and R Papoular, *Phys. Rev.* **B41**, 11 405 (1990)
[17] Sk M Yusuf, L Madhav Rao and P Raj, *Phys. Rev.* **B53**, 28 (1996)
[18] Sk M Yusuf, L Madhav Rao and K B Bhat, *Pramana–J. Phys.* **38**, 669 (1992)
[19] Sk M Yusuf, L Madhav Rao, R Mukhopadhya, S Giri, A Goshray and K Goshray, *Solid State Commun.* (1996) in press
[20] Sk M Yusuf, U Joshi, L Madhav Rao and R G Kulkarni, (to be published)
[21] Sk M Yusuf, L Madhav Rao, P L Paulouse and V Nagarajan *J. Magn. & Magn. Mater.* (1996) in press
[22] V Nagarajan, P L Paulose and R Vijayaraghavan, *J. Phys. (Paris)* **49**, C8–C1135 (1988)
[23] P L Paulose, V Nagarajan, R Krishnan, J Voiron, H Lassri, R Nagarajan and R Vijayaraghavan, *J. Magn. & Magn. Mater.* **144**, 301 (1995)
[24] P Granberg, P Svedlindh, P Nordblad, L Lundgren and H S Chen, *Phys. Rev.* **B35**, 2075 (1987)
[25] Sk M Yusuf, V C Sahni and L Madhav Rao, *J. Phys. Condens. Matter* **7**, 873 (1995)
[26] J L Dormann and M Nogues, *J. Phys. Condens. Matter* **2**, 1223 (1990)
[27] K Muraleedharan, J K Srivastava, V R Marathe and R Vijayaraghavan, *J. Magn. & Magn. Mater.* **54–57**, 66 (1986)
[28] J Nogues, T Puig, R B Jotania, R V Upadhyay, R G Kulkarni and K V Rao, *J. Magn. & Magn. Mater.* **99**, 275 (1991)
[29] M Bozorth, *Ferromagnetism* (Van Nostrand, New York, 1951)
[30] J B Goodenough, in *Magnetism and the chemical bonds* (Wiley, New York, 1963)

The Painlevé property, integrability and chaotic behaviour of a two-coupled Duffing oscillators

S RAJASEKAR and S PAUL RAJ*
Department of Physics, Manonmaniam Sundaranar University, Tirunelveli 627 002, India
*Department of Physics, St. Xavier's College, Tirunelveli 627 002, India

MS received 4 March 1996; revised 25 July 1996

Abstract. Integrability and chaotic behaviour in a two-coupled Duffing oscillators are studied. The coupling is nonlinear. Painlevé test is performed to identify integrable cases of damped- and force-free system. Exact analytical solutions are given for the integrable cases. Effect of external periodic forces for (i) single well with infinite height potential, (ii) potential with a hump at the centre and (iii) single well with finite height hump potential are numerically investigated. Occurrence of multiple attractors and period doubling cascades of coexisting attractors is presented.

Keywords. Coupled Duffing oscillators; Painlevé analysis; chaos.

PACS Nos 05·45; 42·50; 47·20

1. Introduction

The evolution of many phenomena in nature is described by nonlinear ordinary or partial differential and difference equations depending on whether the concerned system is continuous or discrete. During the last decade or so, remarkable progress has been made in understanding the integrability and nonintegrability of nonlinear dynamical systems [1–4]. Integrable systems are rather limited and are in general expected to show regular behaviour whereas nonintegrable systems are capable of showing regular as well as complicated irregular motions in phase space. The knowledge of integrability of a differential equation or a system is very important in physics because we are interested to find a solution to the physical problem. Integrable limits of several physical systems were obtained by Painlevé analysis [4–10].

An ordinary differential equation is said to have the Painlevé property if all movable singularities of the solutions are poles. The term 'strong Painlevé' is used when the solution in the neighbourhood of an arbitrary singularity t^* can be expressed as $\tau = (t - t^*)^{-p}$, where p is an integer determined from the leading order, so that the movable algebraic or logarithmic branch points as well as essential singularities are excluded. Ramani, Dorizzi and Grammaticos [7] have introduced the so-called weak Painlevé property. By weak Painlevé property it is meant that the solution in the neighbourhood of the movable singularity t^* can be expressed as an expansion in powers of $\tau = (t - t^*)^{-1/q}$, where q must be a natural number that depends purely on the leading order behaviour of the singularity and the nature of the potentials. Equations having the Painlevé property might be easier to integrate or solve analytically.

Recently, a series of papers [11–15] devoted to the identification of integrability of damped anharmonic oscillator

$$\ddot{x} + f_1(t)\dot{x} + f_2(t)x + f_3(t)x^3 = 0 \tag{1}$$

using the Painlevé test was published. The integrable choices of the undamped two coupled anharmonic oscillators

$$\ddot{x} = -2A_1 x - 4\alpha_1 x^3 - 2\delta x y^2, \tag{2a}$$

$$\ddot{y} = -2A_2 y - 4\alpha_2 y^3 - 2\delta x^2 y, \tag{2b}$$

has also been studied by various authors [9, 16–18]. System (2) with linear damping is written as

$$\ddot{x} = -d\dot{x} - 2A_1 x - 4\alpha_1 x^3 - 2\delta x y^2, \tag{3a}$$

$$\ddot{y} = -d\dot{y} - 2A_2 y - 4\alpha_2 y^3 - 2\delta x^2 y, \tag{3b}$$

where $2A_i = \Omega_{0i}$, α_i, d and δ are natural frequency, Duffing term, damping coefficient and coupling strength respectively. Equation (3) models two-coupled Duffing oscillators and has been used to model Soret driven Bénard convection [19], vibrations of a stretched string [20], motions of nonlinear circular plates [21] and so forth [2, 22, 23]. Thus the study of integrable and nonintegrable properties of (3) is not only of theoretical but also of practical interest. The choice $d = 0$ reduces to the undamped anharmonic oscillator system. When $\delta = 0$ we have decoupled Duffing oscillators.

In this paper, first we wish to apply Painlevé analysis to study the integrability of (3). It is important to investigate the dynamics of the system including chaotic behaviour in the nonintegrable limit. It is well-known that for chaotic behaviour to occur, a fixed point of a dissipative continuous dynamical system must undergo a Hopf bifurcation thereby developing a limit cycle motion. As the control parameter is varied this limit cycle may bifurcate further leading to chaotic motion. Using linear stability analysis we found that the fixed points of (3) do not undergo Hopf bifurcation for any nonzero value of the parameters. Thus system (3) cannot show chaotic behaviour. However, when the system is subjected to external periodic forces a variety of interesting behaviours such as period doubling phenomenon, coexistence of multiple attractors, chaotic motion and merging of attractors occur.

The paper is organized as follows. To be self-contained, in § 2 we briefly outline the salient features of Painlevé analysis. In § 3 we perform the Painlevé test to the coupled Duffing oscillators. The integrable limits are identified. Then we obtain the explicit analytical solution for the integrable cases in § 4. Section 5 is devoted to the study of the influence of external periodic forces. The dynamics is numerically investigated by varying the amplitude of the forces for three physically interesting potentials. We show the occurrence of multiple periodic attractors and period doubling of coexisting attractors culminating in chaos. Section 6 contains conclusions.

2. Painlevé analysis

where F_i are rational in $x_1, \ldots, x_n$ and analytic in t to have the Painlevé (P-) property is that there is a Laurent series expansion with $(n-1)$ arbitrary expansion coefficients. The P-analysis essentially consists of three steps, dealing with the dominant behaviours, the resonances and the constants of integrations, respectively [5–9].

i) *Dominant behaviours*: The first step is to determine the leading order behaviours of x in the neighbourhood of a movable singularity t^* in the form $x_i \approx a_{i0}(t-t^*)^{p_i}$, as $t \to t^*$, $a_{i0} =$ constant. If all the allowed p_i's are negative integers, the solution may correspond to the strong P-property and if any of the p_i's is a rational fraction, the solution may be associated with the weak P-property. In either case, the solution takes the form of a Laurent series,

$$x_i(t) = (t-t^*)^{p_i} \sum_{k=0}^{\infty} a_{ik}(t-t^*)^k. \tag{5}$$

ii) *Resonances*: The second step is to identify the powers of (5) at which the arbitrary parameters can enter, called resonances. Apart from t^*, we have $(n-1)$ other arbitrary constants for (4). To find the resonances, we substitute

$$x_i \approx a_{i0}(t-t^*)^{p_i} + \Omega_i(t-t^*)^{p_i+r}, \quad r>0, \quad i=1,\ldots,n \tag{6}$$

in (4) and retain the leading order terms in Ω_i. The reduced equation will be of the form

$$Q(r)\cdot\Omega = 0, \quad \Omega = (\Omega_1, \ldots, \Omega_n), \tag{7}$$

where $Q(r)$ is an $n \times n$ matrix with r appearing only in its diagonal elements. Then the resonance values are determined from the roots of the equation $\det Q(r) = 0$.

iii) *The constants of integration*: The final step verifies that in the Laurent series (5) at the resonance values, sufficient number of arbitrary constants exist without the introduction of logarithmic branch points. To do this, we substitute the truncated expansion

$$x_i = a_{i0}(t-t^*)^{p_i} + \sum_{k=1}^{r_s} a_{ik}(t-t^*)^{p_i+k}, \tag{8}$$

where r_s is the largest resonance value in (4) and determines the integration constants. At the resonances, one usually finds some condition termed 'compatibility condition' that has to be satisfied in order to secure arbitrariness of the coefficient.

3. The Painlevé property of nonlinearly coupled Duffing oscillators

3.1 *Leading order behaviours*

Let us apply P-analysis to (3). To start with, we assume the leading orders be

$$x \approx a_0\tau^p, \quad y \approx b_0\tau^q, \quad \tau = (t-t^*) \to 0. \tag{9}$$

To determine p, q, a_0 and b_0, we use (9) in (3) and obtain pairs of leading order equations

$$a_0 p(p-1)\tau^{p-2} = -\mathrm{d}a_0 p\tau^{p-1} - 2A_1 a_0\tau^p - 4\alpha_1 a_0^3\tau^{3p} - 2\delta a_0 b_0^2\tau^{p+2q}, \tag{10a}$$

$$b_0 q(q-1)\tau^{q-2} = -\mathrm{d}b_0 q\tau^{q-1} - 2A_2 b_0\tau^q - 4\alpha_2 b_0^3\tau^{3q} - 2\delta b_0 a_0^2\tau^{2p+q}. \tag{10b}$$

These equations immediately reveal that three different types of leading orders are possible. These are

$$p=-1, \quad q=-1, \quad a_0^2=(2\alpha_2-\delta)/(\delta^2-4\alpha_1\alpha_2),$$
$$b_0^2=(2\alpha_1-\delta)/(\delta^2-4\alpha_1\alpha_2). \tag{11}$$

$$p=-1, \quad q=\tfrac{1}{2}[1+(1+(4\delta/\alpha_1))^{1/2}]\geqslant\tfrac{1}{2},$$
$$a_0^2=-1/(2\alpha_1), \quad b_0^2=\text{arbitrary}. \tag{12}$$

$$p=-1, \quad q=\tfrac{1}{2}[1-(1+(4\delta/\alpha_1))^{1/2}]>-1,$$
$$a_0^2=-1/(2\alpha_1), \quad b_0^2=\text{arbitrary}. \tag{13}$$

The three different solution branches, eqs (11–13) must be tested for the P-property. The next step is to carry out a resonance analysis.

3.2 *Resonances*

To find the resonances, that is, the values of the order r at which arbitrary constants will enter in the expansions of the solutions near the singularity at $t=t^*$, we write

$$x\approx a_0\tau^p+\Omega_1\tau^{p+r}, \quad y\approx b_0\tau^q+\Omega_2\tau^{q+r}. \tag{14}$$

We substitute (14) in (3) to obtain resonances. Retaining leading order terms, we obtain a system of linear algebraic equation

$$M_2(r)\cdot\Omega=0, \quad \Omega=(\Omega_1,\Omega_2), \tag{15}$$

where $M_2(r)$ is a 2×2 matrix dependent on r. In order to have nontrivial set of solutions (Ω_1,Ω_2) we require the determinant of $M_2(r)$ equal to 0.

Case 1: For equation (11), the form of $M_2(r)$ is

$$M_2(r)=\begin{pmatrix}(r-1)(r-2)+8\alpha_1a_0^2-2 & 4\delta a_0b_0\\ 4\delta a_0b_0 & (r-1)(r-2)+8\alpha_2b_0^2-2\end{pmatrix} \tag{16}$$

which then leads to the equation

$$(r^2-3r-4)(r^2-3r-\mu)=0, \quad \mu=4[1+2(\alpha_1a_0^2+\alpha_2b_0^2)]. \tag{17}$$

Thus for (11) the resonances occur at

$$r=-1,4,[3\pm(9-4\mu)^{1/2}]/2. \tag{18}$$

The root -1 corresponds to the arbitrariness of t^* in (9). All the other resonances must have positive integer values as a necessary condition for (14) to be a Laurent series and (3) to possess the P-property. This happens for special values of μ. Equation (18) along with (11) then leads to the following two possibilities:

Case 1(i): $\mu=2, \quad \alpha_1a_0^2+\alpha_2b_0^2=-1/4, \quad r=-1,1,2,4,$ (19a)

$$\delta=2[(\alpha_1+\alpha_2)\pm(\alpha_1^2+\alpha_2^2-\alpha_1\alpha_2)^{1/2}]. \tag{19b}$$

Case 1(ii): $\mu=0, \quad \alpha_1a_0^2+\alpha_2b_0^2=-1/2, \quad r=-1,0,3,4,$ (20a)

$$\delta^2=4\alpha_1\alpha_2. \tag{20b}$$

the P-property, this immediately restricts δ to those values given by (19b) and (20b) for the cases 1(i) and 1(ii) respectively.

Case 2: For eqs (12) and (13), the expression for $M_2(r)$ degenerates to

$$M_2(r) = \begin{pmatrix} r^2 - 3r + 8\alpha_1 a_0^2 & 0 \\ 4\delta a_0 b_0 & r^2 + 2rq - r \end{pmatrix} \tag{21}$$

so that from $\det M_2(r) = 0$, the resonance values are

$$r = -1, 0, (1-2q), 4. \tag{22}$$

In (22), for $(1-2q) \geqslant 0$ we must have $q \leqslant \frac{1}{2}$. But this is in general contradictory to the leading order singularity nature, $q \geqslant \frac{1}{2}$, eq. (12). The only consistent case $q = \frac{1}{2}$ requires both a_0 and b_0 to be arbitrary, which is not true as seen from (12). Thus, the associated P-branch can have less number of arbitrary constants.

Case 3: Using (13) in (21), we infer two possibilities:

Case 3(i): $q = 0$, and so $\delta = 0$, the uncoupled case.

Case 3(ii): $q = -\frac{1}{2}, \quad 3\alpha_1 = 4\delta, \quad r = -1, 0, 2, 4.$ (23)

Thus, for the coupled Duffing equation (3), we identify three sets of full resonances, namely, (19), (20) and (23). The resonance analysis only tells us which coefficients should be arbitrary, and this has to be verified by checking the full recursion relations.

3.3 *Identifying the arbitrary constants of integration*

To verify the existence of a sufficient number of arbitrary constants we introduce series expansion

$$x \approx a_0 \tau^p + \sum_{k=1}^{4} a_k \tau^{p+k}, \quad y \approx b_0 \tau^q + \sum_{k=1}^{4} b_k \tau^{q+k}, \tag{24}$$

in (3) and equating the coefficients of the powers of $(\tau^{p+k-2}, \tau^{q+k-2})$ to zero, we obtain a system of linear algebraic equations for a_k and b_k. For a system containing parameters, say, $a, b, c, \ldots$ one will often find that arbitrariness is only obtained for special values of the system parameters. We will now deal with each one of the cases 1(i), 1(ii) and 3(ii) separately. For the case 1(i) we give the analysis in detail while for the remaining two cases we present main results only.

Case 1(i): The resonance values $r = 1, 2, 4$ imply that in addition to t^*, three arbitrary constants exists. Thus, for system (3) to satisfy P-property a_1 (or b_1), a_2 (or b_2) and a_4 (or b_4) must be arbitrary which we verify here. From the coefficients of (τ^{-2}, τ^{-2}) we obtain

$$da_0 b_0 - 2b_0 a_1 (6\alpha_1 a_0^2 + \delta b_0^2) - 4\delta a_0 b_0^2 b_1 = 0, \tag{25a}$$

$$da_0 b_0 - 2a_0 b_1 (6\alpha_2 b_0^2 + \delta a_0^2) - 4\delta a_0^2 b_0 a_1 = 0. \tag{25b}$$

Then, from (25), for a_1 (or b_1) to be arbitrary we require $\delta = 6\alpha_1$ (or $6\alpha_2$). For this choice of δ values from (19b) we further find that $\alpha_1 = \alpha_2$ and hence $a_0^2 = b_0^2 = -1/(8\alpha_1)$. Proceeding further, for a_2 (or b_2) to be arbitrary, from the coefficients of (τ^{-1}, τ^{-1}) we

obtain $A_1 = A_2$ and hence we have

$$a_2 + b_2 = (2/3)a_0(A_1 - d^2/12). \tag{26}$$

In a similar manner, equating terms of order (τ^0, τ^0) we uniquely determine the coefficients a_3 and b_3 and easily find

$$a_3 + b_3 = (1/27)da_0(9A_1 - d^2). \tag{27}$$

Finally, from the coefficients of (τ^1, τ^1) the compatibility condition for a_4(or b_4) to be arbitrary is

$$\begin{aligned} 2d(a_3 + b_3) &= -(a_2 + b_2)[A_1 + 6\alpha_1(a_1 + b_1)^2 + 12\alpha_1 a_0(a_2 + b_2)], \\ &= (1/a_0)(a_2 + b_2)[d^2 a_0/12 - (3/2)(a_2 + b_2) - A_1 a_0]. \end{aligned} \tag{28}$$

Using (26) the right hand side of (28) is found to be 0. Then, substituting $(a_3 + b_3)$ from (27) in (28) we obtain

$$a_0 d^2(9A_1 - d^2) = 0. \tag{29}$$

This means that a_4(or b_4) is arbitrary only for $d = 0$ and $d = \pm 3\sqrt{A_1}$. The choice $d = 0$ corresponds to the undamped anharmonic oscillator. Thus, the Laurent series (5) for the Duffing equation (3) with $p = -1$, $q = -1$ is seen to have three arbitrary parameters besides t^*. We know that since (3) can be rewritten as four coupled first order ordinary differential equations, its general solution is characterized by four arbitrary parameters. The above analysis shows that these are manifested in the Laurent expansion (5) by the arbitrariness of t^*, a_1(or b_1), a_2(or b_2) and a_4(or b_4). Thus, for case 1(i) the system possesses P-property for

$$\alpha_1 = \alpha_2, \quad \delta = 6\alpha_1, \quad A_1 = A_2, \quad d = 0, \tag{30}$$

$$\alpha_1 = \alpha_2, \quad \delta = 6\alpha_1, \quad A_1 = A_2, \quad d = \pm 3\sqrt{A_1}. \tag{31}$$

Case 1(ii): The resonance values are $r = -1, 0, 3, 4$ with the parametric condition (20b). From the leading order analysis the conditions for a_0(or b_0) to be arbitrary are

$$\alpha_1 = \alpha_2, \quad \delta = 2\alpha_1. \tag{32}$$

Comparing the coefficients of (τ^0, τ^0) in (3) we obtain the following set of equations

$$a_0 a_3 + b_0 b_3 = -d^3/(864\alpha_1), \tag{33}$$

$$\begin{aligned} 0.a_3 + 0.b_3 = d[&(A_1 - A_2)\{1 + (8/3)\alpha_1^2 a_0^2(a_0^2 - b_0^2) - 2\alpha_1 a_0^2\} \\ &+ (2/3)\alpha_1(a_0^2 - b_0^2)(A_2 - d^2/12)]. \end{aligned} \tag{34}$$

Equation (33) implies that a_3(or b_3) is arbitrary while (34) gives the compatibility condition in terms of the parameters of the system. For (34) to be satisfied, we require

$$A_1 = A_2, \quad d^2 = 12A_2. \tag{35}$$

From the coefficients of (τ^1, τ^1) we obtain

$$0.a_4 + 0.b_4 = da_3(1 - \alpha_1 a_0^2 - \alpha_1 a_0 b_0) + db_3(1 - \alpha_1 b_0^2 - \alpha_1 a_0 b_0). \tag{36}$$

Now, using (34) and (36) we can determine both the coefficients a_3 and b_3. But from the resonance condition (20) we require either a_3 or b_3 as arbitrary. Since the coefficients a_3 and b_3 are fixed we conclude that case 1(ii) is of non-P-type for $d \neq 0$. However, for $d = 0$, the right hand side of (36) become zero and so a_4(or b_4) is arbitrary without any further restrictions on the parameters. Thus, for the case 1(ii) the system possesses P-property for

$$\alpha_1 = \alpha_2, \quad \delta = 2\alpha_1, \quad d = 0, \quad A_1 \text{ and } A_2 \text{ arbitrary.} \tag{37}$$

Case 3(ii): Proceeding as before, from the coefficients of $(\tau^{-1}, \tau^{-1/2})$ in (3) we find that b_2 is arbitrary only if

$$3\alpha_1 = 4\delta, \quad d^2 + 3A_1 - 12A_2 = 0, \quad \delta^2 - 18\delta\alpha_2 + 72\alpha_2^2 = 0. \tag{38}$$

From the last condition in (38) we obtain $\delta = 6\alpha_2$ or $12\alpha_2$. From the coefficients of τ^1 in (3) we obtain an equation containing terms b_2, and powers of b_0 and constant terms only. Since b_0 and b_2 are arbitrary we equate the coefficients of b_2 and various powers of b_0 to zero separately which leads to the condition $d = 0$. That is, case 3(ii) is non-P-type for $d \neq 0$. Thus, case 3(ii) passes P-test only if

$$3\alpha_1 = 4\delta, \quad A_1 = 4A_2, \quad \alpha_1 = 8\alpha_2, \quad d = 0, \tag{39}$$

$$3\alpha_1 = 4\delta, \quad A_1 = 4A_2, \quad \alpha_1 = 16\alpha_2, \quad d = 0. \tag{40}$$

Thus, for $d = 0$ system (3) possesses P-property for four sets of parametric restrictions given by (30), (37), (39) and (40) and when $d \neq 0$, (3) passes the P-test only for the parameters set given by (31).

4. Analytical solution for the integrable cases

For $d = 0$, Lakshmanan and Sahadevan [9, 17] explicitly constructed second integrals of motion, the first being the Hamiltonian, in order to substantiate the complete integrability. In this section we find the explicit analytical solution for the integrable cases with $d \neq 0$, namely,

$$\alpha_1 = \alpha_2, \quad \delta = 6\alpha_1, \quad A_1 = A_2, \quad d = \pm 3\sqrt{A_1}. \tag{41}$$

For the above parametric choices, system (3) under the transformation $u = x + y$, $v = x - y$ decouples into two single oscillator

$$\ddot{u} \pm 3\sqrt{A_1}\dot{u} + 2A_1 u + 4\alpha_1 u^3 = 0, \tag{42}$$

$$\ddot{v} \pm 3\sqrt{A_1}\dot{v} + 2A_1 v + 4\alpha_1 v^3 = 0. \tag{43}$$

For positive damping and $\alpha_1 > 0$, under the transformation

$$W = \sqrt{2\alpha_1/A_1}\, u \exp(\sqrt{A_1}\, t), \quad Z = -\sqrt{2}\exp(-\sqrt{A_1}\, t), \tag{44}$$

eq. (42) can be reduced to

$$\mathrm{d}^2 W/\mathrm{d}Z^2 + W^3 = 0. \tag{45}$$

Equation (45) has the Jacobian elliptic function solution [24]

$$W = W_0 cn(W_0 z; k), \quad z = Z - Z_0, \quad k^2 = 1/2 \tag{46}$$

where W_0 and Z_0 are arbitrary integration constants. From (44) and (46) the solution of (42) is written as

$$u(t) = \sqrt{A_1/(2\alpha_1)}\, W_0 \exp(-\sqrt{A_1}\, t) cn(W_0 z; k),$$
$$z = -\sqrt{2}\exp(-\sqrt{A_1}\, t) - Z_0. \tag{47}$$

For $\alpha_1 < 0$, using the transformation (44) with $\alpha_1 = |\alpha_1|$, (42) becomes

$$d^2 W/dZ^2 - W^3 = 0 \tag{48}$$

which has the solution [24]

$$W = W_0/cn(W_0 z; k'), \tag{49a}$$

where

$$z = Z - Z_0, \quad k'^2 = 1 - k^2 = 1/2 \tag{49b}$$

and W_0, Z_0 are the arbitrary constants. The solution of (42) can now be written as

$$u(t) = \sqrt{A_1/(2|\alpha_1|)}\, W_0 \exp(-\sqrt{A_1}\, t)[cn(W_0 z; k')]^{-1},$$
$$z = -\sqrt{2}\exp(-\sqrt{A_1}\, t) - Z_0. \tag{50}$$

The solution for the negative damping $d = -3\sqrt{A_1}$ can be easily obtained from (47) and (50) by replacing t by $-t$.

5. Regular and chaotic dynamics in the coupled Duffing oscillators

In the previous two sections we were concerned with the integrability and exact solutions of the coupled Duffing oscillators in the absence of external periodic forces. In order to study the occurrence of chaotic behaviour we consider the coupled Duffing oscillators driven by external periodic forces [2], namely,

$$\ddot{x} = -d\dot{x} - 2A_1 x - 4\alpha_1 x^3 - 2\delta x y^2 + f_1 \cos\Omega_1 t,$$
$$\ddot{y} = -d\dot{y} - 2A_2 y - 4\alpha_2 y^3 - 2\delta y x^2 + f_2 \cos\Omega_2 t. \tag{51}$$

Equation (51) models a variety of physical systems [2, 20, 22, 23]. Elliott [20] studied the resonance behaviour and Nabergoj *et al* [23] investigated the stability of nonoscillating solution in (51) with $f_2 = 0$. Applying the method of multiple scales Nayfeh and Vakakis [21] analyzed subharmonic frequency response curves. The interaction between high and low frequency modes is analyzed by Nayfeh and Nayfeh [22]. Recently, using Melnikov analytical method we have studied the occurrence of homoclinic bifurcations [25].

Equation (51) can be written as

$$\ddot{x} = -d\dot{x} - \partial V(x, y)/\partial x + f_1 \cos\Omega_1 t,$$
$$\ddot{y} = -d\dot{y} - \partial V(x, y)/\partial y + f_2 \cos\Omega_2 t,$$

where the potential function V is given by

$$V(x, y) = A_1 x^2 + \alpha_1 x^4 + A_2 y^2 + \alpha_2 y^4 + \delta x^2 y^2. \tag{52}$$

Throughout our analysis we assume A_2 and α_2 to have the same signs as A_1 and α_1 respectively. Further, we assume that the coupling is weak. The shape of the potential varies with the signs of $A_1, A_2, \alpha_1, \alpha_2$. We consider the following cases.

Case 1: $A_1, A_2, \alpha_1, \alpha_2 > 0$ – single well with infinite height potential (figure 1a).
Case 2: $A_1, A_2 < 0, \alpha_1, \alpha_2 > 0$ – potential with a hump at the centre (figure 1b).
Case 3: $A_1, A_2 > 0, \alpha_1, \alpha_2 < 0$ – single well with finite height hump potential (figure 1c).
Case 4: $A_1, A_2, \alpha_1, \alpha_2 < 0$ – inverted single well potential (figure 1d).

The nature of the solutions of the system (51) depends on the shape of the potential. In cases (1) and (2) there exists globally bounded solutions since $V(x, y) \to \infty$ as $|x|$ and $|y| \to \infty$. However, for case (3) we may have unbounded solutions of exploding amplitudes for the choices of sufficiently large initial values since $V(x, y) \to -\infty$ as $|x|$ and $|y| \to \infty$. Finally, the potential with $A_1, A_2, \alpha_1, \alpha_2 < 0$ is physically uninteresting since the system has an exploding amplitude $V(x, y) \to -\infty$ as $|x|$ and $|y| \to \infty$. In the following we numerically study the occurrence of regular and chaotic dynamics in (51) for the first three potentials (cases 1–3).

5.1 *Single well with infinite height potential*

We fix the parameters at $A_1 = 0{\cdot}005$, $A_2 = 0{\cdot}01$, $\alpha_1 = 10$, $\alpha_2 = 10$, $\delta = 0{\cdot}05$, $d = 3(A_1)^{1/2}$ and $\Omega_1 = \Omega_2 = 1$. We choose $f_1 = f_2 = f$. The forcing amplitude f is varied from a small value. From our numerical studies we find the following. Figure 2a shows the occurrence of period doubling bifurcations, chaotic motion and window regions. For characterizing the regular and chaotic motion we have calculated the maximal Lyapunov exponent (λ). Variation of λ against f is plotted in figure 2b. Initially for

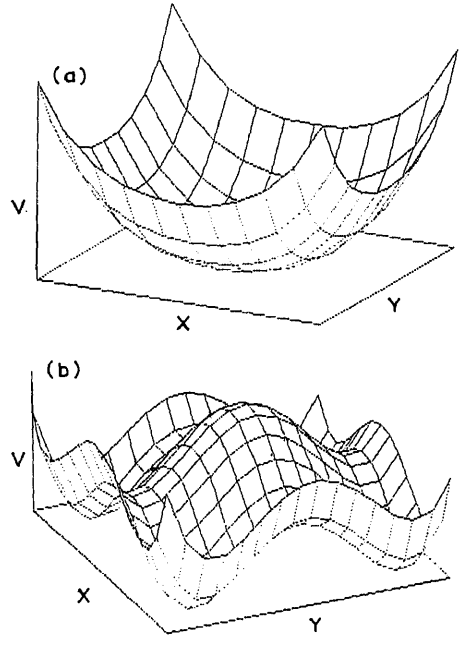

Figure 1. (a) and (b)

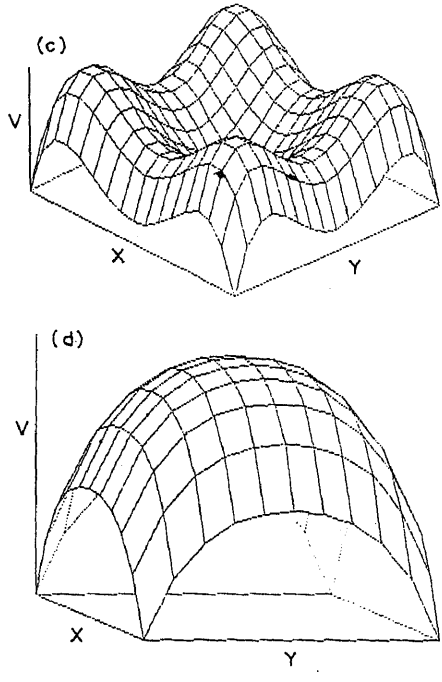

Figure 1. Potential V, equation (52), for (**a**) $A_1, A_2, \alpha_1, \alpha_2 > 0$, (**b**) $A_1, A_2 < 0$, $\alpha_1, \alpha_2 > 0$, (**c**) $A_1, A_2 > 0, \alpha_1, \alpha_2 < 0$ and (**d**) $A_1, A_2, \alpha_1, \alpha_2 < 0$.

small values of f the system exhibits symmetrical orbit. A typical orbit is shown in figure 3a for $f = 0{\cdot}2$. As the parameter f is varied the symmetrical orbit loses its stability and experiences a symmetry breaking bifurcation. The resulting asymmetric orbit is shown in figure 3b for $f = 0{\cdot}8$. As f is further increased the asymmetrical attractor undergoes period doubling cascade to chaos. Period-1, 2, 4 and 8 orbits are found in the interval (0–0·896), (0·896–1·016), (1·016–1·04) and (1·04–1·052) respectively. Onset of chaos is found at $f = 1{\cdot}064$. A feature of chaotic regime is the presence of windows of periodic solutions interspersed throughout the range of their existence. Period-3 window occurs for $f \in (1{\cdot}364–1{\cdot}652)$ in which there is no chaotic behaviour. The developed chaos disappears at $f \approx 2{\cdot}072$ by a period-1 limit cycle. In the chaotic regime as the parameter f is increased the size of the attractor increases gradually as shown in the bifurcation diagram (2a). In figure 4 the Poincaré map of the chaotic attractor in $x - \dot{x}$ plane is plotted for $f = 1{\cdot}7$.

5.2 *Potential with a hump at the centre*

We now fix $A_1 = -0{\cdot}5$, $A_2 = -0{\cdot}055$, $\alpha_1 = 0{\cdot}25$, $\alpha_2 = 0{\cdot}025$, $d = 0{\cdot}4$, $\delta = 0{\cdot}025$, $\Omega_1 = \Omega_2 = 1$. For small values of f coexistence of two limit cycle orbits occur. As the parameter f is increased both the orbits exhibit a cascade of period doubling leading to chaotic motion. Each coexisting attractor possesses its own basin of attraction, defined as the set of initial conditions from which the system evolves to a particular orbit.

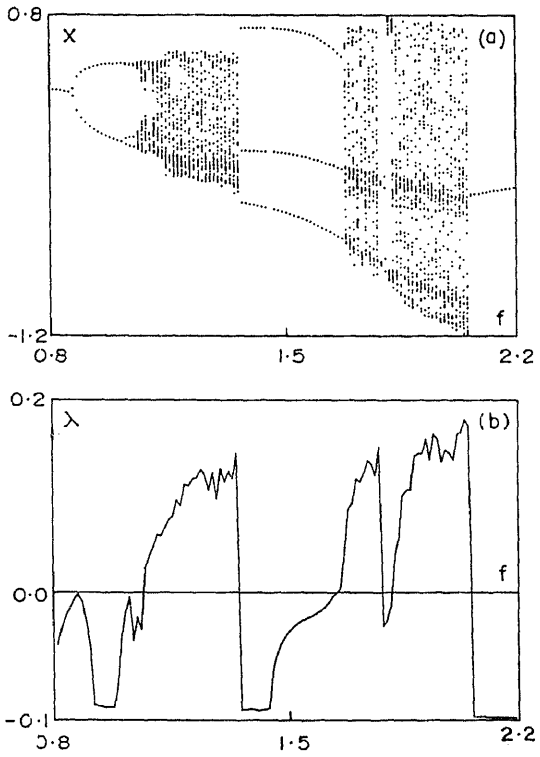

Figure 2. (**a**) Bifurcation diagram illustrating period doubling route to chaos. (**b**) Maximal Lyapunov exponent against the parameter f corresponding to the figure (2a).

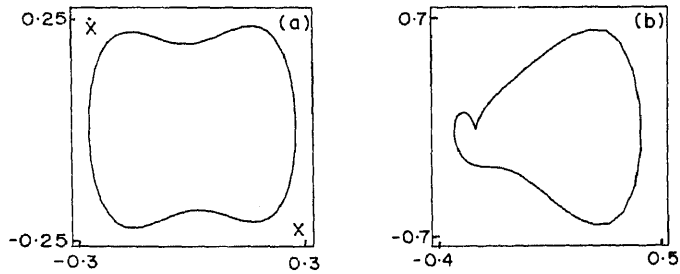

Figure 3. Phase portrait of (**a**) symmetrical orbit for $f = 0{\cdot}2$ and (**b**) asymmetrical orbit for $f = 0{\cdot}8$.

Figures 5a and 5b shows the successive bifurcations of two coexisting attractors. Interestingly, both the attractors underwent bifurcations at the same f values. For example, both the period-1 orbits bifurcate to period-2 orbits at $f \approx 0{\cdot}255$ and period-4 at $f \approx 0{\cdot}26475$. Chaotic motion is first observed at $f = 0{\cdot}267$. The chaotic attractors disappeared at $f = 0{\cdot}281$. Due to crisis two period-1 limit cycles are found. Moreover, these orbits underwent period doubling which is clearly seen in figure 5. Further, we note a sudden expansion in the size of the chaotic attractors at $f \approx 0{\cdot}2715$ and $0{\cdot}3088$.

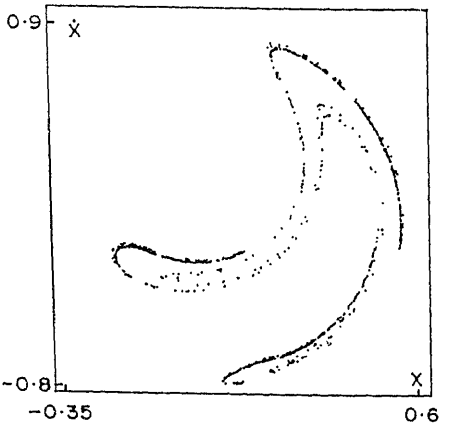

Figure 4. Poincaré map of the chaotic attractor for $f = 1{\cdot}7$.

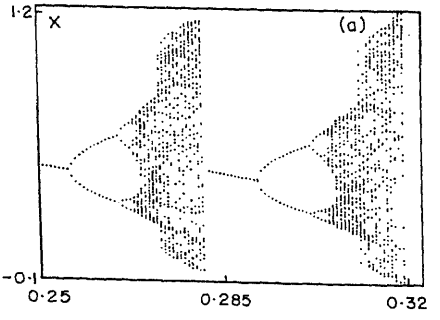

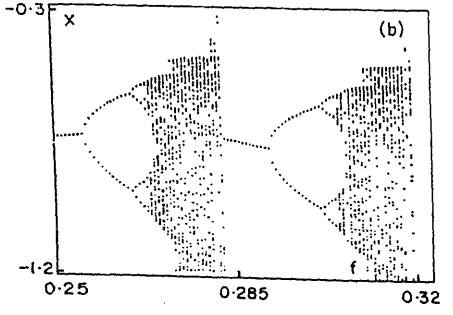

Figure 5. Figures showing successive bifurcations of two coexisting period-1 attractors.

For $f > 0{\cdot}3165$ cross-well chaos is observed. Here, the two chaotic attractors merge into a single attractor. This is shown in figure 6 for $f = 0{\cdot}6$.

5.3 *Single well with finite height hump potential*

Next we consider the case $A_1, A_2 > 0$ and $\alpha_1, \alpha_2 < 0$. The dynamics of the system has been investigated for the following fixed parameters $A_1 = 0{\cdot}5, A_2 = 0{\cdot}55, \alpha_1 = -1, \alpha_2 = -0{\cdot}975$, $\delta = 0{\cdot}025, d = 0{\cdot}4$ and $\Omega_1 = \Omega_2 = 0{\cdot}526$ thereby varying f as done in the other two potential well cases. In this potential well also we have found coexistence of more than one stable periodic orbit and period doubling bifurcations. In contrast to the case 2 potential where both the period-1 orbits underwent period doubling bifurcations at same f value, here the attractors are found to undergo period doubling bifurcations at different f values. Figure 7 shows the phase portrait of three coexisting period-1 orbits for $f = 0{\cdot}1143$. When f is increased the limit cycle labelled as c in figure 7 alone persists while the other two become unstable at certain f values and undergo cascades of period doubling bifurcations. Bifurcations of the period-1 orbit a (b) to period-2 occur at $f = 0{\cdot}1143375(0{\cdot}11448)$; to period-4 at $f = 0{\cdot}114481(0{\cdot}1146225)$; to period-8 at $f = 0{\cdot}1145184(0{\cdot}114645)$.

Figure 8 shows successive period doubling process leading to chaotic motion of coexisting period-1 attractors. The Poincaré map of the two coexisting chaotic attractors at $f = 0{\cdot}11466$ is given in figure 9. For comparison, same scales in x and $\dot{x}$ coordinates are used. For clarity, in figure 9c we show the magnification of the chaotic attractor shown in figure 9b. As the parameter f is increased beyond a certain critical

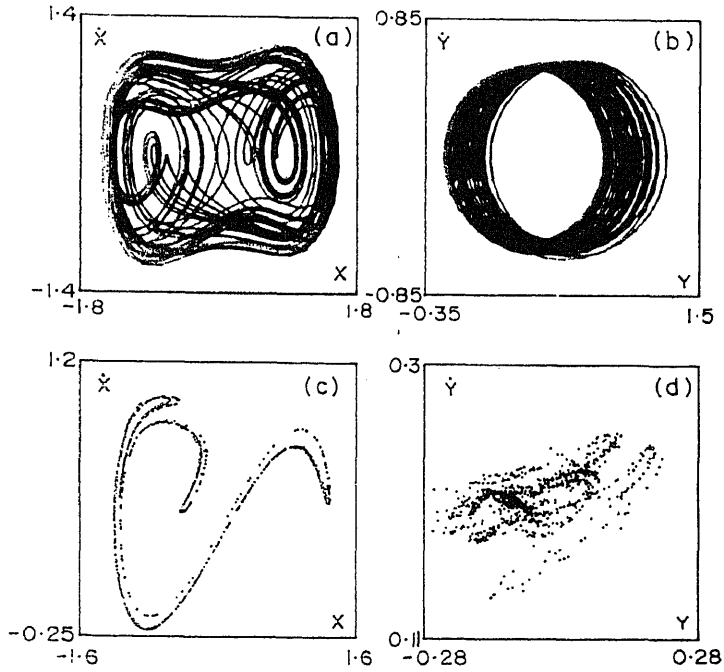

Figure 6. Phase portrait (**a, b**) and Poincaré map (**c, d**) of the chaotic attractor for $f = 0{\cdot}6$.

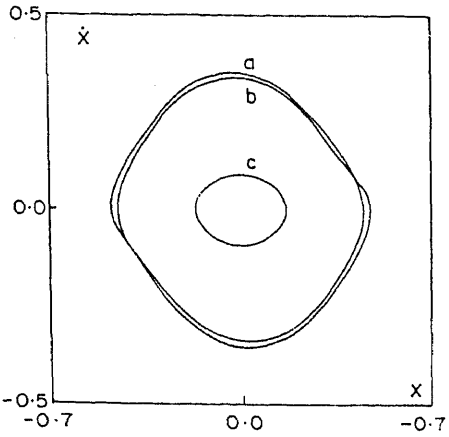

Figure 7. Phase portrait of three different coexisting period-1 attractors for $f = 0{\cdot}1143$. The initial conditions used are $(x, \dot{x}, y, \dot{y}) = (0, 0{\cdot}35, 0, 0)$ (a), $(-0{\cdot}06, 0{\cdot}35, 0, 0)$ (b) and $(0{\cdot}1, 0, 0, 0)$ (c).

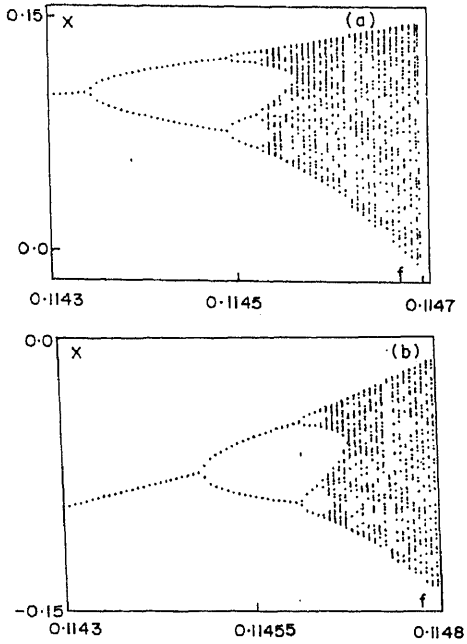

Figure 8. Period doubling bifurcations culminating in chaos of two coexistin attractors.

value of f, both the chaotic attractors merge together and form a single large chaoti attractor. This is caused by a crisis in which both the attractors fuse together and form

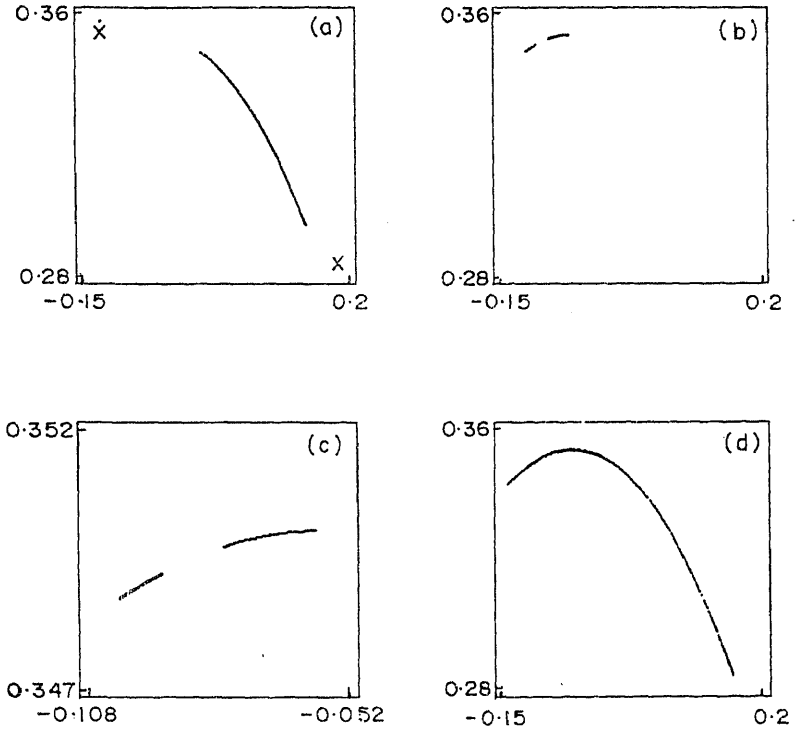

Figure 9. (**a**, **b**) Poincaré map of the two coexisting chaotic attractors for $f = 0{\cdot}11466$. (**c**) Enlargement of the attractor shown in (b). (**d**) Poincaré map of the chaotic attractor for $f = 0{\cdot}11482$.

of the two coexisting attractors found at lower f values. The coexistence of limit cycle c along with the chaotic attractors provides a mode of physical regulation as it allows to switch to a periodic regime upon suitable perturbation.

6. Conclusions

In this paper we have applied the singularity structure analysis (Painlevé analysis) to the nonlinearly coupled Duffing oscillators. Specific sets of parameters for which the system becomes integrable are obtained. For the integrable cases explicit analytical solution is constructed. For the system (3) with $d = 0$ four integrable choices were identified (cf. eqs (30), (37), (39) and (40)), namely,

i) $\alpha_1 = \alpha_2$, $\delta = 6\alpha_1$, $A_1 = A_2$,
ii) $\alpha_1 = \alpha_2$, $\delta = 2\alpha_1$, A_1 and A_2 arbitrary,
iii) $\alpha_1 = 16\alpha_2$, $\delta = 6\alpha_2$, $A_1 = 4A_2$,
iv) $\alpha_1 = 8\alpha_2$, $\delta = 6\alpha_2$, $A_1 = 4A_2$.

However, when the damping term is added the system is found to be integrable only for $\alpha_1 = \alpha_2, \delta = 6\alpha_1, A_1 = A_2$ and $d = \pm 3\sqrt{A_1}$. Further, we have studied the occurrence of chaotic motion for the three potential wells for specific parameter values. Approximate

theories of nonlinear oscillation can be used to get much insight into the occurrenc chaotic motion and locate the chaotic regions in the various parameter space of Chaotic attractor of (51) at critical bifurcations such as onset of chaos, band merg crisis and intermittency can be characterized by the dynamical structure funct [26,27]. It is also of interest to study the effect of the coupling parameter δ on both regular and chaotic dynamics of uncoupled systems. These will be investigate future.

Acknowledgement

The present work forms part of the UGC minor research project of SR.

References

[1] H G Schüster, *Deterministic chaos* (VCH, Weinheim, 1988)
[2] F C Moon, *Chaotic vibrations* (Wiley-Interscience, New York, 1987)
[3] S Wiggins, *Introduction to applied nonlinear dynamical systems and chaos* (Springer-V New York, 1990)
[4] M Tabor, *Chaos and integrability in nonlinear dynamics – An introduction* (Wiley- Int ence, New York, 1989)
[5] M J Ablowitz, A Ramani and H Segur, *Lett. Nuovo Cimento* **23**, 333 (1978)
[6] M J Ablowitz, A Ramani and H Segur, *J. Math. Phys.* **21**, 715 (1980)
[7] A Ramani, B Dorizzi and B Grammaticos, *Phys. Rev. Lett.* **49**, 1538 (1982)
[8] A Ramani, B Grammaticos and T Bountis, *Phys. Rep.* **180**, 159 (1989)
[9] M Lakshmanan and R Sahadevan, *Phys. Rep.* **224**, 1 (1993)
[10] S Paul Raj and S Rajasekar, *Pramana – J. Phys.* **45**, 305 (1995)
[11] S Parthasarathy and M Lakshmanan, *J. Sound Vib.* **137**, 523 (1990)
[12] S Parthasarathy, Ph.D. Thesis (Bharathidasan University, 1993) unpublished
[13] J D Fournier, G Levine and M Tabor, *J. Phys.* **A21**, 33 (1988)
[14] L G S Duarte, N Euler and I C Moreira, *J. Phys.* **A23**, 1457 (1990)
[15] P G Estevez, *J. Phys.* **A24**, 1153 (1991)
[16] M Lakshmanan and R Sahadevan, *Phys. Rev.* **A31**, 861 (1985)
[17] R Sahadevan, Painlevé analysis and integrability of certain coupled nonlinear oscill Ph.D. Thesis (Madras University, 1986) (unpublished)
[18] A Ramani, J Hietarinta, B Dorizzi and B Grammaticos, *Phys. Lett.* **A108**, 55 (1985)
[19] M A F Sanjuan, J L Valero and M G Velarde, *Nuovo Cimento* **13**, 913 (1991)
[20] J A Elliott, *Am. J. Phys.* **50**, 1148 (1982)
[21] T A Nayfeh and A F Vakakis, *Int. J. Non-Linear Mech.* **29**, 233 (1994)
[22] S A Nayfeh and A H Nayfeh, *Int. J. Bifur. Chaos* **3**, 417 (1993)
[23] R Nabergoj, A Tondl and Z Virag, *Chaos, Solitons and Fractals* **4**, 263 (1994)
[24] T Davis, *Introduction of nonlinear differential and integral equations* (Dover Publ. York, 1962)
[25] S Rajasekar and S Paul Raj (submitted for publication)
[26] S Rajasekar, *Phys. Rev.* **E52**, 3234 (1995)
[27] S Rajasekar, *Chaos, soliton and fractals* (1996) (in press)

Stochastic motion of a charged particle in a magnetic field: I Classical treatment

JAGMEET SINGH* and SUSHANTA DATTAGUPTA
School of Physical Sciences, Jawaharlal Nehru University, New Delhi 110 067, India
*Also at: Physics Department, S.G.T.B. Khalsa College, University of Delhi, Delhi 110 007, India

MS received 2 May 1996

Abstract. We study the dissipative, classical dynamics of a charged particle in the presence of a magnetic field. Two stochastic models are employed, and a comparative analysis is made, one based on diffusion processes and the other on jump processes. In the literature on collision-broadening of spectral lines, these processes go under the epithet of weak-collision model and Boltzmann–Lorentz model, respectively. We apply our model calculation to investigate the effect of magnetic field on the collision-broadened spectral lines, when the emitter carries an electrical charge. The spectral lines show narrowing as the magnetic field is increased, the narrowing being sharper in the Boltzmann–Lorentz model than in the weak collision model.

Keywords. Magnetic field-induced dynamics; weak collision-model; Boltzmann–Lorentz model; spectral lineshape; dissipative dynamics.

PACS Nos 32·70; 34·10; 05·40

1. Introduction

The problem of dissipative dynamics of a charged particle in the presence of a magnetic field pervades several areas of basic physics such as classical mechanics, electromagnetic theory and statistical physics. It also has ramifications in plasma physics [1], solid state physics, in particular, diamagnetism [2], and as we shall discuss here, in a branch of optical spectroscopy called "collision broadening" [3]. In its most elementary form, the problem involves reversible dynamics due to the Lorentz force, and its interplay with dissipative effects arising from "collisions". The term is put under quotes to imply that its usage is meant to be understood in a generalized sense to describe either real collisions between the test charge with other foreign particles or effects of interaction with other degrees of freedom, eg. phonons in solids.

Whatever be the source of collisions, its consequence is to make the velocity $\mathbf{v}(t)$ of the charged particle a stochastic process. In the present work, we shall assume this process to be a classical one and that it is a stationary Markov process [4]. Needless to say, the time-integral of $\mathbf{v}(t)$ i.e. the position vector $\mathbf{r}(t)$ is also a stochastic process (albeit a non-stationary one) which can be completely specified by the so-called characteristic function

$$\phi(\mathbf{k}, t) = \langle \exp(i\mathbf{k}\cdot\mathbf{r}(t)) \rangle, \tag{1}$$

where $\mathbf{k}$ is an arbitrary vector and the angular brackets denote the average over the probability function which defines the underlying stochastic process.

It is interesting to note that although the quantity $\phi(t)$ in (1) is introduced as an entirely mathematical object, it has the physical interpretation of the 'phase' of the electromagnetic radiation (of wave vector $\mathbf{k}$) from an emitter whose instantaneous position is $\mathbf{r}(t)$. Indeed, the frequency-Fourier transform of $\phi(t)$ yields the optical lineshape for velocity modulation in gas-phase spectroscopy [5]. This can be readily seen by writing (1) as

$$\phi(\mathbf{k}, t) = \left\langle \exp i\mathbf{k} \cdot \int_0^t \mathbf{v}(t')\mathrm{d}t' \right\rangle, \tag{2}$$

if we assume that $\mathbf{v}(0) = 0$. Note that if the velocity $\mathbf{v}(t)$ were constant in time, the integral in eq. (2) would simply yield $\mathbf{v}t$. We may then perform the average (indicated by the angular brackets), over a stationary Maxwellian distribution of $\mathbf{v}$, thereby yielding a Gaussian in t. The Fourier-transform $\tilde{\phi}(\omega)$, in turn, is also a Gaussian in ω with a width proportional to $T^{1/2}$, T being the temperature characterizing the underlying velocity distribution. Therefore, the spectral line undergoes broadening as temperature increases, which is usually referred to as the Doppler broadening [3]. However, if the emitter suffers *velocity-changing collisions*, its 'effective' velocity is reduced, leading to a narrowing of the Doppler broadened line. This phenomenon is akin to the 'motional narrowing' effect in magnetic resonance [6]. One of our aims in the present paper is to investigate what influence, if any, does an external magnetic field have on the motional narrowing, when the emitter carries an electrical charge.

It is well-known that a stationary Markov process such as $\mathbf{v}(t)$ has an underlying probability function $P(\mathbf{v}, t)$ that obeys the following master equation

$$\frac{\partial P(\mathbf{v}, t)}{\partial t} = \int \mathrm{d}\mathbf{v}' [P(\mathbf{v}', t) W(\mathbf{v}'|\mathbf{v}) - P(\mathbf{v}, t) W(\mathbf{v}|\mathbf{v}')], \tag{3}$$

where $W(\mathbf{v}'|\mathbf{v})$ denotes the probability per unit time that $\mathbf{v}$ jumps (instantaneously) from $\mathbf{v}'$ to $\mathbf{v}$ [7]. The general solution for $P(\mathbf{v}, t)$ is not available in an operationally useful form, except in the following two extreme situations:

(i) *The diffusion process.* In this case the velocity $\mathbf{v}(t)$ is assumed to describe Brownian motion such that the effect of a collision is to alter the velocity of the particle by a 'small' amount. Mathematically, $W(\mathbf{v}'|\mathbf{v})$ can be approximated by a second order Kramers–Moyal expansion (in velocity moments) yielding a Fokker–Planck equation for $P(\mathbf{v}, t)$ [4, 5]. In the literature on collision broadening, such a process goes by the name of weak collision model (WCM), and we shall, henceforth employ this nomenclature for describing the diffusion process. In the sequel, we shall use $P(\mathbf{v}, t)$ in the presence of a magnetic field to investigate the characteristic function $\phi(t)$, and from that, compute the spectral line shape $\tilde{\phi}(\omega)$.

(ii) *The Boltzmann–Lorentz model.* The BLM is a 'strong collision model', in contrast to the WCM, wherein the collisions are viewed to alter the direction of the velocity vector by arbitrary angles, keeping the magnitude fixed [7, 8]. Unlike the WCM, the stochastic process $\mathbf{v}(t)$ is now a jump process, and is applicable to a situation of gas-phase spectroscopy in which the emitter is a small particle that suffers collisions with much heavier buffer-gas particles [5, 8]. In yet another interpretation, borrowed

one to obtain a closed-form solution of the master equation (3), which can then be used to calculate $\phi(t)$. We should emphasize that in the WCM, the particle is continually under the influence of dissipative terms. On the other hand, in the BLM, the trajectory of the particle evolves freely, albeit under a magnetic field, until this evolution is disrupted by the next collision event.

The plan of the paper is to investigate the motion of a charged particle in the presence of a magnetic field in both the WCM and the BLM and make a comparative study of the velocity-correlation, the characteristic function and the spectral line shape. The idea is to explore whether the magnetic field, like temperature or pressure, can be used as a control parameter in the study of collision broadening of spectra. The paper is organized as follows. In § 2, we introduce the WCM and the BLM for describing stochastic motion of a charged particle in the presence of a magnetic field, and make a special reference to the respective velocity auto correlation functions. The results for the characteristic function $\phi(t)$ and the line shape function $\tilde{\phi}(\omega)$ for both the WCM and the BLM are presented in § 3. We discuss in the concluding § 4, how the magnetic field can be used to tune the motional narrowing effect, and also offer some comments on possible quantum generalizations of our results.

2. Two distinct models for stochastic dynamics

a. *The weak collision model.* As introduced in § 1, the weak collision model (WCM) describes the diffusion process or the Brownian motion of a tagged particle in a medium (heatbath). Here we analyze the motion when the particle is charged and is under the influence of an external magnetic field. Most of the results are well known in the literature [9, 10], but we still summarize them in order to make a meaningful comparison, later, with the results derived in the Boltzmann–Lorentz model (BLM).

The WCM is characterized by a Langevin equation for a Brownian particle of mass m and charge q in a fluid at temperature T, under the influence of a uniform magnetic field **B**:

$$m\frac{\mathrm{d}\mathbf{v}}{\mathrm{d}t} = q(\mathbf{v}\times\mathbf{B}) - m\gamma\mathbf{v} + \mathbf{f}(t), \tag{4}$$

where γ is the friction coefficient and $\mathbf{f}(t)$ is a stationary Gaussian white noise with zero mean and correlation given by

$$\langle f_i(t) f_j(t')\rangle = \Gamma\delta_{ij}\delta(t-t'), \tag{5}$$

where the indices i and j denote cartesian co-ordinates and Γ is a positive constant which is related to the friction coefficient γ by the so-called fluctuation-dissipation relationship

$$\Gamma = 2m\gamma k_{\mathrm{B}} T. \tag{6}$$

Equation (6) ensures that $\mathbf{v}(t)$, and its moments and correlations starting from the respective initial values, approach equilibrium, asymptotically (as $t\to\infty$), governed by a Maxwellian distribution at temperature T.

While the Langevin approach is based on the equation of motion of a dynamical variable, in the present instance the velocity $\mathbf{v}(t)$, a completely equivalent picture is provided by the Fokker–Planck equation for the function $P(\mathbf{v}, t)$ which defines the

conditional probability that the velocity is $\mathbf{v}(t)$ at time t, given that the velocity is $\mathbf{v}_0$ at $t = 0$. This equation reads [10]

$$\frac{\partial P(\mathbf{v}, t)}{\partial t} = \gamma \nabla_{\mathbf{v}}(\mathbf{v} P(\mathbf{v}, t)) - \frac{q}{m}(\mathbf{v} \times \mathbf{B}) \cdot \nabla_{\mathbf{v}} P(\mathbf{v}, t) + \frac{\Gamma}{2m^2} \nabla_{\mathbf{v}}^2 P(\mathbf{v}, t) \tag{7}$$

with

$$P(\mathbf{v}, t = 0) = \delta(\mathbf{v} - \mathbf{v}_0). \tag{8}$$

As mentioned earlier, eq. (7) for $\mathbf{B} = 0$ is a limiting case of the integro-differential equation (3). It is straightforward to show, from either the Langevin equation (4) or the Fokker–Planck equation (7) that the correlation function of the velocity is [10]

$$\langle v_i(0) v_j(t) \rangle = \left(\frac{k_B T}{m} \right) e^{-\gamma |t|} [\delta_{ij} \cos \omega_c t - \varepsilon_{ijl} b_l \sin \omega_c t + b_i b_j (1 - \cos \omega_c t)], \tag{9}$$

where ω_c is the so-called cyclotron frequency defined as

$$\omega_c = qB/m (B = |\mathbf{B}|), \tag{10}$$

$b_k = B_k / B$ are the direction cosines of the magnetic field $\mathbf{B}$ and ε_{ijl} is the fully antisymmetric tensor of rank 3. A special case of eq. (9) is the auto-correlation function

$$C(t) \equiv \langle \mathbf{v}(0) \cdot \mathbf{v}(t) \rangle = \left(\frac{k_B T}{m} \right) e^{-\gamma |t|} (1 + 2 \cos \omega_c t). \tag{11}$$

b. *The Boltzmann–Lorentz model.* In this approach, the velocity $\mathbf{v}(t)$ is taken to be a jump process; its magnitude is assumed to remain unaltered due to collisions – only the direction changes at random [8]. We may therefore view the velocity vector as a matrix $\mathbf{V}$ in the 'stochastic' space spanned by the states (Ω), where the set $\{\Omega\}$ specifies the Euler angles of the orientation of the velocity. In this space, the matrix $\mathbf{V}$ is diagonal with its elements being given by the possible values of the velocity. Thus, following the notation of ref. [8]

$$(\Omega | (\mathbf{V}) | \Omega_0) = \hat{u}_{\Omega_0} v \delta(\Omega_0 - \Omega)_. \tag{12}$$

where $\hat{u}_{\Omega_0}$ is the unit vector in the direction of $\mathbf{v}$.

Given an initial velocity at time $t = 0$, the velocity at time t is obtained in terms of the average of the time-evolution operator $U(t)$

$$(\Omega | (\mathbf{V}(t)) | \Omega_0) = (\Omega | (\langle U(t) \rangle \mathbf{V}) | \Omega_0), \tag{13}$$

where the brackets $\langle \cdots \rangle$ denote the average over *only* the statistics of the collisions (not the full average implied in § 1 (cf. eq. (2)). Using (12), the above expression simplifies to

$$(\Omega | (\mathbf{V}(t)) | \Omega_0) = v (\Omega | (\langle U(t) \rangle) | \Omega_0) \hat{u}_{\Omega_0}. \tag{14}$$

In the BLM, the collisions are assumed to be Poisson-distributed with a mean rate γ that depends in general on the instantaneous velocity of the particle. The key expression is that of $\langle U(t) \rangle$ in terms of the 'free evolution operator' (i.e., the 'streaming' operator) $U^0(t)$ and the collision operator $\mathbf{J}$. Following ref. [8], this expression is best

written in terms of the Laplace transform of $\langle U(t)\rangle$,

$$\langle \tilde{U}(z)\rangle = \sum_{n=0}^{\infty} \tilde{U}^0(z+\gamma(v))[(\gamma \mathbf{J})\tilde{U}^0(z+\gamma)]^n$$
$$= \tilde{U}^0(z+\gamma(v)) + \tilde{U}^0(z+\gamma(v))(\gamma(v)\mathbf{J}).\langle \tilde{U}(z)\rangle. \tag{15}$$

Finally, since the velocity is completely randomized in direction due to collisions, the collision operator **J** has the following simple matrix representation

$$(\Omega_0|\mathbf{J}|\Omega) = \frac{1}{4\pi}. \tag{16}$$

Having set up the preliminaries of the BLM, we now make a departure from ref. [8] and consider the expression for the matrix element of the free evolution operator $U^0(t)$, when the particle is charged and is under the influence of a magnetic field. This expression is extracted by first writing down the matrix of the velocity at time t in the collision-free case, from (14)

$$(\Omega|\mathbf{V}(t)|\Omega_0) = v(\Omega|U^0(t)|\Omega_0)\hat{u}_{\Omega_0}. \tag{17}$$

Recalling that the Euler angle Ω_0 in the present case is completely specified by the polar angle θ_0 and the azimuthal angle ϕ_0 (figure 1), the unit vector $\hat{u}_{\Omega_0}$ is

$$\hat{u}_{\Omega_0} = (\sin\theta_0\cos\phi_0, \sin\theta_0\sin\phi_0, \cos\theta_0). \tag{18}$$

Secondly, taking the direction of **B** to be the z-axis (cf. figure 1), a direct solution of the equation of motion (i.e., eq. (4) with only the Lorentz term on the right hand side) yields

$$(\Omega|\mathbf{V}(t)|\Omega_0) = v(\sin\theta\cos\phi, \sin\theta\sin\phi, \cos\theta)$$
$$\times \delta(\cos\theta - \cos\theta_0)\delta(\phi - \phi_0 + \omega_c t). \tag{19}$$

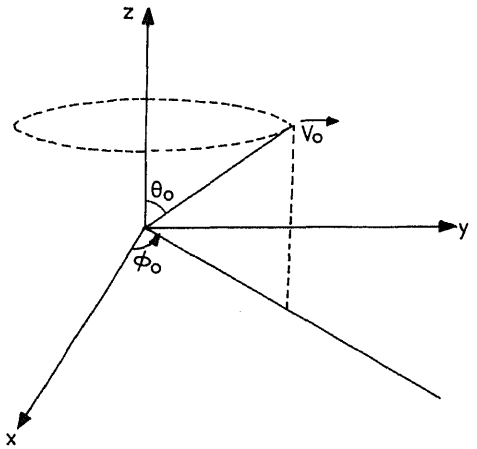

Figure 1. In the absence of collisions, the velocity vector **v** precesses around the direction of the magnetic field **B**, taken along the z-axis. For an initial velocity vector $\mathbf{v}_0 = v\hat{u}_{\Omega_0}$, where $\hat{u}_{\Omega_0} = (\sin\theta_0\cos\phi_0, \sin\theta_0\sin\phi_0, \cos\theta_0)$, the velocity vector after time t is given as $\mathbf{v}(t) = v\hat{u}_{\Omega}(t)$, where $\hat{u}_{\Omega}(t) = (\sin\theta_0\cos\phi(t), \sin\theta_0\sin\phi(t), \cos\theta_0)$ and $\phi(t) = \phi_0 - \omega_c t$.

That is, the velocity vector in the presence of **B** is simply rotated about the z-axis in the clockwise direction by an angle $\omega_c t$, ω_c being the cyclotron frequency. Comparing (19) with (17) and keeping in mind (18), we arrive at

$$(\Omega|\, U^0(t)|\Omega_0) \equiv (\theta, \phi|(U^0(t))|\theta_0, \phi_0) = \delta(\cos\theta - \cos\theta_0)\delta(\phi - \phi_0 + \omega_c t). \tag{20}$$

With the machinery of eqs (15), (16) and (20) at hand, we are now ready to evaluate the autocorrelation function $C(t)$. The latter is given by (cf. eq. (11))

$$C(t) = \langle \mathbf{v}(0)\cdot\mathbf{v}(t)\rangle = \langle v^2 \langle \cos\chi(t)\rangle\rangle, \tag{21}$$

where $\chi(t)$ is the angle between the vectors $\mathbf{v}(0)$ and $\mathbf{v}(t)$, and $\langle\cdots\rangle$ denotes the average over the statistics of collisions, for a fixed value of the magnitude v. (The final average over a Maxwellian distribution of the velocity is indicated by double angular brackets.) For calculational convenience, we rewrite (21) with the aid of the spherical harmonics addition theorem [11]

$$C(t) = \langle v^2 S_v(t)\rangle, \tag{22}$$

where

$$S_v(t) = \frac{4\pi}{3} \sum_{m=-1}^{+1} \langle Y_{1m}(\theta(t), \phi(t))\, Y^*_{1m}(\theta_0, \phi_0)\rangle. \tag{23}$$

In terms of the averaged time-evolution operator $\langle U(t)\rangle$, eq. (23) can be further re-expressed as

$$S_v(t) = \frac{4\pi}{3} \sum_{m=-1}^{+1} \frac{1}{4\pi} \int d\Omega_0 d\Omega\, Y_{1m}(\Omega)(\Omega|\langle U(t)\rangle|\Omega_0)\, Y^*_{1m}(\Omega_0). \tag{24}$$

We turn our attention to the evalution of $S_v(t)$ and in particular its Laplace transform $\tilde{S}_v(z)$ by employing the series solution for $\langle \tilde{U}(z)\rangle$ and the matrix representation of the collision operator **J**, in the BLM (cf. eqs (15) and (16)). Thus

$$\begin{aligned}
\tilde{S}_v(z) = \frac{1}{3} \sum_{m=-1}^{+1} \Bigg[& \int d\Omega_0 d\Omega\, Y_{1m}(\Omega)(\Omega|\, \tilde{U}^0(z+\gamma(v))|\Omega_0)\, Y^*_{1m}(\Omega_0) \\
& + \int d\Omega d\Omega'\, Y_{1m}(\Omega)(\Omega|\, \tilde{U}^0(z+\gamma(v))|\Omega') \\
& \times \frac{\gamma(v)}{4\pi} \cdot \sum_{n=0}^{\infty} \left[\frac{\gamma(v)}{4\pi} \int d\Omega_1\, d\Omega_2 (\Omega_2|\, \tilde{U}^0(z+\gamma(v))|\Omega_1) \right]^n \\
& \times \int d\Omega_0 d\Omega'_0 (\Omega'_0|\, \tilde{U}^0(z+\gamma(v))|\Omega_0)\, Y^*_{1m}(\Omega_0) \Bigg] \\
= \frac{1}{3} \sum_{m=-1}^{+1} \Bigg[& \int d\Omega_0 d\Omega\, Y_{1m}(\Omega)(\Omega|\, \tilde{U}^0(z+\gamma(v))|\Omega_0)\, Y^*_{1m}(\Omega_0) \\
& + \frac{\gamma(v)[\int d\Omega d\Omega'\, Y_{1m}(\Omega)(\Omega|\, \tilde{U}^0(z+\gamma(v))|\Omega')][\int d\Omega_0 d\Omega'_0 \ldots.]}{4\pi \quad 1 - (\gamma(v)/4\pi)\int d\Omega_1 d\Omega_2 (\Omega_2|\, \tilde{U}^0(z+\gamma(v))|\Omega_1)} \Bigg].
\end{aligned} \tag{25}$$

Hence, the special property of the collision operator, indicated in (20), has enabled us to write $S_v(t)$ entirely in terms of the matrix element of the streaming operator: $\tilde{U}^0(z+\gamma(v))$.

In evaluating (25), we use the following definition of the spherical harmonics [11]

$$Y_1^m(\Omega) = \sqrt{\frac{(2l+1)}{4\pi}\cdot\frac{(l-m)!}{(l+m)!}}\, P_l^m(\cos\theta)\mathrm{e}^{im\phi}. \tag{26}$$

It is then straightforward to show from (20) that

$$\int \mathrm{d}\Omega\mathrm{d}\Omega' Y_{1m}(\Omega)(\Omega|\tilde{U}^0(z+\gamma(v))|\Omega')$$

$$= \int \mathrm{d}\Omega_0\,\mathrm{d}\Omega_0'(\Omega_0'|\tilde{U}^0(z+\gamma(v))|\Omega_0)Y_{1m}^*(\Omega_0) = 0. \tag{27}$$

Thus the numerator in the second term on the right of eq. (25) vanishes identically and we are left with simply the first term, which yields

$$\tilde{S}_v(z) = \frac{1}{3}\left[\frac{1}{z+\gamma(v)} + \frac{1}{z+\gamma(v)-i\omega_c t} + \frac{1}{z+\gamma(v)+i\omega_c t}\right]. \tag{28}$$

Taking the inverse Laplace transform of (28) and using (23), we finally obtain

$$C(t) = \tfrac{1}{3}\langle v^2\exp(-\gamma(v)|t|)\rangle(1+2\cos\omega_c t). \tag{29}$$

If the collision rate were velocity independent, i.e., $\gamma(v)=\gamma$, (29) would be identical in form to the correlation function in the WCM, recalling that the mean squared velocity is given by its 'equipartition' value (cf. eq. (11)). However, in the BLM [8]

$$\gamma(v) = \pi n_p a^2 v, \tag{30}$$

where n_p is the number of scatterers per unit volume and a is an effective scattering radius. Hence, under a Maxwell-Boltzmann distribution $p(v)$, (29) reduces to

$$C(t) = \tfrac{1}{3}(1+2\cos\omega_c t)\cdot\int_0^\infty \mathrm{d}v v^2 p(v)\mathrm{e}^{-\gamma(v)|t|}, \tag{31}$$

where

$$p(v) = \sqrt{\frac{2}{\pi}}\left(\frac{m}{k_B T}\right)^{3/2}\cdot\exp\left(-\frac{mv^2}{2k_B T}\right). \tag{32}$$

The integral in (31) may be viewed as a continuous superposition of exponential correlations (in time) leading to a correlation function that would, in general, have a non-exponential behaviour. Such behaviour is known to occur in the theory of jump stochastic processes, such as in the case of the "Kangaroo process" [7, 12, 13]. Substituting the explicit form of $\gamma(v)$ from (30) we obtain

$$C(t) = \frac{k_B T}{m}(1+2\cos\omega_c t)\times[1+4(vt)^2+\tfrac{4}{3}(vt)^4]\exp(v^2t^2)erfc(v|t|)$$

$$-\frac{v|t|}{\sqrt{\pi}}(3+\tfrac{4}{3}v^2t^2), \tag{33}$$

where

$$v \equiv \pi_{,} a^2 \cdot \sqrt{\frac{k_B T}{2m}} \tag{34}$$

and the complementary error function is defined by

$$erfc(v|t|) \equiv \frac{2}{\sqrt{\pi}} \int_{v|t|}^{\infty} dx \exp(-x^2). \tag{35}$$

3. The characteristic function and the spectral lineshape

a. *The weak collision model.* The characteristic function $\phi(t)$ is defined in (1) and (2). If we employ the definition (2), the evaluation of $\phi(t)$ can be carried out, using the Fokker–Planck equation (7). Equivalently, we can calculate $\phi(t)$ from definition (1) by employing the full phase space equation for the probability [10]. However, we follow here a simpler method by taking cognizance of the fact that the underlying stochastic process in the WCM is a Gaussian–Markov process. Thus, all cumulants above the two-point vanish identically [4] and hence, (2) yields

$$\phi(t) = \exp\left[-\frac{1}{2} \sum_{jl} k_j k_l \int_0^t dt' \int_0^t dt'' \langle v_j(t') v_l(t'') \rangle \right]. \tag{36}$$

Further, using stationarity, the above expression simplifies to

$$\phi(t) = \exp\left[-\frac{1}{2} \sum_{jl} k_j k_l \int_0^t d\tau (t-\tau) \langle v_j(0) v_l(t) \rangle \right]. \tag{37}$$

We specialize, now, to the geometry of figure 1 in which the external field is taken along the z-axis, in order to, explicitly, demonstrate the anisotropic nature of the diffusion. The velocity-correlation function is already given in (9) using which we derive

$$\phi(t) = \exp -\tfrac{1}{2}[(k_x^2 + k_y^2) S_\perp(t) + k_z^2 S_\parallel(t)], \tag{38}$$

where $S_\parallel(t)$ and $S_\perp(t)$ are precisely the "variance of the displacement" in the longitudinal and transverse directions respectively [10]

$$S_\parallel(t) = \frac{2k_B T}{m\gamma^2} [\gamma t - 1 + \exp(-\gamma t)], \tag{39}$$

$$S_\perp(t) = \frac{2k_B T}{m(\gamma^2 + \omega_c^2)^2} [\gamma t(\gamma^2 + \omega_c^2) - (\gamma^2 - \omega_c^2) + \exp(-\gamma t)[(\gamma^2 - \omega_c^2)\cos(\omega_c t) - 2\gamma\omega_c \sin(\omega_c t)]]. \tag{40}$$

It is evident that the longitudinal component is associated with the free diffusive behaviour [14], as the motion remains unaffected along the direction of the magnetic field. The transverse component, on the other hand, exhibits the interplay of diffusive motion characterized by the collision rate γ and deterministic orbital motion characterized by the cyclotron frequency ω_c. Of course, in the absence of the magnetic field, $\omega_c = 0$, and (38) reduces to the result in the usual WCM [7].

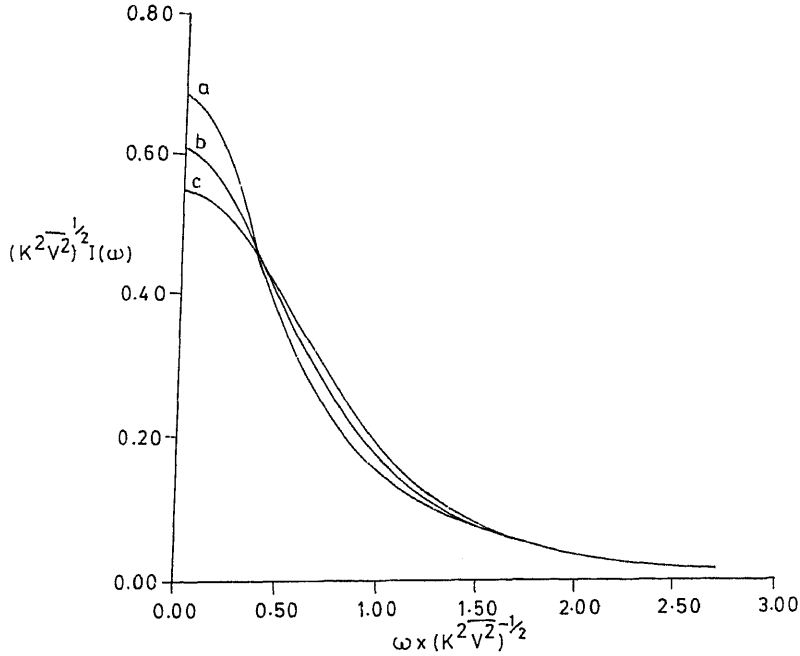

Figure 2. The collision broadened line shape in the weak collision model in the presence of magnetic field. Curves a, b, c correspond to $\bar{\omega}_c = 1$, $\bar{\omega}_c = 0{\cdot}7$ and $\bar{\omega}_c = 0$ respectively, where $\bar{\omega}_c = \omega_c(k^2\overline{v^2})^{-1/2}$ and $\bar{\gamma} = 1$.

We turn our attention to the issue of what influence the magnetic field has on the lineshape, especially, in the context of collision-broadening. For the sake of definiteness, we choose $k_y = k_z = 0$ and $k_x = k$. As mentioned earlier, the spectral lineshape is obtained from [5]

$$I(\omega) = \frac{1}{\pi}\mathrm{Re}\int_0^\infty dt \exp(-i\omega t)\phi(t). \tag{41}$$

We substitute for $S_\perp(t)$ from (40) into (38) and evaluate the integral in (41), numerically. The lineshape is plotted in figure 2 in terms of scaled parameters $\bar{\omega}_c(\bar{\omega}_c \equiv \omega_c(k^2\langle v^2\rangle)^{-1/2})$ and $\bar{\gamma}(\bar{\gamma} \equiv \gamma(k^2\langle v^2\rangle)^{-1/2})$. For a fixed value of $\bar{\gamma}$, which can be ascertained by fixing, say the temperature and pressure, the spectral lines are seen to show narrowing as $\bar{\omega}_c$ is increased. Thus the magnetic field seems to have a similar constraining effect as the collisions do on the velocity of the emitter, leading to a motional narrowing-like phenomenon.

b. *The Boltzmann–Lorentz model.* Our aim in this sub-section is to compute the characteristic function (cf. eq. (2)) and its Fourier transform in the BLM, and compare the respective results with those derived in the WCM (§ 3.a). Before we do this, it is useful to recapitulate the basic premise of the BLM. The time interval 0 to t is divided into $(n+1)$ parts at instants $t_1, t_2, \cdots t_n$, at which time the tagged particle is assumed to undergo collisions with the scatterers. The instants $t_1, t_2 \cdots$ are randomly distributed and assumed to be governed by

Poisson statistics. In-between collisions, the velocity vector of the particle evolves under the influence of the applied magnetic field, and the corresponding evolution operator $G^0(t)$ has matrix elements (cf. eq. (19))

$$(\Omega|G^0(t)|\Omega_0) = \delta(\cos\theta - \cos\theta_0)\delta(\phi - \phi_0 + \omega_c t)\exp\left[iv\left[tk_z\cos\theta_0 + \frac{\sin\theta_0}{\omega_c}[k_x(\sin\phi_0 - \sin\phi) + k_y(\cos\phi - \cos\phi_0)]\right]\right]. \tag{42}$$

With the operator $G^0(t)$ at hand, the full time evolution operator $\langle U(t)\rangle$ has the Laplace transform given by the series solution in (15) except, $\tilde{U}^0(z+\gamma(v))$ is replaced by $\tilde{G}^0(z+\gamma(v))$. The most simplifying result of the BLM that emerges from the structure of the collision operator **J** in (16) is that the matrix of $\langle\tilde{U}(z)\rangle$ is expressible entirely in terms of $\tilde{G}^0(z+\gamma(v))$. Thus [8]

$$\frac{1}{4\pi}\int d\Omega_0 d\Omega(\Omega|(\langle\tilde{U}(z)\rangle)|\Omega_0) = \frac{\tilde{C}_0(z+\gamma(v))}{1-\gamma(v)\tilde{C}_0(z+\gamma(v))}, \tag{43}$$

where

$$\tilde{C}_0(z+\gamma(v)) \equiv \frac{1}{4\pi}\int d\Omega_0 d\Omega(\Omega|(\tilde{G}^0(z+\gamma(v))|\Omega_0). \tag{44}$$

Using (42), we easily obtain

$$\tilde{C}_0(z+\gamma(v)) = \int_0^\infty dt\exp[-(z+\gamma(v))t] \times \frac{1}{4\pi}\int \sin\theta_0 d\theta_0 \int d\phi_0 \exp\left[iv\left(k_z t\cos\theta_0 + \frac{\sin\theta_0}{\omega_c}[k_x(\sin\phi_0 - \sin(\phi_0 - \omega_c t)) + k_y(\cos(\phi_0 - \omega_c t) - \cos\phi_0)]\right)\right]. \tag{45}$$

We are now ready to write down the expression for the spectral lineshape in the BLM. Recall from (41) that

$$I(\omega) = \frac{1}{\pi}\mathrm{Re}\lim_{\delta\to 0}\phi(z), \quad z = -i\omega + \delta, \tag{46}$$

where

$$\tilde{\phi}(z) = \int_0^\infty dv p(v)\frac{\tilde{C}_0(z+\gamma(v))}{1-\gamma(v)\tilde{C}_0(z+\gamma(v))}, \tag{47}$$

$p(v)$ being given by (32). As before, we specialize to the geometry for which $k_y = k_z = 0$ and $k_x = k$ and compute $\tilde{C}_0(z+\gamma(v))$ from (44) by numerical integrations. The results are then substituted in (46) and one additional numerical integration is performed in order to derive $\tilde{\phi}(z)$. The resultant $I(\omega)$ is again plotted (figure 3) in terms of the scaled parameters $\bar{\gamma}$ and $\bar{\omega}_c$, defined earlier, Once again we notice a narrowing of the spectral line with increasing magnetic field although the lines are more intense in this case than in the WCM.

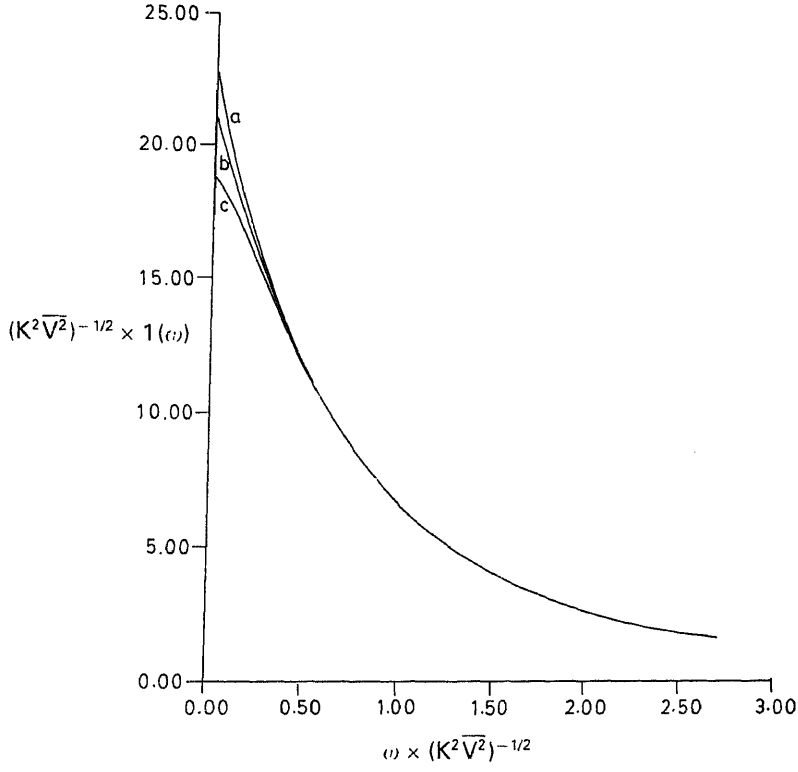

Figure 3. The collision broadened line shape in the Boltzmann Lorentz model in the presence of magnetic field. Curve a corresponds to $\bar{\omega}_c = 1$, and curves b and c to $\bar{\omega}_c = 0{\cdot}7$ and 0 respectively, where $\bar{\omega}_c = \omega_c(k^2\overline{v^2})^{-1/2}$. All curves correspond to $(n_p a^2/k) = 1$ and $\bar{\gamma} = 1$.

4. Summary and conclusions

In this paper, we have employed stochastic modelling for studying classical motion of a charged particle in the presence of a magnetic field. Two distinct stochastic models have been used—one based on diffusion processes, the other on jump processes. These are known in the literature on collision broadening of spectral lines as the weak collision model (WCM) and the Boltzmann–Lorentz model (BLM) respectively. We have made a comparative investigation of the influence of the magnetic field on the spectral line shape, in the WCM and BLM. One of the common features of both these models is *narrowing* of spectral lines, as the magnetic field is increased. Normally, narrowing results from an enhanced rate of collisions, which can be effected by raising the temperature or pressure of the gas. Thus one of our findings in this paper is that the magnetic field can be used as a tuning parameter, in addition to the temperature and pressure, in modulating the width of the spectral lines, in gas-phase spectroscopy.

Apart from the application to spectroscopy, the present study also has a bearing on plasma physics. The magnetic field is, of course a ubiquitous feature in plasma

physics and therefore, the results derived here are expected to be of some relevance in magneto-hydrodynamics. One of the sensitive tools for measuring the temperature inside a hot plasma (such as the one present in a tokomak) is to analyze the width of a spectral line emitted by an ion. This analysis would therefore have to take into account the alteration of the width by the magnetic field, as has been demonstrated in this paper.

Our treatment has been entirely classical. It is important to extend the method to quantum mechanics, especially in the context of magneto-transport of an electron, which is of interest in the measurement of Hall coefficient and magneto resistance, in solid state physics, Another intriguing question is what effect does dissipation (induced by collisions in the present context) have on the Landau diamagnetism, which is inherently a quantum phenomenon. These issues will be discussed in a forthcoming publication.

References

[1] S Ichimaru, *Basic principles of plasma physics-Statistical approach* (Benjamin, Reading, Mass, 1973)

[2] A Jayannavar and N Kumar, *J. Phys.* **A14**, 1399 (1981); also see A Jayannavar, Ph. D. Thesis (Indian Institute of Science, Bangalore, 1982) (unpublished)

[3] R G Breene Jr. *Rev. Mod. Phys.* **29**, 94 (1957)
A comprehensive review of recent activities in the field can be found in spectral line shapes, *Proc. IX Int. Conf. Torun, 1988*, edited by J Szudy (Ossotineum, Wrockaw, 1989) vol. 5

[4] N G Van Kampen, *Stochastic processes in physics and chemistry* (North-Holland, Amsterdam, 1981)

[5] S G Rautian and I I Sobelman, *Usp. Fiz. Nauk* **90**, 209 (1966); [*Sov. Phys. Usp.* **9**, 701 (1967)]
S Dattagupta, *Pramana – J. Phys.* **9**, 203 (1977)

[6] C P Slichter, *Principles of magnetic resonance* (Harper Row, New York, 1963)

[7] S Dattagupta, *Relaxation phenomena in condensed matter physics* (Academic Press, Orlando, 1987)

[8] S Dattagupta and L A Turski, *Phys. Rev.* **A32**, 1439 (1985)

[9] B Kursunoglu, *Ann. Phys. (NY)* **17**, 259 (1962)

[10] S Revathi and V Balakrishnan, *J. Math. Phys. Sci.* **26**, 213 (1992)

[11] See for instance, A Messiah, *Quantum Mechanics* (North-Holland, Amsterdam, 1965) vol. 2, p. 13

[12] V Balakrishnan, in *Stochastic processes–Formalisms and applications, Lect. notes in physics* edited by G S Agarwal and S Dattagupta (Springer Verlag, Berlin, 1983)

[13] A Brissaud and U Frisch, *J. Math. Phys.* **15**, 524 (1974)

[14] S Chandrasekhar, *Rev. Mod. Phys.* **15**, 1 (1943)

PRAMANA
— journal of
physics

© Printed in India

Vol. 47, No. 3,
September 1996
pp. 211–224

Stochastic motion of a charged particle in a magnetic field: II Quantum Brownian treatment

SUSHANTA DATTAGUPTA and JAGMEET SINGH*
School of Physical Sciences, Jawaharlal Nehru University, New Delhi 110067, India
*Also at: Physics Department, S.G.T.B. Khalsa College, University of Delhi, Delhi 110007, India

MS received 2 May 1996

Abstract. We study the quantum Brownian motion of a charged particle in the presence of a magnetic field. From the explicit solution of a quantum Langevin equation we calculate quantities such as the velocity correlation function and the mean-squared displacement. Our calculated expressions contain as special cases the motion of a *classical* particle in a magnetic field and that of a *free* (but quantum) particle, in a dissipative environment.

Keywords. Magnetic field-induced dynamics; quantum Langevin equation; velocity correlation; quantum diffusion.

PACS Nos 05·40; 42·50; 41·70

1. Introduction

In the preceding paper [1] (henceforth referred to as I), we have considered the dissipative dynamics of a charged particle in a magnetic field. Two distinct stochastic models were employed: one based on diffusion processes as appropriate to classical Brownian motion, the other based on jump processes as in the Boltzmann–Lorentz model of classical kinetic theory. Our objective here is to extend the previous classical treatment to the realm of quantum mechanics, for the present to the case of diffusion processes. The case of quantum Boltzmann–Lorentz model will be dealt with later.

The quantum dynamics of a charged particle in the presence of a magnetic field is characterized by coherent (Larmor) precession in circular orbits around the magnetic field. This occurs at a rate given by the cyclotron frequency $\omega_c = |e|B/mc$, where e is the charge, B is the strength of the field, m is the mass of the particle and c is the speed of light. Dissipation leads to incoherence in the motion, brought about by a characteristic rate generally known as the friction coefficient γ. When $\gamma \gg \omega_c$, one expects to see classical-like evolution in an otherwise quantum problem. In addition to γ and ω_c, there is of course a third frequency in the system, $\nu = k_B T/\hbar$, where k_B is the Boltzmann constant, T is temperature and $\hbar$ is the Planck constant. The frequency ν is ubiquitous in a quantum system at a finite temperature characterizing the interplay of thermal and quantal fluctuations. It can be as large as $10^{11}\,s^{-1}$ even at such low temperatures as 1 K which means that one has to probe within a time 10^{-11} s in order to see quantum coherence effects. From the preceding discussion it follows that we are in a situation in which we expect to see different behaviour in different regimes of the three competing

frequency scales set by ω_c, γ and ν. Furthermore, it is also evident that the case at hand belongs to a large class of problems which falls in the domain of quantum dissipative systems. Such problems permeate wide ranging areas of physics including quantum optics, condensed matter physics, chemical physics and quantum measurement theory [2]. Thus, the presently studied system of quantum Brownian motion of a charged particle in the presence of a magnetic field can be viewed as a paradigm of irreversible behaviour of a quantum system which is otherwise governed by unitary evolution.

Having presented the general background to our present investigation, it is important for us to clarify what precisely is meant by "quantum Brownian motion". In answering this question we follow the method of Caldeira and Leggett (CL) in which a system-plus-reservoir approach is adopted [3]. The reservoir is constituted of an infinitely large number of quantum harmonic oscillators which are linearly coupled to the system coordinates. While the details of this model will be discussed later, it suffices for the present to state that by choosing a particular density of states for the reservoir oscillators, CL show that in the appropriate classical limit (i.e. $\nu \to \infty$), the probability distribution in phase space follows a Fokker–Planck equation. Since the latter and its cousin, the Langevin equation for position and momentum variables, are believed to provide a theoretical framework describing classical Brownian motion, CL proceed to extend the validity of the model to the quantum domain, and define the resultant process as the "quantum Brownian motion". We shall follow the same approach here, with an additional input of the magnetic field. In this sense, the present treatment may be viewed as the quantum version of the treatment in I, for diffusion processes.

The CL model is based on a Hamiltonian written down by Feynman and Vernon [4]. There is a lengthy discussion about the justification for the chosen form of the coupling between the system and reservoir oscillators, in a review article [5]. The idea is to consider the time evolution of the so called reduced density operator, obtained from the actual density operator by tracing out the reservoir variables. The Weyl mapping is used to obtain the appropriate Wigner distribution function from the reduced density operator. The Wigner function follows the Fokker–Planck equation in the classical limit, for a specific choice of the density of states for the reservoir oscillators [3]. While this approach may be viewed to be based on the Schrödinger-like picture of quantum mechanics, there is a corresponding Heisenberg-like picture adopted by authors such as Ford *et al* [6], Zwanzig [7] and Ford *et al* [8]. In this, one starts from the same Feynman–Vernon Hamiltonian equations of motion for the position and momentum variables for both the system and the reservoir, integrates out the reservoir variables, and obtains the quantum Langevin equation for the system, under identical assumption about the density of states for the reservoir oscillators, as made by CL. The derivation of the quantum Langevin equation can be easily extended to incorporate the presence of the magnetic field [9]. We find the resultant equation extremely amenable for analyzing the dissipative magneto-transport of a charged particle.

With the preceding background to the aim and scope of the paper the outline is as follows. In § 2, we introduce the basic Feynman–Vernon Hamiltonian, both in the absence and presence of magnetic field and sketch the steps leading to the quantum Langevin equation. The solution of the latter plus the results on velocity correlation function are presented in § 3. The question of mean-squared displacement and the concomitant diffusion behaviour are dealt with in § 4. Finally, § 5 contains a few concluding remarks.

In this section, we give an outline of the derivation of the quantum version of the classical Langevin equation, following the treatment of Ford *et al* [8]. The method uses a system-plus-reservoir approach in which the reservoir coordinates are integrated out from the equations of motion resulting from an underlying Hamiltonian or Lagrangian. In fact, the method is a straight-forward generalization of the derivation of the classical Langevin equation, as in Zwanzig [7]. The starting point is the Hamiltonian, written down by Feynman and Vernon [4]:

$$H = \frac{p^2}{2m} + V(x) + \sum_j [p_j^2/_{2m_j} + \tfrac{1}{2} m_j \omega_j^2 (q_j - x)^2], \tag{1}$$

where p and x are the momentum and position coordinates for the system-particle while p_j and q_j are the corresponding variables for the reservoir. It suffices for the present to consider a one-dimensional case though in the sequel we will be required to treat a three-dimensional model when we discuss the motion of a charged particle in the presence of a magnetic field. The momentum and coordinate variables satisfy the commutation relations

$$[x, p] = i\hbar$$

$$[q_j, p_k] = i\hbar\delta_{jk}. \tag{2}$$

The equations of motion read

$$\dot{x} = [x, H]/i\hbar = p/m,$$

$$\dot{p} = [p, H]/i\hbar = -V'(x) + \sum_j m_j \omega_j^2 (q_j - x),$$

$$\dot{q}_j = [q_j, H]/i\hbar = p_j/m_j,$$

$$\dot{p}_j = [p_j, H]/i\hbar = -m_j \omega_j^2 (q_j - x). \tag{3}$$

Eliminating the momentum variables, we obtain

$$m\ddot{x} + V'(x) = \sum_j m_j \omega_j^2 (q_j - x), \tag{4}$$

$$\ddot{q}_j + \omega_j^2 q_j = \omega_j^2 x. \tag{5}$$

Barring the dependence on the system coordinate x on the right hand side, (5) simply describes harmonic motion and hence the general solution of (5) is given by

$$q_j(t) = q_j^h(t) + x(t) - \int_{-\infty}^{t} dt' \dot{x}(t') \cos[\omega_j (t - t')], \tag{6}$$

where q_j^h is the solution of the homogeneous equation

$$q_j^h(t) = q_j(0)\cos(\omega_j t) + p_j(0)\frac{\sin(\omega_j t)}{m_j \omega_j}. \tag{7}$$

It is interesting to note that our starting Hamiltonian (1) is time independent and hermitian and therefore, would normally yield unitary evolution. However by choosing the *retarded* solution of the inhomogeneous equation (5) we have (tacitly) induced breaking of the time-reversal invariance. Substitute (6) into (4), to obtain the Langevin equation

$$m\ddot{x} + \int_{-\infty}^{t} d\tau \mu(t-\tau)\dot{x}(\tau) + V'(x) = f(t), \tag{8}$$

where the friction or the memory function $\mu(t)$ is given by

$$\mu(t) = \sum_j m_j \omega_j^2 \cos(\omega_j t) \Theta(t), \tag{9}$$

$\Theta(t)$ being the Heaviside step function, and the 'noise' is given by

$$f(t) = \sum_j m_j \omega_j^2 \left[q_j cos(\omega_j t) + \frac{p_j}{m_j \omega_j} \sin(\omega_j t)\right], \tag{10}$$

where q_j and p_j are time independent operators which obey commutation rules given in (2).

It is evident that the noise is a quantum mechanical operator, whose auto correlation and commutator can be obtained by assuming that in the distant past, the harmonic oscillator reservoir is in thermal equilibrium, at a temperature T. Thus, we can write [8]

$$\langle \{f(t), f(t')\} \rangle = \frac{2}{\pi} \int_0^\infty d\omega \, \mathrm{Re}[\tilde{\mu}(\omega + i0^+)] \hbar\omega \coth\left(\frac{\hbar\omega}{2k_B T}\right) \cos[\omega(t-t')], \tag{11}$$

$$\langle [f(t), f(t')] \rangle = \frac{2}{i\pi} \int_0^\infty d\omega \, \mathrm{Re}[\tilde{\mu}(\omega + i0^+)] \hbar\omega \sin[\omega(t-t')]. \tag{12}$$

Here we have defined the Laplace transform of the memory function as

$$\tilde{\mu}(s) = \int_0^\infty dt \exp(ist)\mu(t), \quad \mathrm{Im}\, s > 0. \tag{13}$$

Equations (11) and (12) completely characterize quantum Langevin equation (8).

As in the case of classical Langevin equation, it is useful to consider as a special case, constant "friction". The memory kernel $\mu(t-\tau)$ is then replaced by $m\gamma\delta(t-\tau)$, so that $\mathrm{Re}[\tilde{\mu}(\omega + i0^+)]$ reduces to $m\gamma$, a constant. In that case we have the ordinary Langevin equation:

$$m\ddot{x} + m\gamma\dot{x} + V'(x) = f(t), \tag{14}$$

where now (cf. eqs (11) and (12))

$$\langle \{f(t), f(t')\} \rangle = \frac{2m\gamma}{\pi} \int_0^\infty d\omega \hbar\omega \coth\left(\frac{\hbar\omega}{2k_B T}\right) \cos[\omega(t-t')], \tag{15}$$

$$\langle [f(t), f(t')] \rangle = \frac{2m\gamma}{i\pi} \int_0^\infty d\omega \hbar\omega \sin[\omega(t-t')]. \tag{16}$$

Note the intriguing fact that the underlying stochastic process is still non-Markovian,

of (15) reduces to a term proportional to $\delta(t-\tau)$, restoring Markovianness (cf. eq. (5) of I).

We now turn our attention to the situation in which the particle constituting the system is electrically charged and under the influence of an external magnetic field **B**. The Hamiltonian in (1) is then generalized to [9]

$$H=\frac{1}{2m}\left(\mathbf{p}-\frac{e}{c}\mathbf{A}\right)^2+V(\mathbf{r})+\sum_j\left[\frac{\mathbf{p}_j^2}{2m_j}+\frac{1}{2}m_j\omega_j^2(\mathbf{q}_j-\mathbf{r})^2\right], \tag{17}$$

where e is the charge of the particle and **A** is the vector potential, in terms of which

$$\mathbf{B}=\nabla\times\mathbf{A}. \tag{18}$$

As before (cf. eq. (2)), the commutation relations are

$$[\mathbf{r}_\alpha, p_\beta]=i\hbar\delta_{\alpha\beta},\quad [q_{j\alpha}, p_{k\beta}]=i\hbar\delta_{jk}\delta_{\alpha\beta}, \tag{19}$$

where the Greek symbols stand for the cartesian indices x, y and z.

The equations of motion for the reservoir operators are simply the three-dimensional generalization of the corresponding equations listed in (3), whereas those for the particle have additional terms due to the presence of the magnetic field. In particular, the generalized version of (4) reads [9]

$$m\ddot{\mathbf{r}}+\nabla V(\mathbf{r})=\sum_j m_j\omega_j^2(\mathbf{q}_j-\mathbf{r})+\frac{e}{c}(\mathbf{v}\times\mathbf{B}). \tag{20}$$

We may emphasize that the only additional contribution comes from the quantum form of the Lorenz force term. Furthermore, since there is no dependence on the vector potential **A** in (20), the present treatment is completely gauge-independent [10].

The rest of the steps are exactly as earlier, leading finally to the following quantum Langevin equation for a charged particle in the presence of a magnetic field

$$m\ddot{\mathbf{r}}+\nabla V(\mathbf{r})+\int_{-\infty}^{t}\mathrm{d}t'\,\mu(t-t')\dot{\mathbf{r}}(t')-\frac{e}{c}(\dot{\mathbf{r}}\times\mathbf{B})=\mathbf{f}(t). \tag{21}$$

The spectral properties of $\mathbf{f}(t)$ are the same as before i.e. they are independent of the B-field as one would expect. These are quoted here (see eqs (23) and (24) below) for only the memory-less case in which (21) reduces to

$$m\ddot{\mathbf{r}}+\nabla V(\mathbf{r})+m\gamma\dot{\mathbf{r}}(t)-\frac{e}{c}(\mathbf{v}\times\mathbf{B})=\mathbf{f}(t). \tag{22}$$

The auto-correlation and the commutator of $\mathbf{f}(t)$ are given by (cf. eqs (15) and (16))

$$\langle\{f_\alpha(t), f_\beta(t')\}\rangle=\delta_{\alpha\beta}\frac{2m\gamma}{\pi}\int_0^\infty \mathrm{d}\omega\hbar\omega\coth\left(\frac{\hbar\omega}{2k_\mathrm{B}T}\right)\cos[\omega(t-t')], \tag{23}$$

$$\langle[f_\alpha(t), f_\beta(t')]\rangle=\delta_{\alpha\beta}\frac{2m\gamma}{i\pi}\int_0^\infty \mathrm{d}\omega\hbar\omega\sin[\omega(t-t')]. \tag{24}$$

Equation (22) is of the same form as its classical counterpart (cf. (4) of I) except that the spectral properties of the noise (now an operator) are much richer in structure (compare

(23) and (24) with (5) of I). As commented earlier, the underlying stochastic process is now non-Markovian and therefore, unlike the classical case, there is no appropriate Fokker–Planck description of the dynamics. Hence, for calculational purposes, it is convenient to directly employ the Langevin equation (22), as we shall discuss in the next section.

3. Velocity correlation

In this section we explicitly solve the quantum Langevin equation (22) in the memoryless case, and analyze the velocity auto-correlation function. For the sake of simplicity we ignore the potential energy $V(\mathbf{r})$. Further, we assume that the magnetic field is directed along the z-axis. The motion along z is merely that of a free, quantum particle in a dissipative environment, while that in the xy-plane is described by the equations

$$\ddot{x}+\gamma\dot{x}-\omega_c\dot{y}=\frac{1}{m}f_x(t)$$

$$\ddot{y}+\gamma\dot{y}+\omega_c\dot{x}=\frac{1}{m}f_y(t), \tag{25}$$

where ω_c is the cyclotron frequency (cf. § I)

$$\omega_c=eB/mc. \tag{26}$$

Introducing

$$Z=x+iy,$$

$$F=f_x+if_y,$$

and

$$\bar{\gamma}=\gamma+i\omega_c, \tag{27}$$

(25) can be expressed in the compact form

$$\ddot{Z}+\bar{\gamma}\dot{Z}=\frac{F(t)}{m}, \tag{28}$$

whose solution reads

$$Z(t)=Z(t_0)+\frac{\dot{Z}(t_0)}{\gamma}[1-\exp(-\bar{\gamma}(t-t_0))]$$

$$+\int_{t_0}^{t}d\tau\exp(-\bar{\gamma}\tau)\int_{t_0}^{\tau}dt'\exp(\bar{\gamma}t')\frac{F(t')}{m}. \tag{29}$$

Without loss of generality, we may choose

$$Z(t_0)=0. \tag{30}$$

Corresponding to (29), we have

$$\dot{Z}(t)=\dot{Z}(t_0)\exp[-\bar{\gamma}(t-t_0)]+\exp(-\bar{\gamma}t)\int_{t_0}^{t}dt'\exp(\bar{\gamma}t')\frac{F(t')}{m}. \tag{31}$$

Using the definition of Z as in (27), the correlation function can be alternately expressed as

$$C(t,t') = \langle v_x(t)v_x(t') + v_y(t)v_y(t')\rangle + i\langle(\mathbf{v}(t)\times\mathbf{v}(t'))_Z\rangle. \tag{33}$$

From (31)

$$C(t,t') = \langle|\dot{Z}(t_0)|^2\rangle\exp[-\bar{\gamma}(t-t_0)-\bar{\gamma}^*(t'-t_0)] + \frac{1}{m^2}\exp(-\bar{\gamma}t-\bar{\gamma}^*t')\int_{t_0}^{t}d\tau\int_{t_0}^{t'}d\tau'\exp(\bar{\gamma}\tau+\bar{\gamma}^*\tau')\langle F(\tau)F(\tau')\rangle, \tag{34}$$

where we have used the fact that the initial velocity $\dot{Z}(t_0)$ is uncorrelated with $F(\tau)$ (from causality) and that

$$\langle F(\tau)\rangle = 0. \tag{35}$$

Since we are ultimately going to take the limit $t_0 = -\infty$, we may ignore the first term in (34) from subsequent analysis. Furthermore, we have (cf. eq. (27))

$$\langle F(\tau)F^+(\tau')\rangle = \langle f_x(\tau)f_x(\tau')\rangle + \langle f_y(\tau)f_y(\tau')\rangle, \tag{36}$$

which, from (23) and (24), can be further expressed as

$$\langle F(\tau)F^+(\tau')\rangle = \frac{m\gamma}{\pi}\int_{-\infty}^{\infty}d\omega\hbar\omega\exp[i\omega(\tau-\tau')]\left\{\coth\left(\frac{\hbar\omega}{2k_BT}\right)-1\right\}. \tag{36'}$$

Substituting (36) in (34), and integrating τ and τ', and taking the limit $t_0 = -\infty$, we finally obtain

$$C(t,t') = \frac{1}{m\pi}\int_{-\infty}^{\infty}d\omega\frac{\gamma}{\gamma^2+(\omega+\omega_c)^2}\hbar\omega\left\{\coth\left(\frac{\hbar\omega}{2k_BT}\right)-1\right\}\exp[i\omega(t-t')]. \tag{37}$$

Thus the correlation function is manifestly a function of the time difference $(t-t')$ implying stationarity. Hence, t' can be set equal to zero.

Comparing (37) with (33) we conclude that

$$\langle v_x(t)v_x(0)+v_y(t)v_y(0)\rangle = \frac{1}{m\pi}\int_{-\infty}^{\infty}d\omega\frac{\gamma}{\gamma^2+(\omega+\omega_c)^2}\hbar\omega\left\{\coth\left(\frac{\hbar\omega}{2k_BT}\right)-1\right\}\cos(\omega\tau), \tag{38}$$

and

$$\langle\mathbf{v}(t)\times\mathbf{v}(0)\rangle_Z = \frac{1}{m\pi}\int_{-\infty}^{\infty}d\omega\frac{\gamma}{\gamma^2+(\omega+\omega_c)^2}\hbar\omega \times\left\{\coth\left(\frac{\hbar\omega}{2k_BT}\right)-1\right\}\sin(\omega t). \tag{39}$$

[11]. The latter authors also had started from the Feynman–Vernon Hamiltonian (eq. (1)), but had gone about the calculation in a very different way than the present Langevin treatment. Hakim and Ambegaokar had employed the functional integral representation of the time dependent density matrix of the system, following Caldeira and Leggett [3], and evaluated the so-called influence functional by explicitly diagonalizing the Feynman–Vernon Hamiltonian, in the free-particle case. It is instructive therefore to compare our equations (38) and (39), in the limiting case of $\omega_c = 0$, with the results derived in [11].

Setting $\omega_c = 0$ in (38) and taking cognizance of the (anti-) symmetry of the integrand with respect to ω, we easily find

$$\langle v_x(t)v_x(0) + v_y(t)v_y(0)\rangle = \frac{1}{m\pi}\int_{-\infty}^{\infty} d\omega \frac{\gamma}{\gamma^2+\omega^2}\hbar\omega \coth\left(\frac{\hbar\omega}{2k_B T}\right)\cos(\omega t). \tag{40}$$

In the free particle case, of course, all the three cartesian components of the velocity have the same auto-correlation and hence,

$$\langle \mathbf{v}(t)\cdot\mathbf{v}(0)\rangle = \frac{3}{2m\pi}\int_{-\infty}^{\infty} d\omega \frac{\gamma}{\gamma^2+\omega^2}\hbar\omega \coth\left(\frac{\hbar\omega}{2k_B T}\right)\cos(\omega t). \tag{41}$$

In particular, the equal time correlation leads to

$$\langle \mathbf{v}^2\rangle = \frac{3}{m\pi}\int_{0}^{\infty} d\omega \frac{\gamma}{\gamma^2+\omega^2}\hbar\omega \coth\left(\frac{\hbar\omega}{2k_B T}\right), \tag{42}$$

which agrees with the answer, in equilibrium, derived by Hakim and Ambegaokar (cf. eq. (82) or (83) of [11]).

On the other hand, if we retain the dependence on the initial epoch t_0, we would have obtained from (34) (after some straightforward algebra)

$$\begin{aligned}\langle \mathbf{v}^2(t)\rangle &= \langle \mathbf{v}^2(t_0)\rangle \exp[-2\gamma(t-t_0)] \\ &+ \frac{3\gamma}{m\pi}\int_0^{\infty} d\omega \frac{\hbar\omega}{\gamma^2+\omega^2}\coth\left(\frac{\hbar\omega}{2k_B T}\right) \\ &\times \{1+\exp[-2\gamma(t-t_0)] - 2\exp[-\gamma(t-t_0)]\cos[\omega(t-t_0)],\end{aligned} \tag{43}$$

which for $t_0 = 0$, yields

$$\begin{aligned}\langle \mathbf{v}^2(t)\rangle &= \langle \mathbf{v}^2(0)\rangle \exp(-2\gamma t) \\ &+ \frac{3\gamma}{m\pi}\int_0^{\infty} d\omega \frac{\hbar\omega}{\gamma^2+\omega^2}\coth\left(\frac{\hbar\omega}{2k_B T}\right) \\ &\times \{1+\exp(-2\gamma t) - 2\exp(-\gamma t)\cos(\omega t)\}.\end{aligned} \tag{43'}$$

The difference between (42) and (43′) is precisely due to the choice of the initial epoch. Equation (42) corresponds to the case in which, in the distant past, the particle is

med to be decoupled from the reservoir, which was maintained in thermal librium, at a fixed temperature. It is therefore, not surprising that (43′) is in plete agreement with the result obtained by Hakim and Ambegaokar (cf. eq. (82) of), for the initial condition in which the total density matrix is assumed to be the orized product of the density matrices for the particle and the reservoir.

Classical case

tated earlier (22) provides a description of what we have called quantum Brownian ion, presently of a charged particle moving under the influence of a magnetic field. e quantum mechanics subsumes classical machines we should be able to derive the lts obtained in I, for diffusion processes, in the limit of $\hbar \to 0$. We demonstrate this, icitly, for the velocity auto-correlation.

'e focus our attention to (38) and (39), in which the co-tangent function under the gral can be replaced by the inverse of its argument. Therefore, as $\hbar \to 0$,

$$\langle v_x(t)v_x(0) + v_y(t)v_y(0)\rangle = \frac{2k_B T}{m\pi}\int_{-\infty}^{\infty} d\omega \frac{\gamma}{\gamma^2 + [\omega + \omega_c)^2}\cos(\omega t), \tag{44}$$

$$\langle \mathbf{v}(t) \times \mathbf{v}(0)\rangle_z = \frac{2k_B T}{m\pi}\int_{-\infty}^{\infty} d\omega \frac{\gamma}{\gamma^2 + (\omega + \omega_c)^2}\sin(\omega t). \tag{45}$$

integrals in (44) and (45) can be easily evaluated by contour integration in the plex ω-plane, yielding

$$\langle v_x(t)v_x(0) + v_y(t)v_y(0)\rangle = \frac{2k_B T}{m}\exp(-\gamma|t|)\cos(\omega_c t), \tag{44′}$$

$$\langle \mathbf{v}(t) \times \mathbf{v}(0)\rangle_z = \frac{2k_B T}{m}\exp(-\gamma|t|)\sin(\omega_c t). \tag{45′}$$

e the correlation for the z-component of the velocity is that of a free particle = 0), we have from (44′)

$$\langle \mathbf{v}(t)\cdot\mathbf{v}(0)\rangle = \frac{k_B T}{m}\exp(-\gamma|t|)[1 + 2\cos(\omega_c t)]. \tag{46}$$

xpected (45′) and (46) are in agreement with (9) of I.

Mean-squared displacement

well known that for classical Brownian motion of a particle the mean-squared lacement is (asymptotically) proportional to time, with the coefficient being the ısion constant. This behaviour also remains valid when the particle is charged and er the influence of a magnetic field. In that case the mean-squared displacement is n by [12]

$$\langle \mathbf{r}^2(t)\rangle = 6Dt, \tag{47}$$

where the diffusion coefficient D turns out to be

$$D = \frac{k_B T}{m\gamma} \frac{1 + \omega_c^2/3\gamma^2}{1 + \omega_c^2/\gamma^2}. \tag{48}$$

It is of interest, therefore, to enquire what the mean-squared displacement is, when the charged particle is in quantum Brownian motion. This issue is of basic importance, as certain model calculations suggest that a quantum particle may have "superdiffusive" motion [13].

Before we analyze what the mean squared displacement is, it is useful to consider the following correlation function

$$X(t,t') = \langle Z(t) Z^+(t') \rangle, \quad t \geqslant t'. \tag{49}$$

We note that

$$\mathrm{Re}\, X(t,t') = \langle x(t)x(t') + y(t)y(t') \rangle, \tag{49'}$$

and hence $\lim_{t' \to t} \mathrm{Re}\, X(t,t')$ yields the mean-squared displacement, in the xy plane.

From (29) we obtain

$$\begin{aligned} \langle X(t,t') \rangle = {} & \langle |\dot{Z}(t_0)|^2 \rangle \{ [1 + \exp(-\bar{\gamma}t - \bar{\gamma}^* t' + 2\gamma t_0)] \\ & - \exp(-\bar{\gamma}(t - t_0)) - \exp(-\bar{\gamma}^*(t' - t_0)) \} \\ & + \frac{1}{m^2} \int_{t_0}^{t} d\tau \exp(-\bar{\gamma}\tau) \int_{t_0}^{\tau} dt'' \exp(\bar{\gamma}t'') \int_{t_0}^{t'} d\tau' \exp(-\bar{\gamma}^* \tau') \\ & \times \int_{t_0}^{\tau'} dt''' \exp(\bar{\gamma}^* t''') \langle F(t'') F^+(t''') \rangle, \end{aligned} \tag{50}$$

which, upon using (36) and carrying out the integrals, reduces to

$$\begin{aligned} X(t,t') = {} & \frac{\langle |\dot{Z}(t_0)|^2 \rangle}{\gamma^2 + \omega_c^2} \{ 1 + \exp[-\gamma(t + t' - 2t_0) - i\omega_c(t - t')] \\ & - \exp[-\bar{\gamma}(t - t_0)] - \exp[-\bar{\gamma}^*(t' - t_0)] \} \\ & + \frac{\gamma}{m\pi} \int_{-\infty}^{\infty} d\omega\, \hbar\omega \left[\coth\left(\frac{\hbar\omega}{2k_B T} \right) - 1 \right] \frac{1}{\gamma^2 + (\omega + \omega_c)^2} \\ & \times \left\{ \frac{1}{\omega^2} [1 + \exp(i\omega(t - t')) - \exp(i\omega(t - t_0)) - \exp(i\omega(t' - t_0))] \right. \\ & + \frac{1}{\gamma^2 + \omega_c^2} [1 + \exp(-\bar{\gamma}t - \bar{\gamma}^* t' + 2\gamma t_0) \\ & - \exp(-\bar{\gamma}(t - t_0)) - \exp(-\bar{\gamma}^*(t' - t_0))] \\ & - \frac{i}{\omega\bar{\gamma}} [1 - \exp(-i\omega(t' - t_0))] [\exp(-\bar{\gamma}(t - t_0)) - 1] \\ & \left. + \frac{i}{\omega\bar{\gamma}^*} [1 - \exp(i\omega(t - t_0))] [\exp(-\bar{\gamma}^*(t' - t_0)) - 1] \right\}. \end{aligned} \tag{51}$$

Taking $t' = t$, and setting $t_0 = 0$, we have from (51)

$$\langle x^2(t) + y^2(t) \rangle$$

$$= \frac{\langle \dot{x}(0)^2 + \dot{y}(0)^2 \rangle}{\gamma^2 + \omega_c^2} \{1 + \exp(-2\gamma t) - 2\exp(-\gamma t)\cos(\omega_c t)\}$$

$$+ \frac{1}{m\pi} \int_{-\infty}^{\infty} d\omega \frac{\gamma}{\gamma^2 + (\omega + \omega_c)^2} \hbar\omega \left[\coth\left(\frac{\hbar\omega}{2k_B T}\right) - 1 \right]$$

$$\times \left\{ \frac{4}{\omega^2} \sin^2(\tfrac{1}{2}\omega t) + \frac{1}{\gamma^2 + \omega_c^2} [1 + \exp(-2\gamma t) - 2\exp(-\gamma t)\cos(\omega_c t)] \right.$$

$$+ \frac{2}{\omega(\gamma^2 + \omega_c^2)} [2\omega_c \sin^2(\tfrac{1}{2}\omega t) - \gamma \sin(\omega t)$$

$$+ \exp(-\gamma t)(\omega_c \cos(\omega + \omega_c)t - \omega_c \cos(\omega_c t)$$

$$\left. + \gamma \sin(\omega + \omega_c)t - \gamma \sin(\omega_c t)] \right\}. \tag{52}$$

In order to gain insight into the result in (52) it is instructive to consider certain special cases. The simplest case is of course, that of a free particle ($\omega_c = 0$) in the classical ($\hbar = 0$) Brownian motion. We now have

$$\langle x^2(t) + y^2(t) \rangle = \langle \dot{x}(0)^2 + \dot{y}(0)^2 \rangle \left[\frac{1 - \exp(-\gamma t)}{\gamma} \right]^2$$

$$+ \frac{2k_B T}{m} \left\{ \frac{2}{\gamma^2} [\gamma t - (1 - \exp(-\gamma t))] - \left[\frac{1 - \exp(-\gamma t)}{\gamma} \right]^2 \right\}. \tag{53}$$

Using the equipartition theorem

$$\langle \dot{x}(0)^2 + \dot{y}(0)^2 \rangle = \frac{2k_B T}{m},$$

we finally arrive at the familiar result [14]

$$\langle x^2(t) + y^2(t) \rangle = \frac{4k_B T}{m\gamma^2} [\gamma t - 1 + \exp(-\gamma t)]. \tag{54}$$

Evidently, the right hand side of (54) is quadratic in t for short times (i.e. $\gamma t \ll 1$) and is diffusive for long times (i.e. $\gamma t \gg 1$) with the diffusion coefficient (in two dimensions) being $4k_B T/m\gamma$.

The next case to consider is that of a *free* particle ($\omega_c = 0$) in quantum Brownian

motion [11]. We have from (52),

$$\langle x^2(t)+y^2(t)\rangle = \langle \dot{x}(0)^2+\dot{y}(0)^2\rangle \left[\frac{1-\exp(-\gamma t)}{\gamma}\right]^2 + \frac{1}{m\pi}\int_{-\infty}^{\infty} d\omega \frac{\gamma}{\gamma^2+\omega^2}\hbar\omega \coth\left(\frac{\hbar\omega}{2k_B T}\right) \times \left\{\frac{4}{\omega^2}\sin^2(\tfrac{1}{2}\omega t)+\left[\frac{1-\exp(-\gamma t)}{\gamma}\right]^2 - \frac{2}{\omega}\left[\frac{1-\exp(-\gamma t)}{\gamma}\right]\sin(\omega t)\right\}. \quad (55)$$

Following our discussion in § 3, it is not surprising that (55) is identical to the one derived by Hakim and Ambegaokar (cf. eq. (69a) of [11]), for "factorized" initial condition. Hakim and Ambegaokar have argued that at zero temperature and at long times ($\gamma t \gg 1$), the mean-squared displacement is proportional to $\ln(\gamma t)$ – reminiscent of Sinai-type anomalous diffusion [15]. The logarithmic dependence crosses over to a linear, diffusive one at any finite temperature, for times longer than ν^{-1} where ν has been defined in § 1.

Our final limiting case is that of a charged particle, in classical ($\hbar = 0$) Brownian motion in the presence of a magnetic field. Employing the equipartition theorem (cf. eq. (53)) once again and evaluating the relevant integrals by contour methods, (52) now yields

$$\langle x^2(t)+y^2(t)\rangle = \frac{4k_B T}{m(\gamma^2+\omega_c^2)^2}\{\gamma t(\gamma^2+\omega_c^2)-(\gamma^2-\omega_c^2) + \exp(-\gamma t)[(\gamma^2-\omega_c^2)\cos(\omega_c t)-2\gamma\omega_c \sin(\omega_c t)]\}, \quad (56)$$

the expected result (cf. eq. (40) of I). Asymptotically, for $t \gg \gamma^{-1}$,

$$\langle x^2(t)+y^2(t)\rangle = \frac{4k_B T}{m}\frac{\gamma t}{(\gamma^2+\omega_c^2)}. \quad (57)$$

Since under the same limiting condition, the mean-squared displacement in the direction of the magnetic field is given by the $\omega_c = 0$ limit of eq. (57), we have

$$\langle \mathbf{r}^2(t)\rangle = \frac{2k_B T}{m\gamma}\left(1+\frac{2\gamma^2}{\gamma^2+\omega_c^2}\right)t, \quad (58)$$

which agrees with (47) and (48).

The analysis presented above clearly indicates that the diffusive behaviour in the general case, given by (52) is rather complex, and is not amenable to analytical investigation. The dynamics now is dominated at low temperatures by quantum effects, going over to classical diffusive behaviour at high temperatures.

5. Conclusion

This paper is complementary to I in that we have extended the [illegible] of diffusive

er derivation of a quantum Langevin equation by Ford and coworkers. We have d this equation exactly and the resultant solution has been employed to calculate ity auto-correlation function and the mean-squared displacement. The present oach has been based on a direct analysis of the equation of motion for observables, posed to a master equation for the density matrix or its path integral formulation ade popular in recent years by Leggett and coworkers. However the equivalence een the two approaches has been established by rederiving for the special case of quantum particle, the results obtained earlier by Hakim and Ambegaokar.

ur analysis in §4 on the mean-squared displacement shows that the diffusive viour in the quantum case is rather complicated. This, of course, is not unexpected, ven a free particle is known to have anomalous diffusion, especially at low eratures.

ne immediate application of our present treatment is to the study of Landau agnetism in the presence of dissipation. It is well known that diamagnetism is y a quantum phenomenon [16]. On the other hand, in real materials, electrons are cted to undergo scattering due to phonons, impurities, ion imperfections, etc. ering would naturally lead to dissipative loss and hence the present results are ently suitable to tackle the issue of what happens to Landau diamagnetism when ntum) friction is large. The required analysis inter-alia would be automatically neralization of the corresponding classical treatment of Jayannavar and Kumar Details of this analysis will be reported in a forthcoming paper.

owledgements

eliminary version of the work reported in this and the preceding paper (I) was nted in lectures given by SD at an SERC School organized in December 1995 on gnetic Reconnection in Plasma Physics" at the Institute for Plasma Research, dhinagar. SD is extremely grateful to Dr. P K Kaw and Dr. A Sen for their rous hospitality, and to the participants in the School for lively discussions, which d clarify many of the subtleties.

rences

J Singh and S Dattagupta, *Pramana – J. Phys.* **47**, 199 (1996)
Workshop on *Noise in Macroscopic Quantum Systems* (Institute for Theoretical Physics, Santa Barbara, 1984) Proceedings unpublished
Fluctuations in Macroscopic and Mesoscopic Systems edited by H Cerdeira, F Guinea and U Weiss (World Scientific, Singapore 1991)
Rate Processes in Dissipative Systems: 50 years after Kramers, Ber. Bunsenges. Phys. Chem. **95** (1991)
A O Caldeira and A J Leggett, *Physica* **A121**, 587 (1983)
R P Feynman and F L Vernon, *Ann. Phys.* **24**, 118 (1963)
A O Caldeira and A J Leggett, *Ann. Phys.* **149**, 374 (1983)
G W Ford, M Kac and P Mazur, *J. Math. Phys.* **6**, 504 (1965)
R Zwanzig, *J. Stat. Phys.* **9**, 215 (1973)
G W Ford, J T Lewis and R F O'Connell, *Phys. Rev.* **A37**, 4419 (1988)
X L Li, G W Ford and R F O'Connell, *Phys. Rev.* **A41**, 5287 (1990)
In contrast, the treatment by Y Marathe, *Phys. Rev.* **A39**, 5927 (1989), suffers from a gauge-dependent choice of the vector potential.

[11] V Hakim and V Ambegaokar, *Phys. Rev.* **A32**, 423 (1985)
[12] S Revathi and V Balakrishnan, *J. Math. Phys. Sci.* **26**, 213 (1992)
[13] N Kumar, in *Stochastic processes – formalisms and applications, Lect. Notes in Physics* edited by G S Agarwal and S Dattagupta (Berlin, Springer, 1983)
[14] S Chandrasekhar, *Rev. Mod. Phys.* **15**, 1 (1943)
[15] Ya G Sinai, *Theory Probab. its Appl.* **27**, 247 (1982); and in *Mathematical problems in theoretical physics, Lect. Notes in Physics* edited by J Ehlers (Berlin, Springer, 1982)
[16] J H Van Vleck, *The Theory of Electric and Magnetic Susceptibilities* (London, Oxford University Press, 1932)
[17] A Jayannavar and N Kumar, *J. Phys.* **A14**, 1399 (1981)

Radiative decays of heavy mesons with heavy quark symmetry

A K GIRI, L MAHARANA and R MOHANTA
Physics Department, Utkal University, Bhubaneswar 751 004, India

MS received 3 April 1996; revised 8 July 1996

Abstract. The radiative decays of heavy mesons are considered in heavy quark symmetry formalism. Introducing the interpolating fields for the heavy mesons we obtain the transition matrix element and the corresponding decay widths in the heavy quark symmetry limits. The Isgur–Wise function present in the expression is determined by ISGW quark model. The results obtained agree reasonably well with other estimations.

Keywords. Heavy quark symmetry; interpolating fields; Isgur–Wise function.

PACS Nos 11·30; 13·40; 14·40

1. Introduction

In the last few years considerable progress has been achieved in understanding the physical properties of hadrons containing a single heavy quark because of the development of heavy quark effective theory (HQET) [1–4]. The HQET is an effective theory that arises in a specific limit of QCD where the mass of the heavy quark m_Q, in a hadron is much greater than the scale of the strong interactions Λ_{QCD}. In this limit two new symmetries beyond those usually associated with QCD arise. The first of these is the 'flavor symmetry', which arises from the fact that the long wavelength properties in such a hadron become independent of m_Q for $m_Q \gg \Lambda_{QCD}$ and the Lagrangian is same for all flavors. Thus the light degrees of freedom for B and D meson can be related by a $b \leftrightarrow c$ $SU(2)$ symmetry even though m_b and m_c are very different. The second symmetry is the 'spin symmetry' which arises in QCD because the spin of the heavy quark decoupled from the gluon field. This makes S_Q, the heavy quark spin operator as the generator of another $SU(2)$ symmetry of the light degrees of freedom in meson or baryon containing a single heavy quark. This means that the spectrum of heavy hadrons should show degenerate spin symmetry doublet. Thus for example mesons built from a heavy quark and a light antiquark, the pseudoscalar (0^-) and the vector mesons (1^-) form such a spin symmetry doublet. These symmetries which are not manifest in the original QCD Lagrangian, becomes explicit in the HQET.

Probably, the most fruitful application of the heavy quark spin flavor symmetry is encountered in weak decays of heavy hadrons. Isgur and Wise worked out the consequences of these symmetries for weak decay processes [1]. They have shown that as m_b and $m_c \to \infty$, all the form factors describing the transition between two heavy mesons become related to a single universal function $\xi(v \cdot v')$, the so-called Isgur–Wise function [1, 3]. It depends only on the velocities of the heavy particles and is normalized at zero recoil, where $v \cdot v' = 1$. Similar statements hold for the decays of heavy baryons [5, 6].

In the present investigation we exploit these ideas to study the radiative M1 transitions of the heavy mesons. The assumptions involved in our calculation are mainly as follows. The radiative transitions discussed here are considered to be a predominantly single vertex process induced solely by quark magnetic moment in which a photon is emitted by the confined heavy quark or the light antiquark. Introducing the interpolating fields to describe the ground state of the heavy mesons, the transition amplitude is calculated in the HQET, which comes out in terms of the Isgur–Wise function. Finally the Isgur–Wise function, which is present in the calculation of the matrix element is evaluated using the quark model [7, 8].

The plan of the paper is as follows. In § 2 we give a brief description of the heavy mesons and describe them in terms of the interpolating fields. Using the basic assumption of HQET we obtain the transition amplitude and the corresponding decay widths. Section 3 is devoted to the determination of the Isgur–Wise function using the quark model [7, 8] and § 4 contains results and discussion.

2. Theory

The heavy mesons built from a heavy quark Q and a light antiquark $\bar{q}$ comprise the pseudoscalar 0^- and vector mesons 1^- which are denoted by P and P^* respectively. In terms of the interpolating fields the ground states of these mesons are given as [9]

$$P_i(v) = \bar{q}_v \gamma_5 h_v^i \sqrt{M_P}, \tag{1}$$

and

$$P_i^*(v, \varepsilon) = \bar{q}_v \not{\varepsilon} h_v^i \sqrt{M_{P^*}}, \tag{2}$$

where h_v^i a heavy quark of type 'i' with four velocity v and related to the conventional quark field operator $Q_i(x)$ by

$$Q_i(x) = \exp(-im_Q v \cdot x) h_v^i, \tag{3}$$

and the light quark $\mathbf{q}$, stands for a column vector in flavor $SU(3)$ space as

$$\mathbf{q} = \begin{pmatrix} u \\ d \\ s \end{pmatrix}. \tag{4}$$

ε denotes the polarization vector of the P^* mesons.

To study the heavy flavor conserving radiative M1 transitions $P^* \to P\gamma$ in the HQET, we assume the simple traditional picture of photon emission induced by the quark electromagnetic current. The transition matrix elements describing the process $P^* \to P\gamma$ is given as

$$\mathcal{M}(P^*(v, \varepsilon) \to P(v')\gamma) = \eta^\mu \langle P(v') | J_\mu^{\text{e.m.}} | P^*(v, \varepsilon) \rangle, \tag{5}$$

where η^μ is the polarization vector of the emitted photon. $J_\mu^{\text{e.m.}}$ is the quark electromagnetic current which can be split into heavy quark and light quark components as

$$J_\mu^{\text{e.m.}} = J_\mu^{\text{Q}} + J_\mu^{\text{q}}, \tag{6}$$

where J_μ^{Q} is the heavy quark current given as $J_\mu^{\text{Q}} = e_{\text{Q}} \bar{\text{Q}} \gamma_\mu \text{Q}$, with e_{Q} as the charge of the heavy quark in the units of e and J_μ^{q} is the light quark current. For the purpose of

decay of a heavy meson into another via the heavy quark current, comes out in terms of a single form factor $\xi(v\cdot v')$ known as the Isgur–Wise function. Hence for the heavy quark current sector we obtain the transition amplitude as [3]

$$\langle P(v')|e_Q\bar{Q}\gamma_\mu Q|P^*(v,\varepsilon)\rangle = ie_Q\sqrt{M_P M_{P^*}}\xi(v\cdot v')\varepsilon_{\mu\nu\alpha\beta}v'^\nu v^\alpha\varepsilon^\beta, \tag{7}$$

where $\xi(v\cdot v')$ is the Isgur–Wise function normalized to unity at zero velocity recoil. Momentum conservation for the transition process $P^*(v,\varepsilon)\to P(v')\gamma$ implies

$$M_{P^*}v^\mu = M_P v'^\mu + k^\mu, \tag{8}$$

with k^μ as the momentum of the emitted photon. Substituting the value of v' from (8) into (7) we obtain the transition matrix element for the heavy quark current as

$$\langle P(v')|e_Q\bar{Q}\gamma_\mu Q|P^*(v,\varepsilon)\rangle = -ie_Q\sqrt{\frac{M_{P^*}}{M_P}}\xi(v\cdot v')\varepsilon_{\mu\nu\alpha\beta}k^\nu v^\alpha\varepsilon^\beta. \tag{9}$$

A simple and direct approach can also be followed for the evaluation of the matrix element for the light quark current sector in the HQET. With the states as given in eqs (1) and (2) for P and P^* mesons, one can obtain in a straightforward manner that

$$\begin{aligned}
&\langle P(v')|J^q_\mu|P^*(v,\varepsilon)\rangle \\
&= \sqrt{M_P M_{P^*}}\langle 0|\bar{q}_{v'}\gamma_5 h_{v'}J^q_\mu\bar{h}_v\not{\varepsilon}q_v|0\rangle \\
&= -\sqrt{M_P M_{P^*}}\langle 0|\gamma_5 h_{v'}\bar{h}_v\not{\varepsilon}|0\rangle\langle 0|q_v J^q_\mu\bar{q}_{v'}|0\rangle \\
&= -\sqrt{M_P M_{P^*}}\,\mathrm{Tr}\left(\gamma_5\frac{\not{v}+1}{2}\not{\varepsilon}L_\mu\right),
\end{aligned} \tag{10}$$

where use has been made for the heavy propagator as $\langle 0|h_{v'}\bar{h}_v|0\rangle = (\not{v}+1)/2$ and

$$L_\mu = \langle 0|q_v J^q_\mu\bar{q}_{v'}|0\rangle. \tag{11}$$

From Lorentz covariance L_μ is written as

$$L_\mu = i(C_1(v+v')_\mu + C_2\gamma_\mu + C_3\sigma_{\mu\nu}k^\nu). \tag{12}$$

Substitution of (12) into (10) yields the result

$$\langle P(v')|J^q_\mu|P^*(v,\varepsilon)\rangle = -2iC_3\sqrt{M_{P^*}M_P}\varepsilon_{\mu\nu\alpha\beta}k^\nu v^\alpha\varepsilon^\beta. \tag{13}$$

The coefficient C_3 representing the transition magnetic moment of the light quark present in the heavy meson, comes from the photon coupling to the light quark piece of the electro-magnetic current. In the nonrelativistic quark model the transition magnetic moment of the light quark is given as $\mu_q = e_q/2m_q$, where the charge and mass of the light quark is taken as e_q and m_q respectively. Hence the matrix element of the light sector is given as

$$\langle P(v')|J^q_\mu|P^*(v,\varepsilon)\rangle = -i\sqrt{M_{P^*}M_P}\frac{e_q}{m_q}\varepsilon_{\mu\nu\alpha\beta}k^\nu v^\alpha\varepsilon^\beta. \tag{14}$$

Combining the contributions from both heavy and light quark current sector as given in eqs (9) and (14) respectively, we obtain the transition matrix element for the decay process $P^*(v,\varepsilon)\to P(v')\gamma$ from eq. (5) as

$$\mathcal{M}(P^*\to P\gamma) = -i\sqrt{M_{P^*}M_P}\,\varepsilon_{\mu\nu\alpha\beta}\eta^\mu k^\nu v^\alpha \varepsilon^\beta\left(e_Q\frac{\xi(v\cdot v')}{M_P}+\frac{e_q}{m_q}\right). \tag{15}$$

The corresponding decay width is given by

$$\Gamma(P^*\to P\gamma) = \frac{4\alpha}{3}\left(\frac{M_P}{M_{P^*}}\right)\left(e_Q\frac{\xi(v\cdot v')}{2M_P}+\frac{e_q}{2m_q}\right)^2|\mathbf{k}|^3, \tag{16}$$

where $\mathbf{k}$ is the c.o.m. momentum of the emitted photon in the rest frame of the initial vector meson.

Thus using the basic assumptions of heavy quark effective theory, we obtained a simplified formula (16) for the radiative decay width in terms of the quark and hadron masses in a model independent way. The universal Isgur–Wise function $\xi(v\cdot v')$ present in (16) is normalized at the point of zero velocity transfer i.e. $\xi(v\cdot v'=1)=1$ [1]. For the transition process $P^*(v,\varepsilon)\to P(v')\gamma$, the kinematic variable $v\cdot v'$ is very close to unity, since the P^* and P meson masses are not much different from each other, as is evident from (28). Hence one may expect the Isgur–Wise function not to be deviated from unity near the zero recoil point. For the case $v\cdot v'=1$ (no recoil), $\xi(v\cdot v')$ is model independent. So to calculate the Isgur–Wise function other than the point of zero recoil, one has to make some suitable ansatz. Here we have employed the quark model [7, 8] to calculate the same.

3. Quark model and Isgur–Wise function

In this section we have evaluated the Isgur–Wise function in the quark model following the procedure of Ali *et al* [8]. Since we are dealing with the two body decays, the product $v\cdot v'$ is fixed by the kinematics and hence the Isgur–Wise function has to be taken at this point. In this model the Isgur–Wise function is extracted from the overlap integral

$$\begin{aligned} I(v') &= \int\frac{d^3p}{(2\pi)^3}\tilde{\Phi}_F^*(\mathbf{p}+\Lambda\mathbf{v}')\tilde{\Phi}_I(\mathbf{p}) \\ &= \int d^3x\,\Phi_F^*(\mathbf{x})\Phi_I(\mathbf{x})\exp(-i\Lambda\mathbf{v}'\cdot\mathbf{x}), \end{aligned} \tag{17}$$

where the labels I and F denote wave function of the initial and final mesons respectively. The "inertia parameter Λ" corresponds to the mass of light degrees of freedom and we take the expression for Λ, given by Altomari [10] as

$$\Lambda = \frac{M_P\cdot m_q}{m_Q+m_q}. \tag{18}$$

The wave functions are chosen to be the eigenfunctions of orbital angular momentum L. Since both the initial and final mesons will have $L=0$, the wave functions are given by

$$\Phi_I(\mathbf{x}) = Y_0^0\left(\frac{\mathbf{x}}{|\mathbf{x}|}\right)\phi_I(|\mathbf{x}|) \tag{19}$$

and

$$\Phi_F(\mathbf{x}) = Y_0^0\left(\frac{\mathbf{x}}{|\mathbf{x}|}\right)\phi_F(|\mathbf{x}|), \tag{20}$$

with normalization

$$\int \mathrm{d}^3x\Phi^*_{I/F}(\mathbf{x})\Phi_{I/F}(\mathbf{x}) = \int r^2\,\mathrm{d}r\phi^*_{I/F}(r)\phi_{I/F}(r) = 1. \tag{21}$$

Inserting the wave functions as given in (19) and (20) into the overlap integral (17) and choosing the quantization axis of orbital angular momentum in the direction of velocity, the overlap integral becomes

$$I(v') = \int r^2\,\mathrm{d}r\phi^*_F(r)\phi_I(r)j_0(\Lambda r|\mathbf{v}|), \tag{22}$$

where j_0 is the spherical Bessel function of zeroth order. This expression holds in the rest frame of the heavy meson. In a general frame (22) becomes

$$I(v\cdot v') = \int r^2\,\mathrm{d}r\phi^*_F(r)\phi_I(r)j_0(\Lambda r\sqrt{(v\cdot v')^2 - 1}). \tag{23}$$

This overlap integral is identified as the usual Isgur–Wise function, which is correctly normalized at zero recoil i.e., $v\cdot v' = 1$, since $j_0(0) = 1$. To evaluate the overlap integral, we may take the variational wave functions of harmonic oscillator or hydrogen-like atoms. Here we take the radial wave function of harmonic oscillator as in ref. [7, 8]:

$$\phi(r) = \left(\frac{4\beta^3}{\sqrt{\pi}}\right)^{1/2}\exp(-\beta^2r^2/2), \tag{24}$$

with oscillator strengths $\beta_D = 0{\cdot}39$ and $\beta_B = 0{\cdot}41$ GeV for D and B meson [7] respectively and obtain $\xi(v\cdot v')$ to be

$$\xi(v\cdot v') = \exp(-a^2/4\beta^2), \tag{25}$$

where $a = \Lambda(\sqrt{(v\cdot v')^2 - 1})$.

The product $(v\cdot v')$ is determined by considering the kinematics of the system. Since we are dealing with the two body decays $P^*(v,\varepsilon)\to P(v')\gamma$, momentum conservation implies

$$M_{P^*}v^\mu = M_Pv'^\mu + k^\mu, \tag{26}$$

where k^μ is the momentum of the emitted photon. Using the mass shell condition of the photon as

$$k^2 = 0 = M^2_{P^*} + M^2_P - 2(v\cdot v')M_{P^*}M_P, \tag{27}$$

we obtain

$$v\cdot v' = \frac{M^2_{P^*} + M^2_P}{2M_{P^*}M_P}. \tag{28}$$

Since the pseudoscalar and vector meson masses are not much different from each other, the kinematic variable $(v\cdot v')$ is extremely close to unity and the Isgur–Wise function calculated with (25) also turns out to be unity as shown in table 1.

Table 1. Partial decay widths for the radiative decays of the heavy mesons.

Decay process	$(v\cdot v')$	$\xi(v\cdot v')$	k in MeV	Γ in KeV
$D^{*0}\to D^0\gamma$	1·003	1·000	137·069	32·907
$D^{*+}\to D^+\gamma$	1·003	1·000	135·682	2·413
$D_s^*\to D_s\gamma$	1·002	1·000	136·755	0·415
$B^{*0}\to B^0\gamma$	1·000	1·000	45·603	0·263
$B^{*+}\to B^+\gamma$	1·000	1·000	45·900	0·893
$B_s^*\to B_s\gamma$	1·000	1·000	46·796	0·11

Table 2. Comparison of the partial decay widths Γ(in KeV) for the radiative transitions of the heavy mesons.

Decay process	Present calculation	Experimental values [11]	Barik and Dash [12]	Cheng *et al* [13]
$D^{*0}\to D^0\gamma$	32·907	$<764{\cdot}4\pm58{\cdot}8$	27·94	34
$D^{*+}\to D^+\gamma$	2·413	$<1{\cdot}441^{+1{\cdot}834}_{-0{\cdot}917}$	1·15	2
$D_s^*\to D_s\gamma$	0·415		0·32	0·3
$B^{*0}\to B^0\gamma$	0·263		0·21	0·28
$B^{*+}\to B^+\gamma$	0·893		0·67	0·84
$B_s\to B_s\gamma$	0·11		0·11	–

4. Results and discussion

In this section we calculate the partial decay widths of several possible M1 transitions among the vector and pseudoscalar heavy mesons. Substituting the value of the Isgur–Wise function (which is unity as obtained in table 1) into (16), we obtain the simplified expression for decay width as

$$\Gamma(P^*\to P\gamma)=\frac{4\alpha}{3}\left(\frac{M_P}{M_{P^*}}\right)\left(\frac{e_Q}{2M_P}+\frac{e_q}{2m_q}\right)^2|\mathbf{k}|^3 \tag{29}$$

in terms of the quark and hadron masses. We take the constituent quark masses as $m_u=m_d=330\,\text{MeV}$, $m_s=550\,\text{MeV}$, $m_c=1{\cdot}8\,\text{GeV}$ and $m_b=5\,\text{GeV}$ and the meson masses from [11]. Sunstituting these values in (29) we obtain the partial decay widths for various possible transitions of the heavy mesons as presented in table 1. Comparing our results with that predicted by Barik *et al* [12] and Cheng *et al* [13] we observe a remarkable agreement. Table 2 embodies our results along with their predictions.

In the present investigation we have estimated the partial decay widths for several possible radiative transitions of the heavy mesons in HQET. The spin-flavor symmetries of HQET allow us to deduce a very simple formula for the radiative decay widths. Assuming that the photon emission is induced by the quark electromagnetic current,

we calculate the transition matrix element and the corresponding decay width. The Isgur–Wise function present in the expression for the decay width (16) is determined by the ISGW quark model [7, 8]. Since there is no appreciable mass difference between the vector and pseudoscalar mesons, the kinematic variable $(v \cdot v')$ is very close to unity and the Isgur–Wise function also turns out to be unity. As there is no model dependent parameter in our calculations, the results obtained are quite simple and appreciable. However the results have certain uncertainties due to the $(1/m_Q)$ corrections to HQET. It may be noted that the predicted partial decay widths for $P^* \to P\gamma$ transition are quite satisfactory and in good agreement with the previously calculated results [12, 13] providing the adequacy of the simple traditional picture of the photon emission induced by the quark electromagnetic current.

Acknowledgements

We are thankful to Prof. B B Deo and Prof. N Barik for useful discussions. One of the authors (RM) would like to thank CSIR, Government of India, for a fellowship.

References

[1] N Isgur and M B Wise, *Phys. Lett.* **B232**, 113 (1989); *Phys. Lett.* **B237**, 527 (1990)
[2] H Georgi, *Phys. Lett.* **B240**, 447 (1990); *Nucl. Phys.* **B348**, 293 (1991)
[3] A F Falk, H Georgi, B Grinstein and M B Wise, *Nucl. Phys.* **B343**, 1 (1990)
[4] A F Falk and B Grinstein, *Phys. Lett.* **B247**, 406 (1990); *Phys. Lett.* **249**, 314 (1990)
[5] N Isgur and M B Wise, *Nucl. Phys.* **B348**, 278 (1991)
[6] T Mannel, W Roberts and Z Ryzak, *Nucl. Phys.* **B355**, 38 (1991); *Phys. Lett.* **255**, 593 (1991)
[7] N Isgur, D Scora, B Grinstein and M B Wise, *Phys. Rev.* **D39**, 799 (1989)
[8] A Ali, T Ohl and T Mannel, *Phys. Lett.* **B298**, 195 (1993)
[9] T M Yan, H Y Cheng, C Y Cheung, G L Lin, Y-C Lin and H L Yu, *Phys. Rev.* **D46**, 1148 (1992)
[10] T Altomari, *Phys. Rev.* **D37**, 677 (1988)
[11] Particle Data Group; Review of Particle Properties, *Phys. Rev.* **D50** (1994) part 1
[12] N Barik and P C Dash, *Phys. Rev.* **D49**, 299 (1994)
[13] H Y Cheng, C Y Cheung, G L Lin, Y C Lin, T M Yan and H L Yu, *Phys. Rev.* **D47**, 1030 (1993)

PRAMANA
— journal of
physics

© Printed in India

Vol. 47, No. 3,
September 1996
pp. 233–248

Electromagnetic form factors of nucleons in a relativistic square-root potential model of independent quarks

S N JENA and M R BEHERA
Department of Physics, Berhampur University, Berhampur 760 007, India

MS received 16 March 1996

Abstract. The nucleon electromagnetic form factors $G_E^p(q^2)$, $G_M^p(q^2)$ and the axial-vector form factor $G_A(q^2)$ are studied in a relativistic model of independent quarks confined by an equally mixed scalar-vector square root potential $V_q(r) = \frac{1}{2}(1+\gamma^o)(ar^{1/2}+v_0)$ taking into account the appropriate centre-of-mass corrections. The respective root-mean-square radii associated with $G_E^p(q^2)$ and $G_A(q^2)$ come out as $[\langle r^2\rangle_E^p]^{1/2} = 0{\cdot}86$ fm and $\langle r_A^2\rangle^{1/2} = 0{\cdot}88$ fm. Restoration of chiral symmetry in this model is discussed to derive the pion-nucleon form factor $G_{\pi NN}(q^2)$ and consequently the pion-nucleon coupling constant is obtained as $g_{\pi NN} = 12{\cdot}81$ as compared to $(g_{\pi NN})_{exp} \simeq 13$.

Keywords. Dirac equation; square-root potential; electromagnetic form factors; axial-vector form factor; magnetic moments; charge-radii; axial-vector coupling constant; centre-of-mass correction; pion-nucleon form factor.

PACS No. 13·40

1. Introduction

In a recent work [1] we have found that a relativistic independent-quark model based on the Dirac equation with a confining square-root potential of the form

$$V_q(r) = \tfrac{1}{2}(1+\gamma^0)(ar^{1/2}+v_0),\ a>0 \tag{1.1}$$

explains reasonably well the static properties of the baryons and the mass spectra of the light mesons. It is worthwhile to extend the applicability of the model to the study of nucleon electromagnetic form factors which are essential and useful for the description of the size and compositeness of hadrons. In the recent past, several authors [2] have attempted to study the nucleon form factors based on the bag model and other confining quark potential models. Tegen and collaborators [2] have studied the same in a model with massless quarks in confining scalar potentials of the cr^2 and cr^3 type. They have reasonably accounted for the available experimental data by taking into account the centre-of-mass corrections and the pion-cloud corrections. Here we attempt to study the nucleon form factors in the model with an independent quark confining potential of the form given in (1.1) which corresponds to an equal admixture of scalar and vector parts. We are basically interested to test the applicability of this model in understanding the quark-core contributions to the nucleon electromagnetic

The choice of the effective square-root confining potential in the present study is motivated by the fact that qualitatively the confining potential would be strongly weakened by the screening effects due to the quark pair creation above threshold. On the other hand, evidences for a confinement potential weaker than the linear one also exist [3, 4] because the linear potential has discrepancies with the experimental data only in the domains where either spin dependent effects cannot be explained (such as the hyperfine splittings of p-wave heavy quarkonia) or decay processes (such as leptonic decays) where the derivative of the confining potential is involved. In fact, the increase in linear potential with r seems too fast so that the calculated leptonic widths of higher $c\bar{c}$ and $b\bar{b}$ excited states exceed the experimental data. Olsson and Suchyta III [5] discussed the spin-orbit contribution of the confining interaction and found that the confining potential must fall below the linear potential. More recently, the calculation of lattice QCD for baryon spectrum leads to an effective potential [6] $V(r) = Ar^{\varepsilon}$ ($A = 0{\cdot}508$, $\varepsilon = 0{\cdot}671$) which also shows a potential weaker than linear might be more suitable for describing effective quark confinement in hadrons. Therefore, a phenomenological square-root potential of the form $(ar^{1/2} + v_0)$ which is inspired by the fact that it is weaker than the linear potential has been chosen for the study of nucleon form factors. Recently a square-root potential of the form $ar^{1/2}$ has been used by Xiaotong Song [7] as a Lorentz scalar part along with a Lorentz vector part of the form $br^{-1/2}$ for the study of heavy quarkonia. However, in the present work the potential $ar^{1/2}$ has been used with equally mixed scalar and vector parts in the form given in (1.1) because both the scalar and vector parts in equal proportions at every point render the solvability of Dirac equation for independent quarks by reducing it to the form of Schrödinger-like equation. This Lorentz structure of the potential has also an additional advantage of generating no spin-orbit splitting, as observed in the experimental baryon spectrum.

The organization of the paper is as follows. In § 2, we present a brief outline of the potential model and its consequences in terms of the static properties of baryons as discussed in our earlier work [1]. Using expressions for the ground-state wave functions of the independently confined constituent quarks of the nucleon, the form factors are computed to the order $\eta = |\mathbf{q}|^2/4M_p^2$ in the Breit frame. The $|\mathbf{q}|^2$ dependence of these form factors are studied making comparison with the experimental data in the range $0 \leqslant |\mathbf{q}|^2 < 1\ \mathrm{GeV}^2$. We have only considered the quark core contributions to the form factors taking into account the centre-of-mass corrections but we have not included the pion-cloud contributions. Furthermore, we have computed the nucleon core radii associated with different form factors. Lastly, § 4 contains a brief discussion of the results and conclusion.

2. Formalism

A. *Relativistic potential model of independent quarks*

The potential model and the static nucleon properties on which our present discussion is based upon, has been discussed in detail in our earlier work [1]. In order to make this paper self-contained, we briefly outline some important features of the model, which is based on the following assumptions.

The constituent quarks in a nucleon are assumed to move independently in an average flavour-independent potential taken in the form

$$V_q(r) = \tfrac{1}{2}(1+\gamma^0)\,V(r), \tag{2.1}$$

where $V(r) = ar^{1/2} + V_0$, with $a > 0$. The independent quarks of rest mass m_q are believed to obey the Dirac equation

$$[\gamma^0 E_q - \boldsymbol{\gamma}\cdot\mathbf{p} - m_q - V_q(r)]\psi_q(\mathbf{r}) = 0, \tag{2.2}$$

where $\Psi_q(\mathbf{r})$ is the two-component quark wave function belonging to the energy eigenvalue E_q. It is further assumed that the quarks inside the nucleons in their ground state occupy $1S_{1/2}$ orbits. Then $\Psi_q(\mathbf{r})$ in two component form can be obtained as

$$\Psi_q(\mathbf{r}) = N_q \begin{bmatrix} \phi_q(r) \\ -i\dfrac{\boldsymbol{\sigma}\cdot\hat{r}}{\lambda_q}\phi_q'(r) \end{bmatrix} \chi\uparrow, \tag{2.3}$$

where $\lambda_q = E_q + m_q$ and $\phi_q(r)$ satisfies a Schrödinger-type equation

$$\phi_q'' + \frac{2\phi'}{r} + \lambda_q[E_q - m_q - V(r)]\phi_q = 0 \tag{2.4}$$

which can be solved easily following the discussion given in our earlier work [1].

The overall normalization constant can be obtained as

$$N_q^2 = [1 + (E_q - m_q - V_0 - a\langle\!\langle r^{1/2}\rangle\!\rangle_q)/\lambda_q]^{-1}, \tag{2.5}$$

where $\langle\!\langle r^{1/2}\rangle\!\rangle_q$ stands for the expectation value of $r^{1/2}$ with respect to $\phi_q(r)$.

The solution of (2.4) leads to energy eigenvalue condition for ground state as

$$\varepsilon_q = (\lambda_q/a^4)^{1/5}\,(E_q - m_q - V_0), \tag{2.6}$$

where

$$\varepsilon_q = 1{\cdot}841827.$$

Now with the individual quark binding energy E_q obtained from (2.6) and the wave function $\Psi_q(\mathbf{r})$ given in (2.3), it is straightforward to derive the expressions for the quark-core contributions to certain measurable static quantities like μ_B, (g_A/g_v) and $\langle r^2\rangle_B$ of S-wave baryons which are obtained simply by appropriately adding the contributions of each individual quark in the baryon core.

By the usual approach [1], the quark core contribution to magnetic moment of baryon B is obtained from

$$\mu_B = \langle B\uparrow|\sum_q \mu_q \sigma_z^q|B\uparrow\rangle, \tag{2.7}$$

where μ_q is the constituent quark magnetic moment given by

$$\mu_q = (2M_P N_q^2/\lambda_q)e_q \text{ n.m}, \tag{2.8}$$

and $|B\uparrow\rangle$ represents regular $SU(6)$ state vectors for octet baryons. Here M_P is the proton mass. In this model, the mean square charge radius of the baryon core is

$$\langle r^2\rangle_B = \sum_q e_q \frac{N_q^2}{\lambda_q}[(2E_q - V_0)\langle\langle r^2\rangle\rangle_q - a\langle\langle r^{5/2}\rangle\rangle_q + 3/\lambda_q]. \tag{2.9}$$

The double angular brackets appearing in (2.9) are the expectation values with respect to $\phi_q(r)$ which can be evaluated numerically or by the WKB method [8, 9] through the general expression

$$\langle\langle r^\alpha\rangle\rangle = 2\alpha(2\alpha+1)r_{0q}^\alpha \varepsilon_q^{2\alpha}\beta(2\alpha, 5/2). \tag{2.10}$$

Interpreting the weak β-decays of the baryons $B \to B' + e^- + \bar{\nu}_e$ as quark β-decays like $q_j \to u + e^- + \bar{\nu}_e$ occurring inside the baryon core (where q_j could be a d or S quark), one can obtain in the lines of bag model calculations [10] the axial vector coupling constant ratio g_A/g_V as

$$(g_A/g_V) = (g_A/g_V)^{NR}(1 - 2\Delta_{ju}) \tag{2.11}$$

where g_A and g_V are the axial-vector and vector coupling constants for the baryons, $(g_A/g_V)^{NR}$ is the non-relativistic $SU(6)$ value [11] which for various β-decays can be computed by using $SU(6)$ wave function for $|B\uparrow\rangle$ states [9]. Δ_{ju} is the relativistic correction in the axial coupling for the β-decay of j quark into u quark and is given by

$$\Delta_{ju} = \frac{24}{231}\left(\frac{N_u N_j}{\lambda_u \lambda_j}\right)\frac{\varepsilon_q K^2}{r_{0j}^2} F(\tfrac{1}{4}, 2, \tfrac{15}{4}; k^2), \tag{2.12}$$

where $k^2 = (r_{0j}/r_{0u})^{1/2}$ and $F(\frac{1}{4}, 2, \frac{15}{4}; k^2)$ is the hypergeometric function.

The expressions for the static quantities are modified when corrected for centre-of-mass motion. Following the technique adopted by Bartelski *et al* [12] and Eich *et al* [13], the centre-of-mass corrected expressions for the static quantities in (2.7), (2.9) and (2.11) get modified as

$$\mu_B' = [3\mu_B + Q_B(M_P/M_B)(1 - \delta_B)](1 + \delta_B + \delta_B^2), \tag{2.13}$$

$$\langle r^2\rangle_B' = \frac{\left[3\langle r^2\rangle_B - 3\sum_q \left\{2e_q\left(\frac{E_q}{E_B}\right) - Q_B\left(\frac{E_q}{E_B}\right)^2\right\}\langle r^2\rangle_q\right]}{(2 + \delta_B^2)} \tag{2.14}$$

and

$$(g_A g_V)' = 3(g_A/g_V)/(1 + 2\delta_B), \tag{2.15}$$

where

$$\delta_B = (M_B/E_B) \simeq (1 + \delta_B^2)/2, \tag{2.16}$$

$$\delta_B^2 = (M_B^2/E_B^2) = 1 - \langle \mathbf{P}_B^2\rangle/E_B^2. \tag{2.17}$$

Here $E_B = \Sigma_q E_q$ is the relativistic energy of the quark core and Q_B is the charge of the baryon. The physical mass of the baryon core is

$$M_B = (E_B^2 - \langle \mathbf{P}_B^2\rangle)^{1/2}, \tag{2.18}$$

where $\mathbf{P}_B$ is the centre of mass momentum and $\langle \mathbf{P}_B^2\rangle$ is evaluated with the usual approximation as

$$\langle \mathbf{P}_B^2\rangle = \sum_q \langle \mathbf{P}^2\rangle_q, \tag{2.19}$$

where $\langle \mathbf{P}^2 \rangle_q$ are the mean-square individual quark momenta with respect to $\Psi_q(\mathbf{r})$. In the present model we find

$$\langle \mathbf{P}^2 \rangle_q = N_q^2[2E_q(E_q - m_q) - (3E_q - m_q - V_0)V_0 - (3E_q - m_q - 2V_0)a\langle\langle r^{1/2}\rangle\rangle_q + a^2\langle\langle r\rangle\rangle_q]. \tag{2.20}$$

Evaluation of $\langle \mathbf{P}^2 \rangle_q$, δ_B and δ_B^2 leads to a correct estimate of the static properties due to quark core of octet baryons. However, we do not consider the effect of the coupling of pions to the bare quark core of the baryons.

B. *Electromagnetic form factors of the nucleon core*

The Dirac–Pauli nucleon form factors $F_1(q^2)$ and $F_2(q^2)$ in the space-like region are defined by

$$\langle N(P_2)|J^\mu(0)|N(P_1)\rangle = \bar{u}(P_2, S') \times \left[F_1(q^2)\gamma^\mu + \frac{\sigma^{\mu\nu}q_\nu}{2M_P}F_2(q^2)\right]u(P_1, S), \tag{2.21}$$

where J^μ is the nucleon current, $u(P,S)$ is the positive energy Dirac spinor of the free nucleon of four momentum p and spin S. P_1 and P_2 are the ingoing and outgoing nucleon four-momenta and $q = (P_2 - P_1)$ is the four momentum transferred from the photon to the nucleon. In terms of Sach's form factors [14]

$$G_E(q^2) = F_1(q^2) - \eta F_2(q^2),$$
$$G_M(q^2) = F_1(q^2) + F_2(q^2). \tag{2.22}$$

Equation (2.21) reduces to

$$\langle N(P_2)|J^\mu(0)|N(P_1)\rangle = \frac{1}{1+\eta}\bar{u}(P_2, S')\left[(1+\eta)G_M\gamma^\mu - \frac{G_M - G_E}{2M_P}P^\mu\right]u(P_1, S), \tag{2.23}$$

where

$$P^\mu = (P_1 + P_2)^\mu, \quad \eta = -q^2/4M_P^2.$$

In the Breit frame

$$q^\mu = (0, \mathbf{q}), P_1^2 = P_2 = M_P^2,$$
$$\mathbf{P}_1 = -\mathbf{P}_2 = -\tfrac{1}{2}\mathbf{q}, P_0 = E = M_P(1+\eta)^{1/2}$$

and one obtains

$$\langle N(\mathbf{q}/2)|J^0(0)|N(-\mathbf{q}/2)\rangle = (1+\eta)^{-1/2}\chi_{s'}^\dagger\chi_s G_E(q^2), \tag{2.24}$$

$$\langle N(\mathbf{q}/2)|J(0)|N(-\mathbf{q}/2)\rangle = (1+\eta)^{-1/2}\chi_{s'}^+\frac{\boldsymbol{\sigma}\times\mathbf{q}}{2M_P}\chi_s G_M(q^2). \tag{2.25}$$

Equations (2.24) and (2.25) can now be used to evaluate the form factors of nucleon core.

(i) *Proton electric form factor* $G_E^P(q^2)$: Assuming the quarks to be point-like particles in $1S_{1/2}$ orbits, we take the nucleon current as the sum of the quark currents $\bar{\Psi}_q \gamma^\mu \Psi_q$ where $\Psi_q(\mathbf{r})$ is the single-quark Dirac wave function of the form given in (2.3). Then (2.24) can be written as

$$(1+\eta)^{-1/2} G_E^P(q^2) = \int d^3r \Psi_q^+(\mathbf{r}) \Psi_q(\mathbf{r}) e^{i\mathbf{q}.\mathbf{r}}$$

$$= 4\pi N_q^2 \int_0^\infty dr r^2 J_0(|\mathbf{q}|r)(\phi_q^2 + \phi_q'^2/\lambda_q^2), \tag{2.26}$$

where $J_0(|\mathbf{q}|r)$ is the zeroth-order spherical Bessel function. Now, integrating the 2nd term on the right side of (2.26) and using (2.4) we obtain

$$G_E^P(q^2) = \frac{N_q^2}{\lambda_q}\left(1 + \frac{|\mathbf{q}|^2}{4M_P^2}\right)^{1/2}$$

$$\times [(2E_q - V_0 - |\mathbf{q}|^2/2\lambda_q)\langle\langle J_0(|\mathbf{q}|r)\rangle\rangle - a\langle\langle r^{1/2} J_0(|\mathbf{q}|r)\rangle\rangle], \tag{2.27}$$

where the double angular brackets represent the expectation values with respect to $\phi_q(r)$. In the $q^2 \to 0$ limit, (2.27) gives $G_E^P(0) = 1$, as expected.

(ii) *Proton magnetic form factor* $G_M^P(q^2)$: Using the expression for the current and the ground state wave function, (2.25) becomes

$$(1+\eta)^{-1/2} \frac{(\boldsymbol{\sigma} \times \mathbf{q})}{2M_P} G_M^P(q^2) = -\frac{2N_q^2}{\lambda_q} \int d^3r (\boldsymbol{\sigma} \times \mathbf{r}) e^{i\mathbf{q}.\mathbf{r}} \phi_q(\mathbf{r}) \phi_q'(\mathbf{r}). \tag{2.28}$$

With the choice of the z-axis parallel to $\mathbf{q}$ and equating the x-component on both sides of the above equation, one obtains

$$(1+\eta)^{1/2} \frac{|\mathbf{q}|}{2M_P} G_M^P(q^2) = -\frac{2N_q^2}{\lambda_q} 4\pi \int_0^\infty dr r^2 \phi_q(r) \phi_q'(r) J_1(|\mathbf{q}|r). \tag{2.29}$$

Equation (2.29), on integrating by parts, yields

$$G_M^P(q^2) = \frac{2M_P N_q^2}{\lambda_q}\left(1 - \frac{|\mathbf{q}|^2}{4M_P^2}\right)^{1/2} \langle\langle J_0(|\mathbf{q}|r)\rangle\rangle \tag{2.30}$$

which is easily reduced to

$$G_M^P(0) = 2M_P N_q^2/\lambda_q \tag{2.31}$$

in the limit $q^2 \to 0$. Equation (2.31) is the expression for magnetic moment μ_P of the proton, as can be obtained from (2.7). Therefore, (2.30) can be written as

$$G_M^P(q^2) = \mu_P\left(1 + \frac{|\mathbf{q}|^2}{4M_P^2}\right)^{1/2} \langle\langle j_0(|\mathbf{q}|r)\rangle\rangle. \tag{2.32}$$

As we do not take into account the coupling of the charged pion cloud to the quark core, it is trivial to obtain the electromagnetic form factors of the neutron in this model as

$$G_E^n(q^2) = 0, \quad G_M^n(q^2) = -\tfrac{2}{3} G_M^P(q^2). \tag{2.33}$$

(iii) *The isovector form factors* $F^v_{1,2}(q^2)$: One can conveniently decompose the observed nucleon form factors into isoscalar and isovector components, as the proton and neutron belong to an isotopic doublet. The isovector parts of the form factors $F^v_1(q^2)$ and $F^v_2(q^2)$ can be expressed as

$$F^v_1(q^2)=\frac{1}{2}\left(1+\frac{|\mathbf{q}|^2}{4M_P^2}\right)^{-1}\left[G^P_E(q^2)+\frac{5|\mathbf{q}|^2}{12M_P^2}G^P_M(q^2)\right], \tag{2.34}$$

$$F^v_2(q^2)=\frac{1}{2}\left(1+\frac{|\mathbf{q}|^2}{4M_P^2}\right)^{-1}[-G^P_E(q^2)+\tfrac{5}{3}G^P_M(q^2)]. \tag{2.35}$$

C. *Axial-vector form factor* $G_A(q^2)$ *of the nucleon*

For a nucleon consisting of three point-like quarks $q = u, d$ is their lowest $1S_{1/2}$ orbits. The axial-vector current is the sum of the quark axial-vector currents and is given as

$$A^\mu_\lambda(r)=\sum_q \bar{\Psi}_q(\mathbf{r})\gamma^\mu\gamma^5\frac{\tau_\lambda}{2}\Psi_q(\mathbf{r}). \tag{2.36}$$

Then the axial-vector form factor of the nucleon which measures the spin distribution of the quarks inside the nucleon is given by

$$G_A(q^2)\langle\boldsymbol{\sigma}_N\tau^\lambda_N/2\rangle=\langle N|\int d^3r e^{iq.r}A^\lambda(\mathbf{r})|N\rangle. \tag{2.37}$$

Now substituting (2.36) and (2.3) in (2.37) we get

$$G_A(q^2)\langle\boldsymbol{\sigma}_N\tau^\lambda_N/2\rangle=N_q^2\langle N|\int d^3r e^{iq.r}$$

$$\times\sum_q\left[\phi_q^2\boldsymbol{\sigma}+\frac{(\boldsymbol{\sigma}\cdot\hat{r})\boldsymbol{\sigma}(\boldsymbol{\sigma}\cdot\hat{r})}{\lambda_q^2}\phi_q'^2\right]\frac{\tau^\lambda}{2}|N\rangle. \tag{2.38}$$

After spin algebra and angular integration, we obtain by substitution

$$\langle N|\sum_q\boldsymbol{\sigma}\tau^\lambda/2|N\rangle=\tfrac{5}{3}\langle\boldsymbol{\sigma}_N\tau^\lambda_N/2\rangle, \tag{2.39}$$

$$G_A(q^2)=\tfrac{5}{3}N_q^2\left\{\ll J_0(|\mathbf{q}|r)\gg-\frac{4\pi}{\lambda_q}\int_0^\infty dr r^2\phi_q'^2\right.$$

$$\left.\times[J_0(|\mathbf{q}|r)-2J_1'(|\mathbf{q}|r)]\right\}. \tag{2.40}$$

Equation (2.40) can be simplified further by using (2.4)

$$G_A(q^2)=\frac{10}{3}\frac{N_q^2}{\lambda_q}\left[\ll V_1(r)J_0(|\mathbf{q}|r)\gg+\left\langle\!\!\left\langle r\frac{dV}{dr}\frac{J_1(|\mathbf{q}|r)}{|\mathbf{q}|r}\right\rangle\!\!\right\rangle\right], \tag{2.41}$$

where $V_1(r)=m_q+V(r)$ and

$$V(r)=ar^{1/2}+V_0. \tag{2.42}$$

Hence writing explicity we get

$$G_A(q^2) = \frac{5}{3}\frac{N_q^2}{\lambda_q}\Big[(2m_q + V_0)\langle\langle J_0(|\mathbf{q}|r)\rangle\rangle + a\langle\langle r^{1/2} j_0(|\mathbf{q}|r)\rangle\rangle + \frac{a}{2}\left\langle\left\langle r^{1/2}\frac{J_1(|\mathbf{q}|r)}{|\mathbf{q}|r}\right\rangle\right\rangle\Big]. \tag{2.43}$$

In the $q^2 \to 0$ limit, (2.43) defines the axial-vector constant g_A as

$$G_A(0) = g_A = \tfrac{5}{9}(4N_q^2 - 1) \tag{2.44}$$

which is the expression for g_A/g_V for neutron β-decay as derived in our earlier work [1].

D. *Restoration of chiral-symmetry and pion-nucleon form factor*

The quark-core contribution to the axial-vector current of the nucleon $A_\lambda^\mu(\mathbf{r})$ given in (2.36) breaks chiral symmetry as a necessary consequence of confinement. With the quark fields $\Psi_q(x)$ satisfying the Dirac equation (2.2), it can be shown that

$$\partial_\mu A_\lambda^\mu(x) = iV_1(r)\sum_{j=1}^{3}\bar{\Psi}_j(x)\gamma^\mu\gamma^5\tau_\lambda\Psi_j(x). \tag{2.45}$$

The chiral-symmetry breaking is due to the scalar part of the confining potential $V(r)$ and the quark mass m_q. To restore the chiral symmetry, one usually introduces an elementary pion field $\phi_\lambda(x)$ such that the generalized axial-vector current

$$A_\lambda^\mu(x) = \sum_{j=1}^{3}\bar{\Psi}_j(x)\gamma^\mu\gamma^5\frac{\tau_\lambda}{2}\Psi_j(x) + f_\pi\partial^\mu\phi(x) \tag{2.46}$$

is a quantity satisfying the PCAC (partially conserved axial-vector current) condition

$$\partial_\mu A_\lambda^\mu(x) = -m_\pi^2 f_\pi \phi_\lambda(x), \tag{2.47}$$

where $f_\pi = 93$ MeV is the pion-decay constant. The pion field $\phi^\lambda(x)$ satisfies the resulting equation

$$(\Box + m_\pi^2)\phi^\lambda(x) = J_5^\lambda(x), \tag{2.48}$$

where the source function $J_5^\lambda(x)$ provides the coupling of a pion to the quarks in the nucleon and is given by

$$J_5^\lambda(x) = -i\frac{V_1(r)}{f_\pi}\sum_{j=1}^{3}\bar{\Psi}_j(x)\gamma_5\tau^\lambda\Psi_J(x). \tag{2.49}$$

Now we can define the pion-nucleon form factor $G_{\pi NN}(q^2)$ for the static source $J_5^\lambda(\mathbf{r})$ as

$$G_{\pi NN}(q^2)\langle\sigma_N\cdot\mathbf{q}\tau_N^\lambda\rangle = 2M_N\langle N|\int d^3r\, e^{i\mathbf{q}\cdot\mathbf{r}} j_5^\lambda|N\rangle \tag{2.50}$$

for which the quarks in $1S_{1/2}$ orbits yields

$$G_{\pi NN}(q^2) = \frac{M_P}{f_\pi}\frac{10}{3}\frac{N_q^2}{\lambda_q}\Big[\langle\langle V_1(r)J_0(|\mathbf{q}|r)\rangle\rangle + \left\langle\left\langle r\frac{dV}{dr}\frac{J_1(|\mathbf{q}|r)}{|\mathbf{q}|r}\right\rangle\right\rangle\Big]. \tag{2.51}$$

Now comparing (2.41) and (2.51), we find that

$$G_{\pi NN}(q^2) = \frac{M_P}{f_\pi} G_A(q^2) \tag{2.52}$$

which relates the pion-nucleon form factor to the axial-vector form factor of the quark core of the nucleon. Although at $q^2 = -m_\pi^2$ limit $G_{\pi NN}(q^2)$ defines the pion-nucleon coupling constant $g_{\pi NN}$, we ignore the minor deviation in writing the $q^2 \to 0$ limit in (2.52) as

$$g_{\pi NN} \simeq \frac{M_P}{f_\pi} g_A, \tag{2.53}$$

which is the Goldberger–Treiman relation.

3. Results and conclusion

Our main purpose in the present work is basically to see to what extent the same potential model which is employed with reasonable success in explaining the static baryon properties can explain the nucleon form factors. Therefore, the potential parameters and the quark masses which provide a reasonable fit for the magnetic moments and other static properties of the baryons in the nucleon octet are used to compute the form factors of nucleons.

We find that with a typical set of the parameters

$$(a, V_0) = (0{\cdot}4604\,\text{GeV}^{1{\cdot}5}, \quad -0{\cdot}9087\,\text{GeV}), \tag{3.1}$$

$$m_u = m_d = 0{\cdot}229\,\text{GeV}, \tag{3.2}$$

the energy eigenvalue condition (2.6) yields

$$E_u = E_d = 0{\cdot}405\,\text{GeV}, \tag{3.3}$$

and

$$N_u^2 = N_d^2 = 0{\cdot}745 \tag{3.4}$$

which in turn provide the quark core contributions to the static nucleon properties after the cm-correction as

$$(\mu_P', (\langle r^2 \rangle_P')^{1/2}) = (2{\cdot}7928\,\text{nm}, 0{\cdot}795\,\text{fm}) \tag{3.5}$$

and

$$(g_A/g_V)'_{n \to pe\bar{\nu}} = 1{\cdot}27. \tag{3.6}$$

These results are in close agreement with the corresponding experimental values.

Using the same set of parameters and the corresponding solutions as given in (3.1), (3.2), (3.3) and (3.4), we compute the various form factors like $G_E^P(q^2)$, $G_M^P(q^2)$, $F_{1,2}^V(q^2)$ and $G_A(q^2)$ as provided by the expressions (2.27), (2.30), (2.34), (2.35) and (2.43) respectively. The expectation values $\ll j_0(|\mathbf{q}|r) \gg$, $\ll r^{1/2} j_0(|\mathbf{q}|r) \gg$ and $\ll r^{1/2} j_1(|\mathbf{q}|r)/|\mathbf{q}|r \gg$ appearing in these expressions are evaluated numerically for a range of $|\mathbf{q}|^2$ values, $0 \leqslant |\mathbf{q}|^2 < 1$ GeV, which enables the computation of the q^2 dependence of the form factors. We may note that while calculating $G_M^P(q^2)$ from (2.30) we use the cm-corrected value of the proton magnetic moment for μ_P.

The results for the proton electromagnetic form factors $G_E^P(q^2)$ and $G_M^P(q^2)$ are shown in figures 1 and 2 respectively. Figure 3 shows the $|\mathbf{q}|^2$ dependence of the neutron magnetic form factor $G_M^n(q^2)$. We observed only an overall qualitative agreement with the experimental data [15] with discrepancies more prominent for the higher $-|\mathbf{q}|^2$ region. We obtain $G_M^P(0) = 1$ as expected and $G_E^P(0) = \mu_P = 2{\cdot}7928\,\mu_N$ in exact agreement with $(\mu_P)_{\text{expt}} = (2{\cdot}7928)\mu_N$. It is also instructive to obtain the charge rms radius of the proton which is related to $G_E^P(q^2)$ as

$$\langle r^2\rangle_E^P = -6\frac{dG_E^P(q^2)}{d|\mathbf{q}|^2}\bigg|_{|\mathbf{q}|^2=0}$$

$$= \frac{N_q^2}{\lambda_q}[(2E_q - V_0)\langle\langle r^2\rangle\rangle_q - a\langle\langle r^{5/2}\rangle\rangle_q + 3/\lambda_q] - \frac{3}{4M_P^2}. \tag{3.7}$$

Calculating the above expression we obtain $[\langle r^2\rangle_E^P]^{1/2} = 0{\cdot}86$ fm which is in excellent agreement with the corresponding experimental value of 0·88 fm as against the MIT bag model value [16] of 1·12 fm. Next we obtain the isovector form factors $F_1^V(q^2)$ and $F_2^V(q^2)$ as prescribed in (2.34) and (2.35). Figures 4 and 5 provide a comparison of this result with that of MIT bag-model and the experimental data [17]. We observe that our results are not very different from the MIT bag model calculations [17].

Finally, the results for the axial-vector form factor $G_A(q^2)$ evaluated according to (2.43) are shown in figure 6. Here we have plotted the normalized ratio $G_A(q^2)/G_A(0)$ in comparison with the experimental data [18]. We find the agreement rather poor. Nevertheless, we can derive the rms radius associated with $G_A(q^2)$ which is

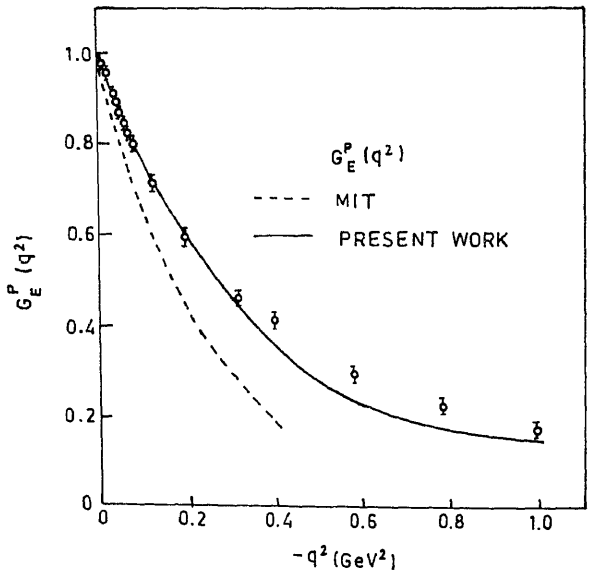

Figure 1. Charge form factor $G_E^P(q^2)$ calculated in the present model in compari-

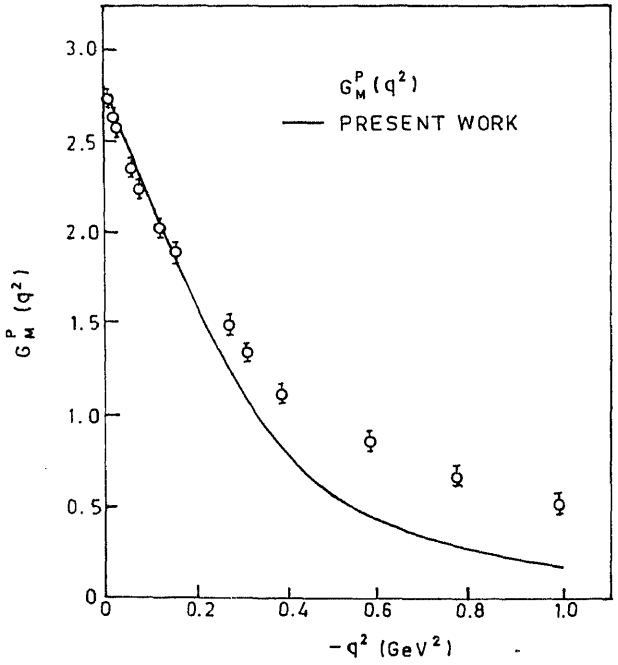

Figure 2. Magnetic form factor $G_M^P(q^2)$, calculated in the present model in comparison with the experimental data taken from [15].

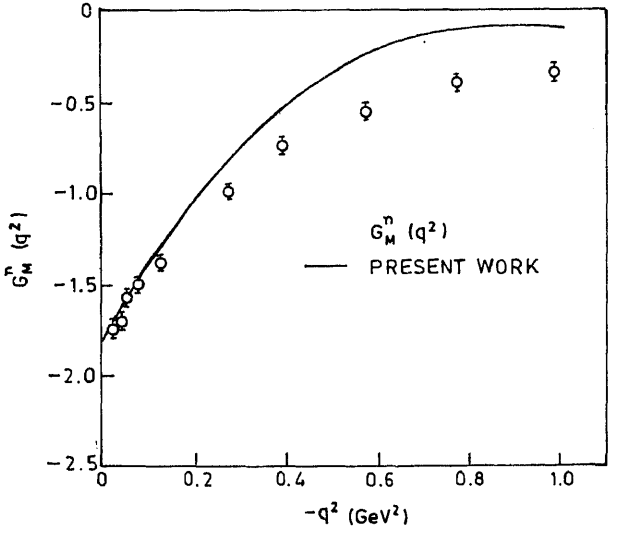

Figure 3. Magnetic form factor $G_M^n(q^2)$, calculated in the present model in comparison with the experimental data taken from [15].

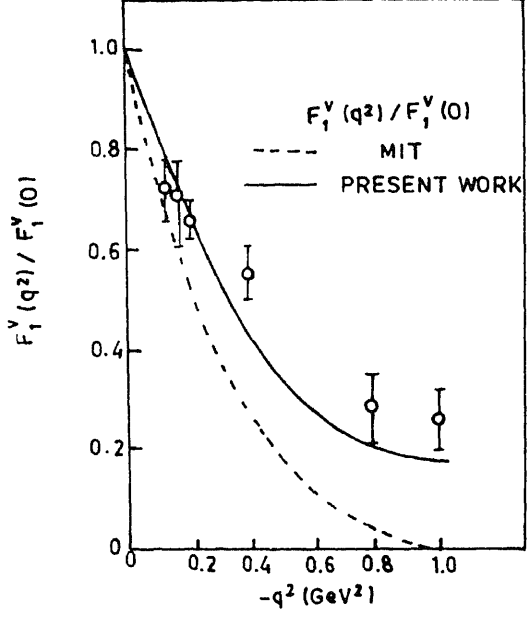

Figure 4. Isovector form factor $F_1^V(q^2)/F_1^V(0)$, as obtained in the present model in comparison with the MIT bag model calculations with bag radius $R = 1$ fm, as well as with the experimental data taken from [17].

given by

$$\langle r_A^2 \rangle = -\frac{6}{g_A}\frac{\mathrm{d}G_A(q^2)}{\mathrm{d}|\mathbf{q}|^2}\bigg|_{|\mathbf{q}|^2=0}$$

$$= \frac{5}{3g_A}\frac{N_q^2}{\lambda_q}[(2m_q + V_0)\langle\langle r^2\rangle\rangle_q + \frac{11}{10}a\langle\langle r^{5/2}\rangle\rangle_q]. \tag{3.8}$$

Calculating this expression with $g_A = G_A(0) = 1{\cdot}10$ we find $\langle r_A^2\rangle^{1/2} = 0{\cdot}88$ fm which is almost the same as $[\langle r^2\rangle_E^P]^{1/2} = 0{\cdot}86$ fm, found in this model without considering the pion-cloud effect. Finally, using the cm-corrected value for g_A in (2.53), we find that $g_{\pi NN} = 12{\cdot}81$ which can be compared with $(g_{\pi NN})_{\text{expt}} \simeq 13$. For completeness, we also obtain the c.m corrected values of magnetic moments, r.m.s. charge radii and axial-vector coupling constant ratios for octet baryons from the expressions (2.21), (2.22) and (2.23) respectively with the same set of potential parameters and quark masses given in eqs (3.1) to (3.4). For this purpose we take $m_s = 0{\cdot}475$ GeV which yields the energy eigenvalues $E_s = 0{\cdot}551$ GeV and $N_s^2 = 0{\cdot}839$ and provides the value of the magnetic moment for Λ^0-baryon after cm-correction as $\mu'_{\Lambda^0} = -0{\cdot}613$ nm in exact agreement with the experimental value. Our calculated results are presented in tables 1–3 in comparison with the corresponding uncorrected values as well as the experimental values.

It is well-known that in models where the pion is introduced by a $f_\pi \partial_\mu \phi$ term in the axial-vector current, the pionic contribution to the axial form factor $G_A(q^2)$ vanishes [19] in the Breit frame. Hence, in such a description $G_A(q^2)$ should be determined

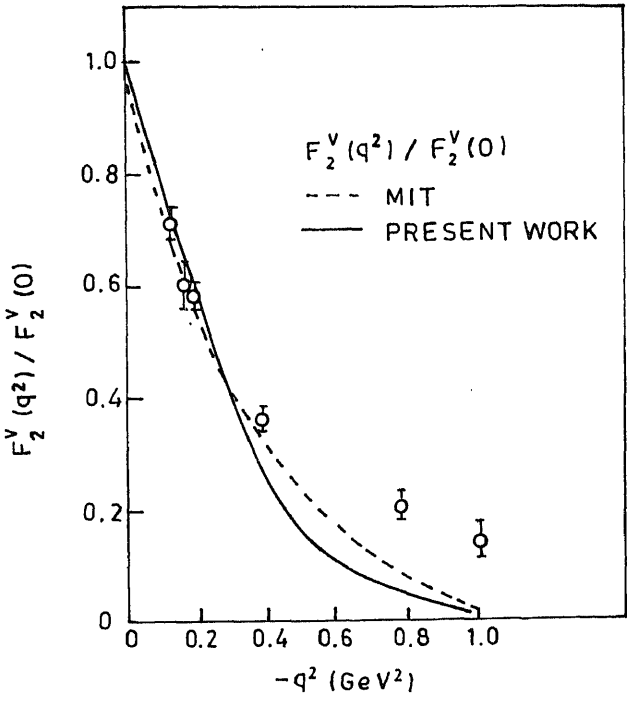

Figure 5. Isovector form factor $F_2^V(q^2)/F_2^V(0)$, as obtained in the present model in comparison with the MIT bag model calculations with bag radius $R = 1$ fm, as well as with the experimental data taken from [17].

entirely by the quark-core alone, while $G_E^p(q^2)$ and $G_M^p(q^2)$ should receive contributions from the pion-cloud effects. Therefore, we believe that the overall discrepancies observed in the present calculations may be because of the absence of possible corrections due to the pion-cloud effects. Also it is noteworthy that in a composite system like the nucleons, the form factors of high $-q^2$ measures the high-momentum tail of the relative-momentum wave function of the constituents which is generated by the short-distance dynamics believed to be governed by the one-gluon-exchange part of the interaction. So the discrepancy in figures 1 and 2 on the high $-q^2$ side may be an *a priori* indicator that this model like the MIT bag model fail to take short-range corrections into account properly. This may be attributed to the absence of any straight-forward and clear-cut mechanism to generate the three-body central potential out of the two-body potential including the short-distance one-gluon-exchange part. The minor discrepancies of our results obtained for the electromagnetic properties of octet baryons are common to most of the phenomenological models of this kind and can be partly accounted for with suitable pionic corrections, as envisaged in the cloudy bag model. The results obtained for nucleon form factors might be improved by incorporating chiral symmetry so as to bring in the pionic effects and by including the cm-corrections in the present model, which is being taken up in our subsequent work. Nevertheless, in testing the applicability of the model in these areas of study, the present

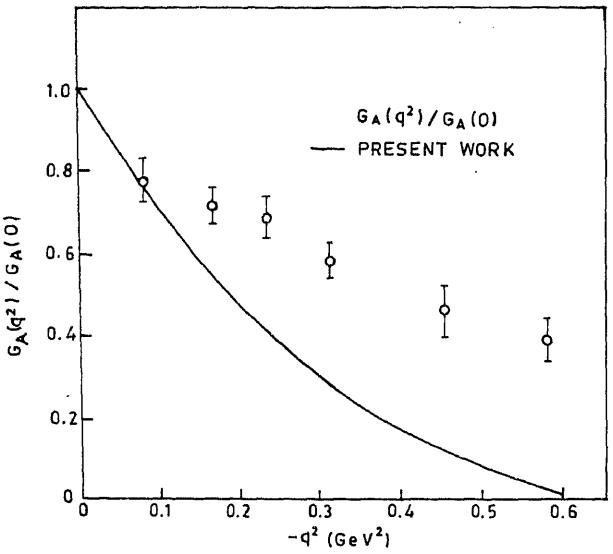

Figure 6. Axial-vector form factor $G_A(q^2)/G_A(0)$, calculated in the present model in comparison with the experimental data taken from [18].

Table 1. Magnetic moments μ_B of the octet baryons calculated by the present model with and without c.m. correction, as compared with the results of the cloudy bag model (CBM) and the experimental data (all numbers in nuclear magnetons).

Baryon	Present calculation of μ_B		μ_B CBM calculation (Ref. [20])	μ_B Experiment (Ref. [21])
	Uncorrected	After cm correction		
P	2·2053	2·7928	2·60	2·7928444 ± 0·0000011
η	−1·4702	−1·8088	−2·01	−1·91304308 ± 0·00000054
Λ^0	−0·5115	−0·6130	−0·58	−0·613 ± 0·004
Σ^+	2·1308	2·6126	2·34	2·379 ± 0·020
Σ^0	0·6605	0·7917	—	0·61 ± 0·08*
Σ^-	−0·8096	−0·9115	−1·08	−1·14 ± 0·05
Ξ^0	−1·1721	−1·3766	−1·27	−1·250 ± 0·014
Ξ^-	−0·4369	−0·5585	−0·51	−0·69 ± 0·04
Λ, Σ^0	−1·2732	−1·5665	—	−1·82 + 0·18† − 0·25

*Values computed according to the definition $\mu_{\Sigma^0} = \frac{1}{2}(\mu_{\Sigma^+} + \mu_{\Sigma^-})_{exp}$, which is quite often referred to as the measured value.
†Ref. [20]

Table 2. Axial-vector coupling-constant ratio (g_A/g_V) calculated in the present model with and without cm correction, as compared to the experiment

Decay mode	Axial-vector coupling-constant ratio (g_A/g_V) Uncorrected	With cm correction	(g_A/g_V) Experiment (Ref. [21])
$\eta \to Pe\bar{\nu}$	1·1004	1·2703	$1{\cdot}254 \pm 0{\cdot}006$
$\Lambda \to Pe\bar{\nu}$	0·7176	0·8130	$0{\cdot}694 \pm 0{\cdot}025$
$\Sigma^- \to ne\bar{\nu}$	−0·2392	−0·2710	$-0{\cdot}362 \pm 0{\cdot}043$
$\Xi^- \to \Lambda e\bar{\nu}$	0·1594	0·1780	$0{\cdot}25 \pm 0{\cdot}05$
$\Xi^- \to \Sigma^0 e\bar{\nu}$	1·1960	1·3356	–
$\Xi^0 \to \Sigma^+ e\bar{\nu}$	1·1960	1·3356	–

Table 3. The rms charge radii $\langle r^2 \rangle_B^{1/2}$ of octet baryons calculated in the present model with and without cm correction, as compared to the experimental and Ferreira–Halayel–Zagury (FHZ) model values (all numbers in fm).

Baryon	$\langle r_B^2 \rangle^{1/2}$ Uncorrected	With cm correction	$\langle r^2 \rangle_B^{1/2}$ Experiment	FHZ model (Ref. [22])
P	0·8816	0·7947	$0{\cdot}87 \pm 0{\cdot}02$	0·932
n	0	0	−0·341	0
Λ^0	0·3035	0·3037		0·346
Σ^+	0·9324	0·8571		0·994
Σ^0	0·3035	0·3037		0·346
Σ^-	0·8276	0·7416		0·86
Ξ^0	0·4293	0·4294		0·48
Ξ^-	0·7700	0·6835		0·79

model has been found to be meaningful, with the simple and straightforward approach yielding encouraging and reasonable results.

We thus find a simple-independent quark model based on the Dirac equation with a square-root confining potential of the form given by (1.1) which provides a reasonable fit for the electromagnetic form factors of nucleons and the static baryon properties in a flavour-independent manner. This effective individual quark potential, phenomenologically representing the confining interaction due to a nonperturbative multigluon mechanism serves as an alternative scheme to the CBM in studying the baryons. The purpose of this paper is not to claim that nature prefers such a square-root confining potential to other potentials advanced earlier in this connection so as to present an analysis that complements studies based on different potential models. Such studies from various quark models, when extended to describe the baryonic properties

and $\mathbf{p}_2$ respectively is given by

$$T_d = \langle \Psi_f^{(-)} | V_i | \Phi_i \rangle, \tag{1}$$

where Φ_i is the initial unperturbed state corresponding to a decomposition of the total Hamiltonian H, say

$$H = H_i + V_i, \tag{2a}$$

where

$$V_i(\mathbf{r}_1, \mathbf{r}_2) = 1/r_{12} - 1/r_2, \tag{2b}$$

$\mathbf{r}_1, \mathbf{r}_2$ being position vectors of the atomic and the incident electron and $\Psi_f^{(-)}$ is the exact final three particle scattering state with converging wave boundary conditions. In hyperspherical coordinates $\Psi_f^{(-)}$ may be represented as (see Das [10, 11], particularly for notations)

$$\Psi_f^{(-)} = \sqrt{\frac{2}{\pi}} \sum_\lambda \left(\frac{F_\lambda(\rho)}{\rho^{5/2}} \right) \phi_\lambda^* \, \phi_\lambda(\alpha, \hat{r}_1, \hat{r}_2). \tag{3a}$$

Here $\rho = PR$, $R = \sqrt{r_1^2 + r_2^2}$, $P = \sqrt{p_1^2 + p_2^2}$, $\alpha = \tan^{-1}(r_2/r_1)$, $\alpha_0 = \tan^{-1}(p_2/p_1)$ and

$$\phi_\lambda(\alpha, r_1, r_2) = P_n^{l_1 l_2}(\alpha) \, Y_{l_1 l_2}^{lm}(\hat{r}_1, \hat{r}_2), \tag{3b}$$

$P_n^{l_1 l_2}(\alpha)$ being the Jacobi polynomial.

The radial waves F_λ's satisfy the coupled set of equations (see Das [10], Lin [12])

$$\left[\frac{d^2}{d\rho^2} + 1 - \frac{\nu_\lambda(\nu_\lambda + 1)}{\rho^2} \right] F_\lambda + \sum_{\lambda'} \frac{2\alpha_{\lambda\lambda'}}{\rho} F_{\lambda'} = 0. \tag{3c}$$

Here λ stands for the multiplet (n, l_1, l_2, l, m) or the eigenvalue $2n + l_1 + l_2$ depending on the context and $\nu_\lambda = \lambda + 3/2$ and

$$\alpha_{\lambda\lambda'} = \left\langle \phi_\lambda \left| \frac{1}{\cos\alpha} + \frac{1}{\sin\alpha} - \frac{1}{|\hat{r}_1 \cos\alpha - \hat{r}_2 \sin\alpha|} \right| \phi_{\lambda'} \right\rangle \Big/ P. \tag{3d}$$

When the off-diagonal matrix elements $\alpha_{\lambda\lambda'} (\lambda \neq \lambda')$ are neglected, the solution of eq. (3c) simply becomes Coulomb waves corresponding to charge parameter $\alpha_{\lambda\lambda} \equiv \alpha_\lambda$. In this approximation which we call *weak correlation approximation* the final three-particle scattering state becomes

$$\Psi_{f0}^{(-)} = \sum_\lambda 2(2\pi)^{5/2} i^\lambda e^{-i\eta_\lambda} \left(\frac{F_\lambda^{(0)}(\rho)}{\rho^{5/2}} \right) \phi_\lambda^*(\alpha_0, \hat{p}_1, \hat{p}_2) \times \phi_\lambda(\alpha, \hat{r}_1, \hat{r}_2). \tag{4}$$

$F_\lambda^{(0)}$ satisfies the boundary conditions

$$F_\lambda^{(0)}(\rho) \sim \rho^{\nu_\lambda + 1}, \quad \rho \to 0$$

$$\sim \sin(\rho - \nu_\lambda \pi/2 + \alpha_\lambda \ln 2\rho + \eta_\lambda), \quad \rho \to \infty,$$

Explicitly F_λ is given by

$$F_\lambda^{(0)}(\rho) = e^{1/2\pi\alpha_\lambda}|\Gamma(\nu_\lambda + 1 + i\alpha_\lambda)|2^{\nu_\lambda}\rho^{\nu_\lambda+1}e^{-i\rho}$$

$$\times {}_1F_1(i\alpha_\lambda + \nu_\lambda + 1, 2\nu_\lambda + 2, 2i\rho)/\Gamma(2\nu_\lambda + 2).$$

Asymptotically $\Psi_f^{(-)}$ (and also $\Psi_{f0}^{(-)}$) behaves as a superposition of a distorted plane wave and incoming converging waves only.

Exchange amplitude is obtained after the substitution $\alpha \to \pi/2 - \alpha$ and $f_1 \rightleftarrows f_2$. Differential cross section is then obtained as usual.

In our present calculation we included terms in the expansion (4) for n, l, l_1, l_2 taking values from zero to certain maximum values n_{max}, l_{max}, l_{1max}, l_{2max} and set $m = 0$. For fixed values of other parameters, convergence is practically obtained with $n_{max} = 5$ or 6 in all the calculations reported here. So we took $n_{max} = 6$ in this calculation. We varied l_{max} from zero to a maximum value of six and for fixed $l_{1\,max}$ we varied $l_{1\,max}(= l_{2max})$ from zero to seven only. With these values convergence is practically obtained in the results. Here we have calculated triple differential cross sections in a plane configuration for incident electron energies of 17·6 eV, 27·2 eV and 54·4 eV in the low energy range for which there are certain experimental results. Results are presented and discussed in the next section.

3. Results

Three sets of results for triple differential cross section are presented in figure 1 for three different incident energies corresponding to the parameters (a) $E_i = 54{\cdot}4$ eV, $E_1 = 5$ eV, $\theta_2 = 4°$; (b) $E_i = 27{\cdot}2$ eV, $E_1 = E_2 = 6{\cdot}8$ eV, $\theta_2 = 15°$; and (c) $E_i = 17{\cdot}6$ eV, $E_1 = E_2 = 2$ eV, $\theta_2 = 140°$. Angles are measured positive or negative depending on if the direction is anticlockwise or clockwise with reference to the incident electron momentum direction.

In figure 1(a) we compare one set of our results for 54·4 eV energy with the theoretical results of convergent close coupling calculation (CCC, Bray *et al* [5]), BBK theory (Brauner *et al* [4]), three-body distorted wave Born approximation (3DWBA, Jones *et al* [2]) and with the experimental results of Ehrhardt *et al* [13] as normalized by Bray *et al*. The experimental results of Ehrhardt and associates are not absolute. For a fixed energy a single multiplicative factor normalizes the results for all scattering angles. Since CCC calculation gives a good total ionization cross section, Bray *et al* [5] normalized these experimental data for each energy by multiplying with a single factor which gives visually the best fit with all of their theoretical results. Thus in normalizing the data of Ehrhardt *et al* for 54·4 eV, they considered all the four sets of results corresponding to $\theta_2 = 4°$, 10°, 16° and 23° during the visual fit (see also figure 2 in ref. [5]). Now the comparison with our results show that our results are really good and are of the right order of magnitude. Inclusion of the effect of coupling are expected to give still better results.

In figures 1(b) and 1(c) we compare one set of our theoretical results for each of energies 27·2 eV and 17·6 eV with the experimental results of Ehrhardt *et al* [13], again

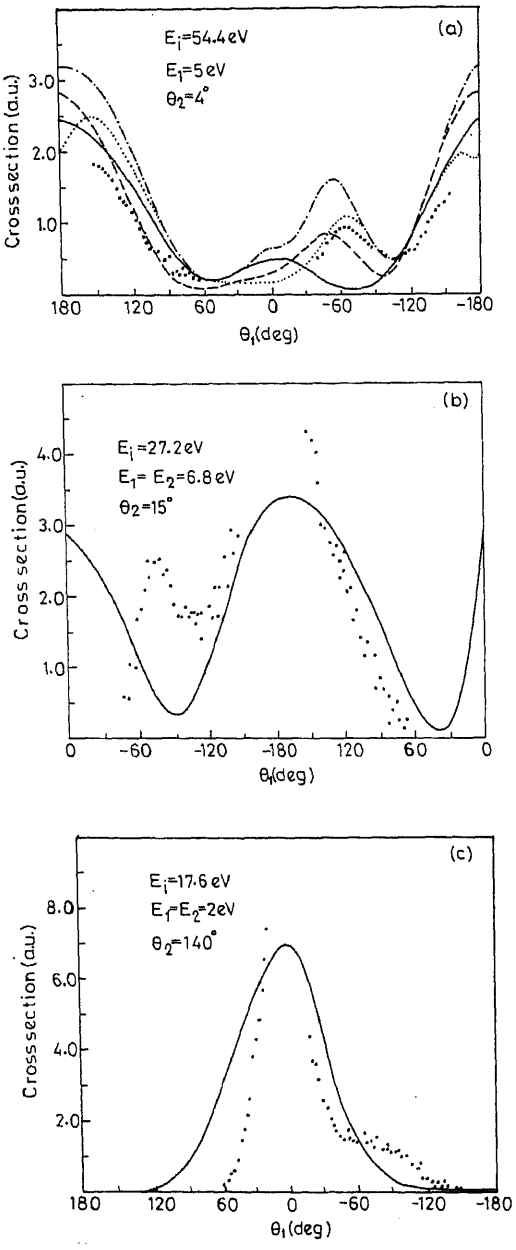

Figure 1a, b, c. Triple differential cross sections for ionization of hydrogen atoms by electrons in a plane for different scattering angles (θ_1) and for three different sets of kinematic conditions. Theory: continuous, present theory; dashed, BBK [4]; dash-dotted, 3DWBA [2]; dotted, CCC [5]. Experiment: points Ehrhardt *et al* [13] suitably normalized.

comparison qualitatively shows that the present results are not bad. Inclusion of coupling effect may be expected to improve the results further. The results are also in conformity with the observations of Murray *et al* [14] regarding contributing partial waves.

The calculations presented here were done on a 486 PC with Linux as operating system. For a single point (i.e. for fixed energy and angles) it took about half an hour computer time for a double precision calculation.

4. Conclusion

The present weak correlation theory is capable of representing gross features of low energy cross section curves. For very low energies, effect of coupling among different partial waves is important and cannot be simply neglected. The calculation will then become much more complicated. Such a calculation is now in progress.

Acknowledgement

One of the authors (KC) is grateful to CSIR for providing a research fellowship.

References

[1] S Jones, D H Madison and M K Srivastava, *J. Phys.* **B25**, 1899 (1992)
[2] S Jones, D H Madison, A Franz and P L Altick, *Phys. Rev.* **A48**, R22 (1993)
[3] J Berakdar and J S Briggs, *Phys. Rev. Lett.* **72**, 3799 (1994)
[4] M Brauner, J S Briggs and H Klar, *J. Phys.* **B22**, 2265 (1989)
[5] I Bray, D A Konovalov, I E McCarthy and A T Stelbovics, *Phys. Rev.* **A50**, R2818 (1994)
[6] J N Das and S Seal, *Phys. Rev.* **A47**, 2978 (1993)
[7] J N Das and S Seal, *Aust. J. Phys.* **47**, 49 (1994)
[8] D A Konovalov, *J. Phys.* **B27**, 5551 (1994)
[9] T Rösel, J Röder, L Frost, K Jung and H Ehrhardt, *Phys. Rev.* **A46**, 2539 (1992)
[10] J N Das, *Aust. J. Phys.* **47**, 743 (1994)
U Fano and A R P Rau, *Atomic collisions and spectra* (Academic Press, New York, 1994) sec. 10
[11] J N Das, Invited talk, Euroconference, Colmar 7–9, December 1994
[12] C D Lin, *Phys. Rev.* **A10**, 1986 (1974)
[13] M Brauner, J S Briggs, H Klar, J T Broad, T Rösel, K Jung and H Ehrhardt, *J. Phys.* **B24**, 657 (1991)
H Ehrhardt (1991) (private communication)
[14] A J Murray, F H Read, N J Bowring, *Phys. Rev.* **A49**, R3162 (1994)

PRAMANA
— journal of
physics

© Printed in India

September 1996
pp. 255–259

Surface enhanced Raman scattering studies of acetophenone on colloidal silver particles

S EDWIN JAYARAJ, V RAMAKRISHNAN*, S PERUMAL† and M GURUNATHAN‡
Laser Laboratory, Department of Microprocessor and Computer, School of Physics; †School of Chemistry; ‡USIC, Madurai Kamaraj University, Madurai 625 021, India

MS received 29 February 1996; revised 3 July 1996

Abstract. Intense Raman scattering by acetophenone molecules adsorbed on colloidal silver particles is reported. Greater enhancement is observed for the ring breathing and ring stretching vibrations. The orientation determination analysis shows that the adsorption of acetophenone molecule is neither through its co-ordinating site nor through its π-orbital system and there is no strong chemical interaction. However significant intensity enhancement for several vibrations suggests that the contribution is from classical electromagnetic field on the rough surface.

Keywords. Acetophenone; adsorption; enhancement orientation.

PACS No. 33·20

1. Introduction

During the early years after the discovery of surface enhanced Raman scattering (SERS), there was more focus on the enhancement of Raman scattered intensity from colourless substances in order to demonstrate the mechanism behind SERS. While there are several theoretical models proposed to explain the SERS process. there has been a consensus among the investigators. The consensus is that, major contribution to SERS originates from electromagnetic and chemical enhancement mechanisms [1].

The determination of the orientation of the adsorbate molecule at the surface is very important in understanding metal adsorbate binding and reactivity of the adsorbate with the substrate. In order to understand the enhancement mechanism and to determine the orientation dynamics of the molecule on the colloidal surface, a simple aromatic ketone namely acetophenone has been chosen for our SERS investigation.

2. Experimental

Acetophenone was immiscible with aqueous silver sol. It was mixed with methanol in the volume ratio 1:1 for carrying out normal Raman and SERS measurements. These studies were also carried out in other alcohols like ethanol, iso-propanol and *t*-butanol to study the effect of solvent on the enhancement process.

*Author to whom correspondence should be addressed.

All the chemicals used were of reagent grade and double distilled water was used for the preparation of the solutions. The silver sol was prepared according to the procedure described by von Raben *et al* [2]. The silver sol and the acetophenone solutions were thoroughly mixed before sampling out for Raman measurements. The details of the Raman apparatus were given elsewhere [3]. The laser power at the sample was about 35 mW.

3. Results and discussion

The normal Raman spectrum (nRs) and the SERS spectrum of acetophenone–methanol, acetophenone–ethanol, acetophenone–isopropanol and acetophenone–*t*-butanol mixtures were recorded under the same experimental conditions. However, significant intensity enhancement was found only in the case of the acetophenone–methanol mixture. Hence, the discussion pertains only to this case. The reason for the enhancement of this particular case has been dealt with, in the latter part of the discussion.

The nRs and SERS spectra of the acetophenone–methanol mixture are given in figure 1. The Raman bands are assigned and listed in table 1. Here the vibrational modes are assigned by considering a molecular model of planar (C_s) symmetry.

Careful analysis of the spectral profile of nRs and SERS shows that the bands at 1002 and 1600 cm^{-1} are greatly enhanced, whereas the remaining bands at 368, 620, 742, 1077, 1268, 1690 and 3065 cm^{-1} are only moderately enhanced. Three new bands at 780, 1442 and 2843 cm^{-1} are observed in the SERS spectrum.

Now let us focus our attention on the strongly enhanced bands in the SERS spectrum (the bands at 1002 and 1600 cm^{-1}). The band due to the ring breathing vibration appears intense between 990–1010 cm^{-1} for mono, *m*-di and sym-tri substitution [4]. The most intense band observed at 1002 cm^{-1} [SERS] is assigned to this ring breathing vibrational mode.

For the mono substituted benzenes having the electron donating groups as substituents, the intensity of the ring stretching vibration is relatively high [5]. In the present investigation of acetophenone, since maximum π–π overlap occurs between the aromatic phenyl ring and the carbonyl group, the ring stretching band is observed as an intense band at 1600 cm^{-1}, the second next to ring breathing vibration. The carbonyl bands are the most characteristic bands in the Raman spectrum. Here in acetophenone, the medium intensity band at 1690 cm^{-1} is assigned to the carbonyl stretching vibration.

Among the five C–H in plane bending vibrations four modes have stable frequencies. The bands due to 9a and 18a vibrations are very intense in the IR spectrum whereas in the Raman spectrum, the vibration 18a is the most prominent one. The band corresponding to the normal mode 3 is weak in general in both IR and Raman spectra and it occurs usually in the range 1253–1351 cm^{-1}. Here in acetophenone the vibrations observed at 1027 cm^{-1} (18a), 1268 cm^{-1} (3), 1162 cm^{-1} (15), 1183 cm^{-1} (9a) and 1077 cm^{-1} (18b) are due to the in-plane CH-deformations. Among these five bands, the 1027 cm^{-1} bands is weak and the 1268 and 1077 cm^{-1} bands are of medium intensity, whereas the 1162 and 1183 cm^{-1} bands overlap and form a broad feature. The strong band at 742 cm^{-1} is assigned to CH out of plane bending vibration.

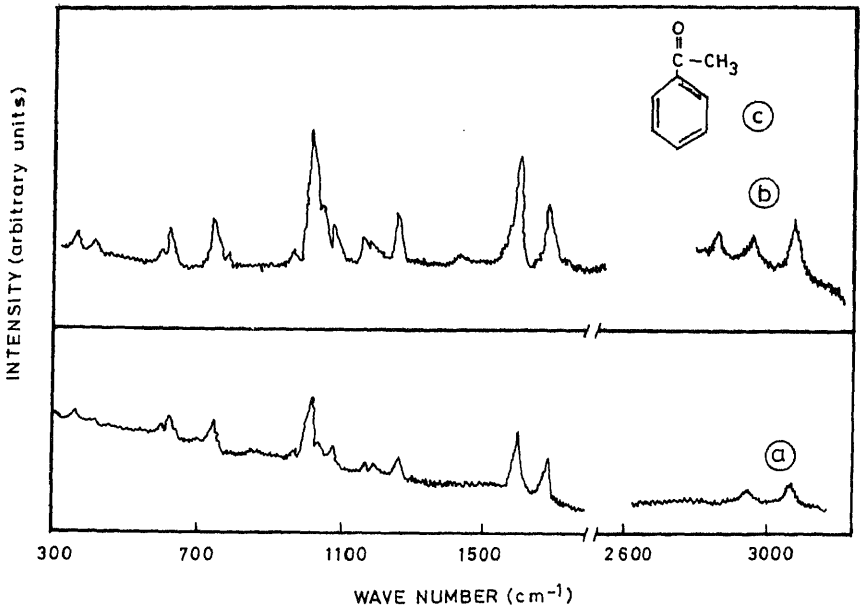

Figure 1. (**a**) Normal Raman spectrum of acetophenone–methanol mixture (1:1 volume ratio); (**b**) SERS spectrum of acetophenone–methanol mixture (1:1 volume ratio); (**c**) Structure of acetophenone molecule.

Table 1. Raman spectral data and assignments for acetophenone–methanol mixture.

NRS (cm^{-1})	SERS (cm^{-1})	Assignments
370 (w)	368 (w)	C–C–C out of plane bending
420 (vw)	418 (vw)	Out of plane skeletal vibration
606 (vw)	606 (vw)	Ring deformation
620 (w)	620 (m)	C–C–C in plane bending
742 (m)	742 (s)	CH-out of plane bending
	780 (vw)	CH-out of plane bending
968 (vw)	966 (vw)	CH-out of plane bending
1004 (s)	1002 (vs)	Ring breathing
1028 (vw)	1027 (s)	In plane CH-deformation
1078 (w)	1077 (m)	In plane CH-deformation
1162 (vw)	1162 (w)	In plane CH-deformation
1185 (vw)	1183 (w)	In plane CH-deformation
1270 (w)	1268 (m)	In plane CH-deformation
	1442 (w)	CH_3 deformation
1600 (s)	1600 (vs)	Ring stretching
1692 (m)	1690 (s)	Carbonyl stretching
	2843 (m)	CH_3-symmetric stretching
2940 (vw)	2940 (m)	CH_3-asymmetric stretching
3065 (w)	3066 (s)	Aromatic CH-stretching

w – weak; vw – very weak; s – strong; m – medium; vs – very strong

The vibrational mode (6) splits into two vibrations in benzene namely 6a and 6b. The frequency of vibration 6a is greatly variable and that of 6b is rather stable. The band at 368 cm^{-1} in the SERS spectrum of acetophenone has been assigned to C–C–C out of plane vibration (6a) whereas the medium intensity band at 620 cm^{-1} is due to the C–C–C in-plane bending vibration.

Of the five CH stretching vibrations only one strong band is observable in Raman spectrum and it occurs around 3065 cm^{-1}. Here in acetophenone the strong band observed at 3066 cm^{-1} is assigned to this CH-stretching vibration. A new band (SERS) observed at 2843 cm^{-1} is due to CH_3-symmetric stretching vibration and another band at 2940 cm^{-1} is assigned to CH_3-asymmetric stretching vibration. Since the solvent mixture contains methanol, its bands also may overlap with the methyl bands.

4. Orientation determination

Acetophenone may bind to the metal surface either via its ring π-system or via the partially negative carbonyl oxygen. When an aromatic molecule is adsorbed on the metal surface through its π-orbital system, the frequencies of ring vibrations are normally shifted and their band profiles are broadened. The frequency shift is caused by either ring-surface π-donation or surface-ring π^* back donation [6]. The increase in bandwidth is due to additional vibrational relaxation caused by interaction between the metal surface and the ring.

The SERS spectrum of acetophenone shows greater enhancement for the ring breathing and ring stretching vibrations. But neither frequency shift nor band broadening is observed in both vibrations which are very essential to demonstrate the 'flat on' adsorption of the molecule.

The frequency of aromatic CH-stretching vibrations was reported to be relatively unambiguous probe for adsorbate orientation based on the surface Raman selection rules [6, 7]. The benzene ring, being easily adsorbed flat on the electrode surface, showed a complete intensity loss of CH-stretching vibration in marked contrast to the large increase in intensity along with frequency downshift and band broadening observed for ring breathing vibration [6]. But here in the SERS spectrum of acetophenone, neither frequency downshift and broadening nor the complete loss of CH-stretching vibration is noticed. Thus the surface selection rules couldn't clearly establish the orientation of the molecule. The alternate possibility is that the molecule is adsorbed through its coordinating site. But if the molecule is adsorbed on the metal surface entirely through its substituents, then enhancement in intensity for the substituents vibrations is observed. The carbonyl group is the coordinating site in the acetophenone molecule. But in the SERS spectrum the intensity of the band due to carbonyl vibration is only slightly enhanced. So, adsorption could not have taken place through this site.

The failure for stronger interaction of the molecule with the metal surface may be due to the following reasons,

(i) The methyl group in acetophenone as in the case of toluene [6] is unlikely to interact strongly with the metal surface,
(ii) the co-planarity of the phenyl ring and the substituent groups leads to greater conjugation and strong π-orbital interaction between them, and

the whole acetophenone molecule participates in a conjugated manner, the lity of interaction through individual group is prevented as adsorption through e of the groups will affect the others.

rboxylic acids [8], a decrease in SERS intensity is observed when the vibrating is separated several angstroms away from the surface. From this, it is inferred e acetophenone molecule necessarily has to be nearer to the Ag metal surface and en the enhancement in intensity for the ring modes can be accounted for. So, the ty enhancement for the vibrational modes could have been derived mainly from ge electric field gradient present on the colloidal silver surface.

influence of alcohol on the SERS can also be accounted for by the above e.m. echanism. Methanol molecules, being small in size and having high dielectric nt relative to other alcohols employed in this SERS investigations, probably ely solvate the acetophenone molecules. Moreover, in methanol the henone molecules are polarized to a larger extent than the other alcohols by the field gradient. This results in higher intensity enhancement in methanol ns than in other alcohols.

clusion

different alcohol–acetophenone mixtures used, significant intensity enhance- s found only in the case of acetophenone–methanol mixture. The bands due to eathing (1002 cm^{-1}) and the ring stretching vibrations (1600 cm^{-1}) are greatly ed. Since adsorption of the acetophenone molecule does not occur through its nating site, the contribution to the intensity enhancement of most of the bands due to the large e.m. field present near the surface.

wledgement

thors are grateful to the Department of Atomic Energy for the financial support is of a project. One of the authors (SEJ) acknowledges the financial support ed by the Council of Scientific and Industrial Research, New Delhi through its Research Fellowship award.

nces

L Garrel, *Anal. Chem.* **61**, 401A (1989)
V von Raben, R K Chang, B L Laube and P W Barber, *J. Phys. Chem.* **88**, 5290 (1984)
Ramakrishnan, N Krishnamurthy, M Gurunathan and V J P Srivatsavoy, *Spectrochim. cta* **A46**, 1615 (1990)
Varsanyi, *Vibrational spectra of benzene derivatives* (Academic Press, New York, 1969) 232, 150, 251, 294
Colthup, L H Daly and S E Wiberly, *Introduction to infrared and Raman spectroscopy* cademic Press, New York, 1975) p. 261
Gao, J P Davies and M J Weaver, *J. Phys. Chem.* **94**, 6858 (1990)
Gao and M J Weaver, *J. Phys. Chem.* **89**, 5040 (1985)
Moskovits and J S Suh, *J. Am. Chem. Soc.* **107**, 6826 (1985)

PRAMANA
— journal of
physics

© Printed in India

Vol. 47, No. 3,
September 1996
p. 261

Errata

Ratios of B and D meson decay constants with heavy quark symmetry

A K GIRI, L MAHARANA and R MOHANTA

(*Pramana – J. Phys.*, 46, pp. 411–416, June 1996)

On p. 413, eq. (6): $\langle 0|\bar{q}\gamma_\mu\gamma_5 c|D_q(v)\rangle = if_{D_q}\sqrt{m_{D_q}}v^\mu$, should be read as

$$\langle 0|\bar{q}\gamma_\mu\gamma_5 c|D_q(v)\rangle = if_{D_q}\sqrt{m_{D_q}}v_\mu.$$

On p. 413, eq. (10) and the sentence preceding it: For the relevant matrix elements of the operator one can write from ref. [18]
$\langle 0|\partial_\mu(\bar{q}\gamma_\mu\gamma_5 h_v^c)|D_q(v)\rangle = \frac{1}{2}\bar{\Lambda}F(\mu)\mathrm{Tr}(v_\mu\gamma_\mu\mathcal{M}(v))$ should be read as
For the relevant matrix elements of the operator one can write from ref. [19]

$$\langle 0|\partial_\mu(\bar{q}\gamma_\mu\gamma_5 h_v^c)|D_q(v)\rangle = \tfrac{1}{2}\bar{\Lambda}F(\mu)\mathrm{Tr}(v_\mu\gamma_\mu\gamma_5\mathcal{M}(v)).$$

IANA
rnal of
hysics

© Printed in India

Vol. 47, No. 4,
October 1996
pp. 263–269

metric scattering in electron and positron impact zation of metastable 2*s*-state hydrogen atoms

AS and S DHAR
ment of Applied Mathematics, University College of Science, 92, Acharya Prafulla ra Road, Calcutta 700 009, India

ceived 1 July 1996; revised 17 September 1996

ct. Triple differential cross sections for ionization of hydrogen atoms in the metastable e by the impact of electrons and positrons have been calculated for coplanar symmetric try. In this calculation a multiple scattering theory due to Das [10] and Das and Seal [11] en used. An analysis of the results reveals that unlike scattering from the ground state, ing from 2*s*-state is essentially a higher order process except for the binary collision on. Moreover, here, the cross section results for 2*s*-state are much larger compared to those ttering from the ground state. It is also found that the ionization mechanism at large ing angles for ionization from the 2*s*-state is different from that for ionization from the l state.

rds. Cross section; collision; ionization; scattering; electron; positron.

No. 34·80

roduction

nar symmetric scattering in electron-atom and positron-atom ionization colli- s now an important field of study [1–9]. Results for ionization from the ground eveals the existence of double peak structure for the cross section curves. The first s the usual binary peak which occurs at about 45° for high energies of incident ons or positrons. The second peak occurs at a large scattering angle and was ned by Briggs [3,4] as due to a double collision effect, first a backward elastic ring from the ion followed by an ionization collision. It will be interesting to see if r double peak structure exist for ionization collisions from excited states. Studies tive magnitudes of cross sections for ionization from the ground state, ionization he 2*s*-state and the study of ionization mechanism in such scatterings will be sting. Hence we made a calculation of ionization cross sections of hydrogen in the metastable 2*s*-state by the impact of electrons and positrons at high es. In this study we used the multiple scattering theory due to Das [10] and Das eal [11]. The above theory was successfully used by Das and Seal in studies of tion of hydrogen and helium atoms under different kinematic conditions [11, ncidentally the wave function for the final three-particle continuum state used in heory is the same as the first order Faddeev wave function [13] except for nalization factor. For ionization from excited states there exist at present very few ations. The first Born and second Born calculation of Vučič *et al* [14], BBK

2s-state and the calculation of Born, BBK and DWIA theory of Berakdar *et al* [17] may be mentioned for ionization from 2p-state. Absence of experimental results is responsible for very slow development of this field of research.

In §2 we describe, in brief, the structure of the scattering amplitude in the multiple scattering theory. Cross section and other results are described in §3 and certain concluding remarks are made in §4.

2. Scattering amplitude

The form of the scattering amplitude in the multiple scattering theory [11] is

$$f(\bar{p}_1, \bar{p}_2) = N[-2f_{\mathrm{PWB}} + f_{eT} + f_{PT} + f_{Pe}], \tag{1a}$$

where the different terms within the braces are given by expressions of the form

$$-(2\pi)^{-1} \int \phi^{(-)*}(\bar{r}_1, \bar{r}_2)(v_{12} + v_2)\exp(i\bar{p}_i \cdot \bar{r}_2)\varphi_{2s}(\bar{r}_1)/(2\pi)^{3/2}. \tag{1b}$$

where $v_{12} = Z/r_{12}$, $v_2 = -Z/r_2$, $Z = 1$ for electron and $Z = -1$ for positron and N is a normalizing factor.

For f_{PWB}, $\phi^{(-)}(\bar{r}_1, \bar{r}_2)$ is given by $\exp(i\bar{p}_1 \cdot \bar{r}_1 + i\bar{p}_2 \cdot \bar{r}_2)$, corresponding to the final two particles represented by plane waves. For f_{eT}, which is also the first Born amplitude, $\phi^{(-)}(\bar{r}_1, \bar{r}_2) = \varphi^{(-)}_{\bar{p}_1}(\bar{r}_1) \times \exp(i\bar{p}_2 \cdot \bar{r}_2)$, corresponding to plane wave for the scattered particle and Coulomb wave (due to Coulomb potential of the target nucleus and the ejected electron) for the atomic electron. The term f_{PT} is similar to f_{eT} except that the role of the electron and the projectile is interchanged. For f_{Pe}, $\phi^{(-)}(\bar{r}_1, \bar{r}_2)$ is given by $\varphi^{(-)}_{\bar{p}}(\bar{r})\exp(i\bar{P} \cdot \bar{R})$, where $\bar{r} = (\bar{r}_2 - \bar{r}_1)/2$, $\bar{R} = (\bar{r}_2 + \bar{r}_1)/2$, $\bar{p} = \bar{p}_2 - \bar{p}_1$ and $\bar{P} = (\bar{p}_2 + \bar{p}_1)$. In this last term the projectile electron interaction is exactly treated in the final channel, where centre of mass moves as a plane wave.

Now each of the scattering amplitude contains two parts, corresponding to v_{12} and v_2 of the interaction potential V_i in the initial channel.

Thus one has for example

$$f_{PT} = f_{PT}(v_{12}) + f_{PT}(v_2). \tag{2}$$

3. Results and discussion

A. *Ionization mechanism*

The present form for the scattering amplitude is specially suitable for an analysis of the scattering mechanism. If in any situation contribution from a single term is dominant, it is indicative of the fact that in the kinematic condition the particular potential, whose effect is taken into account in the corresponding final channel wave function plays the prime role in the scattering process. Thus to unveil the scattering mechanism we look at different components of the scattering amplitude over the entire angular region presented in table 1 for a particular case. We note that except near the binary direction,

Table 1. Different components of scattering amplitude for symmetric ionization of hydrogen atoms in the metastable 2*s*-state by incident electron energy of 500 eV.

$\theta_1 = \theta_2$ (deg.)	f_{PWB}	$f_{eT}(f_B)$		f_{PT}		f_{Pe}	
5	−0·3877E−02	−0·1926E−02	0·4563E−03i	0·9051E−01	−0·6833E−01i	−0·9855E−01	−0·1178E−01i
15	0·4163E−02	−0·2166E−02	0·5148E−03i	0·7523E−01	−0·5046E−01i	−0·2455E−01	0·4836E−03i
30	−0·1123E−01	−0·7426E−02	0·2260E−02i	0·1018E+00	−0·2605E−01i	−0·5465E−01	−0·3220E−01i
45	0·5507E−00	0·3917E−00	−0·3775E+00i	0·4963E+00	−0·2186E+00i	−0·1859E+00	−0·5982E−01i
60	−0·1506E−02	−0·2113E−02	0·3343E−03i	0·7365E−02	0·1017E−01i	−0·9665E−02	−0·5472E−02i
75	−0·2157E−04	−0·1275E−03	−0·1266E−04i	0·2637E−02	0·2479E−02i	−0·2234E−02	−0·5132E−03i
90	0·2457E−04	−0·2049E−04	−0·5022E−05i	0·9259E−03	0·9520E−03i	−0·7522E−03	−0·9468E−04i
120	0·2169E−04	−0·2243E−05	−0·9480E−06i	0·2219E−03	0·3128E−03i	−0·1789E−03	−0·6095E−06i
150	0·1793E−04	−0·7385E−06	−0·3812E−06i	0·1030E−03	0·1817E−03i	−0·6817E−04	0·1222E−04i
175	0·1685E−04	−0·5284E−06	−0·2880E−06i	0·8129E−04	0·1545E−03i	0·1806E−05	0·4015E−05i

Table 2. Contribution to the component f_{PT} from projectile electron (v_{12}) and projectile target (v_2) potentials for the case considered in table 1.

$\theta_1 = \theta_2$ (deg.)	$f_{PT}(v_{12})$		$f_{PT}(v_2)$	
5	0·8980E − 01	− 0·6813E − 01i	0·7093E − 03	− 0·1935E − 03i
15	0·7473E − 01	− 0·5037E − 01i	0·4954E − 03	− 0·8890E − 04i
30	0·1015E + 00	− 0·2605E − 01i	0·2465E − 03	− 0·2599E − 05i
45	0·4961E + 00	− 0·2186E + 00i	0·1350E − 03	0·1745E − 04i
60	0·7282E − 02	0·1015E − 01i	0·8356E − 04	0·2011E − 04i
75	0·2580E − 02	0·2460E − 02i	0·5708E − 04	0·1890E − 04i
90	0·8838E − 03	0·9349E − 03i	0·4214E − 04	0·1709E − 04i
120	0·1944E − 03	0·2987E − 03i	0·2749E − 04	0·1415E − 04i
150	0·8133E − 04	0·1691E − 03i	0·2168E − 04	0·1255E − 04i
175	0·6116E − 04	0·1425E − 03i	0·2012E − 04	0·1206E − 04i

$f_{eT}(=f_B)$ and f_{PWB} are much small compared to f_{PT} and f_{Pe} in magnitude. Thus except near the binary peak direction the scattering is essentially a double or a multiple scattering event. For a large scattering angle, f_{PT} is the most dominating term in the expression 1(a). This indicates further that the projectile nucleus interaction is most important in the final channel. Next we refer to table 2 where separate contribution to f_{PT} from potentials v_{12} and v_2 are presented. From the table it is clear that in the entire angular region, v_{12} gives the dominating contribution. Thus for scattering at a large angle, the projectile first ionizes the atom and then it is back-scattered elastically from the nucleus. In this way we have a good understanding of the ionization mechanism in the present case.

B. *Differential cross sections*

Differential cross section results of our present calculation are presented in figures 1(a)–1(c). Figure 1(a) shows cross section results for 200 eV incident energy. Here we compare our computed results with the first Born results and with the results for ionization from the ground state for a similar calculation [13]. Figures 1(b) and 1(c) show similar results for incident energies of 500 eV and 1000 eV. The results presented here show that unlike for scattering from the ground state there is only one peak, the binary peak, close to 45°. Present cross section results are, generally, much larger than the corresponding Born results. This shows that the coplanar symmetric ionization scattering from the 2*s*-state is essentially a higher order process. From the figure, it appears that present results for $\theta_1 < 25°$ are unlikely to be accurate. There does not exist, at present, measured cross section results for these scattering at high incident energies (however there exists one set of results for low energies [18] in case of ionization from the ground state). The wide difference between the results of the multiple scattering theory and the first Born results calls for other theoretical calculations also, such as by BBK method [8] for the present case. Experimental measurements are most welcome for ionization from the 2*s*-state for different kinematic conditions, such as that considered here.

4. Conclusion

The present calculation shows that for ionization of the 2*s*-metastable state for symmetric geometry, there exist only binary peaks in the cross-section curves. It is also seen that the cross section results are much larger compared to the corresponding Born results or the results for scattering from the ground state. Except at the binary peak

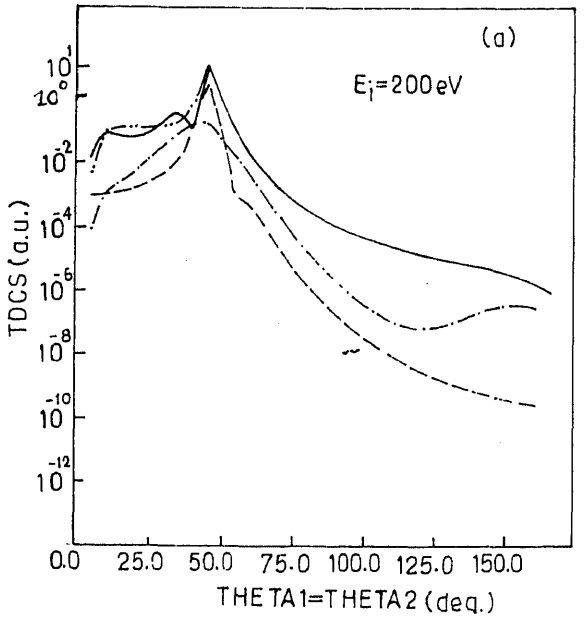

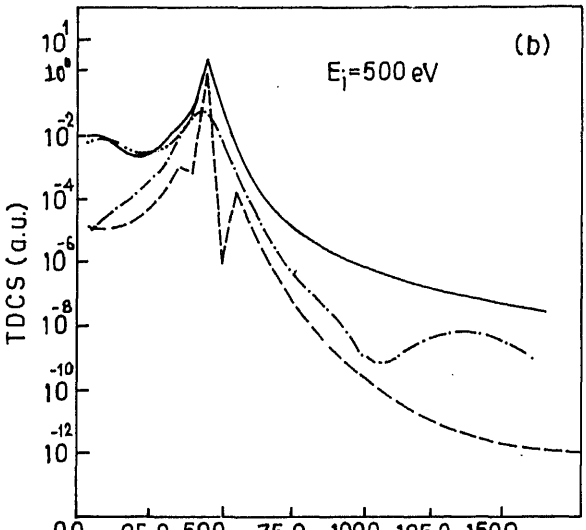

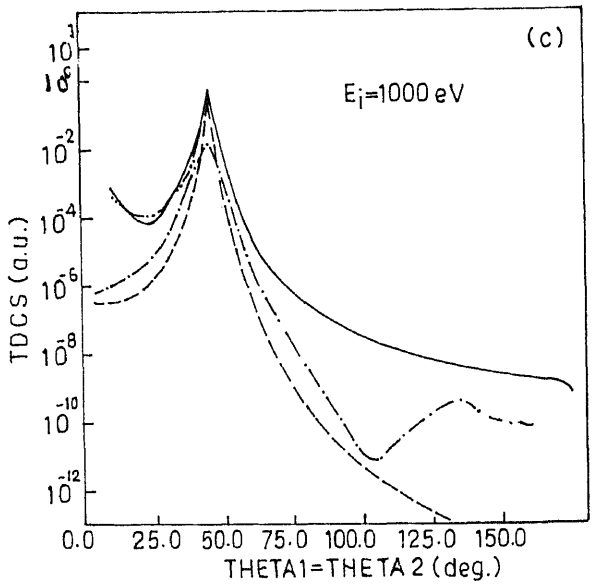

Figure 1. Triple differential cross section with equal energies and angles for symmetric scattering for ionization of hydrogen atoms in the 2*s*-state by electrons and positrons for (**a**) 200 eV energy, (**b**) 500 eV energy, (**c**) 1000 eV energy. Theory: Continuous curve, present calculation for electron; dash double-dotted curve, present calculation for positron; dashed curve, first Born approximation; dash dotted curve, ground state results of Das and Seal [9].

direction the scattering is essentially a double or a multiple scattering event. It is also found that the ionization mechanism for large scattering angles are different for ionization from 2*s*-state. For ionization from 2*s*-state, first a small angle ionization of the atom occurs and then a large angle elastically back-scattering from the atomic nucleus takes place, while it is just the opposite in case of ionization from the ground state.

References

[1] A Pochat, R J Tweed, J Peresse, C J Joachain, B Piraux and F W Jr Byron, *J. Phys.* **B16**, L775 (1983)
[2] F W Jr Byron, C J Joachain and B Piraux, *J. Phys.* **B16**, L769 (1983)
[3] J S Briggs, *J. Phys.* **B19**, 2703 (1986)
[4] J S Briggs, Comments, *At. Mol. Phys.* **23**, 55 (1989)
[5] L Frost, P Frienstein and W Wagner, *J. Phys.* **B23**, L173 (1990)
[6] J Gelebart and R J Tweed, *J. Phys.* **B23**, L641 (1990)
[7] J Botero and J H Macek, *J. Phys.* **B24**, L405 (1991)
[8] M Brauner and J S Briggs, *J. Phys.* **B24**, 2227 (1991)
[9] J N Das and S Seal, *Pramana – J. Phys.* **40**, 253 (1993)
[10] J N Das, *Phys. Rev.* **A42**, 1376 (1990)
[11] J N Das and S Seal, *Phys. Rev.* **A47**, 2978 (1993)
[12] J N Das and S Seal, Z. *Phys.* **D31**, 167 (1994)
S Seal and J N Das, *Aust. J. Phys.* **47**, 49 (1994)

D Faddeev, *Sov. Phys. JETP* **12**, 1014 (1961)
Vučič, R M Potvliege and C J Joachain, *Phys. Rev.* **A35**, 1446 (1987)
I Hafid, B Joulakian and C Dal Cappello, *J. Phys.* **B26**, 3415 (1993)
Dhar, *Aust. J. Phys.* **49**, (1996) [to be published]
Berakdar, A Engelns and H Klar, *J. Phys.* **B29**, 1109 (1996)
T Colm, R J Allan, J Rasch, H R J Walters, X Zhang, J Röder, K Jung and H Ehrhardt,
hys. Rev. **A50**, 4394 (1994)

journal of physics

October 1996
pp. 271–281

Structure of some liquid transition metals using integral equation theory

O AKINLADE, A M UMAR* and L A HUSSAIN†
Department of Physics, University of Agriculture, Abeokuta, Nigeria
*Department of Physics, Uthman dan Fodio University, Sokoto, Nigeria
†Department of Physics, University of Ibadan, Ibadan, Nigeria

MS received 9 August 1996

Abstract. We present the results of calculations of the structure factor $S(q)$ of some liquid $3d$ transition metals using the self consistent hybridized mean spherical approximation (HMSA) integral equation. The local pseudopotential used is composed of the empty core model and a part that takes care of s-d mixing through an inverse scattering approach to model the interionic pair potential. The results presented are in very good agreement with experiment for most of the systems investigated near freezing, as well as for the noble metals Cu, Ag and Au, thus, confirming the reliability of the pseudopotential in the present integral equation scheme.

Keywords. Liquid transition metals; integral equation theory.

PACS No. 61·25

1. Introduction

The central problem of liquid state physics is the determination of the pair distribution function $g(r)$ or its Fourier transform, the static structure factor $S(q)$. At least for a system described solely in terms of volume and pair forces, the knowledge of $g(r)$ is all that we need to know. Among the standard statistical mechanics tools that can be used for this kind of study namely computer simulation, integral equations or perturbation calculations, the thermodynamically self consistent (TSC) integral equation approach has been very successful in recent times. Its success is mainly due to the technical advancement made in the development of two powerful and efficient numerical algorithms for solving nonlinear integral equations [1]. These techniques lead to a drastic reduction in the number of iterations necessary for convergence. Here we intend to adopt the hybridized mean spherical equation of Zerah and Hansen [2] which interpolates between two older closures, the HNC (hypernetted chain) and the soft core mean spherical approximation (SMSA), by means of a switching constant chosen to enforce thermodynamic self consistency. The success of the HMSA is well established for one [3, 4] and two component systems [5].

The other important ingredient for such calculations is the interionic pair potential, usually obtained from a suitable pseudopotential. For transition metals unlike what happens for simple metals, there is not that large number of suitable pseudopotentials. One of the most popular is that based on the first principle study made by Wills and

Harrison (WH) [6] which uses separate treatments for the s-p and d states leading to an effective pair potential that takes into account the effect of s-d hybridization. Despite the success of the theory in the solid state, results for the structure factors of liquid 3d transition metals using molecular dynamics and other complicated liquid state theories have not been that reliable [7, 8]. The root cause of the problem lies in the fact that the position and depth of the first minimum of the WH potential are shifted towards short distances and progressively too deep. An important inference that can be deduced from these is that the liquid state properties apprears to be a severe test of the potential since a correct description is needed to obtain structural properties of such systems.

Essentially, for transition metals, one has to consider the fact that the tightly bound d electrons hybridize with the nearly free-electrons resulting in a partially filled d band, crossing the Fermi energy. The presence of the d band has been a serious impediment to the application of pseudopotential perturbation theory for such systems. Bretonnet and Silbert [9] have developed a pseudopotential which treats the sp states using an Ashcroft type empty core pseudopotential characterized by a core radius R_C, and have made a suitable adjustment to incorporate the s-d mixing by an approximate potential inside the core. The relative success of the model can be deduced from its applications to perturbation calculations [10] and variational modified hypernetted chain integral equations [11]. On the basis of their calculation we feel that it would be worthwhile to look at all the liquid 3d transition metals and consider the modifications that may be necessary in applying the same theories to the noble metals.

The layout of the present paper is as follows. In § 2, we outline the theoretical basis of the work in terms of the pseudopotential used and the HMSA integral equations. In § 3, we compare our results for $S(q)$ with those obtained experimentally in [13]. In § 4 we present our conclusions.

2. Theory

2.1 *Pseudopotential and interatomic pair potential*

Given a system of particles in a volume Ω, and at a given density $\rho = N/\Omega$, assumed to be interacting via a pairwise potential $V(r)$, the pair potential can be expressed as

$$V(r) = \frac{Z_S^2}{r}\left[1 - \int_0^\infty \frac{2}{\pi} F_N(q) \frac{\sin qr}{q} \mathrm{d}q\right], \tag{1}$$

where $F_N(q)$ is the normalized energy wave-number characteristics and Z_S represents the effective number of conduction electrons per ion. For transition metals, in order to account for hybridization, Z_S takes on non-integer values [12]. The pseudopotential to be used [9] is constructed from the superposition of two potentials, one to account for the sp contribution and the other, for the d-band contribution taken together, these results in the following expression for the potential

ourier transformation of eq. (2), the resulting form factor can be expressed as

$$w(q) = 4\pi a^3 \rho \left(\frac{B_1 H_1}{(1 + a^2 q^2)^2} + \frac{8 B_2 H_2}{(1 + 4a^2 q^2)^2} \right) - \frac{4\pi Z_S \rho}{q^2} \cos(q R_C). \tag{3}$$

lly, one requires that the potential and its first derivative be continuous at $r = R_C$. enables us to define B_1 and B_2 as

$$B_1 = \frac{Z_S}{R_C} \left(1 - \frac{2a}{R_C} \right) \exp\left(\frac{R_C}{a} \right), \tag{4}$$

$$B_2 = \frac{2 Z_S}{R_C} \left(\frac{a}{R_C} - 1 \right) \exp\left(\frac{R_C}{2a} \right) \tag{5}$$

$X_n = n^2 a^2 q^2$ and $Y_n = R_C / na$, H_n is given by

$$H_n = 2 - e^{Y_n} \left[[Y_n (1 + X_n) - (1 - X_n)] \frac{\sin(q R_C)}{naq} + [2 + Y_n (1 + X_n)] \cos(q R_C) \right], \tag{6}$$

arameter a being a measure of the softness of the repulsive potential. The dielectric ning function $\varepsilon(q)$ is given by

$$\varepsilon(q) = 1 - \frac{4\pi e^2}{q^2} \chi(q) [1 - G(q)]. \tag{7}$$

s the Lindhard function and $G(q)$ is the local field factor of Ichimaru and Utsumi $F_N(q)$, the normalized energy-wavenumber characteristic can be written as

$$F_N(q) = \left[\frac{q^2}{4\pi Z_s} \right]^2 \left[1 - \frac{1}{\varepsilon(q)} \right] \left[\frac{1}{1 - G(q)} \right] w^2(q). \tag{8}$$

ence the potential $V(r)$ is a function of three parameters: the core radius R_C, the ess parameter a and Z_S, the number of conducting electrons. We shall present the rical values for the systems studied and from the equations above, the pair tial can be constructed.

ntegral equation method

air correlation function $g(r)$ of classical fluid interacting through a pair potential s determined through the solution of the famous Ornstein–Zernike (OZ) equa- With $\gamma(r) \equiv h(r) - c(r)$, we have

$$\gamma(r) = \rho \int h(r') c(|\tilde{r} - \tilde{r}'|) \mathrm{d}\tilde{r}' \tag{9}$$

n decomposes the total correlation function $h(r) = g(r) - 1$ into the direct correla- (r) and the totality of the indirect effects mediated by third particles which itself is lated to the original two. To solve the OZ integral equation, one needs a closure een $h(r)$ and $c(r)$. Here we intend to use the HMSA closure [2]. Implementation of

this integral equation is as follows, first the potential $V(r)$ is split into $\phi_r(r)$ and $\phi_l(r)$, the short range repulsive and long range attractive terms respectively, according to

$$\phi_r(r) = \begin{cases} V(r) - V(r_0) & r \leqslant r_0 \\ 0 & r \geqslant r_0 \end{cases}, \tag{10}$$

$$\phi_l(r) = \begin{cases} V(r_0) & r \leqslant r_0 \\ V(r) & r \geqslant r_0 \end{cases}, \tag{11}$$

where $V(r_0)$ is the pair potential evaluated at its first minimum position r_0. From (10), (11), Zerah and Hansen [2] proposed for $g(r)$ an expression of the form

$$g(r) = \mathrm{e}^{-\beta\phi_r(r)}\left[1 + \frac{\exp(f(r)[\gamma(r) - \beta\phi_l(r)]) - 1}{f(r)}\right], \tag{12}$$

where $f(r)$ is given by

$$f(r) = 1 - \mathrm{e}^{-\alpha r} \tag{13}$$

and the parameter α is varied until full consistency between the virial and compressibility equation of state is achieved. As can be illustrated, the switching functions $f(r)$ satisfies the limiting behaviour

$$\lim_{r\to 0} f(r) = 0 \tag{14}$$

so that (12) reduces in that limit to the soft-core mean spherical approximation closure, and the limiting behaviour

$$\lim_{r\to\infty} f(r) = 1 \tag{15}$$

corresponds to the HNC closure.

In order to obtain α, one follows the standard procedure of relating this adjustable parameter to achieve consistency between the relation arising from the compressibility route in the grand canonical ensemble, which is the inverse long-wavelength limit of the structure factor

$$\chi_T = \beta\rho^{-1}\left[1 + 4\pi\rho\int h(r)r^2\,\mathrm{d}r\right] = \frac{1}{S(0)} \tag{16}$$

and that obtained from the virial equation of state

$$(\chi_T^{\mathrm{v}}) = \rho\beta^{-1} + P_0 + P_1 + P_2, \tag{17}$$

where

$$P_0 = \rho\left[2n\frac{\mathrm{d}u(n)}{\mathrm{d}n} + n^2\frac{\mathrm{d}^2u(n)}{\mathrm{d}n^2}\right], \tag{18}$$

$$P_1 = 2\pi\rho^2\int_0^\infty \mathrm{d}r r^2\left[\frac{r}{3}\frac{\partial}{\partial r} - n\frac{\partial}{\partial n}\right]g(r)\left[\frac{r}{3}\frac{\partial}{\partial r} - n\frac{\partial}{\partial n}\right]V(r), \tag{19}$$

$$P_2 = 2\pi\rho^2\int_0^\infty \mathrm{d}r r^2 g(r)\left[\frac{r}{3}\frac{\partial}{\partial r} - n\frac{\partial}{\partial n}\right]^2 V(r), \tag{20}$$

where the superscript V in (17) refers to the virial pressure route. The number density ρ is related to the electronic density n by $\rho = nZ$, and $u(n)$ is the structure-independent contribution to the energy, consisting of the ground-state electron gas energy, the average interaction between electrons and the noncoulombic part of the bare-ion pseudopotential. The evaluation of (17) could be very delicate and thus aiming only at statistical mechanics self-consistency for liquid structure at fixed density, we determine the parameter α by demanding equality between (16) and the expression to which (17) reduces when the density dependencies of u and $V(r)$ are dropped. This procedure was adopted by Pastore and Kahl [15] and Lai *et al* [3] in their studies.

Essentially the value of α obtained at a given thermodynamic state is used to evaluate $g(r)$ in (12) from which the structure factor can be obtained by Fourier transformation.

3. Numerical results and discussion

Table 1 lists our input parameters for the systems investigated as well as the values of the consistency parameter α. For a given α, the system of equations (9) and (12) is solved, taking advantage of the combination of the Newton–Raphson and successive substitution method as proposed by Gillan [1]. This we have done and in all cases we find that 2048 points with a step size $\Delta r/a = 0{\cdot}025$ (a being the Wigner Seitz radius) are sufficient for our calculations.

The parameters R_C, a and Z_S characterizing the potentials used in the present calculations have been chosen thus; R_C is fitted to reproduce numerically the observed isothermal compressibility. The parameter a is the softness parameter and has an influence on the softness of the potential $V(r)$, which is restricted to the domain $4 < R_C/a < 5$ [11, 16]. This results in a potential that has the required form, i.e. a short ranged repulsive part and an attractive tail. Any value outside this results in a purely repulsive form. For a, we have chosen a value that best reproduces the oscillations of $g(r)$ for the system being investigated. We observe that this works quite well for 3d transition metals but for the 4d and 5d noble metals Ag and Au, the ratio R_C/a is in the range 5·0 to 5·5.

The last parameter is Z_S and following the observation of Moriarty [17] that for 3d and 4d transition metals, Z_S takes on values in the narrow range $1{\cdot}1 < Z_S < 1{\cdot}7$ with a typical value of 1·4. We have used the typical value for all the systems studied here.

Table 1. Temperature (K), atomic volume (Ω), pseudopotential parameters a and R_C and consistency parameter α. We note that in all cases $Z_S = 1{\cdot}4$.

Element	T(K)	Ω(a.u)	a(a.u)	R_C(a.u)	α
Sc	1812	144·90	0·361	1·63	0·346
Ti	1933	130·38	0·400	1·70	0·711
V	2175	102·56	0·380	1·65	0·713
Cr	2130	92·42	0·377	1·60	0·908
Mn	1517	102·04	0·358	1·52	0·673
Cu	1423	89·34	0·247	1·20	0·274
Ag	1273	130·38	0·213	1·10	0·145
Au	1423	128·31	0·185	1·00	0·155

From a perusal of figures 1–4, it is observed that the low q region is well produced for most of the elements studied. This could be adduced to two reasons, firstly, R_C has been fitted to it and secondly, the Ichimaru–Utsumi form of the local field factor appears to be very good in explaining the electronic screening. For most systems studied, the

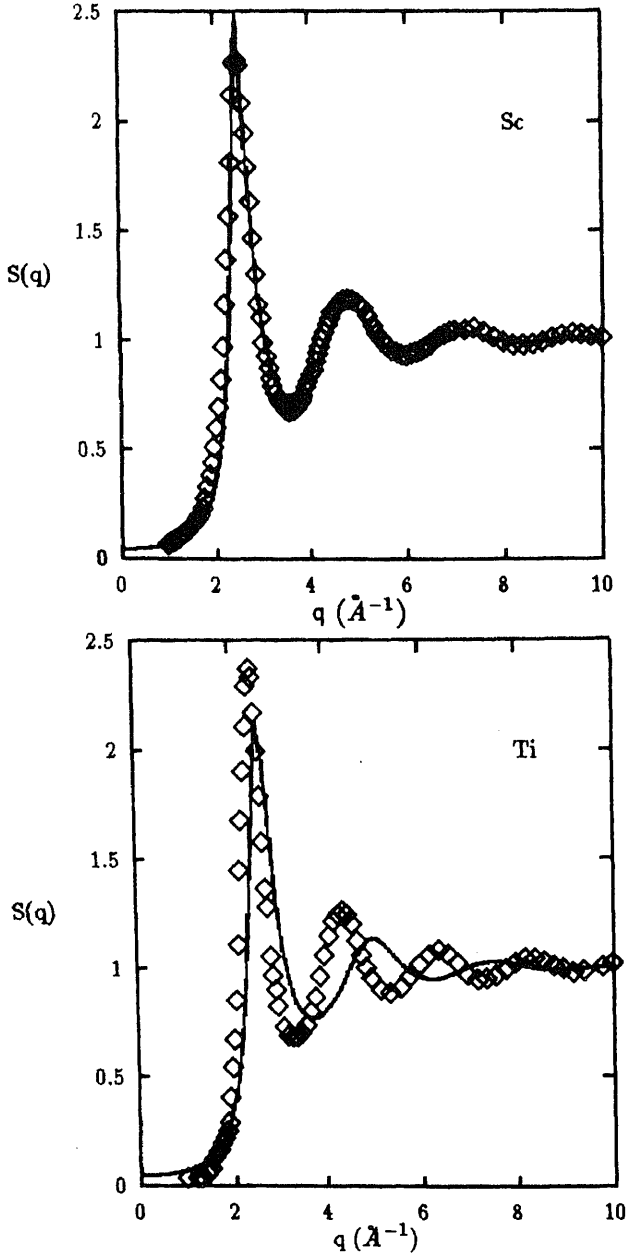

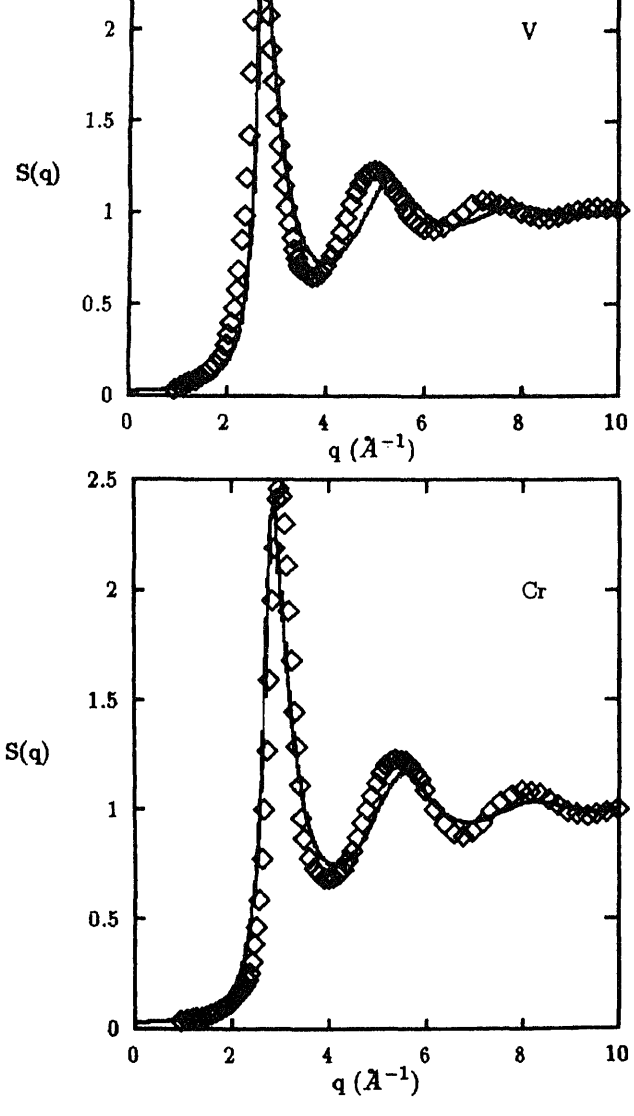

Figure 2. Same as in figure 1 but for V and Cr.

agreement between theoretical and experimental structure factors are quite good especially if one follows the philosophy of Huijben and van der Lugt [18] that for liquid metals, the locations of maxima and minima is $S(q)$ are experimentally more reliable than its detailed shape. We compare our predictions for these locations in table 2. For

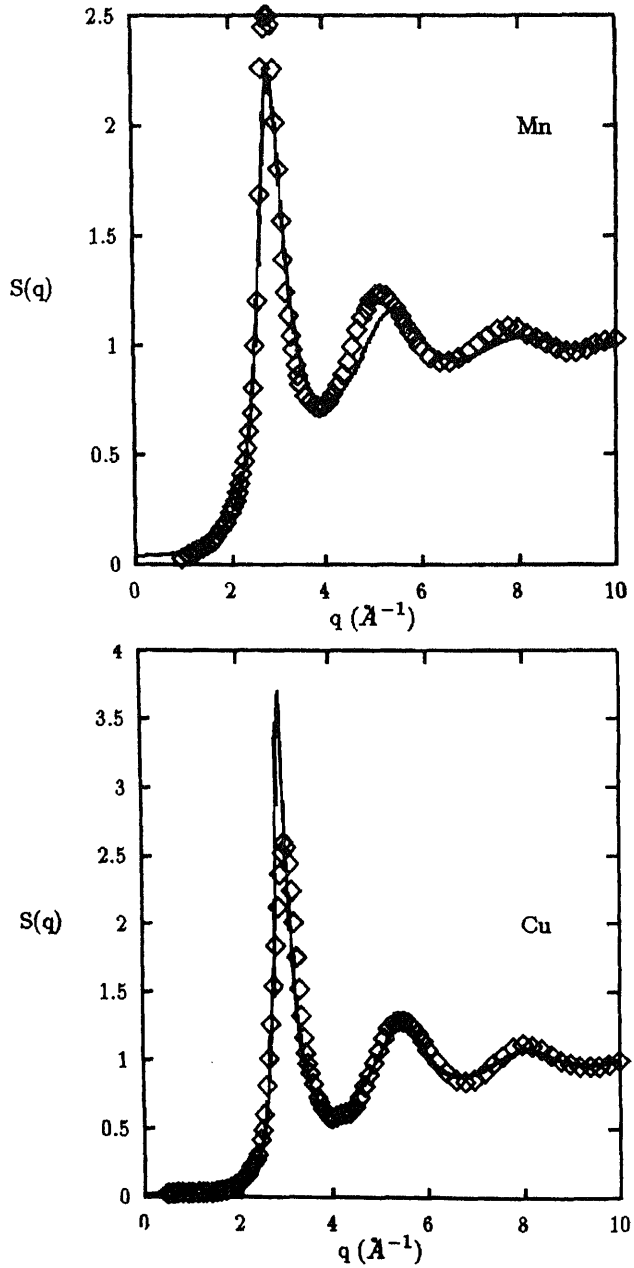

Figure 3. Same as in figure 1 but for Mn and Cu.

all the systems investigated we obtain an accuracy of $\pm 0{\cdot}05$ Å, the first peak, the only exception here is for Ti which is considerably shifted to low q region. Overall, the agreement between theory and experiment is just fair for Ti and V. From table 1, one

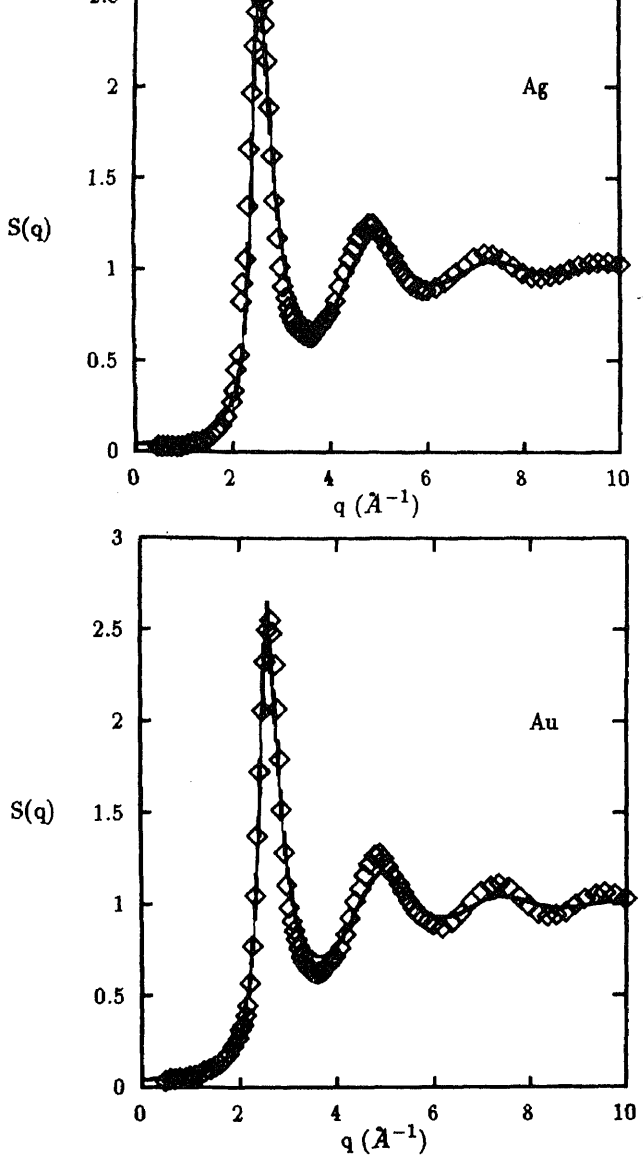

Figure 4. Same as in figure 1 but for Ag and Au.

the core gets progressively lower along the group. It is however comparatively larger for Ti and V and this could be explained on the basis that the gradient of the repulsive core part of the effective interionic potential for liquid Ti and V are relatively small compared with that of the other 3d transition metals. Ideally, one may have to build

Table 2. Comparison of experimental and theoretical locations of the maxima and minima of the liquid structure factor for elements under consideration (in Å). The first line in each case refers to the experimental data [13] while the second line refers to the theoretical values.

		Maxima			Minima	
Metal		1st	2nd	3rd	1st	2nd
Sc	Expt.	2·50	4·80	7·40	3·55	6·00
	Calc.	2·50	4·85	7·20	3·55	6·00
Ti	Expt.	2·45	4·40	6·40	3·30	5·40
	Calc.	2·60	5·00	7·50	3·75	6·25
V	Expt.	2·70	5·00	7·20	3·70	6·20
	Calc.	2·70	5·35	7·90	4·00	6·55
Cr	Expt.	3·00	5·40	8·00	4·00	6·80
	Calc.	2·90	5·60	8·00	4·15	6·95
Mn	Expt.	2·85	5·20	7·80	3·90	6·40
	Calc.	2·80	5·45	8·10	4·00	6·70
Zr	Expt.	2·30	4·40	6·60	3·30	5·40
	Calc.	2·30	4·50	6·65	3·30	5·50
Cu	Expt.	3·00	5·40	8·00	4·00	6·80
	Calc.	2·95	5·50	8·10	4·00	6·70
Ag	Expt.	2·60	4·90	7·20	3·60	6·00
	Calc.	2·60	4·95	7·45	3·70	6·20
Au	Expt.	2·65	4·90	7·40	3·60	6·20
	Calc.	2·60	4·95	7·50	3·70	6·25

into the BS potential a factor to correct for it in these systems. We note that unlike for the VMHNC calculations [11] where convergence to a solution is always obtained for all values of a, the HMSA gives consistency only for some values.

We observe that moving from 3d to the noble metals Ag and Au can be effected trivially and without difficulty using the BS potential. The agreement between theory and experiment for most of the systems studied are quite good and indicates that the HMSA which has so far proved successful for most kinds of simple liquids can be used even for noble metals without much rigour.

The results obtained using the HMSA are of comparable quality as that obtained by Bhuiyan *et al* [11] using the variational modified hypernetted chain approach which has a different philosophy in that it depends on the requirement that the parameter similar to α of the HMSA is chosen to obtain as close as possible a virial- compressibility thermodynamic consistency without enforcing it.

4. Conclusion

The BS nonlocal pseudopotential has been applied successfully to calculate the structure factor of liquid 3d transition metals using the HMSA integral equation. It is found that the theory could be easily extended to noble metals in a consistent way.

Ti and V with a view to improving the result for these systems.

Acknowledgements

One of the authors (OA) is grateful to Dr G Pastore for providing the HMSA computer programs and to the organizers of the 1995 Research Workshop on Condensed Matter Physics and for the hospitality at the International Centre for Theoretical Physics, Trieste, Italy.

References

[1] M J Gillan *Mol. Phys.* **38**, 1781 (1979)
G Zerah, *J. Comput. Phys.* **61**, 280 (1985)
[2] G Zerah and J P Hansen, *J. Chem. Phys.* **84**, 2336 (1986)
[3] S K Lai, L Wang and M P Tosi, *Phys. Rev.* **A42**, 7289 (1990)
[4] J L Bretonnet and N Jakse, *Phys. Rev.* **B50**, 2880 (1994)
[5] G Kahl, *Phys. Rev.* **A43**, 822 (1991)
[6] J M Wills and W A Harrison, *Phys. Rev.* **B28**, 4363 (1983)
[7] C Hausleitner, G Kahl and J Hafner, *J. Phys.: Condens. Matter* **3**, 1589 (1991)
[8] C Regnaut, *Z. Phys.* **179** (1989)
[9] J L Bretonnet and A Deroiche, *Phys. Chem. Liq.* **24**, 169 (1991)
[10] J L Bretonnet, G M Bhuiyan and M Silbert, *J. Phys. Condens. Matter* **4**, 5359 (1992)
[11] G M Bhuiyan, J L Bretonnet, L E Gonzales and M Silbert, *J. Phys.: Condens. Matter* **4**, 7651 (1992)
[12] J A Moriarty, *Phys. Rev.* **B38**, 3199 (1988)
[13] Y Waseda, *The structure of non-crystalline materials* (New York, McGraw-Hill, 1981)
[14] S Ichimaru and K Utsumi, *Phys. Rev.* **B24** 7385 (1981)
[15] G Pastore and G Kahl, *J. Phys.* **F17**, L267 (1987)
[16] J L Bretonnet, G M Bhuiyan and M Silbert, *J. Phys. Condens. Matter.* **4**, 7651 (1992)
[17] J A Moriarty, *Phys. Rev.* **A45**, 3803 (1990)
[18] M T Huijben and van der Lugt, *Acta Cryst.* **A35**, 431 (1979)

Nonlinear travelling waves in ϕ^6 polarizable model

NABONITA D CHOWDHURY* and SANKAR P SANYAL†
Department of Physics, Barkatullah University, Bhopal 462026 India
*Present Address: School of Physical Sciences, Jawaharlal Nehru University, New Delhi 110067, India
†Author for correspondence
†Present Address: Forschung Zentrum Karlsruhe Institut für Nukleare Festkorper-Physik, PB 3640, Karlsruhe, Germany

MS received 10 August 1994; revised 5 August 1995

Abstract. We present a complete theoretical analysis of the periodic and non-periodic travelling waves in a diatomic chain model, in the continuum limit by incorporating nonlinear sixth order polarization potential (ϕ^6) at the anion site. We have formulated a nonlinear lattice dynamical theory in which various energy curves are obtained for different types and magnitudes of the core-shell force constants. For periodic solutions, we have obtained two types of commensurate wave amplitudes which propagate in the opposite direction with respect to each other. For nonperiodic solutions, we have obtained various travelling excitations such as kink, antikink, excitons etc. for different values of the mass ratio and velocity parameter. The dipole moment per unit charge for $SrTiO_3$ has been calculated and it is found that the nonlinear excitations in this model carry large amount of energy as compared to those obtained from harmonic and anharmonic optical phonons in the ϕ^4-polarizable model.

Keywords. Nonlinear dynamics; phase transition.

PACS No. 77·80

1. Introduction

The nonlinear excitations play a dominant role in the dynamical properties of condensed matter systems [1–4]. These excitations are of great importance as they carry large amount of energy in various systems of solids such as photo-ferroelectrics [5] and biomolecules [1]. These type of excitations are obtained from large amplitude solutions which do not obey the principle of superposition. Various types of nonlinear excitations known so far are kinks, periodons and excitons. The kink solution corresponds to finite energy transition from one stable homogenous state (i.e., ferroelectric state) to another, where the time varies from $-\infty$ to ∞. Kink excitation with metastable instantaneous behaviour are called excitons. Periodons are known as nonlinear periodic waves with subharmonic scaling by 3, which locally show the character of excitons but is globally that of phonons.

The nonlinear excitations show their existence in various low dimensional systems and have their connection with the "central peak" phenomena observed in the ferroelectric materials near the structural phase transition [6]. From the theoretical point of view, Behera and Khare [7] suggested that kinks as well as excitons contribute

to the formation of the central peak. Periodons play a role in photo induced effects in ferroelectrics, which suggests their applications to biological systems where nonlinear and nearly loss-free cooperative phenomena such as "active transport" are understood [5]. For the description of the nonlinear dynamical properties of ferroelectrics, a simple diatomic shell model was introduced [2], in terms of strongly anisotropic polarizability of the oxygen and chalcogenide ions which experience a configurationally unstable nonlinear electron-phonon interactions between its core and shell. In the self-consistent phonon approximation, the dynamical properties like soft mode, dielectric constant and phonon dispersion curves are fairly described well in the ϕ^4-polarizability model [1–3]. In one-dimensional picture, exact nonlinear solutions are obtained by Buttner and Bilz [3]. They have also obtained nonlinear periodic solutions (periodons), in addition to the static solutions of kink type. Exact nonlinear travelling wave solutions in the continuum limit are obtained in the ferroelectrics by Benedek *et al* [4]. They have solved the equation of motion of a diatomic chain, considering fourth order (ϕ^4) on-site polarization potential at anion and found the existence of kinks and domain walls. This type of analysis of the travelling wave solutions in the continuum limit helps in the understanding of the nonlinear periodic and nonperiodic excitations.

In the present paper we intend to present the classification and analysis of the travelling wave solutions in a diatomic lattice, in the continuum limit for an anharmonic sixth order polarization potential (ϕ^6) at the anion site. The present work is highly motivated by the experimental facts on certain optical crystals. Adair *et al* [8] have experimentally measured the nonlinear refractive indices in a large number of optical crystals by using the technique of nearly degenerate three wave mixing. The nonlinear refractive index in a crystal arises from the contributions of intraionic and interionic nonlinear polarizations, which gives a very high value of nonlinear dipole moment. For ferroelectric system i.e., $SrTiO_3$, they have measured the nonlinear refractive index as $26{\cdot}7(10^{-19}$ esu) which is a very large value as compared to linear index data i.e., $2{\cdot}31(1{\cdot}06\,\mu m)$. The hyperpolarizability of oxygen ion is responsible for high value of refractive index. We have used the ϕ^6 polarizable potential to understand the high value of refractive indices in ferroelectrics, in terms of the nonlinear travelling waves.

We have considered a model of the one-dimensional diatomic lattice with harmonic coupling between neighbouring sites and anharmonic on-site potential at the polarizable ion as [9]

$$V_p(w_{1,n}) = \sum_n \left[\tfrac{1}{2} g_2 w_{1,n}^2 + \frac{1}{m+2} g_4 w_{1,n}^{m+2} + \frac{1}{2m+2} g_6 w_{1,n}^{2m+2} \right] \tag{1}$$

with $m = 2$. We have started our analytical analysis by first calculating the potential energy of the anharmonic oscillator at the turning point w_0 for different choices of core-shell force constants i.e., (I) $g_2 > 0$, $g_4 > 0$, $g_6 > 0$ (II) $g_2 < 0$, $g_6 < 0$, $g_4 > 0$ (III) $g_2 > 0, g_6 > 0, g_4 < 0$ for $g_2 <, > 2f$ and $g_4^2 >, =, < 4g_2 g_6$. By noticing the variation of energy with displacement coordinate under the conditions mentioned above, we select only case (II) i.e., $g_2 < 2f$ and $g_4^2 = 4g_2 g_6$ for investigating the travelling wave. This potential in case (II) leads to negative value for large $w_{1,n}$, but the harmonic intra-site potential of the diatomic lattice (V_L) stabilizes the potential $V_p(w_{1,n})$. The total potential is the sum of polarization (on-site) (V_p) and harmonic (intra-site) (V_L) potential, which now have a finite energy solution and remain valid for all the conditions. In this case,

energy remains degenerate for three displacements which are close to each other. Hence the present case is a modified ferroelectric case with minima at the displacement $(-g_4/2g_6)^{1/2}$ which is equivalent to $(-g_2/g_4)^{1/2}$, by using the approximation $g_4^2 = 4g_2g_6$. The minima under this approximation reduces to $\sqrt{2}$ times the minima of ϕ^4 potential. This case now corresponds to second order phase transition. The present case discussed is a special case of ϕ^6 polarizable model. We have further, analyzed the periodic and non-periodic travelling wave solutions and obtained kink and antikink solutions, which were not obtained in Benedek's treatment. We have also calculated the dipole moment per unit charge carried by the nonlinear excitations for $SrTiO_3$.

2. Theory

The starting point of the present theory is basically to consider the higher order (i.e. sixth) polarization potential at the site of an anion in a one-dimensional diatomic lattice with nearest and next nearest neighbour interactions (see figure 1). The Hamiltonian can be expressed as

$$H = T + V_L + V_p(w_{1,n}), \tag{2}$$

where

$$T = \tfrac{1}{2}\sum_n [m_1 \dot{u}_{1,n}^2 + m_2 \dot{u}_{2,n}^2 + m_e \dot{v}_{1,n}^2] \tag{3}$$

and

$$\begin{aligned} V_L = \tfrac{1}{2}\sum_n [&f'(u_{1,n+1} - u_{1,n})^2 + f'(u_{1,n-1} - u_{1,n})^2 + f(u_{2,n} - v_{1,n})^2 \\ &+ f(u_{2,n} - v_{1,n-1})^2 + f(u_{2,n} - v_{1,n+1})^2 + f(u_{2,n-1} - v_{1,n})^2 \\ &+ f(u_{2,n-1} - v_{1,n-1})^2]. \end{aligned} \tag{4}$$

Here $u_{1,n}$ and $u_{2,n}$ are the displacements of the core of anion (1) and cation (2) in the nth cell. The respective masses of the ions 1 and 2 are m_1, m_2 and m_e is the mass of the electron shell of anion, which has displacement $v_{1,n}$. f is the nearest neighbour force constant between two ions in the nth cell. f' is the core-core force constant of the anion in two adjacent cells $(n, n \pm 1)$. g_2, g_4 and g_6 are the second, fourth and sixth order anharmonic core-shell force constants. By defining a relative core-shell displacement coordinate of the polarizable ion as $w_{1,n} = v_{1,n} - u_{1,n}$, and using adiabatic approximation ($m_e \sim 0$), we have obtained a nonlinear second order differential equation of motion in relative core-shell coordinate $w_{1,n}$ as

$$\begin{aligned} &(\alpha + \delta w_{1,n}^2 + \gamma w_{1,n}^4)\ddot{w}_{1,n} + 2\delta w_{1,n}\dot{w}_{1,n}^2 + 4\gamma w_{1,n}^3 \dot{w}_{1,n}^2 \\ &+ \frac{2f}{\mu}(g_2 w_{1,n} + g_4 w_{1,n}^3 + g_6 w_{1,n}^5) - f\left(\frac{f}{m_2} - \frac{2f'}{m_1}\right)(u_{1,n+1} + u_{1,n-1} - 2u_{1,n}) \\ &- \frac{f^2}{m_2}(w_{1,n+1} + w_{1,n-1} - 2w_{1,n}) = 0 \end{aligned} \tag{5}$$

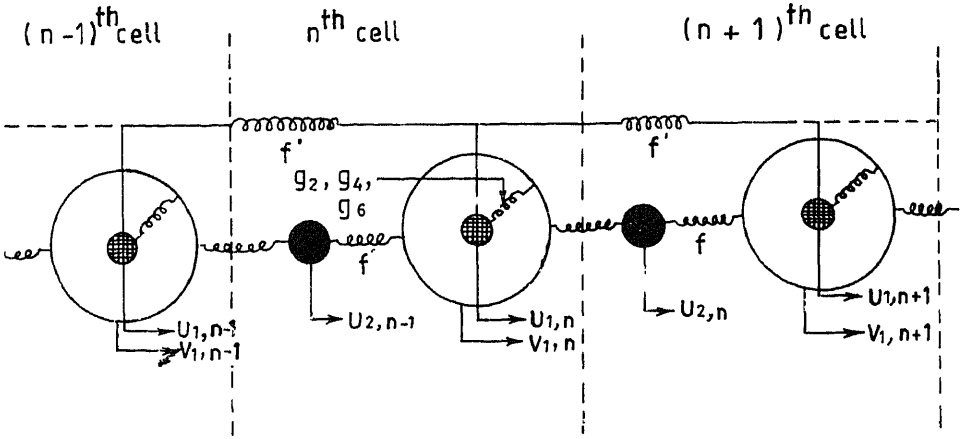

Figure 1. One-dimensional ϕ^6-polarizable model with first neighbour core-shell and core-core force constants of the anion.

with

$$\alpha = 2f + g_2,\ \delta = 3g_4,\ \gamma = 5g_6 \text{ and } 1/\mu = 1/m_2 + 2/m_1.$$

The equation of motion (5) can be solved by first considering the anharmonic oscillators as noninteracting and which are having the same mode of vibration. However, it can be solved for interacting oscillators also by considering the travelling wave type solutions for the core and shell displacements of the respective ions.

In the independent oscillator approximation (ie, $u_{1,n+1} = u_{1,n-1} = u_{1,n}$; $w_{1,n+1} = w_{1,n-1} = w_{1,n}$), the harmonic intra-site potential V_L by using the equation of motion obtained from (2) in (4) reduces to

$$V_L = \frac{g_6^2}{4f}\left[w_{1,n}^{10} + \frac{5}{4}\left(\frac{g_4}{g_6} + \frac{\delta}{\gamma}\right) w_{1,n}^8 + \frac{5}{3}\left(\frac{g_4\delta}{g_6\gamma} + \frac{6g_2}{\gamma}\right) w_{1,n}^6 + \frac{5}{3}\left(\frac{g_2}{g_6}\cdot\frac{2\delta}{\gamma}\right) w_{1,n}^4 + \frac{g_2^2}{g_6^2} w_{1,n}^2 \right]. \tag{6a}$$

For the first integration of (5), the equation of motions are solved by using suitable boundary conditions at the turning point w_0(i.e., at $t = 0$, $w_{1,n} = w_0$). The energy of the anharmonic oscillations at the turning point w_0 will be due to the potential (i.e., onsite and intra-site) energy of the oscillator only, as kinetic energy vanishes (since $\dot{w}_{1,n} = 0$). It can be expressed as [10]

$$E(w_0) = \frac{g_6^2}{4f}\left[w_0^{10} + \frac{5}{4}\left(\frac{g_4}{g_6} + \frac{\delta}{\gamma}\right) w_0^8 + \frac{5}{3}\left(\frac{g_4\delta}{g_6\gamma} + \frac{g_2}{g_6} + \frac{\alpha}{\gamma}\right) w_0^6 + \frac{5}{2}\left(\frac{g_4\alpha}{g_6\gamma} + \frac{g_2}{g_6} + \frac{\delta}{r}\right) w_0^4 + 5\frac{g_2\alpha}{g_6\gamma} w_0^2 \right]. \tag{6b}$$

The above energy expression has its turning point at $w_0 = 0, \pm w_1, \pm w_2, \pm w_3$ and

$\pm w_4$, which are defined as

$$\pm w_1 = \left[-\frac{g_4}{2g_6} \left\{ 1 + \left(1 - \frac{4g_2 g_6}{g_4^2} \right)^{1/2} \right\} \right]^{1/2},$$

$$\pm w_2 = \left[-\frac{g_4}{2g_6} \left\{ 1 - \left(1 - \frac{4g_2 g_6}{g_4^2} \right)^{1/2} \right\} \right]^{1/2} \tag{7}$$

and

$$\pm w_3 = \left[-\frac{\beta}{2\gamma} \left\{ 1 + \left(1 - \frac{4\alpha\gamma}{\beta^2} \right)^{1/2} \right\} \right]^{1/2},$$

$$\pm w_4 = \left[-\frac{\beta}{2\gamma} \left\{ 1 - \left(1 - \frac{4\alpha\gamma}{\beta^2} \right)^{1/2} \right\} \right]^{1/2}. \tag{8}$$

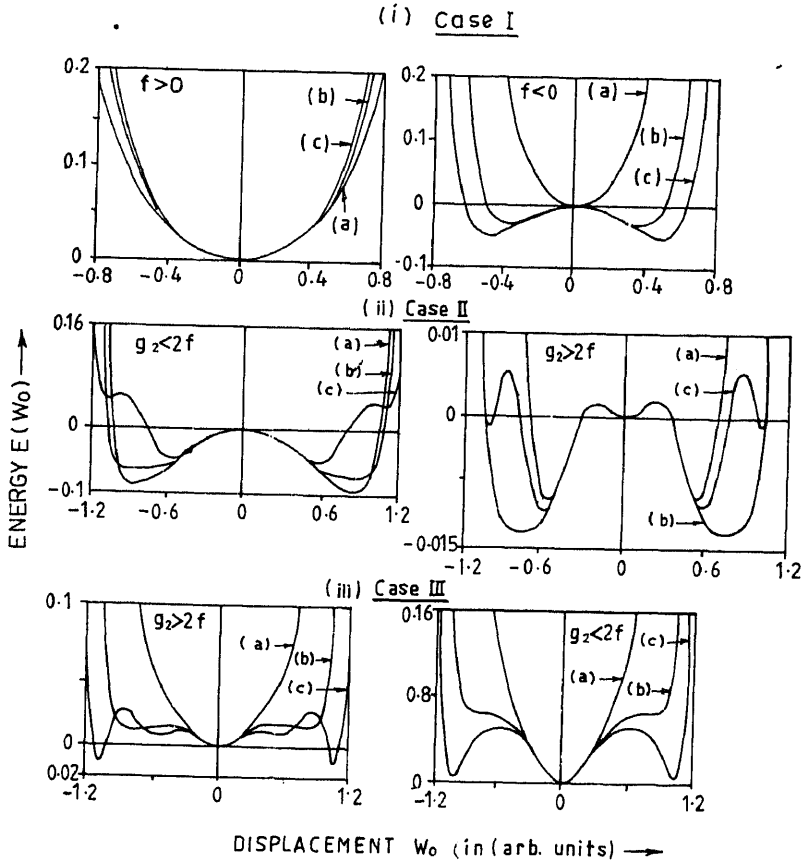

Figure 2. Energy ($E(w_0)$) (in the units of $g_6^2/4f$) versus displacement w_0 for (i) Case I ($g_2 > 0$, $g_4 > 0$ and $g_6 > 0$) with $f > 0$ and $f < 0$, (ii) Case II ($g_2 < 0$, $g_4 > 0$ and $g_6 < 0$) with $g_2 > 2f$ and $g_2 < 2f$, (iii) Case III ($g_2 > 0$, $g_4 < 0$ and $g_6 > 0$) with $g_2 > 2f$ and $g_2 < 2f$ obeying the approximations (a) $g_4^2 < 4g_2 g_6$, (b) $g_4^2 = 4g_2 g_6$ and (c) $g_4^2 > 4g_2 g_6$.

In the approximation $g_4^2 = 4g_2g_6$, the energy expression yields a triple degenerate minima corresponding to the displacements $\pm w_1$, $\pm w_2$ and $\pm w_4$ and maxima at the displacement $\pm w_3$, provided $|g_2| > 2f$. Hence the energy structure develops a harmonic potential at the origin (i.e., for small displacements) and a flattened symmetric double well for large displacements. The energy (in the units of $g_6^2/4f$) versus displacement w_0 for three different cases in the approximations $g_4^2 <, =, > 4g_2g_6$ respectively, are shown in figure 2.

However for the travelling wave solutions, ie, in the interacting oscillator mode, we have taken $g_4^2 = 4g_2g_6$, $g_2 < 0$, $g_4 > 0$, $g_6 < 0$ and $g_2 < 2f$. These conditions lead to the structural phase transition (can be seen from figure 2 (Case II(b))). In the continuum treatment we chose the solutions for the displacements in the travelling wave form as

$$u_{1,n\pm1}\left(t \pm \frac{2a}{v}\right) = u_{1,n}(t),$$

$$u_{2,n\pm1}\left(t \pm \frac{2a}{v}\right) = u_{2,n}(t), \tag{9}$$

where a and v are the interatomic distance and velocity of the travelling wave respectively . We make Taylor's series expansion of displacements in the travelling wave in terms of $\tau(=2a/v)$ (similarly for $u_{2,n\pm1}(t)$ and $w_{1,n\pm1}(t)$) as [4]

$$u_{1,n\pm1}(t) = u_{1,n}(t) \pm \tau \dot{u}_{1,n}(t) + \frac{\tau^2}{2}\ddot{u}_{1,n}(t). \tag{10}$$

Using (2), (9) and (10), the equation of motion (5) in the relative shell-core displacement can be expressed as

$$\left(1 + \beta - 6\beta\frac{w_{1,n}^2}{w_s^2} + 5\beta\frac{w_{1,n}^4}{w_s^4}\right)\ddot{w}_{1,n} - 12\beta w_{1,n}\frac{\dot{w}_{1,n}^2}{w_s^2}$$

$$+ 20\beta w_{1,n}^3\frac{\dot{w}_{1,n}^2}{w_s^4} + \frac{g_2}{M}w_{1,n}\left(1 - 2\frac{w_{1,n}^2}{w_s^2} + \frac{w_{1,n}^4}{w_s^4}\right) = 0, \tag{11}$$

where

$$w_s \equiv \pm\left(-\frac{g_4}{2g_6}\right)^{1/2} = \pm\left(-\frac{2g_2}{g_4}\right)^{1/2}$$

represents the minima of the ϕ^6 potential for the special case, $g_4^2 = 4g_2g_6$ (see figure 2). Here,

$$\beta = \frac{g_2}{2f}\frac{1}{\left(1 - \frac{v_2^2}{v^2}\right)}, \tag{12}$$

$$\frac{1}{\mathrm{M}} = \frac{1}{m_1\left(1 - \frac{v_1^2}{v^2}\right)} + \frac{1}{m_2\left(1 - \frac{v_2^2}{v^2}\right)} \tag{13}$$

$$v_1 \equiv a\left(\frac{4f'}{m_1}\right)^{1/2}, \quad v_2 \equiv a\left(\frac{2f}{m_2}\right)^{1/2} \tag{14}$$

ıe acoustic velocities near the critical temperature [2, 11]. Equation (11) contains meters β and w_s whose values depend upon the magnitude of f, g_2 and g_4. The sign nagnitude of g_6 does not come into picture. Only the knowledge of the nature and itudes of f, g_2 and g_4 are needed in the calculation of dipole moment. Integrating nce, we obtained the equation of motion as

$$\dot{w}_{1,n}^2 = -\frac{1}{M}\left[\frac{V(w_{1,n}^4) - V(w_0^4)}{\left(1+\beta-6\beta\frac{w_{1,n}^2}{w_s^2}+5\beta\frac{w_{1,n}^4}{w_s^4}\right)^2}\right], \tag{15}$$

e $\pm w_0$ are the turning points and

$$V(w_{1,n}^4) = g_2 w_{1,n}^2\left[1+\beta-(1+4\beta)\frac{w_{1,n}^2}{w_s^2}+\left(\frac{1+18\beta}{3}\right)\frac{w_{1,n}^4}{w_s^4}-4\beta\frac{w_{1,n}^6}{w_s^6}+\beta\frac{w_{1,n}^8}{w_s^8}\right]. \tag{16}$$

effective potential relating the anharmonic oscillation is

$$U(w_{1,n}) = -\frac{\mu}{2M}\left[\frac{V(w_{1,n}^4) - V(w_0^4)}{\left(1+\beta-6\beta\frac{w_{1,n}^2}{w_s^2}+5\beta\frac{w_{1,n}^4}{w_s^4}\right)^2}\right]. \tag{17}$$

ime period is obtained from (15) as

$$t = (-M)^{1/2}\int^{w_{1,n}} \frac{\left(1+\beta-6\beta\frac{w_{1,n}^2}{w_s^2}+5\beta\frac{w_{1,n}^4}{w_s^4}\right)}{[(w_{1,n}^2 - w_0^2)\mathrm{R}(w_{1,n}^4)]^{1/2}}\,\mathrm{d}w_{1,n}, \tag{18}$$

e the lower integration limit is arbitary and

$$\mathrm{R}(w_{1,n}^4) = \frac{V(w_{1,n}^4) - V(w_0^4)}{(w_{1,n}^2 - w_0^2)}$$
$$\equiv ax^4 + bx^3 + cx^2 + dx + e \tag{19}$$

iquadratic equation in $x(=w_{1,n}^2)$ with the coefficients

$$a = \beta\frac{g_6^2}{g_2},$$

$$b = \frac{8g_6^2\beta}{g_4} + aw_0^2,$$

$$c = \tfrac{1}{3}g_6(1+18\beta) + bw_0^2,$$

At the turning points ($\pm w_0$), $R(w_0^4)$ is factorized as

$$R(w_0^4) = g_2\left(1 - 2\frac{w_0^2}{w_s^2} + \frac{w_0^4}{w_s^4}\right)\left(1 + \beta - 6\beta\frac{w_0^2}{w_s^2} + 5\beta\frac{w_0^4}{w_s^4}\right). \tag{20}$$

Equation (18) can be solved for both periodic as well as nonperiodic solutions.

2.1 *Periodic solution*

Static periodic waves can be obtained in the limit $v \to 0$. $R(w_{1,n}^4)$ has four roots (w_1^2, w_2^2, w_3^2 and w_4^2) which can be expressed as

$$R(w_{1,n}^4) = \beta\frac{g_6^2}{g_2}(w_{1,n}^2 - w_1^2)(w_{1,n}^2 - w_2^2)(w_{1,n}^2 - w_3^2)(w_{1,n}^2 - w_4^2). \tag{21}$$

We have investigated the anharmonic periodic oscillations, in which a series representation of the integral is preferred as compared to the elliptic integral. For this purpose we assume $w_{1,n}/w_0 = \cos y$ and perform the series representation of the integral. The expression for the time period reduces to

$$t = (M)^{1/2}\int^{y} \frac{\left(1 + \beta - 6\beta\frac{w_0^2}{w_s^2} + 5\beta\frac{w_0^4}{w_s^4}\right)}{R^{1/2}(w_0^4)} \cdot \left[1 + \sum_{m=1}^{\infty} a_m \sin my\right] \mathrm{d}y, \tag{22}$$

where a_m are the coefficients of the periodic function $\sin my$. Further simplification and use of (20), reduces (22) to

$$\Omega t = -\arccos\left(\frac{w_{1,n}}{w_0}\right) - \sum_{m=1}^{\infty}\frac{a_m}{m}P_m\left(\frac{w_{1,n}}{w_0}\right), \tag{23}$$

where

$$\Omega^2 = \frac{g_2}{M} \cdot \frac{\left(1 - 2\frac{w_0^2}{w_s^2} + \frac{w_0^4}{w_s^4}\right)}{\left(1 + \beta - 6\beta\frac{w_0^2}{w_s^2} + 5\beta\frac{w_0^4}{w_s^4}\right)} \tag{24}$$

and

$$P_m\left(\frac{w_{1,n}}{w_0}\right) = 1 - \cos\left[m\arccos\left(\frac{w_{1,n}}{w_0}\right)\right]. \tag{25}$$

At the turning point w_0, the polynomial $P_m(w_{1,n}/w_0)$ vanishes. For obtaining the static periodic waves ($v \to 0$), (23) transforms into the condition

$$\Omega\tau \equiv 2ak = \left[-\frac{2g_2}{f^*}\right]^{1/2}\left(1 - 2\frac{w_0^2}{w_s^2} + \frac{w_0^4}{w_s^4}\right)^{1/2}, \tag{26}$$

where f^* is an effective force constant and is given by $f^* = 2ff'/(f + 2f')$. Periodic wave amplitude is obtained as

$$w_0^2 = w_s^2\left[1 \pm \left\{-\frac{2f^*}{g_2}a^2k^2\right\}^{1/2}\right]. \tag{27}$$

By substitution $2a^2k^2 = 1 - \cos(2ak)$ and the commensurate periodic wave condition

$$w_{0,2}^2 = w_s^2\left[1 \pm \left(-\frac{2f^*}{g_2}\right)^{1/2}\right],$$

$$w_{0,3}^2 = w_s^2\left[1 \pm \left(-\frac{3f^*}{2g_2}\right)^{1/2}\right],$$

$$w_{0,4}^2 = w_s^2\left[1 \pm \left(-\frac{f^*}{g_2}\right)^{1/2}\right],$$

$$w_{0,5}^2 = w_s^2\left[1 \pm \left(2\left\{-\frac{f^*}{g_2}\right\}\sin^2\frac{\pi}{5}\right)^{1/2}\right],$$

$$w_{0,6}^2 = w_s^2\left[1 \pm \left(-\frac{f^*}{2g_2}\right)^{1/2}\right]. \tag{28}$$

Table 1. Static commensurate periodic solutions of electron-ion displacement for periods $N = 1, 2, 3, 4$ and 6.

od $(2\pi/N)$	Electron-ion displacement $(w_{0,N})$	
	ϕ^6 model $(g_4^2 = 4g_2g_6)$	ϕ^4 model [4]
1 oelectric)	$w_0^2 = -\dfrac{g_4}{2g_6} = -\dfrac{2g_2}{g_4}$	$w_0^2 = -\dfrac{g_2}{g_4}$
2 iferroelectric)	$w_0^2 = (-w_1)^2$	
	$w_0^2 = -\dfrac{g_4}{2g_6}\left(1 \pm \left(-\dfrac{4f_r}{g_2}\right)^{1/2}\right)$	$w_0^2 = -\dfrac{g_2}{g_4}\left(1 + \dfrac{4f_r}{g_2}\right)$
3 odon)	$w_0 = 0,\ w_1^2 = (-w_2)^2$	
	$w_1^2 = -\dfrac{g_4}{2g_6}\left(1 \pm \left(-\dfrac{3f_r}{g_2}\right)^{1/2}\right)$	$w_1^2 = -\dfrac{g_2}{g_4}\left(1 + \dfrac{3f_r}{g_2}\right)$
4	$w_0 = w_2 = 0,\ w_1^2 = (-w_3)^2$	
	$w_1^2 = -\dfrac{g_4}{2g_6}\left(1 \pm \left(-\dfrac{2f_r}{g_2}\right)^{1/2}\right)$	$w_1^2 = -\dfrac{g_2}{g_4}\left(1 + \dfrac{2f_r}{g_2}\right)$
6	$w_0 = w_3 = 0,\ w_1^2 = w_2^2 = (-w_4)^2 = (-w_5)^2$	
	$w_1^2 = -\dfrac{g_4}{2g_6}\left(1 \pm \left(-\dfrac{f_r}{g_2}\right)^{1/2}\right)$	$w_1^2 = -\dfrac{g_2}{g_4}\left(1 + \dfrac{f_r}{g_2}\right)$

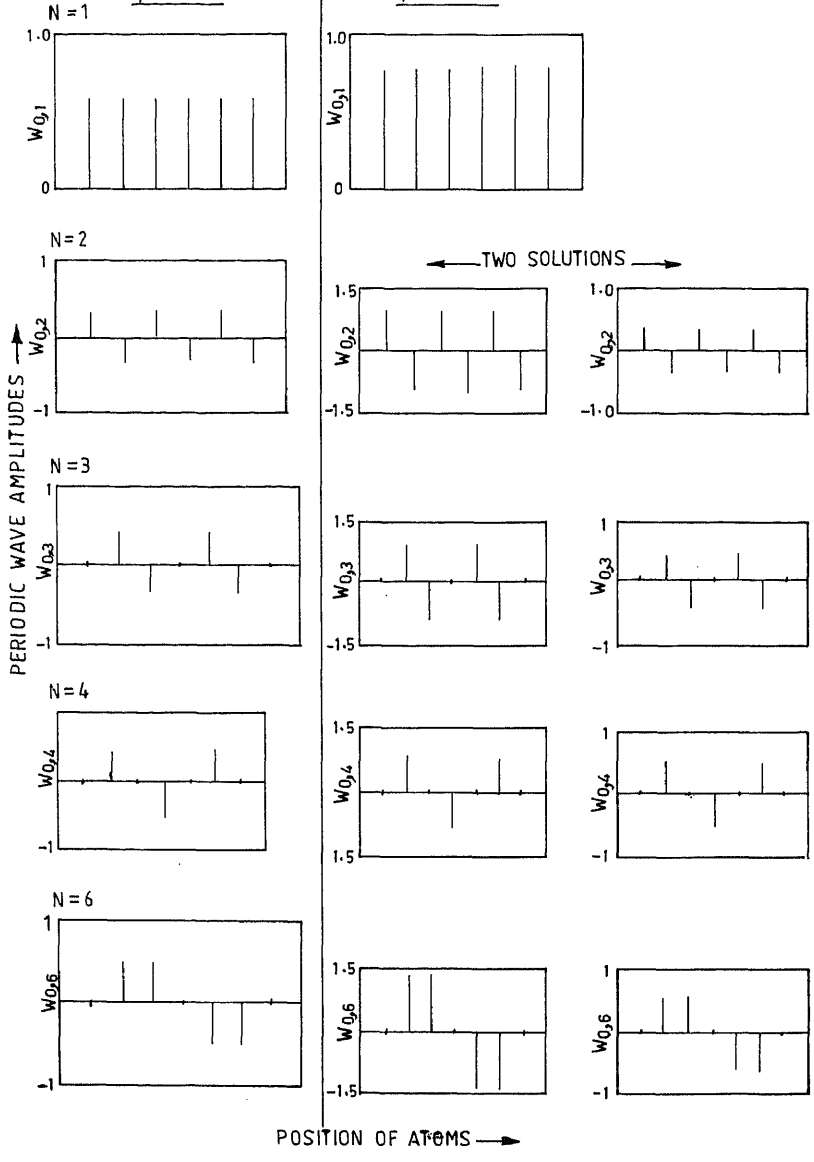

Figure 3. Displacement pattern of static commensurate periodic solutions with periods 1 to 6 for ϕ^4- and ϕ^6-polarizable models.

To have the real static periodic solutions, the value of g_2 is taken to be negative and the force constant f^* as positive. Two different trevelling periodic wave amplitudes are obtained. One travelling amplitude is always smaller than the sixth order amplitude and larger than the sixth order anti-amplitude, i.e., $w_{0,1}^2 < w_{0,N}^2 < w_{0,2}^2$, $N = 3, 4, 5, 6$.

Another travelling wave amplitude exists in the regime which is opposite in order of the previous one $[w_{0,1}^2 < w_{0,N}^2 < w_{0,2}^2]$.

Earlier, Büttner and Bilz [4] have reported the static commensurate solutions for lower order periods for a one dimensional monoatomic chain, where they have considered fourth order electron-phonon interactions at the polarizable ion. Based on the similar model treatment [4], we have calculated the electron-ion displacements for a monoatomic chain with an on-site sixth order electron-phonon coupling, by using the formula

$$w_{n+1} = \frac{1}{f_r}(g_2 w_n + g_4 w_n^3 + g_6 w_n^5) + 2w_n - w_{n-1}, \tag{29}$$

where

$$\frac{1}{f_r} = \frac{1}{f} + \frac{1}{f'}.$$

It has been found that the results obtained from (28) (ie for the sixth order periodic amplitude for a diatomic chain) are identical to the monoatomic case from eq. (26), where the effective force constant f_r corresponds to $f^*/2$. The static commensurate solutions with period 1 to 6 for ϕ^6-polarizable model are given in table 1 and comparison of our model with the ϕ^4-polarizable model are shown pictorially in terms of the relative electron-ion displacement coordinate in figure 3. $w_{0,1}$ is the amplitude of ferroelectric state which has lowest stable energy at the displacement w_s. Above these static ground states, there are nonlinear static kink-like excitations which describe the domain walls between the degenerate ground states of period $N = 2, 3, 4, 6$. As an example, the kink structure in the antiferroelectric state ($N = 2$) has sequence of the ions altered from up, down, up $\cdots$to down, up, down $\cdots$. In the present case, we have obtained two different static periodic amplitudes, in contrast to the one obtained in ϕ^4 model results reported by Benedek [4].

2.2 *Non-periodic solutions*

Non periodic solutions are obtained if the integral of (18) diverges for some values of $w_{1,n}^2$. If one of the roots of $R(w_{1,n}^4)$ is w_0, then the expression $R(w_0^4) = 0$ yields a divergence in time. We have obtained two values of w_0^2 ie,

$$w_0^2 = w_s^2 \quad \text{or} \quad w_0^2 = w_s^2 \left\{ \frac{3}{5} \pm \frac{2}{5}\left(1 + \frac{5}{4\beta}\right)^{1/2} \right\}. \tag{30}$$

It has been found that only the first value of w_0^2 yields a divergence in time (eqs (18) and (20)). Hence the time period is obtained at $w_0^2 = w_s^2$ as

$$\Omega_s t = \int^y \frac{1 + \frac{4}{3}A_s(1 - \frac{3}{2}y + \frac{5}{4}y^2)}{(1-y)^{1/2}\, y^{1/2}(y-1)[1 + A_s(1 - y + y^2)]^{1/2}} \cdot \mathrm{d}y, \tag{31}$$

where

$$y = \frac{w_{1,n}^2}{w_s^2},$$

$$A_s = \frac{3\beta}{(1-3\beta)} = -\left(\frac{3g_2}{2f}\right) \cdot \left[\frac{v_2}{\left(v_2^2 - \left(1 - \frac{3g_2}{2f}\right)v^2\right)} \right] \tag{32}$$

and

$$\Omega_s = \left[\frac{4g_2}{3M}\frac{1}{(1-3\beta)}\right]^{1/2}. \tag{33}$$

The effective potential $U(w_{1,n})$ at $w_0^2 = w_s^2$ is given by

$$U(w_{1,n}) = \tfrac{1}{2}\mu w_s^2 \Omega_s^2 \frac{(y-1)^3(1+A_s(1-y+y^2))}{[1+\frac{4}{3}A_s(1-\frac{3}{2}y+\frac{5}{4}y^2)]^2}. \tag{34}$$

The maxima of the potential $U(w_{1,n})$ lies at $w_0^2 = w_s^2$ (i.e., $y = 1$). The derivative $dt/dw_{1,n}$ has an integrable divergence for the displacement

$$w_{1,n} = \pm\frac{w_s}{2^{1/2}}\left[1 \pm \left(1-\frac{4}{3\beta}\right)^{1/2}\right]^{1/2} \tag{35}$$

provided $\beta \geqslant 4/3$ and $\beta < 0$.

The displacement $w_{1,n}$ can be expressed in terms of the defined parameter, A_s as

$$w_{1,n} = \pm\frac{w_s}{2^{1/2}}\left[1 \pm \left(1-4\left(1+\frac{1}{A_s}\right)\right)^{1/2}\right]^{1/2} \tag{36}$$

with $A_s < 0$. We have categorized the non-periodic solutions into four groups, such as

(1) static and slowly propagating solutions,
(2) large velocity solutions,
(3) pulse solutions,
(4) fast kink and antikink solutions.

2.2.1 *Static and slowly propagating solutions*: The static ($v = 0$) and slowly propagating (for small v) travelling wave solutions exist in between two turning points, $\pm w_s$ for which, A_s is negative. These solutions are travelling kinks obeying the necessary

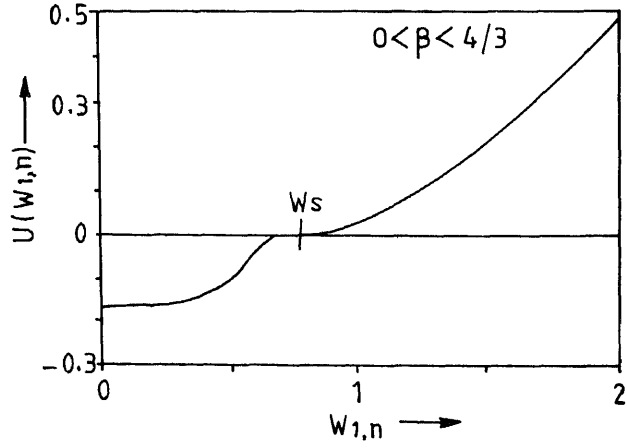

Figure 4. Effective potential $U(w_{1,n})$ as a function of core-shell displacement $w_{1,n}$ for $0 < \beta < \frac{4}{3}$.

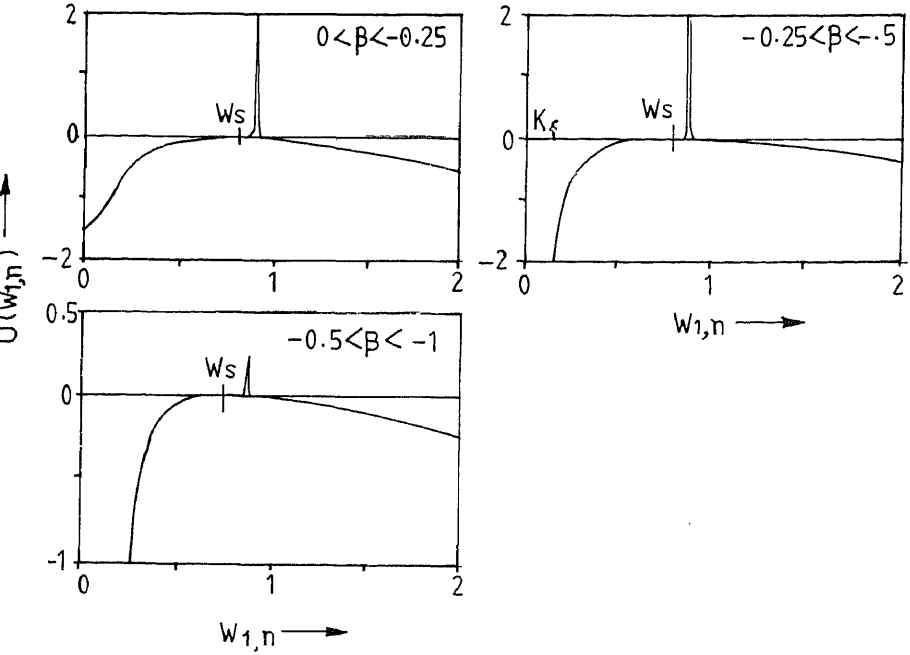

Figure 5. Effective potential $U(w_{1,n})$ as a function of core-shell displacement $w_{1,n}$ for (a) $0 < \beta < -0{\cdot}25$, (b) $-0{\cdot}25 < \beta < -0{\cdot}5$ and (c) $-0{\cdot}5 < \beta < -1$. K_f denotes fast kinks.

tion

$$v^2 < \frac{v_2^2}{(1-2\gamma_{\phi_6})}, \tag{37}$$

$\gamma_{\phi_6} = 3g_2/4f$. It is seen from figure 4, that for slowly moving solutions, no turning is encountered in between $w_{1,n} = \pm w_s$, for the values of the velocity parameter $< \frac{4}{3}$. Turning points are also obtained in the regime $w_{1,n} > w_s$ which are very close . The necessary condition for the mass ratio m_1/m_2 in the regime $0 < \beta < \frac{1}{3}$ is

$$\frac{m_1}{m_2} < \frac{2f'}{f}(1+\gamma_s), \tag{38}$$

$\gamma_s \equiv -3g_2/2f^*$.

this regime, no consequence of the sixth order polarization potential is observed. (34) it can be seen that the effective potential becomes infinite for the displacements

$$w_{1,n} = \pm w_s \left[\frac{3}{5}\left(1 \pm \left(1 - \frac{5}{9}\left(4 + \frac{3}{A_s}\right)\right)^{1/2}\right)\right]^{1/2}. \tag{39}$$

$\beta > 0$, the potential does not exhibit any discontinuity with respect to the acement. The discontinuity can, however be obtained for $\beta < 0$ which are also

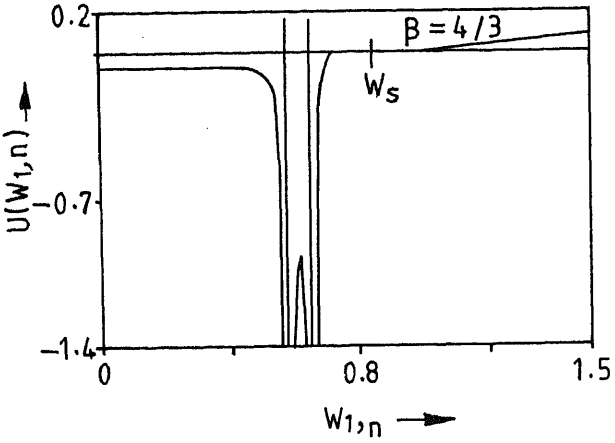

Figure 6. Effective potential $U(w_{1,n})$ as a function of core-shell displacement $w_{1,n}$ for $\beta = 4/3$.

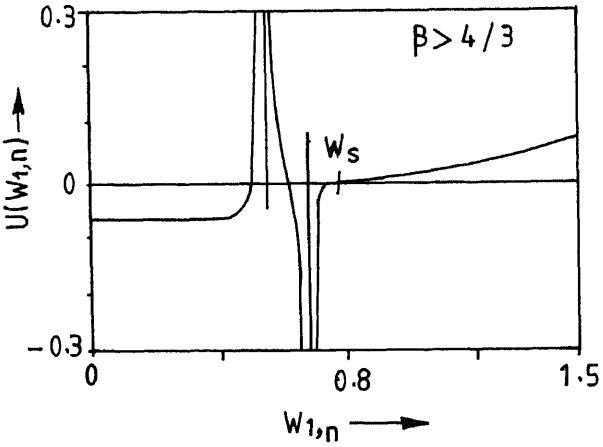

Figure 7. Effective potential $U(w_{1,n})$ as a function of core-shell displacement $w_{1,n}$ for $\beta > 4/3$. E denotes the presence of excitons.

travelling kinks obeying the condition

$$0 < v^2 < \frac{v_2^2}{(1-2\gamma'_{\phi_0})} \quad \text{and} \quad \frac{m_1}{m_2} < \frac{2f'}{f}(1+\gamma'_s) \tag{40}$$

with $\gamma'_{\phi_0} \equiv -g_2/4f$ and $\gamma'_s = g_2/2f^*$. It can be noted from figure 5 that no turning point is encountered in between $w_{1,n} = 0$ and $\pm w_s$. The existence of real turning points in the regime $w_{1,n}^2 > w_s^2$ shows the presence of pulse solutions which start from the ground state polarization and returns back to the same state. Such pulse solutions are known as travelling excitons. Thus, when the velocity, $v^2 = v_2^2(1/(1-2\gamma_{\phi_0}))$ decreases to

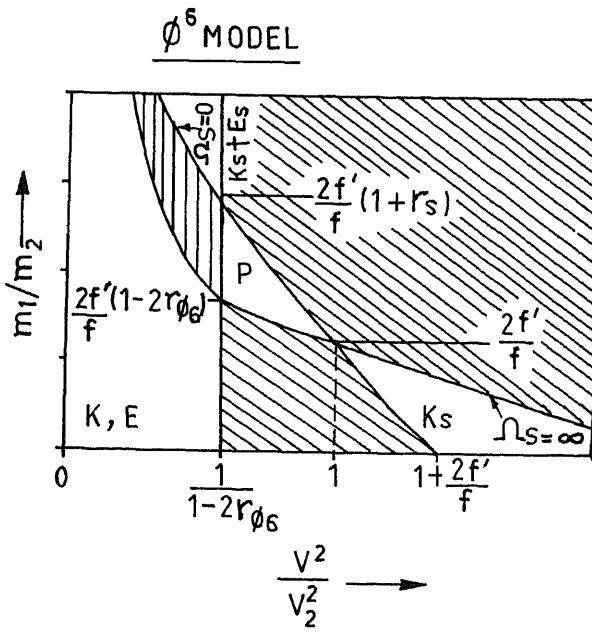

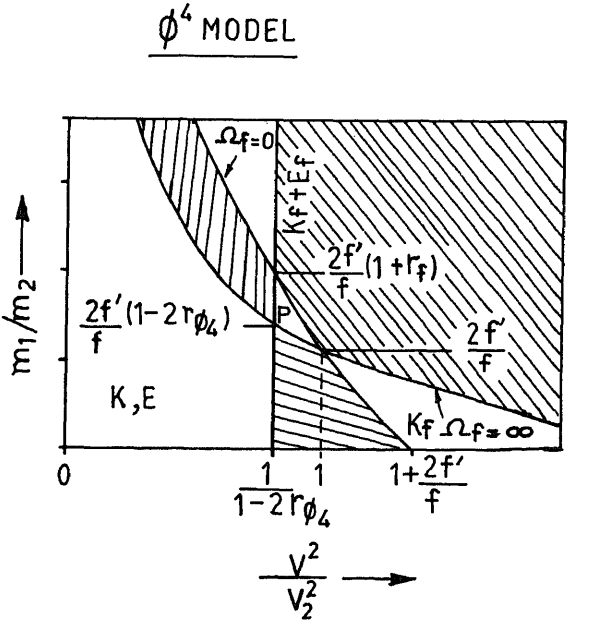

Figure 8. Ratio m_1/m_2 as a function of v^2/v_2^2 in which white areas are represented as an existence domain for (a) ϕ^4 model and (b) ϕ^6 model.

Table 2. The mass ratio m_1/m_2 as a function of velocity ratio v^2/v_2^2. Following values are plotted in figure 8.

	Values of m_1/m_2			
v^2/v_2^2	ϕ^6 model	ϕ^4 model	ϕ^6 model	ϕ^4 model
	$\Omega_s = 0$ ϕ^6	$\Omega_f = 0$ ϕ^4	$\Omega_s = \infty$ ϕ^6	$\Omega_f = \infty$ ϕ^4
0	∞	∞	∞	∞
$\frac{1}{(1-2\gamma_{\phi_{4,6}})}$	$\frac{2f'}{f}\frac{1}{(1+\gamma_s)}$	$\frac{2f'}{f}\frac{1}{(1+\gamma_f)}$	$\frac{2f'}{f}\frac{1}{(1-2\gamma_{\phi_6})}$	$\frac{2f'}{f}\frac{1}{(1-2\gamma_{\phi_4})}$
$\gamma_{\phi_4} = \frac{g_2}{2f}$	$\gamma_s = -\frac{3g_2}{2f*}$	$\gamma_f = -\frac{g_2}{f*}$		
$\gamma_{\phi_6} = \frac{3g_2}{4f}$				
1	$\frac{2f'}{f}$	$\frac{2f'}{f}$	$\frac{2f'}{f}$	$\frac{2f'}{f}$
$1+\frac{2f'}{f}$	0	0	$\frac{2f'}{(f+2f')}$	$\frac{2f'}{(f+2f')}$
∞	0	0	0	0

$v_2^2(1/(1-2\gamma'_{\phi_6}))$, some excitations are associated with the equilibrium state which can be termed as travelling excitons.

2.2.2 *Large velocity solutions*: If the velocity of the travelling wave is increased through the conditions of mass ratio, $m_1/m_2 > (2f'/f)(1+\gamma_s)$ and velocity parameter $\beta \geqslant \frac{4}{3}$, fast kinks and pulse excitons are obtained. The travelling kinks are fast because their velocity v is larger than $v_1((1+\gamma)/(1-2\gamma_{\phi_6}))^{1/2}$. When $\beta = \frac{4}{3}$ and $v^2 = \pm v_2^2(1/(1-(\gamma_{\phi_6}/2)))$, the effective potential becomes infinite for two displacements in the same direction, in between $0 < w_{1,n} < w_s$ (figure 6). As the value of β increases from 4/3, two discontinuities are obtained in the opposite direction of the potential $U(w_{1,n})$. Therefore in ϕ^6-polarizable model there exists fast travelling kinks, excitons and antikinks, as shown in figures 6 and 7.

If the velocity of the travelling wave approaches the value $\pm v_2(1+2\gamma'_{\phi_6})^{-1/2}$ then one discontinuity in $U(w_{1,n})$ is obtained near the origin (see figure 5) and another at $w_{1,n} > w_s$ provided that the mass ratio $m_1/m_2 > (2f'/f)(1+\gamma_s)$.

2.2.3 *Pulse solutions*: For the velocity lying in the range $v_2^2/(1-2\gamma_{\phi_6}) < v^2 < v_2^2(1+2f'/f)$, no kink solution is obtained. Only excitons with pulse wave behaviour exist in a restricted domain of the mass ratio $2f'/f \leqslant m_1/m_2 \leqslant (2f'/f)(1+\gamma_s)$. The parameter Ω_s decides the convergence and divergence of the time period. In the ϕ^4 model [4]

Ω_f serves the purpose ($\Omega_f = 2g_2/(M(1-2\beta))^{1/2}$). Various values of m_1/m_2 as a function of v^2/v_2^2 are given in table 2 and plotted in figure 8. It can be noted that the width of the restricted domain in ϕ^6 model is more than the ϕ^4 model.

2.2.4 *Fast kink solutions*: For the velocity of the travelling wave lying in the range $v \geqslant v_2$ and mass parameter $m_1/m_2 < 2f'/f$, fast kink solutions are obtained. Analysis of the kink solutions in the two regimes, $\beta < 0$ and $\beta > 0$, can be carried out from (31). The complete integral in (31) can be reduced in the form of elliptic integrals of first, second and third kind (given in Appendix 1).

a) $\beta < 0$: The complete analytical expression for the time period is obtained by integrating (31), where the lower limit is taken to be 1/2. The result is

$$\begin{aligned}\Omega_s t = &-\frac{2(A_s+2)(8A_s+3)}{3(3A_s+4)^{1/2}}\Pi(\mu,1,q) - \frac{(21+8A_s)A_s}{3(3A_s+4)^{1/2}}F(\mu,q)\\ &+\frac{5}{6}A_s\frac{(3A_s+4)^{1/2}}{(1+A_s)}E(\mu,q) - \left[\frac{((A_s+2)(8A_s+3)-10A_s y)}{6(1+A_s)^{1/2}}\right.\\ &\left.\times\left(\frac{1-y}{y}+\frac{y}{1-y}+\frac{A_s+2}{A_s+1}\right)^{1/2}\right] + \frac{(3+4A_s)(3A_s+4)^{1/2}}{3}\\ &-\frac{5}{3}(-A_s)^{1/2}\log\left[\frac{2y^{1/2}(1-y)^{1/2}\left(1+\left(1-\frac{2(A_s+1)}{A_s y(1-y)}\right)^{1/2}\right)}{\left(1+\left(-\frac{(3A_s+4)}{A_s}\right)^{1/2}\right)}\right] \qquad (41)\end{aligned}$$

with $y = w_{1,n}^2/w_s^2$, and $E(\mu,q)$, $F(\mu,q)$ and $\Pi(\mu,1,q)$ are the elliptic integrals of first, second and third kind and are expressed as

$$\begin{aligned}E(\mu,q) = &\left(1-\frac{q^2}{4}-\frac{3q^4}{64}\right)\mu + \left[\sin\mu\cos\mu\left(\frac{q^2}{4}+\frac{3q^4}{64}+\frac{q^4}{32}\sin^2\mu\right.\right.\\ &\left.\left.-\left(\frac{8}{15}\right)\left(\frac{172797}{64}\right)q^4\sin^4\mu\right)\right], \qquad (42)\end{aligned}$$

$$\begin{aligned}F(\mu,q) = &\left(1+\frac{q^2}{4}+\frac{9q^4}{64}\right)\mu - \left[\sin\mu\cos\mu\left(\frac{q^2}{4}+\frac{9q^4}{64}+\frac{3q^4}{64}\sin^2\mu\right.\right.\\ &\left.\left.-\left(\frac{8}{15}\right)\cdot\frac{518391}{64}q^4\sin^4\mu\right)\right], \qquad (43)\end{aligned}$$

$$\begin{aligned}\Pi(\mu,1,q) = &I_1\left(1-\frac{q^2}{2}+\frac{3q^4}{8}\right) - \cos\mu\sin\mu\left(\frac{3q^4}{8}\right) + \mu\left(\frac{q^2}{2}+\frac{3}{16}q^4\right)\\ &-\mu\left(\frac{3}{2}\right)q^4, \qquad (44)\end{aligned}$$

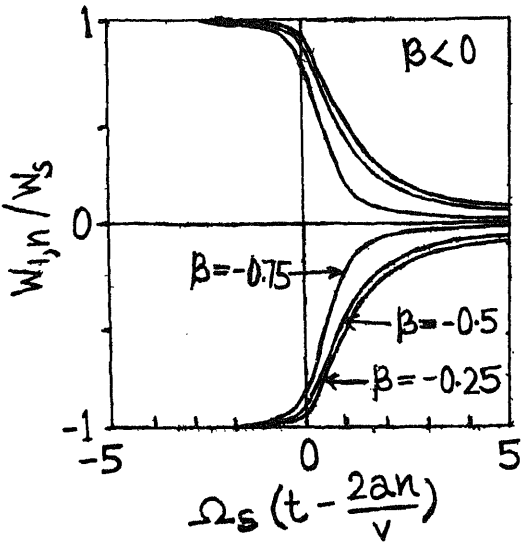

Figure 9. $w_{1,n}/w_s$ plotted as a function of $\Omega_s(t-(2an/v))$ for $\beta<0$.

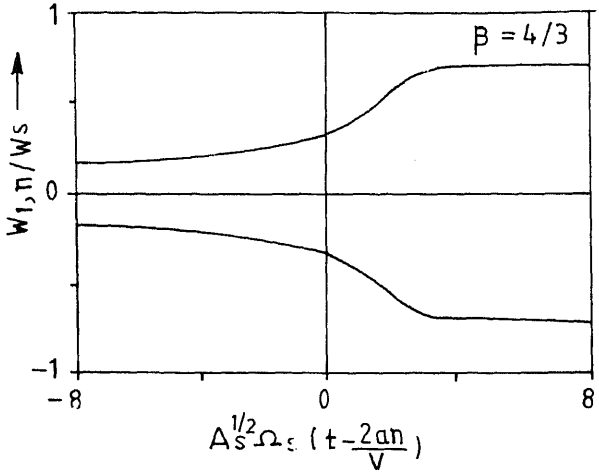

Figure 10. $w_{1,n}/w_s$ plotted as a function of $A_s^{1/2}\,\Omega_s(t-(2an/v))$ for $\beta=\frac{4}{3}$.

$$I_1=\left(1-\frac{1}{2}+\frac{3}{8}+\frac{15}{48}\right)\tan^{-1}(\sin\mu)+\sin\mu\left(\frac{1}{2}+\frac{1}{8}\sin^2\mu+\frac{3}{48}\right)\sin^4\mu$$
$$-\sin\mu\left(\frac{3}{8}+\frac{15}{48}\right), \tag{45}$$

Exact kink and antikink solutions are obtained from (41) and are shown in figure 9 in which $w_{1,n}/w_s$ are plotted as a function of $\Omega_s(t-2an/v)$ for various values of $\beta(<0)$.

It is seen from figure 5 that the potential becomes infinite near the origin for $\beta<0$. In figure 9, kinks and antikinks are obtained in the ϕ^6 model in the regimes $-1<w_{1,n}/w_s<0$ and $0<w_{1,n}/w_s<1$, respectively. The abscissa argument $(t-2an/v)$ has been conveniently multiplied by Ω_s which decides the divergence and convergence of the travelling wave at $\pm w_s$ and 0. In the ϕ^4 treatment, only exact kink solutions are obtained in the limit $w_{1,n}/w_s=-1$ to 1 for various values of A_f (i.e. $2\beta/(1-2\beta)$) [4]. However using the ϕ^6-polarization potential, we have obtained divergence in time at the origin, in addition to $w_{1,n}/w_s=\pm 1$, which is in contrast to the behaviour in the ϕ^4-model.

b) $\beta>0$: For $\beta=\frac{4}{3}$ the expression for the time period is modified as

$$
\begin{aligned}
A_s^{1/2}\Omega_s t = & \frac{(6+19A_s+8A_s^2)(A_s+2)(3A_s+4)}{12(A_s+1)^2}\,\Pi(\mu,1,q) \\
& + \left[\frac{(12+17A_s+8A_s^2)}{3}+\frac{5}{3}\frac{(3A_s+4)A_s}{(A_s+1)}\right]F(\mu,q) \\
& + \frac{5}{6}\frac{A_s^2}{(1+A_s)}E(\mu,q)+\frac{5}{6}\frac{A_s^{3/2}}{(1+A_s)^{1/2}(1-2y)} \\
& \times\left[\frac{1-\left(\frac{A_s}{A_s+1}\right)y+\left(\frac{A_s}{A_s+1}\right)y^2}{2y(1-y)}\right]^{1/2} \\
& - \frac{(3+7A_s+4A_s^2)}{3}\left(\frac{A_s}{(1+A_s)}\right)^{1/2}\left(\frac{1-y}{y}+\frac{y}{1-y}+\frac{A_s+2}{A_s+1}\right) \\
& - \frac{5}{3}A_s\left(\cos^{-1}\left(\frac{A_s y(1-y)}{(A_s+1)}\right)^{1/2}\right),
\end{aligned}
\tag{46}
$$

where

$$
\mu=\arcsin\frac{\left(1-\left(\frac{A_s}{A_s+1}\right)y+\left(\frac{A_s}{A_s+1}\right)y^2\right)^{1/2}}{(1-2y)}
$$

and

$$
q=2\left(\frac{A_s+1}{A_s}\right)^{1/2}.
$$

In figure 10, we have plotted $w_{1,n}/w_s$ as a function of $A_s^{1/2}\Omega_s(t-2an/v)$. In this case the kink and antikink solutions are obtained in the opposite direction in the regimes $-0{\cdot}75<w_{1,n}/w_s<0{\cdot}75$.

(c) $\beta=0$(*static limit*): The expression for the time period for slow solutions (i.e., $v\to 0$) takes a simpler form, since A_s in this case is a small quantity. The slowly moving kink describing the motion of the domain along the diatomic chain is approximately

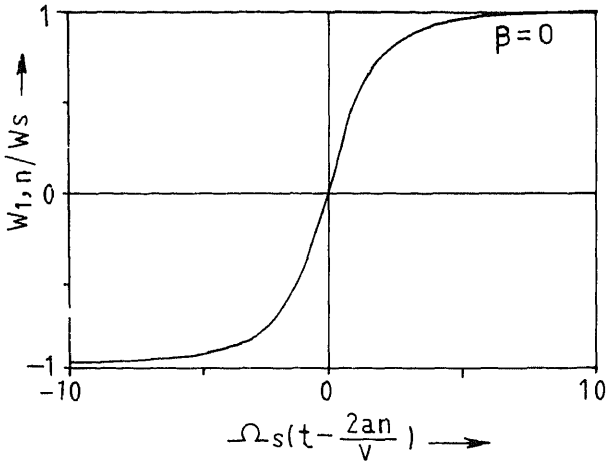

Figure 11. $w_{1,n}/w_s$ plotted as a function of $\Omega_s(t-(2an/v))$ for $\beta=0$

given by

$$w_{1,n}=\left[-\frac{g_4}{2g_6}\right]^{1/2}\sin\left(\arctan\left(\frac{1}{2}\Omega_s\left(t-\frac{2an}{v}\right)\right)\right), \tag{47}$$

$$u_{1,n}=-\frac{4g_2}{3m_1}\frac{1}{\Omega_s^2}w_{1,n}, \tag{48}$$

$$u_{2,n}=\frac{2g_2}{3m_2}\frac{1}{\Omega_s^2}(w_{1,n}+w_{1,n-1}). \tag{49}$$

The variation of $w_{1,n}/w_s$ as a function of $\Omega_s(t-(2an/v))$ is shown in figure 11. The shape of the static ($\Omega_s\to 0$) domain wall with the value of $\Omega_s\sim\frac{2}{3}\gamma_s^{1/2}v/a$ is obtained as

$$w_{1,n}=\left[-\frac{g_4}{2g_6}\right]^{1/2}\sin(\arctan\tfrac{2}{3}\gamma_s^{1/2}n), \tag{50}$$

$$u_{1,n}=\frac{w_{1,n}}{\left(1+\dfrac{2f'}{f}\right)}, \tag{51}$$

$$u_{2,n}=\frac{(w_{1,n}+w_{1,n-1})}{\left(1+\dfrac{f}{2f'}\right)}, \tag{52}$$

where the width of the static domain wall is given by

$$2\left(\frac{3}{2\gamma_s^{1/2}}\right)=2\left(-\frac{3f^*}{2g_2}\right)^{1/2}=2\left(\frac{3f^*}{g_4}\right)^{1/2}\frac{1}{w_s}=2\left(-\frac{3f^*}{2g_6}\right)^{1/2}\frac{1}{w_s}. \tag{53}$$

Table 3. Parameters for calculating the dipole moment per unit charge of $SrTiO_3$.

Parameters	Value [12]
$m_1(10^{-22}\,g)$	1·549
$m_2(10^{-22}\,g)$	1·461
$f(10^4\,g/s^2)$	14·405
$f'(10^4\,g/s^2)$	1·268
$g_2(10^4\,g/s^2)$	−2·629
$g_4(10^{22}\,g/cm^2s^2)$	0·904
$g_6(10^{40}\,cm^4s^2)$	−0·086
β	0·00025
v/v_2	0·3

As the velocity of the travelling wave increases from static value to v_1 or $v_2/((1-2\gamma_{\phi_6})^{1/2})$, the width of the moving kink decreases from the static value (eq. (53)) to zero. The width of the moving kink as a function of v is given by

$$\Gamma_s = 2\cdot\frac{3}{2}\frac{\left(1-\frac{v^2}{v_1^2}\right)^{1/2}\left(1-\frac{v^2}{v_2^2}(1-2\gamma_{\phi_6})\right)^{1/2}}{\left(1-\frac{v^2}{v_0^2}\right)^{1/2}}\cdot\frac{1}{\gamma_s^{1/2}}, \tag{54}$$

where

$$v_0 = \frac{a(2f+4f')}{(m_1+m_2)^{1/2}} \tag{55}$$

is the transverse sound velocity. As far as the size of the static domain is concerned, it has been found that the width of the static domain in ϕ^6-polarizable model is 1·225 times larger than that of the ϕ^4 model.

The various nonlinear excitations obtained in the regimes $\beta>$, <0 are found to carry large amount of energy as compared to ϕ^4 model. The total dipole moment per unit charge of the system is

$$p_s = \frac{vw_s}{2a}\cdot\frac{1}{\Omega_s}\int\frac{w_{1,n}}{w_s}\,d\xi, \tag{56}$$

where ξ is a dimensionless variable and can be taken as $(2a/v)\Omega_s\,(w_{1,n}/w_s)$. It is very difficult to obtain the exact analytical expression for $w_{1,n}/w_s$ as a function of $(\Omega_s t)$ for $\beta<0$ (eq. (41)) and $(A_s^{1/2}\Omega_s t)$ for $\beta>\frac{4}{3}$ (eq. (46)), as the equations (41) and (46) are complicated.

For $SrTiO_3$, Bilz *et al* [2] have calculated the ratio v/v_2 $(v_2 \equiv a(2f/m_2)^{1/2})$ to be equal to 0·3. This value has been obtained by fitting the parameters to the experimental phonon frequencies in the self-consistent phonon approximation [2]. The parameter β is obtained by using the values of g_2, f and v/v_2 in (12). In the present ϕ^6-polarization model, for $SrTiO_3$, the model parameters (m_1, m_2, f, f', g_2 and g_4) are taken from [12] shown in table 3. These parameters are obtained by fitting the experimental data [13]

on the phonon dispersion curves of $SrTiO_3$. For $v/v_2 = 0{\cdot}3$, the value of β in $SrTiO_3$ obtained is 0·00025, whose value lies in the range $0 < \beta < 1/3$. For $0 < \beta < 1/3$, the solution for the time period becomes

$$\begin{aligned}\Omega_s t = &-\frac{(6+19A_s+8A_s^2)(3A_s+4)}{6(A_s+2)(A_s+1)^{1/2}}\Pi(\mu,1,q)\\ &+\left(-\frac{(6+19A_s+8A_s^2)(A_s+2)^{3/2}(3A_s+4)}{12(A_s+1)^{3/2}}+\frac{(3-A_s)}{3(1+A_s)^{1/2}}\right.\\ &\left.-\frac{5A_s(3A_s+4)}{12(1+A_s)^{3/2}}\right)\mathrm{F}(\mu,q)+\frac{5\sqrt{2}A_s}{6(1+A_s)^{1/2}}\mathrm{E}(\mu,q)\\ &-\frac{5A_s(1-2y)}{6(1+A_s)^{1/2}}\left(\frac{(A_s+1)}{2y(1-y)(1+A_s-yA_s+A_sy^2)}\right)^{1/2}\\ &+\frac{(3+7A_s+4A_s^2)}{3(1+A_s)^{1/2}}\left(\left(\frac{3A_s+4}{A_s+1}\right)^{1/2}-\left(\frac{1-y}{y}+\frac{y}{1-y}+\frac{A_s+2}{A_s+1}\right)^{1/2}\right)\\ &-\frac{5}{3}(-A_s)^{1/2}\log\left[\frac{2y^{1/2}(1-y)^{1/2}\left(1+\left(1-\frac{2(A_s+1)}{A_sy(1-y)}\right)^{1/2}\right)}{\left(1+\left(-\frac{(3A_s+4)}{A_s}\right)^{1/2}\right)}\right].\end{aligned} \tag{57}$$

As the equation is complicated, we chose an alternative method for calculating the dipole moment. We have obtained the corresponding numerical values of $w_{1,n}/w_s$ by changing the values of $(\Omega_s t)$ in small increments from $-\infty$ to ∞. Using standard numerical integration techniques we have then computed the integral $\int w/w_s \mathrm{d}\xi$.

Benedek *et al* [4] have found that for this value of velocity ratio, the dipole moment per unit charge in the ϕ^4 model equals to 6·3 nm, which is a large value compared to the polarization induced by ordinary optical phonons. In our model treatment, the dipole moment per unit charge is obtained as 13·325 nm. Thus it is found that the polarization induced by anharmonic phonons in the ϕ^6-model carry very large amount of energy as compared to the ϕ^4-model for a particular value of the velocity parameter β.

3. Conclusion

The present diatomic linear chain model with nonlinear polarizability of sixth order predicts very interesting nonlinear features like the static periodic waves, statics and dynamics of the domain walls, kink and antikink solutions and the existence of the travelling pulse excitons. The pulse excitons are found to carry a large amount of dipole moment for specific relative core-shell displacement, at which the potential energy becomes maximum. We have extended the treatment of Benedek *et al* [4], in which they have considered the nonlinear polarizability of the order four.

We have presented a complete analysis of the travelling wave solutions in a diatomic

(ϕ^6). We have also investigated the periodic and nonperiodic solutions in the limit $g_4^2 = 4g_2g_6$. As compared to the ϕ^4 model [4], we have obtained two types of periodic travelling wave solutions. The sixth order periodic wave amplitudes are found to be identical with the amplitudes obtained in the monoatomic chain with an on-site polarizable potential of sixth order. Regarding nonperiodic solutions, we have obtained kink, antikink and excitons, depending upon different values of the mass ratio and velocity parameter. In our analysis, we have estimated the dipole moment per unit charge for $SrTiO_3$ for a standard value of velocity ratio v/v_2.

The present analytical treatment of the travelling wave solutions can be applied to the study of structural phase transition induced nonlinear dynamical excitations in many biological systems like α-double helix, optical modes of DNA and the materials having hydrogen bonded networks. The cooperative biological phenomena are caused due to the coherent excitations of the nonlinear polar modes in the form of ferroelectric groups. This type of study will help in understanding the nature of many phenomena like transport of ions, energy and the polarization inside biological membranes [14].

Appendix 1

$$
\begin{aligned}
\Omega_s t = & \left(1+\frac{4A_s}{3}\right)\int_{1/2}^{y}\left[\frac{1}{(1-y)^{1/2}y^{1/2}(y-1)(1+A_s(1-y+y^2))^{1/2}}\right]\mathrm{d}y \\
& -2A_s\int_{1/2}^{y}\left[\frac{y^{1/2}}{(1-y)^{1/2}(y-1)(1+A_s(1-y+y^2))^{1/2}}\right]\mathrm{d}y \\
& +\frac{5}{3}A_s\int_{1/2}^{y}\left[\frac{y^{3/2}}{(1-y)^{1/2}(y-1)(1+A_s(1-y+y^2))^{1/2}}\right]\mathrm{d}y \\
= & \frac{(6+19A_s+8A_s^2)}{6\sqrt{2}(1+A_s)^{1/2}}\int_1^z\frac{z\mathrm{d}z}{(z-1)^{1/2}(z+1)^{1/2}\left(z+\dfrac{(A_s+2)}{2(A_s+1)}\right)^{1/2}} \\
& +\frac{(3-A_s)}{3\sqrt{2}(1+A_s)^{1/2}}\int_1^z\frac{\mathrm{d}z}{(z-1)^{1/2}(z+1)^{1/2}\left(z+\dfrac{(A_s+2)}{2(A_s+1)}\right)^{1/2}} \\
& -\frac{5A_s}{6\sqrt{2}(1+A_s)^{1/2}}\int_1^z\frac{(z-1)^{1/2}\mathrm{d}z}{(z+1)^{1/2}\left(z+\dfrac{(A_s+2)}{2(A_s+1)}\right)^{1/2}} \\
& +\frac{(3+7A_s+4A_s^2)}{3(1+A_s)^{1/2}}\left[\left(\frac{3A_s+4}{A_s+1}\right)^{1/2}-\left(\frac{(1-y)}{y}+\frac{y}{(1-y)}+\frac{A_s+2}{A_s+1}\right)^{1/2}\right] \\
& +\frac{5A_s}{6\sqrt{2}(1+A_s)^{1/2}}\int_1^z\frac{\mathrm{d}z}{(z+1)\left(z+\dfrac{(A_s+2)}{2(A_s+1)}\right)^{1/2}}, \qquad \text{(A1)}
\end{aligned}
$$

since $z = \frac{1}{2}[((1-y)/y) + y/(1-y)]$.

The first three integrals in (A1) are known as elliptic integrals. The expression can be reduced to square roots of third and fourth degree polynomial and their products with

rational functions

$$\mu = \arcsin\left(\frac{u-a}{u-b}\right)^{1/2} \quad \text{and} \quad q = \left(\frac{b-c}{a-c}\right)^{1/2}$$

for the integral

$$\int_{\alpha}^{u} \frac{dz}{(z-a)^{1/2}(z-b)^{1/2}(z-c)^{1/2}} = \frac{2}{(a-c)^{1/2}} F(\mu, q) \qquad [u > a > b > c],$$

$$\int_{\alpha}^{u} \frac{z\,dz}{(z-a)^{1/2}(z-b)^{1/2}(z-c)^{1/2}} = \frac{2}{b(a-c)^{1/2}} [a(a-b)\Pi(\mu, 1, q) + b^2 F(\mu, q)] \qquad [u > a > b > c],$$

$$\int_{\alpha}^{u} \frac{(z-a)^{1/2}\,dz}{(z-b)^{1/2}(z-c)^{1/2}} = -2(a-c)^{1/2} E(\mu, q) + 2\left[\frac{(u-a)(u-c)}{(u-b)}\right]^{1/2} \qquad [u > a > b > c].$$

$E(\mu, q)$, $F(\mu, q)$ and $\Pi(\mu, 1, q)$ are the elliptic integrals of first, second and third kind. For $\beta < 0$: $a = 1$, $b = -1$, $c = -(A_s + 2)/2(A_s + 1)$, $u = z$; $\beta \geqslant 4/3$: $a = -(A_s + 2)/2(A_s + 1)$, $b = 1$, $c = -1$, $u = z$; and $0 < \beta < \frac{1}{3}$: $a = 1$, $b = -(A_s + 2)/2(A_s + 1)$, $c = -1$, $u = z$.

The last term in (A1) has its value as

$$-\frac{5}{3} A_s \left(\cos^{-1}\left(\frac{A_s y(1-y)}{(A_s+1)}\right)^{1/2} - \cos^{-1} 1\right) \quad \text{for } \beta = 4/3$$

and

$$-\frac{5}{3}(-A_s)^{1/2} \log\left[\frac{2y^{1/2}(1-y)^{1/2}\left(1 + \left(1 - \frac{2(A_s+1)}{A_s y(1-y)}\right)^{1/2}\right)}{\left(1 + \left(-\frac{(3A_s+4)}{A_s}\right)^{1/2}\right)}\right]$$

for $\beta < 0$ and $0 < \beta < 1/3$.

Acknowledgements

Authors acknowledge the work of A Bussmann-Holder, H Bilz and H Buttner. One of the authors (NDC) acknowledges the financial support of CSIR in the form of Research Associateship. SPS is grateful to UGC for Career Award, financial assistance from UGC, CSIR, DST, New Delhi and DAE, Bombay.

References

[1] R Migoni, H Bilz and D Baurele, *Phys. Rev. Lett.* **37**, 1155 (1976)
J A Krumhansl and J R Schrieffer, *Phys. Rev.* **B11**, 3535 (1975)

[2] H Bilz, A Bussmann-Holder, G Benedek, H Buttner, D Strausch, *Ferroelectrics* **25**, 339 (1980)
H Buttner, in *Nonlinear phenomena at phase transitions and instabilities* edited by T Riste (Plenum, 1981)

[3] H Buttner and H Bilz, *J. Phys.* (*Paris*) **C6**, 111 (1981)
H Buttner and H Bilz, *Recent Developments in Condensed Matter Physics* edited by J T Devreese (Plenum Press, New York, 1981)
[4] G Benedek, A Bussmann-Holder and H Bilz, *Phys. Rev.* **B36**, 630 (1987)
[5] H Frohlich, *Int. J. Quantum Chem.* **2**, 641 (1968)
H Haken, *Synergetics* (Springer-Verlag, Heidelberg, 1978)
F Kaiser, *Z. Naturforsch.*, **A33**, 294, 418 (1978)
H Bilz, H Buttner and H Frohlich, *Z. Naturforsch.* **366**, 208 (1981)
[6] T Riste, E J Samuelson, K Otnes and J Feder, *Solid State Commun.* **9**, 1455 (1971)
S M Shapiro, J D Axe, G Shirane and T Riste, *Phys. Rev.* **B6**, 4332 (1972)
A D Bruce and R A Cowley, *Adv. Phys.* **29**, 219 (1980)
K A Muller, in *Nonlinear phenomena at phase transitions and instabilities* edited by T Riste (Plenum, New York, 1982), p. 1
K A Muller, in *Statics and dynamics of nonlinear systems* edited by G Benedek, H Bilz R Zeyher (Springer, Heidelberg, 1983) **47**, 68
[7] S N Behera and A Khare, *Pramana – J. Phys.* **15**, 245 (1980)
[8] R Adair, L L Chase and S A Payne, *Phys. Rev.* **B39**, 3337 (1989)
[9] E Magwari, *Z. Phys.* **B43**, 345 (1981)
S N Behera and A Khare, *Pramana – J. Phys.* **15**, 245 (1980)
B Dey, *J. Phys.* **C19**, 3365 (1986)
[10] N D Chowdhury, Nonlinear dynamical theory of condensed matter, Ph.D Thesis, University of Bhopal (1993) (unpublished)
[11] A Bussmann-Holder, H Bilz and P Vogl, in *Dynamical properties of IV-VI compounds* (Springer, Berlin, 1983)
[12] A Bussmann-Holder, H Bilz and G Benedek, *Phys. Rev.* **B39**, 9214 (1989)
[13] R A Cowley, *Phys. Rev.* **134**, A981 (1964)
W G Stirling and R Currat, *J. Phys.* **C9**, L519 (1976)
W G Stirling, *J. Phys.* **5**, 2711 (1972)
[14] A J Martin, *Biopolymers* **23**, 471 (1984)

MANA
rnal of
physics

© Printed in India

Vol. 47, No. 4,
October 1996
pp. 309–315

odel of knock-out of oxygen by charged particle diation of Bi-2212

ANDYOPADHYAY, PINTU SEN, P BARAT, P MUKHERJEE,
DAS and B GHOSH
ble Energy Cyclotron Centre, 1/AF, Bidhan Nagar, Calcutta 700 064, India

ceived 27 May 1996; revised 6 August 1996

ct. A model of knock-out of oxygen by charged particle (α and proton) irradiation of $CaCu_2O_{8+x}$ (Bi-2212) is proposed on the basis of Monte Carlo TRIM calculations. In 2, the loosely bound excess oxygen is vulnerable to be displaced by particle irradiation. g energy and hence, displacement energy of this loosely bound excess oxygen is less ared to that of stoichiometric lattice bound oxygen and other atoms. The displaced or ed out oxygen goes to pores or intergranular region and generates large pressure inside the e. Because of porosity of the material, this displaced oxygen diffuses out and there is a net ion of oxygen content of the sample. The irradiation induced oxygen knock-out is ant in the bulk where nonionizing energy loss is maximum.

rds. Oxygen knock-out; Bi-2212; particle irradiation.

Nos 61·80; 74·60

roduction

energy charged particles interact with solids by elastic and inelastic processes Elastic or nuclear energy loss causes displacement of atoms. Inelastic or onic energy loss manifests in ionization and excitation of atoms. In superconduc- it is the nonionizing energy loss (causing displacement of atoms) that plays ificant role in controlling physical properties like critical temperature, resistivity, n conventional superconductors, point defects generated by radiation induced c displacements changes the density of states around Fermi surface, thereby g depression of T_c [3, 4]. In high T_c superconductors also, atomic displacements d by nonionizing energy loss of incident particle control the change of T_c as ction of fluence [5, 6]. For all cuprate superconductors, there is a universal onship between rate of shift of T_c with fluence ϕ, i.e. $dT_c/d\phi$, and nonionizing y loss (NIEL) of the incident particle over a wide range of energies [5–12]. The and hence atomic displacements can be ascertained by Monte Carlo simulation am TRIM (TRansport of Ions in Matter) developed by Biersack *et al* [13]. This am takes into account relative cross-sections for elastic and inelastic processes. n multiatomic system, the total NIEL is given as $S = \Sigma f_i S_i$, where S_i is the NIEL ch atom and f_i its atomic weight fraction given as

$$f_i = x_i A_i / \Sigma x_i A_i,$$

where x_i is the stoichiometric number for the ith element, e.g. 8 for oxygen in $Bi_2Sr_2CaCu_2O_{8+x}$ (Bi-2212) [6]. Hence, it is expected that in Bi-2212, NIEL and hence, displacement of oxygen induced by light charged particle irradiation will be significant.

Oxygen plays a significant role in controlling various physical properties like T_c, resistivity, etc. of high T_c cuprate superconductors (in particular Bi-2212) which are non-stoichiometric with respect to oxygen [14–17]. Bi-2212, based on layered perovskite structure, experiences a tensile stress in Bi–O (bismuth) layer due to small Bi^{3+} ion [17]. This tensile stress is relieved by accommodating extra oxygen in bismuth layer [17–19]. Thus, Bi-2212 is always prone to contain excess oxygen [20, 21]. Oxygen, being an electronegative atom serves as a source of hole to the conducting CuO_2 layer and changes carrier concentration. There is a relation between critical temperature T_c and the excess oxygen content in Bi-2212, which resembles a typical bell-shaped curve [22]. The extra nonstoichiometric oxygen is not strongly bound like other oxygen atoms. Its binding energy is very low and is vulnerable to be knocked out by particle irradiation.

We had earlier observed an increase in T_c by 20 MeV α-irradiation at a dose higher than $1 \times 10^{15}\alpha/cm^2$ on polycrystalline Bi-2212 overdoped with oxygen ($T_c = 65$ K) [23]. We investigated the irradiation at various doses starting from $1 \times 10^{13}\alpha/cm^2$. There was no appreciable increase in T_c up to $1 \times 10^{15}\alpha/cm^2$. The increase after $1 \times 10^{15}\alpha/cm^2$ was monotonic with dose and was presumed to be due to knock-out of oxygen. Annealing of the irradiated sample in oxygen reverted back to original T_c. Irradiation was carried on one surface of the sample. The range of 20 MeV α in Bi-2212 is $\sim 100\,\mu$m. So, in the sample of around 1 mm thickness (as used in earlier irradiation experiments), the damage did not propagate to much depth. Hence, bulk damage and change in oxygen content could not be ascertained by iodometry as the radiation induced oxygen knock-out could not occur in the bulk. To investigate the bulk damage, we adopted the following modifications: (i) Thickness of the sample was reduced from 1 mm to 0·5 mm. (ii) Energy of α was increased from 20 MeV to 40 MeV to have longer range and hence large depth of damage. (iii) Irradiation was carried out on both surfaces of the sample to obtain a fairly uniform bulk damage.

In this paper, we have analyzed oxygen knock-out from the polycrystalline Bi-2212 pellet caused by light charged particle irradiations, where interaction with oxygen is significant. In case of heavy ions, cross-section of interaction with other atoms and their NIEL will be significant. We have considered cases of 20 and 40 MeV α and also 15 MeV proton, which penetrates the sample of 0·5 mm (range of 15 MeV protons in Bi-2212 is $\sim 0{\cdot}8$ mm) and hence causes bulk damage. We have calculated oxygen vacancies generated by particle induced displacements with the help of the program TRIM-95 and the pressure developed due to the displaced oxygen. We have considered the displacement of loosely bound oxygen as these are vulnerable to be displaced more easily. We have then calculated the diffusion of the displaced oxygen through pores or, intergranular region thereby estimating the oxygen content for these particles at various doses. We have verified the results with oxygen content measured iodometrically for Bi-2212 pellets irradiated with 40 MeV α at various doses.

xperimental

rcrystalline samples of Bi-2212 were prepared from nitrates of the respective ents (in nominal composition) by usual solid state reaction [24]. Excess oxygen ent was assayed iodometrically by the method of Appleman *et al* [25]. Often, aerial ation of iodide in strong acid solution catalyzed by Cu(II) gives rise to erroneous lts. We have eliminated it by holding Cu(II) as citrate. Acidity was adjusted to ent aerial oxidation. Excess oxygen content of the sample was 0·204, i.e. it was in verdoped region with respect to oxygen [22].

mples were prepared in the form of pellets of 0·5 mm thickness. Critical tempera- was measured resistively by usual 4-probe method using Lake Shore 120 constant ent source and Keithley 181 digital nanovoltmeter. The current was typically 1 mA. $= 0$) was around 73 K.

few pellets were chosen for irradiation with 40 MeV α from variable energy otron (VEC). They were irradiated from both sides. Defocussed beam was taken to antee uniformity of dose over the sample. Beam current was typically around nA, i.e. $\sim 3 \times 10^{11}$ particles/sec. The area over which the beam was falling was cm^2. Hence, the rate of the incoming particles was $\sim 6 \times 10^{10}/cm^2/sec$. The target mbly was cooled with flowing water at the back of the flange to minimize the ing effect due to particle irradiation. The temperature of the sample was monitored thermocouple and it was around 50°C ($\pm$ 1°C). The whole assembly of the target he flange was in vacuum in the order of $\sim 10^{-6}$ torr. The total doses employed on pellets were 2×10^{15}, 4×10^{15}, 6×10^{15}, 8×10^{15} and $1 \times 10^{16}\alpha/cm^2$. The irra- ed samples were characterized by XRD like the unirradiated one. Their T_c's were sured like the unirradiated sample.

esults and discussion

nd oxygen contents of the irradiated and unirradiated samples are given in table 1. amount of error in iodometric estimation of oxygen contents is indicated in kets. It is seen that T_c increases up to a certain dose. There is a correlation of $= 0$) with excess oxygen content. From table 1, we observe that, oxygen content of rradiated sample decreases with dose. There is a sharp drop in T_c for the dose of $0^{15}\alpha/cm^2$ from that of $6 \times 10^{15}\alpha/cm^2$. This may be due to a large drop in excess en content (0·06) in the dose of $8 \times 10^{15}\alpha/cm^2$. Excess oxygen content 0·06 esponds to a much underdoped region and hence its T_c is much less compared to

Table 1. T_c and excess oxygen as a function of dose.

Dose (α/cm^2)	$T_c(R = 0)$ (K)	Excess oxygen by iodometry
0	73·1	0·204($\pm$0·003)
2×10^{15}	74·3	0·191($\pm$0·002)
4×10^{15}	75·8	0·150($\pm$0·002)
6×10^{15}	76·3	0·102($\pm$0·002)
8×10^{15}	66·46	0·060($\pm$0·002)

the samples of other doses [22]. The behaviour of T_c with change in oxygen content is nearly consistent with the picture of Allgeier and Schilling [22]. The absence of one-to-one correspondence with Allgeier–Schilling picture may be due to some additional factors brought by radiation induced disorder. Displacements of other cations like Cu, Bi, etc. may also play a role. But obviously, oxygen knock-out with irradiation plays a major role.

4. Mechanism of oxygen knock-out

The decrease in oxygen content caused by knock-out of oxygen from the sample can be understood to occur through the following steps: (i) Appreciable oxygen vacancies are created by charged particle irradiation induced displacement of loosely bound oxygen of Bi-2212 at a dose higher than 1×10^{15} particles/cm^2. (ii) The displaced oxygen occupies pores and/or the intergranular region, which are energetically favourable to them and in this process generates pressure. (iii) These 'free' or labile oxygen molecules diffuse from pores to outside (of the sample) which is in vacuum. More porous the sample, more is the absorption or desorption of oxygen. We had earlier seen in the case of textured samples that with decrease of porosity, oxygen absorption decreases during annealing which causes a lower value of excess oxygen content [26]. In the synthesis of Bi-2212 through carbonate and nitrate routes, we observed that the carbonate route gave rise to porous sample and oxygen content was much higher which must have come by absorption of the same through pores during annealing stage. Also, excess oxygen in these porous samples is desorbed after heating to 800–850°C as seen by thermogravimetric analysis [27].

During estimation by iodometry, all the excess oxygen (i.e. those in the pores, intergranular region as well as those in Bi–O layer) are estimated. The net decrease of oxygen content will be the oxygen diffusing out of the pores and/or integranular region. Thus, one can get the net excess oxygen content of the irradiated samples by subtracting the oxygen diffused from excess oxygen content of the unirradiated sample.

We have calculated with the help of the simulation program TRIM (TRIM-95) the number of vacancies created by displacement of loosely bound oxygen due to charged particle irradiation. We have taken binding energy of this loosely bound oxygen as 0·073 eV, supported by experimentally observed ΔH value for the liberation of loosely bound oxygen from the compound as obtained from thermogravimetric analysis (TGA) and differential thermal analysis (DTA) [28]. The numbers for loosely bound oxygen atoms displaced per projectile ion for various doses are given in table 2. The displaced oxygen atoms with enough kinetic energy migrate to pores, interstitials, etc.

Table 2. Number of oxygen vacancies/ion and the partial pressure for various projectiles.

Particle	Loose O-vacancies/ion	Partial pressure (for dose 1×10^{15}/cm^2)	ΔG (kcal)
40 MeV α	110·19	0·6464 atm.	12·12
20 MeV α	77·18	0·4528 atm.	11·95
15 MeV proton	35·26	0·2068 atm.	11·47

We have estimated the partial pressure developed due to oxygen vacancies at a dose of 1×10^{15} particle/cm^2 for a typical sample of mass around 100 mg (total oxygen vacancies being obtained by multiplying the number of vacancies/ion by the dose).

It is seen from table 2 that the partial pressure generated by knocked out loose oxygen atoms is quite high. The free energy change associated with migration of oxygen from inside the sample to outside (or, the free energy difference between inside and outside the sample) is given as

$$\Delta G = RT \ln[\{(P_{O_2})\text{inside sample}\}/\{(P_{O_2})\text{outside sample}\}].$$

(P_{O_2}) outside sample is $\sim 10^{-6}$ torr as the target flange containing the sample during irradiation is under vacuum (of the order 10^{-6} torr). As see from table 2, the free energy change for 100 mg of the sample is $\sim$ 12·12 kcal in case of 40 MeV α-irradiation, which is quite enormous. This is the driving force for migration which is controlled by diffusion. The process of diffusion is controlled by porosity of the sample. The more porous a sample, the higher will be the rate of diffusion. The rate of oxygen atoms/ molecules diffusing out is proportional to the atoms/molecules of oxygen present in the pores.

The rate of net oxygen molecules accumulating at the pores as a result of diffusion is the rate of formation of oxygen through knock-out by charged particles minus the rate of diffusion of oxygen out of pores, which can be given by the following equation

$$d[N_0]/dt = I - D[N_0], \tag{1}$$

where N_0 is the number of oxygen molecules remaining in the pores, I is the rate of oxygen atoms formed per second. D is the diffusion coefficient depending on porosity of the sample. At the beam current of 100 nA of 40 MeV α, $I = 1{\cdot}205 \times 10^{14}$/sec for 0·35 cm^2.

Solution of this first order differential equation (1) yields, for any time t,

$$[N_0 e^{Dt}] = (I/D)(e^{Dt} - 1)$$

or

$$N_0 = (I/D)(1 - e^{-Dt}). \tag{2}$$

Diffusion coefficient of oxygen in this system D is given by following equation [29]

$$D(/\text{sec}) = 2{\cdot}618 \times 10^{-4} \exp[-(1{\cdot}3\ \text{kcal/mole})/RT].$$

The activation energy for diffusion of oxygen from pores is 1·3 kcal/mole as confirmed by thermogravimetric analysis of Bi-2212 [27]. The value of D at the temperature of the sample (around room temperature) $= 3 \times 10^{-5}$/sec.

From the solution of the diffusion equation (2), we can estimate the oxygen remaining in the pores. The total oxygen vacancies can be obtained from the dose. The difference between these two gives the amount diffused out or the net knocked out or, lost oxygen. Subtracting this from the excess oxygen content of the unirradiated sample will give the excess oxygen content for the irradiated sample. The values of excess oxygen thus obtained for 40 MeV, 20 MeV α and 15 MeV protons at various doses are given in table 3. The data for 40 MeV α can be compared with the experimental value obtained by iodometry given in table 1. Figure 1 shows the plots of oxygen contents (theoretically calculated from TRIM and experimentally verified by iodometry) as function of doses for 40 MeV α. It is seen that the two are in close agreement. Thus, it

Table 3. Excess oxygen values calculated from TRIM and diffusion for various particles.

Dose (per cm^2)	40 MeV α	20 MeV α	15 MeV proton
2×10^{15}	0·1854	0·1914	0·1982
4×10^{15}	0·1480	0·1648	0·1861
6×10^{15}	0·1034	0·1335	0·1718
8×10^{15}	0·0553	0·0990	0·1564

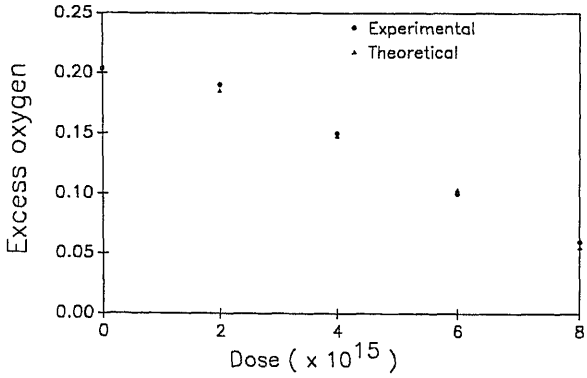

Figure 1. Oxygen contents (experimental and calculated from TRIM) as function of dose.

establishes the mechanism of knock-out of oxygen by charged particle irradiation followed by diffusion from pores. We are now carrying out experiments with 15 MeV proton and 20 MeV α for checking the knock-out of oxygen from bulk polycrystalline Bi-2212 and agreement with the results calculated from TRIM.

For other atoms, displacement energy is ~ 20 eV. TRIM calculation shows number of vacancies to be very less compared to that for loosely bound oxygen (of the order 5/ion). So, the damage due to displacements for other atoms is effective at a dose higher than 1×10^{16} particles/cm^2.

The vacancies of loose oxygen are created mostly in the bulk as little energy is lost at the surface due to ionization. As the projectile particle loses energy with depth, the nonionizing energy loss dominates causing displacement and the knock-out of oxygen. Hence, the knock-out of oxygen is a bulk rather than surface process.

5. Conclusion

We have calculated the knock-out of oxygen by 40 MeV α-irradiation from both sides on polycrystalline Bi-2212 overdoped with oxygen. This was measured experimentally by the difference in oxygen contents of irradiated and unirradiated samples estimated by iodometry. The calculations were done using the code TRIM which showed a large number of vacancies of loose excess oxygen created by α-irradiation. The loose oxygen

ents for irradiated samples for different cases – 15 MeV protons, 20 and 40 MeV various doses. There is fairly good agreement of the calculated results with the en content measured iodometrically in the case of 40 MeV α. We are also carrying tudies with proton to see the knock-out of oxygen and validity of the above ioned mechanism. The knock-out of oxygen is a bulk process.

rences

F Seitz and J S Kohler, *Solid State Physics* edited by F Seitz and D Turnbull (Academic Press, New York, 1956) vol. 2, p. 305
J Lindhard, *Mat.-Fys. Medd. K. Dan. Vidensk. Selsk.* **33**, 1 (1963)
R Viswanathan and R Certon, *Phys. Rev.* **B18**, 15 (1978)
L R Testardi and L F Matthews, *Phys. Rev. Lett.* **41**, 1612 (1978)
B D Weaver, E M Jackson, G P Summers and E A Burke, *Phys. Rev.* **B46**, 1134 (1992); and references therein
G P Summers, D B Chrisley, W G Maisch, G H Strauss, E A Burke, M Nastasi and J R Tesmer, *IEEE Trans. Nucl. Sci.* **36**, 1840 (1989); and references therein
G P Summers, E A Burke, D B Chrisley, M Nastasi and J R Tesmer, *Appl. Phys. Lett.* **55**, 1469 (1989)
B D Weaver, E M Jackson, G P Summers, D B Chrisey, S Horwitz, J M Pond, H S Newman and E A Burke, *IEEE Trans. Nucl. Sci.* **NS-38**, 1284 (1991)
B D Weaver, M E Reeves, D B Chrisey, G P Summers, W L Olson, M M Eddy, T W James and E J Smith, *J. Appl. Phys.* **69**, 1119 (1991)
S Matsui, H Matsutera, T Yoshitake and T Satoh, *Appl. Phys. Lett.* **5**, 2096 (1988)
A Iwase, M Watanabe, T Iwata and T Nihira, *Jpn. J. Apl. Phys.* **28**, 1939 (1989)
J C Barbour, J F Kwak, D S Ginley and P S Peercy, *Appl. Phys. Lett.* **55**, 507 (1989)
J P Biersack and L G Haggmark, *Nucl. Instrum. Methods* **174**, 257 (1980)
J D Jorgensen, *Phys. Today* **44**, 34 (1991)
R J Cava, A W Hewat, B Batlogg, M Marzerio, K M Rabe, J J Krajewski, W F Peck Jr and L W Rupp Jr, *Physica* **C165**, 419 (1990)
J B Goodenough and A Manthiram, *J. Solid State Chem.* **88**, 115 (1990)
H Zhang and H Sato, *Physica* **C214**, 265 (1993)
S B Samanta, P K Dutta, V P S Awana, E Gmelin and A V Narlikar, *Physica* **C178**, 171 (1991)
J B Goodenough and A Manthiram, *Physica* **C178**, 439 (1989)
A K Sarkar and I Maartense, *Physica* **C168**, 591 (1990)
A K Sarkar, B Kumar, I Maartense and T L Peterson, *J. Appl. Phys.* **65**, 2392 (1989)
C Allgeier and J Schilling, *Physica* **C168**, 499 (1990)
S K Bandyopadhyay, P Barat, S K Kar, U Dey, A Poddar, P Mondal and B Ghosh, *J. Solid State Comm.* **82**, 397 (1992)
N Knauf, J Harnischmaker, R Muller, R Borowski, B Roden and D Wohlleben, *Physica* C**173**, 414 (1991)
E H Appleman, L R Morss, A M Kini, U Geiser, A Umezawa, G W Crabtree and K D Carlson, *Inorg. Chem.* **26**, 3239 (1987)
Pintu Sen, S K Bandyopadhyay, P Barat, P Mukherjee, P K Mukhopadhyay and A De, *Physica* **C255**, 306 (1995)
J T S Irvine and C Namgung, *J. Solid State Chem.* **87**, 29 (1990)
J F Marucco and C Gladel, *Physica* **C160**, 73 (1989)
Y Idemoto, K Fueki and H Sugiyama, *J. Solid State Chem.* **92**, 489 (1991)

PRAMANA
— journal of
physics

© Printed in India

Vol. 47, No. 4,
October 1996
pp. 317–324

Enhanced third harmonic generation in periodic structures

V MAHALAKSHMI, JOLLY JOSE and S DUTTA GUPTA*
School of Physics, University of Hyderabad, Hyderabad 500 046, India
*Author for correspondence

MS received 27 May 1996; revised 7 October 1996

Abstract. We consider third harmonic generation in a periodic layered medium with alternate nonlinear media. We show enhanced third harmonic generation when the fundamental frequency matches one of the mode frequencies of the distributed feedback structure. The observed feature is explained in terms of large local field enhancement for the fundamental wave.

Keywords. Third harmonic; periodic structure.

PACS No. 42·65

1. Introduction

In recent years there has been a lot of interest in harmonic generation in nonlinear periodic structures [1–4]. The theory of harmonic generation in periodic structures with undepleted pump approximation is now well understood. In the context of second harmonic generation, periodic structures have been used to achieve phase matching and quasi-phase matching [4]. There is another interesting aspect of periodic structures which can be exploited to enhance the generated harmonics. It is well-known that the linear transmission characteristics of periodic structures have the so called Bragg reflection bands [5–8]. For finite structures there are sharp resonances at the edge of the Bragg bands. The origin of these resonances are due to the excitation of modes of the periodic structure [8]. Such modes possess high quality factors and their excitation corresponds to large local field enhancements. Resonances and associated local field enhancements [9] have been utilized to lower the threshold for nonlinear processes and increase their efficiency [10]. Surface and guided mode resonances and resonances of Fabry–Perot cavities have been used for nonlinear effects like optical bistability [11–14]. The sharper the resonance, the larger is the local field enhancement and hence the nonlinear effect is higher [12]. Keeping in mind the aforesaid we study third harmonic generation in a periodic structure with alternate cubic nonlinear layers. We apply the method developed by Bethune [1] to calculate the generated third harmonic in the forward and backward directions. We show that when the fundamental wavelength is resonant with any of the modes of the periodic structure there is considerable enhancement in the generated third harmonic intensity. This is again because of the large local field enhancement in the fundamental intensity which acts as a source for the third harmonic.

The organization of the paper is as follows: In § 2, we briefly recall the method of Bethune [1] for the calculation of third harmonic intensity. In § 3, we present the results of our numerical investigation and finally in § 4, we conclude the paper.

2. Theory

We follow the analysis of Bethune [1] for evaluating the third harmonic intensity from the layered media. The technique is based on modification of the well-known optical transfer matrix method for layered media to include the nonlinear polarization. This formulation has the advantage that the total third harmonic output field is expressed as the sum of contributions from individual layers and thus the effect of any single layer can be studied separately.

Figure 1 shows the geometry of the layered structure with N periods. Each period consists of two layers A (linear) and B (nonlinear), with refractive indices n_A and n_B and thickness d_A and d_B respectively. The z-axis is normal to the layers and x–z is the plane of incidence. First the electric field at the fundamental frequency in each layer is determined. This is required for the third harmonic calculations. The analysis is presented for the s-polarization. The electric field (at ω) in any ith layer is the plane wave solution of the wave equation and can be written as

$$E_i^{\pm}(r,t) = E_i^{\pm}(r)\exp[(\pm iN_i k_0 z) + i(\kappa x - \omega t)], \tag{1}$$

where $k_0 (= \omega/c)$ is the vacuum wave vector, $N_i (= k_{iz}/k_0)$ is the propagation constant and $\kappa (= k_x)$ is the x-component of the wave vector.

The forward and backward propagating amplitudes at the left and right side of the layer are related through a 2×2 matrix. This matrix is the product of interface and propagation matrices which are given as

$$G_{ij} = \frac{1}{t_{ij}} \begin{pmatrix} 1 & r_{ij} \\ r_{ij} & 1 \end{pmatrix} \tag{2}$$

and

$$\Psi_i = \begin{pmatrix} \psi_i & 0 \\ 0 & \bar{\psi}_i \end{pmatrix}, \tag{3}$$

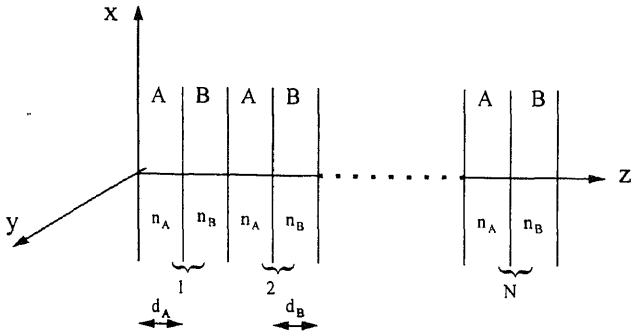

Figure 1. Schematic view of the layered structure.

where r_{ij} and t_{ij} are the reflection and transmission amplitudes for wave incident at $i-$ interface and $\psi_i \exp(iN_i k_0 d_i)$, $\bar{\psi}_i = \exp(-iN_i k_0 d_i)$. Thus, the electric fields at any laye can be related to those at another layer by successive product of the transfer an propagation matrices. In terms of the interface and propagation matrices of all layers the total transfer matrix at the fundamental frequency is given as

$$T = G_{f(f-1)} \Psi_{(f-1)} G_{(f-1)(f-2)} \cdots G_{21} \tag{4}$$

and the overall reflection amplitude $r = -T(2,1)/T(2,2)$. We can now write the electri field amplitudes at the left end of each layer as

$$E_i = G_{i(i-1)} \Psi_{(i-1)} G_{(i-1)(i-2)} \cdots G_{21} \begin{pmatrix} 1 \\ r \end{pmatrix}, \tag{5}$$

where

$$E_i = \begin{pmatrix} E_{i+} \\ E_{i-} \end{pmatrix}. \tag{5a}$$

Knowing the pump field in each layer, we can now calculate the nonlinear polarizatio and the corresponding electric field amplitudes at 3ω. Since we are neglecting the pump depletion, the nonlinear polarization in different layers act as independent sources an the generated third harmonic field will be the sum of contributions from all th nonlinear layers. Let layer j be optically nonlinear. As the pump field is s-polarized, th nonlinear polarization generated and the corresponding third harmonic field will als be s-polarized. Under the pump depletion approximation, the third order nonlinea polarization is written as

$$P_j^{\mathrm{NL}}(3\omega) = \chi^{(3)} [E_j^+(\omega) \exp(iN_j k_0 z) + E_j^-(\omega) \exp(-iN_j k_0 z)]^3, \tag{6}$$

where $\chi^{(3)}$ is the third order susceptibility. The expansion of the RHS of eq. (6) leads t terms with exponential factors like $\exp(\pm iN_j k_0 z)$ and $\exp(\pm 3iN_j k_0 z)$ contributing t the third harmonic. The corresponding effective source dielectric constants can b defined as

$$\varepsilon_s^{(1)} = \left[\left(\frac{N_j}{3} \right)^2 + \kappa^2 \right] \quad \text{and} \quad \varepsilon_s^{(3)} = (N_j^2 + \kappa^2) = \varepsilon_j(3\omega). \tag{7}$$

The total electric field (at 3ω) will be the sum of free waves (solution of homogeneou part of third harmonic wave equation) and bound waves (solution of inhomogeneou wave equation)

$$E_{sj}(3\omega) = E_j^+(3\omega) \exp(3iN_{bj} k_0 z) + E_j^-(3\omega) \exp(-3iN_{bj} k_0 z) + \frac{4\pi}{\varepsilon_s - \varepsilon_j(3\omega)} P_j^{\mathrm{NL}}, \tag{8}$$

where $N_{bj} = N_j(3\omega)$, E^+ and E^- are the forward and backward propagating ampli tudes at 3ω. In every nonlinear layer there will be contribution from each of the sourc dielectric constants $\varepsilon_s^{(1)}$ and $\varepsilon_s^{(3)}$ to the third harmonic electric field.

The continuity of the total (bound plus free) tangential 3ω electric and magneti

$$E_i = M_{ij}E_j + M_{is}E_s, \tag{9}$$

$$M_{kj}\Phi_j E_j + M_{ks}\Phi_s E_s = E_k, \tag{10}$$

where E_j is given by (5a) with amplitudes at 3ω, M and Φ are the interface and propagation matrices at 3ω. Using (9) and (10) we can define source vector for the jth layer as

$$S_j \equiv (\Phi_j M_{js}\Phi_s - M_{js})E_s. \tag{11}$$

In the s-subscripted matrices appropriate ε_s must be used. Now we can write the final reflected and transmitted 3ω field amplitudes $E_1^-(j)$ and $E_f^+(j)$ from the jth layer as

$$\begin{bmatrix} E_f^+(j) \\ E_1^-(j) \end{bmatrix} = \frac{1}{\tilde{T}(1,1)} \begin{pmatrix} 1 & 0 \\ \tilde{T}(2,1) & -\tilde{T}(1,1) \end{pmatrix} S'_j, \tag{12}$$

where $\tilde{T} = L_{j1}^{-1}R_{jf}$ is the total right to left transfer matrix at 3ω, $S'_j = L_{j1}^{-1}S_j$, $R_{jf} = \Phi_j M_{jk}\cdots\Phi_{(f-1)}M_{(f-1)f}$, $L_{j1}^{-1} = \Phi_1 M_{12}\cdots\bar{\Phi}_{(j-1)}M_{(j-1)j}$ and $\bar{\Phi} = \Phi^{-1}$. The total output fields can be obtained by adding the contributions from all values of $|k_{sz}|$ from all the layers.

3. Numerical results and discussion

In this section we present the results of numerical investigation for a periodic medium with alternate nonlinear layers. Silica glass was chosen as the linear medium whereas, we chose CS_2 (with $\chi^{(3)} \approx 6{\cdot}8 \times 10^{-13}$ esu) with linear refractive index $n_B = 1{\cdot}59$ as the nonlinear material. We incorporated dispersion of glass in our calculation. The dispersion data was taken from Palik [15] and they were fitted to yield

$$n_A(\lambda) = 1{\cdot}4507 - 0{\cdot}0032667\lambda^2 + \frac{0{\cdot}002998}{(\lambda^2 - 0{\cdot}0099)}. \tag{13}$$

The rms error in fitting was of the order of 10^{-11}. Due to lack of dispersion data on CS_2 we were forced to assume it to be dispersionless. However, with available data dispersion in CS_2 can trivially be incorporated. In all our calculations we used the same width of the linear layers, namely, $d_A = 0{\cdot}8$ μm. We assume the pump laser to be Nd–YAG operating at the wavelength 1·064 μm. For all our calculations we have taken a periodic system with $N = 100$ periods. It is well known that by varying the structural parameters (in our case d_B since we already fixed d_A) it is possible to make the fundamental wavelength to coincide with the center of the Bragg reflection band or lie at the edge of the Bragg band. For a finite periodic structure the edge of the Bragg band contains sharp resonances characterized by high quality factors [8]. It is well understood that such resonances are associated with large local field enhancements which is instrumental in generating large nonlinear effects. Such sharp resonances in the context of surface/guided modes were exploited to lower the threshold for various nonlinear effects [10–14]. We thus change d_B to make the pump wavelength coincide with one of these sharp resonances at the edge of the Bragg band. For example, for $d_B = 0{\cdot}944$ μm,

$\lambda = 1{\cdot}064\,\mu m$ lies at the center of the rejection band, while for $d_B = 0{\cdot}937\,\mu m$ the fundamental wavelength is resonant with one of the high-Q modes of the periodic structure. We also look at the case when the fundamental wavelength is away from the Bragg bands, say, midway between two Bragg bands. In what follows we present the results for these three cases.

The results for $d_B = 0{\cdot}944\,\mu m$ (pump wavelength $1{\cdot}064\,\mu m$ coincides with the center of the rejection band) are shown in figure 2. In figure 2a we have plotted fundamental transmission coefficient T as a function of the wavelength λ. We have shown the exponential decay of fundamental intensity inside the layers at $\lambda = 1{\cdot}064$ in figure 2b. This is obvious since transmission at $\lambda = 1{\cdot}064\,\mu m$ is minimal (see figure 2a). Since fundamental field distribution (which is almost null over most of the structure) acts as the source for the third harmonic, one expects very little generated third harmonic in this case. This is shown in figure 2c where we have plotted third harmonic intensity generated in the forward and backward directions $T(3\omega)$ (solid curve) and $R(3\omega)$ (dotted curve) as functions of λ. We have multiplied the intensities by the nonlinear susceptibility $\chi^{(3)}$ in order to make $T(3\omega)$ and $R(3\omega)$ dimensionless.

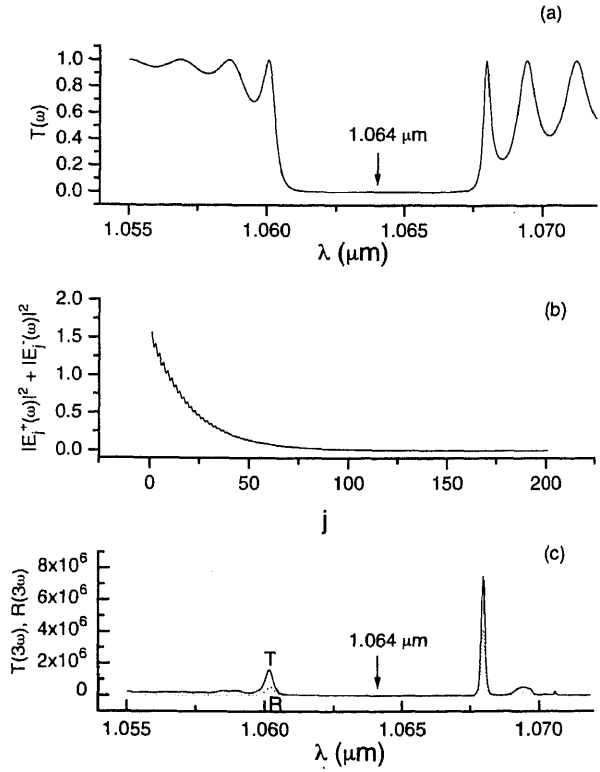

Figure 2. (**a**) Transmission coefficient $T(\omega)$ as a function of λ with $d_A = 0{\cdot}8\,\mu m$, $d_B = 0{\cdot}944\,\mu m$, $n_A = 1{\cdot}59$, n_B is calculated using eq. (13) given in the text, $n_i = n_f = 1{\cdot}0$. (**b**) Plot of fundamental intensity (in arbitrary units) inside the layers at pump wavelength $\lambda = 1{\cdot}064\,\mu m$. (**c**) Third harmonic intensity in the forward (solid) and backward (dotted curve) directions as a function of λ.

The situation is different when d_B is changed to $d_B = 0{\cdot}937\,\mu m$ so as to make the pump wavelength coincide with one of the mode frequencies of the periodic structure. The results for fundamental transmission coefficient as a function of λ for $d_B = 0{\cdot}937\,\mu m$ is shown in figure 3a. Different resonances corresponding to the different modes of the structure are labeled by ± 1, ± 2, etc. The $\pm 1 (\pm 2)$ resonances correspond to single (double) hump field distributions in the layered medium (see figure 3b). Also note that the $+1$ resonance corresponds to the largest enhancements in the local field. Thus if the fundamental wavelength is made to coincide with the $+1$ mode frequency (which is the case for $d_B = 0{\cdot}937\,\mu m$) one expects a large enhancement in the generated third harmonic. This is shown in figure 3c. It is also clear from figure 3c that the generated third harmonic decreases from $+1$ to -1 and from $+2$ to -2 mode resonances. This is explained in terms of the field distributions in figure 3b where the local field enhancement is maximum for the $+1$ mode and minimum for the -2 mode. It is thus clear that by making the fundamental laser resonant with the high quality factor modes of the periodic structure it is possible to enhance the generated third harmonic.

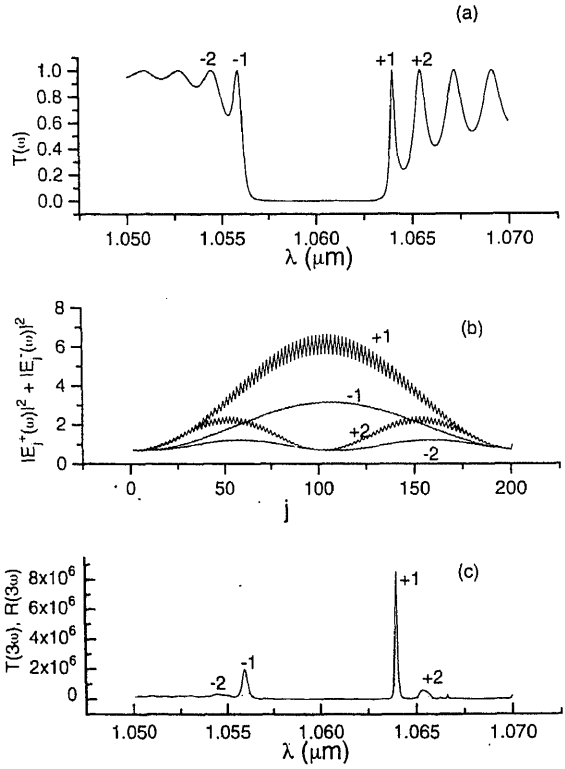

Figure 3. (**a**) Transmission coefficient $T(\omega)$ as a function of λ with $d_B = 0{\cdot}937\,\mu m$, other parameters are same as in figure 2. (**b**) Fundamental intensity (in arbitrary units) distribution when its wavelength coincides with different mode resonances. Different curves are labeled by the mode numbers ± 1 and ± 2. For example curve labeled by $+1$ is for $\lambda = 1{\cdot}064\,\mu m$. (**c**) Third harmonic generated in the forward (solid) and backward (dotted curve) directions as a function of λ.

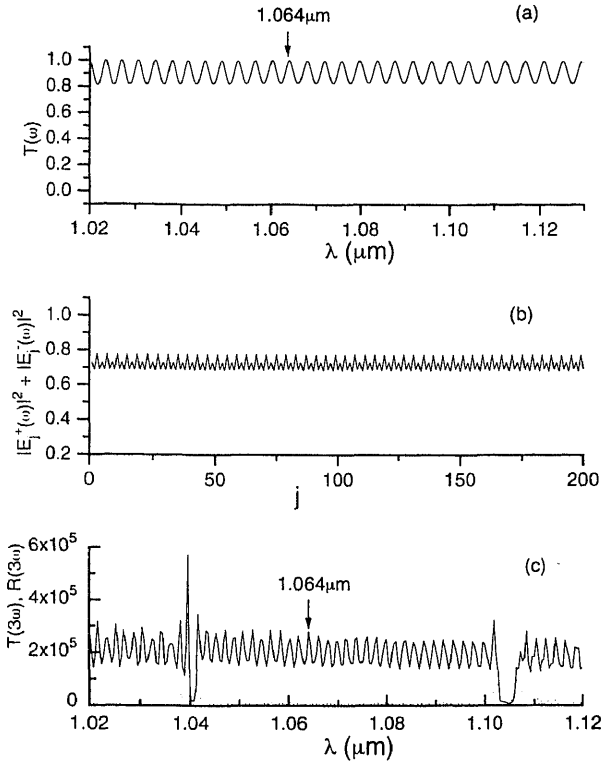

Figure 4. (**a**) Variation of transmission coefficient $T(\omega)$ with λ for $d_B = 1{\cdot}11$ μm, $n_A = 1{\cdot}59$, other parameters are the same as in figure 2. (**b**) Plot of fundamental intensity (in arbitrary units) inside the layers at pump wavelength $\lambda = 1{\cdot}064$ μm. (**c**) Plot of third harmonic intensity in the forward (solid) and backward (dotted curve) directions as a function of λ.

In order to complete the above discussion, we present the results for $d_B = 1{\cdot}11$ μm, when the pump laser wavelength 1·064 μm is midway between two Bragg reflection bands. The results for $T(\omega)$ and the field distribution are shown in figures 4a and 4b respectively. It is clear from figure 4b that the distribution lacks any local enhancements and hence the generated third harmonic (figure 4c) is lower, by an order of magnitude, than the one with enhancement (compare with figure 3c). The gaps close to 1·04 μm and 1·10 μm, which are due to the transmission characteristics of the distributed feedback structures at the third harmonic frequency.

4. Conclusion

In conclusion we studied a periodic layered medium with alternate cubic nonlinear layers for third harmonic generation. Thus one can have enhanced third harmonic generation from the layered medium if the fundamental frequency coincides with one of the mode frequencies of the periodic structure. The high yield of the third harmonic is

explained in terms of the local field enhancements associated with the excitation of the modes at the fundamental frequency.

Acknowledgement

One of the authors (SDG) would like to thank the Department of Science and Technology, Government of India, for supporting this work.

References

[1] Bethune, *J. Opt. Soc. Am.* **B6**, 910 (1989)
[2] Bethune, *J. Opt. Soc. Am.* **B8**, 367 (1990)
[3] N Hashizume, M Ohashi, T Kondo and R Ito, *J. Opt. Soc. Am.* **B12**, 1894 (1995)
[4] G I Stegeman and C T Seaton, *J. Appl. Phys.* **58**, R57 (1985)
[5] P Yeh, *Optical waves in layered media* (New York, Wiley, 1988) pp. 118
[6] A Yariv and P Yeh, *Optical waves in crystals* (New York, Wiley, 1984) pp. 155
[7] P Yeh, *J. Opt. Soc. Am.* **69**, 742 (1979)
[8] S Dutta Gupta and G S Agarwal, *Opt. Commun.* **103**, 122 (1993)
[9] D Sarid, *Phys. Rev. Lett.* **47**, 1927 (1981)
[10] See, for example, S Sarid, R T Deck, A E Crag, R K Hickernell, R S Jameson and J J Fasano, *Appl. Opt.* **21**, 3993 (1982)
G S Agarwal, *Phys. Rev.* **B31**, 3534 (1985)
[11] G S Agarwal and S Dutta Gupta, *Phys. Rev.* **B34**, 5239 (1986)
[12] S Dutta Gupta and G S Agarwal, *J. Opt. Soc. Am.* **B4**, 691 (1987)
[13] M B Pande and S Dutta Gupta, *Opt. Lett.* **15**, 944 (1990)
[14] S Dutta Gupta, *J. Opt. Soc. Am.* **B10**, 1927 (1989)
[15] E D Palik, *Handbook of optical constants of solids* (Academic Press, New York, 1985) pp. 749

Radiation stabilization of U^{5+} in CaO matrix and its thermal stability: Electron paramagnetic resonance and thermally stimulated luminescence studies

V NATARAJAN, T K SESHAGIRI and M D SASTRY
Radiochemistry Division, Bhabha Atomic Research Centre, Trombay, Bombay 400 085, India

MS received 24 May 1996; revised 6 September 1996

Abstract. Electron paramagnetic resonance (EPR) evidence is presented for the radiation stabilization of pentavalent uranium in CaO matrix. From the theoretical predictions of g value for U^{5+} in axial symmetries, it was concluded that U^{5+} at Ca^{2+} site is associated with a second neighbour charge compensating Ca^{2+} vacancy. EPR measurements also revealed the presence of Mn^{2+}, Mn^{4+} and Cu^{2+} impurities in the samples. The thermal stability of U^{5+} was investigated using EPR and thermally stimulated luminescence (TSL) techniques. The TSL and EPR studies on gamma irradiated uranium doped calcium oxide samples had shown that the intense glow peak at 540 K is associated with the reduction in the intensity of EPR signal of U^{5+} ion around this temperature. This peak is associated with the process $U^{5+} + \text{hole} \rightarrow U^{6+*} \rightarrow U^{6+} + h\nu$. The activation energy for this process was determined to be 1·4 eV.

Keywords. Electron paramagnetic resonance; thermally stimulated luminescence.

PACS Nos 33·30; 76·30; 78·60

1. Introduction

Among the different oxidation states of uranium, U^{5+} with $5f^1$ electronic configuration is a very attractive ion for magnetic investigations. Because it is a single electron system, there is no electron–electron repulsion among the $5f$ electrons enabling the description of the energy levels and wave functions with greater certainty. Recently Miyake [1] has reviewed the magnetochemistry of U^{5+} complexes and compounds. U^{5+} was also reported to be stabilized at Nb sites in $LiNbO_3$ [2]. An important aspect of U^{5+} in octahedral symmetry is its relatively long spin-lattice relaxation time when the site symmetry is perfectly octahedral. Under this symmetry, the lowest crystal field state of U^{5+} is a doublet, Γ_2, which takes the form of Γ_7 under spin-orbit interaction. Miyake [1] had discussed the effect of different extents of axial (C_{4v}) and orthorhombic (C_{2v}) distortions on g value of U^{5+}. In spite of low symmetry perturbations on octahedral crystalline field, the g value was reported to be nearly isotropic for small distortions. The absolute g value for overall octahedral symmetry is expected to be around 1·1 which remains constant up to a distortion (ε) of 800 cm^{-1} (for a fixed value of $\tau = -0{\cdot}2464$) beyond which the g value decreases [3]. The axial distortion (ε) and orthorhombic component (τ) were described by the Hamiltonian [1]

$$H_{\text{crystal field}} = H_{\text{Oh}} + \varepsilon(O_2^0 + \tau O_2^2),$$

where O_2^0 and O_2^2 are the appropriate operator equivalents [1]. In C_{4v} symmetry, the g value smoothly increases with increase in ε from the octahedral value of 1·1. Therefore $g = 1{\cdot}1$ can be taken as a finger-print for near-perfect octahedral symmetry at the site of U^{5+}.

U^{5+} can be produced by irradiation of U^{6+}/U^{4+} doped crystals. CaO lattice is an ideal one for stabilizing U^{5+} in perfectly octahedral symmetries in view of its NaCl-like structure. However, there can be charge compensating sites which would reduce the site symmetry. Furthermore, as U^{5+} is a radiation induced defect, γ-irradiation of calcium oxide doped with uranium can produce other concomitant defects which would also be paramagnetic. The thermal stability of U^{5+} in turn depends on the thermal stabilities of these defects and also due to any other paramagnetic impurity that may be present in the starting material. These aspects are investigated in the present work using electron paramagnetic resonance and thermally stimulated luminescence. These two techniques are complimentary. Whereas EPR gives information on the static condition of the trapped charges, TSL gives information on the thermally stimulated electron transfer reactions. In this paper, clear evidence is presented for the stabilization of U^{5+} ion with a weak C_{4v} perturbation and the thermally stimulated electron transfer reactions involving U^{5+} are discussed.

2. Experimental

Analar grade $Ca(NO_3)_2$ was dissolved in distilled water and slightly acidified with 2M HNO_3. Using a slight excess of $(NH_4)_2CO_3$, calcium was precipitated as carbonate. In uranium doped samples, uranyl nitrate solution (at 3 different uranium concentrations – 0·1% (A), 0·5% (B) and 1·0% (C) by weight of CaO) was added to calcium nitrate solution followed by precipitation of $CaCO_3$. The precipitate was filtered, dried and thoroughly ground and then heated in sintered alumina crucibles at 1273 K for 24 h. The samples were immediately transferred to a dessiccator containing P_2O_5 to avoid pick up of moisture/CO_2 from air. The x-ray diffraction patterns of the final products agreed well with those reported for CaO in the literature. The TSL studies were conducted on a home built unit [4] in the 300–650 K range. The samples were wrapped in para films during irradiation and prior to TSL recording to avoid moisture pick-up by samples. Spectral studies were conducted using narrow band interference filters. EPR spectra of the samples were recorded at room temperature and at 77 K on a Bruker ESP-300 X-band EPR spectrometer. For EPR studies, about 60 mg of the samples were sealed in quartz tubes immediately after preparation. Temperature dependence of the EPR spectra was studied by annealing the irradiated samples at different temperatures for 2–3 min and recording the EPR spectra at 77 K. A CTI cryogenic closed cycle helium refrigerator was used for studying the EPR spectra of the uranium doped CaO sample in pellet form in the 10–300 K region. A gamma chamber with ^{60}Co source (dose rate 2 kGy/h) was used for irradiation.

Spectroscopic analysis of the samples using an inductively coupled plasma-atomic emission direct reading spectrometer showed the presence of Mn, Cu and Fe at about 10–20 ppm level in all the samples. The uranium content in all the uranium doped

3. Results

3.1 *EPR studies*

On gamma irradiation to a dose of 4 kGy, a new EPR signal at $g = 1{\cdot}236$ was observed at 77 K in all the uranium doped samples (figure 1). This was absent in undoped CaO sample. The temperature dependence of this signal showed that it is observable between 10 K and 95 K and its g value is temperature independent. This is assigned to U^{5+} [6] at near octahedral symmetry in CaO matrix. On annealing the irradiated CaO:U samples at 540 K, drastic reduction in the intensity of this signal was observed.

EPR signals from Mn^{2+} ($g = 2{\cdot}0015$ and $A = 86{\cdot}3$ G), Cu^{2+} ($g = 2{\cdot}222$, $A = 21$ G) and Fe^{3+} ($g = 2{\cdot}005$) were observed in unirradiated samples. These ions were the residual impurities in the CaO matrix. In one of the samples (C) with relatively higher concentration of the dopant (U_3O_8), a weak signal from Mn^{4+} was also observed. (The stabilization of this higher oxidation state of Mn is probably due to the presence of excess oxygen ions.) In view of the possible role of these impurity ions in the TSL processes, their EPR was also followed in γ-irradiated samples. In sample C, strong signals from Mn^{4+} ($g = 1{\cdot}9948$ and $A = 78$ G were observed on irradiation (figure 2). In gamma irradiated CaO sample, no new signal other than from Mn^{2+}, Cu^{2+} and Fe^{3+} was observed. Temperature dependence studies of the EPR spectra of the irradiated samples did not show any significant change in the intensities of Mn^{2+}, Mn^{4+} and Fe^{3+} in the 300–650 K range.

In γ-irradiated CaO:U pellet sample, a signal at $g_\perp = 2{\cdot}065$ was observed up to 55 K. This was attributed to O^- ion on the basis of earlier reports [7, 8].

3.2 *TSL studies*

The TSL glow curves of CaO samples gamma irradiated at room temperature to a dose of 4 kGy showed weak peaks around 403, 443 and 485 K (heating rate = 5 K/s). In

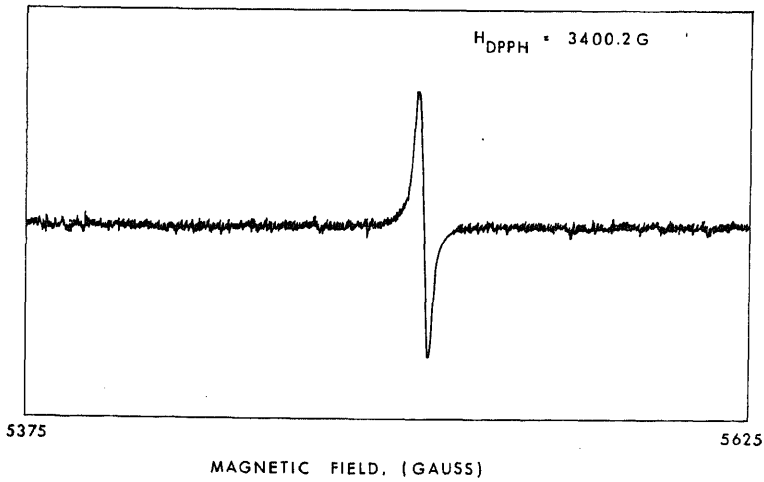

Figure 1. EPR spectra of U^{5+} in gamma irradiated CaO:U sample (dose = 4 kGy) recorded at 77 K.

uranium doped samples, in addition to these peaks, an intense peak around 540 ± 3 K was present. The intensity of this peak was found to be maximum in sample C. Figure 3 shows the TSL glow curves of the different uranium doped CaO samples. Table 1 shows the TSL peaks observed in these samples. The trap parameters for the peaks were evaluated from the different heating rates method [9] and are included in table 1. Thermal bleaching of the lower temperature peaks was done to get the correct T_m for the higher temperature peaks. Spectral studies of the TSL glow peaks at 403, 443 and 485 K showed emission around 600 nm. For the peak at 540 K present in uranium

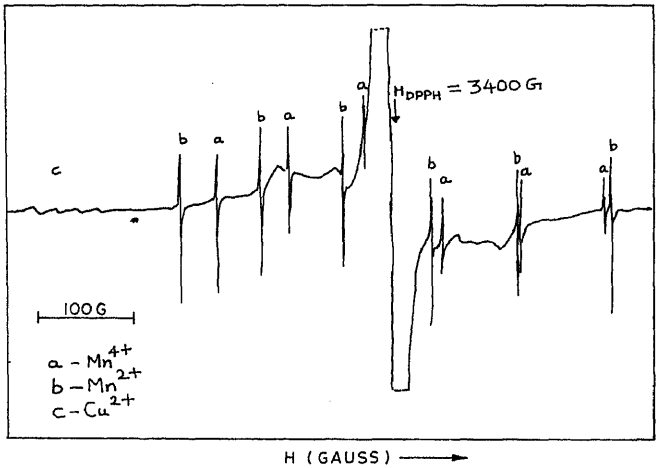

Figure 2. EPR spectrum of CaO:U sample (C) after gamma irradiation to a dose of 4 kGy (recorded at 77 K).

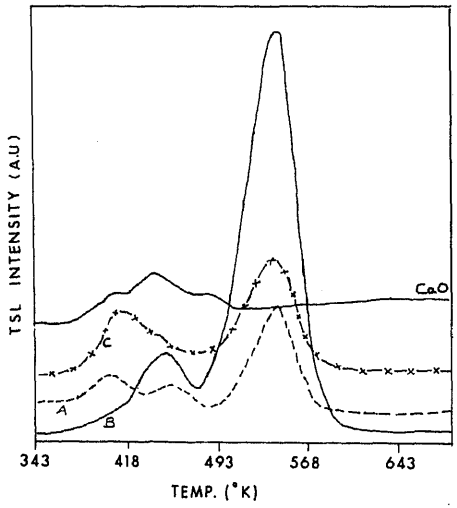

Figure 3. TSL glow curves of gamma irradiated CaO and CaO:U samples.

Table 1. TSL peaks observed in the CaO samples. Peak temperatures are expressed in K (heating rate = 5 K/s^{-1})

	Peak number			
Sample	1	2	3	4
CaO	403	443	485	—
CaO:U-A	403	440	—	538
CaO:U-B	408 (vw)	445 ($E = 0{\cdot}64$ eV, $s = 3{\cdot}7 \times 10^8$)	—	543 ($E = 1{\cdot}4$ eV, $s = 1{\cdot}6 \times 10^{13}$)
CaO:U-C	405 ($E = 0{\cdot}79$ eV, $s = 3 \times 10^{12}$)	438	483 (vw)	538 ($E = 1{\cdot}38$ eV, $s = 2{\cdot}3 \times 10^{12}$)

E = trap depth and s = frequency factor. vw = very weak.
A – 0·1% by weight (20 ppm), B – 0·5% by weight (500 ppm) C – 1·0% (1500 ppm). The % values indicate the amount of uranium added as uranyl nitrate at the precipitation stage whereas figures in the bracket indicate amount of uranium estimated in the final samples.

doped samples, emission around 550, 580 and 598 nm was observed. On the basis of the earlier reports [10, 11], Mn^{2+} was identified as the luminescent centre for the first three weak peaks and U^{6+} for the peak at 540 K.

4. Discussion

CaO matrix has NaCl type of structure and uranium entering in 4 + or 6 + oxidation state would go substitutionally in association with lattice defects for charge compensation. The charge compensation can be achieved either by cation vacancies or interstitial anions O^{2-} in the lattice.

As mentioned earlier, the g value for U^{5+} in perfectly octahedral symmetry (U^{5+} at Ca site with no nearby charge compensating defect) would be 1·1. The present value of 1·236 shows that the local symmetry has small perturbation of axial distortion. The value of ε is estimated to be about 1000 cm^{-1} [1]. The g value greater than 1·1 for U^{5+} suggests that it is more likely due to cation vacancy at the second nearest neighbour site which produces local C_{4v} symmetry. Interstitial O^{2-} ion in close neighbourhood would have increased the coordination number and resulted in a much lower g-value.

When the sample is heated to 540 K, U^{5+} intensity is reduced. This suggests that e^- or hole released from a trap elsewhere recombines at U^{5+} site. The spectral character of emission for the peak (viz. emission around 550, 580 and 598 nm) at 540 K shows that the emission centre is U^{6+}. Therefore the formation of U^{4+} through capture of electron is considered less probable. In view of the nature of the emission centre, the reduction in U^{5+} signal is ascribed to recombination with a hole. The probable mechanism is as follows:

On gamma irradiation,

$$O^{2-} \rightarrow O^{-} + e^{-}, \tag{1}$$

$$U^{6+} + e^{-} \rightarrow U^{5+}. \tag{2}$$

On heating to 540 K,

$$O^{-} \rightarrow O^{2-} + \text{hole}, \tag{3}$$

$$U^{5+} + \text{hole} \rightarrow U^{6+}*, \tag{4}$$

$$U^{6+}* \rightarrow U^{6+} + h\nu, \tag{5}$$

i.e, $U^{5+} + O^{-} \rightarrow U^{6+}* + O^{2-}$; $U^{6+}* \rightarrow U^{6+} + h\nu$. The EPR of O^{-} was observed in the CaO:U pellet sample up to 55 K. This observation of O^{-} only at low temperatures is not surprising since it is reported to have been observed only at 20 K in high symmetry crystals like KCl [12] as it is a Jahn–Teller ion. The annealing behaviour of O^{-} was examined by recording the EPR spectra at 20 K of gamma irradiated CaO: U pellet heated to 540 K. The percentage change in the intensity of O^{-} signal was not large but a definite decrease was noticed. However it may be recalled that sensitivity of TSL is significantly more when compared to EPR [13].

In summary, EPR evidence is presented for radiation stabilization of U^{5+} in CaO. It appears to be associated with a second neighbour cation vacancy, producing low symmetry distortion of about 1000 cm^{-1}. U^{5+} acts as the recombination centre for the TSL glow peak at 540 K.

References

[1] C Miyake, in *Handbook on the physics and chemistry of actinides* edited by A J Freeman and C Keller (Elsevier Science Publishers, Amsterdam, 1991) ch. 7, p. 337
[2] W Burton Lewis, H G Hecht and M P Eastman, *Inorg. Chem.* **12**, 1634 (1973)
[3] A F Leung and Y Poon, *Can. J. Phys.* **55**, 937 (1977)
[4] A G I Dalvi, M D Sastry and B D Joshi, *J. Phys.* **E13**, 1106 (1980)
[5] V Natarajan, T K Seshagiri, S K Thulasidas, A K Pandey, P C Kalsi, M D Sastry and R H Iyer, *Proc. IX National Symposium on Solid State Track Detectors, Bombay* (1995) p. 150
[6] P M Llewellyn, Ph.D. thesis (Oxford University, Oxford, 1956)
[7] W C O'Mara and J E Wertz, *Solid State Commun.* **8**, 807 (1970)
[8] A J Tench and M J Duck, *Solid State Commun.* **15**, 333 (1974)
[9] W Hoogenstraaten, *Philips Res. Rep.* **13**, 515 (1958)
[10] W Lehmann, *J. Lumin.* **6**, 455 (1973)
[11] T K Seshagiri, V Natarajan, A G I Dalvi and M D Sastry, *Pramana – J. Phys.* **33**, 685 (1989)
[12] W Sander, *Naturwissenschaften* **51**, 404 (1964)
[13] M D Sastry, A G I Dalvi, A G Page and B D Joshi, *J. Phys.* **C8**, 3232 (1975)

— journal of
physics

pp. 331–337

Impurity mediated mechanism of photorefractive effect in $BaTiO_3$: A combination of Sangster and piezoelectric effects

M D SASTRY*†, M MOGHBEL† and PUTCHA VENKATESWARLU†

*Radiochemistry Division, Bhabha Atomic Research Centre, Trombay, Mumbai 400 085, India
†Department of Physics, Alabama A & M University, Normal, Alabama 35762, USA

MS received 3 June 1996

Abstract. An impurity mediated mechanism of photorefractive effect in $BaTiO_3$ is proposed. The photoinduced changes in the relative concentration of Fe^{3+} in $BaTiO_3$ results in an electro-optic coupling through a combination of the Sangster and piezoelectric effects. This is based on the examination of the extensive results on the EPR of Fe^{3+} in the $BaTiO_3$ lattice. This model explains the improved photorefractive behavior of $BaTiO_3$ on doping with Co^{2+}.

Keywords. Photorefractive effect; $BaTiO_3$; Electron paramagnetic resonance of Fe^{3+} in $BaTiO_3$.

PACS Nos 42·65; 42·70; 33·30

1. Introduction

The microscopic mechanism of the photorefractive effect and grating formation in $BaTiO_3$ is an important area of current interest particularly with regard to the role of impurities. As in $LiNbO_3$ [1], it is generally accepted that an Fe-impurity plays the role of an acceptor/donor in Kukhtarev's band conduction model [2] in nominally pure $BaTiO_3$. It has become apparent in recent times that the chemical nature of the impurity plays an important role in improving the strength of beam coupling such as Co^{2+} in $BaTiO_3$ [3,4] and Rh in SBN [5]. In $BaTiO_3$, the Debye screening length is shorter than typical fringe width, and the photoinduced charge transfer, more often, results in charge redistribution in the bright region of the interference pattern caused by the writing beam. The net charge transport between bright and dark regions occurs to a significant extent only in the interfacial region between bright and dark regions. Cudney *et al* [6] have shown that the redistribution of charges, on laser illumination between different trapping levels at roughly the same spatial location does not produce any electro-optic coupling due to the absence of electric field, but it does produce an absorption grating. In this note we show that, if the light induced redistribution of charges in the illuminated regions brings changes in the relative concentration of $Fe^{2+}/Fe^{3+}/Fe^{4+}$, then an electro-optic coupling occurs through a combination of Sangster [7] and piezoelectric effects in $BaTiO_3$. In the present note, we propose an impurity mediated mechanism of the photorefractive effect (abbreviated as IMPRE) in $BaTiO_3$, and it is based on the large amount of information available from the electron

paramagnetic resonance (EPR) studies of Fe^{3+} in $BaTiO_3$ [8–15] and its analysis by Müller [12, 14, 15], Müller and Berlinger [13] and Siegel and Müller [11] using superposition model. This IMPRE model convincingly explains why doping with Co^{2+} enhances the photorefractive response in $BaTiO_3$. The description of this model is presented in three sections: (i) EPR information on the cubic crystal field constant and consequence of the Sangster effect, (ii) enunciation of IMPRE model and (iii) consequences of the IMPRE mechanism.

2. EPR information of Fe^{3+}: $BaTiO_3$

The EPR investigations of Fe^{3+} in $BaTiO_3$ were done first by Horning *et al* [8] and by Sakudo and coworkers [9, 10]. Greater insight in this area was obtained by Müller and coworkers [12–15] in their attempt to probe the nature of structural phase transitions in ABO_3 type perovskites and also to get a comprehensive understanding of the local behavior of a number of transition metal dopants at the Ti^{4+} site. It was identified quite early in these studies that Fe^{3+} impurity goes substitutionally at the Ti^{4+} site. Siegel and Müller [11] have shown, using a superposition model for ligand field effects, that Fe^{3+} remains centered in an octahedral environment in all structural modifications of $BaTiO_3$. The cubic field parameter a in the Hamiltonian,

$$H = a/6[S_x^4 + S_y^4 + S_z^4 - (1/5)S(S+1)(3S^2 + 3S - 1)],\ S = 5/2 \text{ for } Fe^{3+}$$

remained constant ($97 \times 10^{-4}\,cm^{-1}$) within 10% in all the structural phases (cubic, tetragonal, orthorhombic and rhombohedral) of $BaTiO_3$. The systematics of a for Fe^{3+} in a number of cubic oxides has revealed that it follows an empirical relation $a = a_0/d^n$ (where $2d$ = lattice spacing), with $n = 7$ and $n = 6$ near $d = 2$ Å, with a significant exception in the case of $BaTiO_3$ and $KNbO_3$. In these two crystals a was found to be 2·5 times smaller than the one expected by the empirical relation $a = a_0/d^n$. This low value of a in $BaTiO_3$ and $KNbO_3$ was found to correlate with the existence of a strongly overdamped and anisotropic soft mode.

The centered position of Fe^{3+} in the octahedral cage of oxygens and the abnormally low value of a were explained by Müller and Berlinger [13] invoking the Sangster effect [7] and the role of electron occupancy of 3d orbitals of Fe^{3+}. Sangster effect [7] predicts that Fe^{3+} at Ti^{4+} site (with no local charge compensation) repels the negative O^{2-} ions. In addition to this repulsion, an extra repulsive force arises due to the electronic configuration of Fe^{3+} ($t_{2g}^3 e_g^2$). The e_g orbitals are antibonding and, therefore, add to the repulsive force between Fe^{3+} and O^{2-}. The t_{2g} orbitals are nonbonding; therefore for an ion-like Mn^{4+} (electron configuration t_{2g}^3) at the Ti^{4+} site, the Sangster effect is absent. (Müller has shown that Mn^{4+} is the most appropriate probe to give a true understanding of the Ti^{4+} site and its dynamics in the $BaTiO_3$ lattice [12]). Using the empirical relationship between a and d, Müller and Berlinger [13] have shown that the probing Fe^{3+} sees the oxygen atom in $BaTiO_3$ at 17% larger distance than what it should be for an inert oxide, i.e., for a situation where the Sangster effect is absent. This was estimated to enhance the anharmonicity of the local potential by 34%. Müller and Berlinger [13] have also shown that the explicit pressure dependence of a in $BaTiO_3$ was three times the average of $3{\cdot}6 \times 10^{-4}\,K^{-1}$ found in other oxides. This has firmly established that the low value of a for Fe^{3+} in $BaTiO_3$ reflects locally expanded

the piezoelectric nature of $BaTiO_3$, and also for other piezoelectric crystals like BSO, in understanding the microscopic nature of photorefraction. To our knowledge, this has not been considered by the 'photorefractive community' so far, and plays a key role in the model proposed in the next section.

3. Enunciation of the model

The model for impurity mediated photorefractive effect (IMPRE) in $BaTiO_3$ may be enunciated as: When $BaTiO_3$ is doped with a transition metal impurity at the Ti^{4+} site whose valence can be changed by laser illumination, any interference pattern produced in the crystal results in a spatial modulation of strain field due to Sangster effect. This results in a modulation of the inter-atomic spacing with spatial period equal to that of the fringe width. As a consequence of the piezoelectric nature of $BaTiO_3$, modulation of internal electric field occurs and hence a phase grating is formed in the crystal. This is illustrated in figure 1.

In this model, the chemical nature of the defect plays an important role in the photorefractive effect. Table 1 gives a summary of the expected Sangster effect for different valence states of transition ions.

4. Consequences of IMPRE mechanism

EPR of Fe^{3+} in $BaTiO_3$ under laser illumination was investigated by Schwartz and coworkers [16] at 25 K and by Moghbel *et al* [17] at room temperature. In both cases it was observed that there is a net change in the concentration of Fe^{3+} even under uniform laser illumination. At room temperature, where most of the photorefractive experiments are conducted, the relative concentration of Fe^{3+} was found to go down on laser illumination. The photoinduced valence change, therefore, involves one or both of the following path ways.

$$Fe^{3+}(t_{2g}^3 e_g^2) \begin{cases} \xrightarrow{h\nu} Fe^{2+}(t_{2g}^4 e_g^2) \\ \xrightarrow{h\nu} Fe^{4+}(t_{2g}^3 e_g^1)_{HS}/(t_{2g}^4)_{LS} \end{cases}$$

where HS and LS refer to high spin and low spin forms respectively. When the spin pairing energy is more than the crystal field splitting, the ion will exist in high spin (HS) form, and in the reverse situation the ion will exist in low spin (LS) form [18]. The valence change $Fe^{3+} - h\nu \rightarrow Fe^{2+}$ implies increased amount of Fe–O repulsion due to larger effective negative charge on Fe. On the other hand, $Fe^{3+} - h\nu \rightarrow Fe^{4+}$ results in considerably lowered Fe–O repulsion, much more so if Fe^{4+} is in low spin form. This obviously implies that, in bright and dark regions of the hologram, there is a strain modulation in view of the alternation of net Fe^{3+} concentration in bright and dark regions. Further, the piezoelectric nature of $BaTiO_3$ obviously helps in the creation of electric field modulation.

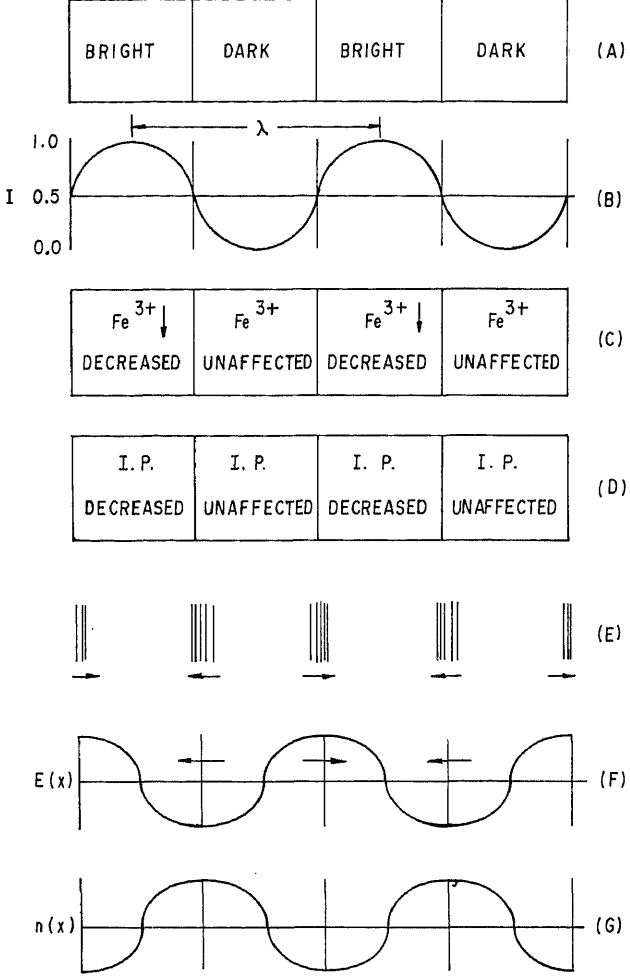

Figure 1. Schematic illustration of IMPRE model. (**A**) Typical illumination pattern. (**B**) Typical intensity profile. (**C**) Photoinduced valence change. (A typical example is $Fe^{3+} \rightarrow h\nu \rightarrow Fe^{4+}$ in Fe: $BaTiO_3$.) (**D**) Change in internal pressure via Sangster effect due to photo induced valence change. (**E**) Change in lattice spacings due to differential pressure in the bright and dark regions. The compression in the lattice spacings is expected to be maximum at the interfacial region. (**F**) The electric field modulation induced by piezoelectric effect due to the strain modulation caused by photo-induced valence change. (**G**) Modulation of refractive index caused by the modulation of electric field.

Schwartz *et al* [16] suggest that photoinduced valence change $[Co^{3+}]_{LS} - h\nu \rightarrow [Co^{2+} + h^+]_{HS}$ is involved in the $BaTiO_3$: Co crystal. It can be seen from table 1, that for high spin Co^{2+}, the Sangster effect is very significant whereas for low spin Co^{3+} it would be substantially smaller. This means that with photoionization of Co^{3+} along with the associated formation of high spin Co^{2+} the lattice is transformed into a more strained

Table 1. Summary of the presence of the Sangster effect for different valence states of transition ions in octahedral fields. The valence states lower than 4 + cause the Sangster effect at the Ti^{4+} site due to purely electrostatic reasons. In this table the contribution to repulsive forces only from the electronic configuration are given. The description of "strong" and "weak" refers to two and one antibonding electrons respectively.

Ions	No. of electrons in d-shell	Electronic configuration in octahedral field		Sangster effect due to antibonding electrons
		High spin form	Low spin form	
Mn^{4+}, Cr^{3+}	d^3	t_{2g}^3	t_{2g}^3	Absent
Mn^{3+}, Fe^{4+}	d^4	$t_{2g}^3 e_g^1$	t_{2g}^4	Weakly present in HS form, absent in LS form
Mn^{2+}, Fe^{3+}	d^5	$t_{2g}^3 e_g^2$	t_{2g}^5	Strongly present in HS, absent in LS form
$Rh^{3+}, Co^{3+}, Fe^{2+}$	d^6	$t_{2g}^4 e_g^2$	t_{2g}^6	Strongly present in HS, absent in LS form
$Ni^{3+}, Rh^{2+}, Co^{2+}$	d^7	$t_{2g}^5 e_g^2$	$t_{2g}^6 e_g^1$	Strong in HS and weak in LS forms
Ni^{2+}, Co^{+}	d^8	$t_{2g}^6 e_g^2$	$t_{2g}^6 e_g^2$	Strongly present in both forms
Cu^{2+}	d^9	$t_{2g}^6 e_g^3$	$t_{2g}^6 e_g^3$	Present equally in both forms

state. Thus the Sangster effect may provide a physical reason why Co^{3+} prefers the low spin state, despite the closeness of ${}^5T_{2g}$ state of its high spin and ${}^1A_{1g}$ of low spin forms [19]. Compared to photoinduced valence change in $BaTiO_3$: Fe, i.e., $Fe^{3+} \leftrightarrow Fe^{2+}/Fe^{4+}$ (both high spin), the corresponding changes for cobalt doped $BaTiO_3$, $[Co^{3+}]_{LS} \leftrightarrow Co^{2+}]_{HS}$ would result in greater contrast in the grating element and hence higher grating efficiency. Similar behavior is expected for the Rh dopant, probably explaining the result reported by Vasquez *et al* [5] in Rh doped SBN. Similarly, the valence changes expected to give good contrast are: $Mn^{4+} \leftrightarrow Mn^{3+}$ and $Mn^{4+} \leftrightarrow Mn^{2+}$. In view of the half filled stability of Mn^{2+}, the latter process ($2e^-$ transfer) is quite probable, and is expected to give high grating efficiency. This is consistent with the reported enhancement of beam coupling in Mn doped $BaTiO_3$ by Wechsler *et al* [3].

The distortion in the lattice arising due to photoinduced strain is a result of the pressure differential generated by valence change and is expected to be maximum in the close vicinity of interfacial region of bright and dark fringes in an interference pattern. This suggests that the phase difference between the interference pattern and the phase grating is about 90° (figure 1). This is known to be responsible for the energy transfer in a two beam coupling experiment [20]. At room temperature, in the tetragonal phase of $BaTiO_3$, if the grating wave vector is parallel to *c*-axis, the crystallographic distortion

axis coincides with that of the spatially periodic distortion caused by the grating formation. Therefore, the tetragonal crystal structure allows their coexistence. However, if the grating formed is in (a, b) plane the superposed distortion destroys the crystallographic equivalence of a and b axes in the tetragonal phase itself. Therefore, the distortions associated with phase grating formation may not be sustained. Furthermore, such distortions may be averaged to zero due to motional averaging of off-centered $[Ti^{4+}]$ along four $\langle 111 \rangle$ directions in tetragonal phase with a time scale of 10^{-9}–10^{-10} s [13]. This probably explains why energy transfer does not take place when the grating wave vector is perpendicular to c-axes and the grating in (a, b) plane acts only as an absorption grating. However, if the phase conjugation studies are conducted in pulse mode with $\tau < 10^{-10}$ s, it may be possible to observe the energy transfer even when the grating vector is perpendicular to c-axis.

There exists a large body of transport data on photo-refractive materials, explaining the basic features of photorefractivity. We do not intend to suggest that photoconductivity is unimportant, but we want to highlight that there exists a possible mechanism which takes into account only the chemical nature of impurity and the photoinduced valence changes. The description of the phenomenon of photorefractive effect invoking only the chemical nature of defects would be incomplete without discussing some simple characteristics of photorefraction which are normally explained using charge transport model. We will attempt to find answers to the following in the framework of our model: (i) why grating formed in $BaTiO_3$ exhibits relatively slow relaxation? (ii) why the response time decreases with application of electric field? and (iii) can erasure with uniform light be explained without transport?

The lifetime of the grating depends upon the trap-depth of the electron/hole trap. Under charge transport model this should correspond to a trap in the darker regions of the interference pattern. The slow relaxation of grating implies that the thermal trap-depth should be more than kT at room temperature. This should be observable as a thermoluminescence (TL) peak above room temperature. In our model this trap can be filled even during uniform illumination and the (Fe) impurity site acts both as donor and acceptor (e/h trap). It is reported that $BaTiO_3$ shows a TL peak at 80°C, when the sample is uniformly irradiated with gamma rays [21]. This peak was found to decay in a few hours at room temperature. This phenomenon is independent of the route through which the traps were filled. They can be filled under conditions of uniform illumination which is analogous to uniform gamma irradiation.

It is known that external electric field decreases the response time. In our proposed mechanism, piezoelectric effect has an important role. In the presence of external field slight distortions produced by the interference pattern get strongly perturbed by the distortion induced by the electric field, resulting in the decrease of response time.

It is a common practice to erase the grating by exposing the $BaTiO_3$ crystals to intense uniform light. In our model, the lattice distortions occur most predominantly at the interfacial regions of the bright and dark fringes (i.e., in the regions of maximum intensity gradient). At the centre of the bright region, the pressure generated at one site gets balanced by that at another neighbouring site. At the interfacial regions the internal pressure differential would be the largest, resulting in the formation of grating 90° out-of-phase with the intensity pattern. Therefore, under the conditions of uniform illumination, the pressure differential goes to zero and the grating gets erased.

5. Conclusion

We have suggested a new mechanism for the photorefractive effect in $BaTiO_3$ doped with transition metal impurities. This is primarily centered around the valence dependent repulsive forces between the impurity ion and the ligand oxygens. This model explains the dependence of photorefraction on the chemical nature of the dopant.

References

[1] E Krätzig and O F Schirmer, in *Photorefractive materials and their applications* edited by P Günter and J-P Huignard, Topics in Applied Physics (Springer-Verlag, Berlin, Heidelberg 1988) ch. 5
[2] N V Kuktharev, *Sov. Tech. Phys. Lett.* **2**, 438 (1976)
[3] B A Wechsler, D Rytz, M B Klein and R N Schwartz, *Materials for nonlinear optics: Chemical perspectives* (American Chemical Society, 1991) ch. 26, p. 394
[4] M H Garrett, J Y Chang, H P Jenssen and C Warde, *J. Opt. Soc. Am.* **B9**, 1407 (1992)
[5] R A Vasquez, R R Neurgaonkar and M D Ewbank, *J. Opt. Soc. Am.* **B9**, 1416 (1992)
[6] R S Cudney, R M Pierce, G D Backer and J Feinberg, *J. Opt. Soc. Am.* **B8**, 1326 (1991)
[7] M J L Sangster, *J. Phys.* **C14**, 2889 (1981)
[8] A W Horning, R C Rempel and H E Weaver, *J. Phys. Chem. Solids* **10**, 1 (1959)
[9] T Sakudo, *J. Phys. Soc. Jpn.* **18**, 1626 (1963)
[10] T Sakudo and H Unoki, *J. Phys. Soc. Jpn.* **19**, 2109 (1964)
[11] E Siegel and K A Müller, *Phys. Rev.* **B19**, 109 (1979)
[12] K A Müller, *Helv. Phys. Acta*, **59**, 874 (1986)
[13] K A Müller and W Berlinger, *Phys. Rev.* **B34**, 6130 (1986)
[14] K A Müller, *Ferroelectrics* **13**, 381 (1976)
[15] K A Müller, *Phys. Rev.* **B13**, 3209 (1976)
[16] R N Schwartz, B A Wechsler and R A McFarlane, *Phys. Rev.* **B46**, 3263 (1992)
[17] M Moghbel, M D Sastry, P Venkateswarlu, A S Jeevarajan and L D Kitspert, *Opt. Soc. Am.* **16**, 6 (1993) Annual Meeting, Technical Digest, Paper # MD5
[18] C J Ballhausen, *Introduction to Ligand Field Theory* (McGraw Hill Inc., 1962)
[19] R N Schwartz and B N Wechsler, *J. Am. Ceram. Soc.* **73**, 3200 (1990)
[20] P Günter and J-P Huignard, in *Photorefractive Materials and their Applications I* edited by P Günter and J-P. Huignard, Topics in Applied Physics (Springer-Verlag, Berlin, Heidelberg, 1988) ch. II
[21] S Lin, R J Vetter and P L Zeimer, *Radiat. Eff.* **38**, 67 (1988)

Dynamics of the logistic map under discrete parametric perturbation

P P SARATCHANDRAN*, V M NANDAKUMARAN and G AMBIKA†
International School of Photonics, Cochin University of Science and Technology, Cochin 682 022, India
†Department of Physics, Maharajas College, Cochin 682 011, India
*Permanent Address: Department of Physics, The Cochin College, Cochin 682 002, India

MS received 30 September 1995; revised 12 August 1996

Abstract. By introducing a periodic perturbation in the control parameter of the logistic map we have investigated the period locking properties of the map. The map then gets locked onto the periodicity of the perturbation for a wide range of values of the parameter and hence can lead to a control of the chaotic regime. This parametrically perturbed map exhibits many other interesting features like the presence of bubble structures, repeated reappearance of periodic cycles beyond the chaotic regime, dependence of the escape parameter on the seed value and also on the initial phase of the perturbation etc.

Keywords. Logistic map; periodic perturbation; bubble structures; fractal basin of escape.

PACS No. 05·45

1. Introduction

Nonlinear difference equations have proved to be efficient mathematical models in the study of many physical and biological systems [1]. The simplest and one of the most extensively studied nonlinear difference equations is the logistic map

$$X_{n+1} = 4\lambda X_n(1 - X_n) \quad 0 \leqslant X, \lambda \leqslant 1. \tag{1}$$

In actual experimental situations the control parameter represents the ambient conditions such as voltage, discharge current, intensity of the electromagnetic field, etc [2, 3] which in turn can often have a time dependence. The simplest case of a time dependence is a linear time dependence [4], where properties like bistability and hysteresis have been observed. One can consider a more general situation in which λ itself evolves as a discrete nonlinear map and most often X gets enslaved to the periodicity of the perturbation [5, 6]. Quadratic maps with additive periodic forcing leading to bistability and co-existence of multiple attractors have also been studied [7]. Time dependence can also be incorporated into the dynamics of (1) as a periodic perturbation [8–11].

In this paper we consider a situation wherein instead of changing λ continuously it is changed in a discrete sequence as a train of pulses repeated periodically, the envelope of the amplitude of the pulses forming a positive sine profile. Such a sequence of pulses may be relevant in the study of biological systems subjected to periodic stimuli [12].

With a similar perturbation, but with a cosine profile that includes both the positive and negative half cycles, it has been found that the map undergoes a transition from a fixed point and gets locked into the periodicity of the perturbation [14]. For odd periodic perturbation, the period locked system undergoes the usual period doubling cascade whereas for even periodic perturbation there are multiple period locked cycles co-existing for an interval and having different basins of attraction. These period locked cycles then undergo period doublings independently. In our work we have restricted the sine profile in the perturbation to its positive half cycle. We have already analyzed the symbolic dynamics of the period-locked cycles in the presence of this perturbation [13] and observed many sequences that do not fall under the MSS prescription. We explain the presence of bubble structures in certain bifurcation diagrams. So also the parameter value for escape is dependent both on the initial phase and on the seed value and that the basin for escape is a fractal. The dimension D_0 of this basin has been computed. The difference in the behaviour of the map for odd and even perturbations as reported in [14] is absent in the present model. The paper is organized as follows. Section 2 discusses the dynamics of the perturbed map for perturbations of various periods with the help of the bifurcation diagrams. Section 3 attempts an explanation for the presence of bubble structures in the bifurcation diagram. In § 4 the phase dependent nature of the escape parameter is detailed. Our concluding remarks are given in the last section.

2. Parametrically perturbed logistic map

In this section we outline the nature of the perturbation employed in the system and its effects on the bifurcation diagrams of the map. The control parameter of the logistic map is perturbed by a periodic perturbation so that it takes the form

$$\lambda_{n+1} = \lambda^0 + \lambda^1 \sin\phi_{n+1} \bmod \pi, \tag{2}$$

where

$$\phi_{n+1} = \phi_n + \pi\omega. \tag{3}$$

Here λ^0 is the time independent part and λ^1 refers to the amplitude of the time dependent part of the control parameter. For a rational ω, say $\omega = p/q$, the control parameter forms a q cycle with cycle elements.

$$\lambda_q = \lambda^0 + \lambda^1 \sin((n-1)\pi/q) \text{ where } n = 0, 1, 2, \ldots, q-1. \tag{4}$$

The logistic map with the sinusoidal perturbation can then be written as

$$X_{n+1} = 4(\lambda^0 + \lambda^1 \sin\phi_n) X_n (1 - X_n). \tag{5}$$

If $L(X) = 4X(1-X)$ the parametrically perturbed map becomes

$$X_{n+1} = \lambda^0 L(X_n) + \lambda^1 \sin\phi_n L(X_n). \tag{6}$$

We can easily identify λ^0 $L(X)$ as the usual logistic map and $\lambda^1 \sin\phi_n L(X)$ as the perturbation component. The dynamics of the parametrically perturbed map (6) has

the unperturbed logistic map possesses only one stable cycle, a stable fixed point x^* (1) so that the full effect of the perturbation can be studied. At $\lambda^1 = \lambda^{1*}$ determined by

$$+1 = \prod_{i=0}^{q-1} 4^q(\lambda^0 + \lambda^{1*}\sin\pi i/q) \tag{7}$$

the fixed point changes stability with a q cycle. This q cycle thereafter undergoes period doubling bifurcations. If λ^0 is such that the unperturbed logistic map has a stable k cycle then the perturbation would result in a transition from k cycle to kq cycle. The transition from a fixed point to a q cycle in such cases can still be observed by a perturbation which is out of phase i.e., $\lambda^1 \sin\phi_n \to -\lambda^1 \sin\phi_n$, the value of λ^{1*} can be obtained from (7). Figures 1 and 2 give the bifurcation diagram for the map (5) for an odd ($q = 3$) and an even ($q = 6$) periodic perturbation respectively. It is clear from table 1 that the stability zone for the various q cycles have increased considerably in comparison with the respective stability zones in the unperturbed logistic map. This perturbation also provides a prescription for period-locking the system to any desired periodicity. It is obvious from figure 1 that the q cycle becomes superstable more than once within a zone of stability. This is in contrast with the behaviour of the unperturbed logistic map (1). The symbolic dynamics of these superstable cycles have already been analyzed [13]. Also the cycles possess sequences which do not fall under the usual MSS prescription in addition to MSS ones.

3. Bubble structures, co-existence of multiple attractors in the parametrically perturbed logistic map

In this section we explain the presence of bubble structures in the bifurcation diagram of (5) for certain q values (for e.g. $q = 10$). A bubble is formed when a periodic cycle of q period doubles but later recombines to form a q cycle again. Such bubble structures

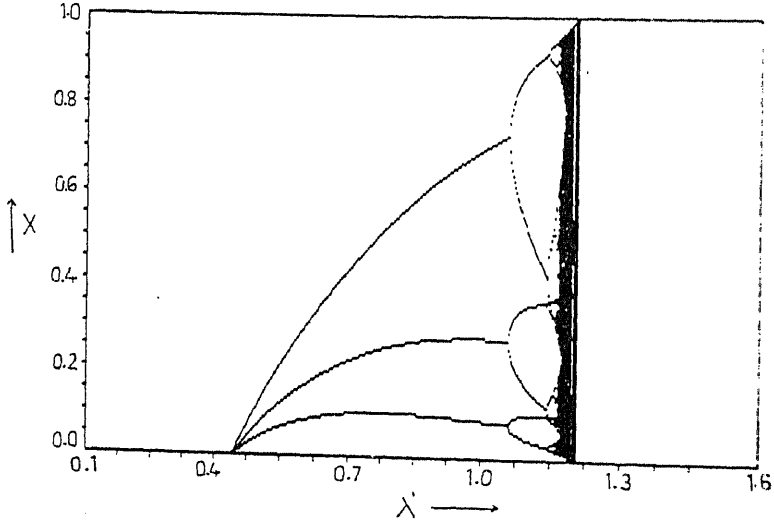

Figure 1. The bifurcation diagram of the map for $q = 3$. Note the widening of the zone of stability for the 3 cycle which appears only as a small window in the logistic map (1).

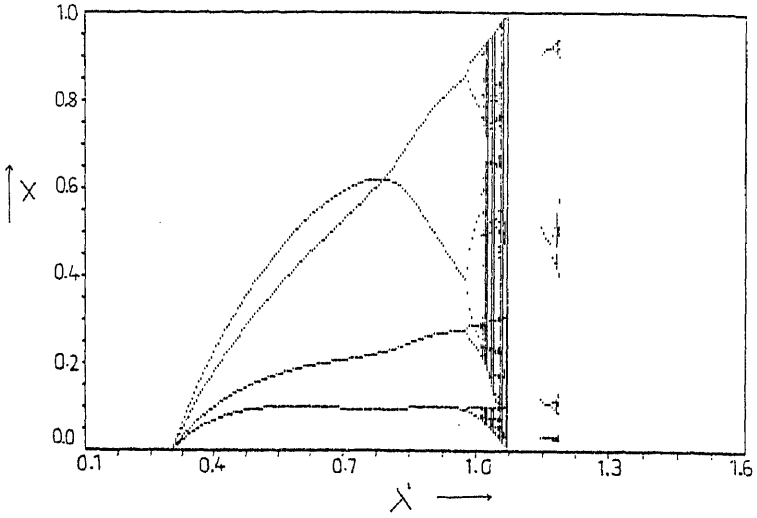

Figure 2. The bifurcation diagram of the map for $q = 4$.

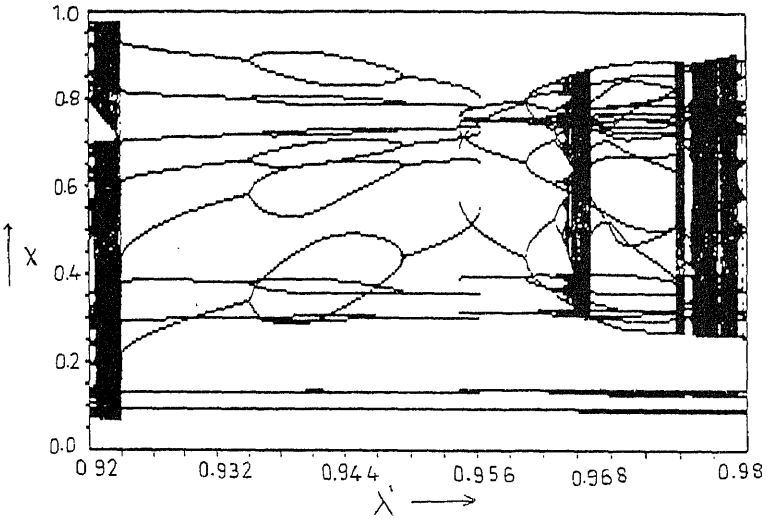

Figure 3. Section of the bifurcation diagram for $q = 10$. The diagram has been drawn using different initial values. Notice the hysteresis region in the range $0{\cdot}953 < \lambda^1 < 0{\cdot}956$.

have been reported earlier [15–17]. We find that the symmetry condition for the bubble structures as reported in [16] is not a necessary condition for the formation of bubbles. Figure 3 plots the bifurcation diagram for $q = 10$ in the parameter range $0{\cdot}9 < \lambda^1 < 1$. Here a 10 cycle reappears after the period doubling cascade and remains stable up to

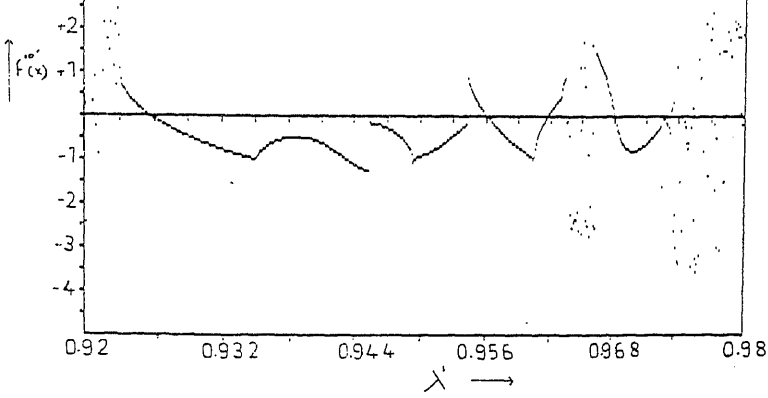

Figure 4. Variation of the $f^{10'}(X)$ with λ^1. Notice the discontinuity in slope in the hysteresis region.

a hysteresis region where a new 10 cycle coexists with this 10 cycle in the parameter range $0{\cdot}953 < \lambda^1 < 0{\cdot}956$. Beyond $\lambda^1 = 0{\cdot}956$ the original 10 cycle loses stability and the new 10 cycle later undergoes period doubling bifurcations. In the region of coexistence the two 10 cycles have their basins of attraction intertwined, which is quite different from earlier reports [7, 14, 18]. Bubble structures have also been found for $q = 5, 8$. We have found that for this map bubble structures are always being followed by a region of co-existing attractors having intertwined basins of attraction. These sequence of events can be visualized in the plot of $f^{10'}(x)$ vs λ^1 given in figure 4. The birth of this new 10 cycle is simultaneous with the discontinuity in the $f^{10'}(x)$ curve. We also find that the range of λ for which the system has bounded orbits is discontinuous, that is there are regions of escape within the tuning range of the parameter λ.

4. Fractal nature of the basin of escape

In this section we discuss the fractal nature of the basin of escape for the perturbed logistic map (5). For the usual logistic map (1) the range of the control parameter for bounded orbits is $0 \leqslant \lambda \leqslant 1$. The value of the control parameter is $\lambda = 1$ beyond which successive iterates of the map speeds away rapidly towards $-\infty$. It has also been found that beyond $\lambda = 1$ those seed values which remain in the $[0, 1]$ after infinite iterations form a cantor set [19]. Therefore $\lambda = 1$ is considered as the parameter value for escape from the interval $[0, 1]$. In map (5) the parameter value for escape λ_e is found to be dependent both on the initial phase and seed value of the iteration. For a given seed value X_0 the iterates may either remain within the interval $[0, 1]$ or go out depending on the initial phase of iteration.Thus for $q = 10$ and $\phi_0 = \pi/10$ the iterates escape towards $-\infty$. If we choose a seed value $X_0 = 0{\cdot}3$ the iterates are unbounded. In fact for $\omega = 1/4$ and $\lambda^1 = 0{\cdot}904$, a parameter value for which a superstable 4 cycle exist we find

Table 1. Stability zone for the q cycle in the parametrically perturbed logistic map

q	Stability zone
2	$0{\cdot}52500 < \lambda^1 < 2{\cdot}0211$
3	$0{\cdot}34096 < \lambda^1 < 0{\cdot}959$
4	$0{\cdot}30034 < \lambda^1 < 0{\cdot}9761$
5	$0{\cdot}28406 < \lambda^1 < 0{\cdot}847$
6	$0{\cdot}27578 < \lambda^1 < 0{\cdot}8541$
7	$0{\cdot}27094 < \lambda^1 < 0{\cdot}907$
8	$0{\cdot}26788 < \lambda^1 < 0{\cdot}883$
9	$0{\cdot}26579 < \lambda^1 < 0{\cdot}9234$
10	$0{\cdot}26432 < \lambda^1 < 0{\cdot}8966$

Table 2. The capacity dimension of the basin of escape for $\omega = 1/10$ for $\phi_0 = \pi/10$.

λ^1	D_0
0·923	0·8526099
0·94	0·9071668
0·948	0·9581154
0·956	0·9728904

that certain seed values do not converge onto the 4 cycle, instead they go out of the interval. This basin of escape is of fractal nature. The fractal dimension D_0 has been calculated and tabulated in table 2.

5. Concluding remarks

We have studied the dynamics of a parametrically perturbed logistic map. The map can be an efficient model in the study of physical systems subjected to periodic stimuli [12]. The map is shown to exhibit many interesting properties like bubble structures, hysteresis region, reappearence of periodic cycles beyond chaotic region. The dynamic region of the control parameter appears to be discontinuous. We find that the escape parameter λ_c depends on the initial phase ϕ_0 and seed value X_0. The basin for escape has a fractal structure. We have also found that the range of λ^1 for which bounded orbits exist is discontinuous.

References

[1] R M May, *Nature (London)* **261**, 459 (1976)
[2] M Ciofini, R Meucci and F T Arecchi, *Phys. Rev.* **E52**, 95 (1995)
[3] R Badii, E Brun, M Finardi, L Flepp, R Holzner, J Parisi, C Reyl and J Simonet, *Rev. Mod. Phys.* **66**, 1389 (1994)
[4] R Kapral and P Mandel, *Phys. Rev.* **A32**, 1076 (1985)

[5] K P Harikrishnan and V M Nandakumaran, *Phys. Lett.* **A125**, 465 (1987); *Pramana – J. Phys.* **29**, 533 (1987); *Phys. Lett* **A133**, 305 (1988)
[6] S Batra and V S Varma *Pramana – J. Phys.* **37**, 83 (1991)
[7] Sanju and V S Varma, *Phys. Rev.* **E48**, 1670 (1993)
[8] R Lima and M Pettini, *Phys. Rev.* **A41**, 726 (1990)
[9] Y C Lai, M Ding and C Grebogi, *Phys. Rev.* **E47**, 86 (1993)
[10] Y C Lai, C Grebogi, *Phys. Rev.* **E49**, 1094 (1994)
[11] W Yang, M Ding, A J Mandell and E Ott, *Phys. Rev.* **E51**, 102 (1995)
[12] S J Schiff, K Jerger, D H Duong, T Chang, M L Spano and W L Ditto, *Nature (London)* **370**, 615 (1994)
[13] P P Saratchandran, V M Nandakumaran and G Ambika, *Proc. of the Seminar on Computational Aspects in Chaos and Nonlinear Dynamics* edited by G Ambika and V M Nandakumaran (Wiley Eastern Ltd., 1994) p. 215
[14] M Lucke and Y Saito, *Phys. Lett.* **A91**, 205 (1982)
[15] M Bier and T C Bountis, *Phys. Lett.* **A104**, 239 (1982)
[16] T Midavaine, D Dangoisse and Glorieux, *Phys. Rev. Lett.* **55**, 1989 (1985)
[17] P R Krishnan Nair, V M Nandakumaran and G Ambika, *Proc. of the Seminar on Computational Aspects in Chaos and Nonlinear Dynamics* edited by G Ambika and V M Nandakumaran (Wiley Eastern Ltd., 1994) p. 144
[18] C Grebogi, E Ott and J A Yorke, *Physica* **D7**, 181 (1983)
[19] R L Devaney, *An introduction to chaotic dynamical systems* (The Bengamin/Cummings Publishing Co., 1989)

Relativistic operator description of photon polarization

ARVIND and N MUKUNDA*
Department of Physics, Indian Institute of Science, Bangalore 560 012, India
*Centre for Theoretical Studies and Department of Physics, Indian Institute of Science, Bangalore 560 012, India
*Also at Jawaharlal Nehru Centre for Advanced Scientific Research, Jakkur, Bangalore 560 064, India

MS received 27 July 1996; revised 16 October 1996

Abstract. We present an operator approach to the description of photon polarization, based on Wigner's concept of elementary relativistic systems. The theory of unitary representations of the Poincarè group, and of parity, is exploited to construct spinlike operators acting on the polarization states of a photon at each fixed energy momentum. The nontrivial topological features of these representations relevant for massless particles, and the departures from the treatment of massive finite spin representations are highlighted and addressed.

Keywords. Photon polarization; Poincaré group representations; massless particles.

PACS Nos 11·30; 14·80; 42·25

1. Introduction

In the framework of relativistic quantum mechanics, elementary systems are described by unitary irreducible representations (UIR's) of the proper orthochronous inhomogeneous Lorentz group, or Poincarè group $\mathscr{P}$ [1]. This is the symmetry group of special relativistic space-time. The adjective 'elementary' here implies that for such systems every physical observable can in principle be constructed as a function of the operators implementing the transformations of $\mathscr{P}$. However, as is well known, not all the mathematically constructible UIR's of $\mathscr{P}$ are physically acceptable. Only the finite mass, finite spin UIR's containing positive time-like energy momenta and the positive lightlike energy momentum finite helicity UIR's, are realized in nature. These two classes of UIR's are closely linked to the rotation subgroup $SO(3)$ of the homogeneous Lorentz group $SO(3,1)$, and to an $E(2)$ subgroup of $SO(3,1)$, respectively. UIR's of $\mathscr{P}$ containing space-like energy momenta and the light like continuous spin or infinite helicity UIR's, are unphysical [2].

On account of the special role played by the $SO(3)$ subgroup in the time-like UIR's, there is a clean kinematic separation between orbital and spin angular momenta in these representations, Indeed the concept of spatial position is well-defined [3], and all the generators of $\mathscr{P}$ can be built up as functions of kinematically independent position, momentum and spin operators. Moreover in these UIR's of $\mathscr{P}$, action by the parity operator P can be accommodated without any enlargement of the representation space. Many of these simplifying features can also be linked to the fact

that the coset space $SO(3,1)/SO(3)$ (equivalently $SL(2,C)/SU(2)$) is $\mathscr{R}^3$ which is topologically trivial.

In the lightlike finite helicity UIR's of $\mathscr{P}$, such as one uses to describe photons, the situation is markedly different in many respects. Here the role of $SO(3)$ is taken over by the $E(2)$ subgroup mentioned earlier, and this is not directly linked to transformations on space alone. Moreover the coset space $SO(3,1)/E(2)$ is topologically nontrivial. For these reasons, there is no longer a clear cut kinematic separation of anything analogous to spin from variables related to space [4]. Indeed for nonzero helicity even position in space is not a well-defined physical observable; and the parity operator P cannot be defined within such a UIR of $\mathscr{P}$.

On the other hand, beginning with classical optics, the treatment of the polarization states of a plane electromagnetic wave, and its extension to the possible polarization states of a single photon, are both physically very well founded. In polarization optics *per se*, intensity preserving linear optical systems–rotators, birefringent media, quarter wave plates, half-wave plates, etc. are effectively treated as realizing various elements of an $SU(2)$ or $U(2)$ group acting on the two-dimensional complex linear space of polarization states [5]. However, from the point of view of the theory of elementary systems, the relevant UIR's of $\mathscr{P}$ lead only to a single polarization state, helicity ± 1 corresponding to right or left circular polarization respectively and helicity is relativistically invariant. One must bring in the action by parity P in an essential manner to connect the states of opposite helicities and so create a two-dimensional space of polarization states which allow for the definitions of linear polarization, general elliptic polarization etc.

The purpose of this paper is to examine this complex of questions taking the relevant UIR's of $\mathscr{P}$ as a fundamental starting point. We wish to bring out the essential role of parity in this context, something not often emphasized, and develop the necessary operator machinery to deal with transformations acting solely on the polarization degree of freedom of a photon. Since one deals here ultimately with an irreducible representation of $\mathscr{P}$ extended by parity, in principle all (physically important) operators can be built up out of the generators of $\mathscr{P}$, finite transformations of $\mathscr{P}$ where necessary, and P. We show that there is an unavoidable momentum dependence in these constructions, including in the building up of generators of $SU(2)$ acting on the polarization states of a photon at fixed energy-momentum.

The contents of this paper are arranged as follows. Section 2 sets up basic notational conventions for dealing with UIR's of $\mathscr{P}$, and includes the statement of the homomorphism from $SL(2,C)$ to the homogeneous Lorentz group. The use of $SL(2,C)$ makes later calculations much simpler than otherwise. The algebraic relations involving parity, the Casimir invariants for $\mathscr{P}$, and the structure of the positive energy timelike UIR's with finite spin are briefly reviewed for the convenience of the reader and for later comparison. In particular the emergence of spin as a separately existing degree of freedom in these UIR's, independent of space variables, is emphasized. In § 3 we take up the mass zero finite helicity UIR's of $\mathscr{P}$. Particular attention is paid to the nontrivial topological features that emerge here, as compared to the finite mass case. Alternative ways to pass from a standard energy-momentum to a general energy momentum, in a singularity-free manner, and the structure of Hilbert space basis vectors including their transition rules, are developed. Finally, the doubling of the Hilbert space to accommodate parity, a feature absent in the massive case, is described. Section 4 shows

how one can construct an $SU(2)$ Lie algebra of operators, in a momentum dependent way, to act on the polarization states of a photon for each fixed energy momentum. Here again the important role of the parity operator P is seen. This construction too has to be done avoiding singularities which would naively occur due to the nontrivial topological features involved. What emerges is that there is no universal or global $SU(2)$ lying behind these momentum dependent constructions, and at the same time there is considerable freedom in the details of the constructions. Section 5 contains some concluding remarks.

2. Notations and the timelike UIR's of $\mathscr{P}$

We begin with some notational preliminaries. The Lorentzian metric will be chosen to be spacelike, with $g_{\mu\nu} = \mathrm{diag}(-1, 1, 1, 1)$, $\mu, \nu = 0, 1, 2, 3$. The two-to-one homomorphism from $SL(2, C)$ to $SO(3, 1)$ is given as follows:

$$\begin{aligned} A \in SL(2, C)\colon\ & A\sigma_\mu A^\dagger = \Lambda(A)^\nu{}_\mu \sigma_\nu, \\ & Ap\cdot\sigma A^\dagger = (\Lambda(A)p)\cdot\sigma, \\ & p\cdot\sigma = p^0\cdot 1 + \mathbf{p}\cdot\boldsymbol{\sigma}, \\ & \Lambda(A) \in SO(3, 1), \\ & \Lambda(A')\Lambda(A) = \Lambda(A'A). \end{aligned} \tag{2.1}$$

Here $\sigma_0 = 1$ and $\boldsymbol{\sigma}$ are the usual Pauli matrices, and p^μ is any (real) four-vector. In any unitary representation (UR) or UIR of $\mathscr{P}$, we have ten hermitian generators $M_{\mu\nu} = -M_{\nu\mu}, P_\mu$ obeying the standard commutation relations

$$\begin{aligned} [M_{\mu\nu}, M_{\rho\sigma}] &= i(g_{\mu\rho}M_{\nu\sigma} - g_{\nu\rho}M_{\mu\sigma} + g_{\mu\sigma}M_{\rho\nu} - g_{\nu\sigma}M_{\rho\mu}), \\ [M_{\mu\nu}, P_\rho] &= i(g_{\mu\rho}P_\nu - g_{\nu\rho}P_\mu), \\ [P_\mu, P_\nu] &= 0. \end{aligned} \tag{2.2}$$

The six components of $M_{\mu\nu}$ generate homogeneous Lorentz transformations and the four P_μ generate space-time translations. In our work we will also have to deal directly with unitary operators $\bar{U}(A)$ representing finite elements of $SL(2, C)$. Using the split notation $M_{jk} = \varepsilon_{jkl}J_l, M_{0j} = K_j$, $j, k, l = 1, 2, 3$, we have for any real three-vectors $\boldsymbol{\alpha}, \mathbf{v}$ the identifications

$$\begin{aligned} \bar{U}(e^{i\boldsymbol{\alpha}\cdot\boldsymbol{\sigma}/2}) &= e^{i\boldsymbol{\alpha}\cdot\mathbf{J}}, \\ \bar{U}(e^{-\mathbf{v}\cdot\boldsymbol{\sigma}/2}) &= e^{i\mathbf{v}\cdot\mathbf{K}}, \end{aligned} \tag{2.3}$$

and the general transformation law for P^μ

$$\bar{U}(A)^{-1} P^\mu \bar{U}(A) = \Lambda(A)^\mu{}_\nu P^\nu. \tag{2.4}$$

Thus if $|p, \ldots\rangle$ is an eigenstate of the energy momentum operators P^μ with eigenvalues p^μ, we have the general rule (up to possible phases and normalization)

$$\begin{aligned} \bar{U}(A)|p, \ldots\rangle &= |p', \ldots\rangle, \\ p' &= \Lambda(A)p. \end{aligned} \tag{2.5}$$

When the action by parity P is defined, it has the following effects

$$P\bar{U}(A)P^{-1} = \bar{U}(A^{\dagger -1}),$$

$$P\mathbf{J}P^{-1} = \mathbf{J},$$

$$P\mathbf{K}P^{-1} = -\mathbf{K},$$

$$P(P^0, \mathbf{P})P^{-1} = (P^0, -\mathbf{P}). \tag{2.6}$$

For a numerical four-vector $p = (p^0, \mathbf{p})$, we shall always write $\tilde{p} = (p^0, -\mathbf{p})$. Then to accompany eq. (2.5) we have, when P is defined,

$$P|p, \ldots\rangle = |\tilde{p}, \ldots\rangle. \tag{2.7}$$

Given any UR of $\mathscr{P}$, the Pauli Lubanski pseudo vector W_μ is defined by

$$W_\mu = \tfrac{1}{2}\varepsilon_{\mu\nu\rho\sigma}M^{\nu\rho}P^\sigma,$$

$$\varepsilon_{0123} = +1, \tag{2.8}$$

and is orthogonal to P^μ. Then the two Casimir invariants for $\mathscr{P}$ are

$$\mathscr{C}_1 = -P^\mu P_\mu,$$

$$\mathscr{C}_2 = W^\mu W_\mu. \tag{2.9}$$

In a UIR of $\mathscr{P}$, both reduce to numbers.

The positive energy timelike UIR's may be labelled by the pair $\{m, s\}$, where $m > 0$ is the rest mass and $s = 0, 1/2, 1, \ldots$ the intrinsic spin. The Casimir invariants have the values

$$\{m, s\}: \mathscr{C}_1 = m^2, \quad \mathscr{C}_2 = m^2 s(s+1). \tag{2.10}$$

In this UIR, P^μ and W^μ are respectively positive timelike and spacelike four-vectors with, however, noncommuting components for W^μ (unless $s = 0$, when W_μ vanishes). The rest-frame energy-momentum, from which all others in this UIR can be obtained by suitable Lorentz transformations, will be written as $p^{(0)}$

$$p^{(0)} = (m, 0, 0, 0). \tag{2.11}$$

The corresponding stability subgroup of $SL(2, C)$ is $SU(2)$

$$Ap^{(0)}\cdot\sigma A^\dagger = p^{(0)}\cdot\sigma \Leftrightarrow A = a \in SU(2). \tag{2.12}$$

An (ideal) basis of momentum eigenstates for the Hilbert space $\mathscr{H}(\{m, s\})$ carrying this UIR may be built up as follows, starting with the vectors $|p^{(0)}, s_3\rangle$ describing a spin s particle at rest [6]. These vectors are characterized by their behaviour under rest-frame rotations, i.e., elements of $SU(2)$:

$$a \in SU(2): \bar{U}(a)|p^{(0)}, s_3\rangle = \sum_{s_3'} D^{(s)}_{s_3' s_3}(a)|p^{(0)}, s_3'\rangle, \tag{2.13}$$

where $D(a)$ is the unitary matrix representing $a \in SU(2)$ in the $(2s+1)$-dimensional spin s UIR of $SU(2)$. Going on now to general energy-momentum we have

$$p = (p^0, \mathbf{p}), \quad p^0 = (m^2 + \mathbf{p}^2)^{1/2}:$$

$$|p, s_3\rangle = \bar{U}(l(p))|p^{(0)}, s_3\rangle, s_3 = s, s-1, \ldots, -s,$$

$$l(p) = \frac{1}{[2m(m+p^0)]^{1/2}}(m + p\cdot\sigma)$$

$$= (p + p^{(0)})\cdot\sigma/[2m(m+p^0)]^{1/2},$$

$$l(p^{(0)}) = 1,$$

$$l(p)p^{(0)}\cdot\sigma l(p)^\dagger = p\cdot\sigma,$$

$$P^\mu|p, s_3\rangle = p^\mu|p, s_3\rangle,$$

$$\langle p', s_3'|p, s_3\rangle = p^0\cdot\delta_{s_3's_3}\delta^{(3)}(\mathbf{p}' - \mathbf{p}). \tag{2.14}$$

A general vector $|\psi\rangle \in \mathscr{H}(\{m, s\})$ has a $(2s+1)$-component momentum space wave function $\psi_{s_3}(\mathbf{p})$ and squared norm given by

$$\langle p, s_3|\psi\rangle = \psi_{s_3}(\mathbf{p}),$$

$$\langle\psi|\psi\rangle = \int \frac{d^3p}{p^0}\sum_{s_3}|\psi_{s_3}(\mathbf{p})|^2. \tag{2.15}$$

The action of $\bar{U}(A)$ on $|p, s_3\rangle$ for general $A \in SL(2, C)$ involves the Wigner rotation, an element of $SU(2)$ acting on the spin projection s_3:

$$\bar{U}(A)|p, s_3\rangle = \sum_{s_3'} D^{(s)}_{s_3's_3}(a(p, A))|p', s_3'\rangle,$$

$$p' = \Lambda(A)p,$$

$$a(p, A) = l(p')^{-1}Al(p) \in SU(2). \tag{2.16}$$

In case $p = p^{(0)}$ and $A \in SU(2)$, we have the simplifications $p' = p^{(0)}$, $a(p^{(0)}, A) = A$, so we recover eq. (2.13).

We notice (as is well known) that the pure Lorentz transformation $l(p)$ given in eq. (2.14) is globally well-defined and singularity free for all $\mathbf{p} \in \mathscr{R}^3$. Related to this is the fact that in the UIR $\{m, s\}$ of $\mathscr{P}$, one can introduce well-defined hermitian position, momentum and spin operators $\mathbf{q}, \mathbf{p}, \mathbf{S}$ out of which all the generators $M_{\mu\nu}$, P_μ of $\mathscr{P}$ can be constructed. The nonvanishing fundamental or primitive commutation relations are

$$[q_j, p_k] = i\delta_{jk}, [S_j, S_k] = i\varepsilon_{jkl}S_l. \tag{2.17}$$

In the momentum basis subject to the normalization given in eq. (2.14) we have

$$\mathbf{q} = i\left(\frac{\partial}{\partial\mathbf{p}} - \frac{1}{2}\frac{\mathbf{p}}{(p^0)^2}\right). \tag{2.18}$$

Starting from the irreducible set $\mathbf{q}, \mathbf{p}, \mathbf{S}$ (where $\mathbf{S}$ generate the spin s UIR of $SU(2)$) we can reconstruct the generators of $\mathscr{P}$ via

$$P^\mu = ((m^2 + \mathbf{p}^2)^{1/2}, \mathbf{p}),$$

$$\mathbf{J} = \mathbf{q} \wedge \mathbf{p} + \mathbf{S},$$

$$\mathbf{K} = \frac{1}{2}\{p^0, \mathbf{q}\} + \frac{\mathbf{p} \wedge \mathbf{S}}{m + p^0}. \tag{2.19}$$

Conversely, $\mathbf{q}, \mathbf{p}$ and $\mathbf{S}$ can be recovered from $M_{\mu\nu}, P_\mu$. This is the so-called Shirokov–Foldy form for the generators of $\mathscr{P}$ in the UIR $\{m, s\}$ [7]. (In the massless finite helicity UIR's, however, no such clean separation of primitive dynamical variables and generators is possible). The action of parity, P, can be taken to be

$$P|p, s_3\rangle = \eta|\tilde{p}, s_3\rangle, \tag{2.20}$$

where $\eta = \pm 1$ is the intrinsic parity. No enlargement of the representation space $\mathscr{H}(\{m, s\})$ is needed, and we have consistency with eqs. (2.6) and (2.7).

3. The lightlike UIR's of $\mathscr{P}$ and the parity doubling

Now we turn to the mass zero finite helicity UIR's of $\mathscr{P}$, to be denoted $\{0, \lambda\}$ with the helicity $\lambda = 0, \pm 1/2, \pm 1, \ldots$. In such a UIR, λ has a fixed value; for definiteness we assume it is nonzero and integral. For photons we need just $\lambda = \pm 1$. In the UIR $\{0, \lambda\}$ both Casimir operators $\mathscr{C}_1$ and $\mathscr{C}_2$ vanish, while the pseudovector W_μ becomes a multiple of P_μ:

$$\{0, \lambda\}: \mathscr{C}_1 = \mathscr{C}_2 = 0,$$

$$W_\mu = \lambda P_\mu. \tag{3.1}$$

This explains why parity P cannot be defined within the space of a single UIR $\{0, \lambda\}$. For the present we will work with a single UIR with fixed λ, and at the end of this section we will turn to the question of accommodating parity.

Towards setting up a basis of energy-momentum eigenfunctions for the Hilbert space $\mathscr{H}(\{0, \lambda\})$ carrying the UIR $\{0, \lambda\}$, analogous to eq. (2.14) for $\mathscr{H}(\{m, s\})$, we begin by noting that the set Σ of all positive lightlike energy-momentum four-vectors is

$$\Sigma = \{p \in \mathscr{R}^4 | p^\mu p_\mu = 0, p^0 > 0\} \tag{3.2}$$

which is topologically nontrivial, since it is essentially $\mathscr{R}^3 - \{\mathbf{0}\}$ [8]. It is therefore convenient to express Σ as the union of two overlapping open subsets Σ_N, Σ_S, each of which is topologically trivial. Using the light cone combinations $p_\pm = p^0 \pm p_3$, we define

$$\Sigma_N = \{p \in \Sigma | p_+ > 0\},$$

$$\Sigma_S = \{p \in \Sigma | p_- > 0\},$$

$$\Sigma = \Sigma_N \cup \Sigma_S;$$

$$\Sigma_N \cap \Sigma_S = \{p \in \Sigma | p_\perp = (p_1, p_2) \neq 0\}. \tag{3.3}$$

The subscripts N, S indicate that the North pole on S^2 is included in Σ_N, the South pole in Σ_S.

Now we need to choose a standard or fiducial energy-momentum four-vector $p^{(0)}$, to replace the choice (2.11) in the time like case. We take $p^{(0)}$ to be

$$p^{(0)} = (1, 0, 0, 1). \tag{3.4}$$

have

$$\tilde{p}^{(0)} = (1, 0, 0, -1);$$

$$p^{(0)} \in \Sigma_N,\ \notin \Sigma_S;\ \tilde{p}^{(0)} \in \Sigma_S,\ \notin \Sigma_N. \tag{3.5}$$

Indeed, the p's omitted from $\Sigma_N(\Sigma_S)$ are all positive multiples of $\tilde{p}^{(0)}(p^{(0)})$. The stability subgroup of $p^{(0)}$ is an $E(2)$ subgroup in $SL(2, C)$

$$Ap^{(0)} \cdot \sigma A^{\dagger} = p^{(0)} \cdot \sigma \Leftrightarrow$$

$$A = h(\varphi, \alpha) \in E(2) \subset SL(2, C),$$

$$h(\varphi, \alpha) = \begin{pmatrix} e^{i\varphi/2} & \alpha \\ 0 & e^{-i\varphi/2} \end{pmatrix},$$

$$0 \leqslant \varphi \leqslant 4\pi, \quad \alpha \in \mathscr{C}. \tag{3.6}$$

The topological nontriviality of Σ is the same as that of the coset space $SL(2, C)/E(2)$, since $\Sigma \simeq SL(2, C)/E(2)$.

In the space of the UIR $\{0, \lambda\}$ the fiducial energy momentum eigenvector $|p^{(0)}, \lambda\rangle$ is characterized by the fact that it provides a one-dimensional representation of $E(2)$,

$$\bar{U}(h(\varphi, \alpha))|p^{(0)}, \lambda\rangle = e^{i\lambda\varphi}|p^{(0)}, \lambda\rangle. \tag{3.7}$$

In terms of the infinitesimal generators $\mathbf{J}, \mathbf{K}$ of rotations and pure Lorentz transformations, this means

$$J_3|p^{(0)}, \lambda\rangle = \lambda|p^{(0)}, \lambda\rangle,$$

$$(J_1 + K_2)|p^{(0)}, \lambda\rangle = (J_2 - K_1)|p^{(0)}, \lambda\rangle = 0. \tag{3.8}$$

These eqs (3.7), (3.8) are the replacements for the earlier eq. (2.13) in the timelike case. Now we need to find, for each $p \in \Sigma$, an $SL(2, C)$ element whose associated Lorentz transformation will carry $p^{(0)}$ to p: this will enable us to set up other energy-momentum eigenvectors $|p, \lambda\rangle$, and so build up a basis for $\mathscr{H}(\{0, \lambda\})$, similar to (2.14). However, in contrast to the timelike case this cannot be done in a globally smooth manner for all $p \in \Sigma$ [8]. This again is a consequence of the nontrivial topology of $\Sigma \simeq SL(2, C)/E(2)$. The problem has to be handled separately over each of Σ_N, Σ_S. To prepare for this, we employ the usual spherical polar angles θ, ϕ on S^2 and define the unit vector $\mathbf{n}(\theta, \phi)$ and an element $a(\theta, \phi) \in SU(2)$ as follows:

$$0 \leqslant \theta \leqslant \pi, \quad 0 \leqslant \phi \leqslant 2\pi:$$

$$\mathbf{n}(\theta, \phi) = \mathbf{n}(2\pi - \theta, \pi + \phi) = -\mathbf{n}(\pi - \theta, \pi + \phi)$$

$$= (\sin\theta\cos\phi, \sin\theta\sin\phi, \cos\theta);$$

$$a(\theta, \phi) = a(-\theta, \pi + \phi) = \exp\left[\frac{i\theta}{2}(\sigma_1 \sin\phi - \sigma_2 \cos\phi)\right] \in SU(2). \tag{3.9}$$

We express a general p as $p^0(1, \mathbf{n}(\theta, \phi))$ and see that Σ_N, Σ_S correspond to $0 \leqslant \theta < \pi$, $0 < \theta \leqslant \pi$ respectively. Whereas $\mathbf{n}(\theta, \phi)$ is well-defined all over S^2, $a(\theta, \phi)$ is undefined at $\theta = \pi$ (south pole). For a general $\mathbf{n} \in S^2$ we have

$$a(\theta, \phi)\mathbf{n}\cdot\boldsymbol{\sigma}a(\theta, \phi)^\dagger = \mathbf{n}'\cdot\boldsymbol{\sigma}, \quad \mathbf{n}' = (\text{right handed rotation by angle } \theta \text{ about } (-\sin\phi, \cos\phi, 0))\mathbf{n}. \tag{3.10}$$

So in particular we get the useful relation

$$a(\theta, \phi)\mathbf{n}(\theta', \phi)\cdot\boldsymbol{\sigma}a(\theta, \phi)^\dagger = \mathbf{n}(\theta' + \theta, \phi)\cdot\boldsymbol{\sigma}. \tag{3.11}$$

Now a possible solution to the problem of constructing Lorentz transformations connecting $p^{(0)}$ to all $p \in \Sigma$ is given by using separate boost and rotation factors in a step-by-step manner

$$p \in \Sigma_N: \; l(p) = a(\theta, \phi)\exp(\tfrac{1}{2}\ln p^0 \cdot \sigma_3),$$

$$l(p)p^{(0)}\cdot\sigma l(p)^\dagger = p\cdot\sigma; \tag{3.12a}$$

$$p \in \Sigma_S: \; l'(p) = a(\theta - \pi, \phi)\exp(-\tfrac{1}{2}\ln p^0 \cdot \sigma_3)\, i\sigma_2,$$

$$l'(p)p^{(0)}\cdot\sigma l'(p)^\dagger = p\cdot\sigma. \tag{3.12b}$$

(Once again, the use of the symbol $l(p)$ here should not cause any confusion with its use earlier in § 2.) In the structure of $l'(p)$, the purpose of the first factor $i\sigma_2$ is to switch $p^{(0)}$ to $\tilde{p}^{(0)}$, and then the rest follows easily. As is to be expected, in the overlap $\Sigma_N \cap \Sigma_S$, $l(p)$ and $l'(p)$ differ by an $E(2)$ element on the right

$$p \in \Sigma_N \cap \Sigma_S: l'(p) = l(p)h(2(\pi - \phi), 0). \tag{3.13}$$

We also have the particular values

$$l(p^{(0)}) = 1,$$

$$l'(\tilde{p}^{(0)}) = i\sigma_2. \tag{3.14}$$

With the aid of these definitions we can set up a basis of energy-momentum eigenvectors for $\mathscr{H}(\{0, \lambda\})$ as

$$p \in \Sigma_N: |p, \lambda\rangle = \bar{U}(l(p))|p^{(0)}, \lambda\rangle = \bar{U}(a(\theta, \phi))e^{-iK_3 \ln p^0 \cdot}|p^{(0)}, \lambda\rangle;$$

$$p \in \Sigma_S: |p, \lambda\rangle' = \bar{U}(l'(p))|p^{(0)}, \lambda\rangle = \bar{U}(a(\theta - \pi, \phi))\cdot e^{iK_3 \ln p^0 \cdot} e^{i\pi J_2}|p^{(0)}, \lambda\rangle;$$

$$p \in \Sigma_N \cap \Sigma_S: |p, \lambda\rangle' = e^{-2i\lambda\phi}|p, \lambda\rangle;$$

$$P^\mu(|p, \lambda\rangle \text{ or } |p, \lambda\rangle') = p^\mu(|p, \lambda\rangle \text{ or } |p, \lambda\rangle'). \tag{3.15}$$

The overlap or transition rule results from eqs (3.7), (3.13). These definitions may be supplemented by the inner products

It is always implied that in $|p,\lambda\rangle(|p,\lambda\rangle')$ the argument p is restricted to $\Sigma_N(\Sigma_S)$. A general $|\psi\rangle\in\mathscr{H}(\{0,\lambda\})$ has a single component momentum space wave function and squared norm given by

$$\psi(\mathbf{p}) = \langle p,\lambda|\psi\rangle,$$
$$\langle\psi|\psi\rangle = \int\frac{\mathrm{d}^3p}{p^0}|\psi(\mathbf{p})|^2. \tag{3.17}$$

Here since the part of Σ omitted in Σ_N is a set of measure zero as far as the integral is concerned, we have used only the basis kets $|p,\lambda\rangle$. Moreover, starting from (3.7) and following through the definitions (3.15), one checks that

$$J_3|p^{(0)},\lambda\rangle = \lambda|p^{(0)},\lambda\rangle;$$
$$\mathbf{J}\cdot\mathbf{p}/p^0|p,\lambda\rangle = \lambda|p,\lambda\rangle,$$
$$\mathbf{J}\cdot\mathbf{p}/p^0|p,\lambda\rangle' = \lambda|p,\lambda\rangle'. \tag{3.18}$$

For a general $A\in SL(2,C)$, the action of $\bar{U}(A)$ on $|p,\lambda\rangle$ or $|p,\lambda\rangle'$ can be computed in a manner similar to the steps leading to (2.16). If $p' = \Lambda(A)p$ is in the overlap $\Sigma_N\cap\Sigma_S$, the result can be expressed as a "Wigner phase" times $|p',\lambda\rangle$ or equally well as another "Wigner phase" times $|p',\lambda\rangle'$; on the other hand, if p is a multiple of either $p^{(0)}$ or $\tilde{p}^{(0)}$, the result can be written in only one way. Since we do not need these results explicitly, we omit the details.

The choices for $l(p)$, $l'(p)$ in eqs (3.12) were based on simple step-by-step constructions to lead from $p^{(0)}$ to p. Alternative choices, $\tilde{l}(p)$ and $\tilde{l}'(p)$ say, more in the spirit of the expressions in (2.14) in the timelike case, are also available [9]

$$p\in\Sigma_N\colon\ \tilde{l}(p) = \frac{1}{\sqrt{2p_+}}(1-\sigma_3+\sigma\cdot p) = \frac{1}{\sqrt{2p_+}}(\tilde{p}^{(0)}+p)\cdot\sigma;$$
$$p\in\Sigma_S\colon\ \tilde{l}'(p) = \frac{1}{\sqrt{2p_-}}(1+\sigma_3-\sigma\cdot p)\sigma_1 = \frac{1}{\sqrt{2p_-}}(p^{(0)}-p)\cdot\sigma\sigma_1;$$
$$p\in\Sigma_N\cap\Sigma_S\colon\ \tilde{l}'(p) = \tilde{l}(p)h(2(\pi-\phi),2(1-p_3)/|p_\perp|). \tag{3.19}$$

Again, these choices are $E(2)$-related to the earlier ones

$$\tilde{l}(p) = l(p)h(0,(1+1/p^0)\cdot\tan\theta/2\cdot\mathrm{e}^{-i\phi}),$$
$$\tilde{l}'(p) = l'(p)h(0,(1-1/p^0)\cdot\cot\theta/2\cdot\mathrm{e}^{i\phi}). \tag{3.20}$$

Since $0\leqslant\theta<\pi$ in the first case and $0<\theta\leqslant\pi$ in the second, these expressions are well-defined in their respective domains. Here the angle arguments in $h(\ldots,\ldots)$ turn out to vanish, hence we get *exactly the same* energy-momentum eigenvectors as before, i.e.

$$\bar{U}(\tilde{l}(p))|p^{(0)},\lambda\rangle = \bar{U}(l(p))|p^{(0)},\lambda\rangle = |p,\lambda\rangle,$$
$$\bar{U}(\tilde{l}'(p))|p^{(0)},\lambda\rangle = \bar{U}(l'(p))|p^{(0)},\lambda\rangle = |p,\lambda\rangle'. \tag{3.21}$$

Having exhibited these alternative choices, we now revert to the earlier ones.

So far the analysis has been limited to the single UIR $\{0, \lambda\}$ of $\mathscr{P}$ for a fixed value of λ. To accommodate parity P we have to adjoin the inequivalent UIR $\{0, -\lambda\}$ and work in the doubled Hilbert space $\mathscr{H}(\{0,\lambda\}) \oplus \mathscr{H}(\{0,-\lambda\})$. This entails bringing in additional basis vectors $|p^{(0)}, -\lambda\rangle$, $|p, -\lambda\rangle$ and $|p, -\lambda\rangle'$ for $\mathscr{H}(\{0,-\lambda\})$ exactly as in (3.15). In this extended space we fix the action of P by assuming $P^2 = 1$ and setting

$$P|p^{(0)}, \pm\lambda\rangle = |\tilde{p}^{(0)}, \mp\lambda\rangle'. \tag{3.22}$$

We need not include an intrinsic parity factor η here as was done in (2.20) since in any case P switches vectors in the two subspaces $\mathscr{H}(\{0, \pm\lambda\})$. One can now follow through the consequences of (3.22) by exploiting the basic relations (2.6) and the constructions (3.15) in each subspace to obtain

$$\begin{aligned} P|p, \pm\lambda\rangle &= |\tilde{p}, \mp\lambda\rangle', \\ P|p, \pm\lambda\rangle' &= |\tilde{p}, \mp\lambda\rangle. \end{aligned} \tag{3.23}$$

To these we adjoin the helicity statements in the extended space

$$\mathbf{J}\cdot\mathbf{p}/p^0(|p, \pm\lambda\rangle \text{ or } |p, \pm\lambda\rangle') = \pm\lambda(|p, \pm\lambda\rangle \text{ or } |p, \pm\lambda\rangle'). \tag{3.24}$$

For photons, we take $\lambda = 1$: then $|p, \pm 1\rangle$, $|p, \pm 1\rangle'$ correspond respectively to right and left circular polarizations.

4. $SU(2)$ generators on the polarization space

For fixed $p \in \Sigma$, the two polarization states $|p, \pm\lambda\rangle$ (or $|p, \pm\lambda\rangle'$) form a basis for a two-dimensional polarization space. The existence of a group of $SU(2)$ transformations acting on this space is obvious. Our aim is to see how to construct the generators of this $SU(2)$ out of the generators of $\mathscr{P}$ and parity P. From (3.24) the helicity operator is already diagonal in this space and acts like the third Pauli matrix σ_3. We need to build up analogues to σ_1 and σ_2.

Now we notice that parity P switches helicity $\pm\lambda$ to $\mp\lambda$, but at the same time changes $p = (p^0, \mathbf{p})$ to $\tilde{p} = (p^0, -\mathbf{p})$. We must therefore supplement action by P with a spatial rotation by amount π, about some axis perpendicular to $\mathbf{p}$, which will bring $-\mathbf{p}$ back to $\mathbf{p}$ but leave helicity unaltered. Here we face the same topological problem which has appeared earlier in another guise – it is impossible to find a $\mathbf{p}$-dependent (unit) vector perpendicular to $\mathbf{p}$, for all $\mathbf{p} \in S^2$, in a singularity-free manner. However such nonsingular choices are available on Σ_N, Σ_S separately. We define $\mathbf{e}(p)$, $\mathbf{e}'(p)$ as follows:

$$p \in \Sigma_N: \mathbf{e}(p) = \mathbf{n}\left(\frac{\pi}{2}, 0\right) - 2\sin\frac{\theta}{2}\cos\phi\,\mathbf{n}\left(\frac{\theta}{2}, \phi\right),$$

$$|\mathbf{e}(p)| = 1, \quad \mathbf{p}\cdot\mathbf{e}(p) = 0; \tag{4.1a}$$

$$p \in \Sigma_S: \mathbf{e}'(p) = \mathbf{n}(\pi/2, 0) - 2\cos\frac{\theta}{2}\cos\phi\,\mathbf{n}(\tfrac{1}{2}(\pi+\theta), \phi),$$

$$|\mathbf{e}'(p)| = 1, \quad \mathbf{p}\cdot\mathbf{e}'(p) = 0. \tag{4.1b}$$

These are by no means unique but suffice for our purposes; each is also unambiguously defined in the corresponding domain. Starting with $p\in\Sigma_N$ we develop

$$\begin{aligned} e^{i\pi e(p)\cdot J} P|p, \pm\lambda\rangle &= e^{i\pi e(p)\cdot J}|\tilde{p}, \mp\lambda\rangle' \\ &= e^{i\pi e(p)\cdot J}\bar{U}(a(-\theta,\pi+\phi))\cdot e^{iK_3\ln p^0}\cdot e^{i\pi J_2}|p^{(0)}, \mp\lambda\rangle \\ &= e^{i\pi e(p)\cdot J}\bar{U}(a(\theta,\phi))e^{i\pi J_2}\cdot e^{-iK_3\ln p^0}\cdot|p^{(0)}, \mp\lambda\rangle \\ &= \bar{U}(a(\theta,\phi))\cdot\bar{U}(a(\theta,\phi)^{-1}\cdot e^{(i\pi/2)e(p)\cdot\sigma}\cdot a(\theta,\phi) \\ &\quad\times e^{(i\pi/2)\sigma_2})\cdot e^{-iK_3\ln p^0}|p^{(0)}, \mp\lambda\rangle. \end{aligned} \tag{4.2}$$

The $SU(2)$ element appearing here can be simplified after some algebra and use of (3.11) to give

$$\begin{aligned} &a(\theta,\phi)^{-1}\cdot e^{(i\pi/2)e(p)\cdot\sigma}\cdot a(\theta,\phi)\cdot e^{(i\pi/2)\sigma_2} \\ &= a(\theta,\phi)^{-1} i\mathbf{e}(p)\cdot\boldsymbol{\sigma} a(\theta,\phi) i\sigma_2 \\ &= -i\sigma_3 = e^{-(i\pi/2)\sigma_3}. \end{aligned} \tag{4.3}$$

Using this in (4.2) we get

$$\begin{aligned} e^{i\pi e(p)\cdot J} P|p, \pm\lambda\rangle &= \bar{U}(a(\theta,\phi))\cdot e^{-i\pi J_3 - iK_3\ln p^0}\cdot|p^{(0)}, \mp\lambda\rangle \\ &= e^{i\pi\lambda}|p, \mp\lambda\rangle. \end{aligned} \tag{4.4}$$

By analogous calculations for $p\in\Sigma_S$ we again find

$$e^{i\pi e'(p)\cdot J} P|p, \pm\lambda\rangle' = e^{i\pi\lambda}|p, \mp\lambda\rangle'. \tag{4.5}$$

Thus these operator expressions act essentially like the first Pauli matrix σ_1 in the polarization space.

For photons we set $\lambda = 1$. At each fixed p, we may then make the following identifications

$$\begin{aligned} \mathbf{J}\cdot\mathbf{p}/p_0 &\to \sigma_3, \\ -e^{i\pi e(p)\cdot J} P &\to \sigma_1, \\ i\frac{\mathbf{J}\cdot\mathbf{p}}{p^0} e^{i\pi e(p)\cdot J} P &\to \sigma_2. \end{aligned} \tag{4.6}$$

Here for definiteness we assumed $p\in\Sigma_N$. The meaning is that we are working in a basis of circular polarization states, and in that basis the Hilbert space operators standing on the left reduce in their actions to the Pauli matrices on the right. Apart from factors of $\frac{1}{2}$, these are the generators of the group of $SU(2)$ transformations familiar in polarization optics.

In the correspondence (4.6) only $\mathbf{J}$ and P are to be treated as Hilbert space operators while p^μ are c-numbers. One may wonder whether the latter could be replaced by the operators P^μ, and whether one would then somehow obtain an $SU(2)$ algebra not tied down to basis states $|p, \pm\lambda\rangle$ for specific p^μ. This however does not work out due to operator ordering problems. One is obliged to *first* pick some numerical p^μ, and then use the correspondence (4.6) *only* for action on the states $|p, \pm\lambda\rangle, |p, \pm\lambda\rangle'$.

5. Concluding remarks

In this paper we have focussed on the operator aspects of the description of photon polarization states, taking as primary inputs the concerned UIR's of $\mathscr{P}$, the operators available in such representations, and the parity operation. This is in the spirit of the definition of elementary systems in relativistic quantum mechanics. We have highlighted many novel features that arise in the treatment of massless particles as compared to massive ones, which can all be traced back to the nontrivial topology of the coset space $SL(2, C)/E(2)$, or of the positive light cone with tip removed. We have emphasized the crucial role played by the parity operation in being able to create a two-dimensional polarization space, and in the construction of operators realizing the $SU(2)$ Lie algebra on this space, at each fixed energy-momentum. In a general sense, we can say that while for electrons the operator description of spin precedes the description in terms of spin states, for photons it is usually the description of various polarization states that is physically immediate. We have tried here to supplement this by an operator description in as straightforward a manner as possible.

Our handling of the topological features involved, and avoidance of singularities in expressions, leaves considerable freedom in the choices of coset representatives $l(p)$, $l'(p)$, fields of vectors $\mathbf{e}(p)$, $\mathbf{e}'(p)$ perpendicular to $\mathbf{p}$, etc. What must be clear is that there is an essential momentum dependence in these constructions which cannot be eliminated. For each $p \in \Sigma$, we do have an $SU(2)$ group acting on the corresponding polarization space; however, these various $SU(2)$'s are not representatives of any single natural globally defined $SU(2)$ at all. In particular there is no relation to the geometrical group of rigid rotations in physical space, as there is in the definition of spin for massive particles.

This helps us answer a question which is not as naive as one may at first imagine. Suppose we have two photons with distinct energy momenta p, p' respectively. Can one treat their separate two-dimensional polarization state spaces as though they were like spin half particle states, couple the two photon polarizations to "total spins" 1 or 0, and handle them just as one would handle the spins of two electrons? The answer is that this is not physically well founded, since the $SU(2)$ groups involved are momentum dependent; there is little meaning to the action of "one and the same $SU(2)$ element" on both photon polarizations on account of the conventions and freedoms involved in identifying the $SU(2)$ generators for each p.

References

[1] E P Wigner, *Ann. Math.* **40**, 149 (1939);
R F Streater and A S Wightman, *PCT, Spin and Statistics, and all that* (W A Benjamin Inc., New York, 1964), ch. 1

[2] These have been discussed in, for example, N Mukunda, *Ann. Phys. (NY)* **61**, 329 (1970) and other references cited therein

[3] T D Newton and E P Wigner, *Rev. Mod. Phys.* **21**, 400 (1949)

[4] See, for instance, ref. [2]

[5] For general introductions to polarization optics one may see R M A Azzam and N M Bashara, *Ellipsometry and Polarized Light* (North-Holland, Amsterdam, 1977
W Swindell (ed), *Polarized Light* (Dowden, Hutchinson and Ross, Stroudsburg, PA, 1975)

[6] A S Wightman, in *Relations de dispersion et particules elementaires*, Les Houches (Paris, Hermann, 1960)
[7] Iu M Shirokov, *Dokl. Acad. Nauk. SSSR* **94**, 857 (1954); **97**, 737 (1954)
LL Foldy, *Phys. Rev.* **102**, 568 (1956)
[8] Some aspects of this situation have been examined in B Dutta and N Mukunda, *Pramana – J. Phys.* **29**, 437 (1987)
[9] These have been developed in refs. [2] and [8], though the notations are slightly different

— journal of
physics

Vol. 47, No. 5,
November 1996
pp. 361–369

Poincaré sphere representation for three state systems

JOSEPH SAMUEL
Raman Research Institute, Bangalore, 560 080, India

MS received 8 August 1996; revised 15 October 1996

Abstract. We point out that the Poincaré sphere can be used to represent the rays of a three state quantum system. Those interested in geometric phase phenomena may find this representation a useful aid to visualize the global structure of ray space.

Keywords. Quantum mechanics; ray space; Poincaré sphere.

PACS No. 03·65

1. Introduction

The Poincaré sphere [1] provides a simple and elegant geometric representation of the rays of a two state system. It was originally introduced in optics, in the context of polarized light and has subsequently been widely used [2]. More recently, the Poincaré sphere has become popular in studies of the geometric phase [3–12] for two state systems. This article shows how the Poincaré sphere can also be used to represent the rays of three or N state systems. There appears to be some current interest [13–15] in this question and we hope that the following exposition will be useful. We will assume that the reader is familiar with the Poincaré sphere for two state systems and with Pancharatnam's work [16, 17, 6, 7, 18, 19] on the interference of polarized light.

This presentation makes use of spinors. While two component (Weyl) spinors are used in some areas of general relativity, their application to the present situation may not be known in the geometric phase community. The purpose of this article is to bridge this gap. In § 2 we briefly summarize the spinorial formulae that will be used in § 3 to show how spinors can be used to represent the ray space of a three state system. Readers desiring to learn more about spinors should consult Penrose and Rindler [20] and Wald [21].

2. Spinorial preliminaries

Let (V, ε) be a two dimensional complex vector space, where ε is an antisymmetric nondegenerate bilinear form on V. Elements of V are called spinors and written ξ^A, $A = 1, 2$. ε provides a natural isomorphism between V and its dual V^*. 'Lowering the index' on ξ^A yields the element $\xi_A := \xi^B \varepsilon_{BA}$ in V^*. Note that $\xi^A \xi_A = 0$. It is usual to pick a basis (ι^A, o^A) in V so that $\iota^A o_A = 1$. Such a frame is called a spin frame. The group of transformations that leaves the structure (V, ε) invariant is $SL(2, \mathbb{C})$, the double cover of the Lorentz group.

One can similarly consider $\bar{V}$, the complex conjugate space of V, whose elements are written $\bar{\xi}^{A'} \in \bar{V}$ and the dual of $\bar{V}$, $\bar{V}^*$ with elements $\bar{\xi}_{A'} \in \bar{V}^*$. The $SL(2,\mathbb{C})$ spinors defined above (while suitable for applications to general relativity) are too general for our purpose. We need to introduce more structure (see p. 376 of ref. [21] or ref. [22]) and reduce the group down to $SU(2)$. This is done by introducing a positive definite, Hermitian inner product $G_{AA'}$ on V. The group of linear transformations on V that preserves both ε and $G_{AA'}$ is $SU(2)$. We can choose our spin frame so that [21]

$$G_{AA'} = \iota_A \iota_{A'} + o_A o_{A'}$$

and use $G_{AA'}$ to define a $\dagger$ operation on spinors.

$$\xi_A^\dagger = \bar{\xi}^{A'} G_{AA'}.$$

We will sometimes use Dirac notation $|\xi)$ for the element ξ^A of V and $(\xi|$ for the element $\xi_A^\dagger$ of V^*. Note that $(\xi|$ is not ξ_A, for $(\xi|\xi)$ is positive definite, whereas $\xi_A \xi^A$ vanishes.

Spinors have some features which take getting used to. These stem from the fact that indices are raised and lowered by an antisymmetric tensor rather than a symmetric one. Here are a few properties that the readers may find useful to verify:

1. $\xi^A \eta_A = -\xi_A \eta^A$. (This is sometimes referred to as 'Penrose's seesaw'.)
2. $\xi^{\dagger\dagger} = -\xi$.
3. $\xi^\dagger$ is orthogonal to ξ: $(\xi^\dagger|\xi) = 0$.

These are all straightforward consequences of the spinorial formalism.

A spinor κ^A can be thought of as representing the state of a spin half system. The ray κ corresponding to the state

$$\kappa^A = z\iota^A + o^A$$

can be represented by z, a point on the extended complex plane $\mathbb{C}^*$. (We allow the possibility $z = \infty$, which is needed to represent $\kappa^A = \iota^A$.) The extended complex plane $\mathbb{C}^*$ can be stereographically mapped onto the Poincaré sphere. The formula

$$z = \cot(\theta/2) e^{i\phi}$$

relates the stereographic coordinate z to the point p on the Poincaré sphere with polar coordinates, θ, ϕ. The group $SL(2,\mathbb{C})$, which acts on spinors, acts on the extended complex plane by Möbius transformations

$$z \to \frac{az+b}{cz+d}, \tag{1}$$

where a, b, c, d are the entries of the $SL(2,\mathbb{C})$ matrix. Composing (1) with the stereographic projection, we get an action of $SL(2,\mathbb{C})$ on the Poincaré sphere [20]. These maps are conformal transformations and map circles to circles on the Poincaré sphere. In the physical interpretation used by relativists, spinors represent null vectors (the momentum four vectors of photons) and rays represent points on the sky [20]. The action of $SL(2,\mathbb{C})$ on the Poincaré sphere can be physically realized as the aberration of light from the sky by Lorentz transformations.

The action of $\dagger$ on the Poincaré sphere is easy to visualize. By explicit computation, one sees that $\iota^\dagger = o, o^\dagger = -\iota$ and so, if $\xi^A = \alpha \iota^A + \beta o^A$,

Since $\xi^\dagger$ is clearly orthogonal to ξ, we see that $\dagger$ sends a point on the Poincaré sphere to its antipode. The subgroup of $SL(2,\mathbb{C})$ which preserves antipodality of points is $SU(2)$, which acts on the Poincaré sphere by rotations. With these preliminaries, we begin our discussion of three state systems.

3. Three state systems

For two state systems, the Poincaré sphere provides a representation of the ray space with the following properties:

P1. All rays of the system are represented exactly once.
P2. Neighboring rays are represented as neighboring points on the Poincaré sphere.

We would like to have a similar representation of the ray space of a three state system.

Since we are only interested in the geometry of the ray space (i.e., kinematic features of the Hilbert space, not dynamical ones like the Hamiltonian), we are free to make any convenient choice of system. The most convenient choice is a spin 1 system ($s = 1$). The physical idea underlying the following discussion is that a spin one ($s = 1$) particle can be thought of as a composite of two spin half ($s = 1/2$) particles. The antisymmetric tensor product of the states of a spin half system is (see p. 204 of ref. [23]) a singlet ($s = 0$) state and need not be further considered. We look at the symmetrized tensor product of spin half states and show how one represents these on the Poincaré sphere.

Let Ψ^{AB} be a symmetric spinor. $\mathscr{H} = V \otimes_s V$ is a three-dimensional complex vector space, whose elements we write in Dirac notation as $|\Psi\rangle$. Let us define

$$\Psi^\dagger_{AB} := \bar{\Psi}^{A'B'} G_{AA'} G_{BB'}.$$

We write elements $\Psi^\dagger_{AB}$ of $\mathscr{H}^*$ as $\langle\Psi|$ and $\Psi^\dagger_{AB}\Psi^{AB}$ as $\langle\Psi|\Psi\rangle$. The elements $(|e_1\rangle, |e_2\rangle, |e_3\rangle)$, where $e_1^{AB} := \iota^A\iota^B$, $e_2^{AB} := 1/\sqrt{2}(\iota^A o^B + \iota^B o^A)$ and $e_3 := o^A o^B$ form an orthonormal set in $\mathscr{H}$. Any element Ψ^{AB} of $\mathscr{H}$ can be expanded in this basis

$$\Psi^{AB} = \Psi^1 e_1^{AB} + \Psi^2 e_2^{AB} + \Psi^3 e_3^{AB}.$$

The inner product of $|\Psi\rangle$ with itself is

$$\langle\Psi|\Psi\rangle = \Psi^\dagger_{AB}\Psi^{AB} = \overline{\Psi^1}\Psi^1 + \overline{\Psi^2}\Psi^2 + \overline{\Psi^3}\Psi^3.$$

Thus $\mathscr{H}$ is a three dimensional complex vector space with a positive definite inner product and can be identified with the Hilbert space of any three state quantum system.

Let us now represent rays in $\mathscr{H}$ on the Poincaré sphere. Let Ψ^{AB} be an (unnormalized, nonzero) symmetric spinor. Consider the quadratic polynomial

$$f(z) = \Psi^{AB}\kappa_A\kappa_B, \tag{2}$$

where $\kappa_A = z\iota_A + o_A$. $f(z)$ has exactly two roots z_1 and z_2 on the extended complex plane and can be factorized as

$$f(z) = C(z - z_1)(z - z_2),$$

where C is a nonzero constant. Defining [21] (for $i = 1, 2$)

$$\kappa_{iA} = z_i\iota_A + o_A, \tag{3}$$

Figure 1. A general state of a three state system represented on the Poincaré sphere.

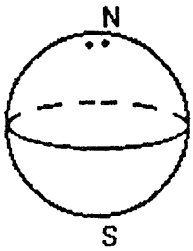

Figure 2. The basis vector $|e_1\rangle$.

we see that

$$z - z_i = \kappa_{iA}\kappa^A.$$

It follows that

$$f(z) = C(\kappa_1^A \kappa_2^B)\kappa_A \kappa_B$$

for any κ_A. Therefore Ψ^{AB} admits the decomposition

$$\Psi^{AB} = C(\kappa_1^A \kappa_2^B + \kappa_1^B \kappa_2^A). \tag{4}$$

(This is the decomposition used in the Petrov classification of gravitational fields [21].) The ray Ψ to which the vector Ψ^{AB} belongs uniquely determines a pair of rays κ_1, κ_2, which can be represented on the Poincaré sphere by points p_1, p_2. Interchanging p_1 and p_2 does not affect Ψ. So a ray of a three state system is represented (figure 1) by an unordered pair (p_1, p_2) (identified with (p_2, p_1)) of points on the Poincaré sphere. The ray space of a three state system is the same as the configuration space of two indistinguishable particles on the surface of a sphere. This is the main observation that we wish to make here.

Note that all rays of the three state system can be thus represented. Neighboring rays are represented by neighboring pairs of points on the Poincaré sphere. This representation correctly captures the global structure of CP^2 and is quite easy to visualize.

We now give a few examples of the general considerations above to gain familiarity with the use of the Poincaré sphere. Let us start with the rays containing the basis vectors: $|e_1\rangle = e_1^{AB} = \iota^A \iota^B$ is represented by two points at the north pole of the sphere. (see figure 2, which shows the points slightly separated for reasons of visibility). Similarly $|e_3\rangle = e_3^{AB} = o^A o^B$ is represented by two points at the south pole of the sphere (figure 3). $|e_2\rangle = 1/(\sqrt{2})(\iota^A o^B + \iota^B o^A)$ is represented by a point at each of the poles (figure 4). One also sees that a general linear combination $1/(\sqrt{2})(\sqrt{2}z|e_1\rangle + |e_2\rangle)$ of $|e_1\rangle$ and $|e_2\rangle$ is

$$\iota^A(z\iota^B + o^B) + \iota^B(z\iota^A + o^A).$$

The ray containing this state is shown in figure 5. The ray containing the state

$$o^A(z\iota^B + o^B) + o^B(z\iota^A + o^A) = 2(e_3^{AB} + \sqrt{2}ze_2^{AB})$$

Figure 3. The basis vector $|e_2\rangle$.

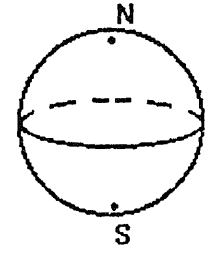

Figure 4. The basis vector $|e_3\rangle$.

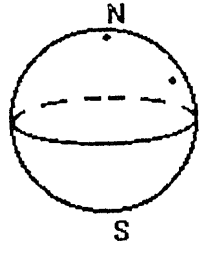

Figure 5. A general vector in the 1–2 plane.

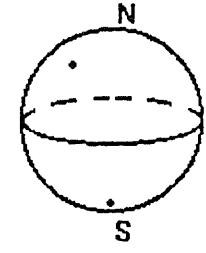

Figure 6. A general vector in the 2–3 plane.

which is in the 2–3 plane is shown in figure 6. Finally, the ray containing a state

$$2(-z^2 e_1^{AB} + e_3^{AB}) = (zl^A + o^A)(-zl^B + o^B) + (zl^B + o^B)(-zl^A + o^A)$$

in the 1–3 plane is represented by a pair of points (shown in figure 7) with the same lattitude but opposite longitudes.

4. Orthogonal rays

Let (p_1, p_2) and (p_3, p_4) be pairs of points representing two rays of a three state system. When are these rays orthogonal? The condition for orthogonality is

$$\kappa_{3A}^{\dagger}\kappa_{4B}^{\dagger}(\kappa_1^A\kappa_2^B + \kappa_1^B\kappa_2^A) = 0, \tag{5}$$

which can be written in Dirac notation as

$$(\kappa_3|\kappa_1)(\kappa_4|\kappa_2) + (\kappa_3|\kappa_2)(\kappa_4|\kappa_1) = 0. \tag{6}$$

To extract the geometrical interpretation of (6) multiply by $(\kappa_2|\kappa_3)(\kappa_1|\kappa_4)$ to rewrite (6) as

$$(\kappa_1|\kappa_4)(\kappa_4|\kappa_2)(\kappa_2|\kappa_3)(\kappa_3|\kappa_1) = -(\kappa_3|\kappa_2)(\kappa_2|\kappa_3)(\kappa_1|\kappa_4)(\kappa_4|\kappa_1). \tag{7}$$

The phase of such a chain of inner products is the geometric phase acquired by a system traversing the path 13241 on the Poincaré sphere. From Pancharatnam's rule [16] this is equal to the solid angle subtended by the broken geodesic curve 13241. The value of say $|\langle\kappa_1|\kappa_4\rangle|$ is $\cos(\delta(\kappa_1, \kappa_4)/2)$, where $\delta(\kappa_1, \kappa_4)$ is the angle between rays 1 and 4. Geometrically, $|\langle\kappa_1|\kappa_4\rangle|$ is the length of the perpendicular bisector dropped from the

Figure 7. A general vector in the 1–3 plane.

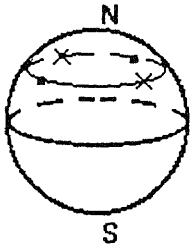

Figure 8. The figure shows the points $(p_1, \tilde{p}_3, p_2, \tilde{p}_4)$ on the Poincaré sphere, when (p_1, p_2) and (p_3, p_4) represent orthogonal rays. (p_1, p_2) are represented by dots and $(\tilde{p}_3, \tilde{p}_4)$ by crosses.

center of the Poincaré sphere to the chord 1–4. Separately equating the phases and amplitudes of these two complex numbers we find:

O1. The curve with geodesic segments connecting $(p_1, p_3, p_2, p_4, p_1)$ on the Poincaré sphere must enclose a solid angle of 2π.

O2. The products of the lengths of the perpendicular bisectors from the origin of the Poincaré sphere to the opposite sides of the rectangle $(p_1, p_3, p_2, p_4, p_1)$ (joined by chords, not along the surface of the sphere) must be equal.

These are necessary and sufficient conditions for the orthogonality of the rays of the three state system. (O1 is irrelevant (and also ambiguous, since there is no unique geodesic in this case) if any of the lengths of the perpendicular bisectors vanish; i.e. the successive vertices are antipodal.)

An alternative characterization of orthogonal rays obtained are as follows. Let us replace (p_3, p_4) by their antipodes $(\tilde{p}_3, \tilde{p}_4)$. Equation (6) implies

$$\kappa_3^{\dagger A} \propto (\kappa_{4B}^{\dagger} \kappa_2^B)\kappa_1^A + (\kappa_{4B}^{\dagger} \kappa_1^B)\kappa_2^A, \tag{8}$$

$$\kappa_4^{\dagger A} \propto (\kappa_{3B}^{\dagger} \kappa_2^B)\kappa_1^A + (\kappa_{3B}^{\dagger} \kappa_1^B)\kappa_2^A, \tag{9}$$

where $\propto$ means equal but for an unimportant (but nonzero) constant.

From (6), (8), (9) it follows that $\kappa_3^{\dagger}, \kappa_4^{\dagger}$ are linear combinations of κ_1 and κ_2 with the same relative amplitude and opposite relative phase. From this one may conclude (see below) that

O'1. The points $(p_1, \tilde{p}_3, p_2, \tilde{p}_4)$ lie on a small circle and (see figure 8) therefore form a rectangle in a plane passing through this circle.

O'2. The products of the lengths (measured along the chord, not along the surface of the sphere) of the opposite sides of this rectangle are equal to each other.

Clearly, any three points of such a set determine the fourth. The space of rays orthogonal to a given ray is two-dimensional.

To see how condition O'1 emerges, recall that the locus of points $\chi(r)$ on the Poincaré sphere traced by the states $\chi(r)^A = \kappa_1^A + r\kappa_2^A$, where r is real, is a small circle passing through the rays p_1 and p_2. This is proved in ref. [2] (see their figure on page 9). An easy

way to see this result is to notice that it is true if p_1 and p_2 are antipodal (in fact, in this case, $\chi(r)$ traces out a great circle through p_1 and p_2). One deduces the result by performing an $SL(2,\mathbb{C})$ transformation, which in general maps antipodal points to non antipodal points and great circles to small circles. As r increases from 0 to infinity, the ray $\chi(r)$ goes along one arc of the circle from p_1 to p_2. As r decreases to minus infinity, $\chi(r)$ traces the other arc of the circle. O'2 is an elementary consequence of condition 2 above and replacing (p_3, p_4) by their antipodes $(\tilde{p}_3, \tilde{p}_4)$. Thus, either set of conditions (O1, O2) or (O'1, O'2) above provides a characterization of orthogonal states.

The condition for orthogonality (6) has a simple interpretation in terms of spinors. Given four rays $(\kappa_1, \kappa_2; \kappa_3, \kappa_4)$ one can form an $SL(2,\mathbb{C})$ invariant, their cross ratio [20]

$$\chi(\kappa_1, \kappa_2; \kappa_3, \kappa_4) := \frac{(\kappa_3 \cdot \kappa_1)(\kappa_4 \cdot \kappa_2)}{(\kappa_3 \cdot \kappa_2)(\kappa_4 \cdot \kappa_1)}, \tag{10}$$

where κ are representative elements from κ and $\kappa_3 \cdot \kappa_1 = \kappa_{3A}\kappa_1^A$. Clearly, (10) depends only on the rays $(\kappa_1, \kappa_2; \kappa_3, \kappa_4)$ and not on the representatives chosen. By $SL(2,\mathbb{C})$ transformations, one can make any set of four rays coincide with any other set if and only if the two sets have the same cross ratio. The condition (6) states that the rays $(\kappa_1, \kappa_2; \kappa_3^\dagger, \kappa_4^\dagger)$ have cross ratio -1. In particular, they can be brought to the vertices of a square on the equatorial plane of the Poincaré sphere by $SL(2,\mathbb{C})$ transformations. Such a set of rays with cross ratio -1 is called harmonic [20]. Conversely, boosting four points in the sky equally spaced on a great circle will generate all sets of points $(p_1, p_2, \tilde{p}_3, \tilde{p}_4)$ which describe orthogonal rays of a three state system.

5. Conclusion

It is easy to generalize the Poincaré sphere representation above to N state systems. $\mathscr{H}$ is then the space of symmetric spinors of rank $N-1$. Such a spinor determines $N-1$ principal spinors $(\kappa_1, \kappa_2, \ldots, \kappa_{N-1})$. These determine $N-1$ indistinguishable points on the Poincaré sphere. As N gets larger, the value of such a visualizable representation of the ray space diminishes because of its complexity. It may be simpler to work directly on the Hilbert space by picking representative elements as in [18] and ensuring gauge invariance explicitly.

Notice that the representation above captures the global properties of the ray space. It represents each ray exactly once and maps neighboring rays to neighboring points. Thus it satisfies (P1, P2) just like the Poincaré sphere. One could introduce a local chart as done for example in ref. [14] on the ray space to label its points. One drawback with this is that neighboring points on the ray space are sometimes widely separated in the representation. Some rays are left out entirely. In other words, a local chart misses some important global information. If one is following the evolution of a system in a local chart, it could happen that the ray 'falls off the edge' of the chart. The main point of this article is that there exists an easily visualizable, globally faithful representation of the rays of a three state system.

The Poincaré sphere representation for three state systems does have a drawback: it does not reflect the full symmetry of the ray space. For two state systems, the Poincaré sphere representation has the desirable feature that the representation displays the full $SU(2)$ symmetry of the ray space. (Recally that unitary transformations of the Hilbert

space are represented as rotations of the Poincaré sphere). The $SU(3)$ symmetry of the three state problem is obscured in the Poincaré sphere representation. Note that some rays are represented by coincident points on the Poincaré sphere. These might appear to be 'different' from other states, which are represented by two distinct points. The difference is illusory. By $SU(3)$ transformations any state can be mapped to any other state. The coincidence of points is not an $SU(3)$ invariant notion. A representation in which $SU(3)$ invariance is manifest is given in [14]. The ray space then appears as a four dimensional subset of S^7. This however has the drawback of not being easy to visualize.

It is very important to remember that the two points (p_1, p_2) are indistinguishable. Else one might think that there is an apparent loss of differentiability at coincidence points. For example, if p_1 and p_2 pass through each other, one could see a 'kink' in their trajectories if one ignored their indistinguishability. Mathematically, one sees that z_1 and z_2 are roots of a quadratic equation, whose coefficients vary smoothly over the ray space. Smooth symmetric functions of (z_1, z_2) (i.e. those which satisfy $f(z_1, z_2) = f(z_2, z_1)$) are smooth functions on CP^2. Examples of symmetric functions are $(z_1 + z_2)$ and $(z_1 z_2)$, both of which can be expressed in terms of the coefficients of the quadratic polynomial (2), and are therefore smooth. Notice that antisymmetric functions like $z_1 - z_2$ involve the square root of the coefficients and are therefore not differentiable at coincidence points.

It would have been entirely possible to make do with $SU(2)$ spinors rather than the more general $SL(2, \mathbb{C})$ ones used in relativity. Our reason for using $SL(2, \mathbb{C})$ spinors is that the extra power of $SL(2, \mathbb{C})$ transformations is sometimes handy for deducing results even about $SU(2)$ spinors! See also the interesting remarks due to Nityananda quoted in [25].

There is another route to the Poincaré sphere representation for N state systems, which does not make use of spinors. One associates the polynomial

$$f(z) = \Sigma_{n=0}^{N-1} \Psi^n z^n / \sqrt{n!} \tag{11}$$

to the state $|\Psi\rangle$ with components $(\Psi^1, \Psi^2, \ldots, \Psi^{N-1}, \Psi^0)$. The roots of this polynomial (which depend only on the ray to which $|\Psi\rangle$ belongs) are $N-1$ points on $\mathbb{C}^*$, which are stereographically mapped to the Poincaré sphere. It is amusing to note that in the Bargmann representation [24] for the simple harmonic oscillator, the Hilbert space of coherent superpositions of the first N energy levels *is* the set of polynomials (11).

Acknowledgements

The author is grateful to Rajaram Nityananda for useful discussions and Supurna Sinha for making suggestions for improving the manuscript.

References

[1] H Poincaré, *Theorie Mathematique de la Lumiere* edited by George Carre (Paris, 1892) p. 275

[2] G N Ramachandran and S Ramaseshan, in *Handbuch der Phys.* (Springer, Berlin, 1961) vol. 25, part I

[3] M V Berry, *Proc. R. Soc. (London)* **A392**, 45 (1984)

[4] B Simon, *Phys. Rev. Lett.* **51**, 2167 (1983)

[5] Y Aharonov and J Anandan, *Phys. Rev. Lett.* **58**, 1593 (1987)
[6] S Ramaseshan and R Nityananda, *Curr. Sci. (India)* **55**, 1225 (1986)
[7] M V Berry, *J. Mod. Opt.* **34**, 1401 (1987)
[8] R Bhandari and J Samuel, *Phys. Rev. Lett.* **60**, 211 (1988)
[9] A Shapere and F Wilczek, *Geometric phases in physics* (World Scientific, Singapore, 1989)
[10] R Simon, H J Kimble, and E C G Sudarshan, *Phys. Rev. Lett.* **61**, 19 (1988)
[11] T H Chyba, L J Wang, L Mandel and R Simon, *Opt. Lett.* **13**, 562 (1988)
[12] P Hariharan, Hema Ramachandran, K S Suresh and J Samuel, *The Pancharatnam phase as a strictly geometric phase: A demonstration using pure projections*, RRI-96-18, to appear in *J. Mod. Opt.*
[13] G Khanna, S Mukhopadhyay, R Simon and N Mukunda, *Ann. Phys.* (in press)
[14] Arvind, K S Mallesh and N Mukunda, Archives quant-ph/9605042
[15] N Mukunda, IISc preprint (1996)
[16] S Pancharatnam *Proc. Indian Acad. Sci.* **A44**, 247 (1956)
[17] S Pancharatnam, *Collected works of S. Pancharatnam* (Oxford University Press, London, 1975)
[18] J Samuel and R Bhandari, *Phys. Rev. Lett.* **60**, 2339 (1988)
[19] N Mukunda and R Simon, *Ann. Phys. (NY)* **228**, 205 (1993)
[20] R Penrose and W Rindler, *Spinors and spacetime* (Cambridge University Press, Cambridge, 1984) vol. I
[21] R M Wald, *General Relativity* (University of Chicago Press, Chicago, 1984)
[22] A Ashtekar, *Lectures on Non-Perturbative Canonical Gravity* (World Scientific, Singapore, 1991)
[23] L D Landau and E M Lifshitz, *Quantum mechanics* (Pergamon Press, Oxford, 1976)
[24] V Bargmann, *Commun. Pure Appl. Math.* **14**, 187 (1961)
[25] See the figure in the article by S Ramaseshan, in *Essays on particles and fields* edited by R R Daniel and B V Sreekantan (Indian Academy of Sciences, Bangalore, 1989)

PRAMANA
— journal of
physics

© Printed in India

Vol. 47, No. 5,
November 1996
pp. 371–377

Quantum motion over a finite one-dimensional domain: With and without dissipation

ASHOK PIMPALE
Inter-University Consortium for Department of Atomic Energy Facilities, University Campus, Khandwa Road, Indore 452 001, India

MS received 7 June 1996

Abstract. Quantum motion of a single particle over a finite one-dimensional spatial domain is considered for the generalized four parameter infinity of boundary conditions (GBC) of Carreau *et al* [1]. The boundary conditions permit complex eigenfunctions with nonzero current for discrete states. Explicit expressions are obtained for the eigenvalues and eigenfunctions. It is shown that these states go over to plane waves in the limit of the spatial domain becoming very large. Dissipation is introduced through Schrödinger–Langevin (SL) equation. The space and time parts of the SL equation are separated and the time part is solved exactly. The space part is converted to nonlinear ordinary differential equation. This is solved perturbatively consistent with the GBC. Various special cases are considered for illustrative purposes.

Keywords. Generalized boundary conditions; free particle; finite domain; dissipation; Schrödinger–Langevin equation.

PACS No. 03·65

1. Introduction

Recently Carreau *et al* [1] has shown that a four parameter infinity of generalized boundary conditions (GBC) exist for the case of a free motion in one dimension over a finite spatial domain. These boundary conditions admit complex wave functions with nonzero current as eigenstates. Such states can find a natural application in many physical problems such as motion of an electron confined in a quantum well or quantum tunneling across a Josephson junction. In most such practical cases dissipation plays an important role. There are two types of approaches to study quantum dissipative systems. In one approach the central system of interest is coupled to extra degrees of freedom and although the total system remains conservative, elimination of the extra degrees of freedom in an appropriate approximation makes the central system dissipative [2, 3]. In the other approach phenomenological quantum equations displaying dissipative behaviour are used. In this category comes the well known Schrödinger–Langevin (SL) equation [4], Gisin equation [5] and the use of complex potential [6]. We report the free particle eigenspectrum explicitly using the GBC and show how the discrete states go over to the plane waves as the spatial domain size increases indefinitely. We introduce dissipation through the SL equation and separate its time and space parts. The time part is solved exactly and the space part is reduced to

a nonlinear ordinary differential equation. A special solution of this equation is obtained and the problems of applying GBC are pointed out. A perturbative scheme for solving the space part consistent with the GBC is developed.

2. Particle in a 1-dimensional box with GBC

Consider a nonrelativistic particle of mass m confined to a spatial domain $0 < x < L$. The commonly used boundary conditions on the wave function are

$$\psi(0) = 0 = \psi(L). \tag{2.1}$$

A more general class of boundary conditions are [1, 7]

$$\begin{bmatrix} -\psi'(L) \\ \psi'(0) \end{bmatrix} = M \begin{bmatrix} \psi(L) \\ \psi(0) \end{bmatrix}, \tag{2.2}$$

where the prime denotes differentiation with respect to x and M is a 2×2 Hermitean matrix

$$M = \begin{bmatrix} a & \alpha + i\delta \\ \alpha - i\delta & b \end{bmatrix}. \tag{2.3}$$

a, b, α and δ are the four real parameters. Using (2.2) it readily follows that the energy eigenvalues are given by

$$E_k = \frac{\hbar^2 k^2}{2m}, \tag{2.4}$$

with k satisfying the dispersion relation

$$2k\alpha + (a+b)k\cos(kL) + [ab - \alpha^2 - \delta^2 - k^2]\sin(kL) = 0. \tag{2.5}$$

The corresponding wave function is given by

$$\psi_k(x) = A[\sin(kx) + C\cos(kx)] \tag{2.6}$$

with

$$C = \frac{[k - (\alpha - i\delta)\sin(kL)]}{[b + (\alpha - i\delta)\cos(kL)]} \tag{2.7}$$

and the constant A is obtained from normalization.
The state (2.6) has a nonzero current

$$j_k = |A|^2 \left(\frac{\hbar k}{m}\right) \delta \frac{[k\cos(kL) + b\sin(kL)]}{\{[b + \alpha\cos(kL)]^2 + \delta^2\cos^2(kL)\}}. \tag{2.8}$$

The usual boundary conditions (2.1) are special cases of (2.2) when

$$a \to \infty, \quad b \to \infty, \quad \alpha \to 0, \quad \delta \to 0. \tag{2.9}$$

It is interesting to consider the large L limit. For usual boundary conditions the states remain discrete and the current zero. Physically, this can be attributed to the fact that any eigenstate is an equal weight linear combination of plane waves moving from left to right and vice versa. Unless an imbalance is introduced in these waves, nonzero current

$$\lim_{L\to\infty} C = \frac{1}{L}\int_{L}^{2L} \frac{[k-(\alpha-i\delta)\sin(kx)]\,dx}{[b+(\alpha-i\delta)\cos(kx)]} \to \pm i \tag{2.10}$$

so that the wave function (2.6) goes over to $\exp(\pm ikx)$.

3. Schrödinger–Langevin equation: t-dependence

We now consider dissipative motion over the domain $0 < x < L, 0 < t < \infty$ for the free particle using the SL equation

$$i\hbar\partial\psi/\partial t = -\frac{\hbar^2}{2m}\partial^2\psi/\partial x^2 + \frac{\lambda\hbar}{2i} ln[\psi/\psi^*]\psi, \tag{3.1}$$

where λ is the dissipation coefficient. The space and time parts of the wave function can be separated by putting

$$\psi(x,t) = \phi(x)\chi(t). \tag{3.2}$$

$\chi(t)$ and $\phi(x)$ then satisfy

$$i\hbar\,d\chi/dt = \frac{\lambda\hbar}{2i}\ln[\chi/\chi^*]\chi + W\chi \tag{3.3}$$

and

$$-\frac{\hbar^2}{2m}d^2\phi/dx^2 + \frac{\lambda\hbar}{2i}\ln[\phi/\phi^*]\phi = W\phi. \tag{3.4}$$

W is the separation constant and in general it can be complex. We first consider the time part (3.3) which can be readily integrated to give the solution

$$\chi(t) = \exp(W_I t/\hbar)\cdot\exp[-iG_R(t)/\hbar], \tag{3.5}$$

were W_I is the imaginary part of W and the real function G_R satisfies the differential equation

$$dG_R/dt + \lambda G_R = W_R, \tag{3.6}$$

W_R being the real part of the separation constant W.

Thus when $W_I > 0$ (2.5) blows up with time t and when $W_I < 0$ it decays to zero. The first case is evidently unphysical and the second is a well known difficulty with quantum dissipative systems [3, 6]. A special solution exists for the spatial part when W_I has a particular negative value as discussed in the next section.

The most general solution of (3.6) is given by

$$G_R(t) = \frac{W_R}{\lambda}[1-\exp(-\lambda t)] + G_0\exp(-\lambda t), \tag{3.7}$$

where G_0 is an arbitrary constant. From (3.5), W_I can be thought of as the imaginary part of particle energy and dG_R/dt as the instantaneous real energy $E(t)$ of the system

$$E(t) = E_0\exp(-\lambda t),\ E_0 = E(t=0) = W_R - G_0\lambda. \tag{3.8}$$

$E(t)$ decays exponentially with time.

4. Schrödinger–Langevin equation: Space part

The space part satisfies (3.4). A special solution of this equation exists when

$$W_I = -\lambda\hbar/2. \tag{4.1}$$

It is given by

$$\phi = \exp[iU(x)/\hbar], \quad U(x) = B_1 + B_2 x - (mW_I/\hbar)x^2,$$

$$B_1\lambda + B_2^2/2m = W_R. \tag{4.2}$$

However, nonlinearity of SL equation does not permit the use of GBC in any simple fashion. We give below a simple perturbative scheme by expanding the separation constant W in powers of the dissipation coefficient. Put

$$W = W_0 + \eta W_1 + \eta^2 W_2 + \ldots, \tag{4.3}$$

$$\phi = \phi_0 + \eta\phi_1 + \eta^2\phi_2 + \ldots, \tag{4.4}$$

where the dimensionless expansion parameter η is

$$\eta \equiv \lambda\hbar/W_0, \tag{4.5}$$

and the wave functions $\phi_0, \phi_1, \phi_2, \ldots$ are mutually orthogonal. The linearity of the GBC then imply that if all the ϕ_i's satisfy them so would (4.4). The various W_i's are in general complex. Using (4.3) and (4.4) in (3.4) and comparing equal powers of η we get

$$(-\hbar^2/2m)\mathrm{d}^2\phi_0/\mathrm{d}x^2 = W_0\,\phi_0, \tag{4.6}$$

$$(-\hbar^2/2m)\mathrm{d}^2\phi_1/\mathrm{d}x^2 + \frac{W_0}{2i}\ln(\phi_0/\phi_0^*)\phi_0 = W_0\phi_1 + W_1\phi_0, \tag{4.7}$$

$$-(\hbar^2/2m)\mathrm{d}^2\phi_2/\mathrm{d}x^2 + \frac{W_0}{2i}\ln\left(\frac{\phi_0}{\phi_0^*}\right)\phi_1 + \frac{W_0}{2i}\left[\frac{\phi_1}{\phi_0} - \frac{\phi_1^*}{\phi_0^*}\right]\phi_0$$

$$= W_0\phi_2 + W_1\phi_1 + W_2\phi_0. \tag{4.8}$$

We can solve these equations consecutively. Thus ϕ_0 is one of the eigenstates ψ_q of the unperturbed i.e. undamped system and W_0 the corresponding energy. The first order correction due to dissipation is then given by

$$\eta W_1 = (\lambda\hbar/2i)\frac{\int\phi_0^*\ln\left[\frac{\phi_0}{\phi_0^*}\right]\phi_0\,\mathrm{d}x}{\int\phi_0^*\phi_0\,\mathrm{d}x} \tag{4.9}$$

and

$$\phi_1 = \sum_{k\neq q} N_k\psi_k \tag{4.10}$$

with

$$N_k = -[E_q/2i(E_k - E_q)]\cdot\frac{\int\psi_k^*\ln(\psi_q/\psi_q^*)\psi_q\,\mathrm{d}x}{\int\psi_k^*\psi_k\,\mathrm{d}x}. \tag{4.11}$$

For the special case when

$$a+b=0, \quad \alpha=0, \quad \delta\neq 0 \tag{4.12}$$

the unperturbed energy eigenvalues correspond to the usual ones given by

$$\sin(kL)=0, \quad \cos(kL)=\pm 1, \quad kL=n\pi, \quad n=1,2,3,\ldots \tag{4.13}$$

Thus for ψ_0 corresponding to $k=q$, the first order correction to the energy becomes

$$\eta W_1=\hbar\lambda\int\rho^2\Theta(x)\mathrm{d}x\Big/\int\rho^2\mathrm{d}x, \tag{4.14}$$

where

$$\rho^2=\frac{q^2\cos^2(qx)+(b^2+\delta^2)\sin^2(qx)+2bq\sin(qx)\cos(qx)}{(b^2+\delta^2)} \tag{4.15}$$

and

$$\tan(\Theta)=\pm\frac{\delta q\cos(qx)}{(b^2+\delta^2)\sin(qx)+bq\cos(qx)}. \tag{4.16}$$

The upper (lower) sign corresponds to $\cos(qL)=1[\cos(qL)=-1]$. From (4.14) it is clear that dissipation acts in opposite directions for alternate states, one state is reduced in energy or pushed down and the other state is pulled up. Further simplification occurs when the parameter b is set equal to zero. Putting $x=L/2+y$ it is seen that the integrand is an odd function of y and the integral vanishes. Thus in this special case dissipation does not affect the energy eigenvalues to first order.

5. Results and concluding remarks

We put the dispersion relation (2.5) in dimensionless form by measuring all distances in units of Bohr radius a_0 and the wave vectors in the units of $1/a_0$, so also the parameters a, b, α and δ in the GBC. The energy E_k then becomes k^2 in Rydberg with k dimensionless for m, the electronic mass. The dependence of the eigenvalues on the size of the box, L, can be absorbed into the changed values of the parameters a, b, α, δ as shown. Multiply (2.5) by L^2 and define

$$q=kL,\ \alpha'=\alpha L,\ \delta'=\delta L,\ a'=aL,\ b'=bL$$

to cast the equation in the L independent form as

$$2q\alpha'+(a'+b')q\cos q+[a'b'-\alpha'^2-\delta'^2-q^2]\sin q=0. \tag{5.1}$$

Roots of this equation correspond to k values for parameters $\alpha=\alpha'/L$ etc. The large k eigenvalues are readily seen to be the usual ones corresponding to

$$\sin q=0 \quad \text{or} \quad q=n\pi, \quad k=n\pi/L, \quad n=1,2,3,\ldots, \tag{5.2}$$

where large k is defined by

$$k\gg|\alpha|,\ |\delta|,\ |a|,\ |b|. \tag{5.3}$$

When $\alpha=0$, $a+b=0$ we again have (5.2).

Another special case of interest occurs when

$$a+b=2\alpha. \tag{5.4}$$

Table 1. Ten lowest roots of the eigenvalue equation (2.5) for some values of the parameters a, b, α, δ. [The values given are in dimensionless form as explained in § 5]

Parameters for $L = 10$	Roots(kL/π)									
$a = b = \alpha = 0{\cdot}001$, $\delta = 1$	1	2	3	4	5	6	7	8	9	10
$a = b = \alpha = \delta = 1$	1	2.49	3	4.48	5	6.43	7	8.37	9	10.32
$a = 1.1$, $b = 0.9$, $\alpha = 1.2$, $\delta = 1$	0·99995	2.46	2.94	4.5	4.94	6.45	6.95	8·4	8.96	10.35

One set of eigenvalues is then given by

$$\cos(kL/2) = 0 \quad \text{or} \quad k = n\pi/L, \quad n = 1, 3, 5, \ldots, \tag{5.5}$$

corresponding to odd n values in (5.2). The other set of eigenvalues is obtained from the solutions of

$$\tan\frac{kL}{2} = \frac{2k\alpha}{\alpha^2 + \delta^2 + k^2 - ab} \tag{5.6}$$

and in general these values are shifted from the even n values of (5.2). Some numerical solutions of the eigenvalue equation (5.6) are given in table 1. It is seen that when a, b, α, δ shift from unity the odd n roots are lowered and even n values are raised thus leading to an apparent pairing of the roots.

The dispersion coefficient λ has dimensions of $1/t$. For the perturbative formulation to be applicable $1/\lambda$ should be substantially larger than the natural time scale of the problem which can be the time taken by the particle to travel from 0 to L. We thus get the condition

$$\frac{1}{\lambda} > \frac{L}{[(\hbar q/m)\mathrm{Im}(C)]}. \tag{5.7}$$

For the simple case of GBC parameter values (4.12), this reduces to

$$\lambda\hbar < \frac{2E_q\delta}{[L(b^2 + \delta^2)]}. \tag{5.8}$$

Thus the dissipation effects would be more important for low lying energy levels.

Acknowledgements

Part of the work was carried out while the author was visiting BESSY Gmbh, Berlin with the help of a short time grant under Indo-German collaboration scheme.

References

[1] M Carreau, E Farhi and S Gutmann, *Phys. Rev.* **D42**, 1194 (1990)
[2] A O Caldeira and A J Leggett, *Ann. Phys. (NY)* **149**, 374 (1983)
[3] M Razavy, *Can. J. Phys.* **69**, 1225 (1991)

[4] M D Kostin, *J. Chem. Phys.* **57**, 3589 (1972)
[5] N Gisin, *J. Phys.* **A14**, 2259 (1981)
[6] M Razavy and A Pimpale, *Phys. Rep.* **168**, 305 (1988)
M Razavy, *Had. J.* **11**, 75 (1988)
[7] G Goertzel and N Tralli, *Some mathematical methods of physics* (McGraw Hill, New York, 1960), Ch. 9.

PRAMANA
— journal of
physics

© Printed in India

Vol. 47, No. 5,
November 1996
pp. 379–385

Nonadiabatic gravitational collapse in multidimensional spacetime

B BHUI
Relativity and Cosmology Research Centre, Department of Physics, Jadavpur University, Calcutta 700 032, India

MS received 19 August 1996

Abstract. We extend to higher dimensions an earlier work of Santos regarding junction conditions for a spherical fluid distribution with heat flux and an electromagnetic field. It is observed that the pressure at the surface of distribution does not vanish when the heat flow is present.

Keywords. Gravitational collapse; higher dimensional spacetime; heat flow.

PACS No. 98·80

1. Introduction

Finding a theory that unifies gravity with other forces in nature remains an elusive goal in quantum field theory. Most recent efforts in this search have been directed at theories in which the dimensions of space-time is greater than the $(3+1)$ of the world that we observe. Further, the advances concerning supergravity in 11 dimensions and superstrings in 10 dimensions indicate that the multidimensionality of space is apparently a fairly adequate reflection of the dynamics of interaction over the distances $r \ll 10^{-16}$ cm where unification of all types of forces is possible [1].

Several attempts have been made to formulate and solve equations of gravitational collapse of a sphere containing heat flow and outgoing radiation flux. Misner and Sharp [2] considered the gravitational collapse problem with energy transport by heat flow. The matching of an interior metric representing an outgoing heat flux is not possible with the exterior Schwarzschild space time for obvious reasons. The matching conditions and other allied matters for non adiabatic flow have been extensively discussed in the literature by de Oliveira and Santos [3] where it is found that when one takes a Reissner–Nordstrom–Vaidya exterior for matching, one gets the interesting result that the pressure of the fluid in the interior does not vanish at the boundary in this case – rather it is related to the heat flow. It may now appear worthwhile to study the above scenario when one introduces space-like extra dimen-

We have already studied in the literature the higher dimensional generalization of Schwarzschild and Vaidya type radiating solutions, which are characterized by spherical symmetry, [4–6] and one can use them for the exterior space-time.

In the present paper, junction conditions are studied at the boundary of a gravitating fluid sphere under very general conditions in higher dimensional space time. It is further assumed that the fluid has some excess charge giving rise to an electric field in the radial direction. We obtain expressions of the extrinsic curvature and the mass function in $(n+2)$ dimensions and to our knowledge such study has not been done so far.

As mentioned earlier, the pressure at the boundary does not vanish when energy momentum tensor contains heat flow. Section 2 addresses primarily the query whether one arrives at the same result when the topology of space time is R^{2+n} and we have spherical symmetry in n-dimensions including the extra ones. Here we get the answer that the dimensionality of space and also the presence of an electric field, does not change the four-dimensional result referred to earlier. It is to be noted that the same boundary conditions can be obtained if one use Synge–O' Brien [7] or Lichnerowicz [8] junction conditions.

2. Interior and exterior higher dimensional space-time and junction conditions

We follow the method of Israel [9] in matching the interior with the exterior at the boundary. We consider an $(n+2)$-dimensional spherically symmetric distribution with its motion described by a time-like $(n+1)$ space Z. The time-like $(n+1)$-space z divides the interior from the exterior and the dividing hypersurface distinguishes between the two $(n+2)$-dimensional manifolds V^- and V^+; both of which contain Z as a part of their boundaries.

The intrinsic metric to z is

$$ds^2 = g_{ij}d\lambda^i d\lambda^j = -d\tau^2 + R^2(\tau)dX_n^2, \tag{1}$$

where $dX_n^2 = d\theta_1^2 + d\theta_2^2\sin^2\theta_1 + \cdots + \sin^2\theta_1\sin^2\theta_2\cdots\sin^2\theta_{n-1}d\theta_n^2$ and the co-ordinates λ^i being $\tau, \theta_1, \ldots, \theta_n$.

The interior metric in $(n+2)$-dimensional space time is taken as

$$ds_-^2 = -A^2dt^2 + B^2(dr^2 + r^2dX_n^2), \tag{2}$$

where A, B and R are functions of the radial co-ordinate 'r' and time 't' and it contains a charged dissipative fluid characterized by radiation and heat flow in the radial direction.

For the exterior spacetime V^+ described by higher-dimensional Reissner–Nordstrom–Vaidya metric [5, 6] which represents radiating Vaidya metric expressed in the null form and including the charge parameter as the source of the electromagnetic field is given by

$$\left[1 - \frac{2m(v)}{r^{n-1}} + \frac{Q^2}{r^{2n-2}}\right.$$

In order to have a unique intrinsic geometry at the boundary hypersurface Z, both $g^-_{\alpha\beta}$ and $g^+_{\alpha\beta}$ must include the same intrinsic metric on Z, so that

$$(ds_-)^2_Z = (ds^2_+)_Z = dS^2_Z. \tag{4}$$

The above condition guarantees the continuity of the metric components across the boundary Z and equations of Z in $V^\pm$ are given by

$$x^\alpha_\pm = x^\alpha_\pm(\lambda^i). \tag{5}$$

The second continuity condition imposed on z takes the form

$$[K_{ij}] = K^+_{ij} - K^-_{ij} = 0. \tag{6}$$

The extrinsic curvature components as given by Eisenhart are expressed as

$$K^\pm_{ij} = -n^\pm_\alpha \frac{\partial^2 x^\alpha_\pm}{\partial\lambda^i \partial\lambda^j} - n^\pm_\alpha \Gamma^\alpha_{ab} \frac{\partial x^a_\pm}{\partial\lambda^i} \frac{\partial x^b_\pm}{\partial\lambda^j}. \tag{7}$$

The equation of the surface which is the boundary Z will have the equation in the interior-co-ordinates

$$f(r,t) = r - r_Z = 0, \tag{8}$$

where r_Z is a constant, being the radial co-ordinates at the boundary in the co-moving system. Since $\partial f/\partial x^\alpha_-$ is a vector orthogonal to Z, the unit normal vector to this surface in the co-ordinates x^α_- will be

$$n^-_\alpha = (0, B(r_Z, t), 0, 0\ldots). \tag{9}$$

The unit tangent vector to Z becomes

$$1^-_\alpha = (A^2 t, 0, 0\ldots). \tag{10}$$

Using equations (2), (7) and (9), we can calculate the following components of the extrinsic curvature

$$K^-_{\tau\tau} = \left(-\frac{\partial A}{\partial r}\middle| AB \right)_Z, \tag{11}$$

$$K^-_{\theta_1\theta_1} = \frac{1}{\sin^2\theta_1} K^-_{\theta_2\theta_2} \equiv \left(r\frac{\partial(Br)}{\partial r} \right)_Z, \tag{12}$$

$$K^-_{ij} = 0, \quad i \neq j, \tag{13}$$

where τ stands for the proper time measured along the stream lines. We consider the junction condition (4) and comparing (1) with (2) with $dr = 0$, we obtain

$$A(r_z, t)\dot{t} = 1, \tag{14}$$

$$r_z B(r_z, t) = R_z(\tau), \tag{15}$$

where overhead dot represents differentiation with respect to τ. As mentioned earlier the interior space-time V^- is due to a spherically symmetric distribution of a charged fluid with radial heat flow. Hence in our problem. we have two energy momentum tensors, one is matter energy momentum tensor and the other is electromagnetic energy

$$T_{\alpha\beta} = (\rho + p)v_\alpha v_\beta + pg_{\alpha\beta} + q_\alpha v_\beta + q_\beta v_\alpha, \tag{16}$$

where ρ is the energy density of the fluid, p the isotropic fluid pressure, v_α is the $(n+2)$-velocity and g_α is the radial heat flux such that

$$v^\alpha = \frac{1}{A}\delta^\alpha_0, \tag{17}$$

$$q^\alpha = (0, q, 0, 0\ldots). \tag{18}$$

The electromagnetic energy tensor is given by

$$E_{\alpha\beta} = \frac{1}{4\pi}\left[F^\nu_\alpha F_{\beta\nu} - \frac{1}{4}g_{\alpha\beta}F^{\nu\delta}F_{\nu\delta}\right], \tag{19}$$

where $F_{\alpha\beta}$ is the electromagnetic field tensor. Maxwell's equations are

$$F_{\alpha\beta} = \varphi_{\beta,\alpha} - \varphi_{\alpha,\beta}, \tag{20}$$

$$F^{\alpha\beta}_{j\beta} = 4\pi J^\alpha, \tag{21}$$

where φ_α is the $(n+2)$ potential and J_α is the $(n+2)$ current. As we have used co-moving co-ordinate system, there will be no magnetic field present in this local co-ordinate system and thus the $(n+2)$ potential and $(n+2)$ current can be given by

$$\varphi_\alpha = [\varphi(r,t), 0, 0\ldots], \tag{22}$$

$$J^\alpha = \sigma v^\alpha, \tag{23}$$

where σ is the charge density.

Einsteins's field equation is

$$G^-_{\alpha\beta} = (T_{\alpha\beta} + E_{\alpha\beta}). \tag{24}$$

Using eq. (22), we get the non-vanishing component of (20) as

$$F_{01} = -F_{10} = -\frac{\partial\varphi}{\partial r}. \tag{25}$$

Putting (23), (25) in Maxwell's equation, straight-forward calculation yields

$$\frac{\partial^2\varphi}{\partial r^2} + \left(\frac{1}{A}\frac{\partial A}{\partial r} + \frac{(n+1)}{B}\frac{\partial B}{\partial r} + \frac{n}{r}\right)\frac{\partial\varphi}{\partial r} = 4\pi AB^2\sigma \tag{26}$$

and

$$\frac{\partial}{\partial t}\left(\frac{1}{A^2B^2}\frac{\partial\varphi}{\partial r}\right) + \left(\frac{1}{A}\frac{\partial A}{\partial t} + \frac{(n+1)}{B}\frac{\partial B}{\partial t}\right)\frac{1}{A^2B^2}\frac{\partial\varphi}{\partial r} = 0. \tag{27}$$

From the above equations (26) and (27), we get after integration

$$\frac{\partial\varphi}{\partial r} = \frac{A}{B}\frac{l(r)}{r^n}, \tag{28}$$

where

$$l(r) = 4\pi\int_0^r \sigma B^{(n+1)}r^n \mathrm{d}r. \tag{29}$$

conclude that $l(r)$ is the total charge distributed up to the radius r.

The non vanishing components of Einstein's field equation (24) with (17), (18) and (28) and metric (2) are given by

$$G_{00}^{-} = -\frac{n(n+1)}{2}\frac{\dot{B}^2}{B^2} + \frac{A^2}{B^2}\left(n\frac{B''}{B} + \frac{n(n-3)}{2}\frac{B'^2}{B^2} + \frac{n^2 B'}{Br}\right)$$

$$= -\left(\rho A^2 + \frac{A^2 l^2(r)}{B^4 r^{2n}}\right), \tag{30}$$

$$G_{11}^{-} = n\frac{A'B'}{AB} + n\frac{A'}{Ar} + \frac{n(n-1)}{2}\frac{B'^2}{B^2} + \frac{n(n-1)B'}{Br} + \frac{B^2}{A^2}$$

$$\times\left(-n\frac{\ddot{B}}{B} - n\frac{n-1}{2}\frac{\dot{B}^2}{B^2} + \frac{n\dot{A}\dot{B}}{AB}\right)$$

$$= \left(pB^2 - \frac{l^2}{B^2 r^{2n}}\right), \tag{31}$$

$$G_2^2 = G_3^3 \cdots = G_n^n = \frac{1}{B^2}\left(\frac{A''}{A} + (n-1)\frac{B''}{B} + (n-1)\frac{A'}{Ar} + \frac{(n-1)(n-4)}{2}\frac{B'^2}{B^2}\right.$$

$$\left. + (n-1)^2\frac{B'}{Br} + (n-2)\frac{A'B'}{AB}\right) - \frac{1}{A^2}\left(n\frac{\ddot{B}}{B} + \frac{n(n-1)}{2}\frac{\dot{B}^2}{B^2} - \frac{n\dot{A}\dot{B}}{AB}\right)$$

$$= \left(p - \frac{1}{B^4}\frac{l^2}{r^{2n}}\right), \tag{32}$$

$$G_{01}^{-} = -\frac{n\dot{B}'}{B} + \frac{n\dot{B}B'}{B^2} + \frac{nA'\dot{B}}{AB} = -qB^2 A. \tag{33}$$

When $n = 2$, the above field equations reduce to four dimensional case. The isotropy of the pressure gives the relation

$$\left(\frac{A'}{A} + (n-1)\frac{B'}{B}\right)' = \left(\frac{A'}{A} + \frac{B'}{B}\right)^2 - \frac{1}{r}\left(\frac{A'}{A} + (n-1)\frac{B'}{B}\right)$$

$$+ 2\left(\frac{A'}{A}\right)^2 - (n-2)\left(\frac{B'}{B}\right)^2. \tag{34}$$

As mentioned earlier the exterior space-time V^+ described by higher dimensional Reissner–Nordstron–Vaidya metric represents spherically symmetric metric with electric field and out going radial flux of unpolarized radiation given in equation (3). The equation of Z in the exterior Vaidya co-ordinate is

$$f(\bar{r}, v) = \bar{r} - r_z(v) = 0 \tag{35}$$

and the unit normal vector on z in the exterior space-time is

$$n_\alpha^+ = \left[1 - \frac{2m}{(n-1)\bar{r}^{n-1}} + \frac{2\mathrm{d}\bar{r}_2}{\mathrm{d}v} + \frac{Q^2}{(n-1)\bar{r}^{2n-2}}\right]\left(-\frac{\mathrm{d}\bar{r}_z}{\mathrm{d}v}, 1, 0, 0\ldots\right). \tag{36}$$

The junction condition (4) yields

$$\bar{r}_Z(v) = R(\tau) \tag{37}$$

and

$$\left(\frac{d\tau}{dv}\right)_z^2 = \left[1 - \frac{2m}{(n-1)\bar{r}^{n-1}} + 2\frac{d\bar{r}_z}{dv} + \frac{Q^2}{(n-1)\bar{r}^{2n-2}}\right]. \tag{38}$$

Using (38) we can write unit-normal vector as

$$n_\alpha^+ = (-\dot{\bar{r}}, \dot{v}, 0, 0, \ldots)_Z. \tag{39}$$

The unit tangent vector to z is

$$1_\alpha^+ = \left(\dot{\bar{r}} - \frac{1}{\dot{v}}, -\dot{v}, 0, 0, \ldots\right). \tag{40}$$

The extrinsic curvature to z is calculated with the help of equations (7), (3), (38) and (39) and we get

$$K_{\tau\tau}^+ = \left[\frac{\ddot{v}}{\dot{v}} - \dot{v}\left(\frac{m}{\bar{r}^n} - \frac{Q^2}{\bar{r}^{2n-1}}\right)\right]_z, \tag{41}$$

$$K_{\theta\theta}^+ = \frac{1}{\sin^2\theta} K_{\varphi\varphi}^+ = \left[\dot{v}\bar{r}\left(1 - \frac{2m}{(n-1)\bar{r}^{n-1}} + \frac{Q^2}{(n-1)\bar{r}^{2n-2}}\right) + \dot{\bar{r}}\bar{r}\right], \tag{42}$$

$$K_{ij}^+ = 0 \text{ for } i \neq j. \tag{43}$$

The Einstein tensor for the metric (3) is

$$G_{\alpha\beta}^+ = (G_{\alpha\beta}^+)_{\text{rad.}} + (G_{\alpha\beta}^+)_{\text{el.}}, \tag{44}$$

$$(G_{\alpha\beta}^+)_{\text{rad.}} = -\frac{n}{\bar{r}^n}\frac{dm}{dv}\delta_\alpha^0\delta_\beta^0, \tag{45}$$

$$(G_{\alpha\beta}^+)_{\text{el.}} = \frac{Q^2}{r^{2n}}\left[1 - \frac{2m}{(n-1)\bar{r}^{n-1}} + \frac{Q^2}{(n-1)\bar{r}^{2n-2}}\right]\delta_\alpha^0\delta_\beta^0 + \frac{Q^2}{\bar{r}^{2n}}\delta_\alpha^0\delta_\beta^1 + \frac{Q^2}{\bar{r}^n}(\delta_\alpha^2\delta_\beta^2 + \sin^2\theta_1\delta_\alpha^3\delta_\beta^3 + \cdots + \sin^2\theta_1\cdots\sin^2\theta_n\delta_\alpha^n\delta_\beta^n). \tag{46}$$

Now from the second continuity condition at the boundary $K_{ij}^+ = K_{ij}^-$ and comparing $K_{\theta\theta}$ at the boundary z from (42) and (12), we get

$$\left[r\frac{\partial(Br)}{\partial r}\right]_z = \left[\dot{v}\bar{r}\left(1 - \frac{2m}{(n-1)\bar{r}^{n-1}} + \frac{Q^2}{(n-1)\bar{r}^{2n-2}}\right) + \dot{\bar{r}}\bar{r}\right]_z. \tag{47}$$

With the help of (14), (15), (37) and (38) we get an expression for higher dimensional mass function as

$$m_z = (n-1)(B\bar{r})^{n-1}\left[\frac{\bar{r}^2\dot{B}^2}{2A^2} - \bar{r}\frac{B'}{B} - \frac{\bar{r}^2B'^2}{B^2} + \frac{Q^2}{2(n-1)(\bar{r}B)^{n-1}}\right]_z. \tag{48}$$

Again comparing (41), (11) and (47), (48) yield the important relations

$$[-(\partial A/\partial r)/AB]_z = \left[\frac{\ddot{v}}{v} - \dot{v}\left(\frac{m}{\bar{r}^n} - \frac{Q^2}{\bar{r}^{2n-1}}\right)\right]_z, \tag{49}$$

$$p_z = (qB)_z. \tag{50}$$

Relation (50) clearly indicates that in the absence of dissipation such as heat flow, the boundary condition reduces to simply $p_z = 0$, but in this case the radiation cannot exist and the exterior space-time V^+ is the higher dimensional Reissner–Nordstron space-time.

In other words, the present analysis extends to higher dimensions an important observation of Santos in 4D case that for a non-adiabatic heat flow pressure does not vanish at the boundary.

Acknowledgement

The author wishes to thank CSIR, India for financial support in carrying out this work.

References

[1] E Witten, *Phys. Lett.* **B149**, 351 (1984)
[2] C W Misner and D H Sharp, *Phys. Lett.* **15**, 279 (1965)
[3] A K G de Oliveira and N O Santos, *Astrophys. J.* **312**, 640 (1987)
[4] R Myer and M Perry, *Ann. Phys. (NY)* **172**, 304 (1986)
[5] S Chatterjee, B Bhui and A Banerjee, *J. Math. Phys.* **31**, 2208 (1990)
[6] S Chatterjee and B Bhui, *Mon. Not. R. Astron. Soc.* **247**, 577 (1990); *Int. J. Theor. Phys.* **32**, 671 (1993)
[7] S O'Brien and J L Synge, *Commun. Dublin Inst. Adv. Stud.* **A9**, 1 (1952)
[8] A Lichnerowicz, *Theories relativities del a Grav. et de l. Electromagnetisme* (Masson, Paris, 1955)
[9] W Israel, *Proc., R. Soc. London* **248**, 404 (1958)

A class of stationary rotating string cosmological models

L K PATEL and NARESH DADHICH*
Department of Mathematics, Gujarat University, Ahmedabad 380 009, India
*Inter-University Centre for Astronomy and Astrophysics, Post Bag 4, Ganeshkhind, Pune 411 007, India
E-mail: naresh@iucaa.ernet.in

MS received 4 July 1996

Abstract. We obtain a one parameter class of stationary rotating string cosmological models of which the well-known Gödel universe is a particular case. By suitably choosing the free parameter function, it is always possible to satisfy the energy conditions. The rotation of the model hinges on the cosmological constant which turns out to be negative. String-dust distribution in Gödel-type universes is also briefly discussed.

Keywords. General relativity; exact solutions; rotating string cosmology.

PACS Nos 04·20; 98·80

1. Introduction

Cosmic strings have been considered in the study of early universe cosmology. They may be one of the sources of density perturbations that are required for formation of large scale structure in the universe [1, 2]. They possess stress-energy and hence couple to gravitational field. Their various features have been considered by some authors [3–5]. Cosmic strings as source of gravitational field in general relativity (GR) was discussed by Letelier [6] and Stachel [7]. Letelier [8] has further constructed string cosmological models for Bianchi I and Kantowski–Sachs spacetimes by introducing the energy-momentum tensor

$$T_{ik} = \rho u_i u_k - \lambda w_i w_k, \quad u_i u^i = 1 = -w_i w^i, \quad u_i w^i = 0 \tag{1.1}$$

as the source term in Einstein's equation

$$R_{ik} - \tfrac{1}{2} R g_{ik} = -8\pi T_{ik} - \Lambda g_{ik}, \tag{1.2}$$

where Λ is the cosmological constant. T_{ik} represents the energy momentum of a cloud of strings attached with mass particles. The density ρ is made up of particle density ρ_p and the string tension density λ, and is given by

$$\rho = \rho_p + \lambda. \tag{1.3}$$

The energy conditions will require $\rho \geqslant 0$, $\rho_p \geqslant 0$ leaving the sign of λ undetermined. However, λ has to be positive whenever $\rho_p = 0$. The matter flow and the string fibre directions are respectively specified by the unit timelike u^i and spacelike w^i vectors.

String cosmological models have been studied for Bianchi type spacetimes by several authors [9–13]. It is also shown that, cylindrically symmetric non-singular spacetimes also admit physically reasonable string cosmological models [14]. So far all the models considered are free of rotation.

In this paper we obtain stationary rotating string solutions of Einstein's equation. We have obtained a one parameter class of rotating string spacetimes and the free function can be suitably chosen to satisfy the energy conditions. The well-known rotating Gödel universe follows as a special case of this class. It turns out that the cosmological constant Λ plays a very important role in the sense that it measures rotation as well as particle density ρ_p. We also consider string dust distribution in Gödel universe.

In § 2 we give the basic equations and their solutions are considered in § 3. String dust distribution in Gödel universe is discussed in § 4 and we conclude with remarks in § 5.

2. Basic equations

We consider the stationary line-element admitting R^3 group of Killing vectors in the form

$$ds^2 = -dx^2 - \alpha^2 dy^2 - dz^2 + (dt + H dy)^2, \tag{2.1}$$

where α and H are functions of x alone.

We introduce the orthonormal tetrad $\theta^1 = dx$, $\theta^2 = \alpha dy$, $\theta^3 = dz$ and $\theta^4 = dt + H dy$ and in what follows all quantities will be referred to the tetrad frame.

The surviving R_{ab} are given as follows:

$$R_{11} = R_{22} = \alpha''/\alpha - H'^2/2\alpha^2,$$

$$R_{44} = -H'^2/2\alpha^2, \quad R_{24} = -(1/2\alpha)(H'' - H'\alpha'/\alpha), \tag{2.2}$$

where overhead prime denotes differentiation with respect to x. Substituting this in (1.2) and using (1.1), we get

$$R_{24} = 0, \tag{2.3}$$

$$R_{11} = -4\pi(\rho + \lambda) - \Lambda, \tag{2.4}$$

$$R_{44} = 2\Lambda = 8\pi(\lambda - \rho), \tag{2.5}$$

where we have used $u_i = \delta_i^4$ and $w_i = \delta_i^3$ (string is along the z-axis).

From eqs (2.2)–(2.5) we readily obtain

$$H' = m\alpha, \quad 8\pi\rho = m^2 - \alpha''/\alpha, \quad 8\pi\lambda = m^2/2 - \alpha''/\alpha, \tag{2.6}$$

where m is a constant of integration. Clearly $\rho \geqslant 0$ is ensured if $\alpha'' \leqslant 0$ and the particle density

$$\rho_p = \rho - \lambda = m^2/16\pi \geqslant 0 \tag{2.7}$$

whereas the cosmological constant

$$\Lambda = -m^2/4 \leqslant 0. \tag{2.8}$$

The vorticity of the velocity field, $\Omega = w_{ab}w^{ab}$ turns out to be

$$\Omega = \sqrt{2}m = 2\sqrt{-2\Lambda} \tag{2.9}$$

which will vanish only when $\Lambda = 0$ and so does the particle density ρ_p.

The metric function α is undetermined and hence we have one parameter class of rotating string spacetimes. In the following we consider some simple interesting cases.

3. Solutions

Solution 1. The simplest case will obviously be $\alpha = x$ leading to

$$\lambda = \rho_p = \rho/2 = m^2/16\pi, \quad H = mx^2/2. \tag{3.1}$$

Then the metric reads

$$ds^2 = -dx^2 - x^2dy^2 - dz^2 + (dt + \tfrac{1}{2}mx^2dy)^2. \tag{3.2}$$

Solution 2. Let us put $\lambda = 0$ which will imply $\alpha = e^{mx/\sqrt{2}}$, $H = \sqrt{2}\alpha$. Then we obtain

$$ds^2 = -dx^2 - e^{\sqrt{2}mx}dy^2 - dz^2 + (dt + \sqrt{2}e^{mx/\sqrt{2}}dy)^2 \tag{3.3}$$

which is the well-known Gödel universe [15] with $8\pi\rho = m^2/2 = -2\Lambda$.

Solution 3. Let us consider the equation of state of the kind $\rho = (1+k)\lambda$ where k is a positive constant. Then we have

$$\alpha'' + \frac{1-k}{2k}m^2\alpha = 0,$$

the solution of which depends upon the sign of $(1-k)/2k$.

Case (i) $a^2 = ((1-k)/2k)m^2 > 0$. In that case,

$$\alpha = \cos ax, \quad 8\pi\rho = \frac{m^2(1+3k)}{2k}, \quad H = -\frac{m}{a}\sin ax$$

and the metric reads

$$ds^2 = -dx^2 - \cos^2 axdy^2 - dz^2 + \left(dt - \frac{m}{a}\sin axdy\right)^2. \tag{3.4}$$

Case (ii) $-b^2 = ((1-k)/2k)m^2$. We then obtain

$$\alpha = e^{bx}, \quad 8\pi\rho = \frac{1+k}{2k}, \quad H = \frac{m}{b}e^{bx}$$

and

$$ds^2 = -dx^2 - e^{2bx}dy^2 - dz^2 + \left(dt + \frac{m}{b}e^{bx}dy\right)^2. \tag{3.5}$$

Solution 4. Let us consider the case of vanishing Λ which means $\rho_p = \Omega = 0$ and $\rho = \lambda$. This is the case of the universe filled with the cosmic strings alone. Note that α still remains free to be chosen. We choose $\alpha''/\alpha = -n^2$, n being a constant. Then we get

$$\rho = \lambda = n^2/8\pi$$

and the metric has the simple form

$$ds^2 = -dx^2 - \cos^2 nx dy^2 - dz^2 + dt^2. \tag{3.6}$$

It is interesting to note that ρ is a constant and switching that off leads to flat spacetime.

This metric can be transformed to the solution for the interior of a string given by Hiscock and Gott [4, 16]. Raychaudhuri [17] criticized their interpretation and suggested that it would represent a homogeneous magnetic universe with Λ. This is what was exactly done by Patel and Vaidya [18] much earlier.

Solution 5. Raychaudhuri and Guha Thakurta [19] have investigated the conditions for the metric (2.1) to be homogeneous from Killing equations without reference to the field equations. These conditions are

$$\alpha''\alpha - \alpha'^2 = \text{const.}, \frac{H'}{\alpha} = \text{const.} \tag{3.7}$$

All the four solutions cited above satisfy the conditions (3.7). Hence they are homogeneous. But our metric function α is arbitrary and therefore it is not necessary to satisfy the first condition in (3.7). For example, let us take α in the form

$$\alpha = A\cosh^2\left(\frac{m}{2}x\right), \tag{3.8}$$

where A is a constant.

In this case we have

$$8\pi\rho = \tfrac{1}{2}m^2\,\text{sech}^2\left(\frac{m}{2}x\right), \quad 8\pi\lambda = -\frac{m^2}{2}\tanh^2\left(\frac{m}{2}x\right),$$

$$H = \tfrac{1}{2}mx + \frac{A}{2}\sinh mx. \tag{3.9}$$

Thus the choice (3.8) of α gives us an inhomogeneous string cosmological model in which the string-dust density is always negative. This solution also satisfies the energy conditions. This is just an illustration of inhomogeneous models.

4. String-dust in Gödel-type universes

We now remove the cosmological constant Λ and bring in an isotropic pressure by considering geometric strings (string-dust) in the Gödel type universes described by the metric (2.1). Here the energy momentum tensor T_{ik} is given by

$$T_{ik} = \lambda(u_i u_k - w_i w_k) + (p + \rho)u_i u_k - p g_{ik}. \tag{4.1}$$

It is easy to see that Einstein's field equation (1.2) for T_{ik} given by (4.1) reduces to the following system of equations:

$$R_{24} = 0, \tag{4.2}$$

$$8\pi p = -\tfrac{1}{2}R_{44} = 8\pi\rho, \tag{4.3}$$

$$8\pi\lambda = -R_{22}. \tag{4.4}$$

Using eqs (2.2) we get

$$\frac{H'}{\alpha} = m = \text{const.}, \; 8\pi p = 8\pi\rho = \frac{m^2}{2},$$

$$8\pi\lambda = \frac{m^2}{2} - \frac{\alpha''}{\alpha}. \tag{4.5}$$

Thus by specifying λ or α the solution gets determined. By taking $\alpha''/\alpha \leqslant 0$, we can make $\lambda > 0$. $\lambda = 0$ gives us the Gödel universe. For different choices of α, we get different string-dust distributions in Gödel universe.

5. Concluding remarks

It can be easily seen that when $H^2 - \alpha^2 < 0$ the curve with constant t, x and z is closed. For example, consider the case (ii) of solution 3. It is clear that when $k < 1$, the curve $t = \text{const.}$, $x = \text{const.}$, and $z = \text{const.}$ is closed. However of late there is a growing opinion to keep the question of causality open. There are two opposing views: (i) the laws of physics forbid the occurrence of closed time-like lines [20] and (ii) the laws of physics allow closed time-like lines and nature exhibits them [21, 22]. Thus the question of occurrence of closed timelike curves is far from resolved.

Acknowledgements

The authors are thankful to A K Raychaudhuri for helpful comments. L K Patel wishes to thank IUCAA for the hospitality.

References

[1] T W S Kibble, *J. Phys.* **A9**, 1387 (1976)
[2] Ya B Zeldovich, *Mon. Not. R. Astron. Soc.* **192**, 663 (1980)
[3] A Vilenkin, *Phys. Rev.* **D24**, 2082 (1981)
[4] J R Gott, *Astrophys. J.* **288**, 422 (1985)
[5] D Garfinkle, *Phys. Rev.* **D32**, 1323 (1985)
[6] P S Letelier, *Phys. Rev.* **D20**, 1294 (1979)
[7] J Stachel, *Phys. Rev.* **D21**, 2171 (1980)
[8] P S Letelier, *Phys. Rev.* **D28**, 2414 (1983)
[9] K D Krori, T Chaudhuri, C R Mahanta and A Mazumdar, *Gen. Relativ. Gravit.* **22**, 123 (1990)
[10] A Banerjee, A K Sanyal and S Chakraborty, *Pramana – J. Phys.* **34**, 1 (1990)
[11] R Tikekar and L K Patel, *Gen. Relativ. Gravit.* **24**, 397 (1992)

[13] S D Maharaj, P G L Leach and K S Govinder, *Pramana – J. Phys.* **44**, 511 (1995)
[14] R Tikekar, L K Patel and N Dadhich, *Gen. Relativ. Gravit.* **26**, 647 (1994)
[15] K Gödel, *Rev. Mod. Phys.* **21**, 447 (1949)
[16] W A Hiscock, *Phys. Rev.* **D31**, 3288 (1985)
[17] A K Raychaudhuri, *Phys. Rev.* **D41**, 3041 (1990)
[18] L K Patel and P C Vaidya, *Curr. Sci.* **40**, 278 (1971)
[19] A K Raychaudhuri and S Guha Thakurta, *Phys. Rev.* **D22**, 802 (1980)
[20] S W Hawking, *The chronology protection conjecture* (University of Cambridge, preprint, 1991)
[21] M S Morris, K S Thorne and U Yuretsever, *Phys. Rev. Lett.* **61**, 148 (1988)
[22] J Friedmann, M S Morris, I D Novikov, F Echeverria, G Klinkhammer, K S Thorne and U Yurestsever, *Phys. Rev.* **D42**, 1915 (1990)

PRAMANA
— journal of
physics

© Printed in India

Vol. 47, No. 5,
November 1996
pp. 393–400

Approximate analytical lower bounds on 'double asymptotic scaling' variables and physics at HERA

A SAIKIA
Department of Physics, Arya Vidyapeeth College, Guwahati 781 016, India

MS received 1 May 1996; revised 29 July 1996

Abstract. We analytically examine the asymptotic solution of gluon evolution equation in terms of the 'double scaling variables' ρ and σ of perturbative QCD and find the approximate lower bounds on these, above which the solution is considered to be valid. Comparison of this asymptotic solution is made with the fit obtained from data and the estimated lower bound on ρ is nearly equal to our analytical finding. To analyze the data below the lower bound on ρ, other analytical solutions of gluon evolution equation are to be used which depend highly on the input x-distributions of gluon to study the physics at low-x of HERA range.

Keywords. Gluon evolution equation; double scaling variable; small-x.

PACS No. 12·35

It has been predicted [1] that, in the HERA range, we will find double asymptotic scaling (DAS) in terms of scaling variables $\sigma(=\sqrt{\ln(x_0/x)\ln[\ln(Q^2/\Lambda^2)/\ln(Q_0^2/\Lambda^2)]})$ and $\rho(=\sqrt{\ln(x_0/x)/\ln[\ln(Q^2/\Lambda^2)/\ln(Q_0^2/\Lambda^2)]})$ if the initial gluon distribution is 'soft', from the solution of DGLAP gluon evolution equation [3, 8] for the gluon evolution at small-x. Phenomenological analysis of DAS has been performed in [1, 2]. Our purpose here is to find the approximate lower bounds on the scaling variables analytically. Comparing the solution obtained in [1] with the fit of [10], we find an approximate lower bound on ρ numerically, which is comparable to the analytical prediction justifying DAS above this lower bound. To identify small-x. physics (that is, whether the gluon is 'soft' or 'hard'), we study the region below this lower bound on ρ covered by HERA data. This can be performed with the help of analytical solutions of DGLAP equation which are sensitive to the initial x-distribution of gluon.

In [1] it has been shown that the DGLAP equation for gluon evolution at small-x can be written as

$$\left[\frac{\partial^2}{\partial\xi\partial\zeta}+\delta\frac{\partial}{\partial\xi}-\gamma^2\right]G(\xi,\zeta)=0, \tag{1}$$

where $G(\xi,\zeta)=xg(x,Q^2)$ is the gluon momentum distribution function,

$$\xi=\ln\frac{x_0}{x},$$

$$\delta = \left(11 + \frac{2n_f}{27}\right) \Big/ \left(11 - \frac{2n_f}{3}\right),$$

$$\gamma = \sqrt{12 \Big/ \left(11 - \frac{2n_f}{3}\right)},$$

$n_f =$ the number of active flavours participating in the process and x_0, Q_0^2 are the starting scales for the perturbative evolution.

In the asymptotic limit $\sigma (\equiv \sqrt{\xi\zeta}) \to \infty$ along any curve such that $\rho (\equiv \sqrt{\xi/\zeta}) \to \infty$, the solution of (1) for soft boundary condition is

$$G(\sigma, \rho) \underset{\sigma \to \infty}{\simeq} \mathrm{N} f_g(y) \frac{1}{\sqrt{4\pi\gamma\sigma}} \left\{ \exp\left[2\gamma\sigma - \delta\left(\frac{\sigma}{\rho}\right) \right] \right\} \left(1 + O\left(\frac{1}{\sigma}\right) \right), \tag{2}$$

where $y = \gamma/\rho$, $f_g(0) = 1$ and N is a normalization factor.

When $\xi\zeta$ is large, (2) can be written in terms of ξ and ζ (in the limit $f_g(y) \to 1$ as $y \to 0$) as

$$G(\xi, \zeta) \simeq \frac{N}{\sqrt{4\pi\gamma}} \cdot \frac{1}{(\xi\zeta)^{1/4}} \cdot \exp(2\gamma\sqrt{\xi\zeta} - \delta\zeta). \tag{3}$$

Now, we try to find the region of validity of (3) in the first quadrant of the ξ–ζ plane. When ζ is fixed (say ζ_1), $G(\xi, \zeta_1)$ has a minimum (figure 1(b)) at

$$\xi = \xi_1 = \left(\frac{1}{4\gamma\sqrt{\zeta_1}} \right)^2 \tag{4}$$

since

$$\left.\frac{\mathrm{d}G(\xi, \zeta_1)}{\mathrm{d}\xi}\right|_{\xi = \xi_1} = 0 \quad \text{and} \quad \left.\frac{\mathrm{d}^2 G(\xi, \zeta_1)}{\mathrm{d}\xi^2}\right|_{\xi = \xi_1} > 0.$$

This implies that, when ξ is increased from 0 up to ξ_1, $G(\xi, \zeta_1)$ decreases. This behaviour is contradictory to QCD predictions [6, 7]. Hence (3) does not depict the nature of gluon evolution with respect to ξ below ξ_1. So, at fixed ζ_1, from (4), the lower bound (σ_1) on σ can be predicted, which is given by

$$\sigma_1 \simeq \frac{1}{4\gamma}. \tag{5}$$

Next, let us study the variation of $G(\xi, \zeta)$ with respect to ζ, when ξ is fixed (say ξ_2) (figure 1(a)). It has a maximum at ζ_2, when $\gamma^2\xi_2 > \delta$, where

$$\zeta_2 = \frac{1}{[2(\gamma\sqrt{\xi_2} - \sqrt{\gamma^2\xi_2 - \delta})]^2} \tag{6}$$

since

$$\left.\frac{\mathrm{d}G(\xi_2, \zeta)}{\mathrm{d}\zeta}\right|_{\zeta = \zeta_2} = 0 \quad \text{and} \quad \left.\frac{\mathrm{d}^2 G(\xi_2, \zeta)}{\mathrm{d}\xi^2}\right|_{\zeta = \zeta_2} < 0.$$

When $\gamma^2\xi_2 < \delta$, ζ_2 is complex and hence within this range of analysis there is no extremum. This evolution pattern contradicts the QCD prediction at small-x and large

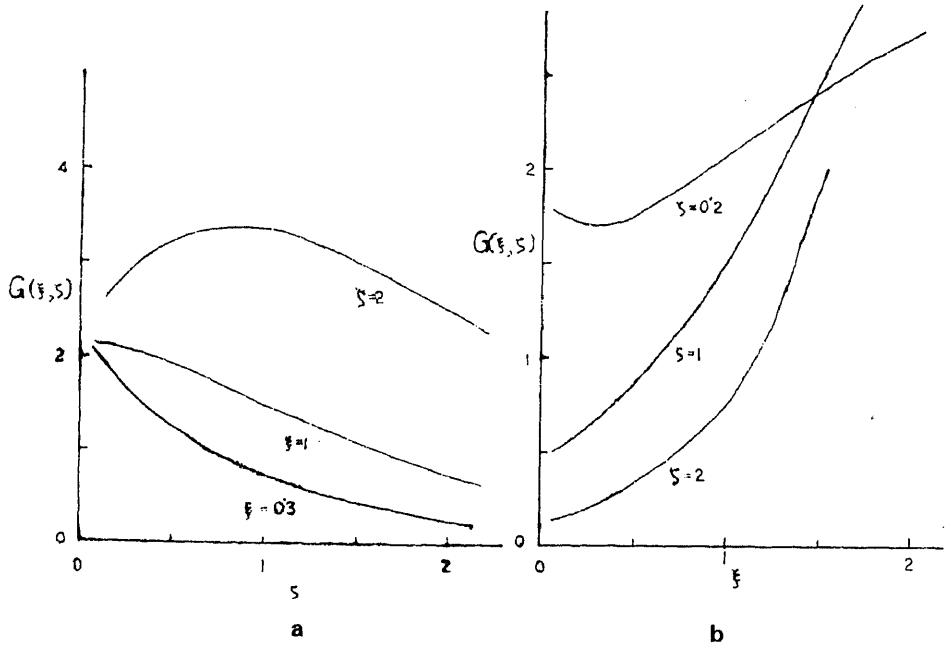

Figure 1. (**a**) Plots of ζ, $G(\xi, \zeta)$ at fixed ξ, and (**b**) plots of ξ, $G(\xi, \zeta)$ at fixed ζ, using (3) considering $N = 1$.

Q^2 [7]. So, the solution (eq. (3)) is valid only when $\xi_2 > \xi_c$, where

$$\xi_c = \delta/\gamma^2. \tag{7}$$

For $\xi_2 \gg \xi_c$, we have

$$\sqrt{\frac{\xi_2}{\zeta_2}} = \delta/\gamma = \rho_2. \tag{8}$$

Therefore, we find that $G(\xi_2, \zeta)$ attains maximum at $\rho_2 = \delta/\gamma$. For $\zeta > \zeta_2$ (i.e. $\rho < \rho_2$), $G(\xi_2, \zeta)$ decreases with increase in ζ which is opposite to the findings of [6, 7]. So, the approximate lower bound on ρ is $\rho_2 (= \delta/\gamma)$. (The lower bounds on ρ and σ evaluated above are approximate, since we are not considering the exact form of $f_g(y)$ in our analysis.) Above these lower bounds, DAS is valid if the gluon is 'soft'. Departures from these lower bounds on ρ and σ may indicate, whether the small-x growth is 'hard' or 'soft', because in the 'hard' gluon case, DAS is violated [1].

For quantitative analysis, we compare DAS prediction (eq. (3)) with the leading order fit of ref. [10], since DAS is a consequence of leading order DGLAP gluon evolution equation. The fit [10] for gluon momentum distribution is

$$G(x, Q^2) = xg(x, Q^2) = \left[x^a (A + Bx + Cx^2) \left(\ln \frac{1}{x} \right)^b + S^\alpha \exp\left(-E + \sqrt{E' s^\beta \ln \frac{1}{x}} \right) \right] (1 - x)^D, \tag{9}$$

where

$$\mu_{LO}^2 = 0{\cdot}25\,\text{GeV}^2, \quad \Lambda = 0{\cdot}232\,\text{GeV}, \quad a = 1{\cdot}00 - 0{\cdot}175,$$

$$\alpha = 0{\cdot}558, \quad \beta = 1{\cdot}218, \quad b = 0, \quad E' = 4{\cdot}066,$$

$$A = 4{\cdot}879s - 1{\cdot}383s^2,$$

$$B = 25{\cdot}92 - 28{\cdot}97s + 5{\cdot}596s^2,$$

$$C = -25{\cdot}69 + 23{\cdot}68s - 1{\cdot}975s^2,$$

$$D = 2{\cdot}537 + 1{\cdot}718s + 0{\cdot}353s^2,$$

$$E = 0{\cdot}595 + 2{\cdot}138s,$$

$$S = \ln[\ln(Q^2/\Lambda^2)/\ln(\mu_{LO}^2/\Lambda^2)].$$

(We use this fit because of its validity over a wide range of x and Q^2; $10^{-5} < x < 1$ and $1 < Q^2 < 10^8$).

For the prediction of DAS (eq. (3)), we use

$$Q_0^2 = 1\,\text{GeV}^2, \quad x_0 = 0{\cdot}1 = 0{\cdot}23\,\text{GeV}$$

because, in ref. [2] it is found that low σ data is well explained by DAS with these values. For our calculations, we take n_f to be four. So, the value of γ is 1·2 and that of δ is 1·3556.

To obtain the predictions of DAS we are to determine the value of N. The method of determination of the normalization constant N is different from [1]. From (3), the prediction from it is accurate when $\xi\zeta \to \infty$. Hence, the prediction from DAS should be nearly equal to the prediction from fit at small-x and large Q^2, that is,

$$G(\xi,\zeta)|_{\text{from DAS}} \simeq \lim_{\substack{x\to 0 \\ Q^2\to\infty}} G(x,Q^2)|_{\text{from fit.}}$$

From such analysis, we found the value of N to be 3·3586 at $x = 10^{-5}$ and $Q^2 = 10^6\,\text{GeV}^2$. Putting this value in (3) we found the predictions of DAS for different values of x and Q^2 which are plotted in figure 2 as dashed curves. The continuous curves in figure 2 represent the prediction from fit using (9). Equation (3) is found to be valid for a wide range of x and Q^2. For $x \in [10^{-5}, 10^{-3}]$ and $Q^2 \in [10^3, 10^6)$ the difference between predictions from fit and DAS is below 7% of the fit; for $x = 10^{-2}$ and $Q^2 \in [10, 10^4]$ the difference is below 10%. But for $x \in [10^{-1}, 10^{-2}]$ and $Q^2 \in [10, 10^6]$ the difference is above 10%. (If we put the exact form of $f_g(y)$ at $x = 10^{-2}$, it will further reduce the prediction of DAS by 8% and at $x = 10^{-3}$ by 6%.) In figure 3 we plot the predictions from (3) and (9) for the values of $x = 10^{-5}, 10^{-2}, 1{\cdot}5 \times 10^{-2}, 2 \times 10^{-2}$ and $Q^2 \in [10, 10^6]$ to represent the difference between the two predictions. (Since $x_0 = 0{\cdot}1$, we are unable to study (3) above 0·1.) In table 1, we show the difference between the two predictions in per cent for different values of x and Q^2 and corresponding values of ρ and σ. (We have omitted from the table the prediction for $x < 10^{-2}$ because for these values of x and $\forall Q^2 \in [10, 10^6]$, $\rho > \rho_2 (\equiv (\gamma/\delta)^{-1} = 1{\cdot}13)$.) From the table we find that the disagreement is more that 10% when ρ is around 1·15 which agrees well with our analytical analysis (the difference is nearly 2%). Hence, it can be inferred that in the region $10^{-2} > x > 10^{-5}$ and $10 < Q^2 < 10^6$, DAS is applicable and 'soft' gluon process is prominent.

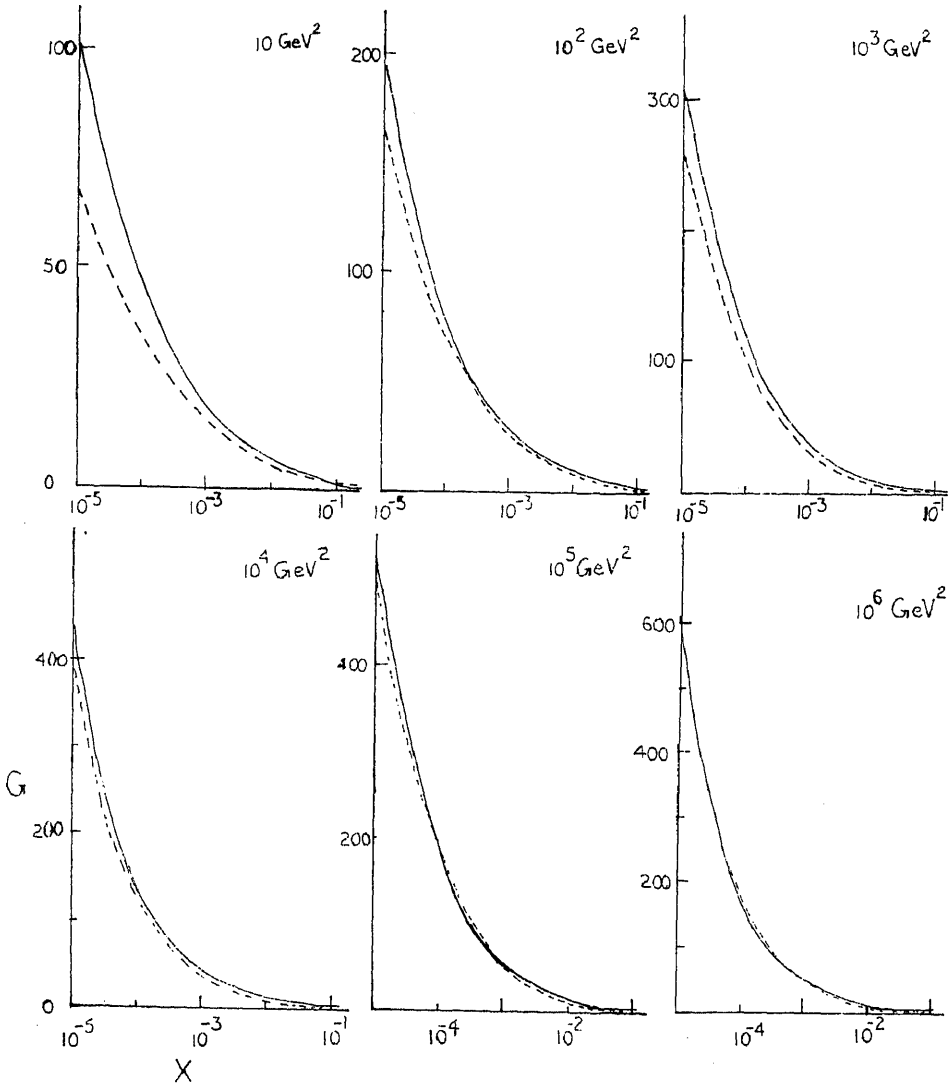

Figure 2. Comparison of the prediction from fit (continuous curves) and DAS (dashed curves) for $Q^2 = 10$, 10^2, 10^3, 10^4, 10^5 and 10^6 GeV^2 for x in the region between $10^{-5} < x < 10^{-1}$.

Almost all of the HERA data lie in the region $\sigma \in [1, 2]$ and $\rho \in [1, 3]$ [1]. Since lower bound on σ is 0·2083 ($\equiv (1/4\gamma)$) which is outside the region probed by HERA, no comparison between fit and DAS is needed for the determination of σ_1.

To complete the exploration of physics at HERA, we study the region $1 \leqslant \rho < 1{\cdot}13$, which is out of reach for DAS. Hence other analytical solutions of DGLAP gluon evolution equation is used which are not only sensitive to the input gluon distribution functions (we need input sensitive one to distinguish between the 'hard' and 'soft'

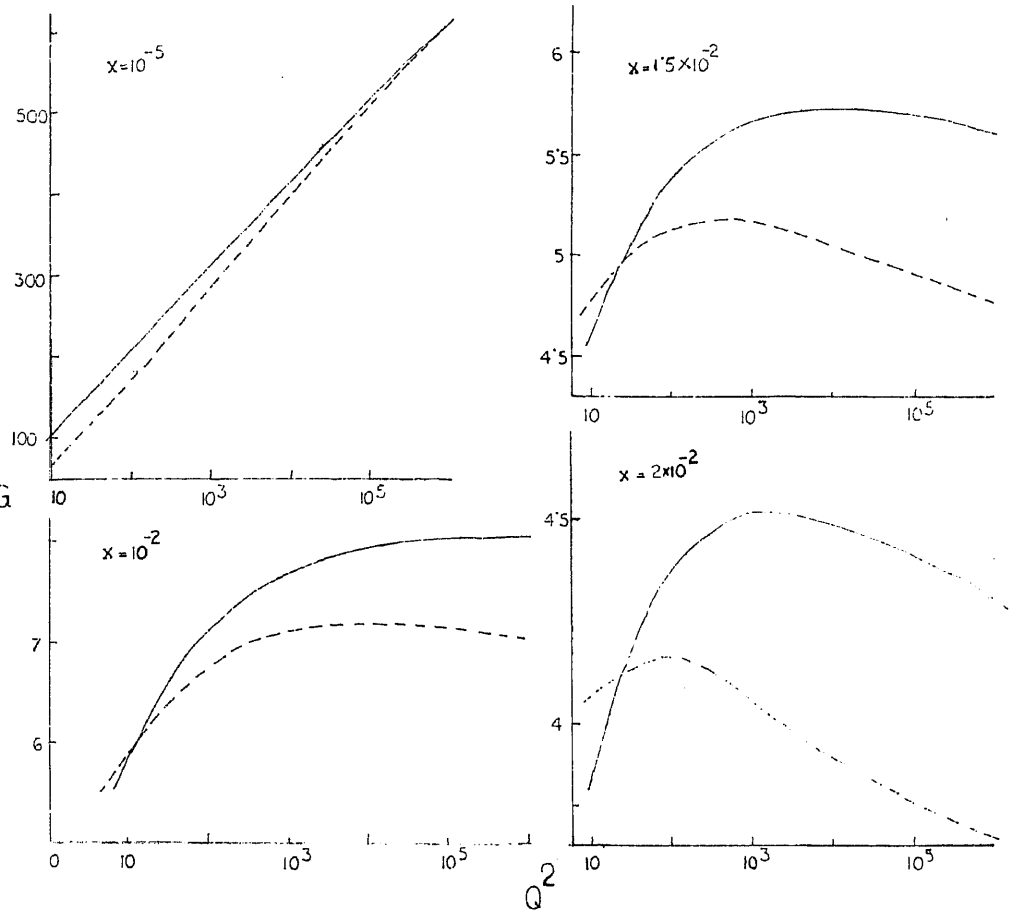

Figure 3. Comparison of the predictions from fit (continuous curves) and DAS (dashed curves) for $x = 10^{-5}$, 10^{-2}, $1{\cdot}5 \times 10^{-2}$ and 2×10^{-2} for $10\,\text{GeV}^2 < Q^2 < 10^6\,\text{GeV}^2$.

processes) but also of the pattern $\exp\sqrt{\xi\zeta}$ which is a consequence of DLA [6, 8, 9]. For the solutions of DGLAP evolution equations for structure functions, we have adopted solutions which are products of some functions of x and Q^2 [4]. This type of analysis is extended to the leading order of gluon sector [5] and to higher order in ref. [11]. This is applicable for the analysis of data around $\rho = 1$, because $\exp\sqrt{\xi\zeta}$ can be written in the factored form of functions of x and Q^2, since

$$\sqrt{\xi\zeta} = \frac{\xi + \zeta}{2}$$

when

$$\xi \simeq \zeta \text{ (i.e. } \rho \simeq 1).$$

When $G(x, Q^2)$ is written in the factored form as

$$G(x, Q^2) = g(x)h(Q^2),$$

Table 1. Difference in per cent between predictions from fit (eq. (9)) and DAS (eq. (3)) in per cent with respect to fit for different values of x and Q^2 and respective values of ρ and σ. Bold figures indicate the start of difference above 10% for respective ρ values.

	$Q = 10\,\text{GeV}^2$	$Q^2 = 10^2$	$Q^2 = 10^3$	$Q^2 = 10^4\,\text{GeV}^2$	$Q^2 = 10^5\,\text{GeV}^2$	$Q^2 = 10^6\,\text{GeV}^2$
$x = 0{\cdot}01$	$-0{\cdot}9\%$	4·1%	7·3%	8·4%	9·8%	**11·8%**
$(\rho, \sigma) =$	(1·9951, 1·1541)	(1·5629, 1·4733)	(1·3801, 1·6685)	(1·2738, 1·8077)	(1·2024, 1·915)	(1·1502, 2·0019)
$x = 0{\cdot}015$	$-3{\cdot}7\%$	4·3%	9%	**11·9%**	13·9%	15·2%
$(\rho, \sigma) =$	(1·811, 1·0476)	(1·4187, 1·3373)	(1·2526, 1·5145)	(1·1562, 1·6408)	(1·0914, 1·7382)	(1·044, 1·817)
$x = 0{\cdot}02$	$-5{\cdot}7\%$	4·9%	**10·7%**	14·3%	16·7%	18·3%
$(\rho, \sigma) =$	(1·668, 0·9649)	(1·3067, 1·2317)	(1·1538, 1·3949)	(1·0649, 1·5113)	(1·0053, 1·601)	(0·9616, 1·6737)
$x = 0{\cdot}025$	$-7{\cdot}1\%$	5·6%	12·3%	16·52%	19·3%	21·2%
$(\rho, \sigma) =$	(1·548, 0·8955)	(1·2127, 1·1432)	(1·0708, 1·2946)	(0·9884, 1·4026)	(0·933, 1·4859)	(0·8925, 1·553)

(where $g(x)$ is the input gluon distribution function and h is a function of Q^2) then.

$$\frac{dG(x,Q^2)}{G(x,Q^2)} = \frac{dg(x)}{g(x)} + \frac{dh(Q^2)}{h(Q^2)}. \tag{10}$$

This shows that the variation of $G(x,Q^2)$ is the sum of the individual variations of the x and Q^2 dependent functions. Keeping Q^2 fixed, variation of $G(x,Q^2$ (fixed)) is equal to the variation of the input gluon distribution function, which makes the solutions to be input sensitive.

Thus, we have demonstrated that the lower limits on the scaling variables of DAS can be obtained analytically in terms of QCD parameters. The lower bound on ρ agrees well with the numerical analysis based on fit obtained from data. Above this lower bound on ρ, 'soft' gluon dominates the physics at small-x validating DAS. For complete analysis of HERA data which are out of DAS, factored form of gluon evolution function can be used near $\rho = 1$.

Acknowledgement

The author is grateful to R Deka and D K Choudhury for useful discussions.

References

[1] R D Ball and S Forte, *Phys. Lett.* **B335**, 77 (1994); **B336**, 77 (1994)
[2] J R Forshaw and R G Roberts, *Phys. Lett.* **B351**, 308 (1995)
[3] V N Gribov and L N Lipatov, *Sov. J. Nucl. Phys.* **15**, 438 (1972)
L N Lipatov, *Sov. J. Nucl. Phys.* **20**, 94 (1974)
G Attarelli and G Parisi, *Nucl. Phys.* **B126**, 298 (1977)
[4] D K Choudhury and A Saikia, *Pramana–J. Phys.* **33**, 359 (1989); **34**, 85 (1990); **38**, 313 (1992)
[5] R Deka and D K Choudhury, *Z. Phys.* (submitted)
[6] L V Gribov, E M Levin and M G Ryskin, *Phys. Rep.* **C100**, 1 (1983)
[7] R G Robert, in *The structure of proton* (Cambridge University Press, Cambridge, 1990)
[8] Y L Dokshitzer, *Sov. Phys. JETP* **46**, 641 (1977)
[9] A De Rujula, S L Glashow, H D Politzer, S B Trieman, F Wilczek and A Zee, *Phys. Rev.* **D10**, 1649 (1974)
T De Grand, *Nucl. Phys.* **B151**, 485 (1979)
J P Ralston and D W Mc Kay, in *Physics simulations at high energies* edited by V Barger (World Scientific, Singapore, 1977)
J P Ralston, *Phys. Lett.* **B172**, 430 (1986)
[10] M Gluck, E Reya and A Vogt, *Z. Phys.* **C53**, 127 (1992)
[11] D K Choudhury, R Deka and A Saikia, *Z. Phys.* (submitted)

Measurement and analysis of excitation functions for alpha induced reactions on iodine and cesium

N P M SATHIK, M AFZAL ANSARI*, B P SINGH and R PRASAD
Department of Physics, Aligarh Muslim University, Aligarh 202002, India
*Present address: Department of Physics, Garyounis University, Benghazi, Libya

MS received 18 March 1996; revised 8 July 1996

Abstract. The excitation functions for the reactions $^{127}I(\alpha,2n)^{129}Cs$, $^{127}I(\alpha,4n)^{127}Cs$, $^{133}Cs(\alpha,2n)^{135}La$ and $^{133}Cs(\alpha,4n)^{133}La$ have been measured up to ≈ 50 MeV α-particle energy using the stacked foil activation technique. Measured excitation functions are compared with pre-equilibrium geometry dependent hybrid model calculations. It has been found that theoretical calculations using an initial exciton number $n_0 = 4$ $(2p + 2n + 0h)$ give good agreement with experimental excitation functions.

Keywords. α-induced reaction on I and Cs; stacked foil activation technique; $E_\alpha \leqslant 50$ MeV.

PACS No. 25·60

1. Introduction

Nuclear reactions induced by intermediate energy α-particles have been a point of interest during the last decade. The highly excited nuclear system, produced by projectile bombardment decays first by emitting a number of fast nucleons or clusters of nucleons at the pre-equilibrium (PE) stage and later on by evaporating low energy nucleons at the equilibrium (EQ) stage. The high energy tail observed in the experimental excitation functions may be explained through the PE emission process. Many semiclassical models [1–5] have been proposed to explain the features of the experimental excitation functions. Among these, the geometry dependent hybrid (GDH) model proposed by Blann [4] has been found to give a satisfactory reproduction of the experimental data. Efforts have been made to develop a fully quantum mechanical (QM) picture of PE reaction in the framework of multistep theories [6–10]. However, on account of the complexity involved in computation, the theoretical calculations for four nucleon systems like α-particle have not been found to give satisfactory results. The work presented here is a part of the programme of precise measurement of excitation functions for α-induced reactions, currently under way [11–19]. We report on the measurement of excitation functions for the alpha induced reactions on ^{127}I and ^{133}Cs. These reactions are important from the point of view of CsI detector design.

2. Experimental details

Excitation functions for the reactions $^{127}I(\alpha,2n)^{129}Cs$, $^{127}I(\alpha,4n)^{127}Cs$, $^{133}Cs(\alpha,2n)^{135}La$ and $^{133}Cs(\alpha,4n)^{133}La$ up to ≈ 50 MeV have been measured using stacked foil

ctivation technique and Ge(Li) gamma-ray spectroscopy. The experiment was per-ɔrmed at the Variable Energy Cyclotron Centre (VECC), Calcutta. Spectroscopically ure (SPECPURE) cesium iodide sample was used as the target material. The purity of ne material was better than 99·9%. Targets were made by vacuum evaporation of bout 1 mg/cm^2 thick cesium iodide on an aluminium backing of thickness ·75 mg/cm^2, placed over the masking plate. In the masking plate there were thirteen pen squares of size 12 mm × 12 mm. Since, CsI is a hygroscopic compound, a thin Al ayer of thickness 200 μg/cm^2 was further deposited by vacuum evaporation onto the pper surface of the prepared CsI target, so that the moisture may not affect the target urface. These targets were cut into pieces and glued on aluminium frames of size 0 mm × 30 mm having a circular hole of diameter 10 mm in the centre. Samples for rradiation were taken in the form of a stack of these targets. Aluminium foil of various hicknesses were used as energy degraders and were sandwiched between the target oils whereever required so as to get the desired α-particle energy incident on each foil. The energy of incident α-particle on each foil in the stack was calculated from the nergy degradation of incident α-particle beam using the stopping power tables of Northcliffe and Schilling [20]. The stack consisting of thirteen such targets was rradiated with a 50 MeV α-particle beam. By using a tantalum collimator placed in ront of the stack the diameter of the beam spot was adjusted to 8 mm. The stack was crewed at the centre of the flange and was electrically insulated from the beam line. During irradiation the stack was cooled by a specially designed assembly through vhich low conductivity water (LCW) circulated. The stack was exposed to the nanalyzed external beam from the 224 cm variable energy cyclotron of VECC, Calcutta. The collimated α-particle beam of ≈ 100 nA falling on the target stack was nonitored by charge collection using a Faraday cup, kept behind the target stack and oupled to an ORTEC current integrator. In many experiments the incident alpha beam flux has also been independently obtained using the standard reactions ^{27}Al(α, 4p 5n)^{22}Na and ^{27}Al(α, 4p 3n)^{24}Na for which the cross-section are said to be ery well known [21]. However, in the present measurements the average incident -beam flux was obtained from the total charge collected in the Faraday cup. After rradiation the induced gamma activities in individual foils were recorded with the help f a pre-calibrated high resolution 100 cm^3 ORTEC Ge(Li) detector (FWHM 2 keV at ·33 MeV) coupled to a CANBERRA-88 multichannel analyzer. The dead time for ounting was kept less then 10% by adjusting the sample detector separation in these neasurements. Several spectra were recorded at suitable time intervals to enable the dentification of the half-lives of various residual nuclei. Various gamma-rays from a calibrated ^{152}Eu source (half-life 13·33 years) were used for the efficiency and the nergy calibration of the counting unit. The expression used for computing the xperimentally measured cross-sections is taken from ref. [22]. The reaction cross-ection $\sigma(E)$ at a given energy E, was calculated using the expression

$$\sigma(E) = \frac{A\lambda \exp(\lambda t_2)}{N_0 \theta \Phi(G\varepsilon) K [1 - \exp(-\lambda t_1)][1 - \exp(-\lambda t_3)]},$$

where $K = [1 - \exp(-\mu d)]/(\mu d)$ is the correction for self absorption of gamma rays in he sample of thickness d (gm/cm^2) and of absorption coefficient μ(cm^2/gm); A is the

area under photo peak, λ is the decay constant of the residual nucleus, t_1, t_2 and t_3 are respectively the period of irradiation, time lapsed between the stop of irradiation and the start of counting and the counting period, N_0 is the number of target nuclei in the sample. Φ is the incident α-beam flux, $(G\varepsilon)$ is the geometry dependent efficiency of the detecting unit and θ the branching ratio for the specific gamma ray.

The activation cross-section for a given reaction has been determined from the intensities of the various identified gamma rays arising from the same residual nuclei. The reported value is the weighted average cross-section corresponding to various identified γ-rays of sufficient intensity. The spectroscopic data used in the cross-section measurement are taken from the table of isotopes [23]. The threshold energy for various reactions involved, half-lives, gamma ray energies and their absolute intensities are given in table 1. A typical observed gamma ray spectrum of CsI irradiated by ≈ 50 MeV α-particles is shown in figure 1. As can be seen from figure 1, various peaks in the spectrum originate due to various residual nuclei produced through different reactions. The reactions were identified by the characteristic γ-rays produced by the residual nuclei. The γ-ray of energy 372 keV (30·8%) is emitted from the residual nuclei ^{129}Cs produced via ^{127}I$(\alpha, 2n)$ reaction. Further, as seen from the observed spectrum (figure 1), the 372 keV γ-ray looks like a doublet. The area under photopeak of interest was obtained using the peak fitting program of the CANBERRA-88 multichannel analyzer and an uncertainty of about $< 10\%$ in the area of photopeak for 372 keV has

Table 1. Reactions, threshold energies, half-lives of residual nuclei, γ-ray energies and branching ratios of gamma-decay.

Reaction	Threshold energy (MeV)	Half life $T_{1/2}$	Gamma-ray energy (MeV)	Absolute gamma-ray intensity (%)
^{127}I$(\alpha, 2n)^{129}$Cs	15·6	1·34 d	0·177	0·27
			0·279	1·33
			0·318	2·46
			0·372	30·80
			0·412	22·50
			0·549	3·42
			0·589	0·61
^{127}I$(\alpha, 4n)^{127}$Cs	33·6	6·25 h	0·125	15·60
			0·321	1·24
			0·412	58·00
			0·462	4·20
			1·197	0·17
			1·307	0·15
^{133}Cs$(\alpha, 2n)^{135}$La	15·6	19·48 h	0·481	1·54
^{133}Cs$(\alpha, 4n)^{133}$La	33·4	3·90 h	0·279	1·90
			0·302	1·24
			0·565	0·51
			0·618	0·80
			0·622	0·49
			0·846	0·48

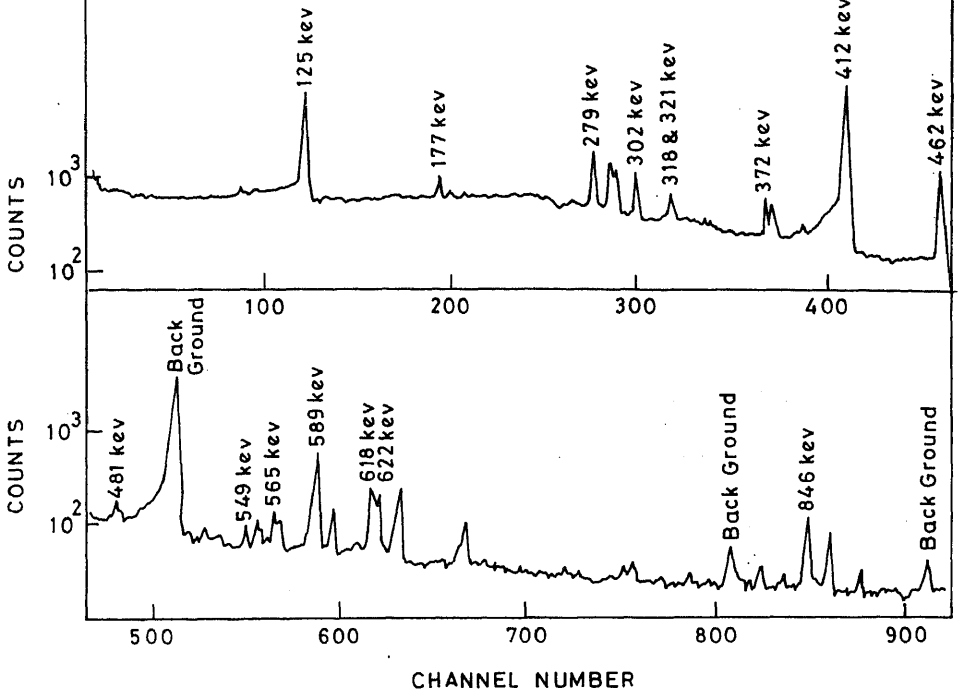

Figure 1. A typical gamma-ray spectrum of CsI irradiated by ≈ 50 MeV α-particle beam.

been obtained. As seen from table 1, the γ-ray of 412·0 keV is produced via two different reactions i.e., $^{127}I(\alpha, 2n)^{129}Cs$ and $^{127}I(\alpha, 4n)^{127}Cs$. Therefore, in the observed γ-ray spectrum beyond 33·6 MeV incident energy of alpha-particles (threshold for $(\alpha, 2n)$ reaction), the intensity of 412·0 keV γ-ray will have a contribution due to both these reaction channels. However, below 33·6 MeV the contribution will be due to $^{127}I(\alpha, 2n)^{129}Cs$ reaction only. In the present calculations the γ-ray of 412·0 keV is used for the measurement of cross-section of $(\alpha, 2n)$ reactions in ^{127}I up to ≈ 33 MeV only. As can be seen from table 1, the γ-ray of 549 keV (3·42%) and 589 keV (0·61%) are emitted from the residual nucleus ^{129}Cs produced in the $^{127}I(\alpha, 2n)$ reaction. Therefore, the intensity of 549 keV γ-ray should be stronger than the 589 keV γ-ray. However, from the observed spectrum (figure 1) it may be seen that the 589 keV γ-ray appears to be stronger than 549 keV γ-ray. The main reason for this anomoly may be that some interfering γ-rays, like $E\gamma \approx 585$ keV (0·2%) from the residual nucleus ^{133}La produced in $^{133}Cs(\alpha, 4n)$, may be emitted which may contribute to the intensity of 589 keV γ-rays. As such the 589 keV γ-ray has not been used for computing the cross-section for $^{127}I(\alpha, 2n)^{129}Cs$ reaction. The presently measured cross-sections at different energies for the reactions $^{127}I(\alpha, 2n)^{129}Cs$, $^{127}I(\alpha, 4n)^{127}Cs$, $^{133}Cs(\alpha, 2n)^{135}La$ and $^{133}Cs(\alpha, 4n)^{133}La$ are tabulated in tables 2 and 3, alongwith the overall errors, including statistical errors of counting, expected due to various factors mentioned in § 2·1.

Table 2. Measured cross-sections for α-induced reaction in ^{127}I.

E_α(MeV)	$^{127}I(\alpha, 2n)^{129}Cs$ Cross-section (mb)	$^{127}I(\alpha, 4n)^{127}Cs$ Cross-section (mb)
18·06 ± 0·57	136·7 ± 17·6	–
19·78 ± 0·56	618·6 ± 74·4	–
21·39 ± 0·56	1040·6 ± 123·9	–
24·26 ± 0·56	1165·9 ± 138·5	–
26·87 ± 0·55	1214·7 ± 144·2	–
30·37 ± 0·55	1346·1 ± 159·2	–
33·63 ± 0·54	628·4 ± 75·3	–
36·68 ± 0·54	255·2 ± 31·6	–
39·57 ± 0·54	187·0 ± 24·6	105·0 ± 17·7
42·36 ± 0·54	99·6 ± 18·0	281·9 ± 41·1
44·99 ± 0·53	75·9 ± 18·5	636·5 ± 92·5
47·50 ± 0·53	62·6 ± 19·9	839·0 ± 123·8
49·93 ± 0·53	51·6 ± 21·3	821·5 ± 128·7

Table 3. Measured cross-sections for α-induced reaction in ^{133}Cs.

E_α(MeV)	$^{133}Cs(\alpha, 2n)^{135}La$ Cross-section (mb)	$^{133}Cs(\alpha, 4n)^{133}La$ Cross-section (mb)
18·06 ± 0·57	118·7 ± 17·7	–
19·78 ± 0·56	545·1 ± 70·3	–
21·39 ± 0·56	961·3 ± 120·0	–
24·26 ± 0·56	1098·8 ± 126·4	–
26·87 ± 0·55	1154·8 ± 133·5	–
30·37 ± 0·55	500·1 ± 57·8	–
33·63 ± 0·54	259·3 ± 37·1	–
36·68 ± 0·54	241·9 ± 34·5	–
39·57 ± 0·54	173·9 ± 28·8	288·4 ± 43·8
42·36 ± 0·54	107·9 ± 25·6	457·0 ± 68·9
44·99 ± 0·53	125·9 ± 41·2	1156·6 ± 167·2
47·50 ± 0·53	98·7 ± 47·9	1684·4 ± 240·7

2.1 *Experimental errors*

The uncertainties may arise in measured cross-sections due to the errors in the estimation of target nuclei in the sample, the variation of the beam current which results in uncertainty of the incident flux, the uncertainty in the detector efficiency determination due to the statistical errors of counting of standard source, the uncertainty due to the solid angle effect due to non-reproducibility of the identical geometries for the standard source and the irradiated samples, etc. The additional uncertainties in measured cross-sections may come up due to the nuclei recoiling out of the sample. In some cases where intensity of activities produced in the irradiated samples were large, the dead time of the detector may also introduce uncertainty in the measured cross-section. The low energy neutrons which are produced when the beam traverses the stack material may also disturb the yield.

electronic microbalance and the thickness of each piece was calculated. The errors in the estimation of the number of target nuclei were analyzed in this way and were estimated to be $< 1\%$. The uncertainty due to flux variation is $< 4\%$. The uncertainty in the detector efficiency due to the statistical error of counting is estimated to be $< 1{\cdot}5\%$. However, the uncertainty due to the solid angle effect, since the irradiated samples were not point sources, is estimated using the prescription given by Gardner and Verghese [24] and is found to be $< 5\%$. Therefore, the total uncertainty in the efficiency is estimated to be $< 6{\cdot}5\%$. To avoid the uncertainty due to recoiling of the nuclei out of the sample, the targets were placed perpendicular to the incident alpha-beam such that CsI deposition faced the incident beam. As such, the recoiling nuclei are likely to be trapped in Al backing. Hence, no correction is applied for that. In order to minimize the errors due to the dead time, particularly for the cases where the activity in the irradiated samples were large, the sample-detector distance was suitably adjusted to keep the dead time $< 10\%$. However, the corrections were applied in the counting rates accordingly. Also, as the beam traverses the stack material, low energy neutrons may be released, which in turn may disturb the yield. However, Ernst *et al* [25] have indicated that such disturbing yields are also negligible.

The overall error due to all these factors, as mentioned above, is expected to be $< 12\%$. The errors mentioned in cross-section in tables 2 and 3 are the overall error including the statistical errors of counting and are generally $< 20\%$ except for a few points. These errors do not include the uncertainty of the nuclear data such as the branching ratio, decay constant, etc., which are taken from the table of isotopes and the nuclear data sheets.

3. Results and discussion

Presently measured excitation functions for the reactions $^{127}I(\alpha, 2n)^{129}Cs$ and $^{127}I(\alpha, 4n)^{127}Cs$ are shown in figure 2 and for reactions $^{133}Cs(\alpha, 2n)^{135}La$ and $^{133}Cs(\alpha, 4n)^{133}La$ are shown in figure 3 respectively. To the best of our knowledge no earlier measurement has been done in the above energy region for these reactions. In these figures dark as well as open circles represent the measured cross section. The horizontal bars are the α-particle energy spread within the target thickness alongwith the inherent uncertainty in the α-particle beam and verticle bars represent the overall uncertainty in the measured cross-sections.

A computer code ALICE/LIVERMORE-82 [26] has been used for calculating the excitation functions theoretically. This code is capable of performing the theoretical excitation function calculations up to an energy range of 200 MeV.

The theoretical calculations of the excitation functions has been done within the framework of Weisskopf–Ewing model [27] for CN calculations while the PE calculations are performed employing geometry dependent hybrid-model of Blann [4]. In the Weisskopf–Ewing formulation, the conservation of angular momentum is not taken into account explicitly. However, an approximate treatment of angular momentum effect is incorporated by using s-wave approximation [[28]. In the GDH model the

intranuclear transition rates may be evaluated both from the imaginary optical potential parameters of Becchetti and Greenlees [29] and from Pauli corrected nucleon-nucleon scattering cross-sections [30]. Both the above methods give similar results [31]. However, optical model parameter set is valid up to 55 MeV projectile energies. In the present calculations the latter option has been used. The nuclear masses were calculated from the Myers and Swiatecki Lysekil mass formula [32]. The mean free path (MFP) is required to calculate the intranuclear transition rates. As the calculated MFP for two-body residual interactions may differ from the actual MFP, an adjustable parameter COST is provided in the code to match the experimental and theoretical excitation functions. The theoretical calculations were performed using different values of the parameter COST and a value of 3 best fits the data. The initial configuration of the initially excited number of particles and holes, also referred to as initial exciton number n_0 is the starting point in any particle induced nuclear reaction. As such the initial exciton number n_0 is an important parameter of PE calculations. In the present calculations the initial exciton configuration $n_0 = 4$ (2 protons + 2 neutrons and no hole) for α-particle is taken.

The level density parameter is also an important parameter in these calculations. In this code the level density $a = (A/PLD)$ is taken, where A is the mass number and PLD is the level density parameter. Though, the default option for the PLD is 9, a value of $PLD = 10$ ($a = A/10$) is found to give satisfactory reproduction of the data. With the

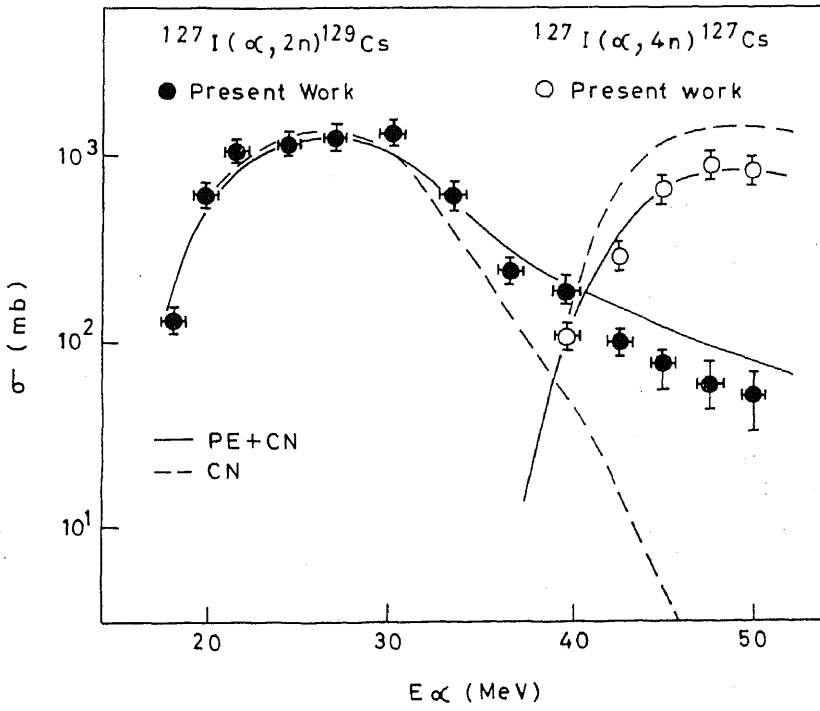

Figure 2. Experimentally measured and theoretically calculated excitation func-

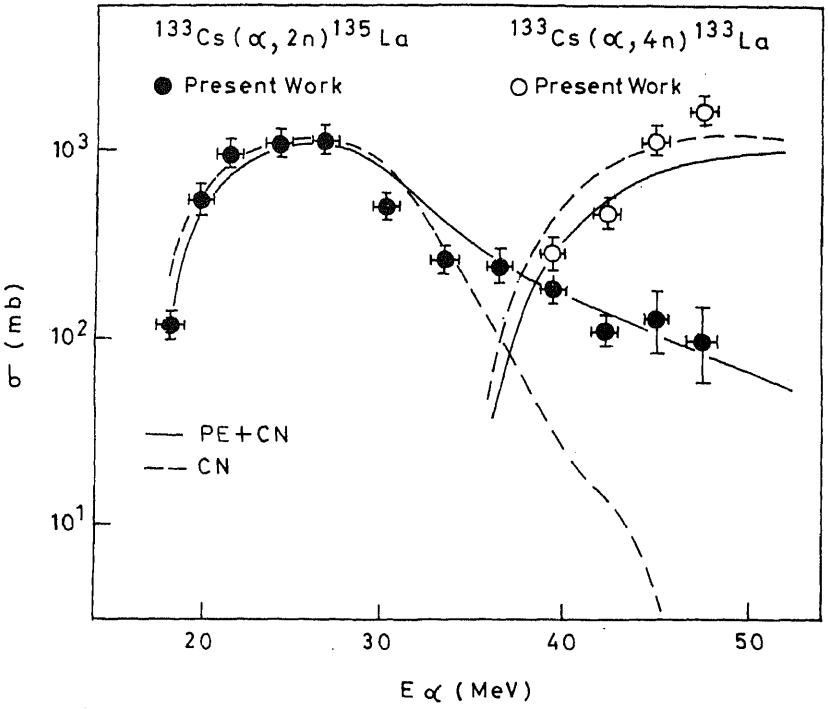

Figure 3. Experimentally measured and theoretically calculated excitation functions for $^{133}Cs(\alpha, 2n)^{135}La$ and $^{133}Cs(\alpha, 4n)^{133}La$ reactions.

choice of the appropriate set of these parameters the theoretical calculations have been performed. In the present calculations the initial exciton number $n_0 = 4(2p + 2n + 0h)$ alongwith the mean free path multiplier equal to 3 and the level density parameter $a = A/10$, have been found to give a satisfactory reproduction of the experimental data. In figures 2 and 3, the excitation functions are represented by solid curves for the calculations obtained by the consideration of both the CN and PE contributions while the broken line is for the CN (Weisskopf–Ewing) calculations. From figures 2 and 3, it may be observed that experimentally measured excitation functions, particularly the tail portions, cannot be reproduced by CN calculations only. However, proper admixture of equilibrium (CN) and PE contributions is needed to explain the excitation functions satisfactorily. In the present experiment, excitation functions for $^{127}I(\alpha, n)^{130}Cs$, $^{127}I(\alpha, 3n)^{128}Cs$, $^{133}Cs(\alpha, n)^{136}La$ and $^{133}Cs(\alpha, 3n)^{134}La$ reactions could not be measured due to short half-lives of the product nucleus. However, the residual nuclei produced in these reactions are also involved in the successive evaporation chain of the other reactions for which excitation function are measured presently.

4. Conclusions

From the above analysis it may be concluded that α-induced excitation functions have high energy tails, which in general cannot be accounted for by pure equilibrium

reaction mechanism. Proper admixture of equilibrium and PE processes is needed in theoretical calculations for better reproduction of experimentally measured excitation functions. It may also be inferred from these figures that for α-particle induced reactions the choice of initial exciton number $n_0 = 4$ with configuration (2 protons, 2 neutrons and no hole) gives satisfactory reproduction of the experimental data.

Acknowledgements

The authors would like to thank Prof M S Z Chaghtai, for providing necessary facilities to carry out this work. They are also thankful to VECC personnel for their help and co-operation during the course of this experimental work. One of the authors (NPMS) acknowledges the financial support in the form of University Research Fellowship awarded by AMU, Aligarh.

References

[1] M Blann, *Ann. Rev. Nucl. Sci.* **25**, 123 (1975)
[2] J J Griffin, *Phys. Rev. Lett.* **17**, 478 (1966)
[3] E Gadioli, E Gadioli-Erba and P G Sona, *Nucl. Phys.* **A217**, 589 (1973)
[4] M Blann, *Phys. Rev. Lett.* **27**, 337 (1971); **27**, 700 (1971); **27**, 1550 (1971)
[5] G D Harp and J M Miller, *Phys. Rev.* **C3**, 1847 (1971)
[6] H Feshbach, A Kerman and S Koonin, *Ann. Phys.* **125**, 429 (1980)
[7] D Agassi, H A Weidenmueller and G Mantzouranis, *Phys. Rev.* **22**, 145 (1975)
[8] T Tamura, T Udagawa, D H Feng and K K Kaur, *Phys. Lett.* **B68**, 109 (1977)
[9] K W McVoy *et al*, *Phys. Rep.* **94**, 140 (1983)
[10] H Gruppelaar *et al*, *La Rivista del Nuovo Cimento* **9**, 7 (1986)
[11] H D Bhardwaj and R Prasad, *Nucl. Instrum. Methods* **A242**, 286 (1986)
[12] I A Rizvi, M Afzal Ansari, R P Gautam, R K Y Singh and A K Chaubey, *J. Phys. Soc. Jpn.* **56**, 3135 (1987)
[13] M Afzal Ansari, R K Y Singh, I A Rizvi, M K Bhardwaj and A K Chaubey, Internal Report IC/88/57 (ICTP, Trieste, 1988)
[14] I A Rizvi, M K Bhardwaj, M Afzal Ansari and A K Chaubey, *Can. J. Phys.* **67**, 870 (1989)
[15] H D Bhardwaj, A K Gautam and R Prasad, *Pramana – J. Phys.* **31**, 109 (1988)
[16] B P Singh, M G V Sankaracharyulu, M Afzal Ansari, R Prasad and H D Bhardwaj, *Int. J. Mod. Phys.* **E1**, 823 (1992)
[17] M Afzal Ansari, N P M Sathik, B P Singh, M G V Sankaracharyulu and R Prasad, Internal Report IC/94/299 (ICTP, Trieste, 1994)
[18] B P Singh, M G V Sankaracharyulu, M Afzal Ansari, H D Bhardwaj and R Prasad, *Phys. Rev.* **47**, 2055 (1993)
[19] N P M Sathik, M Afzal Ansari, B P Singh, M G V Sankaracharyulu and R Prasad, *Int. J. Mod. Phys.* **E5**, 345 (1996)
[20] L C Northcliffe and R F Schilling, *Nucl. Data Tables* **A7**, 256 (1970)
[21] R Michel and G Brinkmann, *Nucl. Phys.* **A338**, 167 (1980)
[22] M Afzal Ansari, R K Y Singh, M Sehgal, V K Mittel and D K Avasthi, *Ann. Nucl. Energy* **11**, 173 (1984)
[23] C M Lederer and V S Shirley, Table of isotopes, 7th edition (Wiley and Sons Inc., New York, 1978)
[24] R P Gardner and K Verghese, *Nucl. Instrum. Methods* **93**, 163–167 (1971)
[25] J Ernst, R Iowski, H Klampfl, H Machner, T Mayer-Kuckuk and R Schanz, *Z. Phys.* **A308**, 301 (1982)
[26] M Blann and J Bisplinghoff, ALICE/LIVERMORE-82, Report UCID-19614 (1982)
[27] V F Weisskopf and D H Ewing, *Phys. Rev.* **57**, 472 (1940)

[28] T Ericson, *Adv. Phys.* **9**, 425 (1960)
[29] F D Becchetti and G W Greenlees, *Phys. Rev.* **182**, 1190 (1969)
[30] K Kikuchi and M Kawai, *Nuclear matter and nuclear interactions* (North-Holland, Amsterdam, 1968)
[31] M Blann, *Nucl. Phys.* **A213**, 570 (1973)
[32] W D Myers and W J Swiatecki, *Ark. Fys.* **36**, 343 (1967)

PRAMANA
— journal of
physics

© Printed in India

Vol. 47, No. 5,
November 1996
pp. 411–417

Radiative decays of heavy baryons with heavy quark symmetry

A K GIRI, L MAHARANA and R MOHANTA
Physics Department, Utkal University, Bhubaneswar 751 004, India

MS received 20 January 1996; revised 30 April 1996

Abstract. The decay widths for the radiative decays of heavy baryons are calculated in the heavy quark effective theory. Introducing the interpolating fields for heavy baryons we obtain the transition matrix elements and the corresponding decay widths. Considering the $SU(6)$ flavor-spin wave functions for heavy baryons, the coupling constants are calculated in the nonrelativistic quark model. Since the masses of the heavy baryons are not available, we have taken the predicted bag model masses. We find our results are quite different from that of the heavy quark bag model calculations.

Keywords. Heavy quark effective theory; interpolating fields.

PACS Nos 11·30; 13·40; 14·20

1. Introduction

In this brief report we intend to study the radiative decays of heavy baryons in the heavy quark effective theory (HQET) [1–4]. Earlier Cheng *et al* [5] had studied these decays using the basic assumptions of heavy quark symmetry alongwith chiral symmetry. Here we have presented a direct and elegant calculation for the radiative decay widths of the heavy baryons. Although we have adopted the procedure as done in [5], our calculations are more reliable than theirs since we have related the coupling constants to the proton magnetic moment which is measurable to a high accuracy whereas they have evaluated them in terms of the quark magnetic moments. Since the experimental masses of the heavy baryons are still unknown, we have taken the predicted bag model masses [6] for them and obtained the decay widths for their radiative transitions. However, a definite prediction can be made only after the experimental masses are known.

2. Theory

A heavy baryon contains a single heavy quark and two light quarks, which are often referred as diquark. Since each light quark is represented as a triplet in $SU(3)$ flavor space, the diquarks form two different $SU(3)$ multiplets. The diquark in the flavor symmetric sextet has spin 1 and when it combines with the spin of heavy quark gives the spin-1/2 (B_6) and spin-3/2 (B_6^*) baryons. In terms of 3×3 matrix the spin-1/2 baryons

are represented as [7]

$$B_6 = \begin{bmatrix} \Sigma_Q^{+1} & \frac{1}{\sqrt{2}}\Sigma_Q^0 & \frac{1}{\sqrt{2}}\Xi_Q'^{1/2} \\ \frac{1}{\sqrt{2}}\Sigma_Q^0 & \Sigma_Q^{-1} & \frac{1}{\sqrt{2}}\Xi_Q'^{-1/2} \\ \frac{1}{\sqrt{2}}\Xi_Q'^{1/2} & \frac{1}{\sqrt{2}}\Xi_Q'^{-1/2} & \Omega_Q \end{bmatrix}. \tag{1}$$

The matrix for B_6^* is similar to B_6. The superscript indicates the value of the isospin quantum number I_3. The diquark in the antisymmetric antitriplet state has spin 0. Thus the combination gives the spin-1/2 baryons ($B_{\bar{3}}$) which are given in terms of an antisymmetric matrix as [7]

$$B_{\bar{3}} = \begin{bmatrix} 0 & \Lambda_Q & \Xi_Q^{1/2} \\ -\Lambda_Q & 0 & \Xi_Q^{-1/2} \\ -\Xi_Q^{1/2} & -\Xi_Q^{-1/2} & 0 \end{bmatrix}. \tag{2}$$

In terms of the interpolating fields [2] these heavy baryons are described as

$$B_{\bar{3}}(v,s) = \bar{u}(v,s)\phi_v h_v, \tag{3}$$

and

$$B_6(v,s,k) = \bar{B}_\mu \phi_v^\mu h_v; \quad k = 1,2, \tag{4}$$

where $k = 1$ for spin-1/2 baryons and $k = 2$ for spin-3/2 baryons. In the above equations ϕ_v and h_v represent the diquark and the heavy quark field respectively. Since the ground state baryons have even parity, the diquarks must also have even parity. Therefore the diquark in $B_{\bar{3}}$ has spin parity 0^+ and represented by the Lorentz scalar ϕ whereas the diquark in B_6 multiplet has spin parity 1^+ and represented by the axial vector field ϕ_μ. The wave functions $\bar{B}_\mu$ as given by Georgi [2] are

$$\bar{B}_\mu(v,s,k=1) = \frac{1}{\sqrt{3}}\bar{u}(v,s)\gamma_5(\gamma_\mu + v_\mu) \tag{5}$$

and

$$\bar{B}_\mu(v,s,k=2) = \bar{u}_\mu(v,s), \tag{6}$$

$u_\mu(v,s)$ and $u(v,s)$ being the Rarita–Schwinger vector spinor field and the usual Dirac spinor respectively, satisfying the relations

$$\not{v} B_\mu(v,s) = B_\mu(v,s) \quad \text{and} \quad v^\mu B_\mu(v,s) = 0. \tag{7}$$

The spin sum of the spinors are taken as

$$\sum_s u_\mu(v,s)\bar{u}_\nu(v,s) = \frac{\not{v}+1}{2}\left[-g_{\mu\nu} + \tfrac{1}{3}\gamma_\mu\gamma_\nu + \tfrac{1}{3}(\gamma_\mu v_\nu - \gamma_\nu v_\mu) + \tfrac{2}{3}v_\mu v_\nu\right], \tag{8}$$

and

$$\sum_s u(v,s)\bar{u}(v,s) = \frac{\not{v}+1}{2}. \tag{9}$$

In the HQET the heavy baryons are taken as bound states of a heavy quark and the diquark fields. Hence in the radiative M1 transitions of the heavy baryons the photon is emitted either from the heavy quark or from the light diquark system. For the transition processes $B_6(B_6^*) \to B_{\bar{3}}\gamma$, the diquark system undergoes a spinflip transition and the heavy quark remains as a spectator whereas for $B_6^* \to B_6\gamma$ the photon may be emitted by the heavy quark and the diquark system remains as spectator.

The transition amplitude describing the process $B_i \to B_f\gamma$ is given by

$$\mathcal{M}(B_i \to B_f\gamma) = \varepsilon^\mu \langle B_f | J_\mu^{\text{e.m.}} | B_i \rangle, \tag{10}$$

where ε^μ denotes the polarization vector of the emitted photon. $J_\mu^{\text{e.m.}}$ is the electromagnetic current which can be split into heavy and light quark components, i.e. $J_\mu^{\text{e.m.}} = J_\mu^{\text{Q}} + J_\mu^{\text{q}}$ with the heavy quark current as $J_\mu^{\text{Q}} = e_{\text{Q}}\bar{\text{Q}}\gamma^\mu \text{Q}$, e_{Q} is the charge of the heavy quark field Q.

To calculate the transition amplitude for $B_6 \to B_{\bar{3}}\gamma$ process

$$\mathcal{M}(B_6(v,s) \to B_{\bar{3}}(v',s')\gamma) = \varepsilon^\mu \langle B_{\bar{3}}(v',s') | J_\mu^{\text{Q}} + J_\mu^{\text{q}} | B_6(v,s) \rangle, \tag{11}$$

it is essential to evaluate the r.h.s. of eq. (11) for both heavy and light quark sector. Using the interpolating fields for heavy baryons from eqs (3) and (4), we obtain the matrix element for the heavy quark current part as

$$\langle B_{\bar{3}}(v',s') | J_\mu^{\text{Q}} | B_6(v,s) \rangle = e_{\text{Q}} \bar{u}_{\bar{3}}(v',s') \gamma_\mu B^\nu(v,s) \langle 0 | \phi_{v'} \phi_{v\nu}^\dagger | 0 \rangle. \tag{12}$$

In the above equation we have used $\langle 0 | h_{v'} \bar{h}_v | 0 \rangle = ((\not{v} + 1)/2)$, the heavy quark propagator, as in the heavy quark limit the velocity of heavy quark before and after interaction is approximately equal i.e. $v \sim v'$. It has been emphasized earlier that the diquark field $\phi_{v'}$ and $\phi_{v\nu}^\dagger$ are scalar and axial vectors respectively, so $\langle 0 | \phi_{v'} \phi_{v\nu}^\dagger | 0 \rangle$ is an axial vector. Since it is impossible to construct an axial vector out of v and v' only, therefore $\langle 0 | \phi_{v'} \phi_{v\nu}^\dagger | 0 \rangle = 0$, hence the heavy quark current sector does not contribute to the transition amplitude. Now for the light quark sector we have

$$\langle B_{\bar{3}}(v',s') | J_\mu^{\text{q}} | B_6(v,s) \rangle = \langle 0 | \bar{u}_{\bar{3}}(v',s') M_{\mu\nu} B^\nu(v,s) | 0 \rangle, \tag{13}$$

where $M_{\mu\nu} = \langle 0 | \phi_v J_\mu^{\text{q}} \phi_{v\nu}^\dagger | 0 \rangle$. Lorentz invariance implies that

$$M_{\mu\nu} = i\eta \varepsilon_{\mu\nu\alpha\beta} k^\alpha v^\beta, \tag{14}$$

where η is the coupling parameter. With (5), (13) and (14) we obtain the transition amplitude for $B_6 \to B_{\bar{3}}\gamma$ process from (11) as

$$\mathcal{M}(B_6(v,s) \to B_{\bar{3}}(v',s')\gamma) = \frac{i}{\sqrt{3}} \eta \bar{u}_{\bar{3}}(v',s') \sigma_{\mu\nu} k^\mu \varepsilon^\nu u_6(v,s) \tag{15}$$

and the corresponding decay width to be

$$\Gamma(B_6 \to B_{\bar{3}}\gamma) = \frac{1}{\pi} k^3 \left(\frac{\eta}{\sqrt{3}} \right)^2. \tag{16}$$

For $B_6^* \to B_{\bar{3}}\gamma$ processes there is also no contribution to the transition amplitude from the heavy quark current sector as the diquark field is same for B_6 and B_6^* baryons,

implying $\langle 0|\phi_{v'}\phi^{\dagger}_{vv}|0\rangle = 0$. For the light quark sector we have

$$\langle B_{\bar{3}}(v',s')|J^{q}_{\mu}|B^{*}_{6}(v,s)\rangle = \bar{u}_{\bar{3}}(v',s')M_{\mu\nu}u^{\nu}(v,s). \tag{17}$$

Substituting the value of $M_{\mu\nu}$ from (14) with η replaced by η_1 we obtain the transition amplitude as

$$\mathcal{M}(B^{*}_{6}(v,s)\to B_{\bar{3}}(v',s')\gamma) = -i\eta_1\varepsilon_{\mu\nu\alpha\beta}\bar{u}_{\bar{3}}(v',s')\varepsilon^{\mu}k^{\nu}\gamma^{\alpha}u^{\beta}(v,s) \tag{18}$$

and the corresponding decay width is

$$\Gamma(B^{*}_{6}\to B_{\bar{3}}\gamma) = \frac{k^3}{12\pi}\eta_1^2\left(3+\frac{m_f^2}{m_i^2}\right), \tag{19}$$

where m_i and m_f are the masses of the initial and final baryons in the decay process.

For $B^{*}_{6}\to B_{6}\gamma$ process, the contribution from the heavy quark current sector is given as

$$\langle B_6(v',s')|J^{Q}_{\mu}|B^{*}_{6}(v,s)\rangle = e_Q\bar{B}^{\alpha}(v',s')\gamma_{\mu}u^{\beta}(v,s)\zeta_{\alpha\beta}(v\cdot v'), \tag{20}$$

where $\zeta_{\alpha\beta}(v\cdot v') = \langle 0|\phi_{v'\alpha}\phi^{\dagger}_{v\beta}|0\rangle$ and in the limit $v\sim v', \zeta_{\alpha\beta}(v\cdot v') = -g_{\alpha\beta}\xi(v\cdot v')$, where $\xi(v\cdot v')$ is the Isgur–Wise function. Equation (20) implies that the heavy quark current does not induce a magnetic coupling and therefore it does not contribute to the radiative M1 transitions. For the light quark current we have obtained the matrix element as

$$\langle B_6(v',s')|J^{q}_{\mu}|B^{*}_{6}(v,s)\rangle = \bar{B}^{\alpha}(v',s')M_{\mu\alpha\beta}u^{\beta}(v,s), \tag{21}$$

where $M_{\mu\alpha\beta} = \langle 0|\phi_{v'\alpha}J^{q}_{\mu}\phi^{\dagger}_{v\beta}|0\rangle$. Taking the general expression for $M_{\mu\alpha\beta}$ from ref. [5] as

$$M_{\mu\alpha\beta} = f_1 g_{\alpha\beta}(v+v')_{\mu} + f_3(g_{\mu\alpha}k_{\beta} - g_{\mu\beta}k_{\alpha}) + f_5 v_{\alpha}v'_{\beta}(v+v')_{\mu}, \tag{22}$$

we obtain

$$\langle B_6(v',s')|J^{q}_{\mu}|B^{*}_{6}(v,s)\rangle = \frac{f_3}{\sqrt{3}}\bar{u}(v',s')\gamma_5(\gamma_{\mu}k_{\beta} - g_{\mu\beta}\not{k})u^{\beta}(v,s). \tag{23}$$

Hence the transition amplitude for the process $B^{*}_{6}\to B_{6}\gamma$ is given by

$$\mathcal{M}(B^{*}_{6}(v,s)\to B_6(v',s')\gamma) = \frac{if_3}{\sqrt{3}}\bar{u}(v',s')\gamma_5\gamma^{\nu}F_{\nu\beta}u^{\beta}(v,s), \tag{24}$$

where $F_{\nu\beta}$ is the electromagnetic field strength tensor i.e. $F_{\nu\beta} = i(k_{\nu}\varepsilon_{\beta} - k_{\beta}\varepsilon_{\nu})$. Using eq. (8) we obtain the decay width to be

$$\Gamma(B^{*}_{6}\to B_6\gamma) = \frac{k^3}{12\pi}\left(\frac{f_3}{\sqrt{3}}\right)^2\left(3+\frac{m_f^2}{m_i^2}\right), \tag{25}$$

with m_i and m_f are the masses of the initial and final baryons in the decay process. Thus the general expression for the decay widths $B_6\to B_{\bar{3}}\gamma$, $B^{*}_{6}\to B_{\bar{3}}\gamma$ and $B^{*}_{6}\to B_{\bar{6}}\gamma$ are given in eqs (16), (19) and (25) respectively. The coupling constants η, η_1 and f_3 present in the expressions are calculated considering the nonrelativistic quark model. In this model the M1 transitions are described by the spin operator of the quarks given as $M = \Sigma_q\mu_q e_q\sigma_q$, where e_q and σ_q are the charge and spin operator of the quarks. μ_q

denotes the quark scale magnetic moment which is identical with the proton magnetic moment for u and d quarks, while for s quark it is taken as $\mu_s = (3/5)\mu_p$ [8]. For the heavy quarks we have taken $\mu_Q = (1/2m_Q)$. Considering the $SU(6)$ flavor-spin wave functions for the heavy baryons from ref. [5] we obtain the transition matrix elements of the spin operator for various possible M1 transitions. Since we have used the flavor-spin wave functions for the baryons to calculate the above matrix elements, the results obtained are equal to the couplings in (15), (18) and (24) which are given as

$$\frac{\eta}{\sqrt{3}}(\Sigma_Q^0 - \Lambda_Q) = -\frac{1}{\sqrt{3}}(\mu_u e_u - \mu_d e_d),$$

$$\frac{\eta}{\sqrt{3}}(\Xi_Q'^{1/2} - \Xi_Q^{1/2}) = -\frac{1}{\sqrt{3}}(\mu_u e_u - \mu_s e_s),$$

$$\frac{\eta}{\sqrt{3}}(\Xi_Q'^{-1/2} - \Xi_Q^{-1/2}) = -\frac{1}{\sqrt{3}}(\mu_d e_d - \mu_s e_s),$$

$$\eta_1(\Sigma_Q^{0*} - \Lambda_Q) = \frac{2}{\sqrt{6}}(\mu_u e_u - \mu_d e_d),$$

$$\eta_1(\Xi_Q'^{*1/2} - \Xi_Q^{1/2}) = \frac{2}{\sqrt{6}}(\mu_u e_u - \mu_s e_s),$$

$$\eta_1(\Xi_Q'^{*-1/2} - \Xi_Q^{-1/2}) = \frac{2}{\sqrt{6}}(\mu_d e_d - \mu_s e_s),$$

$$\frac{f_3}{\sqrt{3}}(\Sigma_Q^{*+1} - \Sigma_Q^{+1}) = \frac{2\sqrt{2}}{3}(\mu_u e_u - \mu_Q e_Q),$$

$$\frac{f_3}{\sqrt{3}}(\Sigma_Q^{*0} - \Sigma_Q^0) = \frac{\sqrt{2}}{3}(\mu_u e_u + \mu_d e_d - 2\mu_Q e_Q),$$

$$\frac{f_3}{\sqrt{3}}(\Xi_Q'^{*1/2} - \Xi_Q'^{1/2}) = \frac{\sqrt{2}}{3}(\mu_u e_u + \mu_s e_s - 2\mu_Q e_Q),$$

$$\frac{f_3}{\sqrt{3}}(\Xi_Q'^{*-1/2} - \Xi_Q'^{-1/2}) = \frac{\sqrt{2}}{3}(\mu_d e_d + \mu_s e_s - 2\mu_Q e_Q)$$

and

$$\frac{f_3}{\sqrt{3}}(\Omega_Q^* - \Omega_Q) = \frac{2\sqrt{2}}{3}(\mu_s e_s - \mu_Q e_Q). \tag{26}$$

3. Results and discussion

Here we have estimated the radiative decay widths for different radiative processes. The masses of the heavy quarks are taken as $m_c = 1{\cdot}6$ GeV and $m_b = 5$ GeV. The masses of the Σ_c, Λ_c, Ξ_c and Λ_b baryons are taken from ref. [9] and the other heavy baryon masses

from ref. [6]. The proton magnetic moment is taken as $\mu_p = 2{\cdot}793$ nm. The centre of mass momentum of the photon k is obtained from the rest frame of the decaying baryon. Substituting the value of the coupling constants from eq. (26) in the expressions for the partial decay widths (16), (19) and (25) we tabulate the results in table 1 and compare them with the results of Izzat *et al* [6]. We observe that our results are quite different from them. Since there is no model dependent parameter in our calculation we expect our results to be more appreciative than that of ref. [6].

In the present investigation we have estimated the radiative decay widths of heavy baryons in heavy quark effective theory. Using the interpolating fields for the heavy

Table 1. The radiative decay widths for the heavy baryons in the HQET as well as in bag model.

$B_i \to B_f \gamma$	k in MeV	$\Gamma(B_i \to B_f \gamma)$ in keV (Present work)	$\Gamma(B_i \to B_f \gamma)$ in keV (from heavy quark bag model [6])
$\Sigma_c^+ \to \Lambda_c^+ \gamma$	162·90	93·17	17
$\Sigma_b \to \Lambda_b \gamma$	137·33	55·82	53
$\Xi_c'^+ \to \Xi_c^+ \gamma$	34·66	0·674	4
$\Xi_c'^0 \to \Xi_c^0 \gamma$	29·52	0·009	0·07
$\Xi_b'^0 \to \Xi_b^0 \gamma$	108·97	20·95	20
$\Xi_b'^- \to \Xi_b^- \gamma$	108·97	0·496	0·3
$\Sigma_c^{*+} \to \Lambda_c^+ \gamma$	194·47	104·676	177
$\Sigma_b^* \to \Lambda_b \gamma$	176·25	77·48	107
$\Xi_c'^{*+} \to \Xi_c^+ \gamma$	131·4	23·87	66
$\Xi_c'^{*0} \to \Xi_c^0 \gamma$	126·46	0·504	1
$\Xi_b'^{*0} \to \Xi_b^0 \gamma$	148·11	34·63	50
$\Xi_b'^{*-} \to \Xi_b^- \gamma$	148·11	0·82	0·7
$\Sigma_c^{*++} \to \Sigma_c^{++} \gamma$	36·63	0·252	9
$\Sigma_c^{*+} \to \Sigma_c^+ \gamma$	35·94	$0{\cdot}598 \times 10^{-3}$	0·08
$\Sigma_b^{*+} \to \Sigma_b^+ \gamma$	39·86	0·574	0·8
$\Sigma_b^{*0} \to \Sigma_b^0 \gamma$	39·86	0·043	0·06
$\Xi_c'^{*+} \to \Xi_c'^+ \gamma$	98·08	0·154	0·3
$\Xi_c'^{*0} \to \Xi_c'^0 \gamma$	98·08	0·93	4
$\Xi_b'^{*0} \to \Xi_b'^0 \gamma$	39·87	0·079	0·09
$\Xi_b'^{*-} \to \Xi_b'^- \gamma$	39·87	0·072	0·1
$\Omega_c^* \to \Omega_c \gamma$	98·15	2·056	3
$\Omega_b^* \to \Omega_b \gamma$	39·87	0·038	0·06

baryons we calculate the decay widths for various possible radiative transitions. The decay widths so calculated contain unknown couplings, which are calculated in the nonrelativistic quark model using the $SU(6)$ flavor-spin wave functions of the baryons. The masses of the heavy baryons are taken from Izatt *et al* [6] as their experimental masses are not available. However there is an uncertainty in the predicted widths which may be removed after experimental values for the baryon masses are available. Although we have followed the procedure of Cheng *et al*, the main difference between our calculation and that of theirs is as follows. We have related the effective coupling constant of the $B_i B_f \gamma$ vertex in the HQET to the proton magnetic moment which is directly measurable to a high accuracy, whereas they have related the couplings to the quark magnetic moments which are not directly observed. We therefore feel that our calculation is more reliable in the spirit of effective field theory where one tries to obtain the branching ratio predictions in terms of directly observable quantities.

Acknowledgements

We are very much thankful to Profs B B Deo, N Barik and Dr S Mohanty for useful discussions. One of the authors (RM) would like to thank CSIR, Govt. of India for fellowship.

References

[1] N Isgur and M B Wise, *Phys. Lett.* **B232**, 113 (1989)
[2] H Georgi, *Nucl. Phys.* **B348**, 293 (1991); *Phys. Lett.* **B240**, 447 (1990)
[3] A F Falk, H Georgi and B Grinstein, *Nucl. Phys.* **B343**, 1 (1990)
[4] N Isgur and M B Wise, *Nucl. Phys.* **B348**, 276 (1991)
[5] H-Y Cheng, C Y Cheung, G Lin Lin, Y C Lin, T-M Yan and H L Yu, *Phys. Rev.* **D47**, 1030 (1993)
[6] D Izatt, C Detar and M Stephenson, *Nucl. Phys.* **B199**, 269 (1982)
[7] P Cho and H Georgi, *Phys. Lett.* **B296**, 408 (1992)
[8] F E Close, in *An introduction to quarks and partons* (Academic Press, London, 1979) p. 64
[9] Particle Data Group, *Phys. Rev.* **D50**, part 1 (1994)

physics pp. 419–433

The partial distribution functions and effective pair potentials of some H-bonded liquids from diffraction data

S SARKAR and R N JOARDER
Department of Physics, Jadavpur University, Calcutta 700 032, India

MS received 21 May 1996; revised 2 September 1996

Abstract. The partial structures and distribution functions are directly linked to structural model of molecular liquids. The comparative study of partial distribution function of different hydrogen-bonded liquids gives the information that hydrogen-bonding is stronger in alcohols than in water and ammonia. The effective pair potential is directly related to the pair correlation function. The comparative study of such potentials for different hydrogen-bonded liquids gives some characteristic features.

Keywords. H-bonded liquid; partial distribution function; pair potential.

PACS No. 61·25

1. Introduction

In our previous laboratory studies, investigations were carried out on the intermolecular structural association of strongly H-bonded liquids, water [1], alcohols [2] and weakly H-bonded liquid ammonia [3]. Devoid of intramolecular terms, the diffraction profile is essentially due to interference in the scattering from different atomic sites present on neighboring molecules so that description in terms of pair correlation functions is more directly linked to the observations. In the present study, the emphasis concerns on the method of evaluating the intermolecular partial structures and correlations in relation to the intermolecular structural association or cluster models of the H-bonded liquids studied earlier. These computed partial structures and correlations provide not only the crucial test [1] of the various association or cluster models but also clearly exhibit the structural distinction from other molecular liquids which are non H-bonded with van der Waals' forces dominating the intermolecular interaction. Like other liquids the pair correlation or distribution functions are directly related to the pair potentials. So if one knows these functions, in principle, the effective pair potential can be evaluated.

Though the intermolecular atom–atom pair distribution function $g_{\alpha\beta}(r)$'s are useful to define the detailed structure of the liquid and these functions have the advantage that their 'definition' do not involve any approximation, the actual extraction of these functions from experimental data is possible only in limited cases [4]. In the case of liquids which consist of two non-equivalent atoms e.g. water and ammonia there are three pair distribution functions and a minimum of three independent scattering experiments (x-ray, neutron, electron or isotopic substitution neutron experiments) are necessary to determine

these distribution functions. The number rapidly increases for molecules with more than two non-equivalent atoms e.g. methanol or acetonitrile [5, 6]. Many organic liquids of considerable importance consist of three or more atomic species, a full description in terms of $g_{\alpha\beta}(r)$ becomes extremely difficult.

The intermolecular atomic site-site pair distribution functions are also obtainable in Monte Carlo (MC) or molecular dynamics (MD) simulations based on effective pair potential models of H-bonded liquids [7]. However, a direct comparison of the partial $g_{\alpha\beta}(r)$ functions with experimentally evaluated values will give a proper test of the potential model [8] used in computation. Evidently the success of this method depends on the modelling of the potential function which itself is a problem for large H-bonded molecules.

In the light of such a situation, the present approach is relevant. The method is based on the assumption that on average, there exist in the liquid one or two types of distinct H-bonded clusters in dominant form. Using a combined analysis of x-ray and neutron diffraction data, we have evaluated [1–3] the center structure factors of several H-bonded liquids through geometrical cluster models. These models then readily yield the intermolecular structures and pair distribution functions. Further, the intermolecular center radial distribution function (CRDF), $g_c(r)$ and center direct correlation function (CDCF) $C_c(r)$ are obtained by Fourier transform of the center structure factor computed from diffraction data. These functions give the average intermolecular picture of the liquid systems with characteristic H-bonding features. From the knowledge of $g_c(r)$ and $C_c(r)$ it is possible to evaluate the average effective pair potentials for several H-bonded liquids using various approximate theories available in the literature [9].

2. Theoretical background

(a) *Partial structures and correlations*

The partial structure factors [9] for a molecule containing several atom types α and β can be expressed as

$$a_{\alpha\beta}(k) = 1 + \rho \int (g_{\alpha\beta}(r) - 1) \exp(i\mathbf{k}.\mathbf{r})\mathrm{d}\mathbf{r}, \tag{1}$$

where $g_{\alpha\beta}(r)$ is defined as follows. The total radial distribution function $g(r)$ consists of a number of independent partial distribution functions $g_{\alpha\beta}(r)$. In a molecular liquid, we can define atom pair distributions $g_{\alpha\beta}(r)$ so that $\rho g_{\alpha\beta}(r)\mathrm{d}\mathbf{r}$ is the number of β sites in a volume element $\mathrm{d}\mathbf{r}$ at a distance r from an α site on another molecule in a fluid of bulk number density ρ. The function $g_{\alpha\beta}(r)$ are obtained from experimentally accessible partial structure factors $a_{\alpha\beta}(k)$ by Fourier inversion relation, i.e.

$$g_{\alpha\beta}(r) = 1 + \frac{1}{(2\pi)^3 \rho} \int_0^\infty (a_{\alpha\beta}(k) - \delta_{\alpha\beta}) j_0(kr)\mathrm{d}k. \tag{2}$$

The atom–atom pair correlation functions $h_{\alpha\beta}(r)$ are given by $h_{\alpha\beta}(r) = g_{\alpha\beta}(r) - 1$. In general, for molecular liquids the intermolecular distinct structure function $H_d(k)$ which

is experimentally accessible contains a weighted sum of the partial functions [10] and is written as

$$H_{\mathrm{d}}(k) = M(k) \sum_{\alpha} \sum_{\beta} f_{\alpha} f_{\beta} H_{\alpha\beta}(k), \tag{3}$$

where f'_{α}s are k-dependent x-ray atomic scattering factors or k independent neutron scattering lengths and $M(k) = [\sum_{\alpha} f_{\alpha}]^{-2}$, the summation extending over all atoms of a molecule. In (3) the partial structure function $H_{\alpha\beta}(k) = \rho h_{\alpha\beta}(k)$ and $\rho h_{\alpha\beta}(k) = a_{\alpha\beta}(k) - \delta_{\alpha\beta}$ for α site on one molecule and β site on another. The diffraction experiments on molecular liquids are interpreted in terms of atom–atom pair distribution functions $g_{\alpha\beta}(r)$. But they do not contain enough information to give the angular dependent pair distribution function.

The estimate of the number of neighboring β site of one molecule surrounding α site of another molecule [9] is obtained by integrating $g_{\alpha\beta}(r)$ as follows

$$n_{\alpha\beta} = 4\pi\rho \int_0^{r_{\min}} g_{\alpha\beta}(r) r^2 \mathrm{d}r, \tag{4}$$

where $r_{\min}$ is the value of the first minimum of $g_{\alpha\beta}(r)$ distribution function.

Partial structures and pair distribution functions via cluster model: In ref. [1, 2] it was shown on the basis of assumptions that the liquid contains distinct molecular clusters due to H-bonding and that these clusters are orientationally uncorrelated as

$$H_{\mathrm{d}}(k) = H_{\mathrm{c}}(k) + F_{2\mathrm{u}}(k)[S_{\mathrm{c}}(k) - f_3(k) - 1], \tag{5}$$

where $H_{\mathrm{c}}(k)$ is the intermolecular cluster structure function defined by

$$H_{\mathrm{c}}(k) = M(k) N_{\mathrm{c}}^{-1} \sum_{1 \neq 1'} \sum_{\alpha,\beta} f_{\alpha_1} f_{\beta_{1'}} j_0(k r_{\alpha_1\beta_{1'}}) \exp(-\lambda^2_{\alpha_1\beta_{1'}} k^2/2) \tag{5a}$$

with N_{c}, the number of molecules in a cluster, α, β denote the atoms while $1, 1'$ denote molecules, $\lambda_{\alpha_1\beta_{1'}}$, the root-mean-square deviation of the local instantaneous atom–atom separation distance $r_{\alpha_1\beta_{1'}}$ and $j_0(x) = x^{-1} \sin x$.

The uncorrelated molecular form factor $F_{2\mathrm{u}}(k)$ is given by

$$F_{2\mathrm{u}}(k) = M(k) \left[\sum_{\alpha} f_{\alpha} j_0(k r_{\mathrm{c}_{\alpha}}) \exp(-\lambda^2_{\mathrm{c}_{\alpha}} k^2/2) \right]^2, \tag{5b}$$

where c refer to the center of a molecule.

The center structure $S_{\mathrm{c}}(k)$ of the liquid is

$$S_{\mathrm{c}}(k) = 1 + N_{\mathrm{m}}^{-1} \sum_{1 \neq 1'} j_0(k r_{\mathrm{c}_{1'}}) \exp(-\lambda^2_{\mathrm{c}_{1'}} k^2/2) \tag{5c}$$

with N_{m} the number of molecules in the system, $f_3(k)$, the structure factor resulting from molecular center pairs within a cluster defined as

$$f_3(k) = N_{\mathrm{c}}^{-1} \sum_{1 \neq 1'} j_0(k r_{\mathrm{c}_{1'}}) \exp(-\lambda^2_{\mathrm{c}_{1'}} k^2/2). \tag{5d}$$

We have in general $H_c(k) \rightarrow H_d(k)$ for moderate to large k values and geometrical modelling of $H_c(k)$ provides information about the existence of dominant molecular clusters [1–3]. Once the dominant clusters are identified it is straightforward to evaluate the partial structures and distribution functions via cluster model. In order to do that we follow the method of Orton [11] and Ohtomo *et al* [12] depicted in ref. [1]. We assume that $H_{\alpha\beta}(k)$'s in (3) are given by the term involving $\alpha - \beta$ interactions from functions $H_c(k)$ and $F_{2u}(k)$ of (5). Thus

$$H_{\alpha\beta}(k) = H_c^{(\alpha\beta)}(k) + F_{2u}^{(\alpha\beta)}(k)[S_c(k) - f_3(k) - 1], \tag{6}$$

where

$$H_c^{(\alpha\beta)}(k) = N_c^{-1} \sum_{1 \neq 1'} \sum_{\alpha,\beta} j_0(kr_{\alpha_1\beta_{1'}}) \exp(-\lambda^2_{\alpha_1\beta_{1'}} k^2/2) \tag{6a}$$

and

$$F_{2u}^{(\alpha\beta)}(k) = (2 - \delta_{\alpha\beta}) j_0(kr_{c\alpha}) j_0(kr_{c\beta}) \exp[-(\lambda^2_{c\alpha} + \lambda^2_{c\beta})k^2/2]. \tag{6b}$$

The function $g_{\alpha\beta}(r)$'s are then given by

$$g_{\alpha\beta}(r) = 1 + \frac{1}{2\pi^2 \rho r} \int_0^\infty k H_{\alpha\beta}(k) \sin(kr)\, dk. \tag{7}$$

Thus, a knowledge of model cluster can yield the required partial structure factors and pair distribution functions from the experimental $H_d(k)$ data. If, however, $S_c(k)$ is calculable theoretically, then the model cluster can generate all the partial structure factors and pair distribution functions for the given molecular system. The results of our calculations are shown in figures 1–4.

(b) *Intermolecular center–center correlations*

The CRDF, $g_c(r)$ and CDCF, $C_c(r)$ are important average correlation functions between two molecules and these are obtained by Fourier inverse transform of center structure factor, $S_c(k)$ using the standard procedure [1]. Thus

$$g_c(r) = 1 + \frac{1}{2\pi^2 \rho r} \int_0^\infty k[S_c(k) - 1] \sin(kr) dk \tag{8}$$

and

$$C_{c(r)} = \frac{1}{2\pi^2 \rho r} \int_0^\infty \frac{S_c(k) - 1}{S_c(k)} \sin(kr)\, dk. \tag{9}$$

The accuracy of $g_c(r)$ can be checked by evaluating the isothermal compressibility of liquid at room temperature using the compressibility equation [9]

$$\rho k_B T \chi_T = 1 + \rho \int [g_c(r) - 1] dr. \tag{10}$$

The evaluation of $C_c(r)$ is important because it is intimately related to the average intermolecular potential energy function $\phi(r)$ [9]. The computed $C_c(r)$'s are shown in figure 5.

(c) *Evaluation of effective pair potential of H-bonded liquids through diffraction data*

The center structure factors evaluated from the combined analysis of x-ray and neutron

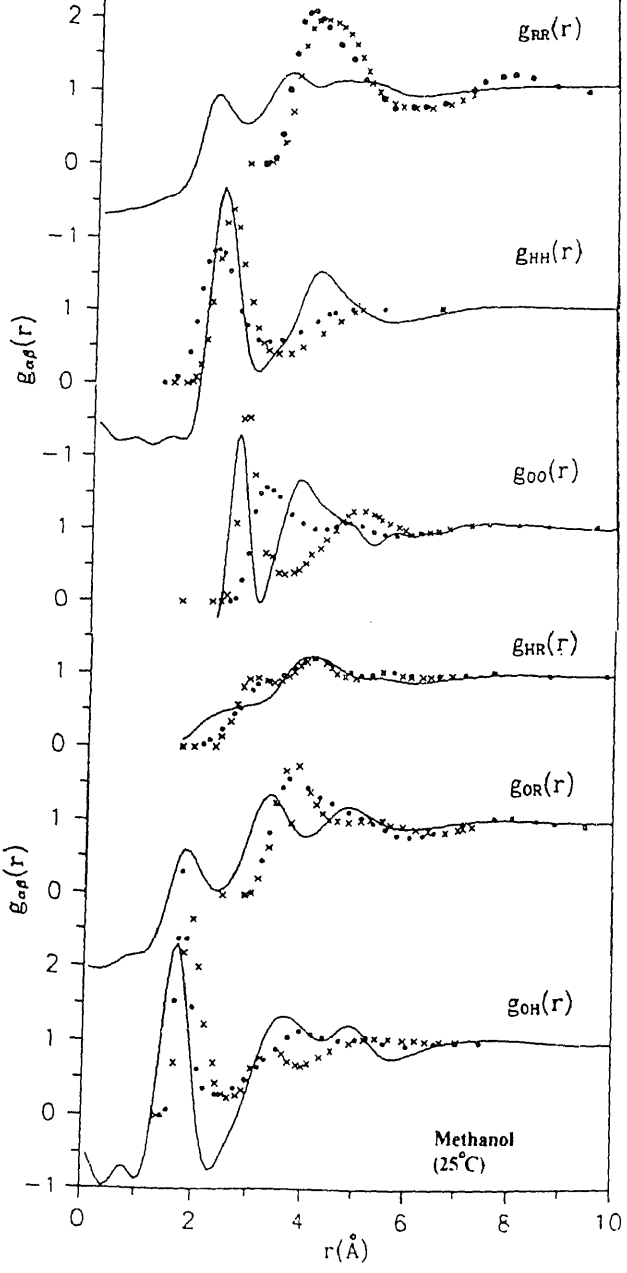

Figure 1. $g_{\alpha\beta}(r)$ for liquid methanol at 25°C. — Hexamer model, x x x simulation results, • • • RISM results.

H-bonded liquids. In [13] average effective intermolecular pair potential of water at room temperature was determined by modified hypernetted chain (MHNC) theory [9]. In the present case we do the computation for liquid ammonia at 4°C (weakly H-bonded) using

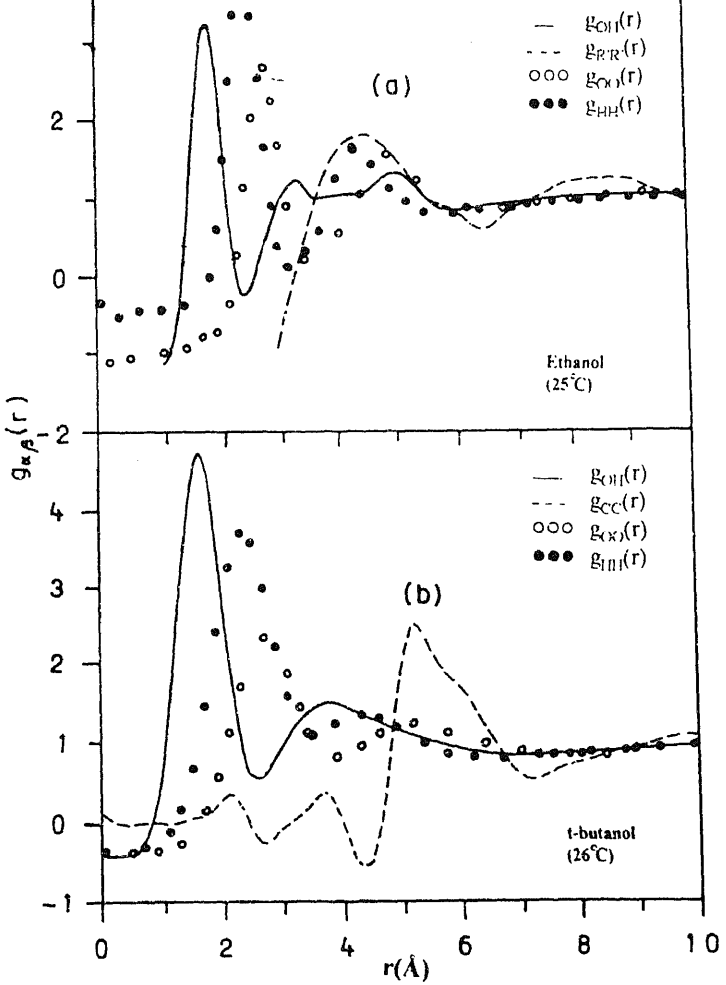

Figure 2. (**a**) Hexamer model $g_{\alpha\beta}(r)$ for liquid ethanol at 25°C; (**b**) Hexamer model $g_{\alpha\beta}(r)$ for liquid *tert*-butanol at 26°C.

the same procedure to bring out the characteristic difference from room temperature water (strongly H-bonded). The MHNC [9] theory of Rosenfeld and Ashcroft is known to be very accurate, quite universal in applications and many recent calculations are based on this theory [14].

The assumption of the existence of an effective pair potential, $\phi_{\text{eff}}(r)$ allows one to write the pair distribution function $g(r)$ as

$$g(r) = \exp[-\beta\phi_{\text{eff}}(r) + h(r) - C(r) + B(r)], \tag{11}$$

where $h(r) = g(r) - 1$, $C(r)$ and $B(r)$ are respectively the DCF and the 'Bridge function'. We have $g(r)$ and $C(r)$ obtainable from center structure factor data. $B(r)$ is not known. It

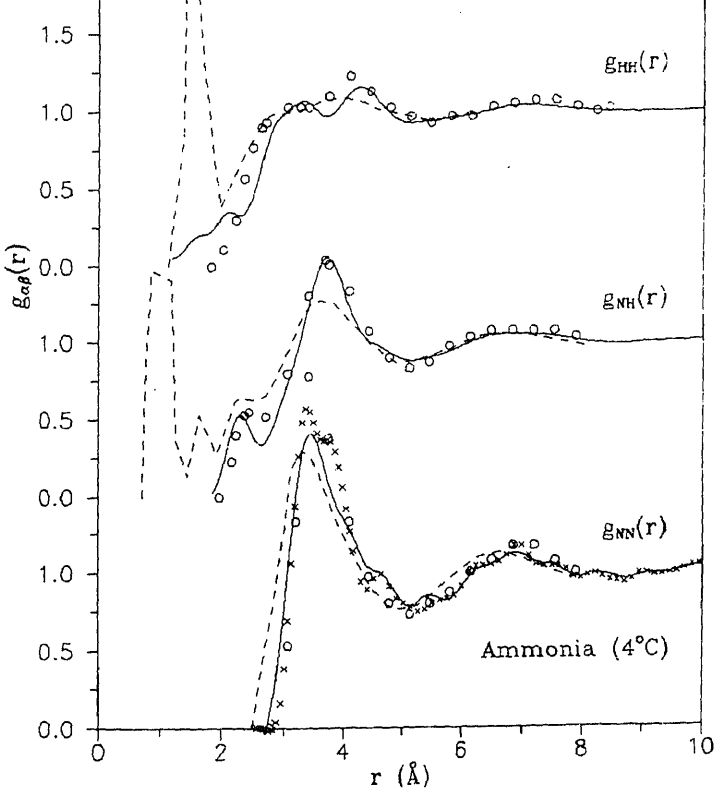

Figure 3. $g_{\alpha\beta}(r)$ for liquid ammonia at 4°C. ———— Symmetrical model, x x x $g_{NN}(r)$ from Narten; o o o simulation results, - - - - - - experimental results.

is however known that for small $r, B(r) \cong B_{hs}(r)$ where $B_{hs}(r, \eta)$ is the Bridge function of hard sphere system with a packing density η. For large r, since $C(r) \sim -\beta\phi_{eff}(r)$ it is easy to show that

$$B(r) \cong B_{hs}(r, \eta) + \tfrac{1}{2}[h^2(r) - h_{hs}^2(r)]. \tag{12}$$

In the MHNC for all r one assumes $B(r)$ to be equal to $B_{hs}(r, \eta)$ with packing density η given by the Lado criterion [15]

$$\int [g(r) - g_{hs}(r, \eta)] \frac{\partial B_{hs}(r, \eta)}{(\partial \eta)} \, dr = 0. \tag{13}$$

Thus, in the MHNC $\phi_{eff}(r)$ is given by

$$\phi_{eff}(r) = -k_B T \, [\ln g(r) + C(r) - h(r) - B_{hs}(r, \eta)]. \tag{14}$$

The computed $\phi_{eff}(r)$ for liquid ammonia (4°C) is shown in figure 6 together with the result for water at room temperature [13]. For comparison we depict the results too for other approximate theories e.g., hypernetted chain (HNC) and Percus–Yeivick (PY) [9].

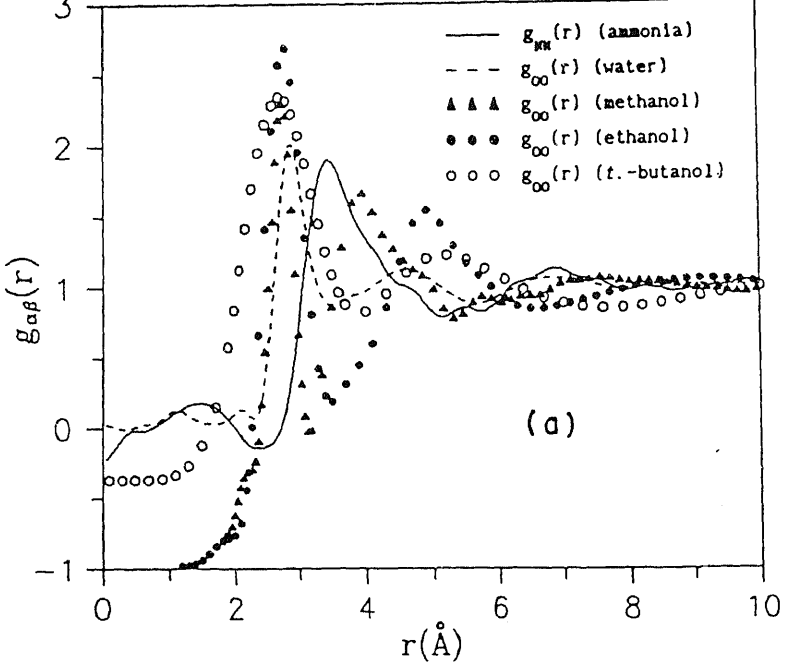
$g_{NH}(r)$ (ammonia)
$g_{OO}(r)$ (water)
$g_{OO}(r)$ (methanol)
$g_{OO}(r)$ (ethanol)
$g_{OO}(r)$ (t.-butanol)
(a)
$g_{\alpha\beta}(r)$
r(Å)

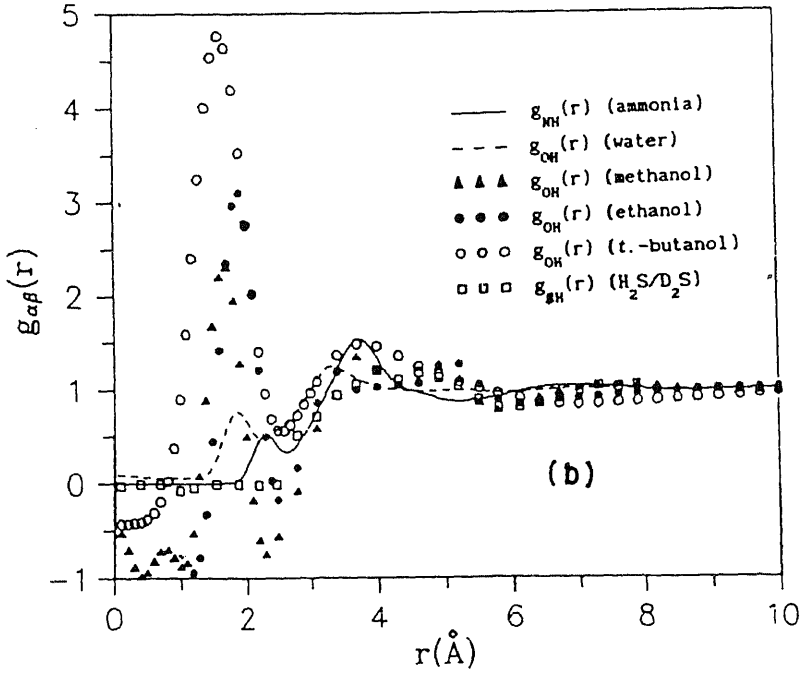
$g_{NH}(r)$ (ammonia)
$g_{OH}(r)$ (water)
$g_{OH}(r)$ (methanol)
$g_{OH}(r)$ (ethanol)
$g_{OH}(r)$ (t.-butanol)
$g_{SH}(r)$ (H_2S/D_2S)
(b)
$g_{\alpha\beta}(r)$
r(Å)

Figure 4a, b.

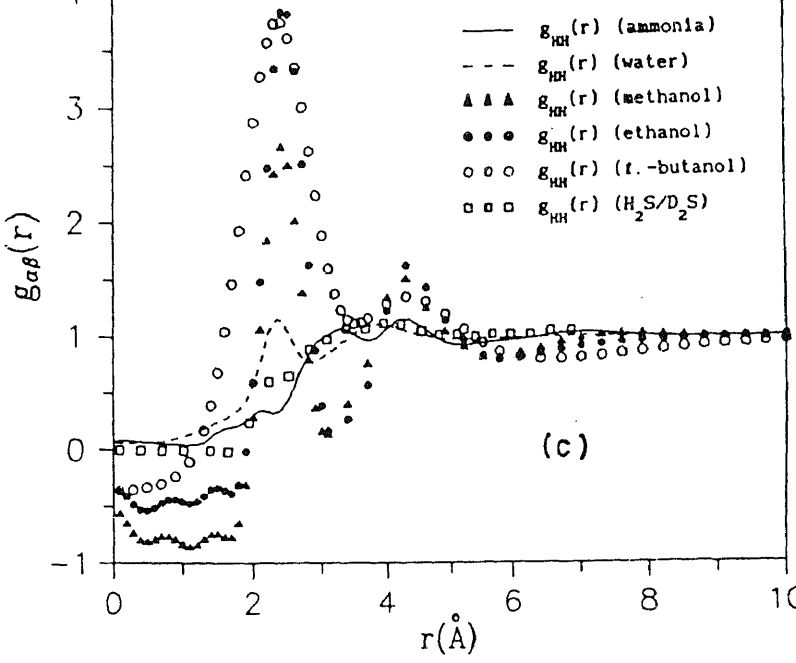

Figure 4. (a) $g_{OO}(r)/g_{NN}(r)$ for different H-bonded liquids; (b) $g_{OH}(r)/g_{NH}(r)$ for different H-bonded liquids; (c) $g_{HH}(r)$ for different H-bonded liquids.

Thus expressions are

$$\text{HNC} : \phi_{\text{eff}}(r) = k_B T[g(r) - \ln g(r) - C(r) - 1], \tag{15}$$

$$\text{PY} : \phi_{\text{eff}}(r) = k_B T \ln\left[1 - \frac{C(r)}{g(r)}\right]. \tag{16}$$

The mean spherical approximation (MSA) for the pair distribution function of the system of particles with impenetrable hard cores was proposed by Lebowitz and Percus [16]. For large r, $\phi_{\text{eff}}(r)$ through MSA is known to be very accurate [17] and gives better results than HNC and PY theories. In MSA,

$$\phi_{\text{eff}}(r) = -k_B T C(r) \qquad \text{for large } r. \tag{17}$$

3. Results and discussions

Water is a prototype of H-bonded liquid and its partial structures and distribution functions have been obtained in details through the cluster model in [1]. In this communication we discuss the cases of three alcohols and ammonia which are also H-bonded liquids. The results for water at room temperature are also shown for comparison. Using hexamer closed chain cluster models as predicted in [1] for liquid methanol, ethanol, *tert*-butanol and heptamer symmetrical cluster model as proposed in [2] for liquid ammonia, we have calculated the cluster structure functions $H_c(k)$ and

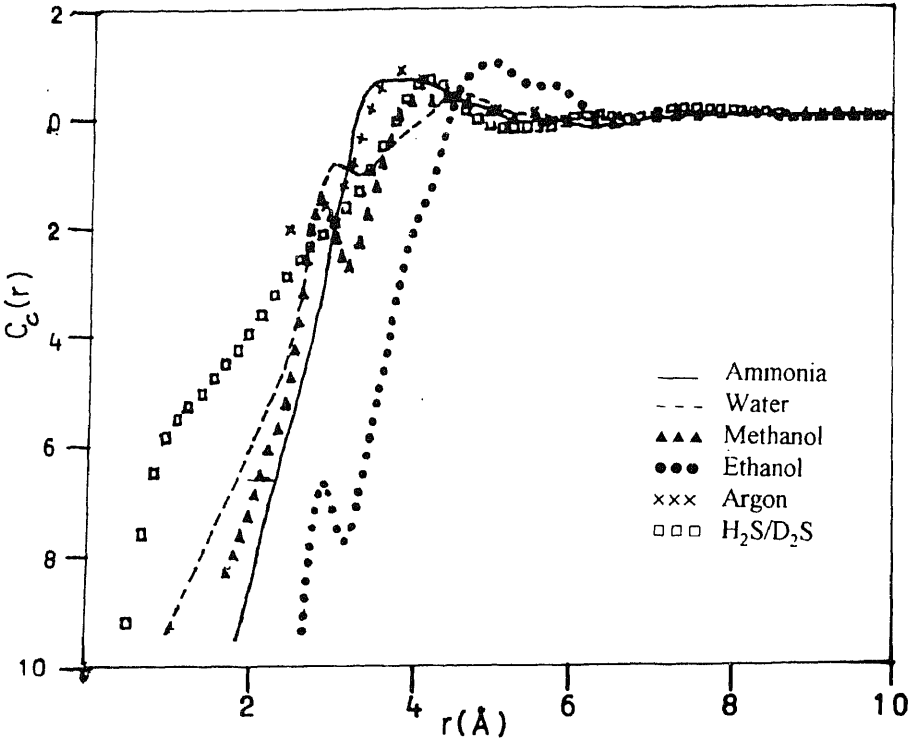

Figure 5. $C_c(r)$ for different H-bonded liquids.

uncorrelated form factor $F_{2u}(k)$ involving interaction of α and β atoms. Using (6) we have then evaluated the partial structure functions using previously evaluated $S_c(k)$ and $f_3(k)$ values.

Methanol has three non-equivalent sites R($\equiv CH_3$), O and H. So there are six partial structure functions such as $H_{OO}(k)$, $H_{HH}(k)$, $H_{RR}(k)$, $H_{OH}(k)$, $H_{OR}(k)$ and $H_{HR}(k)$. In evaluating these for convenience we choose oxygen as the geometric center of bonded methanol monomers. The corresponding partial pair distribution functions have been calculated through (7) taking care of truncation corrections for Fourier transforms. All $g_{\alpha\beta}(r)$'s for liquid methanol are plotted in figure 1. Corresponding results of computer simulation based on potential models, transferable intermolecular potential structure (TIPS) and results from reference interaction site model (RISM) [18] using a slightly modified TIPS model are also shown in these figures. There are some discrepancies between our calculated results and simulation/RISM results. The discrepancies are attributed mainly to the choice of oxygen as geometric center in our calculation.

Ethnol molecule contains four non-equivalent scattering units and hence there are ten partial structure and pair distribution functions. We chose ethylene group (i.e., $CH_2 \equiv R'$) as the center of ethanol monomer. Out of ten, we have evaluated four partial structure functions $H_{OO}(k)$, $H_{HH}(k)$, $H_{OH}(k)$, and $H_{R'R'}(k)$. The corresponding $g_{\alpha\beta}(r)$'s for liquid ethanol are plotted in figure 2(a). Computer simulation and RISM results on partial pair distribution functions for liquid ethanol are not available for comparison. Comparison of the functions with those of methanol shows that these are reasonable.

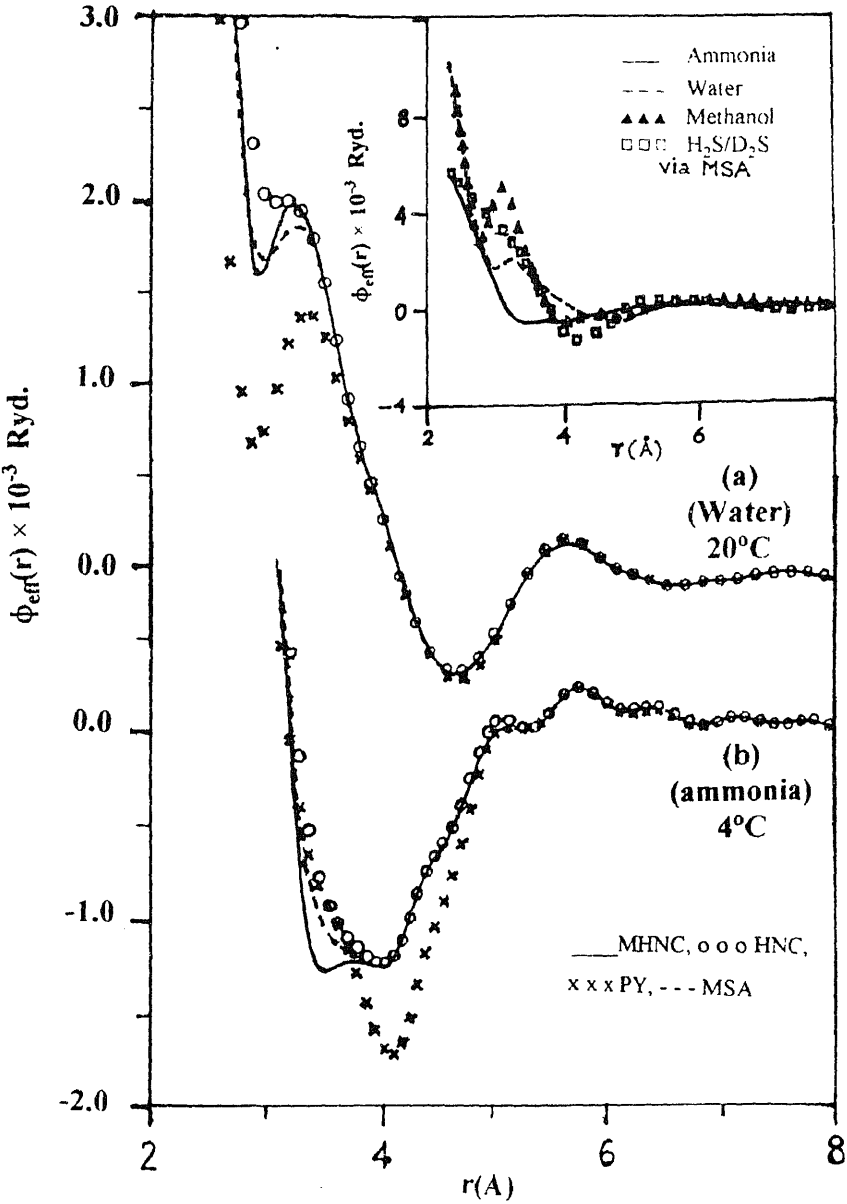

Figure 6. Effective pair potential $\phi_{\text{eff}}(r)$ of H-bonded liquids: (**a**) water at 20°C, (**b**) ammonia at 4°C. Subset: $\phi_{\text{eff}}(r)$ for large r via MSA of several liquids compared.

Tert-butanol molecule also contains four non-equivalent scattering units and hence it has ten partial structures and pair distribution functions. We have taken conveniently carbon as the center of bonded *tert*-butanol molecule. We have considered the center structure factor $S_c(k)$ as the one center hard sphere structure factor given by PY theory [9]

with appropriate core diameter 4·95 Å [2]. We have calculated four partial structure functions $H_{OO}(k)$, $H_{HH}(k)$, $H_{OH}(k)$ and $H_{CC}(k)$ and four partial pair distribution functions $g_{OO}(r)$, $g_{HH}(r)$, $g_{OH}(r)$ and $g_{CC}(r)$ which are shown in figure 2(b). The results of computer simulations are again not available for comparison. The RISM calculations [19] with van der Waals model fail to reproduce the experimental data and hence not shown here for comparison.

Liquid ammonia is a weakly H-bonded liquid. There are three partial structure and pair distribution functions. Our calculation has been based on the assumption that nitrogen is at the center of ammonia molecule. The evaluated $g_{NN}(r)$, $g_{NH}(r)$ and $g_{HH}(r)$ functions are illustrated in figure 3. We have compared our results with simulated $g_{\alpha\beta}(r)$'s based on SCF–MO calculations (model-A) potential [20] in figure 3. There is a remarkable agreement between the simulated results and our calculated results based on cluster model. Narten's [21] center–center distribution function $g_{NN}(r)$ has a splitted peak in the region from $r = 3{\cdot}5$ Å to $r = 4$ Å, which is absent in the calculated and simulated results. Very recently, experiment on isotopic mixtures of hydrogenated and deuterated ammonia has been performed and partial distribution functions could be evaluated [22]. These results are also shown for comparison. It is to be noted that these authors did not separate the intra and inter parts. In $g_{NH}(r)$ and $g_{HH}(r)$ curves the inner prominent peaks are intra peaks. It is however seen that the inter distribution functions agree reasonably well with our cluster model results.

We now compare the partial distribution functions $g_{OO}(r)/g_{NN}(r)$, $g_{OH}(r)/g_{NH}(r)$ and $g_{HH}(r)$ of these liquids (figure 4). We also show the functions for water at room temperature from ref. [1]. The comparison is expected to bring out the relative strength of H-bonding in these liquids. In figure 4(a) we compare the nature of $g_{OO}(r)$ for liquid alcohols and $g_{NN}(r)$ for liquid ammonia studied here together with $g_{OO}(r)$ for liquid water from ref. [1]. For water and methanol $g_{OO}(r)$ and for ammonia $g_{NN}(r)$ give the distribution of molecular centers. The first major peak of $g_{OO}(r)$ for water and alcohols lies at about $r \sim 2{\cdot}8$ Å whereas the first major peak of $g_{NN}(r)$ for ammonia occurs at about 3·5 Å indicating intermolecular H-bonding. In the calculated curve the first minimum of $g_{OO}(r)$ for methanol has the value slightly below the zero line and this is probably due to the fact that our choice of center for methanol at oxygen site is only approximate. The functions $g_{HH}(r)$ and $g_{OH}(r)/g_{NH}(r)$ give the orientational distribution functions between adjacent molecules. Comparative studies of the nature of these distribution functions for three alcohols, water and ammonia are shown in figures (4b) and (c). For comparison we also show $g_{HH}(r)$ and $g_{SH}(r)$ for liquid H_2S/D_2S at or near the room temperature [23] where H-bonding is known to be absent. Both the distribution functions $g_{HH}(r)$ and $g_{OH}(r)$ for water and alcohols show two well-defined peaks which are related to the presence of H-bonds and to the short-range order [6] in the liquid. These characteristics are weakly present in $g_{NH}(r)$ and $g_{HH}(r)$ for liquid ammonia. In liquid H_2S/D_2S these characteristics are practically absent showing the absence of H-bonds. The major peak of $g_{HH}(r)$ occur at about $r \sim 2{\cdot}4$ Å for all the H-bonded liquids studied except ammonia for which a small peak or hump occurs and that too shifted considerably to a larger r. For H_2S/D_2S there exists no peak at all and distribution function has no substantial oscillations. The first peak of $g_{OH}(r)$ occurs at $r \sim 1{\cdot}65$ Å–1·80 Å for alcohols and water. For ammonia, corresponding $g_{NH}(r)$ occurs at about $r \sim 2{\cdot}2$ Å. For H_2S/D_2S system such a peak is practically absent and small

oscillations occur at larger r. The distances at which the first peaks of $g_{HH}(r)$ and $g_{NH}(r)$ for liquid ammonia occur are larger than that for the other H-bonded liquids discussed. The heights of first peak in these two distribution functions are gradually increasing in the order ammonia < water < methanol < ethanol < *tert*-butanol. As far as the peak heights are concerned it can be concluded that H-bonding is stronger in alcohols than in water and ammonia seems to be weakest. The liquid H_2S/D_2S is however seen to be almost without any orientational correlations indicating absence of short-range correlations.

The center–center correlations though represent some average intermolecular correlations which yield very useful information about the characteristics of H-bonded liquids. In figure 5 we show the CDCFs for liquid methanol, ethanol, ammonia and water systems [1–3]. This function for a simple liquid e.g., argon is also shown. $C_c(r)$'s show special feature of a negative peak at about 2·8 Å, the H-bonded O–O distance followed by a positive peak and the function is short-range with no substantial oscillations at large r. The double peak is only slightly present in ammonia and no such peak exists in a simple liquid like argon. We have also computed this function from the x-ray data of liquid H_2S [23]. The function is more similar to that for argon.

In figure 6 we have shown the average effective pair potential $\phi_{eff}(r)$ for ammonia evaluated from the center–center correlations through the accurate MHNC theory [9]. The results via HNC, PY and MSA theories yield similar characteristic features. The results for room temperature water from ref. [13] are also shown for comparison. For water too the basic features of the potentials are more or less same in all the methods. For water, the potential is characterized by two minima, first minimum being a positive one occuring at $r \sim 2{\cdot}8$ Å. This is the position of the RDF first peak. The potential is very different from that for simple liquids. The first minimum in the potential is possibly due to short range hydrogen bonding interaction between neighboring molecules. In ref. [13] it is shown that at about 200°C where most of the H-bonds are broken the potential shows a single minimum at $r \sim 2{\cdot}8$ Å (at the position of RDF first peak) somewhat similar to that in simple liquids. The justification of the double minima potential of room temperature water was presented in ref. [13]. It is noteworthy that $\phi_{eff}(r)$ for ammonia (4°C) also shows feature like that of water but it is only weakly present evidently showing the weak H-bonding of liquid ammonia.

The MHNC method is not straightforward enough to be easily applicable to liquid methanol and ethanol. We have therefore shown through simple MSA to compare $\phi_{eff}(r)$'s for large r of several H-bonded liquids and also of non H-bonded liquid H_2S. MSA is also known to yield accurate potential for large r [17]. The $\phi_{eff}(r)$ values for large r via MSA are shown in the subset of figure 6. What we find here is that the basic features of the potentials for water and methanol are the same having two minima, the first positive minimum being at $r \sim 2{\cdot}8$ Å. For ethanol also the basic feature is the same (not shown). Ammonia has somewhat similar feature at $r \sim 3{\cdot}5$ Å. In literature such potential forms are not uncommon. The liquid semimetals with covalent bonds which exhibit shouldered first peak in their structure factors show characteristic humps in their potentials just outside the core at the position of first RDF peak. The feature is however absent in liquid H_2S for which the potential appears similar to that for simple liquids (e.g. argon). With small oscillations at large r it is more similar to water potential at high temperature [13].

4. Summary

The basic information on the equilibrium structure of H-bonded molecular liquid is represented by the partial pair distribution functions, one of them gives the distribution of molecular centers and the others give the orientational correlations between neighboring molecules. In the present work we compute the partial radial distribution functions of a few H-bonded liquids through geometric cluster models and the comparison gives information about the relative strengths of H-bonding features. From the point of view of chemical physics, informations on the variation of these partials as a function of temperature are more important than the values of these partials at a specific temperature state, say room temperature. Integration of the partial pair distribution functions up to their first minima give the average number of associated neighbors.

For simple molecules, the $g(r)$ formalism is clearly advantageous but as the molecular size and complexity increases, the set of individual partial terms become less informative and it is the behavior of the total molecular units that essentially characterizes the properties of the liquid. The center–center correlations yield characteristic informations. Little work has yet been done on organic liquids of this type but it seems clear that simulation work will be required to provide a physical interpretation of the experimental data in the form which is most appropriate.

We also discuss here a method for finding the average effective intermolecular potential for H-bonded liquids. The curves show that there is some characteristic peculiarity in the average effective intermolecular potential just beyond the core and this feature is totally absent in simple liquids. At high temperature when all H-bonds are broken this feature vanishes [1, 13].

Acknowledgement

The authors are grateful to CSIR, New Delhi and IUC-DAEF, Indore for financial support.

References

[1] A K Karmakar and R N Joarder, *Phys. Rev.* **E47**, 4215 (1993)
A K Karmakar and R N Joarder, *Chem. Phys.* **183**, 11 (1994)
[2] S Sarkar and R N Joarder, *J. Chem. Phys.* **99**, 2032 (1993); **100**, 5118 (1994)
A K Karmakar, S Sarkar and R N Joarder, *J. Phys. Chem.* **99**, 16501 (1995)
[3] S Sarkar, Ph.D. thesis, Jadavpur University (1996)
[4] P A Egelstaff, *Adv. Chem. Phys.* **53**, 1 (1983)
J C Dore, in *Neutron and X-ray Scattering: Complementary Technique*, IOP Conference Series No. 101, (Adam Hilger, Bristol) (pub.), p.1
S H Chen and J Teixeira, *Adv. Chem. Phys.* **64**, 1 (1985)
[5] G Palinkas, E Kalman and P Kovacs, *Mol. Phys.* **34**, 525 (1977)
[6] J C Dore, *J. Mol. Struct.* **250**, 193 (1991)
[7] J P Hansen, in *Hydrogen-Bonded Liquids* edited by J C Dore and J Teixeira, NATO ASI series, **392** (Kluwer, Academic, Dordrecht, 1991)
[8] M Haughney, M Farrario and I R McDonald, *J. Phys. Chem.* **91**, 4934 (1987)
[9] P A Egelstaff, *An Introduction to the Liquid State* (Oxford Science Publication, 1994)

J P Hansen and I R McDonald, *Theory of simple liquids* (Academic Press, New York, 1986) 2nd edition
Y Rosenfeld and N W Ashcroft, *Phys. Rev.* **A20**, 1208 (1979)
[10] A H Narten and A Habenschuss, *J. Chem. Phys.* **80**, 3387 (1984)
[11] B R Orton, *Z. Naturforsch.* **A32**, 863 (1977)
[12] N Ohtomo, K Tokiwano and K Arakawa, *Bull. Chem. Soc. Jpn.* **57**, 329 (1984)
[13] A K Karmakar and R N Joarder, *Phys. Lett.* **A190**, 480 (1994)
[14] G L Masserini and L Reatto, *Phys. Rev.* **B30**, 5367 (1984)
M C Bellissent-Funel, P Chieux, D Lavesque and J J Weis, *Phys. Rev.* **A39**, 6310 (1989)
K Hoshino, N Matsuda, H Mori and M Watabe, *J. Non-Cryst. Solids* **117/118**, 44 (1990)
[15] F Lado, *Phys. Lett.* **A89**, 196 (1982)
[16] J L Lebowitz and J K Percus, *Phys. Rev.* **144**, 251 (1966)
[17] M I Barker and T Gaskell, *Phys. Lett.* **A53**, 285 (1975)
[18] B M Pettitt and P J Rossky, *J. Chem. Phys.* **78**, 7296 (1983)
[19] A H Narten, S I Sandler and T Rensi, *Faraday Discuss. Chem. Soc.* **66**, 39 (1978)
[20] A Hinchliffe, D G Bounds, M L Klein, I R McDonald and R Righini, *J. Chem. Phys.* **74**, 1211 (1981)
[21] A H Narten, *J. Chem. Phys.* **66**, 3117 (1977)
[22] M A Ricci, C Andreani and A K Soper, *J. Chem. Phys.* **102**, 7650 (1995)
[23] C Andreani, C Petrillo and D Rocca, *Europhys. Lett.* **5**, 145 (1988)
C Andreani, V Merlo, M A Ricci and A K Soper, *Mol. Phys.* **73**, 407 (1991)

PRAMANA
—journal of
physics

© Printed in India

Vol. 47, No. 6,
December 1996
pp. 435–445

Higher order elastic constants and generalized Gruneisen parameters of elastic waves and low temperature thermal expansion of gadolinium

S SINDHU and C S MENON
School of Pure and Applied Physics, Mahatma Gandhi University, Kottayam 686 560, India

MS received 10 June 1996; revised 14 October 1996

Abstract. Expressions for the higher order elastic constants are derived using the sublattice displacements to the second degree in strains. These expressions are used to obtain the higher order elastic constants and their pressure derivatives in gadolinium. The higher order elastic constants are used to find out the generalized Gruneisen parameters of the elastic waves propagating in different directions in gadolinium. The Brugger gammas are evaluated and the low temperature limt of the Gruneisen gamma is obtained. The results are compared with the available reported values.

Keywords. Elasticity; elastic constants; thermal expansion.

PACS Nos 63·20; 81·40

1. Introduction

Higher order elastic constants is a measure of the anharmonicity of a solid. The hexagonal system has 6 second order elastic constants (SOEC), 10 third order elastic constants (TOEC) and 19 fourth order elastic constants (FOEC). In this paper the expressions for the six SOEC's, ten TOEC's, and nineteen FOEC's have been derived using the method of homogenous deformation of Born and Huang [1]. These expressions are used to evaluate the higher order elastic constants of gadolinium. The first order pressure derivatives of the second order elastic constants of a crystal are evaluated. The second order pressure derivatives are obtained as a function of the second, third and fourth order elastic constants. Using the finite strain theory of Muranaghan [2] the expressions for the second pressure derivatives of the effective SOEC of a hexagonal solid have been derived in terms of the second, third and fourth order elastic constants by Ramji Rao and Padmaja [3]. These expressions are used in this paper to obtain the second pressure derivatives of gadolinium. These elastic constants are also used to find the low temperature limit of the thermal expansion coefficients of gadolinium.

Gadolinium has importance as a rare earth material of a hexagonal close-packed structure. This metal shows interesting thermal expansion characteristics at low temperatures. The lattice constants of gadolinium are $D = a = 3{\cdot}63$ AU and $C = 5{\cdot}78$ AU and the density of the crystal is 7·89 g/cc. The second order elastic

constants of gadolinium have been experimentally determined by Fisher and Dever [4] and their pressure derivatives by Fisher *et al* [5]. The third order elastic constants are reported by Menon and Ramji Rao [6] using Keatings approach.

2. Theory

2.1 *Higher order elastic constants of gadolinium*

Interactions between atoms only up to the second nearest neighbours of gadolinium are considered. The position coordinates of the two non-equivalent atoms in the unit cell are

$$R\begin{bmatrix}0\\1\end{bmatrix} = D[0,0,0], \qquad R\begin{bmatrix}0\\1\end{bmatrix} = D[1/2\sqrt{3}, 1/2, P/2].$$

Here P is the axial ratio c/a; c and a are the unit cell distances. The PE/unit cell is

$$\phi = \sum_{I=1}^{6} \phi R(I) + \sum_{J=1}^{6} \phi R(J).$$

Here I atoms are the six nearest neighbours of the same type in the basal plane and the J atoms are the six nearest non-equivalent neighbours out of the basal plane. The components of interatomic vector R after deformation is given by

$$R_i'(I) = R_i(I) + \sum_I \varepsilon_{ij} R_j(I),$$

$$R_i'(J) = R_i(J) + \sum \varepsilon_{ij} R_j(J) + W_i.$$

Here ε_{ij} is the deformation parameter related to the macroscopic Lagrangian strain η_{ij} which is given as

$$\eta_{ij} = 1/2\left(\varepsilon_{ij} + \varepsilon_{ji} + \sum_k \varepsilon_{ki}\varepsilon_{kj}\right)$$

and $\overline{W}_i$ are the internal displacements given by

$$\overline{W}_i = W_i + \sum_J \varepsilon_{ji} W_i.$$

Potential energy can be expanded in powers of changes in the squares of vector distances $R(I)$ and $R(J)$ as

$$\begin{aligned}\phi =& \phi_0 + k_2\left[\sum_I [\Delta R^2(I)]^2 + \sum_J [\Delta R^2(J)]^2\right] \\ &+ k_3\left[\sum_I [\Delta R^2(I)]^3 + \sum_J [\Delta R^2(J)]^3\right] \\ &+ k_4\left[\sum_I [\Delta R^2(I)]^4 + \sum_J [\Delta R^2(J)]^4\right]. \qquad (1)\end{aligned}$$

Here k_2 in the harmonic parameter k_3 and k_4 are the third and fourth order anharmonic parameters which are defined as

$$k_2 = \frac{1}{2!}\left[\frac{\delta^2\phi(r)}{\delta(r^2)^2}\right],$$

$$k_3 = \frac{1}{3!}\left[\frac{\delta^3\phi(r)}{\delta(r^2)^3}\right],$$

$$k_4 = \frac{1}{4!}\left[\frac{\delta^4\phi(r)}{\delta(r^2)^4}\right].$$

The term $[\delta\phi(r)/\delta(r^2)]$ does not exist as the derivatives are calculated in the equilibrium configuration. The Lennard–Jonnes potential is given by

$$\phi = -a/r^m + b/r^n.$$

For this potential K_2, K_3 and K_4 are calculated as

$$K_2 = 1/4(\eta M/D^2),$$

$$K_3 = -K_2/6D^2(m+n+6),$$

$$K_4 = K_2/48D^4[(m+n)(m+n+12) - mn + 44],$$

$$\eta = nb(n-m)/2MD^{n+2}.$$

M is the mass of the atom and $D = a$ which is the nearest neighbour distance in the basal plane.

Ramanand *et al* [7] have shown that to evaluate FOEC of an hcp lattice it is enough to obtain the sublattice displacements up to second degree in strain. The internal displacements W_i can be obtained in terms of the Lagrangian strain by minimizing the strain energy with respect to W_i i.e.,

$$\overline{W}_x = [-D/2\sqrt{3}][\eta_{yy} - \eta_{xx}] + [D/2\sqrt{3}][\eta_{yy}^2 - \eta_{xx}^2] + [\sqrt{3}p^2D/4][\eta_{zz}(\eta_{yy} - \eta_{xx})],$$

$$\overline{W}_y = [-D/\sqrt{3}]\eta_{xy} + D/\sqrt{3}[\eta_{xy}(\eta_{yy} + \eta_{xx})] + [\sqrt{3}p^2D/2][\eta_{xy}\eta_{zz}],$$

$$\overline{W}_z = 0. \tag{2}$$

Substituting the value of W_i from (2) to (1) we get the expressions for energy/unit volume of the undeformed state. The resulting expression is compared with that of the elastic energy density

$$U = \frac{1}{2!}\sum_{ijkl} C_{ijkl}\eta_{ij}\eta_{kl} + \frac{1}{3!}\sum_{ijklmn} C_{ijklmn}\eta_{ij}\eta_{kl}\eta_{mn} + \frac{1}{4!}\sum_{ijklmnop} C_{ijklmnop}\eta_{ij}\eta_{kl}\eta_{mn}\eta_{op} + \cdots \tag{3}$$

get the expressions for the fourth, third and second order elastic constants as

$$
\begin{aligned}
C_{1111} &= [\{4390/9\}D^8/V_a]K_4 + [\{4D^6/V_a\}]K_3 - [\{143/6\}D^4/V_a]K_2 \\
C_{1112} &= [\{1474/9\}D^8/V_a]K_4 + [\{23/6\}D^6/V_a]K_3 \\
C_{1113} &= [\{24/9\}D^8p^2/V_a]K_4 + [3D^6p^2/V_a]K_3 - [\{12/6\}D^4p^2/V_a]K_2 \\
C_{1122} &= [\{502/9\}D^8/V_a]K_4 - [\{4/3\}D^6/V_a]K_3 + [\{11/2\}D^4/V_a]K_2 \\
C_{1123} &= [\{24/9\}D^8p^2/V_a]K_4 - [D^6p^2/V_a]K_3 + [6D^4p^2/V_a]K_2 \\
C_{1133} &= [4D^8p^4/V_a]K_4 + [\{3/2\}D^6p^4/V_a]K_3 - [3D^4p^4/V_a]K_2 \\
C_{1144} &= C_{1244} = C_{1255} = [\{24/9\}D^8p^2/V_a]K_4 - [D^6p^2/V_a]K_3 \\
C_{1155} &= [\{24/9\}D^8p^2/V_a]K_4 + [3D^6p^2/V_a]K_3 \\
C_{1166} &= [\{1461/9\}D^8/V_a]K_4 + [\{2/3\}D^6/V_a]K_3 + [\{25/18\}D^4/V_a]K_2 \\
C_{1233} &= [4D^8P^4/V_a]K_4 - [\{3/2\}D^6p^4/V_a]K_3 + [3D^4p^4/V_a]K_2 \\
C_{1333} &= C_{3344} = [6D^8p^6/V_a]K_4 \\
C_{1344} &= [4D^8p^4/V_a]K_4 + [\{3/2\}D^6p^4/V_a]K_3 \\
C_{1355} &= [4D^8p^4/V_a]K_4 - [\{3/2\}D^6p^4/V_a]K_3 \\
C_{2223} &= [\{24/9\}D^8p^2/V_a]K_4 + [3D^6p^2/V_a]K_3 - [6D^4p^2/V_a]K_2 \\
C_{3333} &= [9D^8p^4/V_a]K_4 \\
C_{4444} &= [6D^8p^4/V_a]K_4 \qquad (4) \\
C_{111} &= [\{1099/10\}D^6/V_a]K_3 + [\{23/3\}D^4/V_a]K_2 \\
C_{112} &= [\{83/5\}D^6/V_a]K_3 - [\{7/5\}D^4/V_a]K_2 \\
C_{113} &= [\{5/3\}D^6p^2/V_a]K_3 + [D^4p^2/V_a]K_2 \\
C_{123} &= [\{7/5\}D^6p^2/V_a]K_3 - [D^4p^2/V_a]K_2 \\
C_{133} &= [\{16/5\}D^6p^4/V_a]K_3 \\
C_{344} &= [3D^6p^4/V_a]K_3 \\
C_{144} &= [2D^6p^2/V_a]K_3 \\
C_{155} &= [\{4/3\}D^6p^2/V_a]K_3 \\
C_{222} &= [\{175/2\}D^6/V_a]K_3 + [\{39/5\}D^4/V_a]K_2 \\
C_{333} &= [\{9/2\}D^6p^6/V_a]K_3 \qquad (5) \\
C_{11} &= [\{167/8\}D^4/V_a]K_2 \\
C_{12} &= [\{41/8\}D^4/V_a]K_2 \\
C_{13} &= [\{5/3\}D^4p^2/V_a]K_2 \\
C_{33} &= [3D^4p^4/V_a]K_2 \\
C_{44} &= [2D^4p^2/V_a]K_2 \\
C_{66} &= \tfrac{1}{2}(C_{11} - C_{12}) \qquad (6)
\end{aligned}
$$

where $V_a = \sqrt{3/2}pD^3$ is the volume of the unit cell. These expressions are used to evaluate the fourth, third and second order elastic constants of gadolinium.

2.2 *Low temperature thermal expansion of gadolinium*

Uniaxial crystals are characterized by two principal linear expansion coefficients $\alpha_\parallel$, parallel to the unique axis and $\alpha_\perp$, perpendicular to the unique axis. The behaviour of these expansion coefficients at low temperature is governed by two generalized Gruneisen parameters $\gamma_j'(\theta, \phi)$ and $\gamma_j''(\theta, \phi)$ defined as

$$\gamma_j'(\theta, \phi) = -\frac{1}{v_j(\theta, \phi)} \frac{\partial v_j(\theta, \phi)}{\delta \varepsilon'},$$

$$\gamma_j''(\theta, \phi) = -\frac{1}{v_j(\theta, \phi)} \frac{\partial v_j(\theta, \phi)}{\delta \varepsilon''},$$

where $v_j(\theta, \phi)$ is the velocity of the elastic waves travelling in a direction (θ, ϕ), j is the polarization index of the wave, θ is the angle in the direction the wave propagation makes with the hexagonal axis, ϕ is the azimuthal angle, ε' is a uniform areal strain perpendicular to the unique axis and ε'' is a uniform longitudinal strain parallel to the

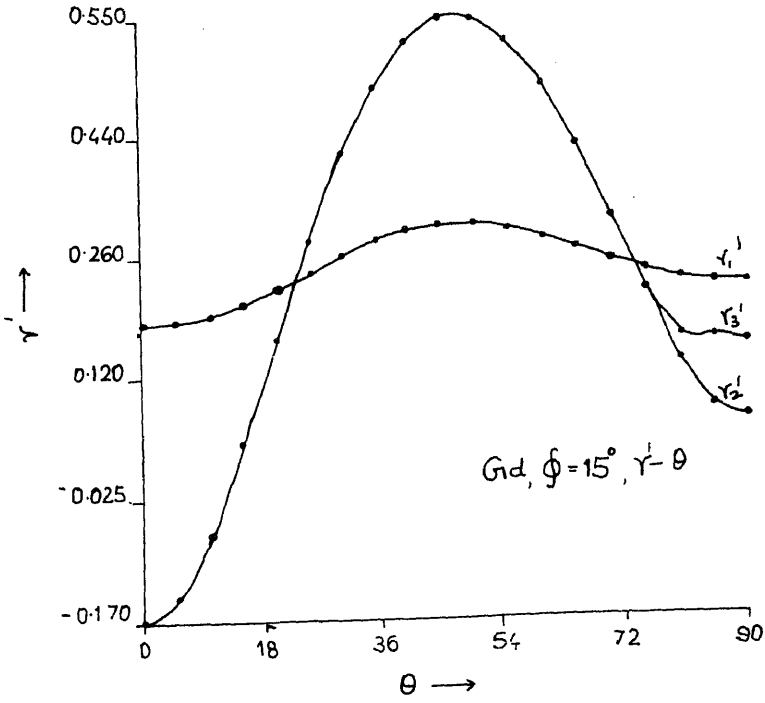

Figure 1A. Variation of generalized GP's γ' with θ for azimuthal angle $\phi = 15°$ in gadolinium.

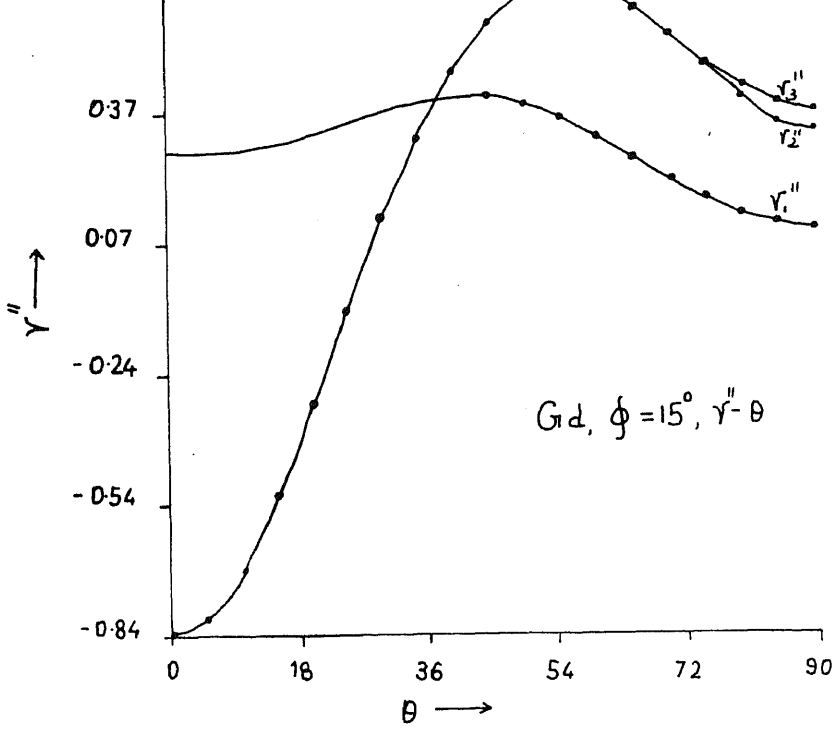

Figure 1B. Variation of generalized GP's γ'' with θ for azimuthal angle $\phi = 15°$ in gadolinium.

unique axis. These generalized Gruneisen parameters can be calculated from the second and third order elastic constants of a solid as shown below by Ramji Rao and Srinivasan [8]. Using the second and third order elastic constants of gadolinium the elastic wave velocities $v_j(\theta, \phi)$, the generalized Gruneisen parameters $\gamma'_j(\theta, \phi)$ and $\gamma''_j(\theta, \phi)$ for different values of θ and ϕ at intervals of 5° for θ and ϕ ranging from 0 to 90° are calculated. The calculations were made on a computer using the programming language Fortran. The linear thermal expansion coefficient of an uniaxial crystal is given by

$$V\alpha_{\parallel} = [2S_{13}\gamma'(T) + S_{33}\gamma''(T)]C_v(T),$$
$$V\alpha_{\perp} = [(S_{11} + S_{12})\gamma'(T) + S_{13}\gamma''(T)]C_v(T). \quad (7)$$

Here V is the molar volume, S_{ij} are the elastic compliance coefficients and $C_v(T)$ is the molar specific heat at temperature T. $\gamma'(T)$ and $\gamma''(T)$ are the effective Gruneisen functions of all the normal modes of the crystal. At very low temperatures, the effective Gruneisen parameters are determined by the mode gammas of the elastic waves and $\gamma'(T)$ and $\gamma''(T)$ attain limiting values γ'_0 and γ''_0. In terms of $v_j(\theta, \phi)$, $\gamma'_j(\theta, \phi)$ and

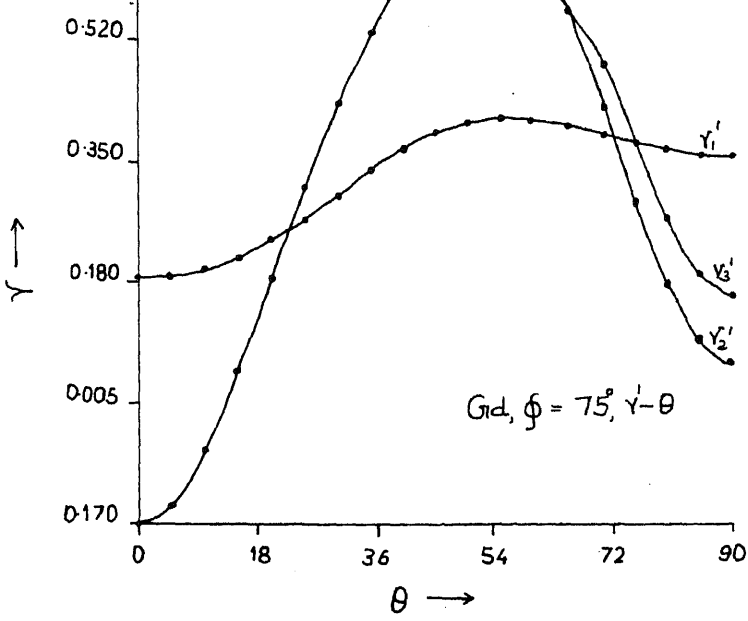

Figure 2A. Variation of generalized GP's γ' with θ for azimuthal angle $\phi = 75°$ in gadolinium.

$\gamma_j''(\theta, \phi)$, these limits are defined by

$$\gamma_0' = \left[\sum_{j=1}^{3} \int v_j^{-3}(\theta,\phi)\gamma_j'(\theta,\phi)\,\mathrm{d}\Omega\right] \Big/ \sum_{j=1}^{3} \int v_j^{-3}(\theta,\phi)\,\mathrm{d}\Omega,$$

$$\gamma_0'' = \left[\sum_{j=1}^{3} \int v_j^{-3}(\theta,\phi)\gamma_j''(\theta,\phi)\,\mathrm{d}\Omega\right] \Big/ \sum_{j=1}^{3} \int v_j^{-3}(\theta,\phi)\,\mathrm{d}\Omega. \tag{8}$$

The integration is over the entire solid angle. We have obtained the values of γ_0' and γ_0'' by numerical integration over the solid angle. The integral was evaluated by dividing θ and ϕ into intervals of 5° and the values were obtained.

Brugger and Fritz [9] have defined the functions

$$\gamma_\perp^{\mathrm{Br}} = V\alpha_\perp / C_v \chi_{\mathrm{iso}},$$
$$\gamma_\parallel^{\mathrm{Br}} = V\alpha_\parallel / C_v \chi_{\mathrm{iso}},$$

where χ_{iso} is the isothermal compressibility. Combining (7) and (8) the low temperature limits of the Brugger gammas are given by

$$\gamma_\perp^{\mathrm{Br}}(0) = [(S_{11} + S_{12})\gamma_0' + S_{13}\gamma_0'']/\chi_{\mathrm{iso}},$$
$$\gamma_\parallel^{\mathrm{Br}}(0) = [2S_{13}\gamma_0' + S_{33}\gamma_0'')]/\chi_{\mathrm{iso}}.$$

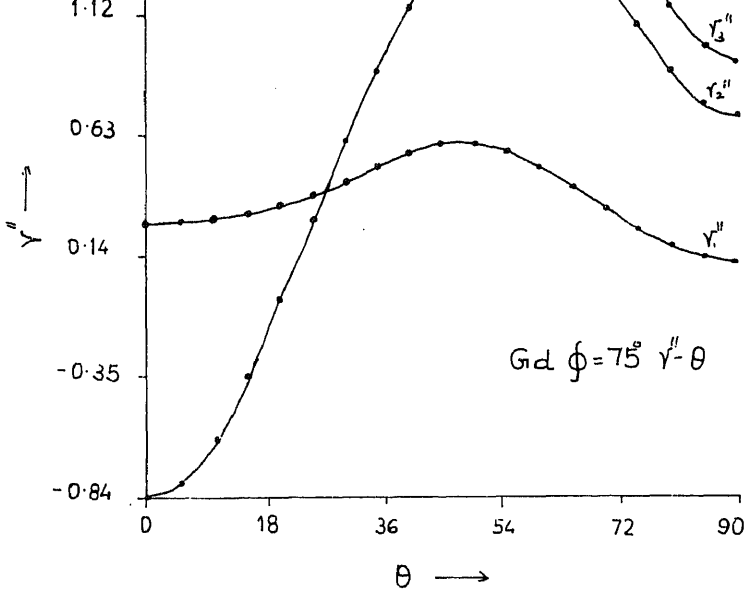

Figure 2B. Variation of generalized GP's γ'' with θ for azimuthal angle $\phi = 75°$ in gadolinium.

e S_{11}, S_{33}, S_{12} and S_{13} are given by

$$S_{11} = \frac{C_{11}C_{33} - C_{13}^2}{(C_{12} - C_{11})2C_{13}^2 - C_{33}(C_{11} + C_{12})},$$

$$S_{33} = \frac{C_{11} + C_{12}}{C_{33}(C_{11} + C_{12}) - 2C_{13}^2},$$

$$S_{12} = \frac{C_{13}^2 - C_{12}C_{33}}{C_{13}},$$

$$S_{13} = \frac{C_{13}}{2C_{13}^2 - C_{33}(C_{11} + C_{12})},$$

$$\chi_{\text{iso}} = 2[S_{11} + S_{12} + S_{13}] + 2S_{13} + S_{33}.$$

g the values of γ_0' and γ_0'' we get $\gamma_\perp^{\text{Br}}(0)$ and $\gamma_\parallel^{\text{Br}}(0)$. Using these two values the low perature limit γ_L of a hexagonal metal can be calculated using the formula

$$\gamma_L = 2\gamma_\perp^{\text{Br}}(0) + \gamma_\parallel^{\text{Br}}(0).$$

Table 1. Second order elastic constants in 10^{10} N/m^2 and first pressure derivative of gadolinium.

C_{ij}	Calculated values	Experimental values	dC_{ij}/dp	Calculated values	Experimental values
C_{11}	7·22	6·67	dC_{11}/dp	3·69	3·018
C_{12}	1·77	2·5	dC_{12}/dp	1·967	2·26
C_{13}	1·406	2·13	dC_{13}/dp	1·472	–
C_{33}	6·68	7·19	dC_{33}/dp	7·061	5·726
C_{44}	1·75	2·07	dC_{44}/dp	1·708	0·185
C_{66}	2·769	2·08	dC_{66}/dp	0·8912	0·377

Table 2. Third order elastic constants of gadolinium in 10^{10} N/m^2.

C_{ijk}	Calculated values	Reported values
C_{111}	−50·25	−50·3
C_{112}	−15·27	−13·3
C_{113}	−1·15	−0·4
C_{133}	−9·92	−9·7
C_{123}	−4·73	−6·3
C_{344}	−9·3	−9·7
C_{333}	−74·72	−76·2
C_{222}	−63·79	−55·2
C_{144}	−3·85	−3·9
C_{155}	−2·56	−2·0

3. Results and discussion

Values of second order elastic constants C_{11} and C_{33} are used to evaluate the harmonic parameter K_2. Third order elastic constants of Menon and Rao [6] are used to evaluate the anharmonic parameter K_3. These SOEC's and first pressure derivatives are given in table 1. These are compared with the experimental SOEC values [4] and first pressure derivatives [5]. The TOEC's are given in table 2. These values are compared with the other reported theoretical values of Menon and Rao [6]. The value of m and n [10,11], are so chosen to give a satisfactory agreement to the reported TOEC of gadolinium. The value of k_2, m and n are used to evaluate the anharmonic parameter k_4.

The calculated fourth order elastic constants of gadolinium are given in table 3. C_{1111} and C_{3333} have large magnitude. The large difference in magnitude of C_{1111} and C_{3333} indicates the higher order elastic anisotropy in the crystal. These higher order elastic constants are used to evaluate the second pressure derivatives of gadolinium. These values are given in table 4. The magnitude of C_{11}^2 and C_{33}^2 is quite large indicating that phase change would occur in this metal when subjected to high pressure. This is confirmed by the experimental evidence. The occurrence of phase change in gadolinium at 25 kbar from hexagonal to orthorhombic structure was reported by Robinson *et al* [12]. The value of Gruneisen coefficients $\gamma_0' = 0{\cdot}258$ and $\gamma_0'' = 0{\cdot}641$ for gadolinium. The Brugger gammas are calculated as

$$\gamma_{\perp}^{\mathrm{Br}}(0) = 0{\cdot}131, \quad \gamma_{\parallel}^{\mathrm{Br}}(0) = -0{\cdot}0069.$$

Table 3. Fourth order elastic constants of gadolinium in $10^{10}N/m^2$ ($m = 5{\cdot}74$, $m = 1{\cdot}42$).

C_{ijkl}	Calculated values
C_{1111}	287·189
C_{1112}	102·99
C_{1113}	−12·12
C_{1122}	37·053
C_{1123}	11·302
C_{1133}	1·735
C_{1144}	6·046
C_{1155}	−1·305
C_{1166}	99·322
C_{1233}	29·555
C_{1244}	6·046
C_{1255}	6·046
C_{1333}	59·33
C_{1344}	22·92
C_{1355}	8·36
C_{2223}	−6·901
C_{3333}	224·99
C_{4444}	23·46
C_{3344}	59·33

Table 4. Second pressure derivatives of gadolinium in $10^{10}\,m^2/N$.

d^2C_{ij}/dp^2	Calculated values
d^2C_{11}/dp^2	0·7417
d^2C_{12}/dp^2	1·984
d^2C_{13}/dp^2	1·0604
d^2C_{33}/dp^2	−0·79
d^2C_{44}/dp^2	−0·247
d^2C_{66}/dp^2	−0·6989

Table 5. Low temperature limit of gadolinium.

Present calculation		Reported value [6]
γ_L	0·2547	0·383

The low temperature limit of the Gruneisen gamma is obtained as 0·2547. This is compared with the available reported value and is given in table 5.

The low temperature limit of the Gruneisen gamma is positive and so we expect the volume expansion to be positive down to 0K for this crystal. The variation of γ with θ for different value of ϕ is shown. The anisotropy in all the graphs of γ vs θ accounts for the pronounced anharmonicity of the solid in certain specific directions. The average Gruneisen function $\gamma_{\perp}^{Br}$ and $\gamma_{\parallel}^{Br}$ are 0·131 and −0·0069 which suggests that the anisotropy in thermal expansion along the c-axis is more pronounced than that along the ab plane.

Acknowledgements

The authors thank Dr N V Eldhose for stimulating discussions. They also wish to thank Mr P C Joseph for his assistance in computing the programme.

References

[1] M Born and K Huang, *Dynamical theory of crystal lattices* (Oxford University Press, New York, 1962)
[2] F D Murnaghan, *Finite deformation of an elastic solid* (New York, Wiley, 1951)
[3] R Ramji Rao and A Padmaja, *Phys. Status Solidi* **B152**, 455 (1989)
[4] E S Fisher and D J Dever, *Proceedings of the Sixth Rare Earth Conference* (Gattinburg, 1967) p. 522
[5] E S Fisher, M H Manghnani and R Kikuta, *J. Phys. Chem. Solids* **34**, 687 (1973)
[6] R Ramji Rao and C S Menon, *Lattice dynamics, third order elastic constants and thermal expansion of some hexagonal metals*, Ph.D. Thesis (IIT, Madras, 1973)
[7] A Ramanand, J V S S Narayana Murthy and R Ramji Rao, *Phys. Lett.* **A81**, 144 (1981)
[8] R Ramji Rao and R Srinivasan, *Phys. Status Solidi* **29**, 865 (1968)
[9] K Brugger and T C Fritz, *Phys. Rev.* **A157**, 524 (1967)
[10] E Gruneisen, *Handbuch der Phys.* (Springer, Berlin, 1926) p. 29, vol. 10
[11] J Goldak, L J Lloyd and C S Barret, *Phys. Rev.* **144**, 478 (1966)
[12] L B Robinson, F Milstein and I Tans, *Physics of solids at high pressure* (Academic Press, New York, 1965) p. 272

A stochastic model for solidification
I. The basic equations, their analysis and solution

SHOBHA DASS, GAUTAM JOHRI* and LAKSHMAN PANDEY*
Govt. M.H. College of Science and Home Science, Jabalpur 482 002, India
*Department of Post Graduate Studies and Research in Physics, Rani Durgavati University, Jabalpur 482 001, India

MS received 4 April 1995; revised 8 November 1995

Abstract. A 3-dimensional (2-space, 1-time) model relating the diffusion of heat and mass to the kinetic processes at the solid-liquid interface, using a stochastic approach is presented in this paper. This paper is divided in two parts. In the first part the basic set of equations describing solidification alongwith their analysis and solution are given. The process of solidification has a stochastic character and depends on the net probability of transfer of atoms from liquid to the solid phase. This has been modeled by a Markov process in which knowledge of the parameters at the initial time only is needed to evaluate the time evolution of the system. Solidification process is expressed in terms of four coupled equations, namely, the diffusion equations for heat and mass, the equations for concentration of the solid phase and for rate of growth of the solid-liquid interface. The position of the solid-liquid interface is represented with the help of a delta function and it is defined as the surface at which latent heat is evolved. A numerical method is used to solve the equations appearing in the model. In the second part the results i.e. the time evolution of the solid-liquid interface shape and its concentration, rate of growth and temperature are given.

Keywords. Stochastic; solidification; binary melt; kinetic phase diagrams.

PACS No. 81.10

1. Introduction

Solidification and melting are the types of phenomenon commonly observed during the production of materials. Most of the materials undergo a process of melting and solidification during their manufacture. Some of the typical manufacturing processes are casting, welding, melt spinning, surface remelting and directional solidification process for growing crystals using Bridgman, Czochralski and Electroslag remelting techniques [1, 2]. In all these techniques the basic objective is to maintain external conditions such that a crystal with desired and reproducible properties is obtained.

Processes such as rapid solidification, directional solidification or surface alloying are often used to create new materials or impart new properties to the existing ones. Many of the production processes of high-tech materials such as high temperature superconductors, magnetic materials, ceramics, composites etc. involve application of high cooling rates and large changes of pressures [8]. Such conditions render these processes far from thermodynamical equilibrium and lead to various metastable states of these materials, for example quasicrystals [3, 4], metallic glasses etc. [5–7], with diverse new properties. Also, properties of materials are governed to a large extent by their microstructure which in turn is greatly influenced by the solidification process.

properties. A qualitative information about this can be obtained by performing a series of experiments by using different solidification parameters. However, the experimentation is quite tedious and crystal defects are difficult to eliminate once they are created. Therefore solidification phenomenon has received considerable theoretical attention with a view to be able to model the process and predict the microstructure and hence the properties.

The existing theories treat solidification process as the one involving nucleation and growth [8–11]. The phenomenological thermodynamics deals with the conditions of phase transformation and the equilibrium co-existence of phases and facilitates the construction of equilibrium phase diagrams [1, 12, 13]. These phase diagrams are often used to predict the constitution of the phases during the solidification of materials, even though their employment is questionable as during solidification the system may be far from thermodynamic equilibrium. Therefore the study of the dynamics of metastable and unstable states becomes essential for a controlled synthesis of new materials with desired and reproducible properties.

Among the modern theories which deal with nucleation process are the stochastic theory [9, 10], the renormalization group method [14] and the field theories [15–17]. However, the kinetics of phase transformation were neglected in all these models. The study of phase transformation kinetics was also developed using other theories such as spinodal decomposition theory [18], the molecular dynamics method [8, 19], the functional density method [20, 21] and the fractal geometry method [22, 23]. The molecular dynamics method [8, 19] is too demanding in terms of computational time. In functional density method [20, 21] the structure of the solid phase is assumed to be known and temperature is taken to be a constant. Fractal geometry method [22, 23] also assumes the structure of the solid phase.

Nonequilibrium thermodynamics was used by Caroli *et al* [24] to study solidification. Some other calculations of the non stationary solidification process have been done based on the Monte Carlo method [25], where growth of only 20 atomic layers was simulated. The concept of kinetic phase diagrams was developed by Cherepanona [26, 27] to describe processes where equilibrium phase diagrams can not be used. In these models constant temperature and concentration was assumed at the interface.

Kinetic phase transformation theories have been formulated dealing with the formation of a new phase (nucleation), growth of the interface and mass and energy transport in the system. In order to predict the structure and properties of materials produced by nonequilibrium experimental conditions under given initial and boundary conditions, a theory must be constructed which takes into account all aspects of phase transformation. Considerable efforts have been made in the past to understand the solidification process of alloys by proposing models which involve heat and mass transfer and shape of the solid-liquid interface [2, 28–30]. From the survey of literature it seems that a treatment of the solidification process taking into account its stochastic nature has not been done except by Chvoj [31–40]. Chvoj [31–40] has proposed a stochastic model by considering the transport of heat and mass simultaneously with the kinetic processes at the phase interface. However, he has not

considered interdependence of heat and mass flow and also has not solved the time evolution of a binary system in three dimensions (2-space, 1-time). which is closer to the real experimental situations.

In this paper a three dimensional (2-space, 1-time) stochastic mathematical model to describe the solidification phenomenon of binary melt taking into account the kinetic processes at the solid-liquid interface is proposed. This model is quite general in nature and can be applied to any material ranging from organic substances to metallic glasses. A preliminary report of the scheme of the model was presented earlier [41].

2. The model

A solid can be grown from the melt if the melt is below its equilibrium melting temperature. Departure from the equilibrium is always required for the solidification process to proceed. Processes responsible for the formation of a solid from the melt are: thermal and density fluctuations governed by stochastic laws, diffusion of mass and heat, evolution of latent heat at the solid-liquid interface, kinetic processes at the interface, convection, radiation and initial and boundary conditions. A stochastic mathematical model has been developed to describe this phenomenon as follows.

The diffusion of mass and heat have been represented with the help of partial differential equations, derived by application of the law of conservation of mass and heat. These equations govern the distribution of mass and heat in the three regions, namely, the solid, the liquid and the solid-liquid interface. The effect of other factors such as latent heat, external fields etc. can also be included in these equations. For the description of the effect of thermodynamic fluctuations in temperature and concentration, Langevin method [42] of stochastic differential equations has been used.

Kinetic processes at the solid-liquid interface have been modeled using a microscopic description of the process of solidification i.e. by assigning probabilities to individual atoms as they make transition from a liquid-like configuration to a solid-like configuration, and then averaging over the corresponding phases to determine the probability of formation of the new phase.

In the solidification process the dominant forces are due to temperature and concentration gradients, which give rise to heat and mass diffusion. The diffusion equations for mass and heat under non steady state growth conditions can be written as

$$\frac{\partial C_L^{(x,y,t)}}{\partial \mathrm{t}} = D_C \nabla^2 C_L(x,y,t) + D_{CT} \nabla^2 T(x,y,t) + \mathbf{R}.\nabla C_L(x,y,t) \tag{1}$$

and

$$\frac{\partial T^{(x,y,t)}}{\partial \mathrm{t}} = D_{TC} \nabla^2 C_L(x,y,t) + D_T \nabla^2 T(x,y,t) + \mathbf{R}.\nabla T(x,y,t) \tag{2}$$

respectively, where C_L is the relative concentration of B atoms in A–B system, T is the temperature of the melt, $D_T = k/C_v\rho$ is the diffusivity in which C_v is the volume specific heat and ρ is the density of the solid, D_C is the diffusion coefficient, D_{CT} and D_{TC} are related to the Onsager's coefficients due to interdependence of mass and heat flow,

and complete translational symmetry. **R** is the rate of growth of the solid phase, x is the direction of growth and y is the coordinate perpendicular to it.

Solidification phenomenon is brought about by a process of heat transfer that is accompanied by a change of phase i.e. from liquid to solid phase. During the phase change, thermal energy is released or absorbed at the solid-liquid interface in the form of latent heat of fusion. For solidification this heat must be drawn from liquid phase at the interface and conducted away through the solid phase. Under certain circumstances, however, the liquid may not remain stagnant and essentially conductive heat transfer may be superimposed with convective heat transfer. This leads to an interface motion coupled nonlinearly to the local temperature field which obeys the diffusion law. Loss of energy can also take place by radiation from the walls of the container of the freezing material. In binary systems the composition of the new phase is different from that of the old phase. The change in composition is governed by the flux boundary condition at the solid-liquid interface. Heat and mass can be produced by chemical reactions also. Solidification process can also be affected by the presence of external fields, for example electric, magnetic or acoustic fields. Finally fluctuations of thermodynamic quantities such as temperature and concentration also contribute to a change in mass and energy of the system. Taking these factors into account the diffusion equations (1) and (2) can be written as

$$\frac{\partial C_L^{(x,y,t)}}{\partial t} = D_C \nabla^2 C_L(x,y,t) + D_{CT} \nabla^2 T(x,y,t) + \mathbf{R}.\nabla C_L(x,y,t) + \operatorname{div} F_C + \operatorname{div} E_C + Q_C \tag{3}$$

and

$$\frac{\partial T^{(x,y,t)}}{\partial t} = D_{TC} \nabla^2 C_L(x,y,t) + D_T \nabla^2 T(x,y,t) + \mathbf{R}.\nabla T(x,y,t) + \operatorname{div} F_T + \operatorname{div} E_T + Q_T, \tag{4}$$

where Q_T and Q_C are respectively the heat and mass produced due to phase transformation, E_T and E_C are the heat and mass flux controlled by external fields, respectively, F_T and F_C are the stochastic terms that represent the flux of heat and mass due to fluctuations, respectively.

The effect of convection and radiation is not included in this model. Also diffusion in the solid phase, effect of capillarity at the solid-liquid interface and change of volume during phase transformation are neglected. The source terms Q_C and Q_T appearing due to the change of phase, at the interface can be expressed as [39]

$$Q_C = \bar{Q}_C \, \delta(\mathbf{x} - \mathbf{X}_r(y,t)), \tag{5}$$

where

$$\bar{Q}_C = (C_{Sr} - C_{Lr})\mathbf{R} \tag{6}$$

and

$$Q_T = \frac{\Lambda \mathbf{R}}{C_v \rho} \delta(\mathbf{x} - \mathbf{X}_r(y,t)), \tag{7}$$

where C_{Sr} and C_{Lr} are the solid and liquid concentrations at the interface $\mathbf{X}_r(t)$, respectively, Λ is the latent heat per unit volume.

Equations (3) and (4) are the stochastic differential equations representing the time evolution of temperature and liquid concentration. For evaluation of the fluctuation terms F_T and F_C the Langevin method of stochastic differential equations has been used [39, 42]. According to this method the average of the random fluctuations is taken equal to zero and it can be written as

$$\langle F_{T,C}(\mathbf{x}, t)\rangle = 0$$

and for $t \neq t'$, $\mathbf{x} \neq \mathbf{x}'$, the fluctuations $F_{T,C}(\mathbf{x}, t)$ and $F_{T,C}(\mathbf{x}', t')$ are statistically independent. Mathematically this can be expressed as

$$\langle F_{T,C}(\mathbf{x}, t)\, F_{T,C}(\mathbf{x}', t')\rangle = K_{TC}(\mathbf{x}, t)\,\delta[\mathbf{x}-\mathbf{x}']\,\delta[t-t']$$

and thus

$$\langle \text{div}\, F_T\rangle = \langle \text{div}\, F_C\rangle = 0,$$

which is characteristic of the Markov process. The function $K_{TC}(\mathbf{x}, t)$ can be derived from the microscopic models. The effect of external fields other than thermal field is considered to be negligible i.e. $E_C = E_T = 0$.

In order to solve equations (3) and (4), the average rate of growth of the solid-liquid interface must be determined. This can be determined by evaluating probability density of formation of a new monoatomic layer. This probability can be obtained by considering the microscopic processes of atom transfer from one phase to the other at the interface.

2.1 *Calculation of growth rate and solid concentration*

Atoms arriving at the solid-liquid interface can make transition to the other phase depending on their activation energies. The number of possible transitions of one B atom from the liquid to the solid phase across the interface per unit time is given by [39]

$$N_B^S = \nu_B^L\, n_B^L, \tag{8}$$

where $n_B^S = C_{Lr}\rho^L$ is the number of B atoms in a monoatomic layer at the interface in the liquid phase, ρ^L is the total number of atoms per unit volume in a monoatomic layer at the interface in the liquid phase.

Similarly, the number of possible transitions of one A atom from the liquid to the solid phase across the interface per unit time is

$$N_A^S = \nu_A^L\, n_A^L, \tag{9}$$

where

$$n_A^L = [1 - C_{Lr}]\rho^L.$$

The corresponding numbers of B and A atoms making a transition from the solid to the liquid phase are given by

$$N_B^L = \nu_B^S\, n_B^S, \tag{10}$$

where

$$n_B^S = C_{Sr}\rho^S.$$

$$N_A^L = \nu_A^S n_A^S, \tag{11}$$

where

$$n_A^S = [1 - C_{Sr}]\rho^S$$

and $\nu_{A,B}^{L,S}$ is the frequency of thermal vibrations of the atoms of A, B component in liquid and solid phase. The subscript r refers to the solid-liquid interface and $C_{Lr} \equiv C_{Lr}(x, y, t)$ and $C_{Sr} \equiv C_{Sr}(x, y, t)$.

The probability of transition of one B atom from the liquid to the solid phase can be written as

$$P_1^B = \exp[-U_B/K_B T_r] \tag{12}$$

and for one A atom can be written as

$$P_1^A = \exp[-U_A/K_B T_r], \tag{13}$$

where $U_{B,A}$ is the activation energy of transition of one B, A atom from liquid to the solid phase across the interface, K_B is the Boltzmann constant and $T_r \equiv T_r(x, y, t)$ is the interface temperature.

Similarly the probability of reverse transition of one B atom from the solid to the liquid phase is

$$P_2^B = \exp\left[-\frac{U_B}{K_B T_r} - \frac{\Delta G_B}{K_B T_r}\right].$$

By using (12) this can be written as

$$P_2^B = P_1^B \exp\left[-\frac{\Delta G_B}{K_B T_r}\right]. \tag{14}$$

Similarly by using (13), for one A atom it is

$$P_2^A = P_1^A \exp\left[-\frac{\Delta G_A}{K_B T_r}\right], \tag{15}$$

where $\Delta G_{B,A}$ is the change in free energy of the system due to one B, A atom transfer from the solid to the liquid phase. These equations are written under the assumptions that A and B atoms are arriving at the interface independently of each other, and the transition to the other phase is also independent. This implies that there are no A – B interactions and the mixture is ideal. The effect of interactions may be taken into account by modifying the expression for the change in the free energy $\Delta G_{B,A}$.

The probability of creation of new monoatomic layer of the solid phase with concentration C'_{Sr} per unit time can be written as [39]

$$P_0(t, C'_{Sr}, C_{Sr}) = \sum_{r_B=0}^{N_B^L} P_{r_B}^- P_{(C_{Sr}\rho^S + r_B)}^+ \sum_{r_A=0}^{N_A^L} P_{r_A}^- P_{((1-C_{Sr})\rho^S + r_A)}^+ \tag{16}$$

where

$$P^-_{r_{A,B}} = \binom{N^L_{A,B}}{r_{A,B}} [P_2^{A,B}]^{r_{A,B}} [1 - P_2^{A,B}]^{[N^L_{A,B} - r_{A,B}]}.$$

and

$$P^+_{m_{A,B}} = \binom{N^S_{A,B}}{m_{A,B}} [P_1^{A,B}]^{m_{A,B}} [1 - P_1^{A,B}]^{[N^S_{A,B} - m_{A,B}]}.$$

Here P^+ and P^- represent the process of atoms joining and leaving the solid phase, respectively. The probability density of creation of a monoatomic layer of concentration C'_{Sr} at time t' can be expressed in terms of P_0 as [39]

$$\omega [C'_{Sr}, C_{Sr}, t', t] = P_0[t', C'_{Sr}, C_{Sr}] \exp\left[- \int_t^{t'} P_0[\tau, C'_{Sr}, C_{Sr}] \, d\tau \right]. \tag{17}$$

The stochastic differential equations for the rate of growth and concentration of the solid phase can be written with the help of probability density ω and by using the assumptions: (i) ω is independent of C_{Sr} i.e. the growth does not depend on the concentration of the solid already formed (ii) the concentration of the solid phase in the new monoatomic layer C'_{Sr} and at the interface C_{Sr} are equal. The stochastic differential equations for growth rate R and concentration C_{Sr}, as written with the help of Ito's formula [42], are

$$dR = \alpha_R \, dt + \beta_R \, dW_R(t) + \beta_{RC} \, dW_C(t) \tag{18}$$

and

$$dC_{Sr} = \alpha_C \, dt + \beta_{RC} \, dW_R(t) + \beta_C \, dW_C(t) \tag{19}$$

where $\alpha_R, \beta_R, \beta_{RC}, \alpha_C$ and β_C are functions of time and their values are given by

$$\alpha_R = \frac{d}{dt} \langle R \rangle, \tag{20}$$

$$\alpha_C = \frac{d}{dt} \langle C_{Sr} \rangle, \tag{21}$$

$$\beta_R^2 + \beta_{RC}^2 = \frac{d}{dt} \langle R^2 \rangle - 2 \langle R \rangle \frac{d}{dt} \langle R \rangle, \tag{22}$$

$$\beta_C^2 + \beta_{RC}^2 = \frac{d}{dt} \langle C_{Sr}^2 \rangle - 2 \langle C_{Sr} \rangle \frac{d}{dt} \langle C_{Sr} \rangle, \tag{23}$$

$$\beta_{RC} \langle \beta_C + \beta_R \rangle = \frac{d}{dt} \langle (R - \langle R \rangle)(C_{Sr} - \langle C_{Sr} \rangle) \rangle \tag{24}$$

and dW_R, dW_C are Wiener's processes obeying the following conditions [42]

$$\langle dW_i \rangle = 0,$$

$$dW_i \, dW_j = \delta_{ij} \, dt; \quad i,j = C, R$$

and

The values of coefficients $\alpha_C, \alpha_R, \beta_C, \beta_R$ and β_{RC} can be obtained by averaging over the growth process as follows

$$\alpha_C = \frac{\mathrm{d}}{\mathrm{d}t}\langle C_{Sr}\rangle = \int_0^\infty \mathrm{d}\tau \int_0^1 \mathrm{d}C_{Sr}\, C_{Sr}\frac{\mathrm{d}\omega}{\mathrm{d}t}. \tag{25}$$

The time derivative of the probability density ω is obtained by differentiating (17) and can be written as [39]

$$\frac{\mathrm{d}}{\mathrm{d}t}\omega[C_{Sr}, t+\tau, t] = \frac{\mathrm{d}P_0(t+\tau, C_{Sr})}{\mathrm{d}(t+\tau)}\exp\left[-\int_t^{t+\tau} P_0(t', C_{Sr})\,\mathrm{d}t'\right], \tag{26}$$

where the term $P_0^2 = P(t+\tau)[P_0(t+\tau) - P_0(t)]$ has been neglected. Under the approximations [39]

$$N_A^L, N_A^S, N_B^L, N_B^S \gg 1,$$

$$C_{Sr}\rho^S, (1-C_{Sr})\rho^S \gg 1,$$

$$\rho^S = \rho^L = \rho^S,\ U_A = U_B = U,\ P_1^B = P_1^A,\ (1-P_2^A) = (1-P_1^A) \cong 1,$$

$$C_{Lr} = (1-C_{Lr}) \cong 0.5,\quad C_{Sr} = (1-C_{Sr}) \cong 0.5,$$

differentiation of (16) yields

$$\frac{\mathrm{d}P_0}{\mathrm{d}t} = -P_0 F(t),$$

where

$$F(t) = a_1\left\langle\frac{\mathrm{d}T_r}{\mathrm{d}t}\right\rangle + a_2\left\langle\frac{\mathrm{d}C_{Lr}}{\mathrm{d}t}\right\rangle, \tag{27}$$

$$a_1 = \nu\rho^S p_1^A\left[-\frac{U}{K_B T_r^2} - \frac{1}{2}\left[\frac{\Delta H_A}{K_B T_r^2} + \Omega_L C_{Lr}^2 - \Omega_S C_{Sr}^2\right]\right.$$
$$\times\exp\left[-\frac{\Delta G_A}{K_B T_r}\right] - \frac{1}{2}\left[\frac{\Delta H_B}{K_B T_r^2} + \Omega_L[1-C_{Lr}]^2 - \Omega_S[1-C_{Sr}]^2\right]$$
$$\left.\times\exp\left[-\frac{\Delta G_B}{K_B T_r}\right]\right] \tag{28}$$

and

$$a_2 = \nu\rho^S p_1^A\left[\exp\left(-\frac{\Delta G_A}{K_B T_r}\right)\frac{\Omega_L C_{Lr}}{K_B T_r}\right.$$
$$\left.-\exp\left(-\frac{\Delta G_B}{K_B T_r}\right)\frac{\Omega_L(1-C_{Lr})}{K_B T_r}\right], \tag{29}$$

where a_1 and a_2 are constants depending on the thermophysical properties of the substances, $\Delta H_{A,B}$ is the latent heat of fusion of pure A, B component and $\Omega_{L,S}$ is the interaction parameter for the liquid, solid phase, for non ideal solutions.

Similarly, other coefficients $\alpha_R, \beta_R, \beta_C, \beta_{RC}$ can be obtained by solving (20), (22)–(24).

The stochastic differential equations for the growth rate and the concentration of the solid phase thus become

$$dR = \bar{\alpha}_R F(t)\, dt + [\bar{\beta}_R\, dW_R + \bar{\beta}_{RC}\, dW_C]\, (F(t))^{1/2} \tag{30}$$

and

$$dC_{Sr} = \bar{\alpha}_C F(t)\, dt + [\bar{\beta}_R\, dW_C + \bar{\beta}_{RC}\, dW_R]\, (F(t))^{1/2} \tag{31}$$

where $\bar{\alpha}_R, \bar{\alpha}_C, \bar{\beta}_R, \bar{\beta}_C$ and $\bar{\beta}_{RC}$ are the stochastic parameters proportional to $\langle R\rangle$, $\langle C_{Sr}\rangle$ $\langle R^2\rangle$, $\langle C_{Sr}^2\rangle$ and $\langle R - \langle R\rangle\rangle\, \langle C_{Sr} - \langle C_{Lr}\rangle\rangle$ respectively.

Similarly (3) and (4) can be written in the form of stochastic differential equations as

$$dT = [\beta_1 + \beta_2 R\delta(\mathbf{x} - \mathbf{x}_r(t)) + \beta_3 R]\, dt + \beta_T dW_T \tag{32}$$

and

$$dC_L = [\beta_4 + (\beta_5 + C_{Sr})\, R\, \delta(\mathbf{x} - \mathbf{X}_r(t)) + \beta_6 R]\, dt + \beta_{CL}\, dW_{CL} \tag{33}$$

where

$$\beta_1 = [\![D_T \operatorname{grad} T + D_{TC} \operatorname{grad} C_L]\!].$$

$$\beta_2 = \frac{\Lambda}{C_v \rho},$$

$$\beta_3 = \operatorname{grad} T,$$

$$\beta_4 = [\![D_C \operatorname{grad} C_L + D_{CT} \operatorname{grad} T]\!],$$

$$\beta_5 = -C_{Lr},$$

and

$$\beta_6 = \operatorname{grad} C_L,$$

where β_T, β_{CL} are stochastic parameters and dW_T, dW_{CL} are Wiener's processes. Writing $F(t)$ with the help of (32) and (33), it becomes

$$F(t) = a_1[\beta_1 + \beta_2\langle R\rangle + \langle R\rangle\beta_3] + a_2[\beta_4 + \beta_5\langle R\rangle + \langle C_{Sr}R\rangle + \beta_6\langle R\rangle]. \tag{34}$$

Equation (32) has been written for the interface.

Here

$$[\![\mathbf{Y}]\!] = \lim_{\varepsilon \to 0} [\mathbf{Y}(\mathbf{X}_r(t) + \varepsilon \mathbf{n}_r) - \mathbf{Y}((\mathbf{X}_r(t) - \varepsilon \mathbf{n}_r)]\, \mathbf{n}_r$$

stands for the divergence in the quantity $\mathbf{Y}$ near the interface, $\mathbf{n}_r$ is normal to the interface, and

$$\mathbf{X}_r(t) = \mathbf{n}_r \int_{t_0}^{t} R(t')\, dt' + \mathbf{X}_r(t_0) \tag{35}$$

gives the position of the interface at time t in which $\mathbf{X}_r(t_0)$ is the initial position of the interface.

(1) $a_1, a_2 \sim 1$. In this case equations (30)–(33) have to be solved simultaneously. The time evolution of the system can be obtained by calculating the probability $P(T, C_L, C_{Sr}, R, t)$; which is the probability that at time t the liquid concentration distribution in the system is C_L, temperature is T, concentration of the solid phase is C_{Sr} and rate of solidification is R. The average values $\langle C_L \rangle$, $\langle T \rangle$, $\langle C_{Sr} \rangle$ and $\langle R \rangle$ can then be obtained by using this probability P. However, this problem is practically unsolvable [40] and further approximations should be made to simplify the problem.

(2) $a_1 \gg 1, a_2 \gg 1$. In this case the method of adiabatic elimination of fast variables [42] can be used. For times $t \gg a_1^{-1}$, $t \gg a_2^{-1}$ the average stationary values of R and C_{Sr} can be substituted in (32) and (33). Also for $t < a_1^{-1}$, a_2^{-1} the memory effects should be included.

(3) $a_1 \ll 1$, $a_2 \ll 1$. In this case, as is evident from (30) and (31), dR and dC_{Sr} are negligible. R and C_{Sr} are thus slowly varying quantities as compared to variation in T and C_L with time. It means that (30) and (31) can be solved by substituting $\langle T \rangle$ and $\langle C_L \rangle$. But the solution of (32) and (33) also depend on the boundary conditions, therefore a stationary solution cannot be pre supposed.

(4) $a_1 \gg 1, a_2 \ll 1$ or $a_1 \ll 1, a_2 \gg 1$. In this case adiabatic elimination of the 'most fast' variable can be done. In the case of metals where $a_1 \approx 10^{20}$ and $a_2 \approx 10^{22}$ [40], these equations can be solved as discussed below.

The probability that at time t, the temperature of the interface is T_r, concentration of the liquid phase is C_{Lr} and the rate of growth is R, is given by Fokker–Planck equation

$$\frac{\partial}{\partial t} P[T_r, C_{Lr}, R, t] = [a_1 L_1 + L_2 + L_3]\, P[T_r, C_{Lr}, R, t]. \tag{36}$$

In writing the probability $P(T_r, C_{Lr}, R, t)$, (31) has been omitted as it does not introduce anything new in the system.

Here

$$L_1 = -\frac{\partial \gamma_1}{\partial R} + \frac{\partial^2}{\partial R^2} \frac{\gamma_2^2}{2},$$

L_2 and L_3 are chosen such that for the projection operator (adiabatic elimination method in terms of operators) P, the following relations hold [42]

$$P L_2 P = 0,$$

$$P L_3 \neq L_3 P$$

and

$$\gamma_1 = \bar{\alpha}_R[\beta_1 + \beta_2\langle R \rangle + \beta_3\langle R \rangle] + \frac{a_2}{a_1}[\beta_4 + \beta_5\langle R \rangle + \langle C_{Sr} R \rangle + \beta_6\langle R \rangle].$$

$$\gamma_2 = \bar{\beta}_R \Big[[\beta_1 + \beta_2\langle R \rangle + \beta_3\langle R \rangle] + \frac{a_2}{a_1}[\beta_4 + \beta_5\langle R \rangle + \langle C_{Sr} R \rangle + \beta_6\langle R \rangle] \Big]^{1/2}.$$

Solution of (36) can be obtained by finding stationary average value of growth rate and taking Laplace transform.

This method of solution is quite cumbersome. An alternative method for evaluating the probability of formation of new monoatomic layer $P_0(t, C_{Sr}, C'_{Sr})$ would be to express it in terms of probabilities of atom attachment/detachment which is discussed below.

2.2 *Calculation of probability*

For ideal mixture the free energies can be written as

$$\Delta G_B = \Delta\mu_B + K_B T_r \ln\frac{C_{Sr}}{C_{Lr}}, \tag{37}$$

$$\Delta G_A = \Delta\mu_A + K_B T_r \ln\frac{[1 - C_{Sr}]}{[1 - C_{Lr}]}, \tag{38}$$

where $\Delta\mu_{A,B}$ is the change in chemical potential per A, B atom transfer from the solid to the liquid phase.

The probability of the event that one B atom is added to the solid phase per unit time is [32]

$$P_3^B = \frac{P_1^B N_B^S - P_2^B N_B^L}{N_B^S}. \tag{39}$$

Substituting the value of N_B^S and N_B^L from (8) and (10) and assuming $\nu_B^L = \nu_B^S$ and $\rho^L = \rho^S$, P_3^B reduces to

$$P_3^B = P_1^B F_B[T_r(x, y, t), C_{Lr}(x, y, t), C_{Sr}(x, y, t)], \tag{40}$$

where

$$F_B = \left[1 - \exp\left[-\frac{\Delta\mu_B}{K_B T_r}\right]\right].$$

Similarly the probability of addition of one A atom to the solid phase per unit time is

$$P_3^A = P_1^A F_A[T_r(x, y, t), C_{Lr}(x, y, t), C_{Sr}(x, y, t)], \tag{41}$$

where

$$F_A = \left[1 - \exp\left[-\frac{\Delta\mu_A}{K_B T_r}\right]\right].$$

By using these probabilities, the average solid concentration and the average rate of growth of the solid phase can be determined as follows.

Let m_A and m_B be the number of atoms of the A- and B-components, respectively that cross the interface from liquid to solid phase per unit area during the time interval Δt. Then

$$m_A = (1 - C_{Sr})\rho^S(y)\Delta x, \tag{42}$$

$$m_B = C_{Sr}\rho^S(y)\Delta x, \tag{43}$$

where $\rho^S(y)$ is the number of atoms per unit volume in the solid phase at the interface

and Δx is the thickness of the solid grown. Therefore probability P_0 can be written as

$$P_0(C_{Sr}, C'_{Sr}, t) = P^{B}_{\rho\Delta\times C_{Sr}}\, P^{A}_{\rho\Delta\times(1-C_{Sr})}, \tag{44}$$

where

$$P^{A,B}_{m_{A,B}} = \binom{N^{S}_{A,B}}{m_{A,B}} [P^{A,B}_{3}]^{m_{A,B}} [1 - P^{A,B}_{3}]^{[N^{S}_{A,B} - m_{A,B}]}.$$

The number of A (B) atoms going to solid on an average is

$$m_A = \overline{(1 - C_{Sr})\,\rho^{S}(y)\,\Delta x} = N^{S}_{A}\, P^{A}_{3}, \tag{45}$$

$$m_B = \overline{C_{Sr}\,\rho^{S}(y)\,\Delta x} = N^{S}_{B}\, P^{B}_{3}, \tag{46}$$

where $C_{Sr} \equiv C_{Sr}(x, y, t)$ and $\Delta x \equiv \Delta x(x, y, t)$.

If Δx and C_{Sr} are considered to be independent of each other, then (45) and (46) can be solved for $\overline{C_{Sr}}$ and $\overline{\Delta x}$. Taking $1/\rho^{S}(y) = a_0$, where a_0 is the lattice constant of the solid, $\overline{C_{Sr}}$ and $\bar{R}$ are given by

$$\bar{C}_{Sr}(x, y, t) = \frac{C_{Lr}\, F_B(T_r, C_{Lr}, C_{Sr})}{C_{Lr}\, F_B(T_r, C_{Lr}, C_{Sr}) + (1 - C_{Lr})\, F_A(T_r, C_{Lr}, C_{Sr})} \tag{47}$$

and

$$\bar{R}(x, y, t) = a_0 \nu\, P^{B}_{1}[C_{Lr}\, F_B[T_r, C_{Lr}, C_{Sr}] + [1 - C_{Lr}]\, F_A[T_r, C_{Lr}, C_{Sr}]] \tag{48}$$

under the approximations $U_A = U_B$ and $\nu^{L}_{B} = \nu^{L}_{A} = \nu$. The average temperature and liquid concentration distribution can be obtained by solving (32) and (33) by substituting average values of rate of growth and concentration of the solid phase ($C_{Sr} \simeq \bar{C}_{Sr}$).

2.3 *Evaluation of $\Delta\mu_{A,B}$ for non ideal solutions*

In order to consider the interaction effects of the constituents of the binary alloy, the corrections to the free energy must be evaluated. The Gibb's energy for liquid solution with components A and B having mole fractions X_A and X_B is given by

$$G^{L} = \mu^{L}_{A} X^{L}_{A} + \mu^{L}_{B} X^{L}_{B} \tag{49}$$

or

$$G^{L} = \mu^{L}_{A} + [\mu^{L}_{B} - \mu^{L}_{A}] X^{L}_{B}, \tag{50}$$

where the condition $X^{L}_{A} + X^{L}_{B} = 1$ has been used and the partial molal free energy μ is by definition the free energy per atom of a component in solution. Differentiation of (50) yields

$$\frac{dG^{L}}{dX^{L}_{B}} = -\mu^{L}_{A} + \mu^{L}_{B}. \tag{51}$$

Substitution of (51) in (50) gives

$$\mu^{L}_{A} = G^{L} - X^{L}_{B} \frac{dG^{L}}{dX^{L}_{B}}. \tag{52}$$

Similarly (51) and (49) give

$$\mu_B^L = G^L + X_A^L \frac{dG^L}{dX_B^L}. \tag{53}$$

The free energy of a non ideal liquid solution can be written as [12, 13]

$$G^L = X_A^L G_A^L + X_B^L G_B^L + K_B T [X_A^L \ln X_A^L + X_B^L \ln X_B^L] + \Omega_L X_A^L X_B^L \tag{54}$$

where the first two terms are the free energies of a mechanical mixture of the two components, the third term is the entropy of mixing and the last term corresponds to the excess enthalpy ($\approx$ excess free energy per atom; ΔH^{XS}) of the non ideal solution. The interaction parameter Ω_L is given by

$$\Omega_L = Z V^L,$$

where Z is the coordination number and

$$V^L = V_{AB}^L - [V_{AA}^L + V_{BB}^L]/2$$

in which V_{AB}^L is the interaction energy between A and B type of atoms in the liquid. V_{AA}^L and V_{BB}^L are the interaction energies between A–A and B–B type of atoms respectively.

Differentiation of (54) with respect to X_B^L gives

$$\frac{dG^L}{dX_B^L} = G_B^L - G_A^L + K_B T \ln \frac{X_B^L}{X_A^L} + \Omega_L [1 - 2X_B^L]. \tag{55}$$

Using (55), (53) can be written as

$$\mu_B^L = G_B^L + K_B T \ln X_B^L + \Omega_L [X_A^L]^2. \tag{56}$$

Similarly (55) and (52) give

$$\mu_A^L = G_A^L + K_B T \ln X_A^L + \Omega_L [X_B^L]^2. \tag{57}$$

The corresponding relations for the solid solution are

$$\mu_A^S = G_A^S + K_B T \ln X_A^S + \Omega_S [X_B^S]^2. \tag{58}$$

and

$$\mu_B^S = G_B^S + K_B T \ln X_B^S + \Omega_S [X_A^S]^2, \tag{59}$$

where

$$\Omega_S = Z V^S$$

and

$$V^S = V_{AB}^S - [V_{AA}^S + V_{BB}^S]/2.$$

Now, subtraction of (59) from (56) yields

$$\Delta\mu_B = \Delta G_B + K_B T_r \ln\frac{C_{Lr}}{C_{Sr}} + \Omega_L [1 - C_{Lr}]^2 - \Omega_S [1 - C_{Sr}]^2, \tag{60}$$

where $X_B^L = C_{Lr}$, $X_A^L = 1 - C_{Lr}$, $X_B^S = C_{Sr}$, $X_A^S = 1 - C_{Sr}$.
Similarly from (57) and (58) we get

$$\Delta\mu_A = \Delta G_A + K_B T_r \ln\frac{[1 - C_{Lr}]}{[1 - C_{Sr}]} + \Omega_L [C_{Lr}]^2 - \Omega_S [C_{Sr}]^2, \tag{61}$$

where $\Delta\mu_{A,B} = \mu_{A,B}^L - \mu_{A,B}^S$ is the chemical potential difference and $\Delta G_{A,B} = G_{A,B}^L - G_{A,B}^S$ is the free energy of fusion for pure component A or B at temperature T_r.

The free energy of fusion for a pure component can be expressed in terms of more commonly available quantity $\Delta H_{A,B}$, the enthalpy of fusion of A, B component at its melting temperature $T_{A,B}$ [12, 43]. For near equilibrium process, it can be written as

$$\Delta G_B = \Delta H_B [T_B - T_r] / T_B, \tag{62}$$

$$\Delta G_A = \Delta H_A [T_A - T_r] / T_A. \tag{63}$$

By using (60) and (62) the expression for chemical potential difference per B atom transfer at the interface can be written as

$$\Delta\mu_B = \frac{\Delta H_B [T_B - T_r]}{T_B} + K_B T_r \ln\frac{C_{Lr}}{C_{Sr}} + \Omega_L [1 - C_{Lr}]^2 - \Omega_S [1 - C_{Sr}]^2 \tag{64}$$

and similarly with the help of (61) and (63) the chemical potential difference for one A atom transfer can be written as

$$\Delta\mu_A = \frac{\Delta H_A [T_A - T_r]}{T_A} + K_B T_r \ln\frac{[1 - C_{Lr}]}{[1 - C_{Sr}]} + \Omega_L [C_{Lr}]^2 - \Omega_S [C_{Sr}]^2. \tag{65}$$

The coupled eqs (32), (33), (35), (47) and (48) can be solved to obtain the time evolution of temperature, concentration of liquid phase, interface shape, concentration of the solid phase and rate of growth respectively.

3. Solution of basic equations

For the study of solidification process it is important to consider the coupling between the temperature, concentrations at the interface and the growth rate. The coupling between temperature and concentration gradients has been taken into account through (47) and (48) for the concentration of the solid phase at the interface and growth rate respectively. Therefore the coefficients D_{CT} and D_{TC} have been neglected from the diffusion equations (32) and (33). The source term $Q_C = [C_{Sr} - C_{Lr}]$ $R(x, y, t)\,\delta(x - x_r(y, t))$ can be accounted for by including it in the flux boundary condition at the interface.

The differential equations (32) and (33) which describe the behaviour of T and C_L in the laboratory frame then reduce to the following equations in the frame (x', y', t')

moving with velocity R, under the steady state conditions

$$D_C \frac{\partial^2 C_L^{(x',y',t')}}{\partial x'^2} + D_C \frac{\partial^2 C_L^{(x',y',t')}}{\partial y'^2} + R(x', y', t') \frac{\partial C_L^{(x',y',t')}}{\delta x'} = 0 \tag{66}$$

and

$$\frac{\partial^2 T^{(x',y',t')}}{\partial x'^2} + \frac{\partial^2 T^{(x',y',t')}}{\partial y'^2} + \frac{R^{(x',y',t')}}{D_T} \frac{\partial T^{(x',y',t')}}{\delta x'}$$

$$+ \frac{\Lambda}{k} R(x', y', t')\, \delta\,(x' - X_r(y', t')) = 0\,, \tag{67}$$

where k is the thermal conductivity and $x' = x - Rt$, $t' = t$ and $y' = y$.

These equations can be solved for a given boundary and initial conditions corresponding to laboratory/manufacturing process. The initial and boundary conditions which have been selected for the present study are as follows.

3.1 *Initial and boundary conditions*

The boundary and initial conditions for temperature T in the interface coordinates are:

(i) $T(-Rt, y, t) = T_1 - \phi t$ for all y where $R \equiv R(x, y, t)$, $x \equiv X_r(y, t)$ represents the interface position, ϕ is the rate of external cooling, T_1 is the equilibrium melting temperature of the substance of composition C_{LO} at position $x = 0$.

(ii) $T(x, 0, t) = T(x, y_{max}, t) = (T_1 - T_2 - \phi t) \exp(-(x + Rt)/\zeta_0) + T_2$ for $x \geqslant X_r(y, t)$ where y_{max} is the width of the sample, T_2 is the temperature at $x = \infty$ and ζ_0 is a constant.

(iii) $T(\infty, y, t) = T_2$ for all y.

(iv) $T(x, y, 0) = (T_1 - T_2) \exp(-x/\zeta_0) + T_2$ for all x, y.

The boundary and initial conditions for concentration C_L are:

(i) $\partial C_L(x, y, t)/\partial t = -R(x, y, t)/D_c\,[C_{Lr} - C_{Sr}]$ at interface $x = X_r(y, t)$ for all y.

(ii) $C_L(\infty, y, t) = C_{LO}$ for all y at a point far from the interface in the liquid.

(iii) $C_L(x, 0, t) = C_L(x, y_{max}, t) = C_{LO}$ for $x \geqslant X_r(y, t)$

(iv) $C_L(x, y, 0) = C_{LO}$ for all x, y.

The experimental conditions compatible with these boundary conditions are shown schematically in figures 1(a, b, c). The sample is considered to be semi infinite on which an exponential external temperature gradient is maintained in the x direction. These boundary conditions are the same as selected by Chvoj [37] for his two dimensional (1-space, 1-time) model.

Equations (66) and (67) together with (47) and (48) are numerically solved for C_L and T respectively using finite difference method [44] and an iterative scheme, namely, the successive overrelaxation method (SOR) [45].

The position of the solid-liquid interface is denoted by delta function in the present model. As the solidification process proceeds latent heat is evolved at the interface $X_r(y, t)$ giving rise to the source term Q_T in (67). The delta function is taken into

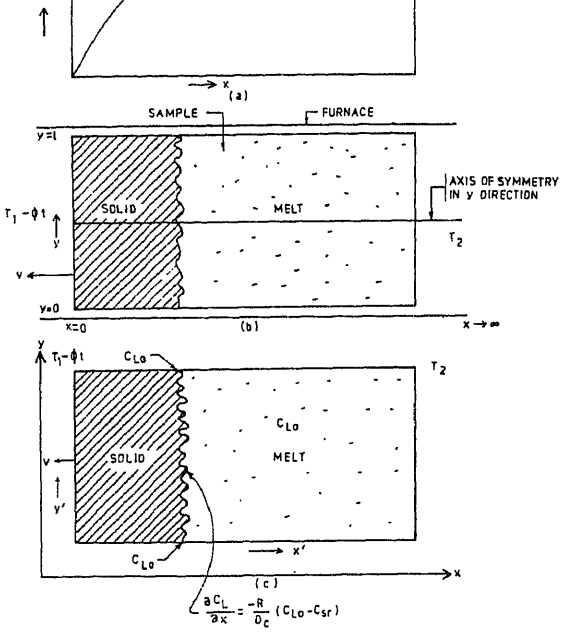

Figure 1. Schematic representation of (**a**) initial temperature distribution in the sample (**b**) boundary conditions on temperature distribution (**c**) boundary conditions on concentration distribution.

$$Q_T = \frac{\Lambda}{C_v \rho}(R(x, y, t))^2 \, \Delta t,$$

where Λ is taken to be

$$\Lambda = C_{Sr}\, Q_B + [1 - C_{Sr}]Q_A - C_{Sr}[W_L[1 - C_{Lr}]^2 - W_S[1 - C_{Sr}]^2] - [1 - C_{Sr}]\,[W_L\, C_{Lr}^2 - W_S\, C_{Sr}^2] \tag{68}$$

in which $W_L = \Omega_L / a_0^3$, $W_S = \Omega_S / a_0^3$ and $Q_{A,B}$ is the latent heat of fusion per unit volume of the pure A, B component.

3.2 *Approximations for the numerical scheme*

The following approximations were made for the numerical calculations:

(i) The effect of diffusion of mass is significant only close to the solid-liquid interface.
(ii) The heat evolved at the interface would spread faster in the transverse direction as compared to the interface movement. The growth of the solid may be visualized as a number of solidification events occurring in succession each in a time interval Δt and the liquid column ahead of the interface comprises small thin segments. These

segments of the system close to the interface stabilizes in the time interval Δt and steady-state equations can be used to express the process during Δt.

(iii) Initial stage of phase transformation i.e. the nucleation process is not considered and the growth is continuous.

(iv) The total domain is divided into two regions, the interface region and the liquid phase. Interface is considered as one of the boundaries moving with time. It is further assumed that the interface temperature at time t constitutes the boundary temperature at time $t + \Delta t$.

(v) Interface concentration C_{L_I} in the flux condition is approximately equal to the equilibrium concentration C_{LO}.

3.3 *System studied and computer software*

The values of the thermophysical properties chosen (table 1) in the present calculations do not correspond to any particular material but they are close to the typical values of many materials, for example Cu–Ni, Cu–Ag etc. [40]. The two components considered here have the same crystal structure (FCC) and they do not exhibit any solid-state allotropic transformations. The interactions parameters Ω_L and Ω_S are taken independent of temperature.

The numerical scheme was applied to six different systems having interaction parameters

System I $\Omega_L = 2{\cdot}8 \times 10^{-20}$ J/atom $\quad \Omega_S = 2{\cdot}33 \times 10^{-20}$ J/atom
System II $\Omega_L = 2{\cdot}8 \times 10^{-21}$ J/atom $\quad \Omega_S = 2{\cdot}8 \times 10^{-20}$ J/atom
System III $\Omega_L = 2{\cdot}8 \times 10^{-19}$ J/atom $\quad \Omega_S = 2{\cdot}8 \times 10^{-20}$ J/atom
System IV $\Omega_L = -2{\cdot}33 \times 10^{-20}$ J/atom $\quad \Omega_S = -2{\cdot}47 \times 10^{-20}$ J/atom
System V $\Omega_L = -2{\cdot}8 \times 10^{-20}$ J/atom $\quad \Omega_S = -2{\cdot}8 \times 10^{-19}$ J/atom
System VI $\Omega_L = -2{\cdot}8 \times 10^{-20}$ J/atom $\quad \Omega_S = -2{\cdot}8 \times 10^{-21}$ J/atom

Table 1. Values of thermophysical parameters used [33, 48].

Constant	Numerical value	Units
ΔH_A	$2{\cdot}12 \times 10^{-20}$	J/atom
ΔH_B	$3{\cdot}11 \times 10^{-20}$	J/atom
a_0	$0{\cdot}36 \times 10^{-9}$	m
T_A	1360	K
T_B	1730	K
K_B	$1{\cdot}38 \times 10^{-23}$	J/K
T_2	1997	K
U	$0{\cdot}5 \times 10^{-19}$	J
ν	3×10^{10}	s^{-1}
D_C	$0{\cdot}73 \times 10^{-7}$	m^2/s
D_T	$5{\cdot}8 \times 10^{-5}$	m^2/s
k	200	J/s/m/K
ζ_0	0.001	m
Q_A	$-1{\cdot}82 \times 10^9$	J/m^3
Q_B	$-2{\cdot}67 \times 10^9$	J/m^3

Each system was studied for 5 to 9 different sets of initial values of equilibrium concentration C_{LO} and temperature T_1. Values of C_{LO}, T_1 and ϕ lies between 0·02–0·98, 1190 K–1703 K and 10^5–$0{\cdot}5 \times 10^8$ K/s respectively. Width of the sample was taken to be 10^{-5} m. It facilitates the construction of nonequilibrium phase diagrams and the study of their time evolution.

A computer program was written in Basic Language and calculations were performed on PC-AT286 at the Department of Physics and the University Computer Centre of Rani Durgavati University and Govt. M.H. College of Science and Home Science, Jabalpur. 100 points on x axis, which is the direction of the external temperature gradient, 20 points on y axis and 5–10 points on t axis were taken. The total computational run time lies between 3 to 7 h for each set of values of initial concentration and temperature. The length of the solid formed lies between $5{\cdot}1 \times 10^{-7}$ m to 6×10^{-5} m for the total evolution time $0{\cdot}28 \times 10^{-5}$ s and 10^{-3} s respectively. The accuracy in the convergence criterion was chosen to be 1%.

4. Results and discussion

The kinetic phase diagrams and their time evolution for the six systems mentioned above are shown in figures 2–7 respectively.

The phase diagram for system I ($\Omega_L \simeq \Omega_S \cdot \Omega_L$ and Ω_S both positive) indicates that the solubility of one component in the other exists over the entire composition range of

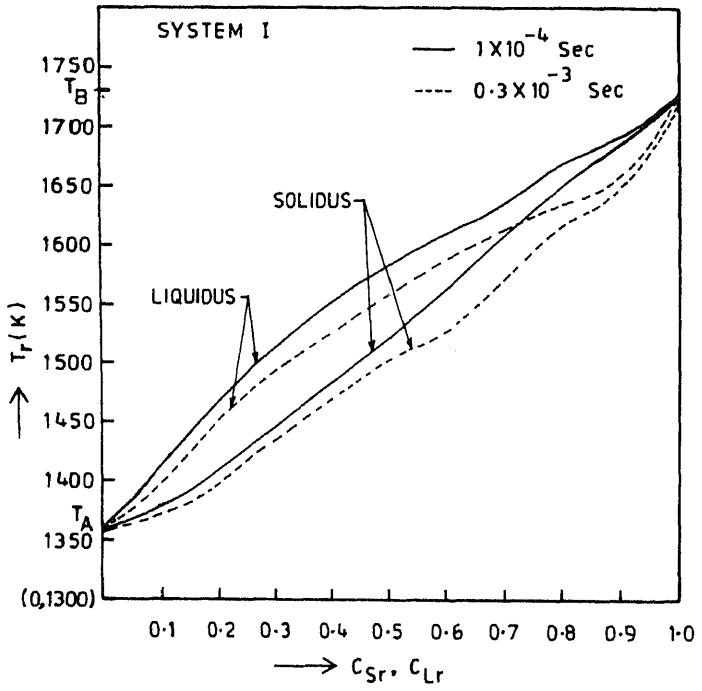

Figure 2. Variation of temperature T_r with compositions C_{Lr} and C_{Sr} for system I with interaction parameters $\Omega_L = 2{\cdot}8 \times 10^{-20}$ J/atom, $\Omega_S = 2{\cdot}33 \times 10^{-20}$ J/atom.

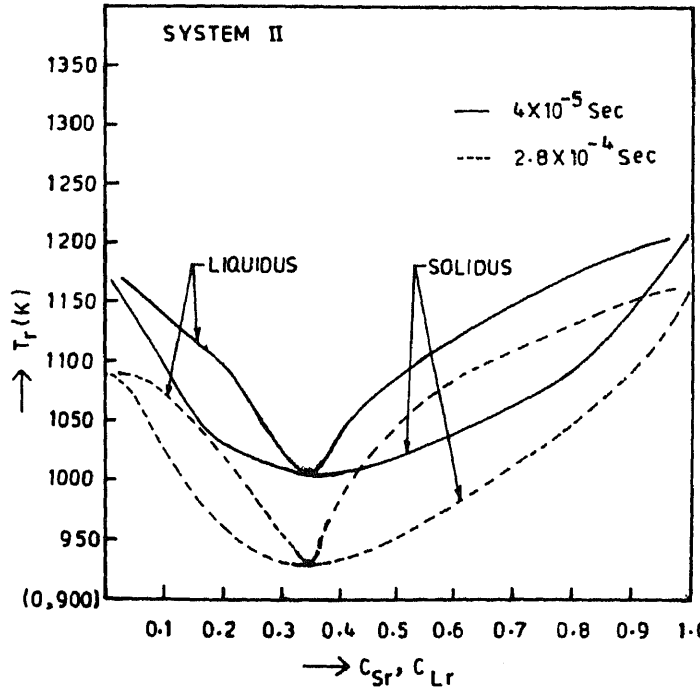

Figure 3. Variation of temperature with compositions C_{L_r} and C_{S_r} for system II with interaction parameters $\Omega_L = 2{\cdot}8 \times 10^{-21}$ J/atom, $\Omega_S = 2{\cdot}8 \times 10^{-20}$ J/atom.

both solid and liquid phases. This also shows co-existence of both solid and liquid phases between the temperature range T_A and T_B for this system, where $T_{A,B}$ is the equilibrium melting temperature of pure A,B component.

In system II ($\Omega_L < \Omega_S$, Ω_L and Ω_S both positive) the positive deviation from ideality in Gibb's mixing energy introduced by positive values of $\Omega_{L,S}$ or ΔH^{xS} ($\Delta H^{xS} = C_{L,S}[1 - C_{L,S}]\Omega_{L,S}$) in both solid and liquid implies a stronger interaction between like atoms (A–A or B–B) than between unlike atoms (A–B). The minima of the liquidus and the solidus curves develop at the same composition, $C_{LO} = 0{\cdot}35$ (figure 3).

For system III with $\Omega_L > \Omega_S$ (Ω_L and Ω_S both positive) the phase diagram shows a maximum both in the liquidus and the solidus curves at an average composition of 0·5 as depicted in figure 4.

The resulting phase diagram for system IV ($\Omega_L \simeq \Omega_S$, Ω_L and Ω_S both negative) as shown in figure 5 depicts the co-existence of both solid and liquid phases over the entire temperature range T_A to T_B.

The phase diagram for system V ($\Omega_L > \Omega_S$, Ω_L and Ω_S both negative) is similar to the phase diagram of system III above. Congruent melting of both the components at an average composition of 0·5 is observed. This is shown in figure 6.

For system VI with $\Omega_L < \Omega_S$ (Ω_L and Ω_S both negative) the phase diagrams obtained are shown in figure 7. A minima at a common point of average composition 0·35, in both solidus and liquidus curves with these values of interaction parameters can be seen.

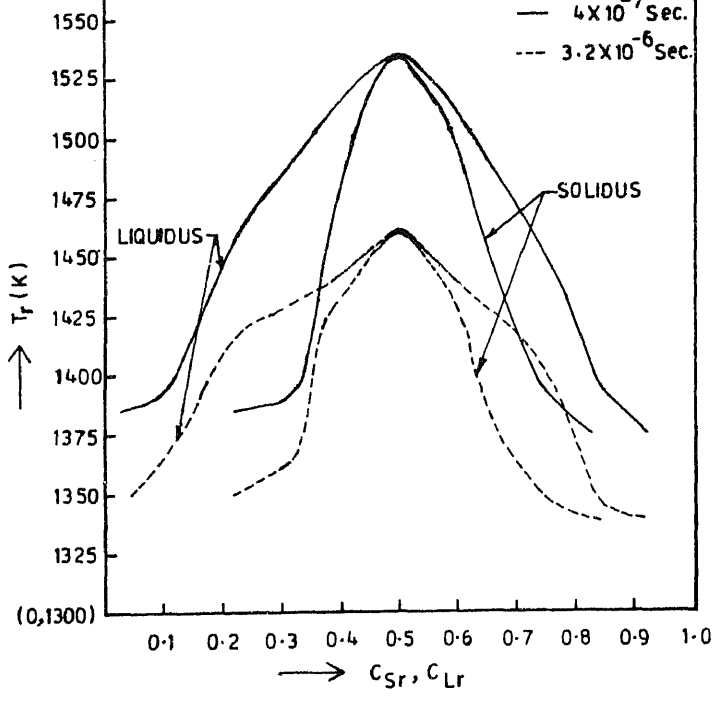

Figure 4. Variation of temperature T_r with compositions C_{L_r} and C_{S_r} for system III with interaction parameters $\Omega_L = 2{\cdot}8 \times 10^{-19}$ J/atom, $\Omega_S = 2{\cdot}8 \times 10^{-20}$ J/atom.

It is evident from these phase diagrams (figures 2 to 7) that as the solutions deviate from ideality, basically three types of phase diagrams are obtained. It is seen by comparison between systems I, II, III and IV, V, VI that all three types of phase diagrams are obtained when the interaction parameters Ω_L and Ω_S are either positive or negative. The liquidus and solidus shapes of these diagrams are similar to those appearing in literature [1, 12] drawn with the help of free energy considerations. However, these phase diagrams cannot be used to predict the sign of the excess Gibb's energy of mixing ($\Delta G^{XS} \simeq \Delta H^{XS}$) for the regular solutions i.e. to predict whether the like atom interactions or the unlike atom interactions dominate. The nature of these phase diagrams also depends on the relative magnitudes of Gibb's mixing energies in liquid and solid solutions. Three cases can be distinguished depending on the relative values of $\Delta H^{XS,liq}$ and $\Delta H^{XS,sol}$.

(i) $\Delta H^{XS\cdot liq} \simeq \Delta H^{XS\cdot sol}$ (*systems I and IV*): The phase diagrams of these systems are lens shaped liquid-solid regions similar to the phase diagrams of ideal systems. These phase diagrams are similar to the experimentally observed equilibrium phase diagrams of many systems, for example Cu–Ni, Au–Pt, ThO_2–ZrO_2 etc.

(ii) $\Delta H^{XS.liq} > \Delta H^{XS.sol}$ (*systems III and V*): These phase diagrams depict a maxima similar to the one observed in Al–Ni system [46]. However these types of phase

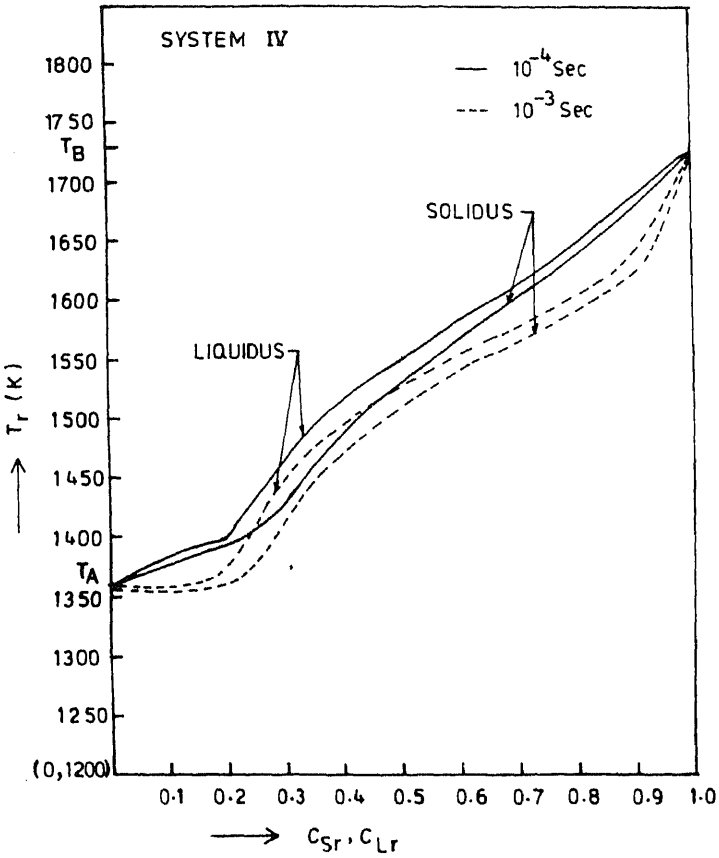

Figure 5. Variation of temperature T_r with compositions C_{Lr} and C_{Sr} for system IV with interaction parameters $\Omega_L = -2{\cdot}33 \times 10^{-20}$ J/atom, $\Omega_S = -2{\cdot}47 \times 10^{-20}$ J/atom.

diagrams are not observed commonly. They are observed in complicated alloy systems that possess more than a single liquid phase (eg. Li–Mg) [47].

(iii) $\Delta H^{XS.liq} < \Delta H^{XS.sol}$ (*systems II and VI*): This type of occurrence of a minima in liquidus and solidus lines is observed in a number of real systems like Cu–Au, Ag–Cu, Au–Ni etc. [1, 46].

The present calculations show that at congruent points (points at which a minima or a maxima occurs in both solidus and liquidus curves, eg. (ii) and (iii) above) freezing can occur with no change in the composition of the solution. Freezing of an alloy at this point is similar to the freezing of a pure metal. These phase diagrams are qualitatively similar to those exhibited by many real systems. They are in agreement with Chvoj's results also [32]. However, Chvoj has drawn these diagrams assuming temperature and liquid concentration to be constant, and he has not covered all the systems. Also time evolution of phase diagram was not determined in his work.

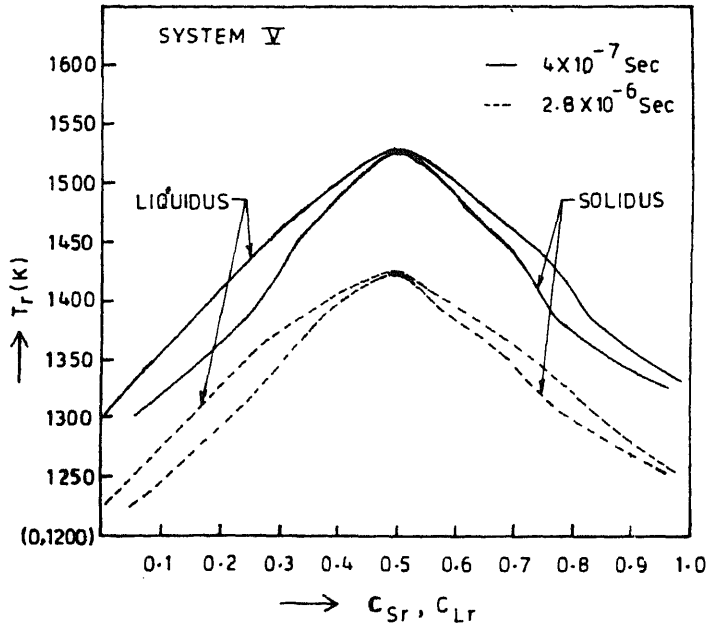

Figure 6. Variation of temperature T_r with compositions C_{Lr} and C_{Sr} for system V with interaction parameters $\Omega_L = -2{\cdot}8 \times 10^{-20}$ J/atom, $\Omega_S = -2{\cdot}8 \times 10^{-19}$ J/atom.

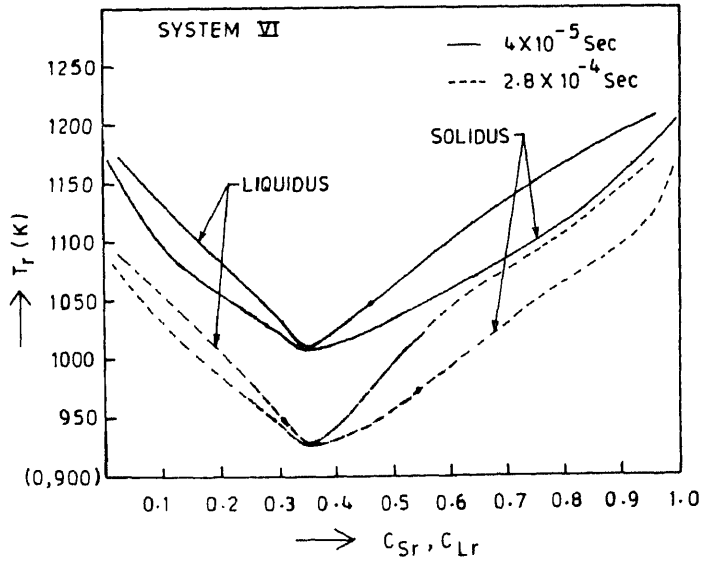

Figure 7. Variation of temperature T_r with compositions C_{Lr} and C_{Sr} for system VI with interaction parameters $\Omega_L = -2{\cdot}8 \times 10^{-20}$ J/atom, $\Omega_S = -2{\cdot}8 \times 10^{-21}$ J/atom.

Figures 2–7 also show the time evolution of phase diagrams. It can be seen from these figures that the phase diagrams shift towards the lower temperature region with time and only a slight change in the shape is observed. Large changes in the shape are not obtained presumably due to the assumption of the linear relationship between currents and gradients, which implies that the system is not very far from equilibrium. Also, the total time elapsed, which has been considered in the calculations is small (10^{-5}–10^{-3}s). This was due to the limitations of the computational time and the numerical scheme.

5. Conclusions

The stochastic model in 3-dimensions (2-space, 1-time) presented here is suitable to study solidification of materials in general, depending on their thermophysical properties. The merit of this model lies in the fact that the growth not necessarily restricted to near equilibrium conditions can also be taken into account. During the nonequilibrium solidification the concentrations of solid and liquid phases, rate of growth, undercooling and the boundary conditions vary with time. These variations are included in this model, enabling the determination of the composition and microstructure of the new phase. Also, interdependence of temperature and concentration together with the effect of kinetic processes at the solid-liquid interface are included in this model. The various approximations can easily be relaxed in this model.

This study is important from the point of view of predicting the outcome of experiments to produce materials with desired and reproducible properties. In order to explain other type of nonequilibrium phase diagrams and microstructures observed, this model can be further extended to multi component systems and 4-dimensions (3-space, 1-time). Also, other type of boundary conditions representing different growth techniques can be studied. This model has been applied to binary alloys having wide range of typical thermodynamic parameters and the kinetic phase diagrams have been obtained. The study of interface movement, shape etc. are given in part II of this paper.

Acknowledgements

One of the authors (LP) is thankful to Prof. P Ramachandrarao for many stimulating discussions. Financial assistance by the University Grants Commission in the form of teacher fellowship to SD is gratefully acknowledged.

References

[1] F C Flemings, in *Solidification processing* (Mc-Graw Hill Inc., New York, 1974)
[2] W Kurz and D J Fisher, in *Fundamentals of solidification* (Trans-Tech Publication, Switzerland, 1986)
[3] P Strimbord, D R Nelson and M Roucheti, *Phys. Rev. Lett.* **47**, 1297 (1981)
[4] P Ramachandrarao, G V S Shastri, L Pandey and A Sinha, *Acta, Cryst.* **A47**, 206 (1991)
[5] D Domb and J L Lebowitz (eds.) in *Phase transitions and critical phenomena.* (Academic, London, 1983)
[6] N Sounders and A P Miodownik, *J. Mater. Res.* **1**, 1803 (1986)
[7] F X Kelly and L H Ungar, *Phys. Rev.* **B. 34**, 1746 (1986)
[8] Z Chvoj, Z Kozisek and J Sestak, *Thermochim. Acta.* **153**, 349 (1989)

[9] D T Gillespie, *J. Chem. Phys.* **74**, 661 (1981)
[10] D Kashchiev, *Cryst. Res. Tech.* **19**, 1413 (1984)
[11] A K Ray, M Chalom and L K Peters, *J. Chem. Phys.* **85**, 2161 (1986)
[12] P Gordon, in *Principles of phase diagrams in materials* (Mc-Graw Hill, 1968; Jersey, 1972)
[13] A K Jena and M C Chaturvedi, in *Phase transformation in materials.* (The Metals Society, Eaglewood Cliffs, New Jersey 1992)
[14] A Bruce and D Wallace, *Phys. Rev. Lett.* **4**, 457 (1982)
[15] J S Langer and L A Turski, *Phys. Rev.* **A8**, 3230 (1973)
[16] J S Langer and A J Turski, *Phys. Rev.* **A22**, 2189 (1980)
[17] J S Langer and A J Swartz, *Phys. Rev.* **A21**, 948 (1980)
[18] V P Skripov and A V Skripov, *Usp. Fiz. Nauk.* **128**, 193 (1979)
[19] V P Skripov and V P Koverda, in *Spontaneous crystallization of undercooled liquids* (Nauka, Moscow, 1984)
[20] A D J Haymet and D W Oxtoby, *J. Chem. Phys.* **84**, 1769 (1986)
[21] A D J Haymet, *Prog. Solid State Chem.* **17**, 1 (1986)
[22] B B Mandelbrot, in *The fractal geometry of nature* (Freeman, San Francisco, 1982)
[23] D S Cannel and C Aubert, in *Fractal and non fractal patterns in physics, in growth and form* edited by H E Stanley and N Ostrowski (Martinus Nijhoff, Dordrecht, 1986)
[24] B Caroli, C. Caroli and B J Roulet, *J. Cryst. Growth* **66**, 575 (1984)
[25] T A Cherepanova, *J. Cryst. Growth* **59**, 371 (1980)
[26] T A Cherepanova, *Phys. Status. Solidi* **A58**, 469 (1980)
[27] T A Cherepanova, *J. Cryst. Growth* **52**, 319 (1981)
[28] L Pandey and P Ramachandrarao, *Acta. Metall.* **35**, 10, 2549 (1987)
[29] R Trivedi, P. Magnin and W Kurz, *Acta Metall.* **35**, 971 (1987)
[30] G S Reddy and J A Sekhar, *J. Mater. Sci.* **21**, 3535 (1985)
[31] Z Chvoj, *Czech. J. Phys.* **B37**, 1256 (1987)
[32] Z Chvoj, *Cryst. Res. Tech.* **21**, 8, 1003 (1986)
[33] Z Chvoj, *Czech. J. Phys.* **B37**, 607 (1987)
[34] Z Chvoj, *Czech. J. Phys.* **B33**, 961 (1983)
[35] Z Chvoj, *Czech. J. Phys.* **B33**, 1060 (1983)
[36] Z Chvoj, *Czech. J. Phys.* **B34**, 548 (1984)
[37] Z Chvoj, *Czech. J. Phys.* **B36**, 863 (1986)
[38] Z Chvoj, *Czech. J. Phys.* **B37**, 1340 (1987)
[39] Z Chvoj, *Czech. J. Phys.* **B40**, 473 (1990)
[40] Z Chvoj, *Czech. J. Phys.* **B40**, 483 (1990)
[41] S Dass, G Johri, L Pandey and P Ramachandrarao, in *II Annual General Meeting of MRSI held at NPL*, New Delhi, February 9–10 (1991)
[42] C W Gardiner, in *Handbook of stochastic methods* (Springer-Verlag, Berlin, 1985)
[43] C N R Rao and K J Rao, in *Phase transitions in solids* (Mc-Graw Hill, Chatham, 1978)
[44] J B Scarborough, in *Numerical mathematical analysis* (Oxford and IBH Publishing Co., New Delhi, 1976)
[45] M Krizek and P Neittaanmaki, in *Finite element approximation of variational problems and applications* (Longman Scientific with John Wiley Inc., New York, 1990)
[46] B Chalmers, in *Principles of Solidification* (John Wiley and Sons, New York, 1967) p.7
[47] R E Reed-Hill, in *Physical metallurgy principles* (EWP, New Delhi, 1975) p. 535
[48] R C Weast (ed.) *CRC Handbook of Chemistry and Physics*, (CRC Press Inc., 1988)

nergy transfer in $CaSiO_3$ phosphors doped ith Ce^{3+} and Tb^{3+}

V SUBRAHMANYAM, SHISHIR JAIN, ASHISH VERMA and S SIVARAMAN
epartment of Physics, Dr. Harisingh Gour Vishwavidyalaya, Sagar 470 003, India

S received 3 January 1995; revised 13 September 1996

ostract. Calcium metasilicate phosphors activated by Ce^{3+} and Tb^{3+} have been studied for their ission characteristics. In two series of phosphors, one activator was kept at its optimum value ile the other was varied. In another two series, one activator was kept below its optimum value d the other was varied. Concentration quenching effects start when each activator gives its aximum emission. There is clear evidence of an energy transfer from Ce^{3+} to Tb^{3+} because the D_3 lines appear on addition of Ce^{3+} while they were conspicuously absent when Tb^{3+} alone was esent. Their absence in singly activated phosphors could not have been due to cross-relaxation. bviously X-ray excitation does not lead to $^5D_3$ transitions which are achieved only by energy nsfer. Further, considering the features of the emission spectra and the concentrations of tivators used, the transfer could only be of the dipole-dipole type.

eywords. Energy transfer; phosphors.

ACS No.

Introduction

is well established that most Ce^{3+} activated phosphors emit in the 300–500 nm spectral nge and that their luminescent decay is fast [1]. These two characteristics make this ass of phosphors especially attractive in fast response optical conversion systems such flying-spot scanners.

Energy transfer from Ce^{3+} to Tb^{3+} ions in inorganic solids has been a subject of umerous investigations [2, 3]. This is because phosphors showing Ce^{3+}–Tb^{3+} energy ansfer may be used industrially as green components in low pressure Hg lamps. Further, ese two rare earth elements combined as activators in a LaOBr matrix, give an efficient een emitting phosphor, which can be used for X-ray intensifying screen [4–6].

In systems containing Ce^{3+} and Tb^{3+} energy transfer is mainly determined by the verlapping between Ce^{3+} and Tb^{3+} excitation spectra [7].

The aim of the present investigation is not only to examine the nature of energy ansfer between Ce^{3+} and Tb^{3+} in the calcium silicate matrix but also to examine a roposition that quenching effects are already prominent when optimum activator oncentrations corresponding to the brightest phosphors are used. If the proposition is alid, then transfer effects should be better when the activator concentration is below its ptimum value.

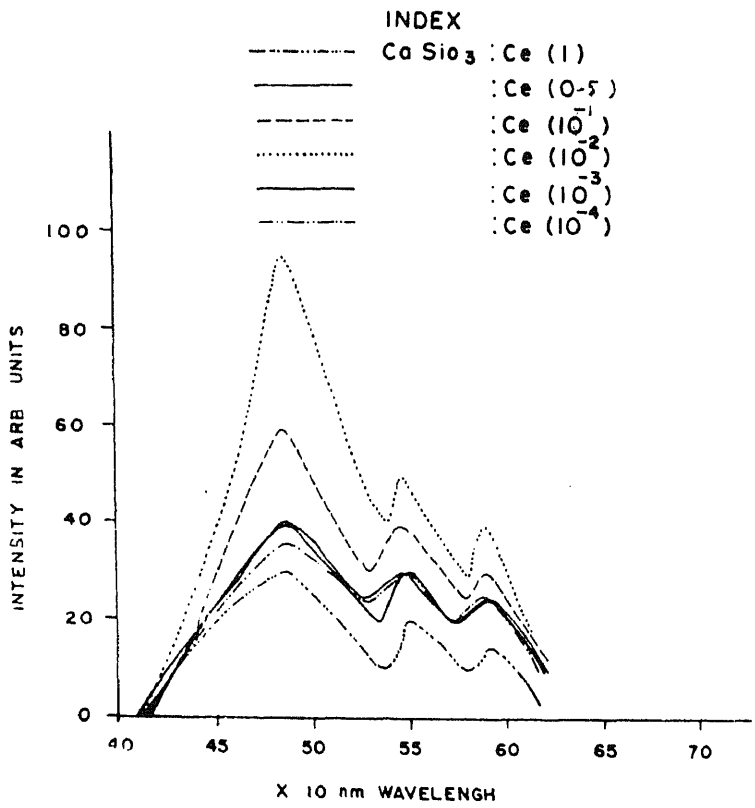

Figure 1. Emission spectra of Ce^{3+} series.

2. Experimental procedure

Analytical grade reagent calcium carbonate and $Si(OH)_4$ were fired with 99% pure oxides of terbium and cerium in a tubular furnace at $1050 \pm 20°C$ for 2 h. Fast cooling was preferred for better emission intensity. In this way six series were prepared.

The terbium concentration in one series was varied from 1 mole % to 10^{-5} mole % and the cerium concentration in the second series was varied from 1 mole % to 10^{-4} mole %. Using the optimum concentration of Tb^{3+} corresponding to maximum emission i.e. 10^{-2} mole %, the Ce^{3+} content was varied from 10^{-7} mole % onward to give a double activated series. Similarly using the optimum of Ce^{3+}, Tb^{3+} was varied from 10^{-7} to 10^{-3} mole % in the fourth series. Two more series were prepared with activator concentrations below their optimum values and the second activator was varied.

The spectral distribution and intensity measurements were studied in the region 400–650 nm, using a Bellingham and Stanley direct recording spectrometer. X-rays are used as

present study. The intensity of the emission was recorded by using the GcA/McPherson photomultiplier model no. Eu 70/30.

3. Results and discussion

3.1 $CaSiO_3: Ce^{3+}$

These phosphors show a broad band emission with three peaks at 485, 545 and 590 nm respectively as shown in figure 1. The emission intensity increases with increase in the concentration of activator, reaches a maximum at 10^{-2} mole % and decreases with further increase in activator concentration. The ground state of Ce^{3+} ion is the doublet $^2F_{5/2} \rightarrow {}^2F_{7/2}$, whose separation remains practically the same as in the free ion because the 4f levels are well shielded from the surroundings. The excited state is derived from the 5d state which is sensitive to the crystal field and is coupled to the lattice vibrations which results in broader band emission rather than line emission. The excited state splits on account of the crystal field into $^2D_{3/2}$ ($^2T_{2g}$) and $^2D_{5/2}$ (^2E_g) from which emission transitions originate [8, 1, 9, 10]. The transition $^2D_{3/2} \rightarrow {}^2F_{7/2}$ is forbidden and one may expect only three transitions. The emissions observed in the present case can therefore be assigned to the transitions $^2D_{5/2} \rightarrow {}^2F_{5/2}$ (485 nm), $^2D_{3/2} \rightarrow {}^2F_{5/2}$ (545 nm) and $^2D_{5/2} \rightarrow {}^2F_{7/2}$ (590 nm).

3.2 $CaSiO_3: Tb^{3+}$

In Tb^{3+} activated phosphors the emission arises from the $^5D_3$ and $^5D_4$ levels to the ground state $^7F_6$ levels, the former transitions being significant only at low concentrations of Tb. In the present work (figure 2) only one peak at 415 nm corresponding to the transition $^5D_3 \rightarrow {}^7F_5$ and four peaks at 490, 550, 590 and 620 nm corresponding to $^5D_4 \rightarrow {}^7F_6$, $^7F_5$, $^7F_4$ and $^7F_3$ were observed [11–13]. Luminescence intensity is highest at 620 nm and increases with concentration of activator, reaches a maximum at 10^{-2} mole % and then decreases as the concentration of the activator is increased.

The separation between $^7F_0$ and $^7F_6$ is 5500 cm^{-1} and that between $^5D_3$ (26300 cm^{-1}) and $^5D_4$ (20500 cm^{-1}) is of the same magnitude. The quenching of $^5D_3$ emission is usually explained by the cross relaxation processes ([14, 15])

$$^5D_3 \rightarrow {}^5D_4 \quad \text{and} \quad {}^7F_6 \rightarrow {}^7F_0,$$

and

$$^5D_3 \rightarrow {}^7F_0 \quad \text{and} \quad {}^7F_6 \rightarrow {}^5D_4.$$

Thus energy can be transferred from the $^5D_3$ level of one Tb^{3+} ion to another, the process depending on the nature of the host lattice (e.g. energy of available phonons, crystal field splitting and index of refraction) [16].

The 4f–4f transitions are in a first approximation spin and parity forbidden and the selection rules can be partially lifted only by spin-orbit coupling and the mixing of the 4f configuration with levels of opposite symmetry. When Tb^{3+} occupies a site with inversion symmetry, only magnetic dipole transition with $\Delta J = 0, \pm 1$ and

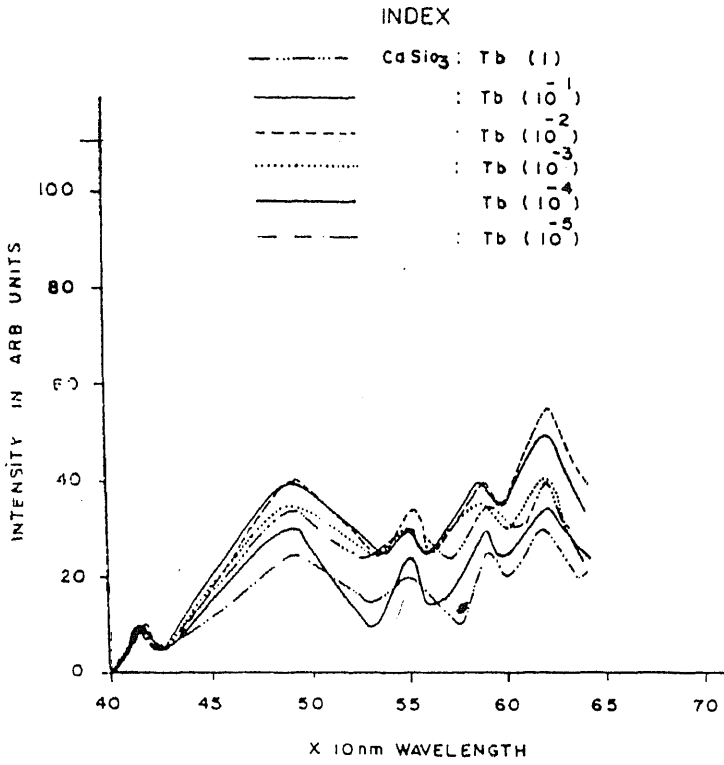

Figure 2. Emission spectra of Tb^{3+} series.

vibronically induced electric dipole transitions with $\Delta J = 2$ can occur. Quantitative calculations have shown that in this case the relative contribution of $^5D_4$ to $^7F_5$, $^7F_4$ and $^7F_3$ will be 89, 1 and 10 respectively, the value being close to the experimental values for SBO_3 and $NaSO_2$ activated by Tb^{3+}. The $^5D_4 \rightarrow {}^7F_6$ transition is 'hypersensitive' to variations of the surroundings [17]. As opposed to Eu^{3+} where even small deviations from inversion symmetry are sufficient to induce intense electric-dipole transitions, Tb^{3+} is less sensitive. The total departure of the $^5D_4$ lines from the standard intensity distribution is an indication of a strong departure from inversion symmetry of the Tb^{3+} site.

3.3 $CaSiO_3: Tb^{3+}$, Ce^{3+}

Keeping the Tb^{3+} concentration at 10^{-2} mole % optimum value and at 10^{-3} mole %, the Ce^{3+} concentration was varied. The emission now consisted of seven and eight lines respectively, the brightest phosphors being obtained for cerium concentrations of 10^{-6} and 10^{-4} mole % respectively. The additional lines observed are 435 nm ($^5D_3 \rightarrow {}^7F_4$), 455 nm ($^5D_3 \rightarrow {}^7F_3$) and 520 nm for which no transition can be ascribed. The last line was observed in the series with 10^{-3} mole % Tb^{3+} (figures 3(a–d)).

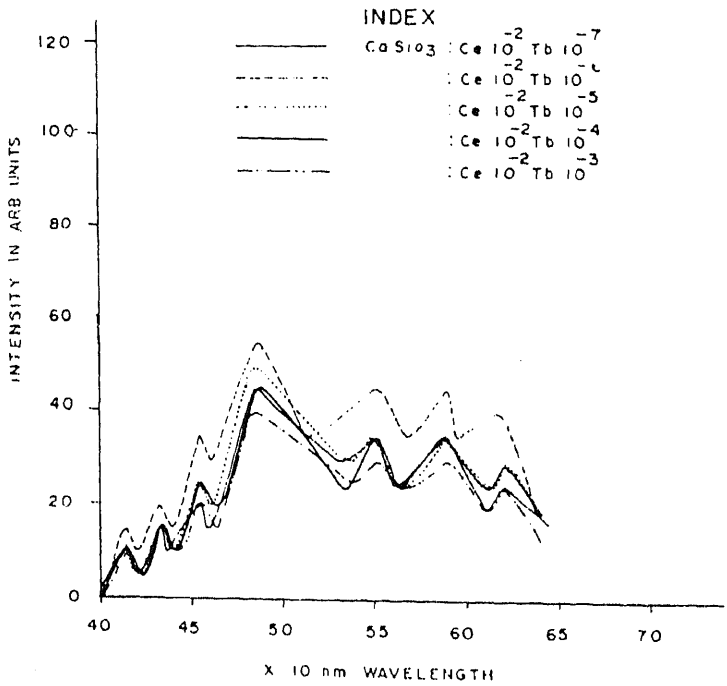

Figure 3a.

At the optimum value of activator concentration, quenching effects begin because of activator–activator interactions. Hence further addition of the activator decreases the intensity. Because of this consideration the value of Tb^{3+} was fixed below optimum in one series. The argument appeared justified from the results obtained. For this series, addition of cerium enhances Tb emission, the maximum sensitization being achieved at 10^{-4} mole % of Ce^{3+}. Three lines of Tb^{3+} and Ce^{3+} [490 and 485, 550 and 545 and 590 nm] overlap when both activators are present. In the absence of any transfer of energy, the intensities at these locations should just be the sum of the individual intensities when the activators are present singly. Also, the already existing lines of Tb^{3+} should have the same intensity as before. In these phosphors the 490 nm emission is predominant. This is understandable since it was the strongest emission of Ce^{3+} and the second best emission of Tb^{3+}. The next intense line is 455 nm which was not present in the terbium series. This is followed by the two overlapping lines 550 and 590 nm. The 435 nm line which is new is comparable to the 620 nm line which was the brightest when terbium is alone.

In the series with optimum Tb^{3+}, maximum sensitization effect was observed for only 10^{-6} mole % addition of Ce^{3+} after which the emission decreased. Here too, the 620 nm intensity was reduced from the start. The 490 and 550 nm lines have greater intensity while 455 nm has the same intensity as the overlaping lines at 590 nm. The decrease in

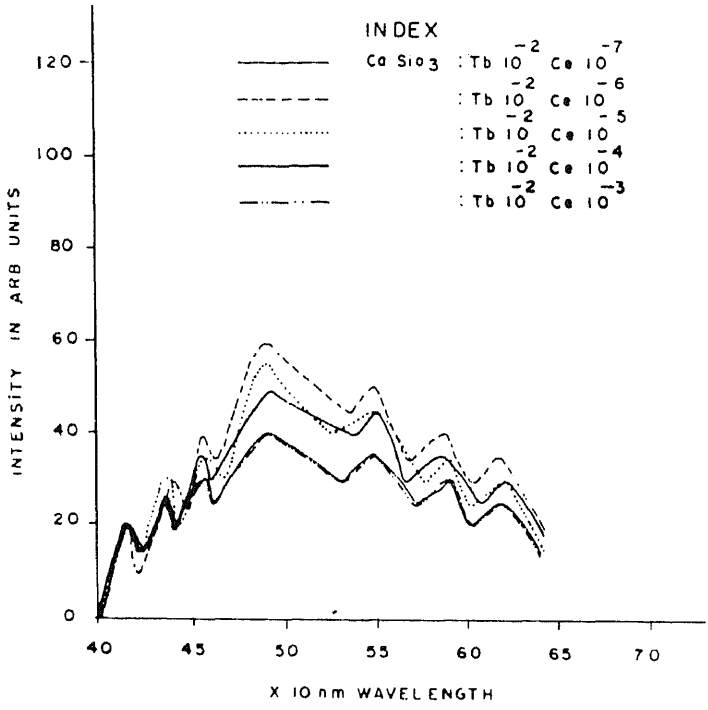

Figure 3b.

There is clearly a sensitization of the emission from $^5D_3$ which is conspicuous by its absence in the Tb^{3+} phosphors except for a weak line at 415 nm. The fact that this emission is now obtainable in the same lattice argues against the earlier absence being due to cross-relaxation on account of either higher activator concentration or radiationless loss at donor acceptor pairs. Obviously X-ray excitation is not capable of exciting this emission which is achieved by a transfer of energy from Ce^{3+} directly to the $^5D_3$ levels. Strontium orthophosphate activated by Tb^{3+} along with Sn^{2+} as sensitizer shows $^5D_3$ lines which are absent when activator alone is present [18]. As for the $^5D_4$ lines, the intensity of the 620 nm emission is slightly less and the other three lines where there is overlap between cerium and terbium emission, the intensity is not far greater than the sum of individual intensities and at times a little less. For the series with optimum Tb^{3+} the $^5D_4$ lines have less intensity than the sum of individual intensities. Sensitization is evident however because of good emission obtained in the $^5D_3$ lines practically absent when Tb^{3+} alone is present.

Where the transitions in both the sensitizer and the activator are 'allowed', i.e. the interaction is of the dipole-dipole type, the transfer of energy may take place by the emission and re-absorption of a photon or by a radiationless resonance process. The former will in general depend on the size and shape of the specimen. If the overlap between emission of sensitizer and absorption spectrum of the activator is not perfect, not only the magnitude but the shape of the former will also be altered as activator concentration is changed. In the present case no dips corresponding to

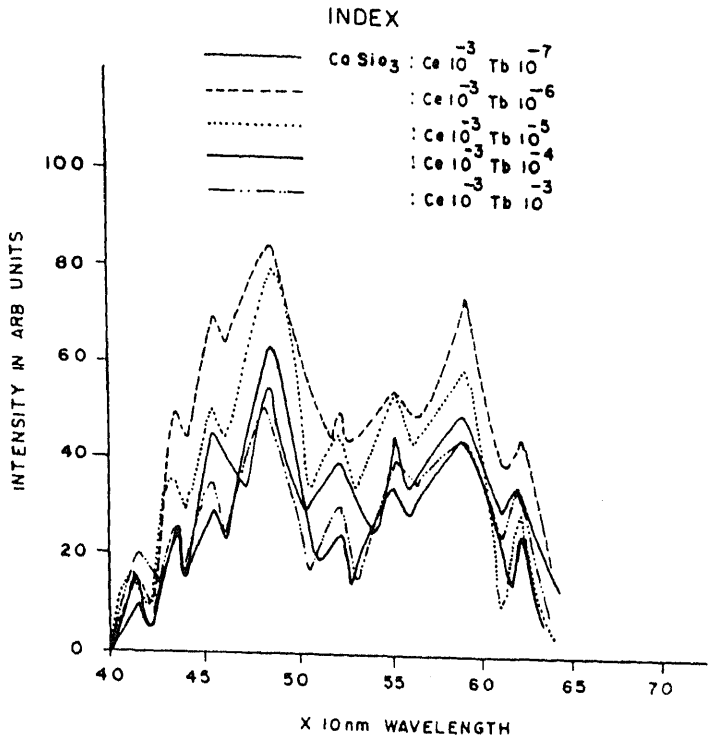

Figure 3c.

Tb^{3+} absorption appear in the Ce^{3+} emission and hence a radiative transfer of energy may be ruled out.

Exchange interaction require a large direct or indirect overlapping between donor and acceptor orbitals leading to easy electronic exchange. Because Ce^{3+} and Tb^{3+} are both reducing ions, an exchange would require too high energies. Also, exchange transfer mechanism is operative over very short distances only, while multipolar interactions can be active over a distance of 10 Å and more [3]. The concentration of active ions used in the present study are low and hence sensitizer-activator distances would be large. It is also known that at low sensitizer concentrations the dipole-dipole transfer predominates. Since both terbium and cerium gives efficient fluorescence when present alone, we are dealing with effectively allowed transitions and the interaction could be of the dipole-dipole type [2, 3].

In the two series with optimum cerium and below optimum cerium, when 10^{-6} mole % of Tb^{3+} is added there is maximum sensitization. The sample with less cerium gives better emission as is to be expected.

In the two series with below optimum values of Tb and Ce, there is a line at 520 nm which is not obtained in any of the other three series containing Tb. This line has been reported among the lines obtained in the terbium spectra [19, 20], although no transition

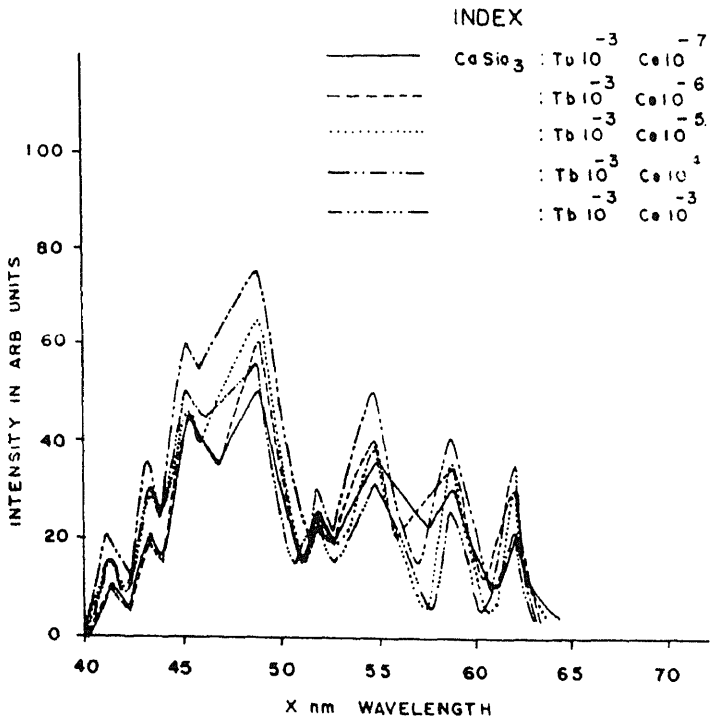

Figure 3d.

Figure 3. Emission spectra of Ce^{3+}; Tb^{3+} series.

4. Conclusions

(1) Addition of cerium to terbium activated phosphors resulted in sensitization of the latter reflected in the appearance of additional peaks at 435 and 455 nm due to transition from $^5D_3$. The results indicate that the transfer of energy from cerium takes place predominently to $^5D_3$ of Tb^{3+}. (2) Quenching effects are already strong at 'optimum' concentrations of activator and sensitization effects are better observed when activator concentration is less than optimum. (3) The absence of $^5D_3$ lines in terbium samples and their appearance on addition of cerium indicates that the quenching of $^5D_3$ emission is not due to high activator concentration but rather due to the mode of excitation. Addition of Ce^{3+} is able to populate this excited state directly. (4) The energy transfer from Ce^{3+} to Tb^{3+} may be due to a dipole-dipole interaction.

References

[1] P Jr Victor Kelsey and J J Jr Brown, *J. Electrochem. Soc.* **123**, 184–85 (1976)
[2] A M Srivastav, *J. Electrochem. Soc.* **137**, 2959 (1990)
[3] R Reisfeld and J Hormadaly, *J. Solid State Chem.* **13**, 283 (1975)
[4] J Holsa, M Leskela and L Miinisto, *J. Solid State Chem.* **37**, 267 (1981)

[5] J G Rabatin, *U.S. Pat.* **3**, 617, 743 (1971)
[6] K Nomota and R Kubo, *Jpn. Kokai* **76**, 378 (1976)
[7] D L Dexter, *J. Chem. Phys.* **21**, 826 (1953)
[8] S Asano, N Yamashita and T Ohnishi, *Phys. Status Solidi* **B99**, 661 (1980)
[9] T Hoshina, *J. Phys. Soc. Jpn.* **48**, 1261 (1980)
[10] Ravindra Pandey and S Sivaraman, *J. Phys. Chem. Solids* **52**, 211–225 (1991)
[11] W Lehmann, *J. Luminescence* **5**, 87 (1972)
[12] A Bril, W L Wanmaker and J W Ter Vrugt, *J. Electrochem. Soc.* **115**, 776 (1968)
[13] R N Tripathi and S Sivaraman, *Phys. Status Solidi* **A55**, K123 (1979)
[14] A D Pearson, G F Peterson and W R Northover, *J. Appl. Phys.* **37**, 729 (1966)
[15] L G van Uitert and L F Johnson, *J. Chem. Phys.* **44**, 3514 (1966)
[16] G Blasse and A Bril, *Philips Res. Rep.* **22**, 481–504 (1967)
[17] C K Jorgensen and B R Judd, *Mol. Phys.* **8**, 281 (1964)
[18] H Mizuno and M Masuda, *Proc. Int. Conf. Luminescence*, Budapest (1966) p. 1703
[19] G E Rindone, *Luminescence in inorganic solids* edited by P Goldberg (Academic Press, New York, London, 1968) 419–461
[20] B V Shulgin, A A Kulesskii, A M Korovkin, V L Petrov and S V Podurovskii, *Opt. Spectrosc. (USSR)* **68**, 491–492 (1990)

Electron paramagnetic resonance studies in photorefractive crystals I: Hyperfine interaction and photoinduced charge transfer in $^{233}U^{5+}$ and $^{238}U^{5+}$ doped $LiNbO_3$

N K PORWAL, MITHLESH KUMAR and M D SASTRY
Radiochemistry Division, Bhabha Atomic Research Centre, Mumbai 400 085, India

MS received 7 June 1996

Abstract. Electron paramagnetic resonance studies were conducted on the photoinduced charge transfer and also hyperfine interaction of U^{5+} stabilized in photorefractive matrix $LiNbO_3$. This work deals with: (i) first observation of hyperfine structure due to ^{233}U ($I = 5/2$) in its pentavalent state at octahedral sites and comparison with other possible site symmetries, (ii) photoinduced charge transfer as observable by EPR and its relevance to photorefractive behaviour of $LiNbO_3$. The effect of chemical bonding on the hyperfine interaction of $5f^1$ configuration was also studied by converting the existing literature data on $^{235}U^{5+}$ to that of $^{233}U^{5+}$ by standard methods. This suggests that progressive substitution of oxygen by F^-, in the series UO_6^{7-}, $(UO_5F)^{6-}$ and $(UO_4F_2)^{5-}$ drastically decreases the hyperfine coupling constant $A_{\|}$, along the local distortion axis. This trend is explained as being due to the absence of ligand ion along the distortion axis at U^{5+} site in trigonal $LiNbO_3$. The effects of illumination by copper vapor laser (CVL) on the intensity of the U^{5+} signal was studied in the 10–300 K region. The kinetics of decay and restoration of U^{5+} was also studied between 10–100 K range. The decay kinetics was found to obey double exponential. The reduction of concentration of U^{5+} with CVL-illumination and its restoration in the absence of light show that pentavalent uranium takes part in the photorefractive effects in $LiNbO_3$.

Keywords. Electron paramagnetic resonance; photorefraction; $LiNbO_3$; uranium; hyperfine interaction.

PACS No. 76·30

1. Introduction

Lithium niobate is ferroelectric at room temperature [1] and it has exhibited many interesting properties. Notable among them is the first observation of photorefractive effect and the associated possibility of storing information in terms of holograms [2–4]. Mechanism of this process has been identified as due to the photoinduced charge transfer involving Fe^{3+} impurity. In the early years of the discovery of photorefractive effects in $LiNbO_3$, the effect of impurities, particularly those of 3d-group, on photorefractive properties has been investigated [3]. The possibility of stabilizing Fe and Mn in different valence states facilitating the photoinduced charge transfer appears to be important for photorefraction. As multivalence is important, the trivalent lanthanides may not be good candidates for this process. On the other hand, uranium

exhibiting multivalence is potentially a good candidate to enhance photorefractive behaviour of $LiNbO_3$. Work of Okamoto *et al* [5] suggests that the uranium dopant enhances photorefractive sensitivity in U:$LiNbO_3$, however, the hologram is nearly permanent. It may be noted that in the sample of Okamoto *et al*, uranium may be in tetravalent/hexavalent states.

Burton Lewis *et al* [6] have shown that U^{5+} gets stabilized at Nb^{5+} sites in $LiNbO_3$, with six-fold oxygen coordination, on doping with U_3O_8. They have shown that the symmetry of site is almost perfectly octahedral. Among all the oxidation states of uranium the pentavalent ion, U^{5+}, with outer electronic configuration, $5f^1$, is an interesting candidate for electron paramagnetic resonance (EPR) investigations. In the case of U^{5+} ion in perfectly octahedral coordination, the 7-fold degenerate $5f$-orbitals split into $a_{2u}(\Gamma_2)$, $t_{2u}(\Gamma_4)$ and $t_{1u}(\Gamma_5)$ (Γ's are Bethe's notation) with the orbital singlets a_{2u} as the ground state [7,8]. The quenching of orbital angular momentum increases the spin-lattice relaxation time making its EPR observable at easily accessible temperatures. When spin orbit interaction is taken into account the symmetry classification of these levels would change, the lowest state being Γ_7. In the present work we have carried out a similar investigation with $^{238}U^{5+}/^{233}U^{5+}$ doped $LiNbO_3$ directed at getting information on the hyperfine interaction between $I = 5/2$ of ^{233}U and $5f^1$ electron having a_{2u} character under octahedral symmetry and also to investigate the possible role of uranium ion in photoinduced charge transfer processes. The only published report on the hyperfine structure of ^{233}U in EPR is of trivalent uranium in $LaCl_3$ by Dorain *et al* [9]. In this paper we present the results of three important aspects of U^{5+} in $LiNbO_3$: (i) The first report of hyperfine structure of ^{233}U in its pentavalent form and in octahedral symmetry. (ii) The systematics of the hyperfine coupling constant of $^{233}U^{5+}$ in $(UO_6)^{7-}$ with progressive substitution of O^{2-} by the more ionic ligand F^-. This was made possible by using the h.f.s. data available on $^{235}U^{5+}$ in $(UO_5F)^{6-}$ and $(UO_4F_2)^{5-}$ sites stabilized in alkali fluorides [7, 10, 11]. (iii) The first report of the valence change of pentavalent uranium on illumination with copper vapor laser between 10–100 K.

2. Experimental

The sample of $^{233}U^{5+}$: $LiNbO_3$ was prepared by the flux method described by Lewis *et al* [6]. Appropriate quantities of Li_2CO_3, Nb_2O_5 and U_3O_8 (8% by weight) were mixed and the mixture was slowly added to the molten LiCl. After cooling the melt, the LiCl was easily leached out by dissolving in pure water leaving behind insoluble uranium doped in $LiNbO_3$. Further, the residue was washed with alcohol and dried under I.R. lamp. The XRD patterns of the sample showed that the $LiNbO_3$ formation was complete. Finally, the sample was sealed in quartz tubes for recording EPR spectra. This work was done in glove-box specially made for handling radioactive materials. The outer surface of the quartz tube was decontaminated by nitric acid, teepol and water before recording the spectra, which were measured at 77 K using a Bruker ESP-300 EPR spectrometer operating at the X-band frequency.

The effect of laser illumination on the EPR spectrum was studied using an optical transmission cavity. The sample $LiNbO_3$ in single crystal form doped with ^{238}U was

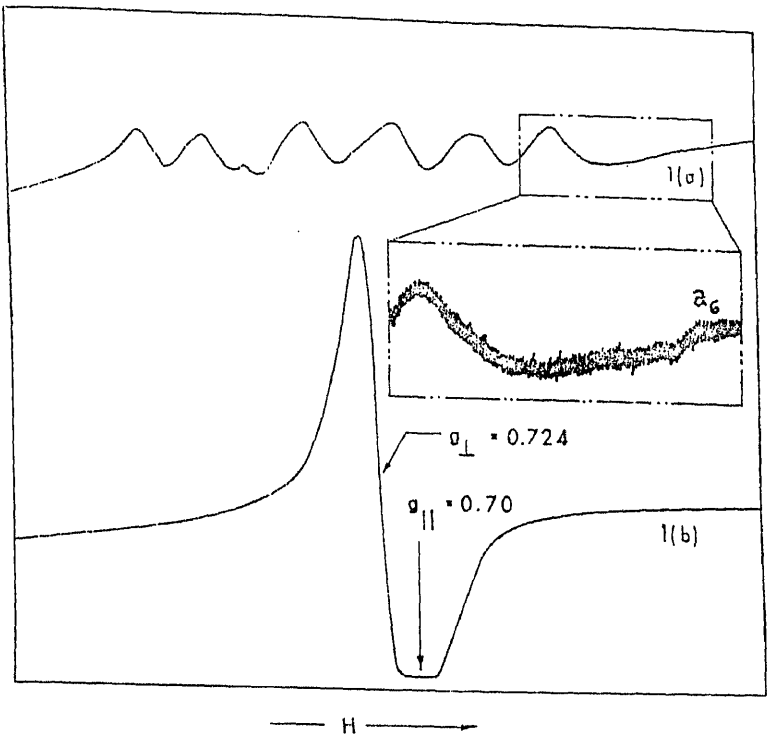

Figure 1. EPR spectrum of U^{5+} in $LiNbO_3$ powder at 77 K: (**a**) doped with $^{233}U_3O_8$; (**b**) doped with natural U_3O_8. As expected the perpendicular spectrum is more intense than the parallel one. The $g_{||}$ value was calculated from $^{238}U^{5+}$ spectrum. The separation between field corresponding to $g_{||}$, and high field hyperfine components of the parallel spectrum (a_6 in the inset) were used for calculating $A_{||}$.

illuminated *in situ* using a 10 W copper vapor laser. The temperature of the sample was varied between 10 and 300 K using a closed cycle helium refrigerator supplied by M/S APD Cryogenics.

3. Experimental results

3.1 *EPR spectra of* $^{233}U^{5+}$

The EPR spectra obtained on $^{233}U^{5+}$ doped $LiNbO_3$ at 77 K is shown in figure 1(a). The EPR spectra obtained under identical condition for natural U^{5+} in $LiNbO_3$ are also shown in figure 1(b) for comparison. The spectrum of $^{233}U^{5+}$ consists predominantly of a sextet arising from hyperfine interaction with $I = 5/2$ of ^{233}U. In view of the powder nature of the sample it is attributed to the perpendicular components. From the natural uranium (V) spectrum it can be unambiguously seen that there is a slight g-anisotropy with $g_{||} = 0{\cdot}70$ and $g_\perp = 0{\cdot}724$. These values are slightly different from the isotropic g reported by Lewis *et al* [6]. The g anisotropy as defined by Ursu and Lupei [7] is

Table 1. g-values of U^{5+} centre in $LiNbO_3$ and other reported U^{5+} complexes with oxygen coordination.

Nature of the complex	$g_{\parallel}$	$g_{\perp}$	Reference
$^{233}UO_6 : LiNbO_3$	$0{\cdot}710 \pm 0{\cdot}001$	$0{\cdot}724 \pm 0{\cdot}001$	Present work
$UO_5V_F : LiF$ (Tg3)	0·13	0·595	10
$UO_6 : LiF$ (Tg4)	0·326	0·362	10

Table 2. Systematization of ^{233}U hyperfine coupling constant in $[UO_6]^{7-}$ with progressive fluoride substitution. The ^{233}U data on UO_5F and UO_4F_2 were calculated from the ^{235}U-h.f.s. data available.

Complex	$A_{\parallel}$ (in 10^{-4} cm^{-1})	$A_{\perp}$ (in 10^{-4} cm^{-1})	A_{iso} (in 10^{-4} cm^{-1})
$UO_6 : LiNbO_3$	145 ± 10	128 ± 2	134
$UO_5F : NaF$	119·6	146·9	137·8
trans $UO_4F_2 : NaF$	88·4	150·8	130·0
trans $UO_4F_2 : KF$	93·6	153·5	133·5

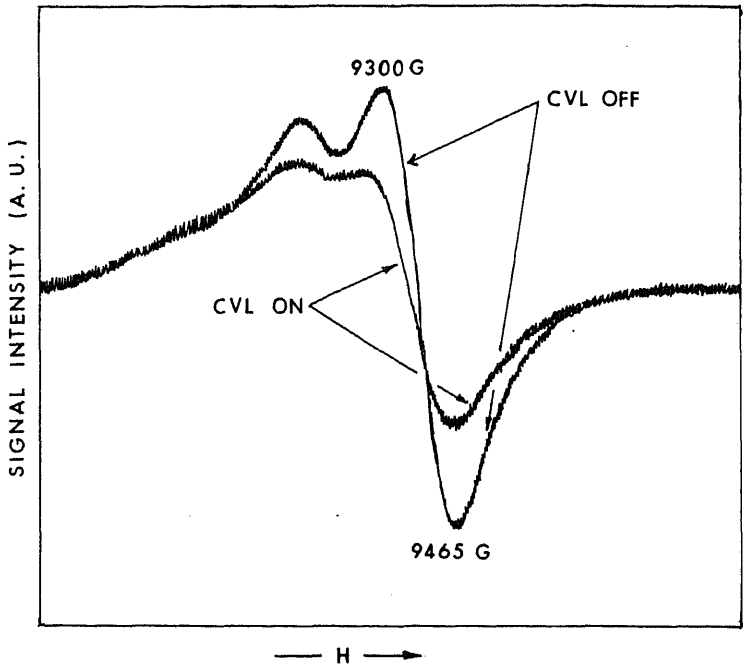

Figure 2. The effects of laser illumination on the EPR spectrum of U^{5+} in $LiNbO_3$ at 10 K. (**a**) Without laser, (**b**) with CVL illumination.

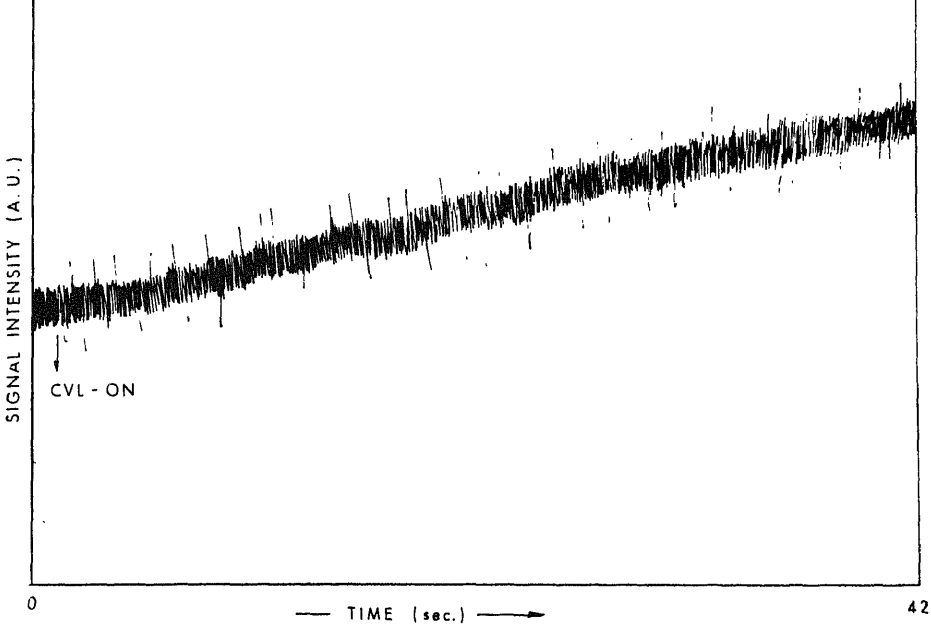

Figure 3a. The decay of EPR of U^{5+} signal on laser illumination. The apparent rise in the signal is due to locking of the field on the lower inflection point of the derivative signal.

which is considerably less than the corresponding values for U^{5+}in other octahedral oxy-fluoro coordinations. This point is of relevance in analyzing the hyperfine spectrum of $^{233}U^{5+}:LiNbO_3$ powder, in which the perpendicular component is most intense. In the EPR spectra of $^{235}U^{5+}$ in oxyfluoro coordinations in NaF and LiF, the quadrupole interaction has been reported [7] to be of the order of or stronger than the electron-nuclear (magnetic) interaction. The interaction term contains the product of z-component of electric field gradient (e.f.g.) produced by fluoride substitution in the first coordination and the quadrupole moment of ^{233}U nucleus. This gave rise to unusual hyperfine structure in the 'perpendicular' spectrum of $^{235}U^{5+}:LiF$ and it has been analyzed by a new perturbation scheme developed by Lupei *et al* [12]. This predicted a number of intense forbidden transitions ($\Delta m_I > 1$) and more interestingly, that the splitting of $m_I = +5/2$ and $+7/2$ ($I(^{235}U) = 7/2$) transitions should vanish at $\theta = 90°$ resulting in an intense line at the centre (i.e. the field position corresponding to A.I.S = 0). It can be seen in figure 1(a) that these features are completely absent for $^{233}U^{5+}:LiNbO_3$ ($\theta = 90°$) suggesting that quadrupole terms can be neglected, despite small anisotropy seen in the g-tensor. Therefore the hyperfine sextet was analyzed by standard methods and the spin Hamiltonian constants along with reported ones for other U^{5+} ions in oxy-fluoro coordinations are given in tables 1 and 2. As mentioned earlier this is the first report of hyperfine coupling constants for ^{233}U in pentavalent form. The only other report of

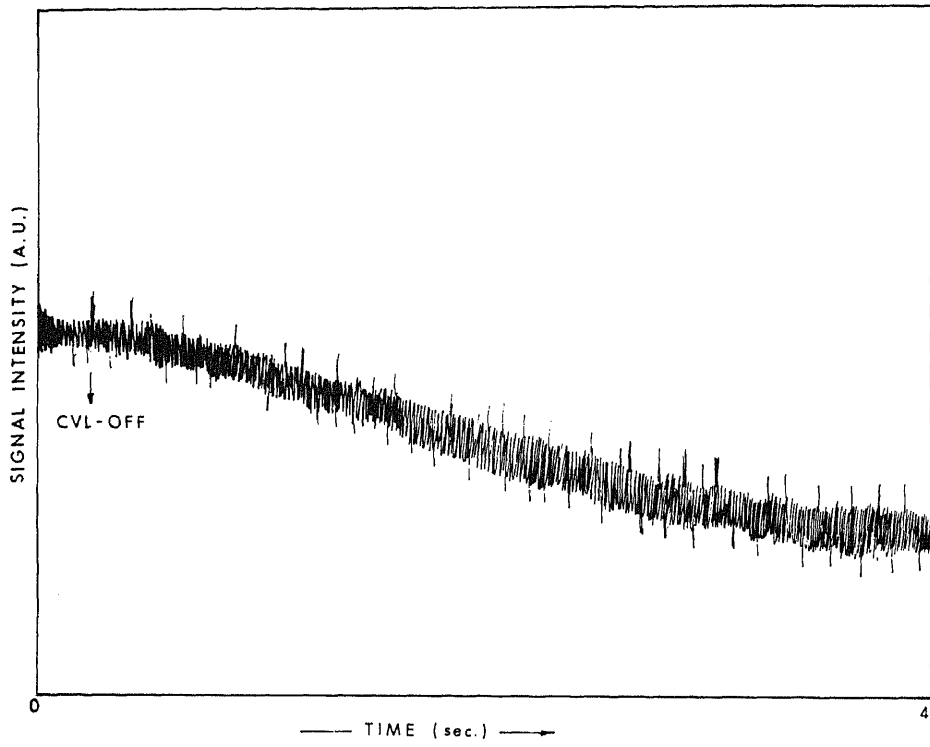

Figure 3b. The recovery of EPR signal of U^{5+} on switching off the laser.

similar data for ^{233}U was in trivalent form reported by Dorain *et al* [9] for $^{233}U^{3+}$ in $LaCl_3$.

3.2 *Effects of illumination with copper vapour laser*

As mentioned earlier $LiNbO_3$ single crystals doped with ^{238}U were used for these studies. U^{5+} was stabilized by gamma irradiation. The single crystal loaded in an optical transmission cavity (Bruker ER4104 OR) was illuminated using light from CVL (510 and 578 nm). Figure 2 shows the effect of laser illumination on the intensity of U^{5+} signal at 10 K. By locking the magnetic field on the EPR derivative peak (on the lower inflection point) the decay of the signal with laser illumination and recovery after CVL was put off and were recorded as a function of time. Figures 3(a) and (b) show the decay and recovery of the signal. (The apparent increase and decrease occurred respectively, for decay and growth as the field was locked on the lower inflection point of EPR signal.)

4. Discussion

4.1 *Structure of pentavalent U-complex*

EPR of U^{5+} was reviewed by Ursu and Lupei [7] and also more recently by Miyake [13]. Miyake discussed the dependence of g-value as a function of axial and orthorhombic

and orthorhombic distortions. By analysis it may be concluded that for a perfect octahedral symmetry the g-value of U^{5+} is expected to be around 1·1 and under C_{2v} distortion the $|g|$ value decreases from this value. Further it was seen that the position of ground Γ_7 and excited Γ_7' states were found to be independent of ϵ (axial distortion parameter) for small distortion and hence g-value is not expected to be highly anisotropic despite the lower site symmetry. From the g-value in the present case which is nearly isotropic, the axial distortion ϵ is estimated to be (from figure 6 of Miyake) $1100\,cm^{-1}$ and orthorhombic distortion $|\epsilon\tau| = 270\,cm^{-1}$. U^{5+} ion in $LiNbO_3$ takes the position of Nb^{5+} site, having three long (2·113 A) and three short (1·889 A) Nb–O bonds in $LiNbO_3$ [3]. Therefore the g-value obtained is consistent with that expected at this site symmetry. The deviation from the expected g-value of $|J = 5/2, \Gamma_7\rangle$ state is also attributed for the crystal field admixing of upper $|J = 7/2, \Gamma_7\rangle$ state [8]. The expected g-value is

$$g = (-10/7)\cos^2\alpha + (16/7\sqrt{3})\cos\alpha\sin\alpha + (24/7)\sin^2\alpha,$$

where $\cos\alpha$ and $\sin\alpha$ give the admixture of $|J = 5/2, \Gamma_7\rangle$ and $|J = 7/2, \Gamma_7\rangle$ states in the ground doublet. Using the g_{iso} value $\{g_{iso} = (g_\parallel + 2g_\perp)/3\}$, the ground state doublet is found to have the form

$$|\pm\rangle = 0{\cdot}905|J = 5/2, \Gamma_7\rangle + 0{\cdot}308|J = 7/2, \Gamma_7\rangle.$$

The hyperfine constant for $^{233}U^{5+}$ ($5f^1$) depends upon the nature of ground state and it is given in terms of cos α and sin α by the expression [8]

$$\begin{aligned} A = 2g_n\beta\beta_n < r^{-3} > [&(-16/7)\cos^2\alpha - (8/7\sqrt{3})\cos\alpha\sin\alpha \\ &+ (16/7)\sin^2\alpha - k\{(5/21)\cos^2\alpha + (16/7\sqrt{3})\cos\alpha\sin\alpha \\ &+ (3/7)\sin^2\alpha\}], \end{aligned}$$

where k is the constant related contribution from core polarization, $< r^{-3} >$ is the expectation value for the radial distribution of the $5f$ electron and other symbols have their usual meaning. By taking A_{iso} as $134 \times 10^{-4}\,cm^{-1}$, $< r^{-3} >= 5{\cdot}6$ a.u. and the values of $\cos^2\alpha$ and $\sin^2\alpha$, the hyperfine coupling constant takes the expression

$$A_{iso} = -2g_n\beta\beta_n < r^{-3} > \{2{\cdot}045 + k\ 0{\cdot}643\},$$

the value of k for $^{233}U^5$ being $-3{\cdot}18$.

4.2 *Comparison with perturbed $(UO_6)^{7-}$ centres*

Extensive EPR work has been reported on $^{238}U^{5+}$ and $^{235}U^{5+}$ in $(U(O_{6-x}F_x)_{x=1,2})^{7-}$ and $UO_5{\cdot}V_F$ centres stabilized in LiF and NaF matrices [10, 12]. Among these, two centres with no fluorides in the immediate coordination were reported by Lupei and Lupei [10] on the basis of the absence of ^{19}F-s.h.f.s. These were designated as Tg3 and Tg4. The Tg3 centre was assumed to correspond to an U^{5+}–O_5 associated with an F-vacancy taking the place of Li–F_6 octahedron. Therefore Tg3 takes the form of $(U^{5+}O_5V_F)$. This centre was reported to have the following g-values: $g_\parallel = 0{\cdot}13$ and $g_\perp = 0{\cdot}595$. The Tg4 centre was assumed to correspond to $(UO_6)^{7-}$ octahedron at a $(LiF_6)^{5-}$ site slightly perturbed by a

cation impurity such as Cu, Ag or Au. This centre was reported to have the g-values: $g_{\parallel} = 0{\cdot}326$ and $g_{\perp} = 0{\cdot}362$. The Tg4 centre is closest to the U^{5+} centre in $LiNbO_3$ and next comes the Tg3 centre. In view of the apparent high symmetry of $(UO_6)^{7-}$ in $LiNbO_3$, as well as in cubic LiF, it is rather intriguing that the g-values of Tg4 are widely different from those in $LiNbO_3$. This is probably due to lower symmetry components of the crystalline field arising from associated lattice defects in alkali fluoride lattices.

4.3 *Systematics of* $(^{233}UO_{6-x}F_x)$ *hyperfine coupling constants with* F^-*-substitutions*

To understand the systematics of the effect of F-substitution in $(^{233}UO_6)^{7-}$, on the hyperfine coupling constant, the hyperfine data for $^{235}U^{5+}$ in oxyfluoro coordinations is used. The ratio of magnetic moments of two isotopic species of the same paramagnetic ion will be the ratio of the respective products AI [13]. Therefore $(AI)^{233}/(AI)^{235} = 0{\cdot}65/-0{\cdot}361$ [14]. This gives the value of $|(A)^{233}| = 2{\cdot}6\ (A)^{235}$. Using this, the values of A^{233} were calculated for $(UO_4F_2)^{5-}$ and $(UO_5F)^{6-}$ complexes from the data published by Lupei *et al* [12]. These values are summarized in table 2. It can be seen that the value of $A_{\parallel}$ decreased drastically with fluoride ion substitution, with an associated increase in the value of $A_{\perp}$. The value of A_{iso} was found to be essentially unaltered.

The systematic decrease of $A_{\parallel}$, with fluoride substitution looks rather surprising in the first instance as substitution with a more ionic ligand is expected to increase the hyperfine coupling constant. It can be understood by considering the site symmetry of the U^{5+} complex, the shape of $5f$ orbitals and their relative energies at the respective sites. In perfectly octahedral symmetry the ground a_{2u} orbital is directed away from the ligands and therefore no direct overlap is expected. However, lowering of symmetry together with spin-orbit interaction brings in Γ_7 character to the upper sigma antibonding t_{1u} orbital set. As the ground state a_{1u} orbital transforms as Γ_7, the lowering of symmetry admixes the antibonding t_{1u} into the ground state. This enhances the electron density in the direction of distortion (z-axis). The $[UO_4F_2]^{5-}$ and $[UO_5F]^{6-}$ complexes in alkali fluorides have D_{4h} and C_{4v} symmetries respectively, whereas the symmetry axis of U^{5+} site in $LiNbO_3$ is a three-fold axis coincident with the centre of an octahedral face. Therefore for the oxyfluoro complexes in alkali halide matrices, there is an increased covalency in the axial direction thereby decreasing the A value. For U^{5+} in $LiNbO_3$ there is no bond in the direction of z-axis and hence a larger value is found for the magnitude of the parallel component of the hyperfine coupling constant.

4.4 *Effects of laser illumination*

Okamoto *et al* [5] investigated the effect of uranium dopant on the photorefractive sensitivity for $LiNbO_3$. They have reported that the hologram is stable for an unusually long time. The main aspect where our work differs from that of Okamoto *et al* is that we have stabilized U^{5+} in $LiNbO_3$, and that we have focussed our attention only on the role of U^{5+} in photoinduced charge transfer thereby formation of phase grating. The results shown in figure 2 give evidence for photoinduced reduction in U^{5+} concentration. The uranium dopant exists in tetravalent and/or probably hexavalent form in $LiNbO_3$ crystal. It may be noted that U^{4+} in octahedral symmetry does not give EPR signal. The decay of

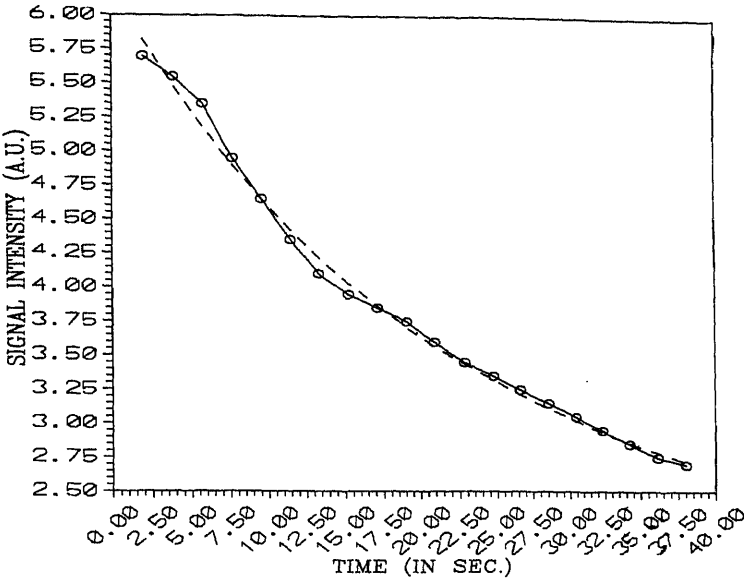

Figure 4. The fitting of the decay of EPR signal of U^{5+} to a double exponential ($\tau_1 = 16$ s, $\tau_2 = 146$ s at 10 K). The dashed curve is the theoretical fit.

the signal was fit to both single and double exponential forms. The double exponential decay gave a very satisfactory fit. A typical calculated decay curve along with experimental points is shown in figure 4. The two decay constants τ_1 and τ_2 corresponding to various temperatures are given in table 3. It may be seen that the decay consists of one faster component which is temperature independent and another one which is slower but temperature dependent. The logarithmic temperature dependent decay constant vs. $1/T$ yielded a straight line with slope of 2·9. Fitting with two exponentials suggests the possibility of two types of trapping centres/mechanisms due to the photoinduced charge transfer process. Temperature independent process might imply a direct electron transfer photoexcitation between two trapping centres without involving mobility of charge carriers through conduction band. The temperature dependent process on the other hand would involve temperature dependence of mobility, dielectric relaxation time, number of charge carriers, etc. [13]. The temperature dependence of τ_2 can fit to an Arrhenius kind of equation with associated activation energy $0{\cdot}25 \times 10^{-3}$ eV. This shows the trap is extremely shallow and that probably was the reason for observing these effects in 10–80 K region. The band gap of $LiNbO_3$ is 3·8 eV. Therefore excitation with CVL is not expected to give inter-band transition. The reduction in U^{5+} signal, on CVL illumination and its restoration suggest that the photoinduced processes may be electron transfer between defect centers. If it is between U^{5+} and U^{4+} it can be of the form

$$U^{5+} + h\nu \rightarrow U^{6+} + e^-$$

$$U^{4+} + e^- \rightarrow U^{3+}$$

$$\text{i.e. } (U^{5+} + U^{4+}) \xrightarrow{h\nu} (U^{6+} + U^{3+}).$$

Temperature (K)	τ_1(s)	τ_2(s)
10	16	146
40	16	178
80	16	183
100	16	210

The reverse electron transfer would restore the U^{5+} signal on putting off the laser illumination. This transition between two different valence states of uranium, may be identified with the temperature independent process with time constant of ~ 16 s. The intrinsic instability of the lower valence states of uranium at Nb^{5+} site could be responsible for this.

Another possible pathway may be

$$O^{2-} - h\nu \rightarrow O^- + e^-$$
$$U^{5+} + e^- \rightarrow U^{4+}.$$

In this process the recovery of the signal may be very slow as U^{4+} is stable in this lattice. Further O^- should be detectable by EPR. As O^- was not detected, this pathway is considered less probable.

5. Conclusion

The hyperfine interaction data of $^{233}U(V)$ in octahedral (UO_6):$LiNbO_3$ is presented. The systematics of variation of hyperfine coupling with F^--substitution can be explained using a simple crystal field approach. It is observed that uranium in pentavalent state takes part in photoinduced valence change which is the basic mechanism for photorefraction.

Acknowledgement

The authors are thankful to Dr J C Vyas for his help during the growth of $LiNbO_3$ single crystal.

References

[1] R Orlowski and E Kratzig, *Ferroelectrics* **26**, 831 (1980)
[2] A Ashkin, G D Boyd, J M Dziedzic, R G Smith, A A Ballmann and K Nassau, *Appl. Phys. Lett.* **9**, 72 (1966)
[3] F S Chen, J T LaMacchia and D B Fraser, *Appl. Phys. Lett.* **13**, 323 (1968)
[4] P Günter and J P Huignard (eds), *Topics in applied physics: Photorefractive materials and their applications I* (Berlin, Heidelberg, 1988) vol. 61
[5] E Okamoto, H Ilkeo and K Muto, *Appl. Opt.* **14**, 2543 (1975)
[6] W Burton Lewis, H G Hecht and M P Eastman, *Inorg. Chem.*, **12** 1634 (1973)

[7] I Ursu and V Lupei, *Bull. Magn. Reson.* **6**, 162 (1984)
[8] A Abragam and B Bleaney, *Electron Paramagnetic Resonance of Transition Ions* (Clarendon Press, Oxford, 1970)
[9] Paul B Dorain, Clyde A Hutchinson Jr and Eugene Wong, *Phys. Rev.* **105**, 1307 (1957)
[10] V Lupei and A Lupei, *Phys. Status Solidi* **B94**, 301 (1979)
[11] A Lupei, V Lupei and I Ursu, *J. Phys.* **C15**, 5489 (1976)
[12] V Lupei, A Lupei, S Georgescu and I Ursu, *J. Phys.* **C9**, 2619 (1976)
[13] C Miyake, in *Handbook of physics and chemistry of the actinides* edited by A J Freeman and C Keller (Elsevier Science Publishers, Amsterdam, 1991) ch. 6
[14] EPR/ENDOR Frequency Table, Bruker Almnac (1001) p. 98

PRAMANA
—journal of
physics

© Printed in India

Vol. 47, No. 6,
December 1996
pp. 493–504

Determination of thermal effusivity of solids by a photoacoustic scanning technique

J PHILIP and A A SUDHAKARAN
Department of Instrumentation, Cochin University of Science and Technology, Cochin 682 022, India

MS received 22 May 1996; revised 19 August 1996

Abstract. A new method is proposed to determine the thermal effusivity of solid samples using a one dimensional photoacoustic scanning technique. The method employs a sample configuration in which the backing for a good light absorber layer is changed from a reference sample to the unknown sample by scanning the absorber surface with an incident modulated light beam. From the measured phase difference or amplitude ratio one can determine the thermal effusivity of the unknown sample, knowing the effusivity of the reference sample. The Rosencwaig–Gersho theory of photoacoustic effect has been extended to the present experimental situation and expressions have been derived for photoacousitc phase difference and amplitude ratio as the backing is changed. Values calculated using these expressions are found to agree well with measured values for different sample combinations except in amplitude ratio values when the thermal effusivities of the samples differ very widely. The reason for this disagreement is discussed.

Keywords. Photoacoustic effect; thermal effusivity; scanning technique.

PACS Nos 44·50; 43·85; 66·90

1. Introduction

The photoacoustic (PA) technique has emerged as a very powerful technique to study optical and thermal properties of solid samples [1]. It is now the best alternative analytical technique for samples in which conventional absorption spectroscopic techniques often fail. The technique has proved its power over a very wide variety of samples ranging from human blood to superlattices. A number of review articles have appeared in literature on this subject [1–3]. Since the amplitude and phase of the PA signal ultimately depend upon material parameters such as optical absorption coefficient, thermal conductivity, heat capacity and density, it has proved its ability to detect and measure thermodynamic changes such as phase transitions in solids [4]. In photoacoustic effect, since optically generated thermal waves propagate through the sample causing pressure variations in the surrounding gas medium, it finds application in thermal wave depth profiling, microscopy and nondestructive testing of materials [5–7].

A number of papers have appeared in literature on the determination of thermal parameters such as thermal diffusivity (α) and effusivity (e) of solid samples using PA technique. Measurement of thermal diffusivity and effusivity lead to the determination of thermal conductivity (k) and heat capacity (C). The PA technique belongs to the category

of periodic heat flow methods of measuring thermal diffusivity in contrast to the conventional transient heat-flow methods. A number of different methods have been developed to measure the thermal diffusivity of solids by the photoacoustic technique. The most popular among these involves a chopping frequency analysis of the PA amplitude or phase and determination of the critical frequency, f_0, at which the sample goes from a thermally thick to a thermally thin regime [8–10]. Adams and Kirkbright [11] calculated α for different samples coated with a thin layer of absorber by measuring the variation of the phase φ of the PA signal obtained from a rear illumination with frequency. For a thermally thick sample, $l_s a_s \gg 1$, where l_s is the sample thickness and a_s is the thermal diffusion coefficient defined by $a_s = (\omega/2\alpha)^{1/2}$. For a thermally thick sample, the PA phase ceases to vary beyond the critical frequency corresponding to $l_s a_s = 1$ so that $\alpha = f_0 l_s^2$. An equivalent procedure is to measure the variation of the PA amplitude with frequency and obtain the critical frequency at which there is a distinct change in slope. Determination of f_0 is rather straightforward here because, for a thermally thick sample the Rosencwaig–Gersho (R–G) theory [12] predicts an ω^{-1} dependence for the PA amplitude. So, when a sample with a definite thickness changes over from a thermally thin to a thermally thick regime with increase in frequency, the slope of the PA amplitude versus $\omega^{1/2}$ plot changes from -2 to -3 from which the critical frequency can be determined and thermal diffusivity evaluated.

An alternative to the above method is to vary the distance between the point where the heat is generated and the point at which the thermal oscillations are detected. Cesar *et al* [13] have adopted this method by varying the position of a laterally incident laser beam on a transparent sample. A plot of the photoacoustic amplitude and phase against the distance x provides α by a data fit to expression with an exponential and linear dependence on $-a_s x$. A related technique has been adopted to determine the thermal conductivity and specific heat of an opaque sample by measuring the variations in photoacoustic phase with frequency for different sample thicknesses [14]. By adopting the R–G theory to specialized experimental conditions and analyzing the generated PA signal amplitude and phase, different authors have determined thermal diffusivity [15] or thermal conductivity and specific heat simultaneously [16] of a variety of samples.

Another technique to measure the thermal diffusivity of a solid sample involves determination of the amplitude ratio or phase lag of the photoacoustic signal between the front and rear surface illuminations at a single chopping frequency. This method is attractive in the sense that the measurement is independent of the sample thickness and chopping frequency. Measurement of the amplitude ratio was adopted by Yasa and Amer [17], but phase lag measurements are found to give better results. For phase lag measurement, Pessoa *et al* [18] have used two beams of light derived from the same source to illuminate the front and rear surfaces of the sample simultaneously, whereas Thomas *et al* [19] have adopted the technique of illuminating the front surface and then rotating the PA cell by 180° to illuminate the rear surface of the sample with the same light beam.

All the techniques described above suffer from the limitation that the measurement accuracy is dependent on photoacoustic cell calibration. Measurements involving variations in sample thickness or chopping frequency can cause errors in measurement. Measurement of amplitude ratio or phase lag between front and rear surfaces also depend

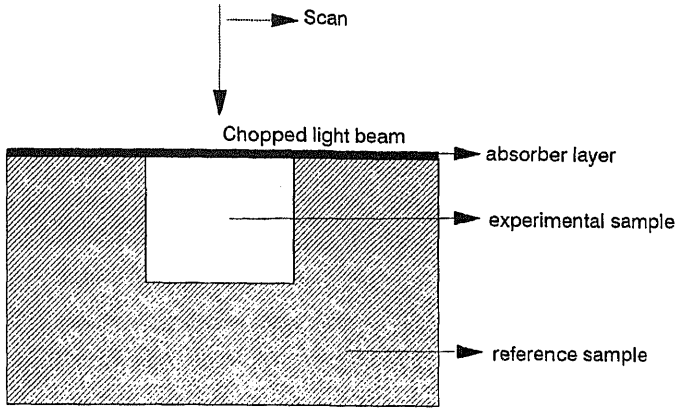

Figure 1. Sample configuration used in the experiment.

on the experimental conditions. Moreover, these measurements are laborious and difficult to automate.

In this paper we describe a convenient technique to measure thermal effusivity of solid samples using a photoacoustic scanning method. Principle of the method, adaptation of the R–G theory to this experimental situation, experimental details, results obtained and discussion of the results analyzing the advantages and limitations of this technique, are given in the following sections.

2. Principle of the technique

Consider the experimental configuration shown in figure 1. The experimental sample, whose thermal parameters are to be determined, is inserted inside a reference sample, whose thermal parameters such as thermal conductivity, k, and heat capacity, C, are known. The experimental sample is tightly inserted into the reference samples in such a way that the top of both the samples are flat and are at the same level. A thin layer of a highly light absorbing material such as carbon black is coated over the top surface. The top surface can be irradiated with a chopped beam of light and the light beam can scan the surface in a step by step fashion. The sample configuration can be kept in a photoacoustic cell and the PA amplitude as well as phase can be measured. In this configuration the absorber layer acts as the thermally thin photoacoustic sample and the thermally thick backing medium is changed from the reference sample to the experimental sample and back to the reference sample as the absorber surface is scanned with the chopped beam of light in a step by step fashion.

If the samples are made in such a way that they have thickness larger than their thermal diffusion lengths at the chopping frequency used, one can apply the one dimensional R–G theory to this configuration and evaluate the ratio of the PA amplitude as the backing is changed from the reference to the experimental sample. An expression for the corresponding difference in PA phase can also be obtained. Once the thermal effusivities of the reference sample and absorber layer are known, we show that the effusivity of the

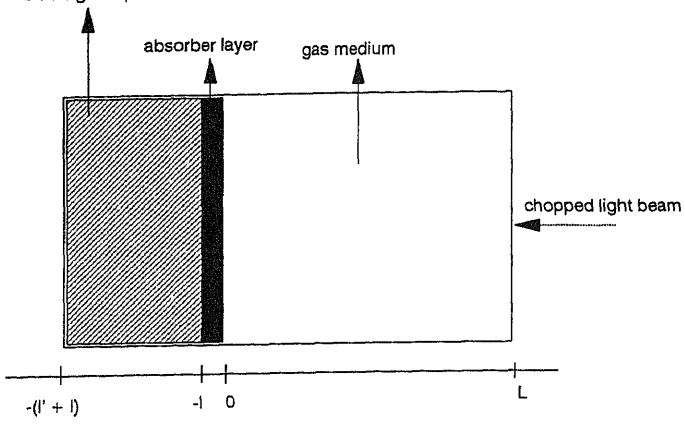

Figure 2. Sample geometry with the absorber layer on a backing sample.

experimental sample can be determined without involving any of the cell parameters and experimental conditions.

In the following section we adapt the one dimensional R–G theory to the sample configuration shown in figure 1.

3. Theoretical background

Consider the sample geometry shown in figure 2 where we have a good light absorber such as carbon black coated over a backing medium enclosed in a cylindrical photoacoustic cell. Let us apply the Rosencwaig–Gersho (R–G) one-dimensional theory for the production of photoacoustic signal to this configuration. The backing material has thermal conductivity k_b, density ρ_b and specific heat C_b and the corresponding parameters for carbon black are k_c, ρ_c and C_c respectively. The parameters for the air medium in front of the absorber layer are k_a, ρ_a and C_a respectively. For the three media, the thermal diffusivity is $\alpha = k/\rho C$, the thermal diffusion coefficient is $a = [\omega/2\alpha]^{1/2}$ and the thermal diffusion length is $\mu = 1/a$, with the corresponding subscripts as before. Here ω is the modulation frequency of the light beam. Assume that a sinusoidally chopped monochromatic beam of light of wavelength λ is incident on the absorber sample so that the modulated intensity of the light can be written as

$$I = (1/2)[I_0(1 + \cos \omega t)], \tag{1}$$

where I_0 is the incident light flux. If β is the optical absorption coefficient of the absorber sample, then the heat produced at any point x due to the absorbed light is given by

$$(1/2)[\beta I_0 e^{\beta x}(1 + \cos \omega t)],$$

where x is negative as per figure 2. Now, one can write the thermal diffusion equation for the absorber sample, backing sample and the air medium in front, and follow the algebra

as been done by Rosencwaig and Gersho [12] and obtain an expression for the plex amplitude of the periodic temperature at the absorber layer–air boundary. This odic temperature variation within the absorber sample produces a corresponding ng of the boundary layer which in turn causes a corresponding expansion and raction of the boundary layer of air, which in turn causes a corresponding periodic sure variation which is detected by a microphone as the photoacoustic signal. One apply the gas laws and show that the complex envelope of the sinusoidal pressure tion is of the form [1]

$$\delta P = A\mathrm{e}^{-i\varphi}, \tag{2}$$

re A and φ are the amplitude and phase of the generated PA signal. This expression be written more explicitly as

$$\delta P = Y\left[\frac{(r-1)(b+1)\mathrm{e}^{\sigma l} - (r+1)(b-1)\mathrm{e}^{-\sigma l} + 2(b-r)\mathrm{e}^{-\beta l}}{(g+1)(b+1)\mathrm{e}^{\sigma l} - (g-1)(b-1)\mathrm{e}^{-\sigma l}}\right], \tag{3}$$

re

$$b = \frac{k_\mathrm{b}a_\mathrm{b}}{k_\mathrm{a}a_\mathrm{a}},$$
$$g = \frac{k_\mathrm{c}a_\mathrm{c}}{k_\mathrm{a}a_\mathrm{a}},$$
$$r = \frac{(1-i)\beta}{2a_\mathrm{a}},$$
$$\sigma = (1+i)a_\mathrm{a} \tag{4}$$

l is the thickness of the absorber sample.

or a good absorber such as carbon black, optical absorption coefficient β is very high. eover, the absorber sample is thermally thin at the chopping frequencies used. er these physically realistic assumptions, the magnitude of the PA amplitude term olifies to

$$A = Y\left[\frac{b^2(g+b)^2}{4a^2[(g^2+b^2)^2 + 4gb[(g+b)^2 - gb]]}\right]^{1/2}, \tag{5}$$

re

$$Y = \frac{\beta I_0 \gamma P_0}{2\sqrt{2}T_0\, k_\mathrm{c} l_\mathrm{a} a_\mathrm{a}}$$

constant. Here P_0, T_0 and γ are the ambient pressure, temperature and ratio of specific s respectively. Substituting for b and g and defining thermal effusivity as $(\rho Ck)^{1/2}$, one finds that the amplitude term can be expressed in terms of thermal sivity. In one dimensional photoacoustic scanning, as one changes the backing from reference sample to the experimental sample, the ratio between the amplitudes, after braic simplifications, works out to be

$$\frac{A_\mathrm{R}}{A_\mathrm{E}} = \left[\frac{e_\mathrm{R}^2(e_\mathrm{c}+e_\mathrm{R})^2[(e_\mathrm{c}^2+e_\mathrm{E}^2)^2 + 4e_\mathrm{c}e_\mathrm{E}(e_\mathrm{c}+e_\mathrm{E})^2 - e_\mathrm{c}e_\mathrm{E}]}{e_\mathrm{E}^2(e_\mathrm{c}+e_\mathrm{E})^2[(e_\mathrm{c}^2+e_\mathrm{R}^2)^2 + 4e_\mathrm{c}e_\mathrm{R}(e_\mathrm{c}+e_\mathrm{R})^2 - e_\mathrm{c}e_\mathrm{R}]}\right]^{1/2}, \tag{6}$$

where e_R, e_E and e_c are the thermal effusivities of the reference sample, experimental sample and the absorber sample respectively. Under the same assumptions, as one changes the backing material from the reference sample to the experimental sample, the difference in PA phase works out to be

$$\varphi_R - \varphi_E = \tan^{-1}\left(1 + \frac{e_R}{e_C}\right) - \tan^{-1}\left(1 + \frac{e_E}{e_c}\right). \tag{7}$$

If R_R and R_E are the thermal wave reflection coefficients at the absorber-backing boundaries defined by

$$R_R = (1 - e_R/e_c)/(1 + e_R/e_c)$$

and

$$R_E = (1 - e_E/e_c)/(1 + e_E/e_c),$$

one can consider three cases depending upon whether both R_R and R_E are negative or both are positive or one of them positive and the other negative. When both R_R and R_E are negative, (6) simplifies to

$$\frac{A_R}{A_E} = \left[\left(\frac{e_R}{e_E}\right)\frac{e_E + 4e_c - (e_c/e_E)/(1/e_E)}{e_R + 4e_c - (e_c/e_R)/(1/e_R)}\right]^{1/2}. \tag{8}$$

When both R_R and R_E are positive, (6) simplifies to

$$\frac{A_R}{A_E} = \left[\left(\frac{e_R}{e_E}\right)\gamma_1\left[\frac{m_2 + e_c(4P_2 - 1)}{m_1 + e_c(4P_1 - 1)}\right]\right]^{1/2}, \tag{9}$$

where

$$m_1 = \frac{(e_c^2 + e_R^2)^2}{e_R},$$

$$m_2 = \frac{(e_c^2 + e_E^2)^2}{e_E},$$

$$P_1 = (e_c + e_R)^2,$$

$$P_2 = (e_c + e_E)^2,$$

and

$$\gamma_1 = (e_c + e_R)^2/(e_c + e_E)^2.$$

Similarly, when R_R is positive and R_E negative, (6) simplifies to

$$\frac{A_R}{A_E} = \left[\left(\frac{e_R}{e_E}\right)\left[\frac{(m_2/P_2) + e_c(4 - 1/P_2)}{e_R + e_c(4 - 1/e_R^3)}\right]\right]^{1/2}. \tag{10}$$

An inverse relation results when R_R is negative and R_E is positive. Once the thermal parameters of the absorber and the reference samples are known, the above equations can be used to determine the thermal effusivity and related parameters of the experimental sample. The values of φ_E and φ_R in (7) cannot be separated and treated independently because one does not know the absolute phase in the experiment.

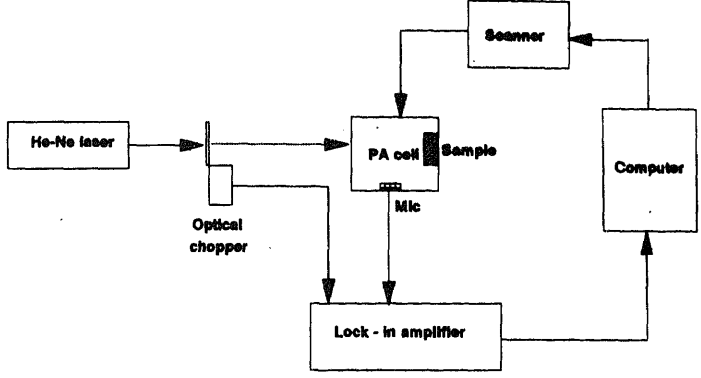

Figure 3. Block diagram of the experimental set up.

4. Experimental method

A photoacoustic spectrometer has been set up around a small volume PA cell in which the light beam can scan the surface of the absorber sample. Scanning is done under computer control in a step by step fashion so that photoacoustic amplitude and phase can be measured at different points on the absorber surface as the backing is changed. The scanner is designed in such a way that one step corresponds to a distance of 0.25 mm. A block diagram of the experimental set up is shown in figure 3. A 10 mW He–Ne ($\lambda = 632.8$ nm) laser is used as the radiation source and a chopping frequency of 40 Hz has been chosen to correspond to the best performance of the PA cell. An electret microphone (Knowles model BT 1759) has been used to detect the PA signal and the PA amplitude and phase, as usual, are measured with a lock-in amplifier.

The PA cell is mounted over a movable platform which moves step by step in one dimension. Range of movement, interval between steps etc. are software controlled. During measurements, the experimental parameters such as chopping frequency as well as the PA cell parameters remain unaltered as the light beam scans the absorber surface changing the backing from one to the other. PA signal amplitude and phase from each point are recorded after ensuring that the readings are stabilized. The changes in PA amplitude or phase due to change in distance between the acoustic source point and the detector as a consequence of PA cell movement are negligibly small as this distance is extremely small compared to the wavelength of the acoustic wave with frequency 40 Hz.

The sample configuration shown in figure 1 is so designed that it is circular with a reference sample diameter of 12 mm and experimental sample diameter of 4 mm. So we can go from backing boundary to the other in 16 steps. Obviously, it is ensured that the thickness of the backing sample is more than the thermal diffusion length at the chopping frequency used. Moreover, the thickness of the absorber layer is very small, of the order of a few microns, so that it is much smaller than its thermal thickness. The absorber layer used in our experiment is carbon black with thickness of a few tens of microns which is applied by keeping the backing samples in a benzene flame. The set up has been tested several times by having the reference and experimental samples the same, in which case the system just senses the boundaries without causing any change in PA phase or amplitude as the backing is changed.

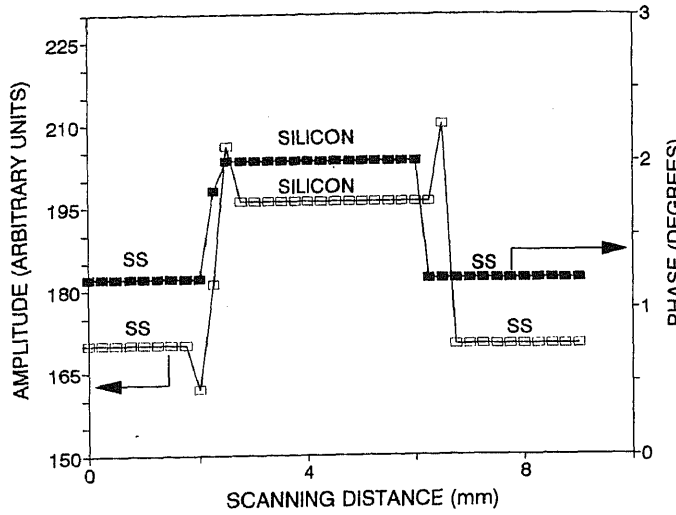

Figure 4. Variation of PA amplitude and phase with distance for a sample configuration with stainless steel (SS) as reference sample and silicon as experimental sample.

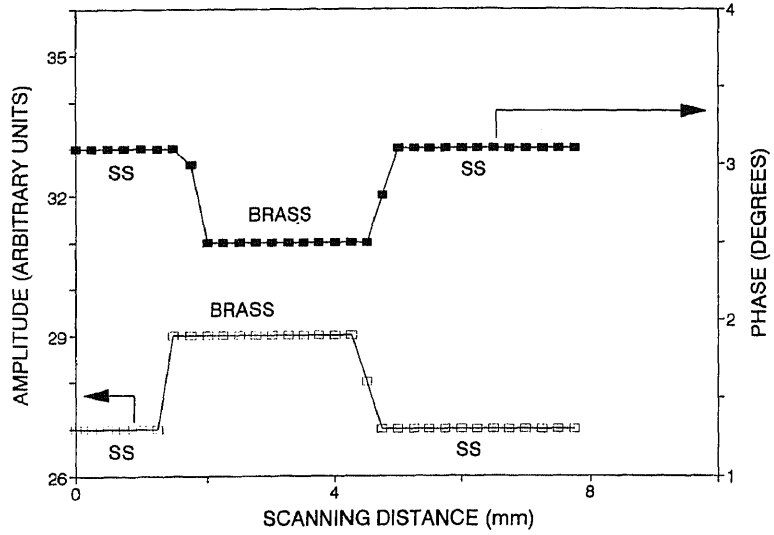

Figure 5. Variation of PA amplitude and phase with distance for a sample configuration with stainless steel (SS) as reference sample and brass as experimental sample.

5. Results

The PA amplitude ratio and phase difference have been recorded for a series of sample combinations with varying thermal parameters. They include copper, brass, stainless

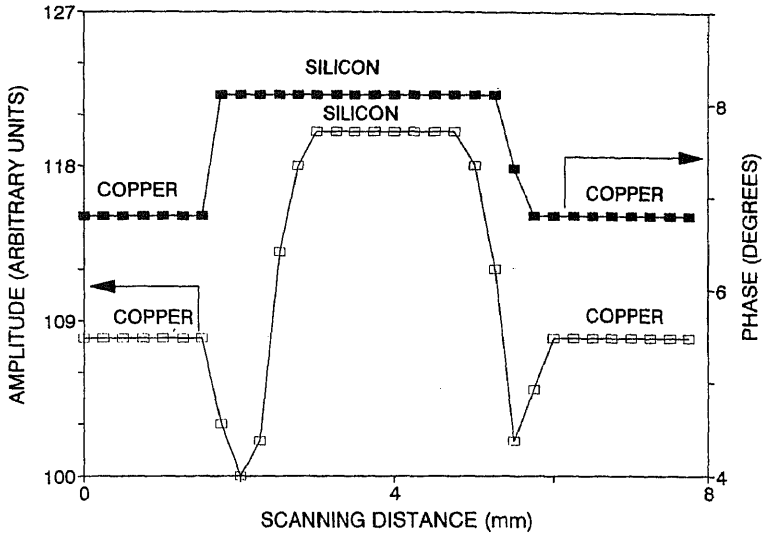

Figure 6. Variation of PA amplitude and phase with distance for a sample configuration with copper as reference sample and silicon as experimental sample.

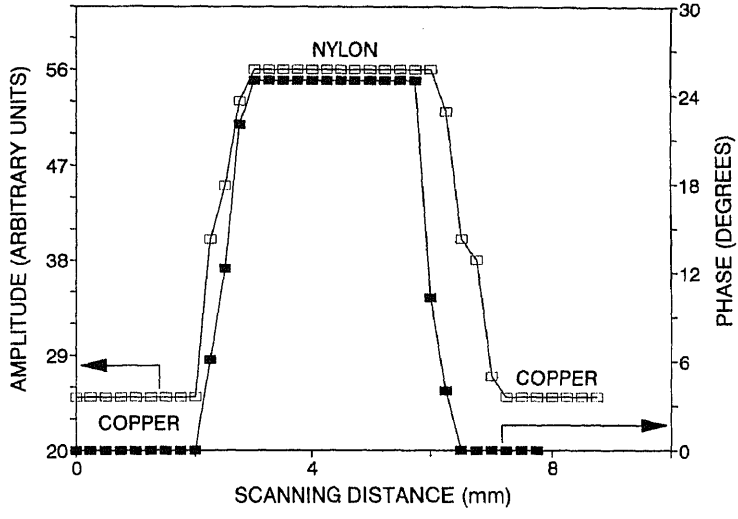

Figure 7. Variation of PA amplitude and phase with distance for a sample configuration with copper as reference sample and nylon as experimental sample. This is a case where the R values have opposite signs. Consequently there is large difference between measured and calculated amplitude ratio values.

steel, silicon, nylon, and teflon. A few plots are shown in figures 4–7. The sharp changes in amplitude and phase as a function of distance correspond to the boundaries. The direction in which the PA amplitude or phase vary in the experimental sample relative to the reference sample clearly indicates whether the experimental sample has a higher or lower thermal effusivity compared to the reference sample. Obviously, there is no

Table 1. Measured and calculated values of phase difference and amplitude ratios for different sample configurations.

Sample configuration E-experiment sample R-reference sample	Thermal wave reflection coefficients	Phase difference (degrees)		Amplitude ratio	
		Measured	Calculated	Measured	Calculated
E-Brass R-Copper	$R_E = -0.91$ $R_R = -0.96$	1·2 ±0·05	1·2	0·87 ±0·04	0·93
E-Stainless steel R-Copper	$R_E = -0.93$ $R_R = -0.96$	0·6 ±0·04	0·62	0·97 ±0·05	0·98
E-Silicon R-Copper	$R_E = -0.91$ $R_R = -0.96$	1·3 ±0·05	1·4	0·9 ±0·05	0·92
E-Nylon R-Copper	$R_E = +0.08$ $R_R = -0.96$	26 ±1·2	27·5	large difference as R_E is +ve and R_R is −ve	
E-Brass R-Stainless steel	$R_E = -0.91$ $R_R = -0.93$	0·7 ±0·04	0·62	0·93 ±0·05	0·95
E-Copper R-Nylon	$R_E = -0.96$ $R_R = +0.08$	26 ±1·3	27·5	large difference as R_E is −ve and R_R is +ve	
E-Nylon R-Stainless steel	$R_E = +0.08$ $R_R = -0.93$	24·5 ±1·2	26·9	large difference as R_E is +ve and R_R is −ve	
E-Silicon R-Stainless steel	$R_E = -0.91$ $R_R = -0.93$	0·75 ±0·04	0·77	0·9 ±0·04	0·93
E-Teflon R-Nylon	$R_E = +0.05$ $R_R = +0.08$	0·6 ±0·03	0·64	0·96 ±0·06	0·95
E-Brass R-Nylon	$R_E = -0.91$ $R_R = +0.08$	24 ±1·2	26·3	large difference as R_E is −ve and R_R is +ve	
E-Teflon R-Copper	$R_E = +0.05$ $R_R = -0.96$	23·6 ±1·2	26·5	large difference as R_E is +ve and R_E is −ve	

An estimated value of $e_c = 0.02\,\text{cal}\,\text{cm}^{-2}\,\text{K}^{-1}\,\text{s}^{-1/2}$ has been used in these calculations.

variation in amplitude or phase, except for variations at the boundaries, when the same material is used in places of the reference and experimental samples leading to a value zero for the phase difference in equation (7) and unity for the amplitude ratio in equations (8), (9) or (10). For a sample in two different experiments the measured PA phases need not be the same as the initial phases in the two situations could very well be different. This is why the phases for the same sample in different figures show difference in values.

In table 1 we tabulate the results obtained from a series of sample combinations with different thermal effusivity values. The measured phase difference and amplitude ratio values along with the corresponding values calculated using (7) and (8), (9) or (10) using data taken from handbooks are tabulated in this table for comparison. The thermal effusivity of carbon black layer used as absorber is estimated by measuring the amplitude ratio and phase difference in one experiment in which both backings used have known thermal properties. It can be noted from the table that the agreement between calculated and experimental phase difference values is good irrespective of the thermal effusivity values of the backings. Again, the agreement between calculated and experimental ratios is very good when both the backings have higher or lower thermal effusivities compared

Table 2. Values of thermal effusivity determined for a few selected samples.

ıental	Reference sample used	Effusivity values determined experimentally cal cm^{-2} K^{-1} s$^{-1/2}$ Phase difference method	Amplitude ratio method	Calculated effusivity of the experimental sample available data cal cm^{-2} K^{-1} s$^{-1/2}$
	Stainless steel	0·42 ± 0·01	0·41 ± 0·01	0·44
	Copper	0·4 ± 0·01	0·38 ± 0·01	0·37
s steel	Copper	0·59 ± 0·02	0·54 ± 0·02	0·585
	Nylon	0·018 ± 0·001	0·018 ± 0·001	0·018

of the absorber layer. Large differences between experimental and calculated in amplitude ratio values is found when the thermal effusivity values of the two es are widely different leading to a difference is sign for R_E and R_R, as in copper–combination tabulated in table 1. This point is discussed in greater detail in the next ı. The thermal effusivity values of a few samples determined from PA amplitude ınd phase difference measurements are tabulated in table 2. The corresponding calculated from available data are also tabulated for comparison.

cussion and conclusion

work we have demonstrated a rather simple and direct method for determining the ıl effusivity by a photoacoustic scanning technique. Since measurements are made e to a reference sample, the technique is free of PA cell calibration and other mental conditions. The only requirement is that the thermal parameters of the ıce sample should be known accurately. Experimentally it is found that providing a m coating over the surfaces of the two samples is not difficult. Of course, one must that the samples have flat top surfaces and must be in the same level. But in a e experiment, one can have a standard reference sample and the experimental e can be inserted into an appropriate cavity made in the reference sample.

is evident in some of the plots shown in figures, the boundary between the two es gives rise to abrupt increase or decrease in amplitude and phase. But the regions ponding to reference and experimental samples are quite clear and explicit.

lysis of the results presented in table 1 shows that we have a good agreement en measured and calculated values of amplitude ratios when the thermal wave ion coefficient R at the absorber-backing sample boundaries are both positive or ve. Negative value for R corresponds to the situation when the thermal effusivity of cking is more than that of the absorber layer. In this situation, more of the thermal generated in the absorber sample by photothermal conversion which propagate and the boundary, are transmitted into the backing medium. The extent to which these

the thermal effusivity of the backing is smaller than that of the absorber layer, more of thermal waves get reflected back into the absorber layer reducing the PA amplitu When R_R and R_E are both positive the reflected thermal waves from the two backings in phase and in this case equation (9) holds good and we have good agreement betw calculated and experimental values. When R_R is positive and R_E is negative or vice ve an extra phase factor between the transmitted and reflected thermal waves at the boundaries will appear which is not accounted for in (10). So there is large differe between calculated and experimental amplitude ratio values in this case. This aspec under further investigation. However, with a suitable choice of the reference sample limitation can easily be got over.

In any case, phase difference measurement do not suffer from any such limitati Taking into account the approximations used to get equation (7), it must be said that agreement is very good irrespective of the sign of R_E or R_R. In this regard, one must take into account the errors in the values used to calculate the numbers quoted in tabl and experimental uncertainties. Since phase difference measurement is enough determine the effusivity of any sample, the method works for all samples irrespective thier effusivity values.

Since these measurements do not involve any variations in frequency, sample thickn or backing material as in other experiments, the technique is quite straightforward fast. This method could be developed into a standard experiment set up with wh thermal analysis of unknown samples can be done in a routine way.

Acknowledgements

This work was supported by the Department of Science and Technology.

References

[1] A Rosencwaig, *Photoacoustics and photoacoustic spectroscopy* (Wiley, New York, 1980
[2] C K N Patel and A C Tam, *Rev. Mod. Phys.* **53**, 517 (1981)
[3] A C Tam, *Rev. Mod. Phys.* **58**, 381 (1986)
[4] P Korpiun and R Tilgner, *J. Appl. Phys.* **51**, 6115 (1980)
[5] J Ospal and A Rosencwaig, *J. Appl. Phys.* **53**, 4240 (1982)
[6] J Baumann and R Tilgner, *J. Appl. Phys.* **58**, 1982 (1985)
[7] U Seidel, K Haupt, H G Walther, J Burt and B K Bein, *J. Appl. Phys* **75**, 4396 (1994)
[8] P Charpentier, F Lepoutre and L Bertrand, *J. Appl. Phys.* **53**, 608 (1982)
[9] A Lachaine and P Poulet, *Appl. Phys. Lett.* **45**, 953 (1984)
[10] K N Madhusoodanan, M R Thomas and J Philip, *J. Appl. Phys.* **62**, 1162 (1987)
[11] M J Adams and G F Kirkbright, *Analyst* **102**, 281 (1977)
[12] A Rosencwaig and A Gersho, *J. Appl. Phys.* **47**, 64 (1976)
[13] C L Cesar, H Vargas, J Mendes Filho and L C M Miranda, *Appl. Phys. Lett.* **43**, 555 (19
[14] A Lachaine, *J. Appl. Phys.* **57**, 5075 (1985)
[15] B Bonne, J L Laporte and Y Rousset, *J. Appl. Phys.* **67**, 2253 (1990)
[16] U Zammit, M Marinelli, R Pizzo Ferrato, F Scudieri and S Martellucci, *J. Phys.* **E21**, (1988)
[17] Z Yasa and N Amer, in *Topical meeting on acoustic spectroscopy* (Ames, Iowa, 1979) WA
[18] O Pessoa Jr, C L Cesar, N A Patel, H Vargas, C C Ghizoni and L C M Miranda, *J. Appl. P* **59**, 1316 (1986)
[19] S Thomas, J Isaac and J Philip, *Rev. Sci. Instrum.* **66**, 3907 (1995)

SUBJECT INDEX

General and Mathematical Physics

Quantum theory of continuous measurements and its applications in quantum optics — *M D Srinivas* — 1–24

The Painlevé property, integrability and chaotic behaviour of a two-coupled Duffing oscillators — *S Rajasekar and S Paul Raj* — 183–198

Stochastic motion of a charged particle in a magnetic field: I Classical treatment — *Jagmeet Singh and Sushanta Dattagupta* — 199–210

Stochastic motion of a charged particle in a magnetic field: II Quantum Brownian treatment — *Sushanta Dattagupta and Jagmeet Singh* — 211–224

Dynamics of the logistic map under discrete parametric perturbation — *P P Saratchandran, V M Nandakumaran and G Ambika* — 339–346

Relativistic operator description of photon polarization — *Arvind and N Mukunda* — 347–360

Poincaré sphere representation for three state systems — *Joseph Samuel* — 361–370

Quantum motion over a finite one-dimensional domain: With and without dissipation — *Ashok Pimpale* — 371–378

Relativity and Gravitation

Magnetized cylindrically symmetric universe in general relativity — *Raj Bali and Mahbub Ali* — 25–32

Stationary rotating string world models with a magnetic field — *L K Patel and S D Maharaj* — 33–40

A model of the universe with decaying vacuum energy — *Abdussattar and R G Vishwakarma* — 41–56

Nonadiabatic gravitational collapse in multidimensional spacetime — *B Bhui* — 379–386

A class of stationary rotating string cosmological models — *L K Patel and Naresh Dadhich* — 387–392

Particle Physics

Radiative decays of heavy mesons with heavy quark symmetry
A K Giri, L Maharana and R Mohanta 225–232

Electromagnetic form factors of nucleons in a relativistic square-root potential model of independent quarks *S N Jena and M R Behera* 233–248

Approximate analytical lower bounds on 'double asymptotic scaling' variables and physics at HERA *A Saikia* 393–400

Nuclear Physics

Measurement and analysis of excitation functions for alpha induced reactions on iodine and cesium
N P M Sathik, M Afzal Ansari, B P Singh and R Prasad 401–410

Atomic and Molecular Physics

Cross sections and other parameters of e^--H_2O scattering ($E_1 \geqslant 50$ eV)
K N Joshipura and Minaxi Vinodkumar 57–64

New method for the evaluation of the RKR potential-integrals for diatomic molecules *Suresh Chandra, A K Sharma and Z H Khan* 65–78

$(e, 2e)$ triple differential cross section for ionization-excitation of helium
Seema Gupta and M K Srivastava 79–86

Positron scattering from alkaline-earth elements
Ritu Raizada and K L Baluja 87–98

Weak correlation theory of electron hydrogen atom ionization collisions
J N Das and K Chakrabarti 249–254

Symmetric scattering in electron and positron impact ionization of metastable 2*s*-state hydrogen atoms *J N Das and S Dhar* 263–270

Lasers, Optics and Spectroscopy

Enhanced third harmonic generation in periodic structures
V Mahalakshmi, Jolly Jose and S Dutta Gupta 317–324

Impurity mediated mechanism of photorefractive effect in $BaTiO_3$: A combination of Sangster and piezoelectric effects
M D Sastry, M Moghbel and Putcha Venkateswarlu 331–337

The origins of phase stability in ordered and disordered Ni–Pt alloys
Prabhakar P Singh 99–108

Analytic solution of the BCS gap equation in D dimensions ($D = 1, 2, 3$), at finite temperatures *Arun Bhardwaj and Satish K Muthu* 109–124

Internal irradiation effects in ^{239}Pu doped $K_2Ca_2(SO_4)_3$: EPR, TSL and PAS investigations
T K Seshagiri, V Natarajan, A R Dhobale and M D Sastry 125–132

Temperature dependent photoluminescence studies of ZnSe: I single crystals grown by chemical vapor transport
Suruchi Anand, Prabhat Verma, S C Abbi, K P Jain, M J Tafreshi, K Balakrishnan and R Dhansekaran 133–144

Raman study of phase transition in ferroelectric $Ba_{0.95}Ca_{0.05}TiO_3$
Rekha Rao, A P Roy, B A Dasannacharya, S Balakumar, R Ilangovan and P Ramasamy 145–150

Pressure-induced structural and electronic transition in $KTb(MoO_4)_2$ through Raman and optical studies
A Jayaraman, S K Sharma, S Y Wang, S R Shieh, L C Ming and S-W Cheong 151–162

Surface enhanced Raman scattering studies of acetophenone on colloidal silver particles
S Edwin Jayaraj, V Ramakrishnan, S Perumal and M Gurunathan 255–260

Structure of some liquid transition metals using integral equation theory
O Akinlade, A M Umar and L A Hussain 271–282

Nonlinear travelling waves in ϕ^6 polarizable model
Nabonita D Chowdhury and Sankar P Sanyal 283–308

A model of knock-out of oxygen by charged particle irradiation of Bi-2212
S K Bandyopadhyay, Pintu Sen, P Barat, P Mukherjee, S K Das and B Ghosh 309–316

Radiation stabilization of U^{5+} in CaO matrix and its thermal stability: Electron paramagnetic resonance and thermally stimulated luminescence studies *V Natarajan, T K Seshagiri and M D Sastry* 325–330

The partial distribution functions and effective pair potentials of some H-bonded liquids from diffraction data *S Sarkar and R N Joarder* 419

Higher order elastic constants and generalized Gruneisen parameters of elastic waves and low temperature thermal expansion of gadolinium
S Sindhu and C S Menon 435

A stochastic model for solidification I. The basic equations, their analysis and solutions *Shobha Dass, Gautam Johri and Lakshman Pandey* 447

Energy transfer in $CaSiO_3$ phosphors doped with Ce^{3+} and Tb^{3+}
R V Subrahmanyam, Shishir Jain, Ashish Verma and S Sivaraman 471

Electron paramagnetic resonance studies in photorefractive crystals I: Hyperfine interaction and photoinduced charge transfer in $^{233}U^{5+}$ and $^{238}U^{5+}$ doped $LiNbO_3$ *N K Porwal, Mithlesh Kumar and M D Sastry* 481

Techniques and Instrumentation

Measurement of optical constants of thin polymer films using spectrally resolved white light interferometry
Nirmal Kumar, Y Chandrasekhar and D Narayan Rao 163–170

Magnetic studies in mesoscopic length sclae using polarized neutron spectrometer at Dhruva reactor, Trombay
Sk Mohammad Yusuf and L Madhav Rao 171–182

Determination of thermal effusivity of solids by a photo-acoustic scanning technique *J Philip and A A Sudhakaran* 493

Brief Report

Radiative decays of heavy baryons with heavy quark symmetry
A K Giri, L Maharana and R Mohanta 411–417

AUTHOR INDEX

Abbi S C
see Anand Suruchi 133
Abdussattar
A model of the universe with decaying vacuum energy 41
Akinlade O
Structure of some liquid transition metals using integral equations theory 271
Ali Mahbub
see Bali Raj 25
Ambika G
see Saratchandran P P 339
Anand Suruchi
Temperature dependent photoluminescence studies of ZnSe: I single crystals grown by chemical vapor transport 133
Ansari M Afzal
see Sathik N P M 401
Arvind
Relativistic operator description of photon polarization 347

Balakrishnan K
see Anand Suruchi 133
Balakumar S
see Rao Rekha 145
Bali Raj
Magnetized cylindrically symmetric universe in general relativity 25
Baluja K L
see Raizada Ritu 87
Bandyopadhyay S K
A model of knock-out of oxygen by charged particle irradiation of Bi-2212 309
Barat P
see Bandyopadhyay S K 309
Behera M R
see Jena S N 233
Bhardwaj Arun
Analytic solution of the BCS gap equation in D dimensions ($D = 1, 2, 3$), at finite temperatures 109
Bhui B
Nonadiabatic gravitational collapse in multidimensional spacetime 379
Chakrabarti K
see Das J N 249
Chandra Suresh
New method for the evaluation of the RKR potential-integrals for diatomic molecules 65
Chandrasekhar Y
see Nirmal Kumar V 163
Cheong S-W
see Jayaraman A 151
Chowdhury Nabonita D
Nonlinear travelling waves in ϕ^6 polarizable model 283
Dadhich Naresh
see Patel L K 387

Das J N
Weak correlation theory of electron hydrogen atom ionization collisions 249
Symmetric scattering in electron and positron impact ionization of metastable 2*s*-state hydrogen atoms 263
Das S K
see Bandyopadhyay S K 309
Dasannacharya B A
see Rao Rekha 145
Dass Shobha
A stochastic model for solidification I. The basic equations, their analysis and solution 447
Dattagupta Sushanta
see Singh Jagmeet 199
Stochastic motion of a charged particle in a magnetic field: II Quantum Brownian treatment 211
Dhansekaran R
see Anand Suruchi 133
Dhar S
see Das J N 263
Dhobale A R
see Seshagiri T K 125
Dutta Gupta S
see Mahalakshmi V 317

Edwin Jayaraj S
Surface enhanced Raman scattering studies of acetophenone on colloidal silver particles 255

Ghosh B
see Bandyopadhyay S K 309
Giri A K
Radiative decays of heavy mesons with heavy quark symmetry 225
Radiative decays of heavy baryons with heavy quark symmetry 411

Gupta Seema
(e, 2e) triple differential cross section for ionization-excitation of helium 79
Gurunathan M
see Edwin Jayaraj S 255

Hussain L A
see Akinlade O 271

Ilangovan R
see Rao Rekha 145

Jain K P
see Anand Suruchi 133
Jain Shishir
see Subrahmanyam R V 471
Jayaraman A
Pressure-induced structural and electronic transition in KTb $(MoO_4)_2$ through Raman and optical studies 151
Jena S N
Electromagnetic form factors of nucleons in a relativistic square-root potential model of independent quarks 233
Joarder R N
see Sarkar S 419
Johri Gautam
see Dass Shobha 447
Jose Jolly
see Mahalakshmi V 317
Joshipura K N
Cross sections and other parameters of $e^- - H_2O$ scattering ($E_i \geq 50$ eV) 57

Khan Z H
see Chandra Suresh 65
Kumar Mithlesh
see Porwal N K 481

Madhav Rao L
see Yusuf Sk Mohammad 171
Mahalakshmi V
Enhanced third harmonic generation in periodic structures 317
Maharana L
see Giri A K 225, 411
Menon C S
see Sindhu S 435
Ming L C
see Jayaraman A 151
Moghbel M
see Sastry M D 331
Mohanta R
see Giri A K 225, 411
Mukherjee P
see Bandyopadhyay S K 309
Mukunda N
see Arvind 347
Muthu Satish K
see Bhardwaj Arun 109

Nandakumaran V M
see Saratchandran P P 339
Narayana Rao D
see Nirmal Kumar V 163
Natarajan V
see Seshagiri T K 125
Radiation stabilization of U^{5+} in CaO matrix and its thermal stability: Electron paramagnetic resonance and thermally stimulated luminescence studies 325
Nirmal Kumar V
Measurement of optical constants of thin polymer films using spectrally resolved white light interferometry 163

Pandey Lakshman
see Dass Shobha 447
Patel L K
Stationary rotating string world models with a magnetic field 33
A class of stationary rotating string cosmological models 387
Perumal S
see Edwin Jayaraj S 255
Philip J
Determination of thermal effusivity of solids by a photoacoustic scanning technique 493
Pimpale Ashok
Quantum motion over a finite one-dimensional domain: With and without disipation 371
Porwal N K
Electron paramagnetic resonance studies in photorefractive crystals I: Hyperfine interaction and photoinduced charge transfer in $^{233}U^{5+}$ and $^{238}U^{5+}$ doped $LiNbO_3$ 481
Prasad R
see Sathik N P M 401

Raizada Ritu
Positron scattering from alkaline-earth elements 87
Raj S Paul
see Rajasekar S 183
Rajasekar S
The Painlevé property, integrability and chaotic behaviour of a two-coupled Duffing oscillators 183
Ramakrishnan V
see Edwin Jayaraj S 255
Ramasamy P
see Rao Rekha 145

Rao Rekha
Raman study of phase transition in ferroelectric $Ba_{0.95}$ $Ca_{0.05}$ TiO_3 145
Roy A P
see Rao Rekha 145

Saikia A
Approximate analytical lower bounds on 'double asymptotic scalling' variables and physics at HERA 393
Samuel Joseph
Poincaré sphere representation for three state systems 361
Sanyal Sankar P
see Chowdhury Nabonita D 283
Saratchandran P P
Dynamics of the logistic map under discrete parametric perturbation 339
Sarkar S
The partial distribution functions and effective pair potentials of some H-bonded liquids from diffraction data 419
Sastry M D
see Seshagiri T K 125
see Natarajan V 325
Impurity mediated mechanism of photorefractive effect in $BaTiO_3$: A combination of Sangster and piezoelectric effects 331
see Porwal N K 481
Sathik N P M
Measurement and analysis of excitation functions for alpha induced reactions on iodine and cesium 401
Sen Pintu
see Bandyopadhyay S K 309
Seshagiri T K
Internal irradiation effects in ^{239}Pu doped $K_2Ca_2(SO_4)_3$: EPR, TSL and PAS investigations 125
see Natarajan V 325
Sharma A K
see Chandra Suresh 65
Sharma S K
see Jayaraman A 151
Shieh S R
see Jayaraman A 151
Sindhu S
Higher order elastic constants and generalized Gruneisen parameters of elastic waves and low temperature thermal expansion of gadolinium 435
Singh B P
see Sathik N P M 401
Singh Jagmeet
Stochastic motion of charged particle in a magnetic field: I Classical treatment 199
see Dattagupta Sushanta 211
Singh Prabhakar P
The origins f phase stability in ordered and disordered Ni–Pt alloys 99
Sivaraman S
see Subrahmanyam R V 471
Srinivas M D
Quantum theory of continuous measurements and its applications in quantum optics 1
Srivastava M K
see Gupta Seema 79
Subrahmanyam R V
Energy transfer in $CaSiO_3$ phosphors doped with Ce^{3+} and Tb^{3+} 471
Sudhakaran A A
see Philip J 493

Tafreshi M J
see Anand Suruchi 133

Umar A M
see Akinlade O 271

Venkateswarlu Putcha
see Sastry M D 331
Verma Ashish
see Subrahmanyam R V 471
Verma Prabhat
see Anand Suruchi 133
Vinodkumar Minaxi
see Joshipura K N 57
Vishwakarma R G
see Abdussattar 41

Wang S Y
see Jayaraman A 151

Yusuf Sk Mohammad
Magnetic studies in mesoscopic length scale using polarized neutron spectrometer at Dhruva reactor, Trombay 171

End of the forty seventh volume